

Shielding Aspects of Accelerators, Targets and Irradiation Facilities - SATIF 6

Workshop Proceedings
Stanford, CA, USA
10-12 April 2002



Nuclear Science

Proceedings of the Sixth Meeting of the Task Force on
**Shielding Aspects of Accelerators,
Targets and Irradiation Facilities**

**Stanford Linear Accelerator Center (SLAC)
Menlo Park, CA, USA
10-12 April 2002**

Jointly organised by

Organisation of Economic Co-operation and Development
Stanford Linear Accelerator Center (SLAC)
Radiation Safety Information Computational Center (RSICC)
Shielding Working Group of the Reactor Physics Committee of Japan

© OECD 2004
NEA No. 3828

NUCLEAR ENERGY AGENCY
ORGANISATION FOR ECONOMIC CO-OPERATION AND DEVELOPMENT

ORGANISATION FOR ECONOMIC CO-OPERATION AND DEVELOPMENT

Pursuant to Article 1 of the Convention signed in Paris on 14th December 1960, and which came into force on 30th September 1961, the Organisation for Economic Co-operation and Development (OECD) shall promote policies designed:

- to achieve the highest sustainable economic growth and employment and a rising standard of living in member countries, while maintaining financial stability, and thus to contribute to the development of the world economy;
- to contribute to sound economic expansion in member as well as non-member countries in the process of economic development; and
- to contribute to the expansion of world trade on a multilateral, non-discriminatory basis in accordance with international obligations.

The original member countries of the OECD are Austria, Belgium, Canada, Denmark, France, Germany, Greece, Iceland, Ireland, Italy, Luxembourg, the Netherlands, Norway, Portugal, Spain, Sweden, Switzerland, Turkey, the United Kingdom and the United States. The following countries became members subsequently through accession at the dates indicated hereafter: Japan (28th April 1964), Finland (28th January 1969), Australia (7th June 1971), New Zealand (29th May 1973), Mexico (18th May 1994), the Czech Republic (21st December 1995), Hungary (7th May 1996), Poland (22nd November 1996), Korea (12th December 1996) and the Slovak Republic (14th December 2000). The Commission of the European Communities takes part in the work of the OECD (Article 13 of the OECD Convention).

NUCLEAR ENERGY AGENCY

The OECD Nuclear Energy Agency (NEA) was established on 1st February 1958 under the name of the OEEC European Nuclear Energy Agency. It received its present designation on 20th April 1972, when Japan became its first non-European full member. NEA membership today consists of 28 OECD member countries: Australia, Austria, Belgium, Canada, the Czech Republic, Denmark, Finland, France, Germany, Greece, Hungary, Iceland, Ireland, Italy, Japan, Luxembourg, Mexico, the Netherlands, Norway, Portugal, Republic of Korea, the Slovak Republic, Spain, Sweden, Switzerland, Turkey, the United Kingdom and the United States. The Commission of the European Communities also takes part in the work of the Agency.

The mission of the NEA is:

- to assist its member countries in maintaining and further developing, through international co-operation, the scientific, technological and legal bases required for a safe, environmentally friendly and economical use of nuclear energy for peaceful purposes, as well as
- to provide authoritative assessments and to forge common understandings on key issues, as input to government decisions on nuclear energy policy and to broader OECD policy analyses in areas such as energy and sustainable development.

Specific areas of competence of the NEA include safety and regulation of nuclear activities, radioactive waste management, radiological protection, nuclear science, economic and technical analyses of the nuclear fuel cycle, nuclear law and liability, and public information. The NEA Data Bank provides nuclear data and computer program services for participating countries.

In these and related tasks, the NEA works in close collaboration with the International Atomic Energy Agency in Vienna, with which it has a Co-operation Agreement, as well as with other international organisations in the nuclear field.

© OECD 2004

Permission to reproduce a portion of this work for non-commercial purposes or classroom use should be obtained through the Centre français d'exploitation du droit de copie (CCF), 20, rue des Grands-Augustins, 75006 Paris, France, Tel. (33-1) 44 07 47 70, Fax (33-1) 46 34 67 19, for every country except the United States. In the United States permission should be obtained through the Copyright Clearance Center, Customer Service, (508)750-8400, 222 Rosewood Drive, Danvers, MA 01923, USA, or CCC Online: <http://www.copyright.com/>. All other applications for permission to reproduce or translate all or part of this book should be made to OECD Publications, 2, rue André-Pascal, 75775 Paris Cedex 16, France.

FOREWORD

Nuclear energy covers a field much wider than that of nuclear power. In fact, atomic and nuclear energy applications involve a large range of scientific and technological activities using a variety of machines and analysis techniques. Activities in this area have increased over the years and consequently the OECD/NEA Nuclear Science Committee sponsors an increasing amount of work in this domain.

One of these activities concerns “Shielding Aspects of Accelerators, Targets and Irradiation Facilities” (SATIF). A series of workshops has been held over the last decade: SATIF-1 was held on 28-29 April 1994 in Arlington, Texas; SATIF-2 on 12-13 October 1995 at CERN in Geneva, Switzerland; SATIF-3 on 12-13 May 1997 at Tohoku University in Sendai, Japan; SATIF-4 on 17-18 September 1998 in Knoxville, Tennessee; SATIF-5 on 17-21 July 2000 at the OECD in Paris, France; and SATIF-6 on 10-12 April 2002 at the Stanford Linear Accelerator Center (SLAC), Menlo Park, California. SATIF-7 is scheduled to take place on 17-18 May 2004 at the ITN, Sacavém, Portugal, and SATIF-8 is planned to be held in 2006 in Pohang, Republic of Korea.

Each workshop is hosted by organisations having accelerator facilities and experts, which enhances the interaction between local expertise and experts from the international community. SATIF-6 was held at the prestigious Stanford Linear Accelerator Center (SLAC) in California; the chairman of the workshop, Sayed H. Rokni, arranged visits to the different facilities. It was also an opportunity to become acquainted with the work being carried out on the Next Linear Collider (NLC). This powerful new instrument will provide a frontier facility for basic research on elementary particles. Stretching some 20 miles, it will smash electrons into their antimatter counterparts, creating exotic new particles from pure energy. Scientists expect research at this facility to answer fundamental questions about the behaviour of matter and the origins of the universe. It will involve the creativity of scientists and engineers from many nations in its design, construction and use.

SATIF-6 was jointly organised by:

- the OECD Nuclear Energy Agency;
- the Stanford Linear Accelerator Center (SLAC);
- the Radiation Safety Information Computational Center (RSICC);
- the Shielding Working Group of the Reactor Physics Committee of Japan.

These proceedings provide a summary of the discussions, decisions and conclusions, as well as the texts of the presentations made at the workshop.

The proceedings are published on the responsibility of the OECD Secretary-General. The views expressed are those of the authors and do not necessarily correspond to those of the national authorities concerned.

Professor Kazuo Shin
(1950-2001)

Associate Professor
Nuclear Engineering Department, Kyoto University, Japan



*These proceedings are dedicated to the memory of our colleague,
who made major contributions to the progress of SATIF.*



Acknowledgements

Acknowledgements are due to the members of the SATIF-6 Technical Programme Committee: S. Rokni (SLAC, Chairman), A. Fassò (CERN), H. Hirayama (KEK), B.L. Kirk (RSICC), N. Mokhov (FNAL), T. Nakamura (U. Tohoku, Vice-Chair), M. Silari (CERN), G. Stevenson, P. Vaz (ITN), L. Waters (LANL) and E. Sartori (OECD/NEA, Secretary) for their contribution in shaping the technical programme, and to all participants who contributed the valuable work and ideas described in these proceedings. Special thanks go to Amanda Costa for her dedication in preparing these proceedings for publication.



TABLE OF CONTENTS

Foreword		3
Executive Summary.....		9
Annex – SATIF-6 Programme.....		13
SESSION I	Source Term and Related Data – Proton and Ion Accelerators and Spallation Source.....	17
	<i>Chairs: T. Nakamura, A. Fassò</i>	
	<i>T. Nakamura, T. Kurosawa, T. Kato</i>	
	Double-differential Thick-target Neutron Yields Bombarded by High-energy Heavy Ions.....	19
	<i>H. Nakashima, H. Takada, Y. Kasugai, S. Meigo, F. Maekawa, T. Kai, C. Konno, Y. Ikeda, Y. Oyama, N. Watanabe, M. Arai, T. Ino, M. Kawai, M. Numajiri, S. Sato, K. Takahashi, Y. Kiyonagi, H. Conrad, D. Filges, R. Neef, H. Stechemesser, H. Spitzer, G.S. Bauer, E. Jerde, D. Glasgow, J. Haines, T. Gabriel, P. Montanez, A. Carroll, H. Ludewig, J. Hastings</i>	
	Current Status of the AGS Spallation Target Experiment.....	27
	<i>S. Teichmann, B. Amrein, J. Gerig, W. Hajdas, H. Temnitzner</i>	
	Dose Rate Measurements Behind Different Shielding for 250 MeV Protons on a Thick Copper Target.....	37
	<i>I. Koprivnikar, E. Schachinger</i>	
	The Biological Shield of a High-intensity Spallation Source: A Monte Carlo Design Study.....	47
	<i>S. Agosteo, T. Nakamura, M. Silari</i>	
	Attenuation Curves in Concrete of Neutrons from 100-400 MeV per Nucleon He, C and Ne Ions	65
	<i>M. Silari, H. Vincke</i>	
	The Effect of a Beam Loss at the PS/nTOF Interface of the CERN PS Complex.....	77
	<i>V. Vlachoudis, C. Borcea, S. Buono, P. Cennini, M. Dahlfors, A. Ferrari, Y. Kadi, A. Herrera-Martinez, V. Lacoste, E. Radermacher, C. Rubbia, L. Zanini, nTOF Collaboration</i>	
	Radioprotection and Shielding Aspects of the nTOF Spallation Source	87

	<i>L. Heilbronn, Y. Iwata, T. Murakami, H. Iwase, T. Nakamura, H. Sato, R. Ronningen</i>	
	Neutron Production Measurements Relevant to Shielding for Space-related Activities	99
	<i>M. Brugger, G.R. Stevenson</i>	
	Radiation Calculations for the NA60 Experiment	107
	<i>N. Pauwels, F. Clapier, J. Proust, M. Mirea</i>	
	Experimental and Calculated Neutron Production by Deuterons Impinging on Be, C and U Thick Targets (17, 20, 28, 80, 160 and 200 MeV)	121
SESSION II	Measurements and Calculations of Induced Radioactivity	129
	<i>Chair: M. Silari</i>	
	<i>S.H. Rokni, T. Gwise, J.C. Liu, A. Fassò, S. Roesler</i>	
	Induced Radioactivity of Materials by Stray Radiation Fields at an Electron Accelerator	131
	<i>H. Vincke, I. Brunner, M. Huhtinen</i>	
	Production of Radioactive Isotopes in Al, Fe and Cu Samples by Stray Radiation Fields at a Proton Accelerator	143
	<i>A. Puryear, J.C. Liu, S. Rokni</i>	
	FLUKA Calculations of Radionuclides, Star and Neutron Fluence in Soil Around High-energy Electron and Proton Linear Accelerators	153
	<i>H. Yashima, H. Sugita, T. Nakamura, Y. Uwamino, A. Fukumura</i>	
	Induced Radioactivities of Spallation Products by Various Projectile Ions	163
SESSION III	Benchmarking – Calculations and Results	171
	<i>Chairs: H. Hirayama, R. Prael</i>	
	<i>H. Hirayama, Attenuation Length Sub-working Group in Japan</i>	
	Intercomparison of Medium-energy Neutron Attenuation in Iron and Concrete (4)	173
	<i>D. Ridikas, P. Vertes</i>	
	Code and Data Benchmarking with the New IAEA Photonuclear Data Library	183
	<i>S.G. Mashnik, R.E. Prael, A.J. Sierk, K.K. Gudima, N.V. Mokhov</i>	
	Event Generator Benchmarking for Proton Radiography Applications	193
	<i>S. Roesler, J.C. Liu, S.H. Rokni</i>	
	Calculation of Neutron Time-of-flight and Energy Spectra Behind Thick Shielding of an Electron Accelerator and Comparison to Experimental Data	207

	<i>S. Taniguchi, M. Sasaki, T. Nunomiya, H. Iwase, S. Yonai, T. Nakamura, K. Kase, J.C. Liu, S.H. Rokni, S. Roesler</i>	
	Measurement of Neutron Energy Spectra Behind the Lateral Shield of a High-energy Electron Beam Dump	221
	<i>T. Nunomiya, H. Iwase, T. Nakamura, N. Nakao</i>	
	Deep-penetration Calculation with an 800 MeV Proton Beam Compared with the Shielding Experiment at ISIS	227
	<i>G. Maino, E. Menapace</i>	
	Nuclear Photoreactions in the Context of a Nuclear Data Review for Radiation Shielding in Advanced Technology Applications	235
SESSION IV	Dose and Related Issues	245
	<i>Chairs: M. Pelliccioni, A. Leuschner</i>	
	<i>M. Pelliccioni</i>	
	Conversion Coefficients: An Addition to Existing Data	247
	<i>V. Mares, H. Schraube</i>	
	The Effect of the Fluence-to-dose Conversion Coefficients Upon the Dose Estimation to Cosmic Radiation	257
	<i>A. Leuschner</i>	
	Feasibility Study on an Active Neutron Dosimeter Based on Carbon Activation for the Linear Collider TESLA	279
	<i>Y. Sakamoto, S. Tsuda, T. Sato, N. Yoshizawa, H. Hirayama</i>	
	Benchmark Calculations with Simple Phantom for Neutron Dosimetry (2)	287
	<i>P.K. Job, J. Alderman</i>	
	Radiation Levels Experienced by the Insertion Devices of the Third-generation Synchrotron Radiation Sources	299
SESSION V	Status of Computer Codes, Cross-sections and Shielding Data Libraries.....	305
	<i>Chairs: H. Hunter, N. Mokhov</i>	
	<i>H.T. Hunter, J.B. Mannes Schmidt, B.L. Kirk, M. Greene, E. Sartori, T. Suzuki, P. Vaz</i>	
	Progress Report on the Available Analytical Tools for Accelerator Shielding Analysis 2002	307
	<i>S.G. Mashnik, K.K. Gudima, A.J. Sierk</i>	
	Merging the CEM2k and LAQGSM Codes with GEM2 to Describe Fission and Light-fragment Production	337
	<i>N. Sobolevsky, I. Gudowska, P. Andreo, D. Belkic, A. Brahme</i>	
	Interaction of Ion Beams with Tissue-like Media: Simulations with the SHIELD-HIT Monte Carlo Transport Code	367

<i>K. Hayashi, R. Tayama, H. Handa, K. Shin, H. Hirayama, H. Nakano, F. Masukawa, H. Nakashima, N. Sasamoto</i> Analytical Method for Multi-scattered Neutrons in Cavity Used in the DUCT-III Code.....	377
<i>H. Iwase, K. Niita, T. Nakamura</i> Development of a General-purpose Heavy-ion Transport Code	389
<i>A. Fassò, A. Ferrari, P.R. Sala, G. Tsileidakis</i> Implementation of Xenon Capture Gammas in FLUKA for TRD Background Calculations.....	397
<i>N.V. Mokhov</i> Status of MARS Code	407
SESSION VI Shielding in Medical Accelerator Applications.....	417
<i>Chairs: J.C. Liu, P. Vaz</i>	
<i>B. Mukherjee</i> Principle of Radiological Shielding of Medical Cyclotrons.....	419
<i>W.D. Newhauser, U. Titt</i> An Overview of Shielding Considerations in Constructing a Proton-radiation Cancer-therapy Facility	431
List of Participants.....	439

EXECUTIVE SUMMARY

Scope

The Expert Group on Shielding of Accelerators, Targets and Irradiation Facilities (SATIF) deals with multiple aspects related to the modelling and design of accelerator shielding systems including electron accelerators, proton accelerators, ion accelerators, spallation sources and several different types of facilities, such as synchrotron radiation facilities, very-high-energy radiation facilities, accelerator production of tritium and free electron lasers.

Objectives

Objectives of the SATIF-6 meeting include:

- to promote the exchange of information among scientists in this particular field;
- to identify areas in which international co-operation could be fruitful;
- to carry on a programme of work in order to achieve progress in specific priority areas;

Deliverables

Deliverables emerging from this meeting include:

- assessment of needs in experimental data for the validation of models and codes;
- organisation of shielding experiments;
- collection and compilation of experimental data sets;
- assessment of models, computer codes, parametrisations and techniques available for accelerator shielding design purposes;
- validation of computer codes and models available to perform particle transport simulation;
- organisation of international benchmark and intercomparison exercises;
- organisation of workshops and co-organisation of conferences relevant in the area of its scope and computing radiation dosimetry (e.g. QUADOS);
- publication of workshop proceedings;
- editing of an “Accelerator Shielding Handbook”;
- maintenance of SATIF listserver and archive of technical discussion between members.

SATIF-6 workshop

Introduction

The sixth SATIF workshop was hosted by the Stanford Linear Accelerator Center (SLAC), Menlo Park, California, USA. The objectives were to present and assess achievements on agreed actions agreed upon at the previous meeting held in Paris in 2000, and to discuss and recommend actions where a strong need is identified for further work in theoretical model development, experimental work and benchmarking for model validation.

The workshop was opened and the participants welcomed by the General Chair Sayed Rokni (SLAC Radiation Physics Group). He also called to mind the passing away of Professor Kazuo Shin of Kyoto University. This is a great loss to the SATIF group; Professor Shin contributed much to the success of the SATIF activities. It was agreed that the proceedings of SATIF-6 would be dedicated to him. The Chair then noted that Professor Nakamura was accompanied by five of his students, and commented that this is an effective means of transmitting know-how to the younger generation.

Professor Paterson, Associated Director for the Technical Division of SLAC also welcomed the participants to SLAC. He presented a brief history of SLAC, including the construction, 40 years ago, of what was at the time the world's largest linear accelerator. He continued in this vein, mentioning the SPEAR rings, the PEP-I and PEP-II double rings, the linear collider SLC, the establishment of a BIO-X satellite for structural molecular biology and finally the work being carried out on the Next Linear Collider. He then emphasised the importance of international collaboration in this area and at SLAC in particular.

Enrico Sartori welcomed participants on behalf of the OECD/NEA and thanked SLAC for hosting this workshop.

The workshop was attended by about 50 participants from 10 different countries, representing 26 organisations. Thirty-three (33) presentations were made, organised into six topical sessions:

- source term and related data – proton and ion accelerators and spallation source;
- measurements and calculations of induced radioactivity;
- benchmarking – calculations and results;
- dose and related issues;
- status of computer codes, cross-sections and shielding data libraries;
- shielding in medical accelerator applications (special topic).

The workshop was concluded with sessions on follow-up of past SATIF agreements and actions, and discussion/summary and future actions.

Specific actions agreed upon are:

- Collection of the different data produced on dose conversion coefficients, store them in comparative tables and make them available internationally through the NEA Data Bank, along with the descriptions of codes and methods used. This should help to resolve the remaining discrepancies.

- All authors of the major computer codes for accelerator shielding problems should be invited to the next SATIF meeting to present the latest features of codes, to discuss further needed developments and share new physics models and developments.
- The know-how and experience gathered by the SATIF group over recent years should be synthesised into a handbook – “Accelerator Shielding Handbook” – for the benefit of an increasingly larger community of accelerator shielders. No current handbook exists on this subject and, a strong need for it being expressed, its production was agreed upon. The editors of the handbook were designated among those SATIF members having editing experience. This should be prepared over a period of two years and be available in draft form for the next SATIF workshop. The chapters will cover: physics basics for accelerator shielding, facilities and their shielding and dosimetry approaches, simple fast methods for estimating orders of magnitude, existing state-of-the-art transport codes (MC and deterministic), data for accelerator shielding and experimental benchmark data.
- Sharing of modules for translating geometries for different radiation transport codes. This will reduce efforts in benchmarking and ensure that input to codes is coherent among different users.
- At the special session on shielding in medical accelerator applications it was concluded that medical accelerator physicists greatly benefit from SATIF activities, and as some of the medical-accelerator-related activities are equally of interest to SATIF, it was recommended that benchmarks of common interest to the two communities be carried out, in particular benchmarking of simplified methods that are more widely used in the medical area; standardisation of mazes for developing analytical tools was recommended. A general need for increased intercommunication between these fields was identified.
- Much progress was achieved as concerns the intercomparison of medium-energy neutron attenuation in iron and concrete. However, participants should provide further results in order to resolve discrepancies found for iron and the study should be extended up to 100 GeV to enable improved formulation of attenuation length trends at high energies. Also, results of appropriate experiments need to be selected to benchmark and verify the calculations and models.
- Newly developed codes for hadron transport, transport in complex ducts and cascades of particles have been developed. These should be acquired by the code centres for sharing among the community of experts.
- Additional (γ,n) data for accelerator shielding applications need to be collected and made available. Neutron shields are becoming increasingly important for electron accelerators as they increase in energy and power.
- The group has expressed interest in contributing to the EU Quality Assurance for Numerical Dosimetry (QUADOS) initiative.

The mandate of this expert group has been extended until 2005. As this group meets only every two years, a period judged as required for a consistent progress to be reported, it will seek a further extension of the mandate during the 2005 NSC meeting. In view of the number of large accelerator facilities in planning and under construction within the OECD area, the need for extended and improved databases, methods and codes in accelerator and target shielding is growing. Over the years, the

radiation shielding community has benefited from the co-operation which takes place under the aegis of SATIF, and the group has established itself as the international forum for addressing priority issues in this area. SATIF will contribute shared research results to emerging priority areas.

The seventh NSC meeting on Shielding Aspects of Accelerators, Targets and Irradiation Facilities (SATIF-7) will be hosted by ITN, Portugal from 17-18 May 2004 in connection with the ICRS10 and RPS-2004 conferences. The group organising these series of meetings should prepare a new draft mandate proposal for discussion at the NSC bureau meeting and subsequent decision at the next NSC meeting in June 2003.

Sponsors

This event was jointly organised by the:

- OECD Nuclear Energy Agency;
- Stanford Linear Accelerator Center (SLAC);
- Radiation Safety Information Computational Center (RSICC);
- Shielding Working Group of the Reactor Physics Committee of Japan.

Scientific Committee

The members of the Scientific Committee of SATIF-6 were:

A. Fassò (CERN)	E. Sartori (OECD/NEA, Secretary)
H. Hirayama (KEK)	M. Silari (CERN)
B. Kirk (RSICC)	G. Stevenson (CERN)
N. Mokhov (FNAL)	P. Vaz (ITN)
T. Nakamura (U. Tohoku, Vice Chair)	L. Waters (LANL)
S. Rokni (SLAC, Chair)	

Executive Committee

The members of the Executive Committee, in charge of preparing the Technical Programme for SATIF-6 and submitting it to the Scientific Committee, were:

B. Kirk (RSICC)	E. Sartori (OECD/NEA, Secretary)
T. Nakamura (U. Tohoku, Vice Chair)	G. Stevenson (CERN)
S. Rokni (SLAC, Chair)	P. Vaz (ITN)

Annex
SATIF-6 PROGRAMME

10-12 April 2002
Stanford Linear Accelerator Center
2575 Sand Hill Road, Menlo Park, CA 94025

General Chair: Sayed Rokni • General Vice-chair: Takashi Nakamura

Wednesday, 10 April

Registration

Introductory and welcome remarks (*Rokni, Paterson, Sartori*)

Session I: Source Term and Related Data – Proton and Ion Accelerators and Spallation Source

Chairs: T. Nakamura, A. Fassò

T. Nakamura, T. Kurosawa, T. Kato

Double-differential Thick Target Neutron Yields by Heavy Ions

H. Nakashima and ASTE Collaboration Team

Current Status on AGS Spallation Target Experiment

S. Teichmann, B. Amrein, J. Gerig, W. Hajdas, H. Temnitzer

Dose Rate Measurements behind Different Shielding for 250 MeV Protons on a Thick Copper Target

I. Koprivnikar, E. Schachinger

The Biological Shield of a High-intensity Spallation Source: A Monte Carlo Design Study

S. Agosteo, T. Nakamura, M. Silari

Attenuation Curves in Concrete of Neutrons from 100-800 MeV per Nucleon He, C and Ne Ions

M. Silari and H. Vincke

The Effect of a Beam Loss at the PS/n_TOF Interface of the CERN PS Complex

C. Borcea, P. Cennini, A. Ferrari, Y. Kadi, V. Lacoste, E. Radermacher, C. Rubbia, V. Vlachoudis, L. Zanini

Radioprotection and Shielding Aspects of nTOF Spallation Source

*L. Heilbronn, H. Iwase, Y. Iwata, T. Nakamura, R. Ronningen, L. Townsend,
Y. Tozawa*
Neutron Production Measurements Relevant to Shielding for Space-related
Activities

M. Brugger, G.R. Stevenson
The Radiological Situation in the NA60 Experiment

Thursday, 11 April

Session II: Measurements and Calculations of Induced Radioactivity

Chair: M. Silari

S.H. Rokni, A. Fassò, T. Gwise, J.C. Liu, S. Roesler, R. Sit
Comparison of Calculations and Measurements of Induced Activity of Different
Materials at SLAC

H. Vincke, I. Brunner, M. Huhtinen
Production of Radioactive Isotopes in Al, Fe and Cu Samples by Stray Radiation
Fields at a Proton Accelerator

A. Puryear, J.C. Liu, S. Rokni
FLUKA Calculations of Radionuclides, Star and Neutron Fluence in Soil around
the High-energy Electron and Proton Linear Accelerators

H. Yashima, H. Sugita, T. Nakamura, Y. Uwamino, S. Ito, A. Fukumura
Induced Radioactivities of Spallation Products by Various Projectile Ions

Session III: Benchmarking Calculations and Results

Chairs: H. Hirayama, R.E. Prael

H. Hirayama
Intercomparison of the Medium-energy Neutron Attenuation in Iron and Concrete (4)

D. Ridikas and P. Vertes
Code and Data Benchmarking with the New IAEA Photonuclear Data Library

S.G. Mashnik, K.K. Gudima, N.V. Mokhov, R.E. Prael, A.J. Sierk
Benchmarking Codes for Proton Radiography Applications

S. Roesler, J.C. Liu, S.H. Rokni
Calculation of Neutron Time-of-flight and Energy Spectra behind Thick Shielding
of an Electron Accelerator and Comparison to Experimental Data

*S. Taniguchi, M. Sasaki, T. Nunomiya, H. Iwase, S. Yonai, T. Nakamura, S.H.
Rokni, J.C. Liu, S. Roesler, K. Kase*
Shielding Experiment of Neutrons through Concrete Outside the Beam Dump of
28.4 GeV Electron Linear Accelerator

N. Nakao, N.V.Mokhov, Y.Irie, K.Yamamoto, A.Drozhdin (Withdrawn)
Deep Penetration Calculation Along the Whole Ring Tunnel of JAERI-KEK
3 GeV Proton Synchrotron Using MARS Code

*T. Nunomiya, N. Nakao, P. Wright, T. Nakamura, E. Kim, T. Kurosawa,
S. Taniguchi, M. Sasaki, H. Iwase, Y. Uwamino, T. Shibata, S. Ito, D.R. Perry*
Deep Penetration of Neutrons Produced by 800 MeV Protons through Concrete and
Iron at ISIS

G. Maino, E. Menapace
Photonuclear Reaction Data Calculations by Algebraic Model Approach for
Radiation Shielding Purposes in the International Context

Session IV: Dose and Related Issues

Chairs: M. Pelliccioni, A. Leuschner

M. Pelliccioni
Conversion Coefficients: An Addition to Existing Data

V. Mares, H. Schraube
The Effect of the Fluence-to-dose Conversion Coefficients Upon the Dose
Estimation to Cosmic Radiation

A. Leuschner
Feasibility Study on an Active Neutron Dosimeter Based on Carbon Activation for
the Linear Collider TESLA

Y. Sakamoto, S. Tsuda, T. Sato, N. Yoshizawa, H. Hirayama
Benchmark Calculation with Simple Phantom for Neutron Dosimetry (2)

P.K. Job, J. Alderman
Radiation Levels Experienced by the Insertion Devices of the Third-generation
Synchrotron Radiation Sources

General discussion on Sessions I-IV

Friday, 12 April

Session V: Status of Computer Codes, Cross-sections and Shielding Data Libraries

Chairs: H. Hunter, N. Mokhov

H.T. Hunter, B.L. Kirk, J.B. Manneschildt, E. Sartori
Progress Report on the Available Analytical Tools for Accelerator Shielding
Analysis 2002

S.G. Mashnik, K.K. Gudima, A.J. Sierk
Merging the CEM2k and LAQGSM Codes with GEM2 to Describe Fission and
Light-fragment Production

N. Sobolevsky, I. Gudowska

Interaction of Ion Beams with Tissue-like Media with the Shield Transport Code

K. Hayashi, R. Tayama, H. Handa, K. Shin, H. Hirayama, H. Nakano,

F. Masukawa, H. Nakashima, N. Sasamoto

Analytical Method for Multi-scattered Neutron in Cavity Used in DUCT-III Code

H. Iwase, T. Kurosawa, T. Nakamura, N. Yoshizawa, J. Funabiki

Development of Heavy-ion Transport Monte Carlo Code

A. Fassò, A. Ferrari, P.R. Sala, G. Tsileidakis

Implementation of Xenon Capture Gammas in FLUKA for Background Calculations in a Transition Radiation Detector

N. Mokhov

Status of MARS Code

Session VI: Shielding in Medical Accelerator Applications

Chairs: J.C. Liu, P. Vaz

B. Mukherjee

Principle of Radiological Shielding of Medical Cyclotrons

W.D. Newhauser, U. Titt, D.T. Dexheimer

A Perspective on Shielding Design Methods for Future Proton Therapy Facilities

Discussions

Session VII: Follow-up of Past SATIF Agreements and Actions

Co-ordinators: A. Fassò, H. Hirayama, H. Hunter

Session VIII: Discussion/Summary and Future Actions

Co-ordinators: M. Silari, N. Mokhov, T. Nakamura, P. Vaz

Closing remarks (*Sartori, Rokni*)

SESSION I

Source Term and Related Data – Proton and Ion Accelerators and Spallation Source

Chairs: T. Nakamura, A. Fassò

DOUBLE-DIFFERENTIAL THICK-TARGET NEUTRON YIELDS BOMBARDED BY HIGH-ENERGY HEAVY IONS

Takashi Nakamura

Department of Quantum Science and Energy Engineering, Tohoku University, Japan

Tadahiro Kurosawa

Advanced Institute of Science and Technology, Japan

Takashi Kato

Nikken Sekkei Co. Ltd., Japan

Abstract

The angular and energy distributions of neutrons produced by 100 to 400 MeV/nucleon He, C, Ne, Ar, Fe, Xe ions and 800 MeV/nucleon Si ions stopping in thick C, Al, Cu and Pb targets were systematically measured using the Heavy Ion Medical Accelerator (HIMAC) of the National Institute of Radiological Sciences, Japan. The neutron spectra spread to almost twice as much as the projectile energy per nucleon, and were integrated over energy to produce neutron angular distributions. The total neutron yields obtained by integrating over the angular distributions could be fitted to a simple semi-empirical formula. The phenomenological hybrid analysis, based on the moving source model and the Gaussian fitting of the break-up and knock-on processes, could also well represent the measured thick target neutron spectra. This phenomenological analytical equation is expressed with several parameters as functions of atomic number Z_p , mass number A_p , energy per nucleon E_p for projectile, and atomic number Z_T , mass number A_T for target. This equation is quite useful for estimating the neutron source term in the neutron shielding design of high-energy heavy-ion accelerators.

Introduction

Recently, high-energy heavy ions have been used in various fields of nuclear physics, material physics, space physics and medical application, especially cancer therapy. Data on double-differential cross-sections (DDX) in energy and angle, DDX of secondary neutrons from a thin target, and the data on the double-differential neutron production yield from a thick (stopping-length) target, (TTY) are indispensable to estimate source terms for accelerator shielding design and exposure during a long-term space mission.

For DDX, there exist only a few published data [1,2], and our group performed a series of systematic studies to measure the double-differential neutron production cross-sections by heavy ions for energies from about 100 to 800 MeV/nucleon [3,4]. For TTY, only a few experimental works are available [5,6,7], and our group also performed a systematic study to measure the double-differential neutron yields from thick targets of C, Al, Cu and Pb bombarded by various heavy ions having energies of 100 to 800 MeV/nucleon using the Heavy Ion Medical Accelerator (HIMAC) in Chiba, at the National Institute of Radiological Sciences (NIRS) in Japan [8,9,10].

We also introduced a systematic estimation of secondary neutron energy spectra from thick targets thus-obtained, using a simple moving source model [11], and determined the parameters of the model by fitting the data calculated by the model to the experimental data.

Experimental procedure

The measurements were carried out using the HIMAC heavy-ion synchrotron. The energy of neutrons produced in the target was measured by the time-of-flight (TOF) method. Figure 1 shows the experimental geometry. A beam extracted from the synchrotron has a time pulse width of 0.5 s at every 3.3 s time interval, and each pulse has a microtime structure of 5 MHz. A thin NE102A plastic scintillator (30 mm diameter by 0.5 mm thick) was placed just behind the end window of the beam line as a beam pick-up scintillator. The output pulses of this scintillator were used as start signals for the TOF measurement and were also used to count the absolute number of projectiles incident to the target. A target was set on the beam line 10 cm behind the beam pick-up scintillator. The NE213 liquid scintillator (12.7 cm diameter by 12.7 cm thick) was used for the neutron detector (E counter) and the NE102A plastic scintillator (15 × 15 cm square by 0.5 cm thick) was placed in front of the E counter for a dE counter to discriminate charged particles from non-charged particles, neutrons and photons. Three sets of E and dE counters were used for simultaneous angular distribution measurements at three different angles. The detection angles are 0, 7.5, 15, 30, 60 and 90 degrees. The detectors were located 2-5 m away from the target to provide good energy resolution. By interposing an Fe shadow bar (15 × 15 cm square by 60 cm long) between the target and detector, the background neutron components from room scattering were estimated.

The incident energies of heavy ions and the target materials with their thickness are given in Table 1. Each target has a shape of 10 × 10 cm square and its thickness was determined to stop the incident particles completely.

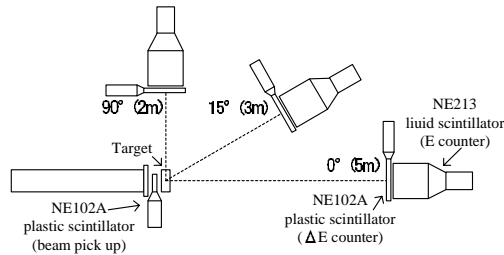
Table 1. Projectile type with its incident energy per nucleon and target thickness used in the experiment

Projectile type and energy (MeV/u)	Target thickness (cm)			
He (100)	C (5.0)	Al (4.0)	Cu (1.5)	Pb (1.5)
He (180)	C (16.0)	Al (12.0)	Cu (4.5)	Pb (5.0)
C (100)	C (2.0)	Al (2.0)	Cu (0.5)	Pb (0.5)
C (180)	C (6.0)	Al (4.0)	Cu (1.5)	Pb (1.5)
C (400)	C (20.0)	Al (15.0)	Cu (5.0)	Pb (5.0)
Ne (100)	C (1.0)	Al (1.0)	Cu (0.5)	Pb (0.5)
Ne (180)	C (4.0)	Al (3.0)	Cu (1.0)	Pb (1.0)
Ne (400)	C (11.0)	Al (8.0)	Cu (3.0)	Pb (3.0)
Ar (400)	C (7.0)	Al (5.5)	Cu (2.0)	Pb (2.0)
Fe (400)	C (4.0)	Al (3.0)	Cu (1.5)	Pb (1.5)
Xe (400)	C (3.0)	Al (2.0)	Cu (1.0)	Pb (1.0)
Si (800)	C (23.0)		Cu (6.5)	

Data analysis

To eliminate charged particles, we used two-dimensional dE-E graphical plots. As the dE counter does not scintillate by neutrons and photons, the neutron and photon events could be selected from the charged particle events. After this discrimination, the neutron and photon events were separated by using two-dimensional total-slow pulse-height graphical plots. By using this plot, we could clearly separate the components of neutrons and photons. After the experimental run, each E counter was calibrated with a ^{60}Co photon source, and the Compton edge in the photon spectrum was used as the bias point (1.15 MeV).

Figure 1. Experimental geometry



Using this low-bias setting, low-energy neutrons could be measured down to about 3 MeV. After obtaining the TOF spectrum, it was converted into the energy spectrum of neutrons using the detection efficiency. The detection efficiency for this scintillator was calculated with the Monte Carlo code by Cecil, *et al.* [12].

The energy resolutions of measured neutron spectra are from 5-40% as a function of neutron energy for three flight path lengths. The experimental uncertainties are divided into statistical uncertainties and normalisation uncertainties. The statistical uncertainties vary in a range of 2-5% for the low- to medium-energy (5-400 MeV) region of the spectra and increase to about 30% at the highest energies. The normalisation uncertainties were estimated to be about 15% in total. The fraction of background

components was found to be less than 1%. The uncertainty in the number of beam particles incident on the target was estimated to be less than 3%. The uncertainty in the solid angle subtended by the target is less than 10%, and the uncertainty in the calculated detection efficiencies is estimated by Nakao, *et al.* [13] to be about 10% from the comparison with experimental results.

Experimental results

Measured neutron spectra for C, Al, Cu and Pb targets bombarded by 400 MeV/nucleon C and Fe ions are shown in Figures 2 and 3, respectively, as examples [8,9,10]. For all projectiles and target combinations, the spectral shapes at each angle are generally similar to each other and they indicate the following general tendencies:

- These experimental spectra in the forward direction have a broad peak at the high-energy end. The peak energy of these bumps is about 60 to 70% of the projectile energy per nucleon, and this peak becomes more prominent for lighter targets and for larger projectile mass. This indicates that these high-energy neutron components are produced in the forward direction by the knock-on and break-up processes and the momentum transfer from projectile to target nuclei are higher for lighter nucleus than for heavier nucleus.
- The neutron spectra have two components: One below about 10 MeV corresponds to neutrons produced isotropically in the centre-of-mass system mainly by the equilibrium process; the other above 10 MeV corresponds to those produced by the pre-equilibrium process. Since the neutron emission by the pre-equilibrium process has forwardness in the angular distribution, the neutron spectra become softer at large emission angles, where the equilibrium process is prominent.
- The high-energy neutrons in the forward direction spread up to the energy that is about 2.5 times higher than the incident particle energy per nucleon. This phenomenon may be explained from the rough assumption that the projectile nuclei are highly excited through the direct collision with some nucleons moving in the target nucleus to produce the project-like fragments, and the high-energy neutrons are produced from the thus-excited project-like fragments.

The total neutron yields above 5 MeV were obtained by integrating the spectra above 5 MeV and then over a hemisphere from 0-90°. The thus-obtained total neutron yields were found to be well fitted to the following formula:

$$Y = 1.5 \times 10^{-6} N_T^{-1/3} E_p^2 (A_p^{1/3} + A_T^{1/3})^2 N_p A_p Z_p^{-2} \text{ (neutrons/particle)} \quad (1)$$

where N_T and N_p are the respective neutron numbers of target and projectile, E_p is the incident particle energy per nucleon (MeV/nucleon), A_T and A_p are the respective mass numbers of target and projectile, and Z_T and Z_p are the respective atomic numbers of target and projectile.

Systematic analysis with moving source model

The measured differential thick target yields were analysed phenomenologically using the moving source model. This model was originally developed to evaluate differential cross-sections of particle production by light ions, that is thin target yield. We applied this model to estimate the TTY induced

Figure 2. Neutron energy spectra at 0-90° from 400 MeV/nucleon C ions on C, Al, Cu and Pb targets

The experimental data are shown by the open dots. The dashed lines are from the best parameter fitting with Eq. (2) and the solid lines are from the recalculation with Eq. (2) using the generalised parameters given in Ref. [14].

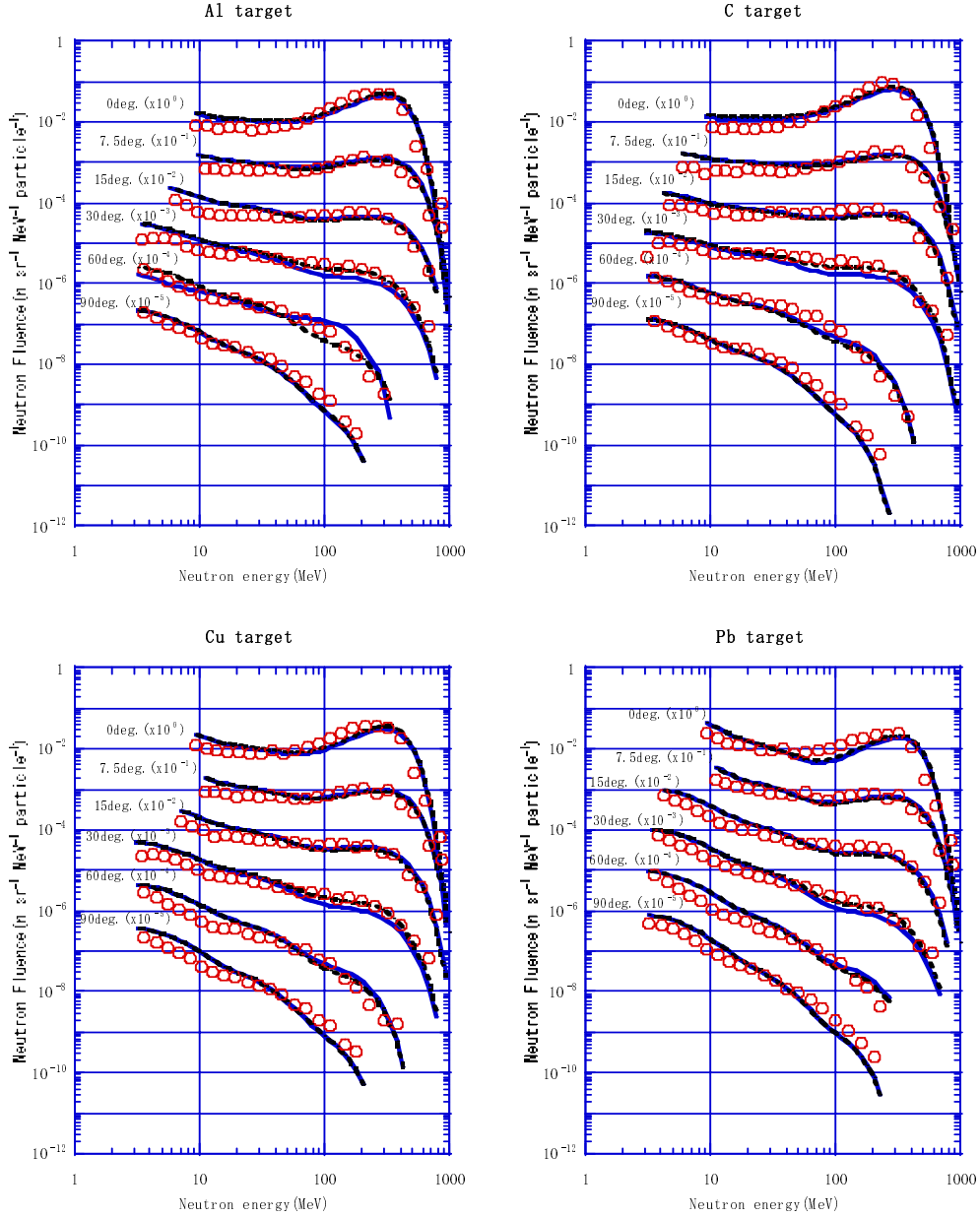
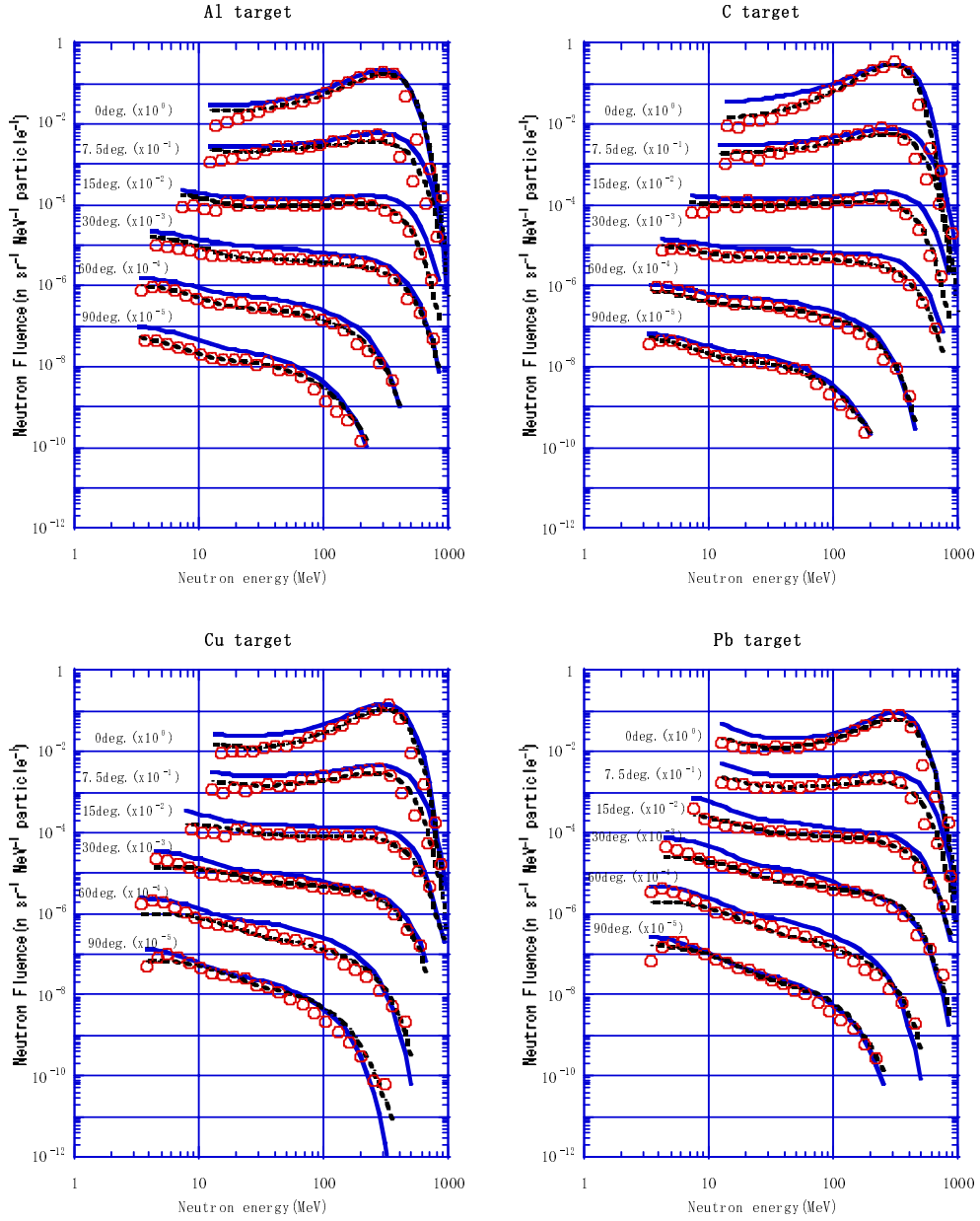


Figure 3. Neutron energy spectra at 0-90° degrees from 400 MeV/nucleon Fe ions on C, Al, Cu and Pb targets

The experimental data are shown by the open dots. The dashed lines are from the best parameter fitting with Eq. (2) and the solid lines are from the recalculation with Eq. (2) using the generalised parameters given in Ref. [14].



by heavy ions after revision by adding the quasi-free collision term having a Gaussian distribution for high-energy neutron components produced by impulsive direct collisions, as follows:

$$\begin{aligned}
 Y(E_n, \theta) &= \frac{m_0}{\sqrt{2\pi\sigma_c(\theta)^2}} \exp\left(-\frac{(E_n - E_c(\theta))^2}{2\sigma_c(\theta)^2}\right) \\
 &+ \sum_{i=1}^2 m_1 \frac{\sqrt{E_n}}{2(\pi\tau_i)^{3/2}} \times \exp\left(-\frac{E_s}{\tau_i}\right) \\
 E_s &= E_n - 2\sqrt{\varepsilon_i E_n} \cos\theta + \varepsilon_i
 \end{aligned} \tag{2}$$

where E_n is the neutron energy and θ is the emission angle.

The nine parameters, m_1 , τ_1 , ε_1 , m_2 , τ_2 , ε_2 , m_0 , E_c , and σ_e , of this equation were derived through fitting to the measured TTY spectra. The results of the phenomenological hybrid analysis using Eq. (2) are also shown in Figures 2 and 3. By selecting the adequate parameters in Eq. (2), the neutron spectra are well reproduced within a factor of 2 margin of accuracy.

We then searched for generalised fitting parameters for all TTY neutron spectra obtained in our systematic experiments. These parameters can be expressed simply as functions of atomic number Z_p , mass number A_p , energy per nucleon E_p for projectile, and atomic number Z_T , mass number A_T for target [14]. The formulae which give nine generalised parameters are given in Ref. [14].

The spectra recalculated using these generalised fitting parameters are also shown in Figures 2 and 3. The recalculated spectra are in good agreement with the measured spectra within a factor of 2 margin of accuracy, except for a few cases. This analytical formula with generalised parameters is quite useful to estimate the TTY neutron spectra which are the source terms of shielding calculation for heavy ion accelerators.

Conclusion

The angular and energy distributions of neutrons produced by 100 to 400 MeV/nucleon He, C, Ne, Ar, Fe, Xe ions and 800 MeV/nucleon Si ions stopping in thick C, Al, Cu and Pb targets were systematically measured using the Heavy Ion Medical Accelerator, HIMAC of the National Institute of Radiological Sciences, Japan. The measured differential thick target yields were phenomenologically analysed using a revised moving source model with generalised parameters.

Acknowledgements

We gratefully acknowledge the support and assistance of the HIMAC accelerator operation staffs. We also wish to thank the many colleagues in our group for their help during these experiments. This work was supported in part by the Research Project with Heavy Ions at NIRS-HIMAC.

REFERENCES

- [1] Cecil, T.A., B.D. Anderson, A.R. Baldwin, *et al.*, *Phys. Rev.*, C24, 2013 (1983).
- [2] Baldwin, A.R., R. Madey, W.M. Zhang, B.D. Anderson, D. Keane, J. Varga, *et al.*, *Phys. Rev.*, C46, 258 (1992).
- [3] Sato, H., T. Kurosawa, H. Iwase, *et al.*, *Phys. Rev.*, C64, 034607 (2001).
- [4] Iwata, Y., T. Murakami, H. Sato, *et al.*, *Phys. Rev.*, C64, 054609 (2001).
- [5] Cecil, R.A., B.D. Anderson, A.R. Baldwin, *et al.*, *Phys. Rev.*, C21, 2481 (1980).
- [6] Heilbronn, L., R.S. Cary, M. Cronqvist, *et al.*, *Nucl. Sci. Eng.*, 132, 1 (1999).
- [7] Heilbronn, L., R. Madey, M. Elaasar, *et al.*, *Phys. Rev.*, C58, 3451 (1998).
- [8] Kurosawa, T., N. Nakao, T. Nakamura, *et al.*, *Nucl. Sci. Eng.*, 132, 30 (1999).
- [9] Kurosawa, T., N. Nakao, T. Nakamura, *et al.*, *J. Nucl. Sci. Technol.*, 36, 41 (1999).
- [10] Kurosawa, T., N. Nakao, T. Nakamura, *et al.*, *Phys. Rev.*, C62, 044615 (2000).
- [11] Mantzouranis, G., H.A. Weidenmuller, D. Agassi, *Z. Phys.*, A276, 145 (1976).
- [12] Cecil, R.A., B.D. Anderson, R. Madey, *Nucl. Instrum. Methods*, 161, 439 (1979).
- [13] Nakao, N., T. Nakamura, M. Baba, *et al.*, *Nucl. Instrum. Methods*, A362, 454 (1995).
- [14] Kato, T., T. Kurosawa, T. Nakamura, *Nucl. Instrum. Methods*, A, in press.

CURRENT STATUS OF THE AGS SPALLATION TARGET EXPERIMENT

**H. Nakashima, H. Takada, Y. Kasugai, S. Meigo, F. Maekawa,
T. Kai, C. Konno, Y. Ikeda, Y. Oyama, N. Watanabe**
Japan Atomic Energy Research Institute, Tokai, Ibaraki 319-1195, Japan

M. Arai, T. Ino, M. Kawai, M. Numajiri, S. Sato, K. Takahashi
High Energy Accelerator Research Organisation, Oho, Tsukuba, 305-0801 Japan

Y. Kiyanagi
Hokkaido University, Kita-13, Nishi-8, Kita-ku, Sapporo 060-8628, Japan

H. Conrad, D. Filges, R. Neef, H. Stechemesser
Forschungszentrum Jülich, GmbH, D-52425, Jülich, Germany

H. Spitzer, G.S. Bauer
Paul Scherrer Institut, CH-5232, Villigen, Switzerland

E. Jerde, D. Glasgow, J. Haines, T. Gabriel
Oak Ridge National Laboratory, PO Box 2008 Oak Ridge, TN 37831-6364, USA

P. Montanez, A. Carroll, H. Ludewig, J. Hastings
Brookhaven National Laboratory, Upton, NY 11973, USA

Abstract

In preparation for the construction of next-generation neutron sources, a series of experiments were performed using a mercury target assembly with a water moderator and a lead reflector at the AGS accelerator. In a bare target experiment, neutron spatial and energy distributions around the target were obtained at proton energies of 1.6-24 GeV using an activation method. The radioactivities induced in activation samples placed around the mercury target were also measured. Using a mercury target with a water moderator and a lead reflector, the spectral intensity of slow neutrons from the moderator was measured with only a few proton pulses with a newly developed technique, a current mode time-of-flight detector. A shielding experiment was also carried out to measure neutron attenuation in lateral shields of ordinary concrete and steel. This paper reviews the experimental results and the current status of the analyses.

Introduction

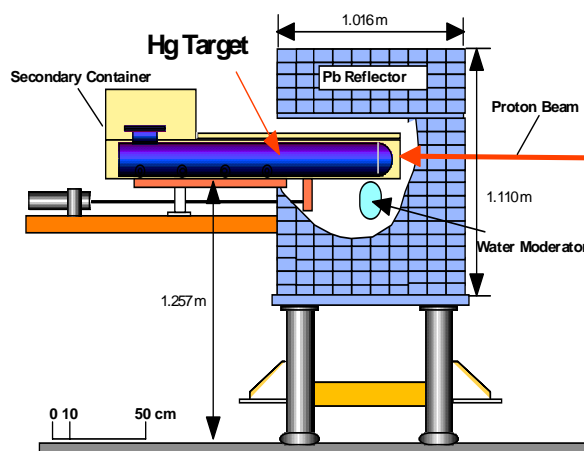
Aiming at next-generation short-pulse spallation neutron sources with an average proton power of 1 MW or more, a series of neutron and shielding experiments have been performed since 1997 in the framework of an international collaboration among laboratories in Japan, the US and Europe. This collective effort is known as the AGS Spallation Target Experiment (ASTE) collaboration. The experiments were carried out using short-pulse high-peak-power GeV proton-beams from the Alternating Gradient Synchrotron (AGS) of Brookhaven National Laboratory. In the experiment, mercury, being identified as one of the best candidates from the neutronic and thermodynamic points of view, was used as a spallation target material. The main purpose of the experiment is to provide experimental data on neutronic performances of the mercury target assembly and on shielding design parameters, and to validate predictions from theoretical calculations on neutronics and shielding. For this purpose, three kinds of experiments were carried out: an experiment with only a mercury target (a bare target experiment), an experiment with a water moderator and a lead reflector, and a shielding experiment. This paper reviews the current status of these experiments [1-13].

Experimental

The experiments were carried out using proton beams of extraction energies between 1.6 and 24 GeV delivered by AGS. The available power per pulse of proton beams was 240 kJ at 24 GeV and 0.86 kJ at 1.6 GeV with a repetition rate of 0.6 Hz. The peak beam intensity per pulse was over 10^{12} protons for all energies. Intensities of incident proton beams were precisely monitored by an integrating current transformer, a secondary emission chamber and an activation method with the $^{nat}\text{Cu}(p,x)^{24}\text{Na}$ reaction during the measurements. An imaging plate technique with an Al activation method monitored the beam profiles integrated during the measurement and a segmented parallel-plate ion chamber was applied to measure the profiles per proton pulse.

Figure 1 shows the cross-sectional view of the mercury target assembly. Mercury was contained in a cylindrical container 1.3 m long and 0.2 m in diameter having a hemispherical front window 0.2 m in diameter. The vessel was made of 2.5 mm thick stainless steel. The cylindrical container was set up inside the secondary rectangular container to protect against leakage of mercury. A cubic lead reflector of about 1 m surrounded the target and a light water moderator of $0.1 \times 0.1 \times 0.05 \text{ m}^3$ in an aluminium container was placed under the target.

Figure 1. Schematic vertical cross-sectional view of mercury target assembly [5]



Experimental results and analyses

Bare target experiment

Neutron spatial and energy distribution

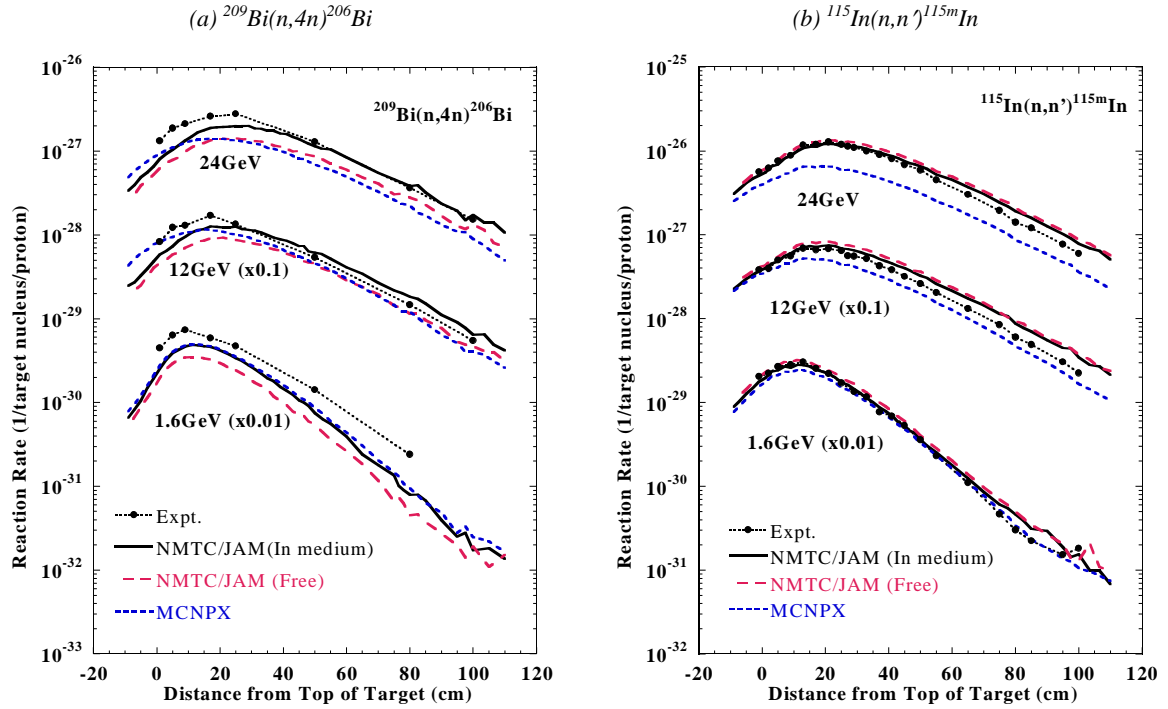
An experiment with only the mercury target (“bare target” configuration) was carried out in order to study the neutronic performance of the target. The spatial distribution of neutron reaction rates along the target was measured by activation foils attached on removable fixtures around the target. Many kinds of activation foils with different threshold energies such as Bi, Al and In were used to obtain information on the energy spectra of neutrons leaking from the target.

The experimental results were analysed by a code system composed of the NMTC/JAM [14] and MCNP4A [15] codes to estimate the precision of theoretical calculations for a spallation target. The JAM code [16] was implemented in the NMTC/JAM code for the nucleon-induced nuclear reaction calculations above 3.5 GeV and meson calculations above 2.5 GeV, while the Bertini model is adopted to treat the intranuclear cascade calculation below these energies. The nucleon–nucleon cross-sections in free space and in-medium cross-sections according to the Cugnon parametrisation [17] were applied in the analyses in order to estimate their applicability. The MCNPX code [18] was also used for the analyses to compare the precision between both codes.

Figure 2(a) shows measured spatial distributions of the rate of the $^{209}\text{Bi}(n,4n)^{206}\text{Bi}$ reaction (threshold energy: E_{th} 22.6 MeV) due to neutrons generated in the mercury target by incident protons of 1.6, 12 and 24 GeV. In the figure, the measurements are compared with calculations by the NMTC/JAM code with both cross-section options and by the MCNPX code. The calculations of NMTC/JAM with the in-medium cross-section underestimate the measurement at 1.6 GeV and at positions less than 40 cm from the front of the target at 12 and 24 GeV. The NMTC/JAM calculations with the free cross-section underestimate all measurements. The NMTC/JAM (in-medium) calculation is larger and closer to the measurements than the NMTC/JAM (free) calculations. It seems that angular distributions of neutron production cross-sections of mercury for proton in the lateral direction used in the JAM code are underestimated at 12 and 24 GeV [19]. The MCNPX calculation at 1.6 GeV gives almost the same result as the NMTC/JAM (in-medium) calculation, while the shape of the distributions at 12 and 24 GeV given by the MCNPX code are different from those by the NMTC/JAM code. It should also be noted that angular distributions of neutron production cross-sections for protons on mercury used in the MCNPX code are different from the measurements at 12 and 24 GeV.

Comparisons of the $^{115}\text{In}(n,n')^{115\text{m}}\text{In}$ reaction (E_{th} : 0.5 MeV) among the measurements and calculations with the NMTC/JAM+MCNP4A and MCNPX codes at 1.6, 12 and 24 GeV protons are shown in Figure 2(b). Both NMTC/JAM and MCNP4A calculations with in-medium and free cross-sections agree among each other, as neutrons having energies lower than 20 MeV predominantly contribute to the reaction. Both calculations agree with the measurement except for the overestimation at positions longer than 40 cm from the front of target. The overestimation is caused by the slight overestimation of angular distribution of neutron production cross-section of protons on mercury in the forward direction. The MCNPX calculation shows a difference in peak position relative to the measurement, and underestimates the measurement at 12 and 24 GeV more clearly than in case of the $^{209}\text{Bi}(n,4n)^{206}\text{Bi}$ reaction.

Figure 2. Neutron reaction rate spatial distributions parallel to the axis of the mercury target



Induced radioactivity

An experiment on induced radioactivities and residual nuclei distributions of mercury was carried out to estimate the precision of activation calculation code systems. HgO samples were put around the target irradiated by 2.83 and 24 GeV proton beams in order to study the activities induced by the primary proton beam and secondary particles generated at the target. The radioactivities of residual nuclides in the HgO samples were measured using HP-Ge detectors. The measured radioactivities were analysed by an induced radioactivity calculation code system composed of the NMTC/JAM, MCNP4A and DCHAIN-SP [20] codes. The time evolutions of the measured radioactivities of residual nuclei: $^{197\text{m}}\text{Hg}$, $^{198\text{g}}\text{Au}$, ^{181}Re , ^{203}Hg and ^{185}Os , generated in a HgO sample put in front of the target are compared with the calculations in Figure 3. It is shown that the total activity is mainly dominated by ^{197}Hg during two weeks after the irradiation and ^{203}Hg after 15 days. The comparison shows that the calculations agree with the measurements within a factor of 2 for $^{197\text{m}}\text{Hg}$ and ^{203}Hg and a factor of 3 for others, although all calculations underestimate the measurements slightly. The measurements of radioactivities for other long-lived residual nuclei and other irradiation materials are in progress.

Experiment with water moderator and Pb reflector

Neutron spatial and energy distributions

In order to estimate the neutronic performance of a lead reflector, neutron spatial and energy distributions around the mercury target were measured by the same activation method as for the bare target experiment. The effect of the lead reflector can be seen from the ratios of measured $^{115}\text{In}(n,n')^{115\text{m}}\text{In}$ and $^{93}\text{Nb}(n,2n)^{92\text{m}}\text{Nb}$ (E_{th} : 0.5 and 9.1 MeV) reaction rates with and without the lead reflector shown in Figure 4. Data were taken parallel to the axis of the target for proton energies of 12 and 24 GeV. There

Figure 3. Radioactivities of residual nuclei

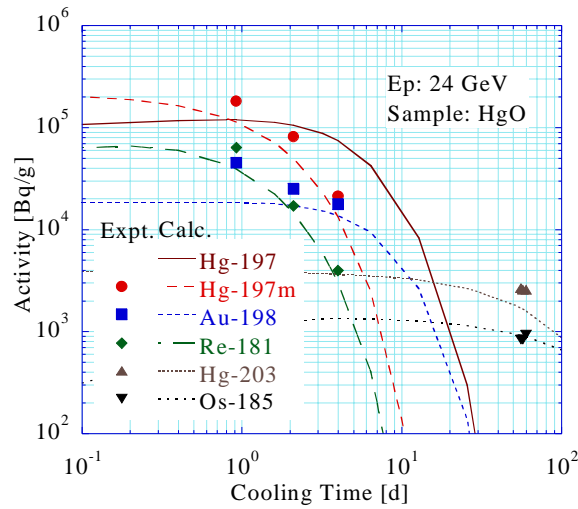
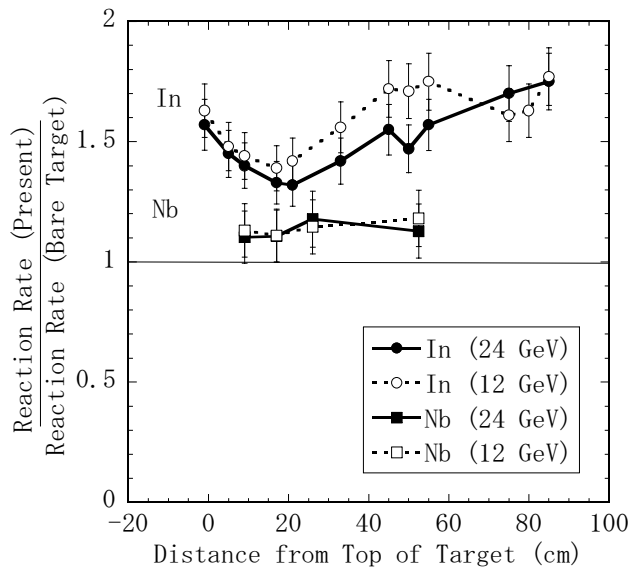


Figure 4. Ratios of reaction rates parallel to the axis of the target with and without lead reflector [13]

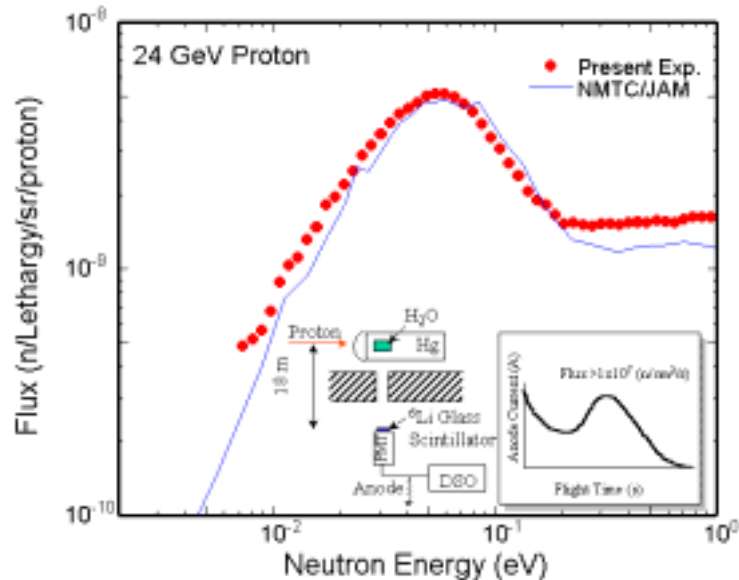


is no clearly observable dependency on the energy of the incident protons in the measured data. The larger effect in the case of the In reaction, which has a low threshold energy of 0.5 MeV, means that the lead reflector plays an important role in slowing down neutrons around the mercury target. The ratios for the In reaction rates decrease from the front end of the mercury target to the peak position of the In reaction rate and increase from the peak position to the far end. This is because the ratio of neutrons produced in the lead reflector to neutrons coming directly from the target is relatively smaller at the peak position than at other positions. In other words, the lead reflector makes the In reaction rate distribution, which mainly represents the low-energy neutron distribution, flatter than in the case of a bare mercury target. Thus, the lead reflector increases the intensity of low-energy neutrons around the mercury target and makes their axial distribution flat independent of the incident proton energy.

Spectral intensity of slow neutron from the water moderator [6]

The spectral intensity of slow neutrons from the moderator placed under the mercury target was also measured in order to obtain experimental data on neutronic performance of the water moderator and to estimate the precision of the calculation code system. Only few proton pulses were needed in the measurement of the intensity by using a newly developed technique, a current mode time-of-flight detector system. A schematic view of the experiment is shown in the insert in Figure 5 along with the measured anode current spectrum as a function of flight time. The flight path length from the water moderator to the detector was 18 m. Anode currents generated at ^6Li and ^7Li glass scintillation detectors were measured by a digital storage oscilloscope and the difference of the currents was converted to a neutron spectral intensity. The measurement on the spectral intensity of slow neutrons at 24 GeV protons is compared with the calculation using the NMTC/JAM and MCNP4A code system in Figure 5 without any normalisation (absolute scale). Excellent agreement between the measurement and calculation with the code system can be observed. Thus, the accuracy of the NMTC/JAM and MCNP4A code system has been validated on neutron flux calculations from a few tens of GeV down to the meV region.

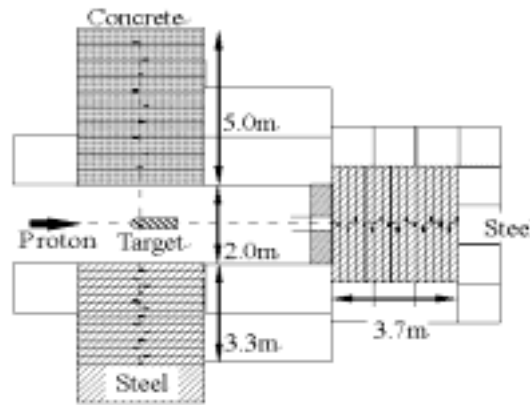
Figure 5. Measured neutron spectral intensity from water moderator [6]



Shielding experiment

A shielding experiment was carried out using 2.83 and 24 GeV proton beams with steel and ordinary concrete shields set on both sides of the bare mercury target in order to estimate the calculation accuracy of code systems and the parameters of empirical formulae for shielding calculations. Figure 6 shows the arrangement of the shielding experiment. The mercury target was placed inside a cave of ordinary concrete, the inside dimensions of which were 2 m in width and 2.7 m in height. The lateral shields of ordinary concrete (5.0 m thick) and of steel (3.3 m thick) started at 1 m from the mercury target and the forward shield of steel (3.7 m thick) started at 3.5 m from the far end of the mercury target. All shields had cross-sections of more than 2 m \times 2 m, and densities of steel and ordinary concrete are 7.74 g/cm³ and 2.45 g/cm³, respectively. Activation samples of Bi, Al, In and Au were set deep inside the shields to measure the neutron spatial distributions in the shields. Neutron reaction rates of $^{209}\text{Bi}(n,xn)$, $^{27}\text{Al}(n,x)^{24}\text{Na}$, $^{115}\text{In}(n,n')^{115m}\text{In}$ and $^{197}\text{Au}(n,\gamma)^{198}\text{Au}$ reactions with various threshold

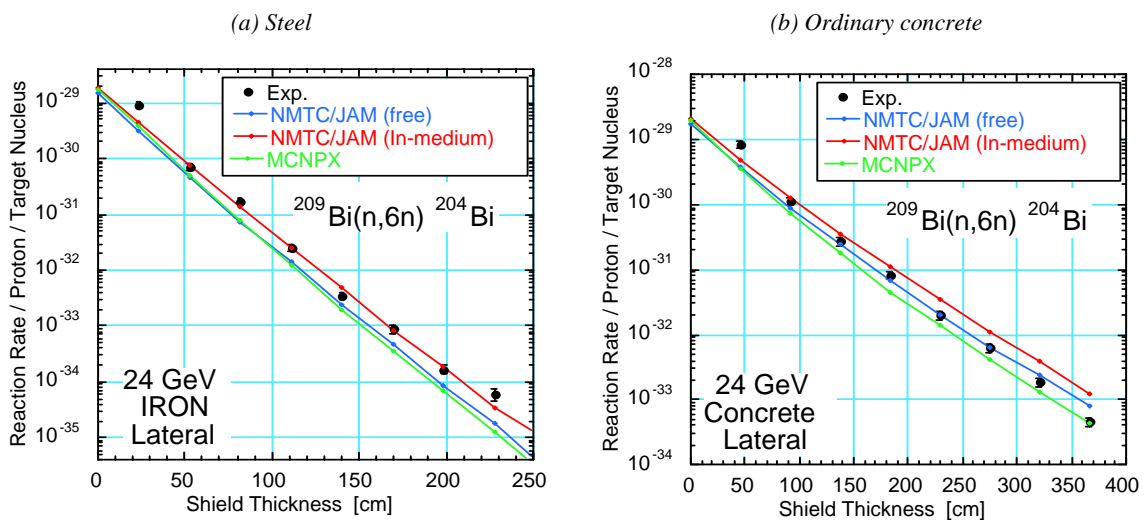
Figure 6. Horizontal cross-sectional view of arrangement for shielding



energies were measured by the HP-Ge detectors to obtain information on the energy spectra inside the shields. A high beam intensity of about 10^{12} protons per pulse, totally over 10^{16} protons, was needed to measure data up to about 2.5 m deep inside the lateral steel shield and about 4 m deep for the lateral concrete shield.

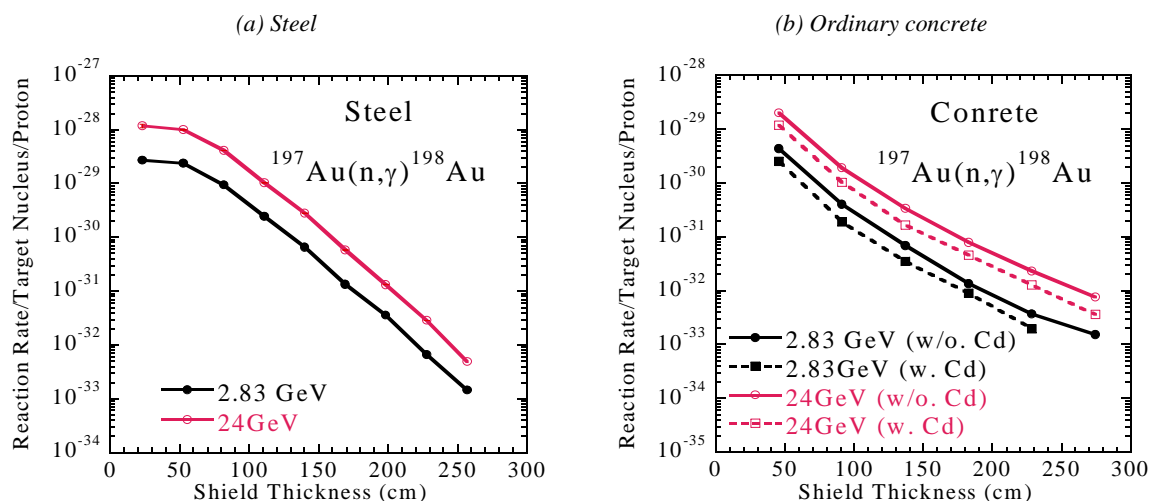
The measured spatial distributions of neutron reaction rates of the $^{209}\text{Bi}(n,6n)^{204}\text{Bi}$ reaction (E_{th} : 38.0 MeV) inside the steel and ordinary concrete shields are compared with the NMTC/JAM (free) and (in-medium) calculations and the MCNPX calculations at 24 GeV protons in Figure 7. In the case of the steel shield, the NMTC/JAM (in-medium) calculation agrees very well with the measurement almost at all positions. The NMTC/JAM (free) and MCNPX calculations show the same topology of neutron attenuation and agree with the measurement within a factor of 2, although the calculations yield slightly lower values than the measurement. In the case of the ordinary concrete shield, all calculations agree with the measurement within a factor of 3. However the calculated neutron attenuation with distance slightly differs from the measured one and also among the different calculations. It is noted that the difference between the measurement and calculations at 25 cm from the surface of the shield is due to the fact that the actual geometry around the target was too complicated to make an exact geometry model for the calculations. On the whole, all calculations predict the neutron attenuation in the shields satisfactorily, over 5 orders of magnitude within a factor of 3.

Figure 7. $^{209}\text{Bi}(n, 6n)^{204}\text{Bi}$ reaction rate spatial distributions in shields



Attenuations measured by the $^{197}\text{Au}(n,\gamma)^{198}\text{Au}$ reaction rates in the steel and ordinary concrete shields at 2.83 and 24 GeV incident protons are shown in Figure 8. Measured reaction rates with a 1 mm thick Cd cover over the foils are also compared with the reaction rate without the cover to study the behaviour of thermal neutrons in the ordinary concrete shield. It is found that the attenuations are convex curves in the case of the steel shield, while the curves are concave in the case of the ordinary concrete shield. Thus, it is revealed experimentally that the attenuations of low-energy neutrons in steel and concrete shields are different from those of reaction rates having high threshold energy.

Figure 8. $^{197}\text{Au}(n,\gamma)^{198}\text{Au}$ reaction rate spatial distributions in the shields



Summary

A series of neutronic and shielding experiments were carried out using a mercury target assembly irradiated by intense GeV energy protons from AGS. The experiment provided various valuable insights and data for the designs of the next-generation spallation neutron sources. The experimental data were used for neutronic code system validation. It is found that the code systems are reliable for neutron flux calculations and induced activation calculations, although some experimental analyses for activation and shielding experiments are still in progress.

Acknowledgements

The authors would like to express their gratitude to all other members of the ASTE collaboration and the operation team of the AGS accelerator. The experimental work at BNL was supported in part by the US Department of Energy (DOE) under contract no. DE-AC02-98-CH10996 with Brookhaven Science Associates.

REFERENCES

- [1] Jerde, E.A., *et al.*, “Neutron Activation by Neutrons Produced via Proton-induced Spallation in a Liquid-mercury Target: Measurements and Assessment of Uncertainties”, *J. Radioanalytical and Nuclear Chemistry*, Vol. 242(2), 473 (1999).
- [2] Nakashima, H. *et al.*, “Measurement of Incident Proton Beam Characteristics for AGS Spallation Target Experiment”, *Proc. ICANS-XIV*, Illinois, USA, June 1998, 457 (1998).
- [3] Takada, H., *et al.*, “Measurement of Reaction Rate Distributions on a Mercury Target Bombarded with High-energy Protons”, *Proc. ICANS-XIV*, Illinois, USA, June 1998, 468 (1998).
- [4] Meigo, S., *et al.*, “Development of Current Mode Time-of-flight Technique for Measurement of Thermal Neutron Spectrum”, *J. Nucl. Sci. Technol.* (Suppl.), 789 (2000).
- [5] Ikeda, Y., *et al.*, *Status of the ASG Experiment for Mercury Spallation Target Development*, JAERI-Conf 2000-005, 38 (2000).
- [6] Meigo, S., *et al.*, “Measurement of Spectrum for Thermal Neutrons Produced from H₂O Moderator Coupled with Mercury Target”, *Proc. ICANS-XV*, Tsukuba, Japan, November 2000, 941 (2000).
- [7] Kasugai, Y., *et al.*, “Measurement of Induced Radioactivity in a Spallation Neutron Field of a Mercury Target for GeV-proton Bombardment”, *Proc. ICANS-XV*, Tsukuba, Japan, Nov. 2000, 995 (2000).
- [8] Maekawa, F., *et al.*, “Analysis of the AGS Experiment on a Mercury Target with a Moderator and a Lead Reflector Bombarded by GeV Energy Protons”, *Proc. ICANS-XV*, Tsukuba, Japan, November 2000, 983 (2000).
- [9] Maekawa, F., *et al.*, “Analysis of Neutronic Benchmark Experiment on a Simulated Mercury Spallation Neutron Target Assembly Bombarded by GeV Protons”, to be submitted to *Nucl. Sci. Eng.*
- [10] Takada, H., *et al.*, *Measurements of Activation Reaction Rate Distributions on a Mercury Target Bombarded with High-energy Protons at AGS*, JAERI Data/Code 2000-008 (2000).
- [11] Kasugai, Y., *et al.*, *Measurements of Activation Reaction Rate Distributions on a Mercury Target with a Lead-reflector and Light-water-moderator for High-energy Proton Bombardment Using AGS Accelerator*, JAERI Data/Code 2000-042 (2001).
- [12] Meigo, S., *et al.*, *Measurement of Profile and Intensity of Proton Beam by an Integrating Current Transformer and a Segmented Parallel-plate Ion Chamber for the AGS-spallation Target Experiment (ASTE)*, JAERI Data/Code 2001-014 (2001).

- [13] Nakashima, H., *et al.*, “Research Activities on Neutronics Under ASTE Collaboration at AGS/BNL”, to be published as *Proc. Int. Conf. on Nuclear Data for Science and Technology*, Tsukuba, Japan, 7-12 Oct. 2001 (2002).
- [14] Niita, K., *et al.*, *High-energy Particle Transport Code NMTC/JAM*, JAERI-Data/Code 2001-007 (2001).
- [15] *MCNP – A General Monte Carlo N-particle Transport Code Version 4A*, J.F. Briesmeister, ed., LA-12625 (1993).
- [16] Nara, Y., *et al.*, “Study of Relativistic Nuclear Collisions at AGS Energies from p+Be to Au+Au with Hadronic Cascade Model”, *Phys. Rev.*, C61, 24901 (1999).
- [17] Cugnon, J., T. Mizutani and J. Vandermeulen, *Nucl. Phys.* A352, 505 (1981).
- [18] *MCNPXTM User’s Manual*, L.S. Waters, ed., TPO-E83-G-UG-X-00001, Los Alamos National Laboratory (1999).
- [19] Maekawa, F., private communication.
- [20] Takada, H. and K. Kosako, *Development of the DCHAIN-SP Code for Analyzing Decay and Build-up Characteristics of Spallation Products*, JAERI-Data/Code 99-008 (1999).

DOSE RATE MEASUREMENTS BEHIND DIFFERENT SHIELDING FOR 250 MeV PROTONS ON A THICK COPPER TARGET

S. Teichmann, B. Amrein, J. Gerig, W. Hajdas, H. Temnitzer
Paul Scherrer Institut, Villigen, Switzerland

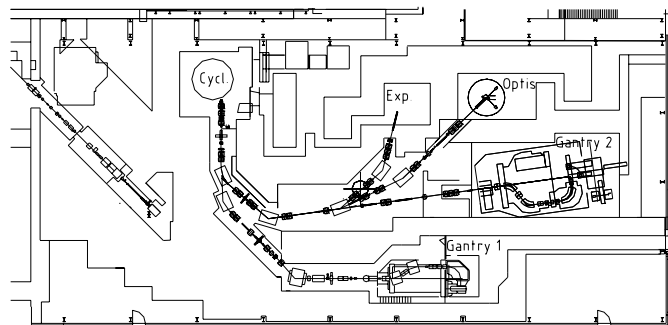
Abstract

A dedicated cyclotron for proton therapy will be installed at the Paul Scherrer Institut, feeding two treatment rooms and one experimental area. It will produce 250 MeV protons at a maximum current of 500 nA. The shielding calculations for these facilities are based on published parameters. To support the calculations, an experiment has been carried out in an existing experimental area with 250 MeV protons stopped in a thick copper target. Neutron and photon dose rates were measured (a) at 90° and 78° on the roof, for concrete shielding thicknesses of 0.5-3 m and (b) at 20° behind a shielding wall of concrete and iron. The dose rate component due to neutrons above 20 MeV was determined using a $^{12}\text{C}(n,2n)$ -monitoring system; a measurement with this monitor was possible only for 0.5-1.5 m roof thickness. Comparisons with the calculational method show good agreement in case of the forward shielding (b); for the lateral shielding (a) the calculations in general underestimate the dose rate.

Introduction

In August 2000, project PROSCAN was initiated at the Paul Scherrer Institut (PSI) and is expected to be completed by the end of 2005. By installing a dedicated cyclotron (Cycl.) for proton therapy, the already existing facilities for the treatment of eye tumours and of deep-seated tumours (the latter is labelled Gantry 1) will become independent from the operational schedules of PSI's Injector 1 and the Ring Cyclotron. The new cyclotron will produce 250 MeV protons at a maximum current of 500 nA. A degrader can be used to produce lower-energy protons. Figure 1 shows a provisional layout for PROSCAN.

Figure 1. Provisional layout of the PROSCAN area



A second gantry for proton therapy of deep-seated tumours (Gantry 2) will be installed in one of the treatment rooms, using up to 250 MeV protons at a current of about 1 nA. Another patient treatment room is foreseen for eye tumour treatment (Optis) with up to 10 nA of 70 MeV protons and possibly for new therapy methods using up to 250 MeV protons at currents of about 1 nA. Gantry 1 will be disconnected from the old beam line (still partly shown in Figure 1) and hooked up to the new cyclotron. In addition, an experimental area (Exp.) will be used for proton irradiation experiments at various beam energies up to 250 MeV with an intensity of up to 10 nA. The shielding layout for the PROSCAN facilities is currently being designed, based on calculations and on results of a shielding experiment, which support them.

The calculational method is briefly summarised and a detailed description of the shielding experiment and its results is given. The measured and the corresponding calculated dose rates behind different shielding are then compared.

Calculational method

The shielding calculations for PROSCAN use the concept of exponential dose attenuation:

$$H(E_p, \theta, d(\theta)) = \frac{H_0(E_p, \theta)}{r^2} e^{-\frac{d(\theta)}{\lambda(\theta)}}$$

where E_p is the proton beam energy, r is the distance from the target to the measuring point and $d(\theta)$ is the effective shielding thickness (i.e. the length of shielding material that is being traversed). Parameters for the angle-dependent source terms $H_0(E_p, \theta)$ and for the attenuation lengths $\lambda(\theta)$ in normal concrete were taken from S. Agosteo, *et al.* [1]. The source terms include dose rate contributions from neutrons at all energies and of photons. Contributions from other secondary

particles produced in the shielding are also included, but are negligible. Based on other published results [2,3] and preliminary Monte Carlo calculations at PSI using MCNPX, the following dose attenuation lengths are being used in the case of iron shielding: $\lambda = 140 \text{ g/cm}^2$ at 0° and $\lambda = 120 \text{ g/cm}^2$ at 90° with respect to the beam direction; interpolated values are used for the angles in-between. Table 1 shows the parameters being used for $E_p = 250 \text{ MeV}$ on iron and tissue targets. Since the neutron production and the shape of the neutron energy spectrum varies with target material, the values of H_0 and λ also change with target material. The uncertainties of the parameters, which were derived using Monte Carlo simulations, are not known.

Table 1. Parameters for the shielding calculations ($E_p = 250 \text{ MeV}$). Source terms H_0 and attenuation lengths λ in concrete for Fe and tissue targets are taken from [1].

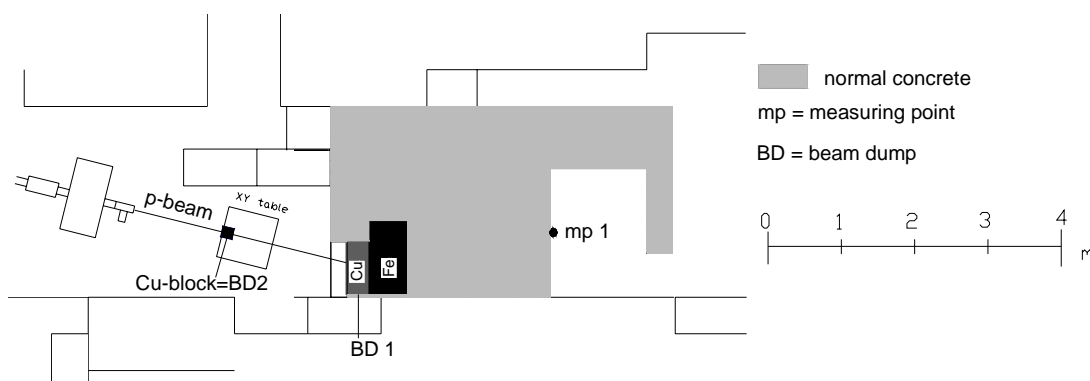
Angular bin [degrees]	Fe target			Tissue target	
	H_0 [$\text{Sv m}^2 \text{ p}^{-1}$]	λ concrete [g cm^{-2}]	λ iron [g cm^{-2}]	H_0 [$\text{Sv m}^2 \text{ p}^{-1}$]	λ concrete [g cm^{-2}]
0-10	9.0E-15	109.0	140.0	7.4E-15	100.0
10-20	7.5E-15	106.0	137.7	5.4E-15	101.0
20-30	6.8E-15	110.0	135.3	3.5E-15	96.7
30-40	3.9E-15	98.7	133.0	3.3E-15	90.5
40-50	3.3E-15	92.9	130.6	2.0E-15	84.5
50-60	2.5E-15	89.0	128.3	1.2E-15	79.8
60-70	2.0E-15	83.7	125.9	7.1E-16	76.7
70-80	8.1E-16	78.2	123.6	4.1E-16	68.9
80-90	6.2E-16	62.8	121.2	2.5E-16	61.8
90-100	3.8E-16	60.1	118.9	1.6E-16	56.5

Shielding experiment

To verify the shielding calculations, an experiment was carried out in an existing experimental area (see Figure 2) normally used for proton irradiation tests of electronic devices and various other materials (PIF = Proton Irradiation Facility).

Figure 2. Horizontal cut of the experimental layout at beam height

*BD2 was put in place for the second set of dose rate measurements.
 "mp 1" indicates the measurement point when the beam was stopped in BD1.*



Layout

590 MeV protons from the ring cyclotron were degraded down to 250 MeV and stopped either:

- In the regular copper beam dump (BD1) set into the forward wall of the experimental area.
- In a cylindrical copper block (BD2) located at the irradiation position, about 1.5 m in front of the forward wall.

The proton beam current was measured in two ionisation chambers, one of which was directly in front of BD2. Due to the degradation, the beam was very wide with a diameter at FWHM of about 60 mm. Table 2 shows the parameters of the beam and of the beam dumps.

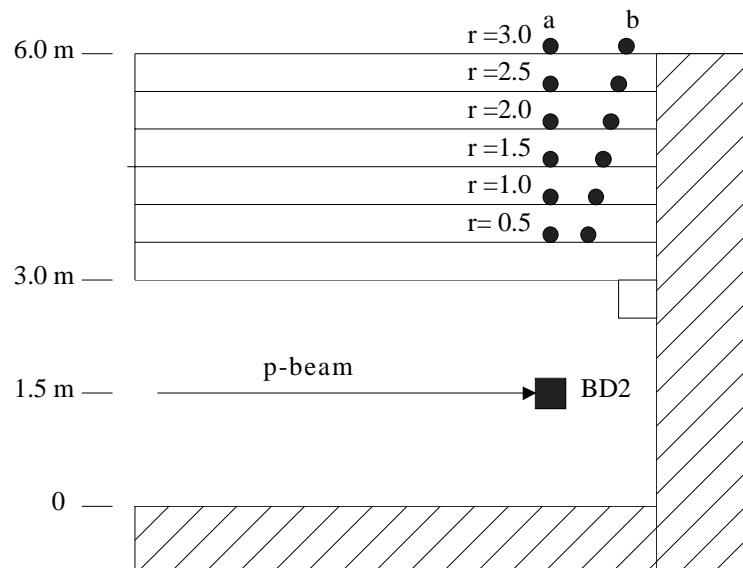
Table 2. Parameters of the proton beam and of the copper beam dumps

E_p [MeV]	Beam		BD1		BD2	
	I_p (on BD2) [nA]	\varnothing_{FWHM} [mm]	Area [mm × mm]	Thickness [mm]	\varnothing [mm]	Thickness [mm]
250	3.1	60	500 × 750	300	100	70

The shielding wall behind BD1 consisted of localised iron shielding, 0.5 m thick, and of 2 m normal concrete. Dose rate measurements were made directly behind the shielding wall at beam height and at an angle of about $20 \pm 2^\circ$ with respect to the beam entrance point in BD1. The roof shielding consisted of normal concrete and was varied in 0.5 m steps from 0.5 m thickness to 3 m thickness, starting at 1.5 m above BD2. Dose rate measurements were made directly above BD2, i.e. at $90 \pm 2^\circ$, and at $78 \pm 2^\circ$ with respect to the beam direction. Due to the layout of the experimental area it was not possible to take measurements at more forward angles. Figures 2 and 3 show the experimental layout and the measurement points.

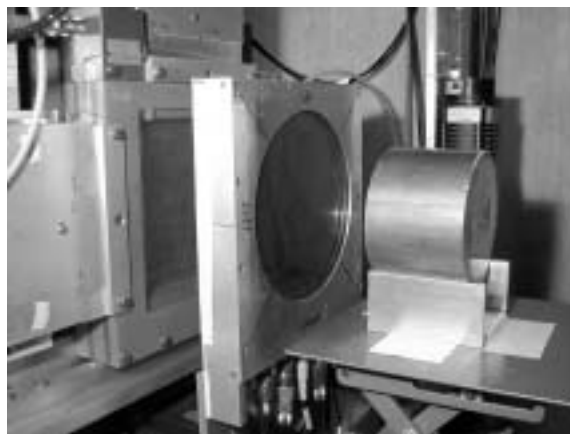
Figure 3. Vertical cut of the experimental layout

Roof shielding (normal concrete) was added in 0.5 m steps, starting at 1.5 m above BD2. The measurement points are indicated.



The first set of dose rate measurements were made without BD2 in place and at a roof thickness of 0.5 m. For the second set of dose rate measurements, BD2 was put in place and the roof thickness was varied. Figure 4 shows part of the set-up with BD2 in position. Figure 5 shows BD1 with its iron shielding during the dismantlement of the shielding wall.

Figure 4. Cu block (BD2) behind the ionisation chamber



Figures 5. The copper beam dump BD1 with its iron shielding during dismantlement of the forward shielding wall



Dose rate measuring systems

All dose rate measurements were made by radiation protection personnel. Gamma dose rates were measured either with a Teletektor Graetz or with a Bicorn/Low Energy instrument. Dose rates due to neutrons below 20 MeV were measured with a Berthold LB 123/LB 6411 REM counter. This detector consists of a ^3He proportional counter with a spherical polyethylene moderator. Dose rates due to high-energy neutrons ($E_n > 20$ MeV) were determined using a ^{11}C monitor, which is based on the measurement of the induced ^{11}C activity in a plastic scintillator. The latter could be used only for 0.5-1.5 m concrete shielding due to the low intensity of high-energy neutrons behind thicker shielding. Table 3 provides an overview of the measuring systems, their measuring uncertainties and their use during the experiment.

Table 3. Overview of dose rate measuring systems, their measuring uncertainties and their use during the experiment

	γ	n < 20 MeV	n > 20 MeV
Instrument	Graetz X 1000 W, Bicron/Low Energy	LB 123/LB 6411	¹¹ C monitor
Uncertainty	± 15%	± 30%	± 30-50% *
Use	All measurement points	All measurement points	Roof: 90°, 0.5-1.5 m shielding

* Estimated uncertainty.

Measurement results

Tables 4 and 5 provide the results of the dose rate measurements for the measurement points shown in Figures 2 and 3. The dose rates due to neutrons above 20 MeV were derived from the measured high-energy neutron flux assuming an average energy of about 60 MeV (derived from Monte Carlo simulations using MCNPX) and using the corresponding flux-to-dose conversion factor of 370 pSv cm² [4].

Table 4. Measured dose rates behind the forward shielding wall (mp 1) and on the roof for 0.5 m shielding. The beam was stopped in BD1. Measurement uncertainties are listed in Table 3.

	mp 1 [μ Sv/h]	r = 0.5a [μ Sv/h]	r = 0.5b [μ Sv/h]
n < 20 MeV	5.5	390	360
γ	0.5	150	150

Table 5. Measured dose rates on the roof for 0.5-3 m shielding. The beam was stopped in BD2. Measurement uncertainties are listed in Table 3.

	a: 90° [μ Sv/h]			b: 78° [μ Sv/h]	
	n > 20 MeV	n < 20 MeV	γ	n < 20 MeV	γ
r = 0.5	650	2 500	500	3 100	550
r = 1.0	80	180	30	210	30
r = 1.5	11	22	3.0	25	3.0
r = 2.0	Not meas.	3.5	0.3	4.5	0.4
r = 2.5	Not meas.	0.7	0.1	1.2	0.2
r = 3.0	Not meas.	0.2	0.1	0.3	0.1

The contributions due to high-energy neutrons at the measuring points r = 1.0(a) and r = 1.5(a) correspond to about 45-50% of the dose rate due to low-energy neutrons ($E_n < 20$ MeV), indicating that equilibrium is reached at about 1.5 m shielding thickness. For thicker shielding it is assumed that the shape of the neutron spectrum does not change. Furthermore, it is assumed that the shape of the neutron spectrum at 78° does not differ significantly from the one at 90°. For the subsequent analysis, the following assumptions were therefore used:

- For a shielding thickness of more than 1.5 m, the dose rate contribution due to high-energy neutrons corresponds to 50% of the dose rate due to low-energy neutrons ($E_n < 20$ MeV).
- For 78° and a shielding thickness up to 1.5 m, the dose rate contribution due to high-energy neutrons is the same as for 90°.

Table 6 shows the total dose rates H_{tot} ($\gamma + n < 20$ MeV + $n > 20$ MeV) and their uncertainties (using the values from Table 3) at measurement points used for the subsequent comparison with calculations.

Table 6. Total dose rates H_{tot} for measurement points, using the above assumptions for the high-energy neutron contributions

	H_{tot} [μ Sv/h] beam stop in BD2						H_{tot} [μ Sv/h] beam stop in BD1	
	r = 0.5	r = 1.0	r = 1.5	r = 2.0	r = 2.5	r = 3.0	mp 1	
a: 90°	3650±800	290±63	36±8	5.5±1.3	1.3±0.3	0.4±0.1	20°	8.8±2.0
b: 78°	4460±980	335±73	40±9	7.1±1.6	2.0±0.4	0.5±0.1		

Comparison with the calculational method

Forward shielding

Table 7 shows the measured total dose rate H_{tot} and the corresponding calculated result at the measuring point behind the forward shielding wall (mp 1) for the case that the beam is stopped in BD1. The values agree within the measurement uncertainty. For the calculation, the shielding effect of copper was assumed to be the same as that for iron. After subtracting the range of protons in copper (62.5 mm), the total effective thickness of iron used for the shielding calculation was 0.75 m; that for normal concrete was 2.0 m.

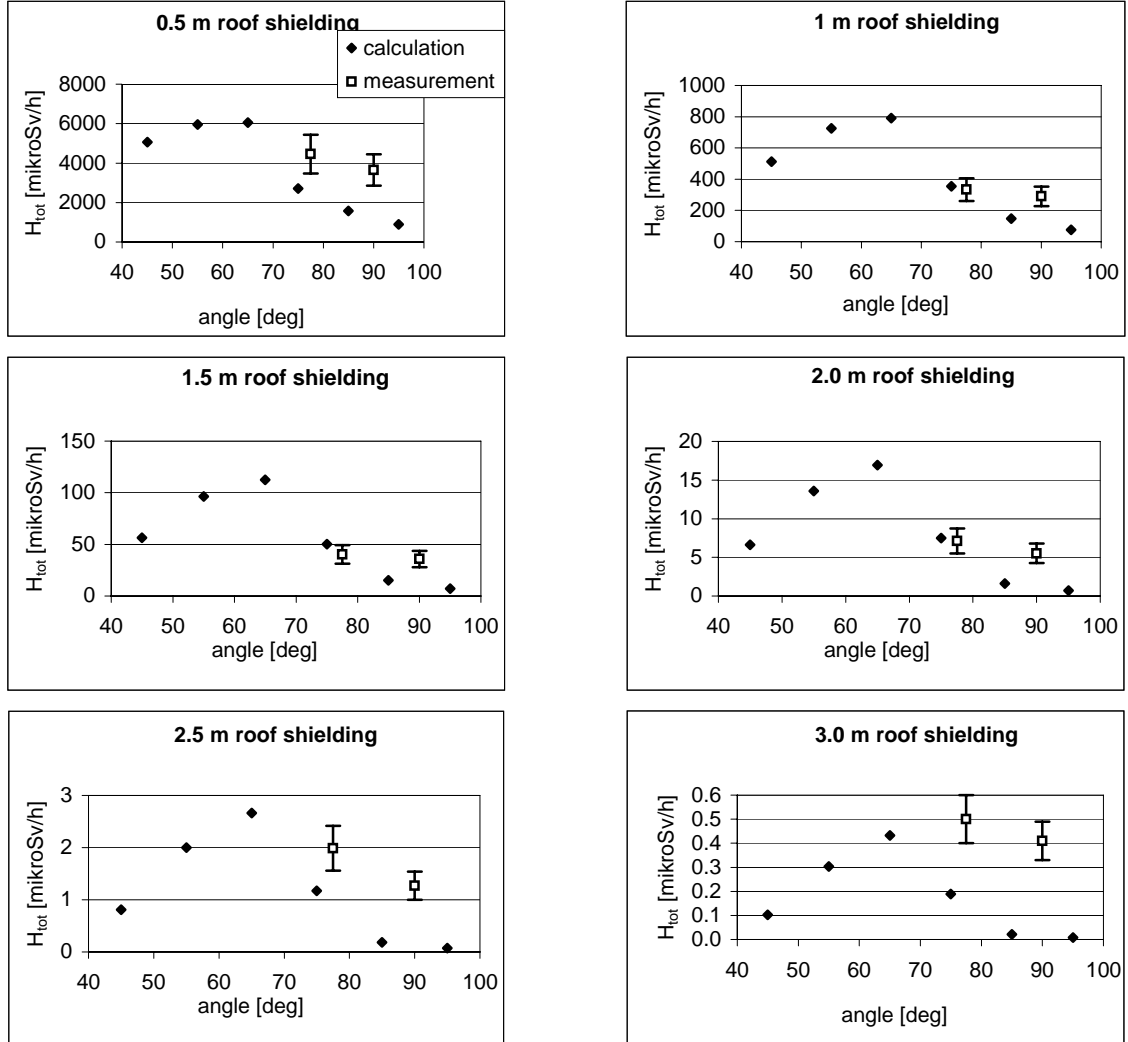
Table 7. Comparison of measured and calculated total dose rates at point mp 1 (beam stop in BD1)

	H_{tot} [μ Sv/h]	
	Measured	Calculated
mp 1	8.8±2.0	8.1

Lateral shielding

Figure 6 shows a comparison of the measured total dose rates H_{tot} on the roof (values from Table 6) with results from the calculational method, as a function of angle with respect to the beam direction and for different normal-concrete shielding thicknesses. The calculations predict a dose rate maximum at 65°. The occurrence of such a maximum is explained by the fact that while the source term H_0 becomes larger at more forward angles, the effective shielding thickness also becomes larger with $1/\sin(\theta)$. In general, the calculations underestimate the dose rates. The difference between calculation and measurement is the worse for 3 m roof shielding. However, for this shielding thickness, the measured dose rates are close to the detection limit of about 0.1 μ Sv/h and may therefore have a larger uncertainty than shown. For 0.5-2.5 m shielding, the measured dose rates at 78° agree within a factor of about 2 with the calculated results; the measured dose rates at 90° are higher by factors of about 3-10 (the worse case being observed at 2.5 m shielding).

Figure 6. Comparison of measured and calculated total dose rates on the roof. The plotted calculated points represent angular bins of $\pm 5^\circ$. The angular uncertainty of the measured points is about $\pm 2^\circ$.



Conclusions

The agreement between calculated and measured dose rates behind the forward shielding wall, consisting of iron/copper and concrete, is very good. For the case of the lateral roof shielding, the calculations tend to underestimate the dose rates. At 78° , the agreement seems to be better than at 90° , possibly indicating a smaller angular dependency than that predicted by the calculations. Additional measurements at more forward angles would be necessary to confirm this. However, disregarding the measurements at 3 m roof shielding, which were near the detection limits, the trend seems to be that the angle-dependent maximum measured dose rate would not significantly exceed the calculated dose rate at 65° (the predicted “hot spot”). In practice, therefore, the lateral shielding for PROSCAN will be designed in such a way that the calculated dose rate at the “ 65° hot spot” is below the limiting value as defined by the radiation protection specifications. For the design of the forward shielding for PROSCAN, the calculational method is considered to be sufficiently accurate.

REFERENCES

- [1] Agosteo, S., *et al.*, “Double Differential Distributions and Attenuation in Concrete for Neutrons Produced by 100-400 MeV Protons on Iron and Tissue Targets”, *Nucl. Instr. and Meth.*, B 114, 70-80 (1996).
- [2] Hirayama, H., “Intercomparison of Medium Energy Neutron Attenuation in Iron and Concrete”, *Proceedings of the Workshop on Shielding Aspects of Accelerators, Targets and Irradiation Facilities (SATIF-5)*, 18-21 July 2000, 189.
- [3] Handa, H., *et al.*, “Deep Penetration Calculations of Neutrons Up to 1.5 GeV”, *Proceedings of the Workshop on Shielding Aspects of Accelerators, Targets and Irradiation Facilities (SATIF-5)*, 18-21 July 2000, 205.
- [4] *Verordnung über die Personendosimetrie*, Swiss federal publication SR 814.501.43, Oct. 1999.

THE BIOLOGICAL SHIELD OF A HIGH-INTENSITY SPALLATION SOURCE: A MONTE CARLO DESIGN STUDY

I. Koprivnikar and E. Schachinger

Institute for Theoretical Physics, TU-Graz, Austria

Abstract

The design of high-intensity spallation sources requires the best possible estimates for the biological shield. The applicability of three-dimensional Monte Carlo simulation in the design of the biological shield of a spallation source will be discussed. In order to achieve reasonable computing times along with acceptable accuracy, biasing techniques are to be employed and it was the main purpose of this work to develop a strategy for an effective Monte Carlo simulation in shielding design. The most prominent MC computer codes, namely MCNPX and FLUKA99, have been applied to the same model spallation source (the European Spallation Source) and on the basis of the derived strategies, the design and characteristics of the target station shield are discussed. It is also the purpose of the paper to demonstrate the application of the developed strategy for the design of beam lines with their shielding using as an example the target-moderator-reflector complex of the ESS as the primary particle source.

Introduction

Spallation, the bombardment of a heavy metal target by an intense proton beam, has developed to become an important technique for the production of high-intensity neutron flux. Several new projects for high-intensity spallation sources (Spallation Neutron Source (SNS) [1] in the USA, European Spallation Source (ESS) [2] in the EU and the Neutron Science Project (NSP) [3] at JEARl in Japan) are all based on neutron production by means of a high-intensity proton beam with proton energies typically in the range of 1 to 2 GeV and beam powers of at least 1 MW. These new conditions require reinvestigating the numerical methods applied so far in the design of the biological shield of the target station. It is expected that a careful design will result in an optimal layout of the shielding and the instrumentation around the target-moderator-reflector complex (TMRC) by reducing the beam lines to minimum length under the required shield design criteria. Furthermore, the shielding costs of the spallation source comprise a significant part of the total facility costs.

Intrinsic to the simulation of radiation transport through a bulk-biological shield, heterogeneous in material, are accuracy problems as a radiation flux attenuation over several orders of magnitude is to be traced by the computer code. In the TMRC of the spallation source neutrons are produced within an energy spectrum which covers 14 decades. In addition, secondary protons and photons will also be generated but they constitute a problem of little importance compared to the shielding problems which are connected with deeply penetrating high-energy neutrons as long as a typical multi-layered shield of iron followed by concrete is investigated. These neutrons have a strong angular dependence and can, in the forward direction with respect to the proton beam, reach the energy level of the incident protons. They also cause nucleon-nucleon spallation processes deep inside the shield which additionally complicate its design. Neutrons are attenuated by elastic and inelastic scattering, and below the lowest threshold energy for inelastic scattering (the pion production threshold is about 290 MeV) they can build up and penetrate the shield in large numbers. Thus, high-energy neutrons in forward direction constitute the most important problem in shielding design.

There are, in principle, two methods which can be employed in shielding design. The classical methods are based on the discrete ordinate expansion of the transport equations [4] or on semi-empirical algorithms based on the Moyer Model [5], and, on the other hand, methods based on Monte Carlo (MC) simulation. The latter are about to become a method of great importance due to the implementation of variance reduction techniques, but also due to the increased speed and memory capacity of modern computer technology. The obvious advantages of MC simulations are:

- The particles, their spectra and distributions in the complicated geometry of the TMRC which serves as the particle source for the bulk shielding calculations can be precisely calculated.
- Charged particles and photons can be treated within one run.
- The shield with its beam lines, holes and narrow gaps which give rise to radiation leaks can be modelled in necessary detail.
- Energy deposition, material damage and activation can be determined.
- It is possible to study time-dependent processes.
- No high-energy cross-section library which is material dependent is required.

The goal of this paper is to develop a strategy for the design of a biological shield of a high-intensity spallation source using as an example the TMRC and the surrounding shielding structure of the European Spallation Source (ESS). Particular emphasis is placed on the application of variance-reducing

methods, as they are available in the two most prominent MC computer transport codes, namely MCNPX [6] and FLUKA99 [7]. These two codes use different hadron event generators and the low-energy transport (<150 MeV) uses different cross-section libraries and methods. A comparison between the results generated by MCNPX and FLUKA will, therefore, also be a prominent part of this paper.

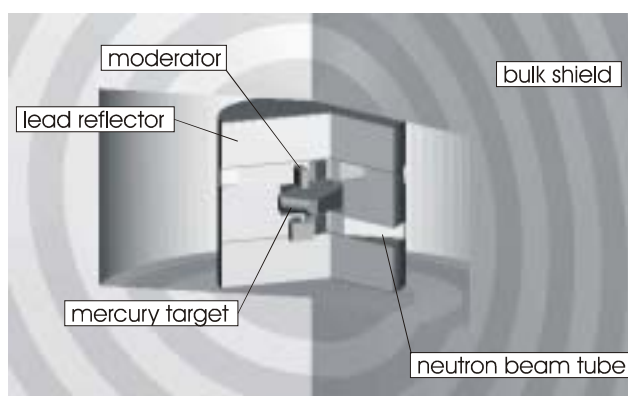
The following section investigates the applicability of three-dimensional Monte Carlo simulation in the design of the biological shield of the high-intensity neutron spallation source. In the first part we concentrate on the simulation of the particles and their energy spectra as they are generated by the TMRC. Using these results as particle source, the second part of this section develops the necessary strategies that will allow a shielding design with Monte Carlo within reasonable time and with necessary accuracy. On the basis of the derived strategies, the bulk shielding design is studied. Shielding characteristics of the biological shield are discussed in detail. We thus demonstrate the application of the strategy developed for the design of beam lines with their shielding using as an example the TMRC of the ESS as the primary particle source. We then present our conclusions in the final part of the paper.

Monte Carlo bulk shielding calculations

The TMR complex as secondary particle source

The TMRC of a typical high-intensity spallation source consists of a liquid-metal target (mercury is the main candidate), a target container built of stainless steel, a number of moderators, all encased by a cooled reflector. To calculate the secondary particles and their energy spectra as they are leaking through the outer TMRC surface, a simple cylindrical model describing the gross features of the TMRC was developed. Figure 1 presents a view of the TMRC geometry based on the preliminary design parameters of ESS [2]. The target is of slab type and has a curved front end. It is 14 cm high and 30 cm wide in the interaction region. We also added, for completeness, four ambient water moderators, two on top and two below the target, they are of dimension $12 \times 15 \times 5 \text{ cm}^3$ and they serve three beam channels which split into 18 beam lines. The moderator case consists of aluminium, 3 mm thick. Finally, the reflector has a diameter of 150 cm and is 120 cm high. It consists of lead rods which are cooled by heavy water. This heterogeneous reflector structure was homogeneously approximated so as to conserve the number of atoms and the average atomic density for representative materials.

Figure 1. Cutaway view of the TMRC geometry used in MC calculations to provide the particle source for the shielding design



The target is hit by a monoenergetic proton beam of 1.334 GeV within an elliptic cross-section of 6 cm vertical axis and 20 cm horizontal axis. Using the LAHET [8]/MCNP [9] code merger MCNPX (version 2.2.3) [6], the angular distribution and the energy spectrum of the hadron leakage (due to the spallation processes in the target region) through the surface of the TMRC have been calculated. The pre-equilibrium model [10] which describes the situation after the intranuclear cascade was set active in all calculations. Thus, an analogue simulation of the multi-particle transport is performed and a detailed description of the nucleon-meson cascade is obtained. As low-energy hadrons generated in the immediate vicinity of the TMRC are of little importance for the layout of the biological shield, this calculation has a low energy cut-off of 1 MeV for neutrons and 10 MeV for charged hadrons. The MCNPX code uses the Bertini-model [11] in the high-energy regime and below 150 MeV the continuous nuclear data library LA150 [12] is applied to generate the required cross-sections.

Figure 2 presents the energy spectrum of the hadrons leaking through the TMRC cylindrical surface at the target level in various directions relative to the incident proton beam (0 degrees). For angular resolution a 30 degrees interval has been chosen. The hadrons have been scored using a surface current tally and the cylindrical reflector surface was segmented into scoring zones 40 cm high. The data are normalised to one incident proton and presented per unit lethargy and per unit area. Figure 3(a) supplements the detailed results of Figure 2 presenting a three-dimensional plot of the energy spectrum of neutrons escaping the TMRC surface in an angular interval from 0 to 180 degrees relative to the incident proton beam. Moreover, Figure 3(b) demonstrates a mesh tally depiction of the neutron flux density distribution for energies >10 MeV important for the shielding design in the transverse section of the TMRC. The cross-section of the TMRC at target level has been divided into a rectangular grid of 1 cm³ scoring cells to create this plot. The anisotropy of the energy spectrum in its angular dependence becomes particularly transparent due to contour lines added to both graphs of Figure 3.

The statistical error in Figure 2 is below 5% in the interval 0-90 degrees and about 10% in the interval 90-180 degrees. It becomes evident from these results that the high-energy hadron radiation is strongly anisotropic in its angular distribution and that high-energy hadrons (>100 MeV) which

Figure 2. Particle leakage per incident proton, unit lethargy and unit area on the outer surface of the TMRC for various directions with respect to the incident proton beam

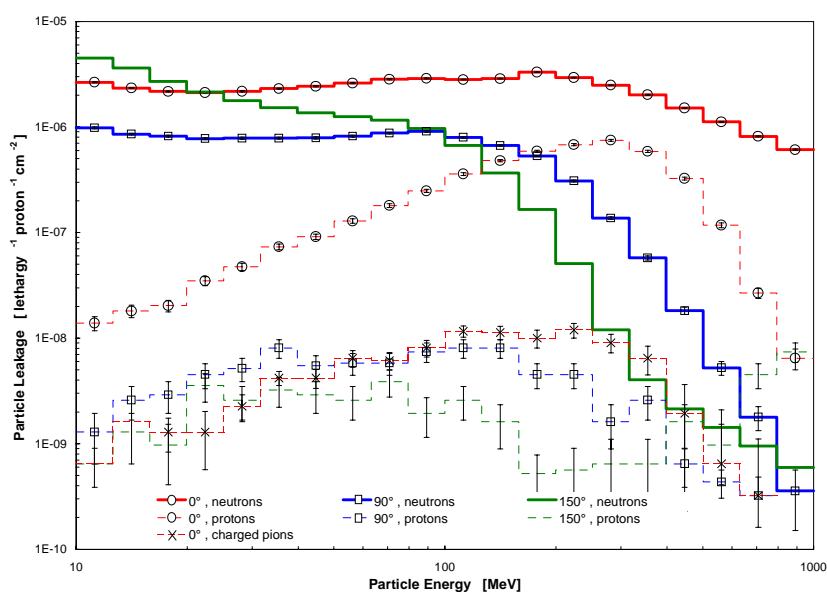
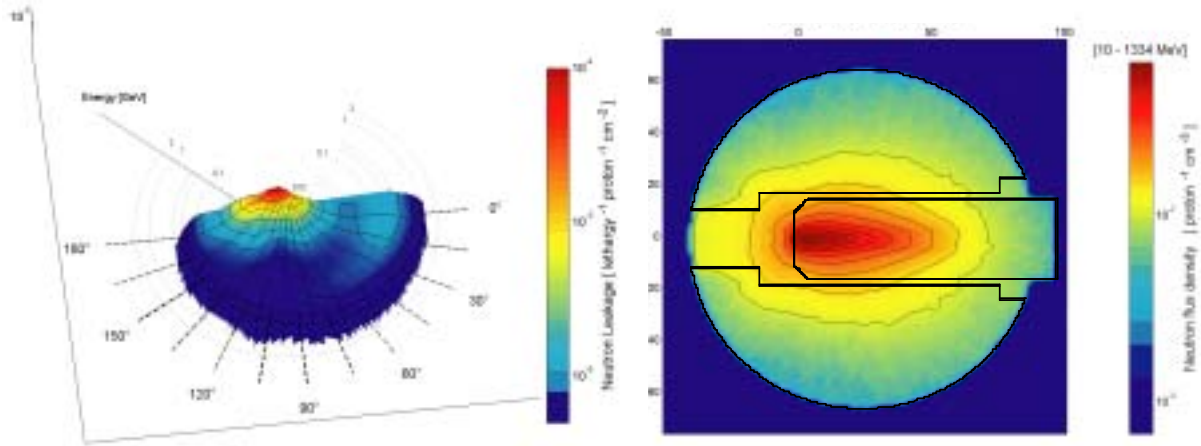


Figure 3

a) Angular distribution of the neutron leakage in neutrons per incident proton, unit lethargy and unit area at the outer surface of the TMRC for energies >1 MeV.

b) Neutron flux density in neutrons per incident proton and per area unit along the transverse section of the TMRC. Axis units are given in cm.



constitute the most significant problem in the shielding design appear predominantly in a rather small cone around the forward direction of the incident proton beam [see also Figure 3(a)]. Low-energy neutrons display a nearly isotropic angular distribution, which is not presented in this figure.

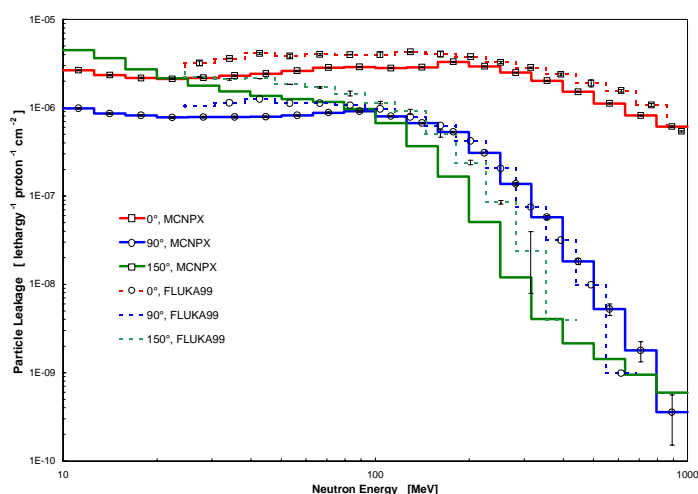
Finally, we compare our results with data generated by the other major MC particle transport code, FLUKA99, which is widely used at CERN. This code treats nuclear inelastic interactions above 20 MeV within the pre-equilibrium cascade model PENAUT [13]. To treat the particle transport below 20 MeV, the FLUKA99 code employs cross-section data based on the ENEA neutron cross-section library [7]. In these calculations the statistical error is up to 15% in the angular interval 0-90 degrees and below 40% otherwise. The reason for this greater error in comparison to the MCNPX calculations is prohibitive computing times of our FLUKA99 implementation which has not been optimised to our LINUX-PC installation. Nevertheless, Figure 4 demonstrates a surprisingly good agreement between MCNPX and FLUKA99 results despite the quite different physical models and nucleon cross-section databases implemented in these two codes. There is certainly a systematic difference to be observed as FLUKA99 gives (particularly below 100 MeV) a slightly higher hadron current leaking through the TMRC surface. The gross difference is about +10% for neutrons and about +20% for protons in the energy range considered here.

The transport data of hadrons leaving the TMRC surface are saved on file and used later on as source particles in the detailed analysis of computational strategies necessary for design of the biological shield.

Shielding design

It is the purpose of this section to develop a strategy for the design of the biological shield of the target station in its spatial dimensions and material composition in order to meet direct radiation criteria outside the shield's surface under normal conditions of operation. Moreover, the biological shield should be of minimum size and weight, it should be geometrically compact and easily be constructed. We discuss different shielding configurations of the target station (including a standard double-layered shield as well as a "sandwich" option consisting of a multiple of iron-concrete layers) on the basis of the results of our MC simulations.

Figure 4. Comparison between MCNPX and FLUKA99 results of neutron leakage spectra on the TMRC surface



Strategy for a 3-D Monte Carlo simulation

In a first step in the realisation of acceptable neutron source statistics, the results obtained for the neutron leakage at the surface of the TMRC have been parameterised in energy, position and flight angle. The neutrons penetrating the inner surface of the shield as source particles of our MC simulation are then generated on the basis of such a parameterisation. Furthermore, numerous preliminary calculations revealed that the dose rate on the outer surface of the biological shield in a given direction relative to the incident proton beam is affected by neutrons emitted from the TMRC surface only with energies greater than 1 MeV and within a radiation cone centred around the direction of interest having an opening angle of 60 degrees. Figure 5 sketches the geometrical layout in the forward direction of the incident proton beam. The top of the radiation cone is placed right at the geometrical centre of the TMRC. The source neutrons for the deep penetration calculation are then sampled from the cross-section of the TMRC's surface with the radiation cone. This cross-section is divided into three areas of same size and uniformly distributed source particles are then sampled from these areas using the parameterised source data. Furthermore, in order to achieve an adequate statistical significance of high-energy source neutrons which are only infrequently generated, a source particle biasing in the energy domain has been applied. All other source hadrons in the energy region above 10 MeV are started as they appear at the surface of TMRC (i.e. no parameterisation of the relevant transport data).

In shielding design, incident source particles have to be traced down to thermal energy, but it is also necessary to allow for spallation processes to occur in the shielding material because of the high-energy source particles emitted by the TMRC. All this requires the use of biasing techniques to assure suitable statistical significance throughout the calculated particle energy spectra as well as to allow for acceptable computer times. A combination of two biasing techniques proved to be most successful: (i) energy-dependent weight windows and (ii) source energy biasing. A weight window is a space-energy-dependent splitting and Russian roulette technique in which each space-energy phase-space cell defines a window of acceptable particle weights. If this weight is below a lower bound, Russian roulette is played and the particle is eventually eliminated. If, on the other hand, the particle is above the upper weight limit, it is split in such a way that all split particles are again within the weight window.

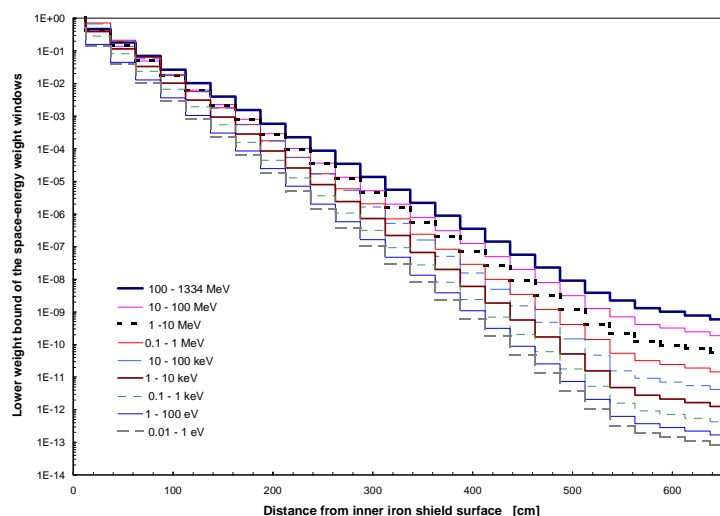
The parameters for the energy-dependent weight windows which are assigned to the spherical shells (Figure 6) have been obtained from an empirical three-step procedure. (1) Geometry sampling: Geometry importances are assigned to the different cells in such a way that an approximately constant track density with increasing penetration depth is maintained. (2) Spatial weight windows which are independent of the particle energy are then introduced with bounds inversely proportional to the geometry importances, this ensuring a roughly constant mean score of any track [14]. (3) Finally, the energy-dependent weight windows are then adjusted in an iterative procedure in a way that the track density distribution is kept constant in any energy region with increasing penetration depth. Figure 7 presents the lower weight bounds of the weight windows attached to the shells shown in Figure 6. The ratios between upper and lower weight bounds are kept constant through the geometry.

Particular care was taken to match the space-energy weight windows at those boundaries where the equilibrium neutron spectrum is disturbed due to changes in the shielding material. Calculation efficiency was also increased by space-dependent energy cut-offs which allow to terminate particle tracks of negligible influence on the dose rate outside the shield. Finally, to ensure the correct treatment of spallation processes, the pre-equilibrium model following the intranuclear cascade has been activated. Furthermore, to properly consider backscattering processes, regions of 30 cm thickness behind the TMRC surface were taken into account. All photons generated by neutrons within the shield were transported and traced.

Deep penetration characteristics

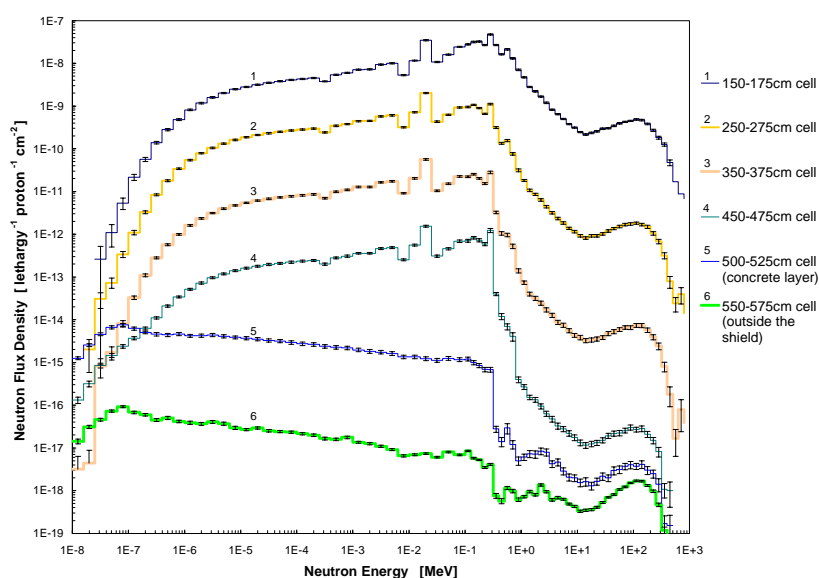
Figure 8 presents the results of a MCNPX calculation in which the strategy presented in the previous section has been utilised. What is shown is the energy distribution of neutron flux densities down to thermal energies for positions inside and outside the iron-concrete shield configuration (475 cm iron and 50 cm concrete in the forward direction). The figure presents results in the forward direction with respect to the incident proton beam. The statistical fluctuations are below 5% for each energy interval. The scoring zones are cylindrical cells of 75 cm diameter placed inside the various cylindrical shells and a track length estimator was used to calculate the neutron flux density per incident proton, per unit lethargy and per unit area.

Figure 7. Example of space-energy weight windows parameters for the forward direction as they were used in the shielding design



The figure shows clearly the attenuation of the neutron spectrum with increasing shield thickness and the major energy component shifts towards the low-energy region mainly due to elastic scattering and due to the 24 keV resonance of iron. Because of the inelastic scattering of high-energy neutrons in the iron layer the low-energy neutron flux spectrum (particularly below a few hundred keV) attenuates slower than its high-energy tail. Therefore, low-energy neutrons generated by the TMRC contribute only negligibly to the neutron spectra deep within the shield and the chosen energy threshold of 1 MeV for the source neutrons is obviously justified. The influence of the concrete component in absorbing low-energy neutrons for >475 cm is also nicely depicted in Figure 8 (line no. 5). At $r \approx 500$ cm the spectrum is already close to a $1/E$ distribution.

Figure 8. Neutron flux density energy spectra for Model 1 (in neutrons per unit lethargy, incident proton and unit area) across the shield in forward direction with respect to the proton beam

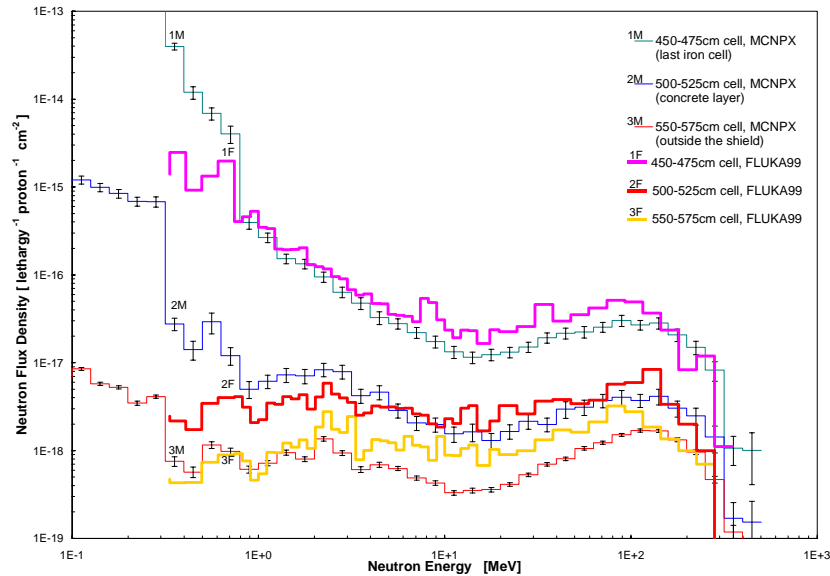


Finally, Figure 9 presents a comparison with FLUKA99 calculations for neutron energies >0.1 MeV. There are some systematic differences in the energy distribution of the neutron flux. In the high-energy region, at $r > 500$ cm, FLUKA99 reports a neutron flux which is higher by about 30% than the MCNPX result. On the other hand, in the energy range below 1 MeV the neutron flux is below the MCNPX result by almost one order of magnitude. These differences can probably be explained by differences in the cross-section libraries used by FLUKA99 and MCNPX.

Dose rates and attenuation length

Neutron dose equivalent rates have been calculated by folding the local neutron fluence with appropriate fluence-to-dose-equivalent conversion factors taken from the neutron ambient dose conversion coefficients based on the ICRP74 recommendations [15] which cover neutron energies up to 200 MeV. For higher neutron energies the conversion data have been augmented from data by Sannikov and Savitskaya [16]. Conversion factors for photons are given by A. Ferrari [17]. In actual MCNPX calculations these conversion factors simply constitute a response function for the appropriate tally.

Figure 9. Comparison of MCNPX results with FLUKA99 spectra for neutron energies >0.1 MeV in the forward direction with respect to the incident proton beam for Model 1



For all model configurations of the biological shield discussed here we assumed a 5 MW incident proton beam (average current of 3.75 mA, or 2.34×10^{16} protons/s [18] at 1.334 MeV). As a first example we study the shield (Model 1) consisting of an inner steel layer (475 cm thick in the forward direction) and an outer concrete layer (50 cm thick). The neutron equivalent dose attenuation across the shield is presented in Figure 10 for three different directions, namely 0, 45 and 90 degrees relative to the proton beam. Please note that, because of the anisotropic distribution of the source particles on the TMRC surface in 45 degree, 450 cm iron and in the 90 degree direction, only 425 cm iron is needed to get an ambient neutron dose rate the person is exposed to significantly below the design criterion of $5 \mu\text{Sv/h}$. According to Table 1, which summarises our results for the horizontal geometry of the shield there is a difference of 1 m in the thickness of the iron shield in going from forward to backward direction of the incident proton beam. In Figure 10, the solid lines correspond to the “total” neutron dose rate while dashed lines are used to show the dose rate due to “high-energy” neutrons (>10 MeV). In general, the neutron dose decreases exponentially with increasing thickness of the iron layer. The same holds for the dose rate due to high-energy neutrons but it is falling more steeply. The characteristics are quite similar in the different directions. It also becomes apparent that due to the build up of low-energy neutrons (Figure 8) in the iron layer the dose rate is dominated by the contributions of low-energy neutrons in the outer regions of this iron layer. In the low-energy region concrete has a higher shielding performance than iron due to the elastic scattering effect of hydrogen contained in concrete. Therefore, it is then the purpose of the outer concrete layer to reduce quite effectively the dose rate contribution of low-energy neutrons. This becomes particularly transparent in Figure 11, in which we compare the attenuation of the dose per incident proton in $\mu\text{Sv} \times \text{m}^2/\text{p}$ as a function of the distance from the inner shield surface for different multi-layer models in the direction of the incident proton beam. The different shield configurations investigated in this study are compared in Table 1. For the second model (Model 2), which consists of an inner iron shield (425 cm) and an outer concrete layer (100 cm), the solid line without crosses in Figure 11 corresponds to the “total” neutron dose, while the corresponding dashed line represent the “high-energy” dose. The latter shows a steep exponential decay within the iron layer and a slightly flatter decay within the concrete part. The total dose decays exponentially but with a smaller exponent until the concrete layer has been

Figure 10. Attenuation of neutron ambient dose equivalent in $\mu\text{Sv/h}$ along different directions across the shield (Model 1)

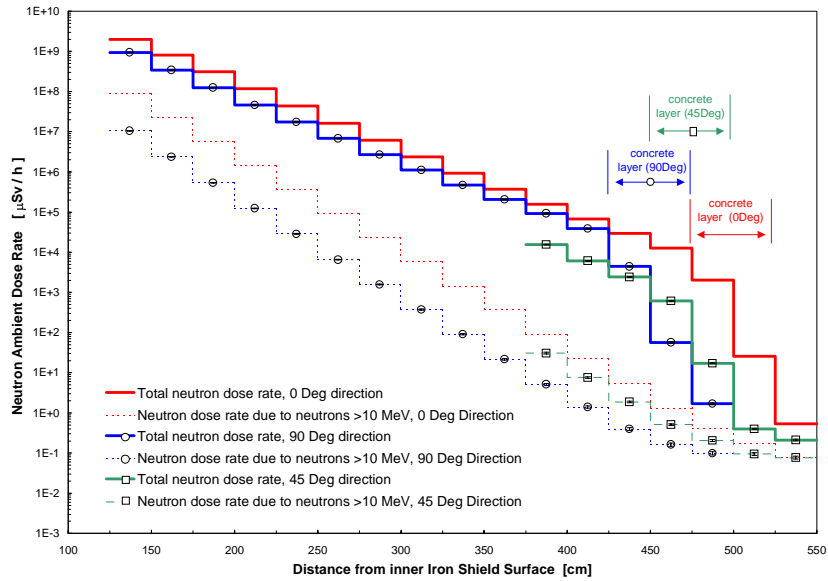
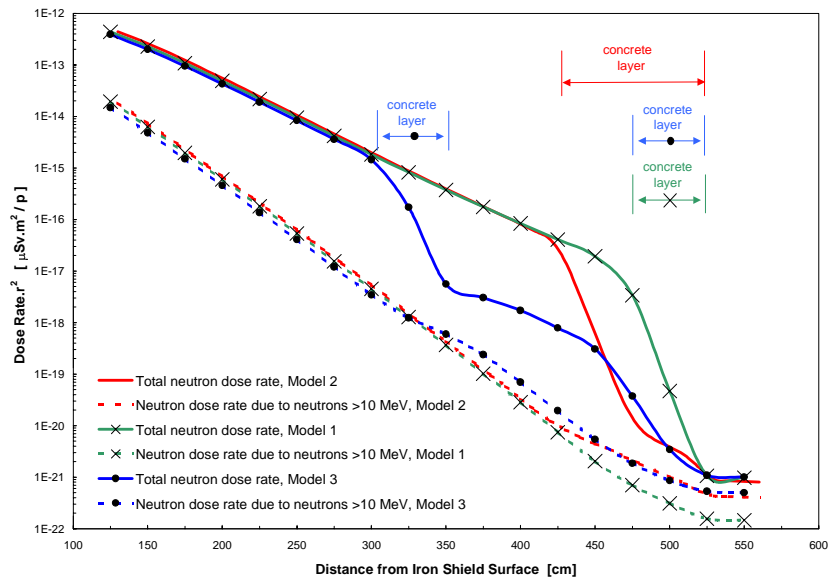


Figure 11. Attenuation of neutron dose in forward direction as a function of the distance from the inner shield surface for various shield configurations



reached. Inside this layer we see a sharp drop in the local dose rate which turns into a much flatter decay at about 70 cm concrete. This is to be compared with the results for Model 1: 475 cm iron and 50 cm concrete in the direction of the incident proton beam. The solid line represents the total and the dashed line the high-energy part of the dose rate. There is, of course, no difference between the two models up to the distance of 425 cm. The total dose rate then follows its previous course until the end of the iron layer is reached. We observe the sharp drop in the concrete layer which is now not fully utilised in its shielding potential because it ends after only 50 cm. In Model 3 we studied a “sandwich” configuration: a 325 cm thick iron layer is followed by 50 cm concrete, then there is a second iron

layer, 100 cm thick, and a final outer concrete layer with a thickness of 50 cm. This configuration results in about the same ambient dose and thus has no advantage over the much simpler two-layer configurations. Table 2 summarises our results for the neutron ambient dose equivalent rates for all three models considered in this study. It is clear from the table that the concrete layer should be about 1 m thick to take full advantage of the low-energy neutron absorption in the concrete layer.

Table 2. Comparison of the neutron ambient dose equivalent rates at the shield's surface for the three models. The statistical errors associated to the results are below 5%.

Direction with respect to the incident proton beam	Shield thickness (cm)		Total neutron dose rate ($\mu\text{Sv/h}$)	High-energy neutron dose rate ($\mu\text{Sv/h}$)	Contribution of the high energy to the total dose rate (%)
	Iron	concrete			
Model 1					
0°	475	50	0.8	0.2	25
45°	460	50	0.8	0.3	40
90°	423	50	2.0	0.3	15
180°	375	50	2.0	0.3	15
Model 2					
0°	425	100	0.75	0.6	80
Model 3					
0°	325 + 50 + 100 + 50		0.8	0.6	75

Using the results of Figure 11 it is easy to determine the neutron attenuation length in iron and in concrete. For distances beyond 200 cm from the inner surface the transmission curve becomes exponential, i.e. the neutron spectrum has reached its equilibrium. Thus, we use the results in the region 200-400 cm from the inner surface to estimate the attenuation length λ for iron, and the region beyond 450 cm for concrete. The values of the calculated dose equivalents multiplied by the square of the penetration depth were fitted with an exponential function, and Table 3 lists our results of the neutron attenuation lengths for the total and for the high-energy (>10 MeV) spectrum of neutrons generated by the 1.334 GeV incident proton beam. These numbers are of quite some importance in comparing our results with other model calculations or experiments. The literature [19] gives an attenuation length of 19 cm in iron for secondary neutrons (>20 MeV) generated by 1.3 GeV protons, which is in quite good agreement with our results.

Table 3. Attenuation of the neutron dose equivalent inside iron and concrete

Energy range [MeV]	Neutron attenuation length [cm]		
	Iron		Concrete
	0° direction	90° direction	0° direction
10 – 1 334	22±1	20±1	38±2
1E-8 – 1 334 (total)	35±1	31±1	/

It should be noted that photons contribute a maximum of 2% to the total dose rate for all configurations investigated here. The photons might be more important for lower energies of incident protons (see [20], where results are reported for a concrete shield in which neutron capture generates a high gamma component). The little photon contribution to the total dose equivalent may thus also be due to the fact that most of the shield is made of iron. Components coming from secondary protons certainly have some relevance in the forward direction of the incident proton beam. Thus, secondary

protons have been transported in all calculations (in contrast to photons), but their contribution is only a few per cent (<5%) of the total dose rate which obviously is dominated by neutrons, as was to be expected.

Finally, it is evident from our results that the double-layer shield with an inner iron layer (max. 425 cm thick) and an outer concrete layer (100 cm thick) is economically the best choice of the three models investigated here. Nevertheless, all models fulfil the requirement of an ambient dose equivalent rate of less than 5 $\mu\text{Sv/h}$.

Neutron beam line shielding design

The biological shield of the target station is penetrated by numerous neutron beam lines serving the instruments outside the bulk shield. It has been recognised that the neutronics of the neutron beam lines and their shielding is one of the very important issues in the design of intense spallation neutron sources. It is the purpose of this section to demonstrate the application of the strategy developed in the previous section for the design of beam lines with their shielding using as an example the TMRC of the ESS as the primary particle source. The target station shield of the ESS contains 18 neutron beam lines (nine on each side) viewing the moderators. The neutron beam lines are equally spaced in angle. We concentrate on the design of one beam line neglecting possible interactions between neighbouring beam lines. The most forward directed beam lines are the most problematic cases in view of shielding design and therefore, a beam line at 45 degrees with respect to the incident proton beam has been chosen for our investigation. It is important to mention that this tube has a square of cross-section 100×100 mm and views to the downstream ambient water moderator placed below the target. The calculations were again performed in two steps: a source term simulation and beam line shielding design.

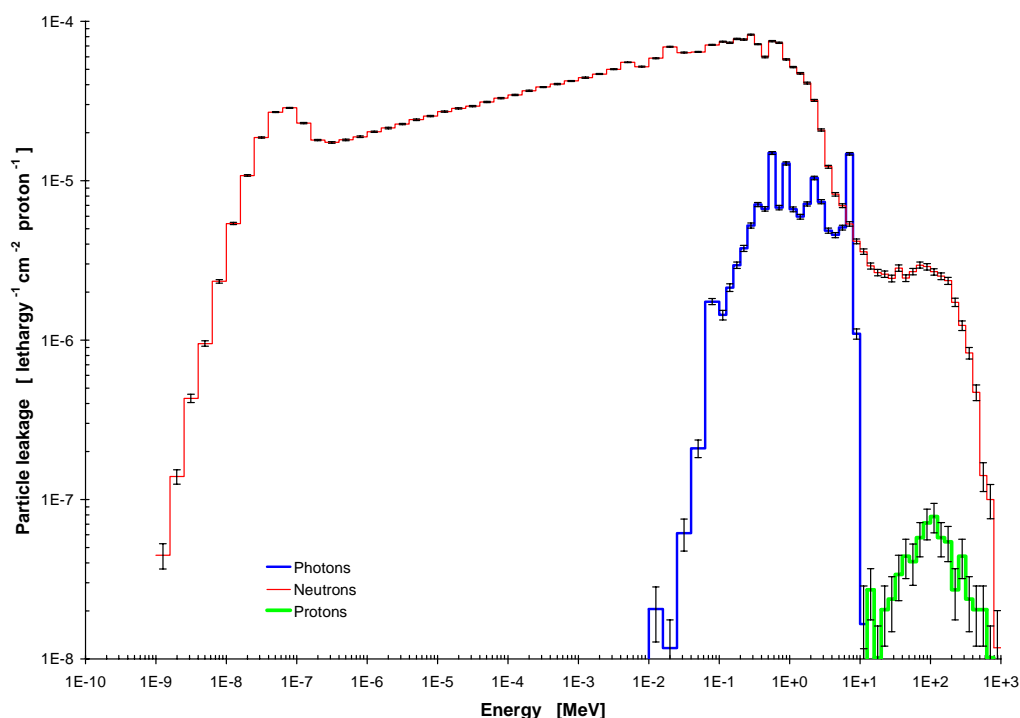
Source term simulations

For the source term simulation, the proton interaction with the mercury target and its surroundings as well as the production and transport of particles to the entrance of the neutron beam line at 45 degrees was simulated using the MCNPX code. The LA-150 transport cross-section library was used for the MCNPX calculations. To properly consider the backscattering processes in the iron shield, regions of the surrounding iron shield of 100 cm thickness behind the TMRC surface were taken into account. Spectral leakage of particles passing the TMRC outer surface were registered with a segmented tally scoring the particles leaking the TMRC within a cylinder of radius of 30 cm centred around the beam line axis. Numerous preliminary calculations revealed that this radius is properly chosen and that only particles passing the TMRC within a cylinder with a radius of 30 cm significantly affect the beam line design. Figure 12 shows the calculated distributions of neutrons, photons and protons as a function of their energy at the entrance in the neutron beam line. We can easily identify the typical spallation neutron spectrum with a thermal peak due to the presence of the hydrogenic moderator. The photon energy spectrum extends from several keV up to several MeV.

Neutron beam line neutronics and shielding design

To obtain acceptable particle neutron source statistics in the second step of the simulation, a parametrisation of the particle distribution on energy, position and angle, at the entrance to the neutron beam line was prepared. For the parametrisation, the geometric cross-section of the TMRC with the radiation cylinder was segmented in three concentric areas. For the resolution of the neutron starting

Figure 12. Distributions of neutrons, photons and protons as a function of their energy at the entrance in the 45° neutron beam line



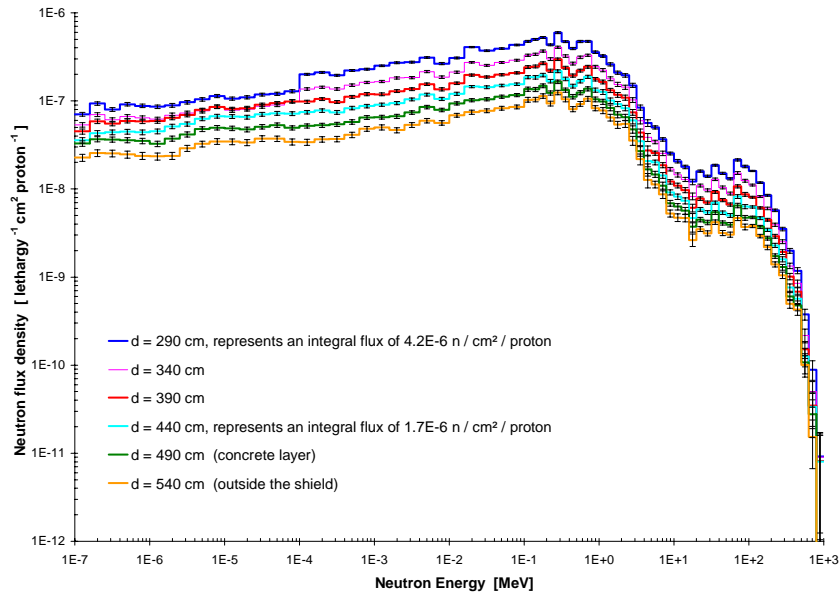
angles, an interval of 1° for directions within a declination of 10° from the neutron beam line axis, and then toward every 15° with respect to the neutron beam line axis was chosen. Thus, for each of these angular ranges a parametrised energy spectrum of emerging neutrons was obtained. The source neutrons for the beam line simulation are then sampled uniformly from the selected areas on the basis of such a parametrised distribution. All other source hadrons and prompt photons are started as they appear at the surface of TMRC (i.e. no parameterisation of the relevant transport data is used).

For variance reduction of the MCNPX results, the weight window technique was used and the weight window parameters were carefully selected.

Figure 13 presents an example of the MCNPX neutron flux in which the strategy described here and in the previous sections has been utilised. What is shown is the energy distribution of neutron flux densities down to thermal energies for positions inside the beam line as a function of the distance from the TMRC surface. It is evident from these calculations that the shape of the flux spectra does not change significantly, and that the neutron flux in the beam line decreases monotonically by about one order of magnitude every 5 m distance

Furthermore, this strategy allows the design of the beam line shield outside the target station shield. In case of the ESS, the preliminary results for the investigated beam line surrounded with a typical multi-layered shield of iron followed by a polyethylene layer have indicated that the beam line iron shield should be at least 90 cm thick perpendicular to the beam line axis. The polyethylene layer should have a thickness of 30 cm. Thus, the requirement of an ambient dose rate less than 1 μSv/h outside the shield of this beam line is fulfilled.

Figure 13. Neutron energy spectra in the neutron beam line at 45° for different distances d from the TMRC outer surface



Conclusions

The applicability of three-dimensional Monte Carlo simulation in the design of the biological shield of a high-intensity neutron spallation source has been investigated. To be concrete we considered as an example the target-moderator-reflector complex of the European Spallation Source. The task can be divided into two major steps. In a first step the particle fluences in their spatial and energy distribution on the TMRC surface are to be calculated using a not-too-detailed model of this complex. This data constitutes the source of incident particles for shielding design. For optimum data handling the neutron source particle data are further on parametrised in energy, position and flight angle. The second step concerns the actual shielding design. Variance improving techniques as they are nowadays offered by all good MC computer codes are essential in achieving acceptable computing performance and are therefore a major part in the development of a design strategy.

Iterative refinement of the various variance improving methods finally results in a stable strategy for the calculations which then allows to study various design models with only little modification of the basic set-up. The techniques discussed here can easily be extended to design studies of biological shields of accelerators, beam dumps and other high intensity, high particle energy installations.

In this study two of the most prominent MC computer codes, MCNPX and FLUKA99, have been employed. Despite major differences in the physical models and cross-section databases implemented in these two codes the final geometric layout of the biological shield is identical which is a quite satisfactory result.

REFERENCES

- [1] *National Spallation Neutron Source Conceptual Design Report*, NSNS/CDR-1/V1&2, Oak Ridge National Laboratory, Oak Ridge, TN (1997). See details in the home page at <http://www.sns.gov>.
- [2] “The European Spallation Source Study”, Vol. III, *The ESS Technical Study Report ESS-96-53-M, European Spallation Neutron Source* (1996).
- [3] Furusaka, M., H. Ikeda, “Overview of the Spallation Neutron Source Project at JHF”, *Proc. 2nd Int. Topical Meeting on Nuclear Application of Accelerator Technology*, 20-23 Sept. 1998, Gatlinburg, TN, USA, 345 (1998).
- [4] Engle, W.W., Jr., “ANISN”, *Union Carbide Nuclear Division Report*, K-1693 ORNL-TN (1969).
- [5] Moritz, L., “Using the Moyer Model at Energies Less than 1 GeV”, *Proc. of 9th Int. Conference on Radiation Shielding (ICRS-9)*, 17-22 Oct. 1999, Tsukuba, Ibaraki, Japan, *Journal of Nuclear Science and Technology*, Supplement 1, 180 (2000).
- [6] Waters, L.S., *MCNPX User’s Manual, Version 2.1.5*, Los Alamos National Laboratory, Los Alamos, NM, TPO-E83-G-UG-X-00001 (1999); <http://mcnpx.lanl.gov>.
- [7] Fassò, A., *et al.*, *FLUKA-99 User’s Manual* (2000), see details in the home page at <http://fluka.web.cern.ch/fluka/>.
- [8] Prael, R.E. and H. Lichtenstein, *User Guide to LCS: The LAHET Code System*, Los Alamos National Laboratory, Los Alamos, NM, LA-UR-89-3014 (1989).
- [9] Briesmeister, J.F., *MCNPTM – A General Monte Carlo N-particle Transport Code, Version 4B*, Los Alamos National Laboratory, LA-12625-M (1997).
- [10] Prael, R.E., “A Review of Physics Models in the LAHETTM Code”, *Proceedings of a Specialists Meeting on Intermediate Energy Nuclear Data: Models and Codes*, Issy-les-Moulineaux, France, 145 (1994).
- [11] Bertini, H.W., *Phys.Rev.* 188, 1711 (1969).
- [12] Chadwick, M.B., *et al.* “Cross-section Evaluations to 150 MeV for Accelerator-driven Systems and Implementation in MCNPX”, *Nuclear Science and Engineering*, 131, 293 (1999).
- [13] Fassò, A., *et al.* “FLUKA: Performances and Applications in the Intermediate Energy Range”, *Proc. of an AEN/NEA Specialists Meeting on Shielding Aspects of Accelerators, Targets and Irradiation Facilities*, 28-29 April 1994, Arlington, OECD Documents (1995).

- [14] Both, E.B., *A Sample Problem for Variance Reduction in MCNP*, Los Alamos National Laboratory, Los Alamos, NM, LA-10363-MS (1985).
- [15] *Conversion Coefficients for Use in Radiological Protection Against External Radiation*, International Commission on Radiation Units and Measurements (ICRU), Report 57, Bethesda, Maryland, USA (1998).
- [16] Sannikov, A.V. and E.N. Savitskaya, “Ambient Dose Equivalent Conversion Factors for High-energy Neutrons Based on the ICRP 60 Recommendations”, *Radiation Protection Dosimetry*, 70, 383 (1997).
- [17] Ferrari, A. and M. Pelliccioni, “On the Conversion Coefficients from Fluence to Ambient Dose Equivalent”, *Radiat. Prot. Dos.*, 51, 251 (1994).
- [18] Filges, D., *et al.* “Nuclear Simulation and Radiation Physics Investigations of the Target Station of the European Spallation Neutron Source”, *Nuclear Technology*, 132, 30 (2000).
- [19] Hirayama, H., “Intercomparison of Medium-energy Neutron Attenuation in Iron and Concrete”, *Proc. of the 4th Specialists Meeting on Shielding Aspects of Accelerators, Targets and Irradiation Facilities*, 17-18 September 1998, Knoxville, TN, USA (1998).
- [20] Agosteo, S., *et al.*, “Double-differential Distributions and Attenuation in Concrete for Neutrons Produced by 100-400 MeV Protons on Iron and Tissue Targets”, *NIM*, B 114, 70-80 (1996).

ATTENUATION CURVES IN CONCRETE OF NEUTRONS FROM 100-400 MeV PER NUCLEON He, C AND Ne IONS

S. Agosteo

Politecnico di Milano, Dipartimento di Energia Nucleare
Via Ponzio 34/3, 20133 Milano, Italy

T. Nakamura

KEK, Dept. of Quantum Science and Energy Engineering
Cyclotron and Radioisotope Centre, Tohoku University
Aoba, Aramaki, Aoba-ku, Sendai-shi 980-8578, Japan

M. Silari

CERN
1211 Geneva 23, Switzerland

Abstract

Data on transmission of neutrons in concrete generated by heavy ions of intermediate energies (typically of up to 1 GeV per nucleon) are of interest for shielding design of accelerators for use in both the research and in the medical field. The energy distributions of neutrons produced by ions of different species (from He to Xe) striking various targets at energies from 100 to 800 MeV per nucleon were recently measured by Kurosawa, *et al.* in the angular range 0-90°. These spectra were used as input data for Monte Carlo simulations performed with the FLUKA code to determine source terms and attenuation lengths in ordinary concrete. Here, calculations are presented for 100 MeV/u helium ions on a Cu target, 100 MeV/u carbon ions on C and Cu, 100 MeV/u neon ions on Cu and Pb, 400 MeV/u carbon ions on C, Al, Cu and Pb. The results include the contributions of all secondaries. Some of the resulting attenuation curves are best fitted by a double exponential function rather than the usual single one. The effect of various approximations introduced in the simulations is discussed.

Introduction

Experimental data on neutron emission from the interaction of heavy ion beams with matter are less abundant than data on neutron production from protons. In addition, the various Monte Carlo codes applicable for radiation protection calculations, such as FLUKA [1,2], MCNPX [3] and MARS [4], do not treat secondary particle production from ions with masses larger than one atomic mass unit. Development work is under way to implement ion transport in FLUKA, but the new version of the code has not yet been released.

Thus there is a general lack of knowledge on shielding data, i.e. source terms and attenuation lengths, for neutron produced by heavy ions in all energy ranges. Recent experimental results obtained at CERN have shown that at very high energies the spectral fluence of the secondary neutrons outside a thick shield is similar for light (protons) and heavy (lead) ions of comparable energy per nucleon stopped in a thick target. It was also shown that the approach of considering a high-energy lead ion as an independent grouping of free protons is sufficiently accurate for the purpose of evaluating the ambient dose equivalent of secondary neutrons outside thick shielding [5].

Measurements of the neutron emission from comparatively thin, unshielded, targets have shown that the neutron spectral fluence has two peaks, i.e. an isotropic evaporation component centred at 3 MeV and a high-energy peak with a maximum around 100-150 MeV. A comparison with Monte Carlo simulations for protons and experimental results for lead ions has demonstrated that a reasonable prediction can be carried out by scaling the result of a Monte Carlo calculation for protons by the projectile mass number to a power law which slightly depends on the target [6,7].

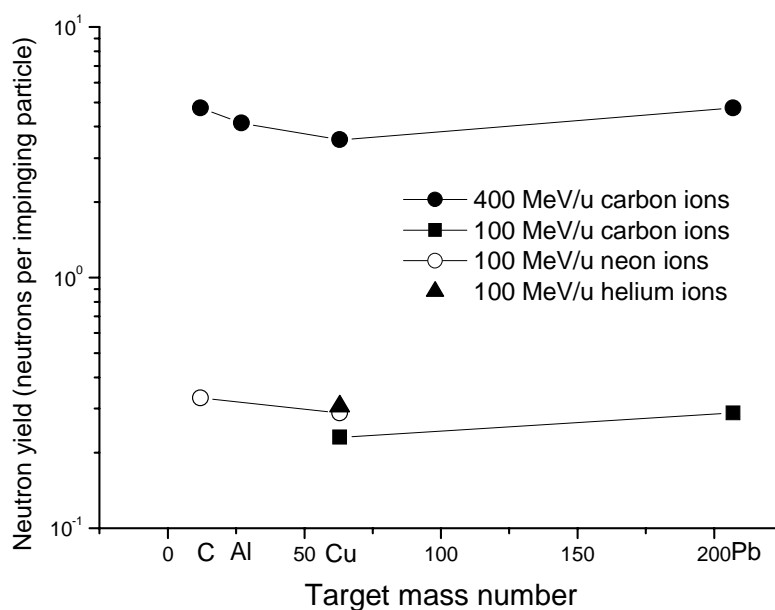
Data on transmission in concrete of neutrons generated by heavy ions of intermediate energies (typically up to several hundreds of MeV per nucleon) are of interest for shielding design of accelerators for use in both the medical and the research field. For the former, we shall mention here the various medical hadron accelerators being built for radiation therapy with ion beams. An example of the latter type of machines is the transformation of the former Low-energy Antiproton Ring (LEAR) at CERN into a Low-energy Ion Ring (LEIR) for the LHC injector chain.

Systematic measurements of yield and energy distribution in the angular range 0-90° of neutrons produced by the interaction with various targets of ion beams from carbon to xenon with energy of up to 800 MeV per nucleon were recently published by Kurosawa, *et al.* [8-10]. These spectra were used as input data for Monte Carlo simulations performed with the FLUKA code to determine source terms and attenuation lengths in ordinary concrete. Calculations are presented here for 100 MeV/u helium ions on a Cu target, 100 MeV/u carbon ions on C and Cu, 100 MeV/u neon ions on Cu and Pb, 400 MeV/u carbon ions on C, Al, Cu and Pb. The results include the contributions of all secondaries. The effect of various approximations introduced in the simulations is discussed. The means of employing the present results in shielding estimates using the Moyer model is addressed.

Neutron sources

Figure 1 shows the thick-target neutron yield (forward 2π) [8-10] as a function of the projectile mass number for the ion-target combinations considered in the present work. It should be noted that, for 400 MeV/u carbon ions, the neutron yield decreases with target mass number up to copper. The lead target yield is higher than that of copper and aluminium and is very close to that from a carbon target. A decreasing trend of the yield with target atomic number (for C and Cu) can also be observed for carbon ions at 100 MeV/u.

Figure 1. Thick-target neutron yield (forward 2π) [8-10] as a function of the projectile mass number for the ion energies considered in this work



It should be mentioned that the energy distribution of secondary neutrons exceeds the energy per nucleon of the projectile, mainly at forward angles [8-10]. The maximum energy of the neutron spectra at forward angles is about 250 MeV and 1 GeV for 100 MeV/u and 400 MeV/u ions, respectively. Therefore the corresponding attenuation lengths in concrete are expected to be larger than those of proton beams of the same energy.

Monte Carlo calculations

The following simulation geometry was used for calculating the source terms and the attenuation lengths. A point neutron source was placed at the centre of a spherical shell, 6 m thick, made up of concrete TSF-5.5 [11], with inner radius large enough (90 m) to make effects related to curvature negligible. Effects due to neutron scattering are also negligible, since the fluence of neutrons diffusing inside the concrete shell is inversely dependent on its inner surface area [12]. The fluence of outward-directed particles was scored in boundary crossings placed at various depths inside the concrete shell. The latter was also subdivided into polar sectors to account for the angular distribution of the fluence. At projectile energies of 400 MeV/u, where the energy distribution of the secondary neutrons exceeds the threshold energy for pion production (about 280 MeV [13]), the fluence of pions generated in concrete was scored in addition to that of neutrons, photons (from neutron absorption and residual nucleus de-excitation) and secondary protons. The ambient dose equivalent was estimated with the conversion coefficients of Refs. [14,15]. Geometry splitting and Russian roulette were used as variance reduction techniques for neutron transport inside the concrete shield.

As mentioned above, fluence scoring in each boundary crossing inside the concrete shells accounted only for outward-directed particles. This should minimise the effect of reflection (especially for neutrons) from the outer concrete shells, which leads to overestimate the fluence and consequently $H^*(10)$. However, reflection is not eliminated completely because, as a second-order effect, neutrons can be backscattered more than once inside the shield. Each time a multi-reflected neutron crosses a boundary outwards, it is counted in this one-way fluence scoring. Moreover, since neutrons are slowed

down in scattering events, the prompt gamma-ray component from low-energy neutrons may also be overestimated. The exact evaluation would have required a set of different simulations, each one with the correct shielding thickness, and a much longer computing time. The effect of this approximation was investigated with separate simulations considering shells with different thickness, for the case of 400 MeV/u carbon ions on copper [16]. Data were fitted with the classical two-parameter formula (single-exponential function), given by Eq. (1) in the following section. As expected, the source terms resulted to be slightly lower (in the range 2-13%, excluding the angular bins 30-40° and 80-90°) than those calculated with fictitious shells. The difference in the attenuation lengths was found to be comparatively small (a few per cent at maximum). It can therefore be concluded that, at least for 400 MeV/u carbon ions on copper, the data obtained with the fictitious shell model are sufficiently correct and representative of the real situation, if the overall non-statistical uncertainties (i.e. cross-sections, nuclear models, concrete composition, etc.) are also taken into account.

Results

The attenuation curves in concrete at 0-10° and 80-90° for 100 MeV/u neon and 400 MeV/u carbon ions on copper are shown as an example in Figures 2 and 3, respectively. It has been shown previously [16] that neutrons are responsible for most of the dose equivalent, but also that the contribution of secondary protons cannot be completely neglected.

The data at forward angles (up to 50°) for 400 MeV/u projectiles are characterised by a build-up behaviour. No build-up is observed at larger angles and small depths (up to about 60 cm), where the curves decrease with a slope steeper than at equilibrium. This double-exponential trend also characterises the attenuation curves for 100 MeV/u ions at all angles. This effect may be explained by observing how the neutron spectra vary with depth in concrete. The following discussion refers to the spectral fluences at 80-90° in concrete shown in Figure 4 for 400 MeV/u carbon ions on copper, but holds generally for the other ion-target combinations considered in this work. At a depth of 20 cm a broad peak is present with a maximum at around 50 MeV. At larger depths, up to about 100 cm, the

Figure 2. Attenuation curves in concrete at 0-10° and 80-90° for 100 MeV/u neon ions on copper

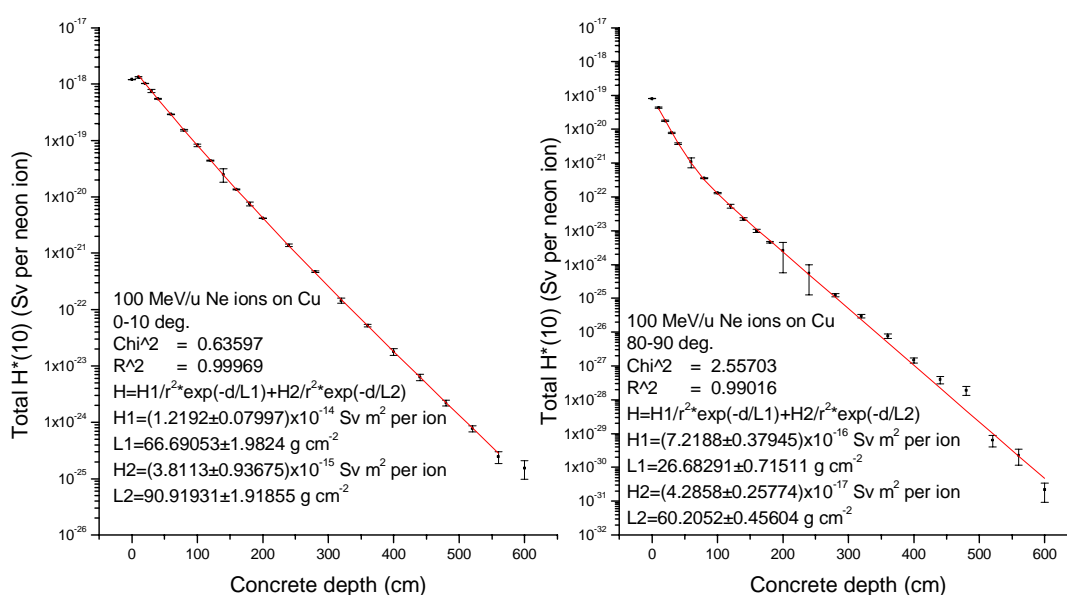


Figure 3. Attenuation curves in concrete at 0-10° and 80-90° for 400 MeV/u carbon ions on copper

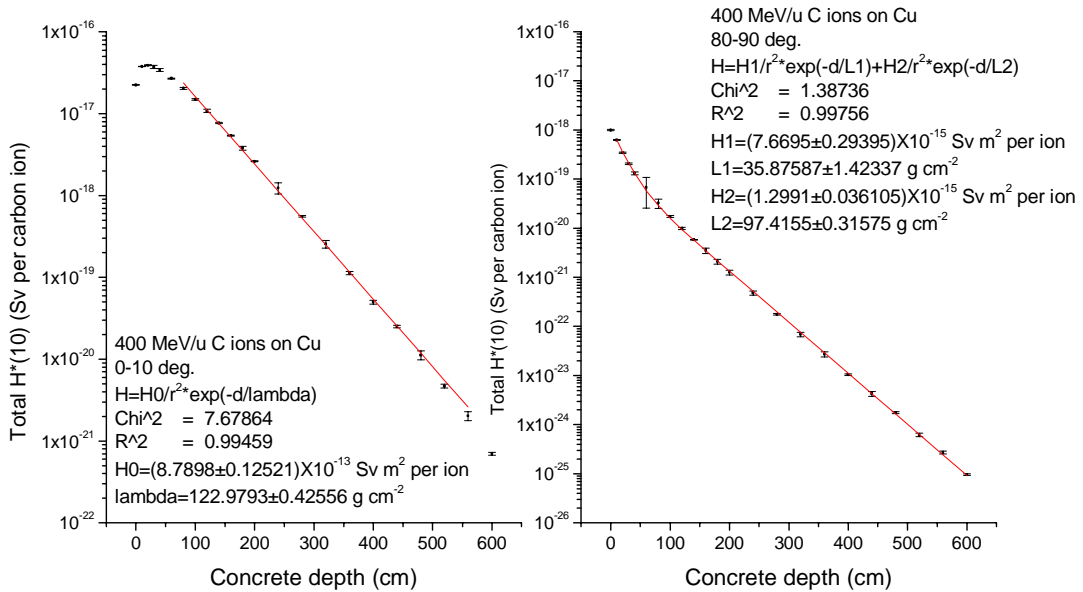
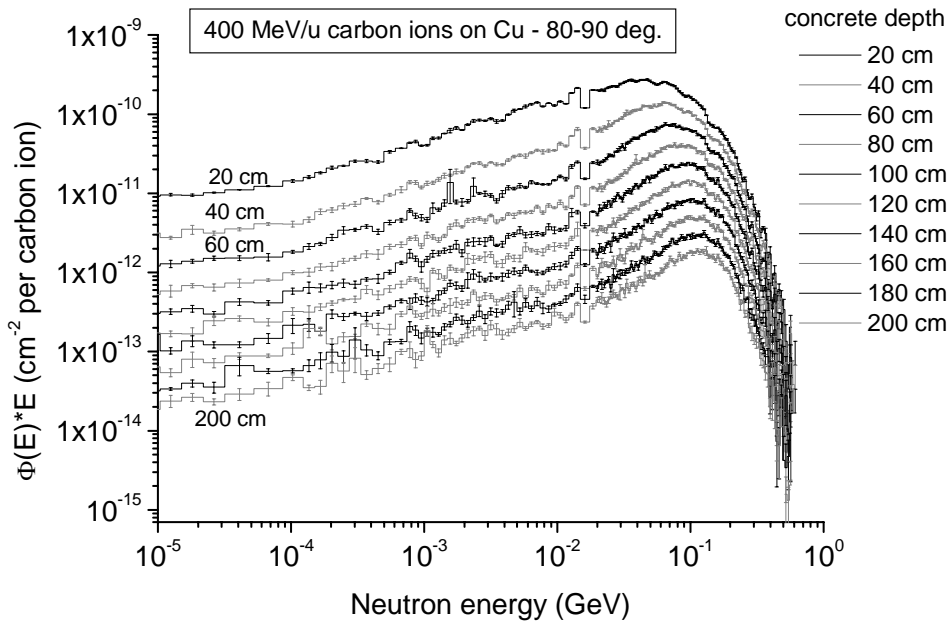


Figure 4. Neutron spectral fluences at various depths in concrete, at 80-90°, for 400 MeV/u carbon ions on copper



peak tends to get narrower and to be displaced towards higher energies (about 100 MeV). This trend is quite smooth below 100 cm and yields to a “quasi-equilibrium” situation. The spectral fluence then reaches its equilibrium. In other words, the lower-energy components of the spectrum are attenuated mostly up to about 100 cm concrete depth with a short attenuation length, giving rise to a harder and more penetrating spectral distribution (even if less intense), which is characterised by a larger attenuation length.

The attenuation curves of 400 MeV/u carbon ions on carbon, aluminium, copper and lead were fitted with the classical two-parameter formula for angles up to 50° (40° for 400 MeV/u C ions on lead):

$$H(E_p, \theta, d/\lambda) = \frac{H_0(E_p, \theta)}{r^2} \exp\left[-\frac{d}{\lambda_\theta g(\alpha)}\right] \quad (1)$$

where H is the ambient dose equivalent beyond the shield, E_p is the energy per nucleon of the primary particle (neutrons in the present case), r is the distance between the radiation source and the scoring position, θ is the angle between the direction \vec{r} and the beam axis, H_0 is the neutron source term, d is the shield thickness, λ_θ is the attenuation length and α is the angle between the direction \vec{r} and the normal to the shield surface. The function $g(\alpha) = 1$ for the spherical geometry is used in the present simulations and $g(\alpha) = \cos \alpha$ in all other cases.

A double-exponential function was used for fitting the attenuation curves of 400 MeV/u carbon ions on carbon, aluminium, copper and lead for angles above 50° and those of 100 MeV/u helium, carbon and neon ions:

$$H(E_p, \theta, d/\lambda) = \frac{H_1(E_p, \theta)}{r^2} \exp\left[-\frac{d}{\lambda_{1,\theta} g(\alpha)}\right] + \frac{H_2(E_p, \theta)}{r^2} \exp\left[-\frac{d}{\lambda_{2,\theta} g(\alpha)}\right] \quad (2)$$

where $(H_1, \lambda_{1,\theta})$ and $(H_2, \lambda_{2,\theta})$ are the source terms and the attenuation lengths of the low-depth and high-depth exponential functions, respectively. The second term of Eq. (2) describes the attenuation above 60-100 cm and obviously cannot be applied at lower depths, because it would lead to an underestimate of the ambient dose equivalent. In practice, Eq. (2) includes Eq. (1) by setting $H_0 = H_2$, $\lambda_\theta = \lambda_{2,\theta}$ and setting the first term to zero (i.e. $H_1 = \lambda_{1,\theta} = 0$).

The resulting source terms and the attenuation lengths are listed in Tables 1-9, for 100 MeV/u helium ions on a Cu target, 100 MeV/u C on C and Cu targets, 100 MeV/u Ne ions on Cu and Pb targets and 400 MeV/u C ions on C, Al, Cu and Pb targets.

Table 1. Source terms and attenuation lengths in concrete for neutrons generated by 100 MeV/u helium ions on Cu. The data were fitted using Eq. (2).

Angular bin	H_1 (Sv m ² per ion)	λ_1 (g cm ⁻²)	H_2 (Sv m ² per ion)	λ_2 (g cm ⁻²)
0-10°	$(6.43 \pm 0.76) \times 10^{-15}$	64.17 ± 4.58	$(7.11 \pm 0.92) \times 10^{-15}$	94.12 ± 1.22
10-20°	$(4.57 \pm 0.17) \times 10^{-15}$	51.11 ± 2.46	$(3.43 \pm 0.19) \times 10^{-15}$	92.34 ± 0.67
20-30°	$(3.88 \pm 0.15) \times 10^{-15}$	47.78 ± 1.69	$(1.12 \pm 0.09) \times 10^{-15}$	90.59 ± 0.94
30-40°	$(3.29 \pm 0.18) \times 10^{-15}$	35.97 ± 1.23	$(6.46 \pm 0.37) \times 10^{-16}$	82.55 ± 0.74
40-50°	$(2.23 \pm 0.15) \times 10^{-15}$	33.62 ± 1.16	$(2.64 \pm 0.16) \times 10^{-16}$	81.61 ± 0.64
50-60°	$(1.64 \pm 0.12) \times 10^{-15}$	29.43 ± 0.95	$(9.94 \pm 0.39) \times 10^{-17}$	77.22 ± 0.54
60-70°	$(1.34 \pm 0.08) \times 10^{-15}$	27.02 ± 0.74	$(4.91 \pm 0.34) \times 10^{-17}$	66.56 ± 0.77
70-80°	$(1.27 \pm 0.05) \times 10^{-15}$	24.82 ± 0.43	$(5.40 \pm 0.62) \times 10^{-17}$	50.57 ± 0.82
80-90°	$(1.33 \pm 0.08) \times 10^{-15}$	20.98 ± 0.52	$(7.40 \pm 0.80) \times 10^{-17}$	42.30 ± 0.63

Table 2. Source terms and attenuation lengths in concrete for neutrons generated by 100 MeV/u carbon ions on C. The data were fitted using Eq. (2).

Angular bin	H_1 (Sv m ² per ion)	λ_1 (g cm ⁻²)	H_2 (Sv m ² per ion)	λ_2 (g cm ⁻²)
0-10°	$(2.84 \pm 0.10) \times 10^{-14}$	59.10 ± 1.40	$(9.06 \pm 1.24) \times 10^{-15}$	86.91 ± 1.07
10-20°	$(1.31 \pm 0.04) \times 10^{-14}$	54.08 ± 1.97	$(4.08 \pm 0.46) \times 10^{-15}$	88.31 ± 1.03
20-30°	$(5.40 \pm 0.39) \times 10^{-15}$	47.99 ± 1.87	$(1.77 \pm 0.10) \times 10^{-15}$	87.59 ± 0.64
30-40°	$(2.53 \pm 0.16) \times 10^{-15}$	46.37 ± 1.82	$(6.83 \pm 0.43) \times 10^{-16}$	88.14 ± 0.68
40-50°	$(1.91 \pm 0.05) \times 10^{-15}$	40.92 ± 0.95	$(3.87 \pm 0.15) \times 10^{-16}$	87.62 ± 0.54
50-60°	$(1.10 \pm 0.06) \times 10^{-15}$	37.64 ± 1.37	$(2.14 \pm 0.09) \times 10^{-16}$	85.64 ± 0.57
60-70°	$(8.40 \pm 0.40) \times 10^{-16}$	33.13 ± 0.92	$(8.97 \pm 0.43) \times 10^{-17}$	82.52 ± 0.69
70-80°	$(5.70 \pm 0.40) \times 10^{-16}$	32.70 ± 1.24	$(3.89 \pm 0.30) \times 10^{-17}$	73.23 ± 0.73
80-90°	$(3.97 \pm 0.14) \times 10^{-16}$	31.32 ± 0.42	$(1.07 \pm 0.07) \times 10^{-17}$	73.47 ± 0.67

Table 3. Source terms and attenuation lengths in concrete for neutrons generated by 100 MeV/u carbon ions on Cu. The data were fitted using Eq. (2).

Angular bin	H_1 (Sv m ² per ion)	λ_1 (g cm ⁻²)	H_2 (Sv m ² per ion)	λ_2 (g cm ⁻²)
0-10°	$(1.65 \pm 0.64) \times 10^{-14}$	58.72 ± 1.80	$(4.44 \pm 0.80) \times 10^{-15}$	89.32 ± 1.66
10-20°	$(8.77 \pm 0.20) \times 10^{-15}$	49.23 ± 0.93	$(2.34 \pm 0.12) \times 10^{-15}$	89.70 ± 0.60
20-30°	$(4.74 \pm 0.17) \times 10^{-15}$	42.28 ± 1.23	$(1.22 \pm 0.06) \times 10^{-15}$	87.06 ± 0.57
30-40°	$(2.75 \pm 0.12) \times 10^{-15}$	37.73 ± 1.47	$(5.75 \pm 0.37) \times 10^{-16}$	81.11 ± 0.70
40-50°	$(1.91 \pm 0.05) \times 10^{-15}$	40.92 ± 0.95	$(3.87 \pm 0.15) \times 10^{-16}$	87.62 ± 0.54
50-60°	$(1.70 \pm 0.15) \times 10^{-15}$	39.34 ± 1.58	$(2.15 \pm 0.19) \times 10^{-16}$	76.87 ± 0.87
60-70°	$(1.27 \pm 0.13) \times 10^{-15}$	31.47 ± 1.50	$(1.88 \pm 0.12) \times 10^{-16}$	64.74 ± 0.61
70-80°	$(6.56 \pm 0.83) \times 10^{-16}$	30.91 ± 1.31	$(5.51 \pm 0.32) \times 10^{-17}$	70.40 ± 0.57
80-90°	$(4.44 \pm 0.25) \times 10^{-16}$	33.27 ± 0.60	$(2.16 \pm 0.11) \times 10^{-17}$	82.88 ± 0.50

Table 4. Source terms and attenuation lengths in concrete for neutrons generated by 100 MeV/u neon ions on Cu. The data were fitted using Eq. (2).

Angular bin	H_1 (Sv m ² per ion)	λ_1 (g cm ⁻²)	H_2 (Sv m ² per ion)	λ_2 (g cm ⁻²)
0-10°	$(1.22 \pm 0.08) \times 10^{-14}$	66.69 ± 1.98	$(3.81 \pm 0.94) \times 10^{-15}$	90.92 ± 1.92
10-20°	$(6.61 \pm 0.23) \times 10^{-15}$	62.68 ± 1.42	$(1.75 \pm 0.27) \times 10^{-15}$	94.15 ± 1.43
20-30°	$(3.64 \pm 0.06) \times 10^{-15}$	47.27 ± 0.94	$(1.44 \pm 0.07) \times 10^{-15}$	93.38 ± 0.63
30-40°	$(2.72 \pm 0.45) \times 10^{-15}$	39.06 ± 0.81	$(8.13 \pm 0.21) \times 10^{-16}$	94.28 ± 0.51
40-50°	$(2.04 \pm 0.04) \times 10^{-15}$	38.43 ± 0.65	$(3.14 \pm 0.13) \times 10^{-16}$	92.73 ± 0.70
50-60°	$(1.62 \pm 0.22) \times 10^{-15}$	30.75 ± 0.50	$(1.54 \pm 0.06) \times 10^{-16}$	85.70 ± 0.58
60-70°	$(1.12 \pm 0.05) \times 10^{-15}$	30.65 ± 0.65	$(5.95 \pm 0.36) \times 10^{-17}$	79.97 ± 0.76
70-80°	$(9.42 \pm 0.40) \times 10^{-16}$	27.95 ± 0.56	$(5.48 \pm 0.33) \times 10^{-17}$	67.15 ± 0.61
80-90°	$(7.22 \pm 0.38) \times 10^{-16}$	26.68 ± 0.71	$(4.29 \pm 0.26) \times 10^{-17}$	60.20 ± 0.46

Table 5. Source terms and attenuation lengths in concrete for neutrons generated by 100 MeV/u neon ions on Pb. The data were fitted using Eq. (2).

Angular bin	H_1 (Sv m ² per ion)	λ_1 (g cm ⁻²)	H_2 (Sv m ² per ion)	λ_2 (g cm ⁻²)
0-10°	$(7.68 \pm 0.80) \times 10^{-15}$	58.15 ± 4.16	$(5.47 \pm 1.09) \times 10^{-15}$	81.31 ± 1.35
10-20°	$(4.63 \pm 0.22) \times 10^{-15}$	54.60 ± 2.89	$(2.34 \pm 0.30) \times 10^{-15}$	85.69 ± 1.14
20-30°	$(3.52 \pm 0.06) \times 10^{-15}$	46.27 ± 1.24	$(1.03 \pm 0.06) \times 10^{-15}$	87.68 ± 0.69
30-40°	$(2.74 \pm 0.17) \times 10^{-15}$	36.31 ± 1.68	$(6.70 \pm 0.35) \times 10^{-16}$	83.54 ± 0.62
40-50°	$(2.01 \pm 0.11) \times 10^{-15}$	37.50 ± 1.26	$(2.88 \pm 0.17) \times 10^{-16}$	87.32 ± 0.72
50-60°	$(1.65 \pm 0.07) \times 10^{-15}$	32.24 ± 0.73	$(1.76 \pm 0.01) \times 10^{-16}$	82.24 ± 0.60
60-70°	$(1.06 \pm 0.07) \times 10^{-15}$	33.51 ± 1.07	$(7.35 \pm 0.48) \times 10^{-17}$	81.99 ± 0.87
70-80°	$(7.03 \pm 0.40) \times 10^{-16}$	37.63 ± 0.78	$(3.00 \pm 0.29) \times 10^{-17}$	77.52 ± 0.95
80-90°	$(1.03 \pm 0.04) \times 10^{-15}$	28.11 ± 0.45	$(2.26 \pm 0.14) \times 10^{-17}$	74.47 ± 0.59

Table 6. Source terms and attenuation lengths in concrete for neutrons generated by 400 MeV/u carbon ions on C. The data were fitted using Eq. (2).

Angular bin	H_1 (Sv m ² per ion)	λ_1 (g cm ⁻²)	H_2 (Sv m ² per ion)	λ_2 (g cm ⁻²)
0-10°			$(1.93 \pm 0.02) \times 10^{-12}$	120.98 ± 0.21
10-20°			$(4.37 \pm 0.02) \times 10^{-13}$	120.21 ± 0.14
20-30°			$(1.50 \pm 0.01) \times 10^{-13}$	122.15 ± 0.20
30-40°			$(5.75 \pm 0.03) \times 10^{-14}$	122.18 ± 0.21
40-50°			$(2.28 \pm 0.02) \times 10^{-14}$	117.03 ± 0.21
50-60°	$(1.03 \pm 0.05) \times 10^{-14}$	49.28 ± 2.27	$(7.53 \pm 0.15) \times 10^{-15}$	111.74 ± 0.34
60-70°	$(8.98 \pm 0.33) \times 10^{-15}$	50.07 ± 1.59	$(3.19 \pm 0.14) \times 10^{-15}$	103.86 ± 0.65
70-80°	$(7.62 \pm 0.28) \times 10^{-15}$	48.43 ± 1.40	$(1.49 \pm 0.07) \times 10^{-15}$	102.23 ± 0.64
80-90°	$(6.11 \pm 0.33) \times 10^{-15}$	39.88 ± 1.07	$(9.54 \pm 0.26) \times 10^{-16}$	95.87 ± 0.36

Table 7. Source terms and attenuation lengths in concrete for neutrons generated by 400 MeV/u carbon ions on Al. The data were fitted using Eq. (2).

Angular bin	H_1 (Sv m ² per ion)	λ_1 (g cm ⁻²)	H_2 (Sv m ² per ion)	λ_2 (g cm ⁻²)
0-10°			$(1.38 \pm 0.01) \times 10^{-12}$	117.92 ± 0.18
10-20°			$(2.69 \pm 0.01) \times 10^{-13}$	121.15 ± 0.19
20-30°			$(1.14 \pm 0.01) \times 10^{-13}$	119.69 ± 0.20
30-40°			$(5.61 \pm 0.05) \times 10^{-14}$	117.67 ± 0.21
40-50°			$(2.03 \pm 0.01) \times 10^{-14}$	114.30 ± 0.22
50-60°	$(9.60 \pm 0.95) \times 10^{-15}$	45.22 ± 3.02	$(7.51 \pm 0.18) \times 10^{-15}$	109.87 ± 0.32
60-70°	$(8.14 \pm 0.38) \times 10^{-15}$	53.92 ± 2.75	$(2.85 \pm 0.21) \times 10^{-15}$	106.68 ± 0.98
70-80°	$(7.33 \pm 0.43) \times 10^{-15}$	48.25 ± 1.73	$(1.73 \pm 0.06) \times 10^{-15}$	102.60 ± 0.45
80-90°	$(5.96 \pm 0.22) \times 10^{-15}$	46.32 ± 1.30	$(9.05 \pm 0.47) \times 10^{-16}$	99.41 ± 0.50

Table 8. Source terms and attenuation lengths in concrete for neutrons generated by 400 MeV/u carbon ions on Cu. The data were fitted using Eq. (2).

Angular bin	H_1 (Sv m ² per ion)	λ_1 (g cm ⁻²)	H_2 (Sv m ² per ion)	λ_2 (g cm ⁻²)
0-10°			$(8.79 \pm 0.12) \times 10^{-13}$	122.98 ± 0.43
10-20°			$(2.13 \pm 0.01) \times 10^{-13}$	121.62 ± 0.14
20-30°			$(8.75 \pm 0.06) \times 10^{-14}$	121.21 ± 0.19
30-40°			$(3.58 \pm 0.01) \times 10^{-14}$	122.47 ± 0.15
40-50°			$(1.93 \pm 0.02) \times 10^{-14}$	119.16 ± 0.19
50-60°	$(1.11 \pm 0.13) \times 10^{-14}$	30.93 ± 2.28	$(8.10 \pm 0.09) \times 10^{-15}$	120.91 ± 0.24
60-70°	$(7.83 \pm 0.56) \times 10^{-15}$	47.47 ± 2.63	$(2.91 \pm 0.10) \times 10^{-15}$	116.03 ± 2.53
70-80°	$(6.78 \pm 0.51) \times 10^{-15}$	45.61 ± 2.05	$(1.88 \pm 0.06) \times 10^{-15}$	102.46 ± 0.39
80-90°	$(7.67 \pm 0.29) \times 10^{-15}$	35.88 ± 1.42	$(1.30 \pm 0.04) \times 10^{-15}$	97.42 ± 0.32

Table 9. Source terms and attenuation lengths in concrete for neutrons generated by 400 MeV/u carbon ions on Pb. The data were fitted using Eq. (2).

Angular bin	H_1 (Sv m ² per ion)	λ_1 (g cm ⁻²)	H_2 (Sv m ² per ion)	λ_2 (g cm ⁻²)
0-10°			$(7.17 \pm 0.10) \times 10^{-13}$	118.11 ± 0.25
10-20°			$(1.68 \pm 0.01) \times 10^{-13}$	121.67 ± 0.22
20-30°			$(7.05 \pm 0.06) \times 10^{-14}$	121.44 ± 0.23
30-40°			$(3.05 \pm 0.02) \times 10^{-14}$	115.65 ± 0.25
40-50°	$(2.12 \pm 0.24) \times 10^{-14}$	30.99 ± 2.40	$(1.29 \pm 0.02) \times 10^{-14}$	108.64 ± 0.32
50-60°	$(1.50 \pm 0.13) \times 10^{-14}$	37.18 ± 2.03	$(6.17 \pm 0.14) \times 10^{-15}$	100.52 ± 0.40
60-70°	$(1.67 \pm 0.10) \times 10^{-14}$	33.88 ± 1.26	$(3.67 \pm 0.09) \times 10^{-15}$	95.55 ± 0.37
70-80°	$(1.01 \pm 0.10) \times 10^{-14}$	41.37 ± 2.05	$(2.26 \pm 0.08) \times 10^{-15}$	98.40 ± 0.35
80-90°	$(1.08 \pm 0.06) \times 10^{-14}$	37.67 ± 1.38	$(1.03 \pm 0.47) \times 10^{-15}$	99.84 ± 0.34

The source terms and attenuation lengths tend to decrease with increasing angle, according to the yield and the energy distribution of secondary neutrons [8-10]. In the interval 0-30° the source terms for 400 MeV/u carbon ions on carbon are higher (up to a factor 1.6) than those for aluminium. At forward angles the source terms for C ions on C and Al are higher than those for copper and lead. This difference tends to vanish at larger angles, where the attenuation lengths are also comparable. This is in agreement with the high-energy components (above about 20 MeV) of the neutron yield for C ions on C, Al, Cu and Pb targets [8], which do not differ too much at large angles. The source terms and the attenuation lengths for 400 MeV/u carbon ions on carbon and copper targets are also given in Ref. [16], where a single-exponential function was used for data fitting. The resulting parameters at large angles agree satisfactorily with the H_2 and λ_2 calculated in the present work for the same ion-target combinations.

Conclusions

The approach of considering an ion of mass A equivalent to a bunch of A protons is most likely not a good approximation in the energy range discussed here. This is correct at ultra-relativistic energies, i.e. hundreds of GeV/u, as has been experimentally verified in recent years [5-7,17], but here

it may lead to underestimates rather than overestimates. A quick comparison of shielding data for 100 MeV/u Ne ions on a copper target (resulting from the present Monte Carlo calculations) with those for 100 MeV protons on an iron target [18], seems to indicate that assuming the ion as a bunch of free protons would underestimate the shielding requirement by a factor which becomes increasingly larger with increasing shielding thickness. This is most likely because secondary neutrons from ion beams have a spectrum that extends to a maximum energy which is almost twice the projectile energy per nucleon, as has been shown above. This penetrating component would dominate the radiation dose past a thick shield. This trend will be studied in more detail in the continuation of this work.

REFERENCES

- [1] Fassò, A., A. Ferrari, P.R. Sala, “Electron-photon Transport in FLUKA: Status”, *Proc. of the Monte Carlo 2000 Conference*, Lisbon, 23-26 October 2000, A. Kling, F. Barao, M. Nakagawa, L. Tavora, P. Vaz, eds., Springer-Verlag, Berlin, pp. 159-164 (2001).
- [2] Fassò, A., A. Ferrari, J. Ranft, P.R. Sala, “FLUKA: Status and Prospective for Hadronic Applications”, *Proc. of the Monte Carlo 2000 Conference*, Lisbon, 23-26 October 2000, A. Kling, F. Barao, M. Nakagawa, L. Tavora, P. Vaz, eds., Springer-Verlag, Berlin, pp. 955-960 (2001).
- [3] Prael, R.E., H. Lichtenstein, *User Guide to LCS: The LAHET Code System*, LA-UR-89-3014, Los Alamos National Laboratory, Los Alamos, New Mexico (1989).
- [4] Mokhov, N.V., S.I. Striganov, A. Van Ginneken, S.G. Mashnik, A.J. Sierk and J. Ranft, “MARS Code Developments”, *Proc. of the 4th Workshop on Simulating Accelerator Radiation Environments (SARE-4)*, Knoxville (TN, USA), 14-16 September 1998, T. Gabriel, ed., ORNL, 87-99 (1998).
- [5] Agosteo, S., C. Birattari, A. Foglio Para, M. Silari and L. Ulrici, “Neutron Measurements Around a Beam Dump Bombarded by High-energy Protons and Lead Ions”, *Nuclear Instruments and Methods*, A 459, 58-65 (2001).
- [6] Agosteo, S., C. Birattari, A. Foglio Para, A. Mitaroff, M. Silari and L. Ulrici, “90° Neutron Emission from High-energy Protons and Lead Ions on a Thin Lead Target”, *Nuclear Instruments and Methods*, A 476, 63-68 (2002).
- [7] Agosteo, S., C. Birattari, A. Foglio Para, L. Gini, A. Mitaroff, M. Silari and L. Ulrici, “Neutron Production from 158 GeV/c per Nucleon Lead Ions on Thin Copper and Lead Targets in the Angular Range 30°-135°”, submitted for publication in *Nuclear Instruments and Methods B*.
- [8] Kurosawa, T., N. Nakao, T. Nakamura, Y. Uwamino, T. Shibata, N. Nakanishi, A. Fukumura and K. Murakami, “Measurements of Secondary Neutrons Produced from Thick Targets Bombarded by High-energy Helium and Carbon Ions”, *Nuclear Science and Engineering*, 132, 30-57 (1999).

- [9] Kurosawa, T., N. Nakao, T. Nakamura, Y. Uwamino, T. Shibata, A. Fukumura and K. Murakami, "Measurements of Secondary Neutrons Produced from Thick Targets Bombarded by High-energy Neon Ions", *Journal of Nuclear Science and Technology*, 36, 41-53 (1999).
- [10] Kurosawa, T., N. Nakao, T. Nakamura, H. Iwase, H. Sato, Y. Uwamino and A. Fukumura, "Neutron Yields from Thick C, Al, Cu and Pb Targets Bombarded by 400 MeV/Nucleon Ar, Fe, Xe and 800 MeV/Nucleon Si Ions", *Physical Review*, C 62, third series, No. 4 (2000).
- [11] National Council of Radiation Protection, *Radiation Protection Design Guidelines for 100 MeV Particle Accelerators Facilities*, NCRP Report 51 (1977).
- [12] McCall, R.C., T.M. Jenkins, R.A. Shore, "Transport of Accelerator-produced Neutrons in a Concrete Room", *IEEE Trans. Nucl. Sci.*, NS-26, 1593-1602 (1979).
- [13] Ferrari, A., P.R. Sala, "The Physics of High-energy Reactions", *Proceedings of the Workshop on Nuclear Reaction Data and Nuclear Reactor Physics, Design and Safety, International Centre for Theoretical Physics, Miramare-Trieste (Italy)*, 15 April-17 May 1996, A. Gandini and G. Reffo, eds., Vol. 2, *World Scientific*, 424-532 (1998).
- [14] Ferrari, A. and M. Pelliccioni, "Fluence-to-dose Equivalent Conversion Data and Effective Quality Factors for High-energy Neutrons", *Radiation Protection Dosimetry*, 76, 215-224 (1998).
- [15] Pelliccioni, M., "Overview of Fluence-to-effective Dose and Fluence-to-ambient Dose Equivalent Conversion Coefficients for High-energy Radiation Calculated Using the FLUKA Code", *Radiation Protection Dosimetry*, 88, 279-297 (2000).
- [16] Agosteo, S., "Radiation Protection at Medical Accelerators", *Radiation Protection Dosimetry*, 96, 393-406 (2001).
- [17] Agosteo, S., C. Birattari, A. Foglio Para, E. Nava, M. Silari and L. Ulrici, "Neutron Measurements in the Stray Field Produced by 158 GeV/c Lead Ion Beams", *Health Physics*, 75, 619-629 (1998).
- [18] Agosteo, S., A. Fassò, A. Ferrari, P.R. Sala, M. Silari and P. Tabarelli de Fatis, "Double-differential Distributions and Attenuation in Concrete for Neutrons Produced by 100-400 MeV Protons on Iron and Tissue Targets", *Nuclear Instruments and Methods*, B 114, 70-80 (1996).

THE EFFECT OF A BEAM LOSS AT THE PS/nTOF INTERFACE OF THE CERN PS COMPLEX

Marco Silari, Helmut Vincke
CERN, 1211 Geneva 23, Switzerland

Abstract

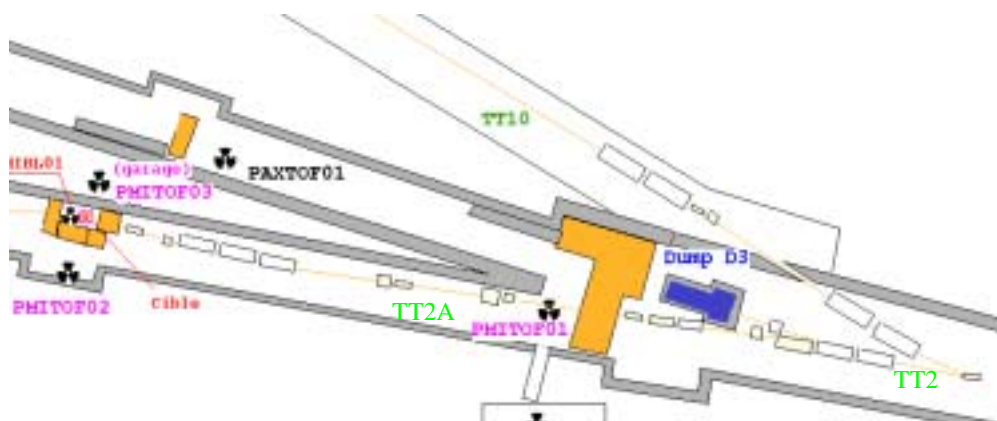
This paper discusses the potential radiation hazard caused by beam losses in one of the transfer lines (TT2) of the CERN Proton Synchrotron, close to the point where the beam is split and can be directed towards the Super Proton Synchrotron via the TT10 tunnel, sent to the nTOF experiment installed in the extension of TT2 (TT2A tunnel), or stopped in a massive dump. The TT2 area is separated from the downstream TT2A zone of nTOF by a 4.8 m thick concrete wall. A full beam loss in TT2 could generate a serious radiation hazard on the TT2A side of the shielding wall. Several beam loss scenarios were investigated through Monte Carlo simulations performed with the FLUKA code. The various radiation components making up the dose equivalent rate in TT2A were assessed. It was found that the dose equivalent is dominated by either muons (mainly originating from pion decay) or neutrons produced in hadronic cascades inside the shielding wall, depending on the point at which the beam is lost. A comparison between simulation results and measurements is made.

Introduction

The CERN Proton Synchrotron (PS) accelerates protons up to 26 GeV/c with an intensity of up to 3×10^{13} protons per pulse and has a cycle of 1.2 s. Two pulses are transferred to the Super Proton Synchrotron (SPS) each SPS super-cycle (a typical 14.4 s SPS super-cycle containing 12 PS pulses) to be further accelerated to 450 GeV/c. One to four pulses per super-cycle are sent to the nTOF experiment. The rest of the beam is partly used for fixed target experiments in the East Experimental Hall, and partly sent to a conversion target to generate antiprotons for the Antiproton Decelerator (AD) and related experiments. This paper discusses the potential radiation hazard caused by beam losses in the TT2 transfer line close to the point where the PS beam is split. Here, the beam can be directed towards the SPS via the TT10 tunnel, sent to the nTOF experiment installed in the prolongation of TT2 (called TT2A), or stopped in a massive dump (called D3). This dump consists of an iron core 7.2 m thick, surrounded by 80 cm of concrete. Figure 1 shows a sketch of the area. The TT2 area is separated from the downstream TT2A zone of nTOF by a concrete wall 4.8 m thick. The nTOF area is accessible with beam present in TT2 if two independent interlock conditions are met (the magnets bending the beam into TT2A are off and two stoppers are inserted in the beam line). However, a catastrophic beam loss in TT2 could generate a serious radiation hazard on the TT2A side of the shielding wall.

Figure 1. Schematic view of the area around the dump D3

*The dimensions of the shielding walls are not to scale.
The PAX and the PMI symbols indicate the position of the installed radiation monitors.*



This study was triggered due to an accidental condition in which a beam loss in TT2, caused by a failure of a corrector magnet installed about 100 m upstream of the shielding wall, generated a high radiation level in TT2A. At this moment TT2 was dumping two AD pulses and two nTOF pulses onto D3, with intensities of 1×10^{13} and 5×10^{12} protons per pulse, respectively. At the time of the incident the beam was lost somewhere a few tens of metres upstream of D3. A radiation monitor in TT2A, located close to the wall, generated an alarm and alerted people present in the area of the abnormal dose equivalent rate. These people left immediately but their film badges registered doses of 400 μ Sv, half of it due to neutrons and the other half due to low LET radiation.

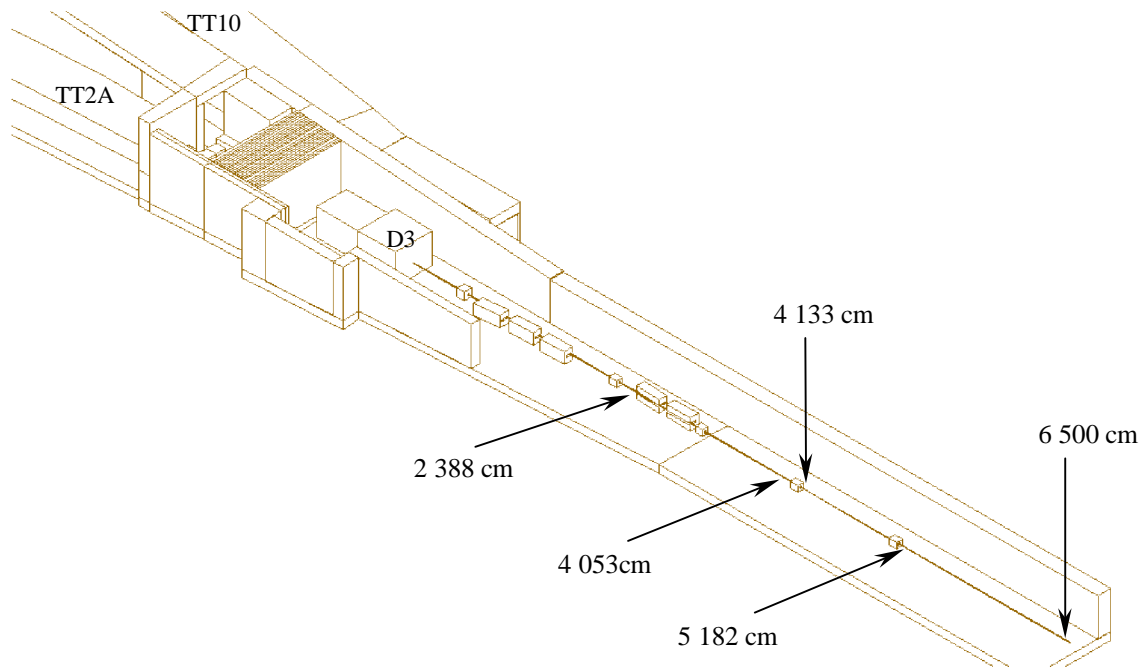
This accidental condition was investigated using Monte Carlo simulations, as well as a number of other beam loss scenarios. The various radiation components making up the dose equivalent rate in TT2A were assessed as a function of the various loss positions in the TT2 beam line upstream of the shielding wall. All calculations were performed with the latest version of the FLUKA code [1,2]. A comparison between simulation results and measurements is made.

Monte Carlo simulations

Only a comparatively simple model of the geometry was implemented in the FLUKA calculations, omitting unnecessary details. However, the “key points” of this area are considered correctly. Figure 2 shows the area as coded into the FLUKA geometry, including the TT2 proton beam line. Around the beam pipe the various dipoles and quadrupoles present in the beam line were simulated in order to take into account the shielding effect of the iron of these magnets.

Figure 2. Overview of the TT2 area as simulated with FLUKA

The arrows indicate hypothetical beam loss points along the vacuum pipe. The indicated distances are the distances between the various beam impact points and the front face of the dump D3. All FLUKA geometry pictures presented in this paper were produced by using the programme FLUKACAD [3].



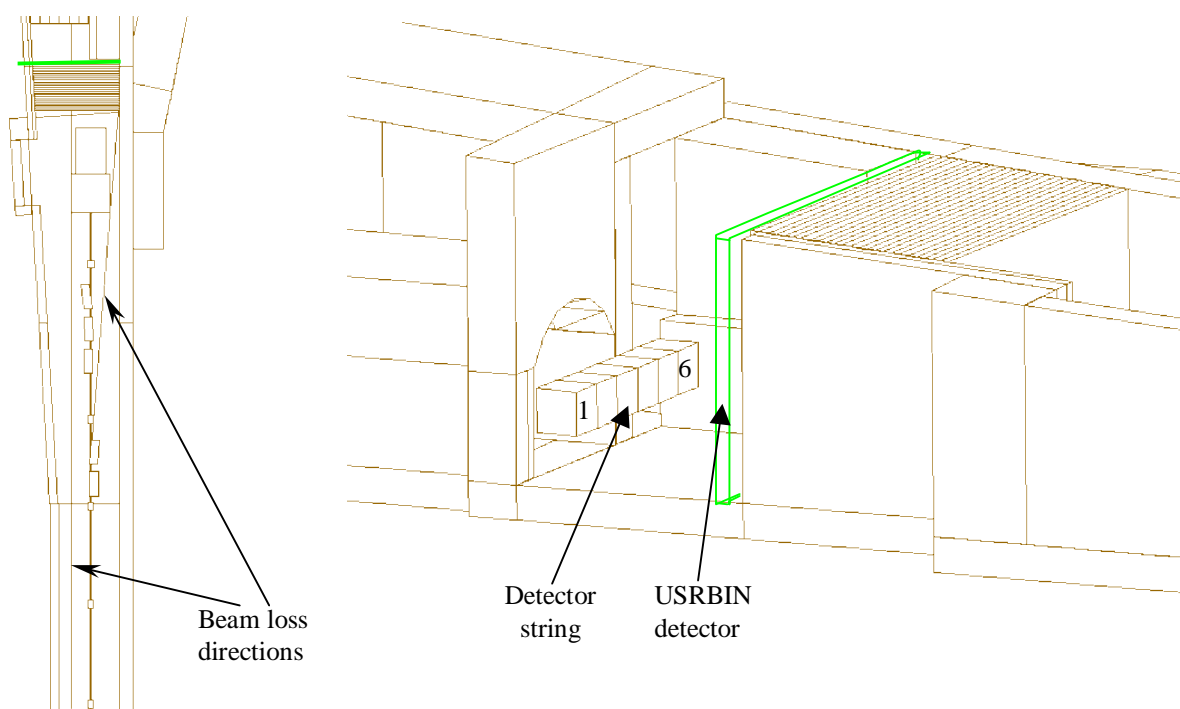
Some information was not available, such as the exact location of impact of the beam in the vacuum pipe, its angle of incidence at the impact point, the exact shape of the vacuum pipe, the exact number of lost particles during the incidental condition, as well as the strength of the magnetic field in the dipoles and in the corrector magnet. Reasonable assumptions were made for all these parameters. The beam parameters used in the simulations were the following:

- Particles: protons.
- Momentum: 26 GeV/c.
- Average beam intensity: 1.6×10^{12} protons/s.

The average beam intensity is based on the SPS cycle length of 14.4 s. Over this period one AD pulse (1.1×10^{13} p) and two TOF pulses ($2 \times 0.6 \times 10^{13}$ p) were assumed to be lost, in order to reproduce the real experimental conditions (see below). Since no precise information on the beam size was available, the simulations were performed using a pencil beam at the various interaction points. This is a sufficiently good approximation for the purpose of the present study.

Seven hypothetical loss scenarios were considered. The first scenario simulates a beam loss occurring more than 100 m upstream of dump D3. This beam loss location enables the beam to miss the dump D3, as shown in Figure 3. Although this scenario seems unlikely, it represents the worst possible accident condition. No interaction with the pipe wall material and the air was taken into account in these calculations. Approximately 13% of the beam particles undergo a hadronic interaction with the air molecules in a path length of 100 m, but this effect can be neglected for the purpose of the present calculations. The energy loss by ionisation in 100 m of air is negligible.

Figure 3. Detectors used in the Monte Carlo simulations. The picture on the left shows the two directions of the mis-steered beam hitting the wall on the left and on the right of dump D3.



In a second loss scenario a malfunction of the magnets, which normally bend the protons towards TT10, was assumed. Due to such a malfunction the beam misses the dump and directly hits the wall (see Figure 3). Furthermore, five other cases in which the beam hits the wall of the vacuum pipe at a very grazing angle were simulated. The beam loss points investigated are located upstream of D3 at the following distances from the front face of the dump: 23.88 m, 40.53 m, 41.33 m, 51.82 m and 65.00 m (Figure 2).

In order to tally particles reaching the area of interest, six detectors (labelled with indices 1 to 6 in Figure 3) each of volume of 1 m^3 were positioned at the beginning of the TT2A tunnel, a few metres downstream of the shielding wall. For the scenarios in which the beam hits the wall unshielded, particle detectors, covering the whole backside of the separation wall, were used (called USRBIN in Figure 3).

Depending on the beam loss situation, either shower particles originating from interactions inside the wall or muons, produced via pion or kaon decay, form the dominant part of the radiation field behind the separation wall. These effects require different simulation procedures and thus two types of calculations were performed.

Simulation of the muon-induced radiation

In order to generate a sufficient number of muons, the decay lengths of all possible parent particles of muons were artificially shortened. To compensate for this artificial decay length, the statistical weight of the produced muons was adapted automatically in FLUKA. To obtain a reduction of the simulation time, all stable particles reaching a kinetic energy below 100 MeV were killed. In this simulation only the dose caused by muons was taken into account.

Simulation of the electromagnetic and hadronic shower-induced radiation

The simulation procedure concerning the radiation caused by shower particles generated inside the shielding wall differs from the muon radiation calculation discussed above. In order to increase the number of particles traversing the wall, importance biasing was implemented. The lower transport energy threshold for electrons and positrons was set to 200 keV. Photons produced in the simulation were tracked until they reached an energy of 100 keV, whereas neutrons were followed down to thermal energies. All other charged particles were tracked until they reached energies of 100 keV.

In both simulation procedures the particle fluences were folded with energy- and particle-dependent fluence-to-dose conversion factors [4] to provide dose equivalent values.

For calculating the radiation exposure caused by a beam impact in the vacuum pipe, a combination of both simulation procedures was used. Muons, mainly produced by pions and kaons decaying outside the wall, were calculated using procedure 1, whereas dose contributions from particles other than muons were calculated via procedure 2. The simulations regarding direct impact of the beam on the wall used only procedure 2 to calculate the dose equivalent level behind the wall.

Results

Radiation caused by a direct beam impact onto the wall

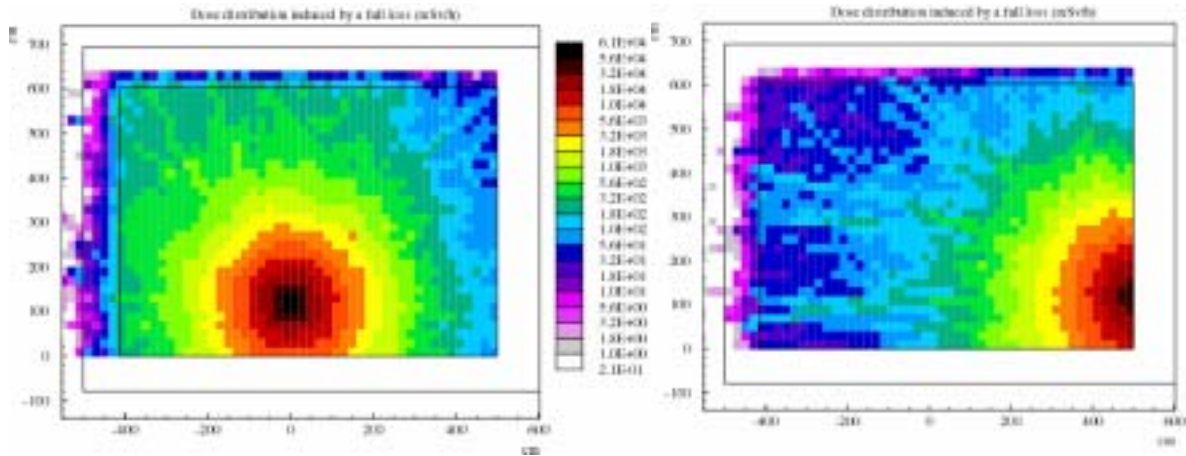
Two scenarios define the accident triggered by a direct loss of the beam into the wall. On the one hand, the beam impacting on the wall on the left-hand side of the dump is due to protons lost far upstream in TT2. Interactions in the pipe material and in the air, between the beam exit point from the pipe and the impact point on the wall, were neglected. Although this scenario is purely hypothetical, in terms of radiation protection it represents the worst possible accident in the area. On the other hand, a beam loss on the right-hand side of the dump can be caused by a malfunction of one of the magnets bending the beam towards TT10. This is an example of a possibly more realistic scenario.

Figure 4 shows the radiation levels in TT2A behind the shielding wall separating TT2A from the area around the dump in TT2. The figure on the left shows the radiation level that would be caused by the beam impacting on the wall on the left-hand side of the dump. The dose equivalent around the beam axis behind the wall would reach 250 mSv within one single super-cycle. Although this value is very localised, it would obviously be unacceptably high.

In case the protons are lost due to a malfunction of one of the magnets bending the beam into TT10, the beam hits the wall on the right-hand side of the dump. This scenario is similar to the one previously described. The difference is that the highest dose equivalent rate would now be located in a more inaccessible area. Nevertheless, the radiation level in all accessible areas behind the wall would still be far too high.

Figure 4. Radiation levels obtained behind the separation wall

The picture on the left shows the dose equivalent rate obtained if the beam hits the separation wall on the left-hand side of the dump D3. The figure on the right shows the dose equivalent rate in case the beam is lost due to a malfunction of one of the TT10 bending magnets.



The dose in the detector string (see Figure 3) located about 5 m behind the wall is shown in Figure 5 and Figure 6. If the beam hits the wall on its left-hand side, the dose equivalent rate could exceed 1 Sv/h (Figure 5). Here neutrons are the dominant component. Protons, pions and photons produced inside the wall represent the second largest contribution to the radiation field. In an accidental condition of a direct beam loss in the wall, the muon contribution plays only a minor role. This is because pions, which are produced inside the wall by hadronic cascades, cause further hadronic collisions. Therefore, most of them do not have time to decay to muons.

Figure 5. Radiation levels in the detector string (in front of TT2A) in case the beam would hit the wall on the left-hand side of the dump

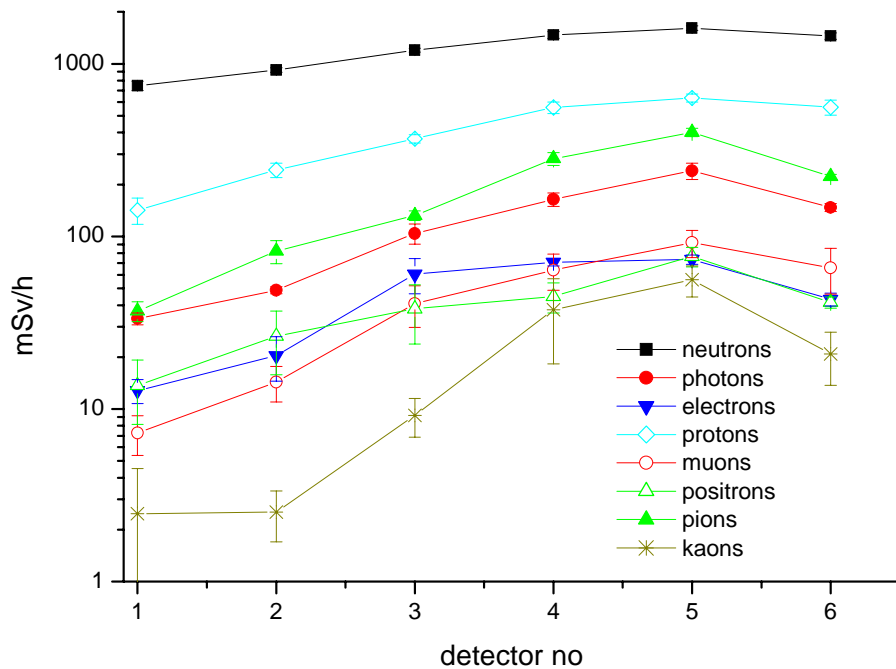
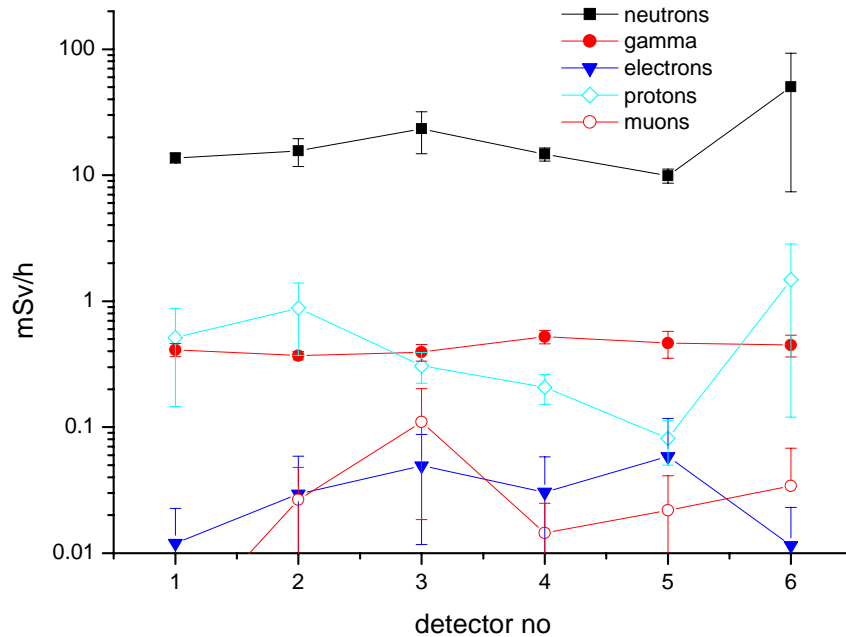


Figure 6. Radiation levels in the detector string (in front of TT2A) in case the beam would hit the wall on the right-hand side of the dump



In case the beam hits the wall on the right hand side of the dump, the radiation in the detector string is much lower than in the scenario described above (see Figure 6). Since the detector string is well shielded against the main radiation source, which is located along the beam axis (Figure 3, left), the dose equivalent in this region is comparatively low. Neutrons are the main contributor to the dose equivalent; the contribution of other particles is more than a factor of 10 lower.

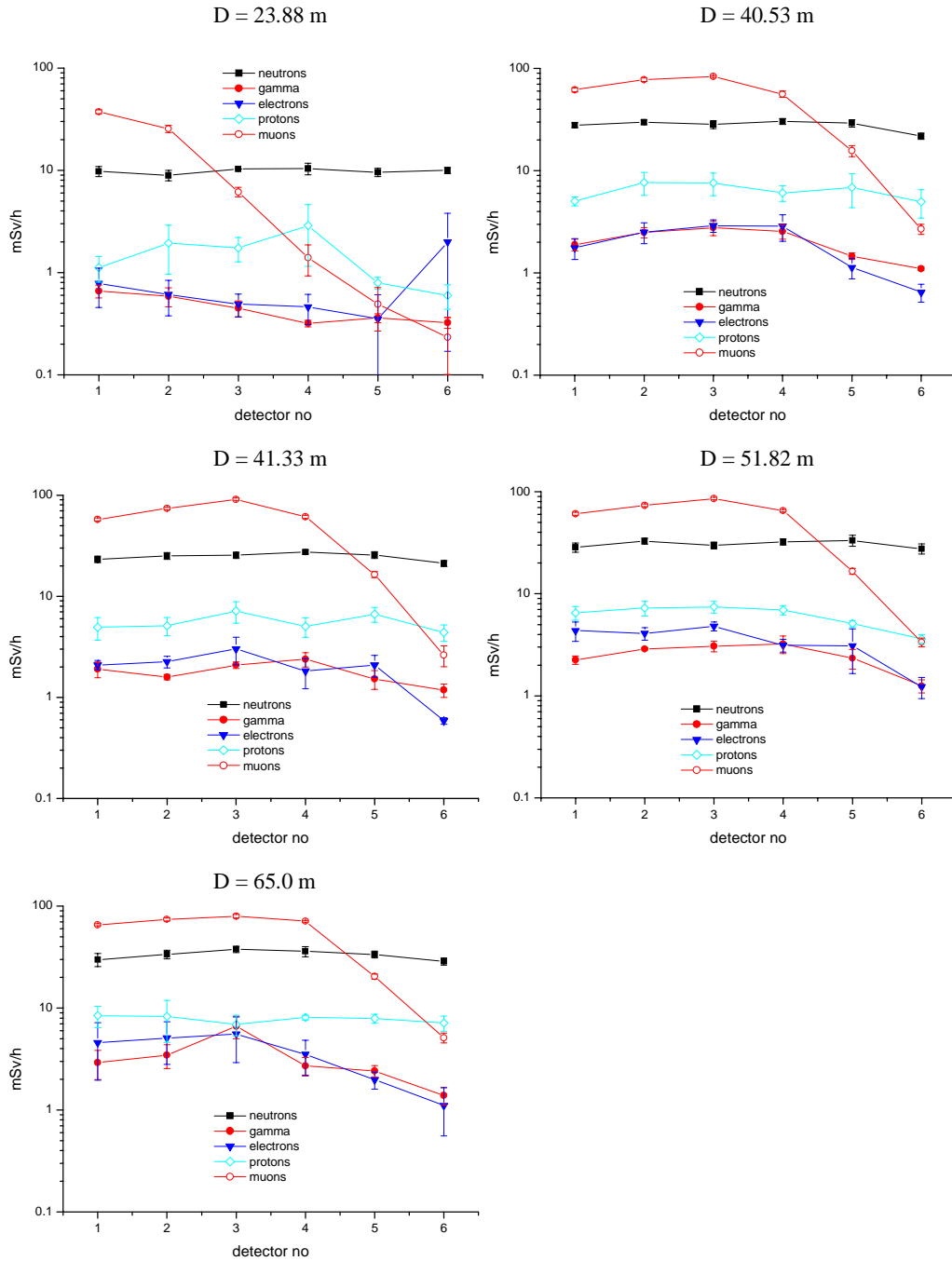
Radiation caused by a beam loss in the TT2 vacuum pipe

If the beam is lost in the beam pipe, the situation is very different from the above scenario. The beam is assumed to hit the pipe at a very grazing angle. Due to this small angle, most of the protons entering the pipe material perform a hadronic interaction. In these interactions pions and kaons are also produced, most of which leave the pipe material without making further hadronic interactions. Depending on their energy and the position from where they leave the pipe, a certain number of them decay into muons.

Figure 7 shows the radiation level in the detector string. These results correspond to the five impact positions of the beam along the beam line as shown in Figure 2. The graph representing the dose equivalent rate caused by a beam impacting 2 380 cm upstream of the front face of the dump shows that muons dominate only in detectors 1 and 2. The other detectors are fully or partly shielded by the magnets and by the dump, which are located between the primary interaction point and the wall; the higher the detector number, the lower the dose contribution from muons.

The further upstream the loss point in the pipe, the smaller the “shadowing effect” of the dump and the magnets. This effect can be observed in the increasing muon dose equivalent rate in the first four detectors (especially in detector 4) with increasing distance between the loss point and the dump. Only the fifth and sixth detector of the string are always fully shielded by the dump. The contribution to the radiation exposure of particles, other than muons, is fairly constant in all six detectors.

Figure 7. Dose levels seen in the detector string (in front of TT2A) in case the beam hits the beam pipe at the labelled distances (D) to the dump



From the above results one can draw the following conclusion. If there is no shielding material, the radiation exposure behind the wall is dominated by muons. The dump, consisting of a thick iron core surrounded by 80 cm of concrete on all sides, the shielding wall and part of the dipole magnets provide enough shielding to stop most of the produced muons. On average 0.7 m of iron is needed to reduce the muon energy by 1 GeV. The majority of muons produced by decay do not have energies higher than a few GeV, such that they are completely stopped in the D3 dump.

If the beam loss is caused by a failure of the corrector magnet, a combination of the scenarios presented here best describes the real situation. Depending on the size of the beam and on the bending power of the corrector, a possible scenario is the following: the beam is assumed to be bent upwards. Due to the lateral extension of the beam, not all particles enter the pipe wall at the same position. If the bending power of the corrector is weak, the first interactions occur close to the dump and some of the protons interact with the dump without hitting the beam pipe. In case the corrector provides a stronger bending power, the first interactions with the pipe occur far upstream. This increases the radiation contribution of muons on the other side of the wall. Since the real beam extension is not infinitely small, the misguided beam essentially provides a line source along the beam pipe. Depending on the strength of the magnetic field, all or only a part of the proton beam interacts with the pipe. The rest hits the dump without contributing to the dose equivalent behind the wall. In most of the simulated scenarios the muons represent the main contribution to the radiation field in the first four detectors of the string. Therefore, the line source scenario will also be dominated by muons if the first interactions occur at a distance at least 40 m upstream of the dump.

Measurements

Several weeks after the incident mentioned in the introduction, the PS operating team attempted to reproduce the anomaly that caused the beam loss. Several passive and active radiation detectors were deployed across TT2A to monitor the dose equivalent rate and determine the dominant radiation components, namely: an argon-filled high pressure ionisation chamber to detect photons, muons and high-energy charged particles, a REM ion chamber for neutrons up to about 15 MeV, a plastic scintillator to detect hadrons of energy above ~20 MeV via ^{11}C production, and ^6LiF and ^7LiF thermoluminescent dosimeters inside polyethylene moderators to discriminate the fast neutron and photon components.

It was found that beam mis-steering by the corrector, which is positioned approximately 100 m upstream of D3, caused the beam to exit the vacuum chamber. The actual location at which the beam centre exits the chamber corresponds to the second dipole bending the beam to TT10 (the component located 2 388 cm upstream of D3 in Figure 2). Under these conditions the radiation monitors in TT2A indicated a dose equivalent rate of approximately 30 mSv/h, split in the ratio 2/3 due to low-LET radiation (that is, muons) and 1/3 to neutrons. If we compare this result with our simulations we can conclude as follows: the beam centre crosses the vacuum pipe at the location corresponding to the loss point simulated in the scenario shown in Figure 7, top left. Since the beam has a lateral extension, about half of the protons interacted with the wall of the vacuum chamber well upstream of this point. The interactions, which are distributed over several tens of metres upstream, contribute to the dose equivalent rate with 2/3 of muons and 1/3 of neutrons (Figure 7). The other half of the primary particles interact either with the vacuum chamber downstream of this point or with the dump. Due to the shadowing effect of the dump discussed above, the contribution to the dose equivalent rate of these interactions is negligible. With the results presented in Figure 7 and the fact that only 50% of the primary particles contribute to the radiation behind the wall we can conclude that the simulated dose equivalent rate is 30-40 mSv/h. This result is in very good agreement with the measurements.

Conclusions

Several hypothetical beam loss scenarios of the PS beam in TT2 were investigated by Monte Carlo simulations. Although the geometry of the area and the beam parameters were not precisely known, the results provide a sufficiently clear picture of the radiological situation following various potential accidental conditions. A full beam loss directly into the shielding wall on the left-hand side of the

dump, although hypothetical, would represent the worst possible accident and generate the highest dose equivalent rate in the upstream end of the TT2A tunnel. One single pulse would be sufficient to deliver a dose equivalent largely exceeding 15 mSv, which is the annual limit for occupationally exposed workers at CERN. A beam loss in the vacuum pipe at various distances upstream of the wall would also cause too-high radiation levels in TT2A. The dose equivalent is dominated by either muons, mainly originating from pion decay, or neutrons produced in hadronic cascades inside the shielding wall, depending on the point where the beam is lost. The predictions of the Monte Carlo simulations are in good agreement with experimental results obtained under a well-defined loss condition.

The first action that followed the incident described above was to implement a new interlock condition. With TT2A in access condition and presence of beam in TT2 (i.e. beam transferred to TT10, to the AD and/or dumped in D3), a radiation monitor was interlocked to the beam in TT2. In case of abnormal radiation level due to beam mis-steering, beam extraction from the PS was inhibited. As a result of the present study, no access is currently allowed in TT2A when beam present in TT2. This directive will remain in effect until a detailed risk analysis has been performed to prove that none of the worse case scenarios described here can occur.

Acknowledgements

The authors wish to thank André Muller of the CERN Radiation Protection group for the measurements.

REFERENCES

- [1] Fassò, A., A. Ferrari, P.R. Sala, "Electron-photon Transport in FLUKA: Status", *Proc. of the Monte Carlo 2000 Conference*, Lisbon, 23-26 October 2000, A. Kling, F. Barao, M. Nakagawa, L. Tavora, P. Vaz, eds., Springer-Verlag, Berlin, pp. 159-164 (2001).
- [2] Fassò, A., A. Ferrari, J. Ranft, P.R. Sala, "FLUKA: Status and Prospective for Hadronic Applications", *Proc. of the Monte Carlo 2000 Conference*, Lisbon, 23-26 October 2000, A. Kling, F. Barao, M. Nakagawa, L. Tavora, P. Vaz, eds., Springer-Verlag, Berlin, pp. 955-960 (2001).
- [3] Vincke, H., "FLUKACAD/PIPSICAD: Three-dimensional Interfaces Between FLUKA and AutoCAD", *Proceedings of the 5th Workshop on Shielding Aspects of Accelerators, Targets and Irradiation Facilities (SATIF-5)*, Paris, 18-21 July 2000, NEA/OECD, pp. 361-370 (2001).
- [4] Pelliccioni, M., "Overview of Fluence-to-effective Dose and Fluence-to-ambient Dose Equivalent Conversion Coefficients for High-energy Radiation Calculated Using the FLUKA Code", *Radiat. Prot. Dosim.*, 88, 279-297 (2000).

**RADIOPROTECTION AND SHIELDING
ASPECTS OF THE nTOF SPALLATION SOURCE**

**V. Vlachoudis¹, C. Borcea¹, S. Buono¹, P. Cennini¹, M. Dahlfors^{1,3},
A. Ferrari¹, Y. Kadi¹, A. Herrera-Martinez¹, V. Lacoste¹,
E. Radermacher¹, C. Rubbia², L. Zanini¹ and the nTOF Collaboration**

¹CERN, European Organisation for Nuclear Research, Switzerland

²Dipartimento di Fisica e INFN Università di Pavia, Italy

³Dept. of Radiation Sciences Uppsala Univ., Uppsala Sweden

Abstract

The neutron Time of Flight (nTOF) facility at CERN is a high flux neutron source obtained by the spallation of 20 GeV/c protons onto a solid lead target. The first experimental measurements performed in April 2001 have revealed an important neutron background, 50 to 100 times higher than expected, along with some secondary effects such as air activation, with a strong presence of ⁷Be and ⁴¹Ar. In a subsequent study this neutron background was accounted to the strong presence of charged particles and especially negative muons, resulting from the interaction of the high-energy proton beam with the lead target. The present paper reports the study and solutions to the radioprotection and shielding aspects related to the nTOF spallation source.

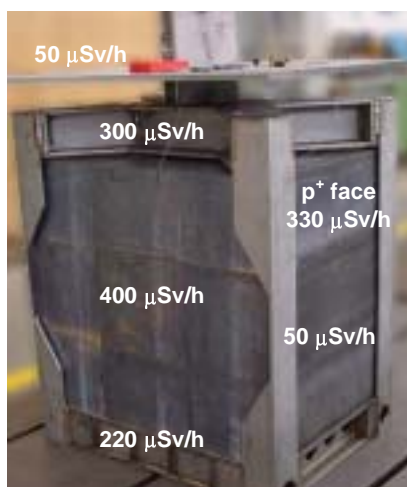
Introduction

The neutron Time of Flight (nTOF) [1,2] facility at CERN is a high flux neutron source obtained through the spallation of 20 GeV/c protons onto a solid lead target. The proton beam is delivered by the CERN Proton Synchrotron [3], capable of providing up to four sharp bunches (6 ns) with an intensity of 7×10^{12} protons per bunch, within a 14.4 s super cycle. The new facility is operational and was commissioned in November 2000 and April 2001 with the main goal of verifying the conformity of its characteristics. Part of the commissioning programme was dedicated to measurements on the safety of the installation. During the measurements performed up to the end of June 2001, a high background was observed [4], roughly two orders of magnitude higher than that expected. This background was later related to neutrons generated by the negative muon capture on the material near the experimental area, and the appropriate actions have been taken. The present paper describes the study and solutions to the background problem, along with radioprotection and shielding aspects related to the nTOF spallation source, with emphasis on the conditions required for neutron-induced cross-section measurements.

The lead spallation target

The major part of the design phase of the nTOF facility was focused on the lead spallation target. The target is made with pure lead blocks and its shape is $80 \times 80 \times 60 \text{ cm}^3$, except for the spallation area where a volume of $30 \times 55 \times 20 \text{ cm}^3$ was removed to obtain the nominal design dimension [5] (Figure 1). The target is mounted on a steel support and is submerged in water contained in an aluminium alloy vessel. The water layer surrounding the lead block is 3 cm thick except at the exit face of the target where it is 5 cm thick. The walls of the aluminium container are 0.5 cm thick, except the exit wall that consists of a thin single metallic aluminium window [5] of 1.6 mm thickness, 80 cm diameter. During operation the maximum dose recorded by the Safety Division (TIS) detectors was of the order of 10 Sv/h in the target area. The target was removed at the end of the first commissioning period (14 February 2001) for inspection. After exposing the lead target to 2×10^{16} protons of 20 GeV/c and two months of cooling the maximum dose record was 1.1 mSv/h at the hot spot and an average of 400 $\mu\text{Sv/h}$ was measured in the front face of the target. The measurements are compatible with the simulations [6] reporting a maximum dose of $\sim 2 \text{ mSv/h}$ at the hot spot. The aluminium container had a dose of 5 $\mu\text{Sv/h}$ and 15 $\mu\text{Sv/h}$ was measured on the inox screws.

Figure 1. Activity of the spallation lead target after two months of cooling



The total volume of water used in the cooling system is about 700 litres; 20% of it remains in the aluminium container. We can reasonably assume that the specific dose of the whole water volume is five times lower than the specific activity in the water inside the container, as this water permanently circulates in the cooling system. After one day of decay, the activity is mainly due to ^7Be and tritium, with 53.3 d and 12.33 y half-lives respectively. For an irradiation of 3×10^{15} protons on the lead target and 1 day cooling the simulations [6] gave a tritium level of 700 Bq/l and 20 000 Bq/l from ^7Be . The measurements showed 600 Bq/l for the tritium and the 30 Bq/l for the ^7Be . The difference in the ^7Be shows the effectiveness of the resin filter. The water was also contaminated by other isotopes, namely: ^{51}Cr originating from the canalisation, ^{122}Sb , $^{198,200-202}\text{Tl}$ and $^{200,202,202m,203}\text{Pb}$ coming from the lead target.

Thermodynamic behaviour of the lead target

The energy deposited by the proton beam in the lead target induces a temperature increase. Thus, the temperature behaviour of the target was monitored by means of six thermocouples inserted in different positions in the lead block. At proton intensities of $\leq 10^{12}$ protons/pulse no visible structure in the temperature behaviour could be observed. For the highest proton intensities of 7×10^{12} protons/pulse a clear temperature rise was observed. However, the maximum temperature remained below 70°C , in agreement with the calculations [7].

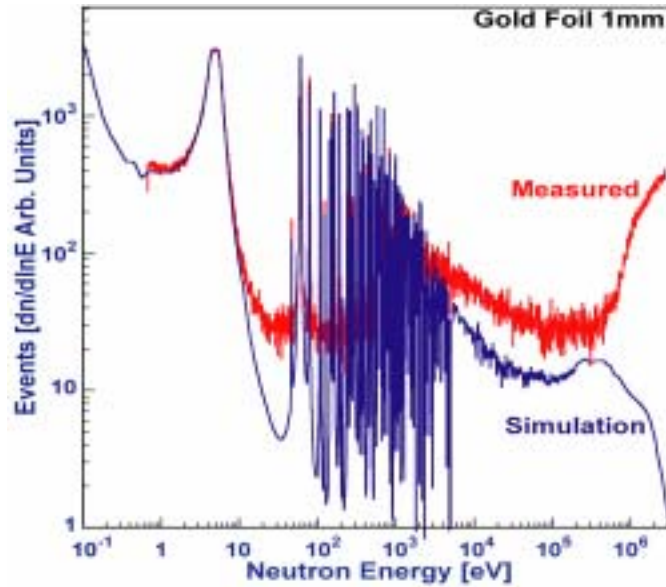
Sound waves

At proton intensities above 3×10^{12} protons/pulse a clear acoustic signal could be perceived coming from the target region. The signal was audible even behind 10 m of concrete shielding. The energy deposited in the centre of the target is mainly converted to heat almost instantaneously. Due to the large mass-inertia and the short time a pressure is created and the equilibrium inside the material is disturbed. The potential energy is converted into kinetic energy, which creates elastic vibrations resulting in a sound wave travelling through the material. These elastic vibrations travel through the target and only ~15% goes into the water. Analytical calculations [7] showed a maximum displacement of the lead target of a few μm and a maximum pressure at the hot spot of 7 bar. The calculations indicate that the appearing forces are such that possible damages to the window, the welds of the water tank and other structures can be excluded. Recent studies [8] have shown that a displacement of $1 \mu\text{m}/\text{m}^2$ can produce up to 75 dB noise. Several detectors have been mounted on the lead target to measure the effect: accelerometers, strain gauges and crack detection gauges.

The background in the experimental area

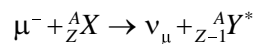
During the measurements performed up to the end of June 2001, a significant background (Figure 2) was observed [4], roughly two orders of magnitude higher than expected. This background has consequences on capture measurements both in terms of accuracy and required beam time. The background was visible with various detectors: liquid scintillators C_6D_6 , TLD-7, Bicron 702, CR-39 track edge detectors. However, it was not possible to identify the mechanism responsible for producing it. The most important characteristics were the strong left-right asymmetry (with respect to the beam line), the intense prompt flash appearing outside the beam line and the long time component up to few ms. In order to understand the origin of this background, several scenarios have been proposed, such as fast neutrons coming directly from the target area, muon interactions, the collimation system, imperfections in the shielding, the neutron escape line, etc. We have demonstrated that the most likely explanation of the neutron background in the nTOF experimental zone is negative muon captures occurring in the walls and materials of the experimental hall.

Figure 2. Experimental spectrum from 1 mm thick gold sample compared to the expected effect constructed from the cross-section and the simulated flux. The spectra are normalised via the strong resonance at 4.9 eV. The difference between the two curves is due to the presence of the background.



Neutron generation by muons is a process that has been acknowledged to exist for quite some time [9]. It is particularly important in situations such as underground sites or atmospheric showers at ground level where muons are known to dominate the radiation environment. Actually, muons can produce hadronic interactions through two different mechanisms:

- Photo-nuclear interactions via virtual photons.
- Negative muon capture with μ^- brought to rest through the weak process:

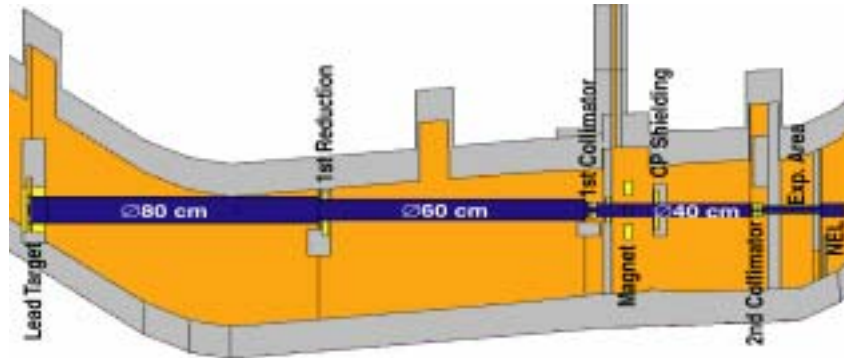


The former process involves muons of (relatively) high energy and has a mean free path of a few hundred meters in earth. Thus, it is not supposed to significantly contribute in the nTOF. The assumptions used in our simulation models predict that ~50% of μ^- stopping in concrete undergoes nuclear capture. Experimental spectra of neutrons emitted following μ^- captures show an evaporation peak consistent for multiplicity and excitation with single nucleon excitation, plus a low intensity tail extending up to several tens of MeV which cannot be explained without resorting to more complex interactions. The model embedded in FLUKA [10] uses a combination of single and two-nucleon absorption within a cascade pre-equilibrium evaporation model, with the relative importance of the two components set in such a way to obtain a satisfactory description of the experimental data.

Simulation studies

An intensive simulation programme [11] was launched to identify the mechanism responsible for the background. All the simulations were carried out using the general purpose Monte Carlo code FLUKA [10]. The TT2A tunnel geometry (Figure 3) with all the details was modelled, in conformance

Figure 3. Top view of TT2A tunnel geometry used in the simulations



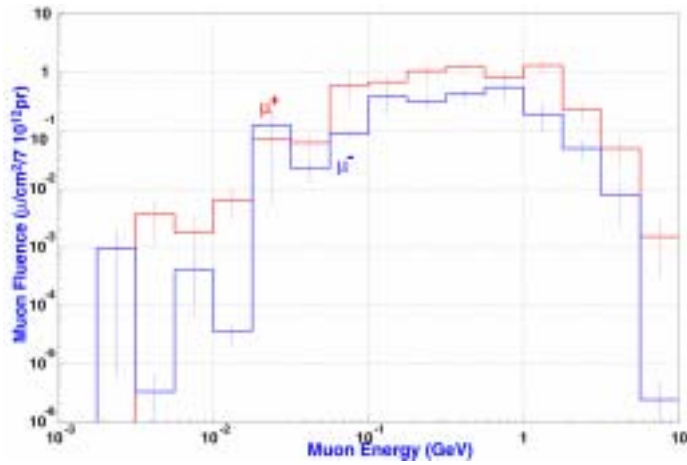
to the technical drawings and civil engineering plans, apart from a couple of shielding pieces, which were not included in the technical drawings. None of these details are felt to be relevant for the calculations. However it must be stressed that the simulation did not include imperfections in the shielding, which could contribute to the observed background. In particular, no penetrations (cable trays, air and water pipes, etc.) have been modelled.

Initially, a special “simulation” was performed to find possible weak points in the shielding of the nTOF tunnel. This was calculated using a special particle in FLUKA [10] known as “RAY”, being a straight-line trajectory through the geometry. The program tracks all the objects lying in a given direction, calculating a number of various quantities like distance traversed in each material, mass, number of interaction lengths, etc. This simulation revealed straight paths from the target area to the experimental area where the shielding might be insufficient with a minimum range of $1\,400\text{ g/cm}^2$ (corresponding to 5.2 m of concrete). This range is equivalent to at least 2 GeV/c energy losses by ionisation for minimum ionising particles.

The 20 GeV/c proton beam interacting with the lead target is a source of many charged and neutral particles [12]. The suppression of charged particles inside the neutron tube is achieved with the sweeping magnet located at 145 m. The spectrum of the muons peaks at $\sim 1\text{ GeV/c}$ with a significant fraction above the 2 GeV/c ionisation losses limit calculated before. Therefore, we expect to have a considerable fraction of muons penetrating the experimental area through the concrete shielding. The measurement with TLD ^7Li demonstrated the presence of an ionising signal outside the neutron tube with a strong left-right asymmetry coming directly from the target area, which was interpreted as muons. These results were validated with a subsequent simulation biased in such a way to enhance the muon fluence in the experimental area. This simulation (Figure 4) showed that a significant muon component is present in the nTOF experimental area and that such a component is highly asymmetric due to the asymmetry of the material density along the tunnel. The flux of muons is enhanced up to 100 times, at the right-hand side of the tunnel. The maximum muon flux is of the order of a few $10^2\ \mu/\text{cm}^2/7 \times 10^{12}$ protons. The muon spectrum is peaking at energies somewhat lower than 1 GeV, with a ratio μ^+/μ^- of 2.5 ± 0.6 . The maximum muon energy observed with the present statistics is around 10 GeV, consistent with the primary beam momentum (20 GeV/c), pion decay kinematics and minimum thickness along the flight direction.

According to the minimum mass calculation and the muon simulation, it was recognised that the asymmetry could be naturally explained if a penetrating component is streaming through the tunnel up to the experimental area. Hence a complete simulation of the whole set-up was performed. Due to the statistical difficulties, extensive use was made of several variance reduction techniques, most of them specific to the FLUKA [10] code. The simulation predicted a background neutron fluence of the order

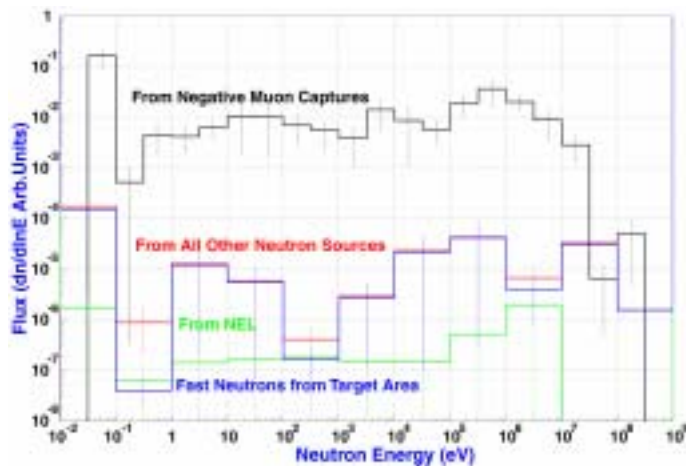
Figure 4. Energy spectrum $[d\mu/d\ln(E)]$ of the muons entering the experimental area



of a few $n/cm^2/7 \times 10^{12}$ protons with a slight asymmetry due to the predominant contribution of neutrons being moderated in the experimental area. This intensity is in reasonable agreement with the measurements available.

Figure 5 shows the neutron energy distribution divided into various components. The most important contribution results from the capture of negative muons in the walls surrounding the experimental area. Neutrons coming directly from the target area can be seen clearly, even though they represent a small fraction. The contribution of the Neutron Escape Line (NEL) is very small. The rest are neutrons originating mostly from interactions in the second collimator area. It is worthwhile to emphasise that more than 50% of the entries are thermal neutrons. The neutron spectra are quickly softened with increasing time. After a few ms only thermal neutrons are left.

Figure 5. Neutron background fluence at the experimental area split into different sources



Initially, the neutrons originating from muon captures are as asymmetric as their parents. However, they rapidly diffuse through multiple scattering in the walls and in the experimental room. Therefore, the time- and energy-averaged neutron fluence is expected to show only a slight asymmetry as indeed we measured with the neutron detector. A strong signal from stopping muon decays was observed at μ s level in the C_6D_6 spectrum, due to the decay electrons.

Possible remedies

There are two means of reducing the background at nTOF. One possibility implies devising extra shielding effective in removing the largest source of the background, which is the penetrating muon component. A shielding effective against muons will, of course, be oversized against neutrons originating from the target area, which will disappear as well. Another approach could be a local reduction of the effect of the neutron background by means of quick moderation and following capture. This approach will be effective whatever the neutron source. However it will not reduce the problems associated with the muons themselves and it will not cure the fast neutron background component. The two approaches are complementary and a combination of both could be a very effective solution.

Preventing pions from decay would require much less material. However, the simulations showed that roughly 50% of the pions that will generate muons reaching the experimental hall are inside the vacuum tube at the exit of the shielding of the target area and 10% of them are still inside the vacuum pipe as far as 60 m from the proton target. Therefore a shielding in the first part of the tunnel will not be fully effective due to the impossibility of intercepting those particles still flying inside the vacuum pipe. Therefore, a 3.2 m thick iron shield has been introduced downstream of the sweeping magnet at a distance of 150 m from the lead target. This thickness corresponds to ~ 3.2 GeV energy loss for minimum ionising particles, and to more than 13 interaction lengths for the most penetrating neutrons (80-300 MeV). A reduction factor close to 1 000 can be achieved with this simple solution. Of course in reality, the overall reduction factor would be somewhat smaller, because of unavoidable penetrations in the shielding (cables, clearances, water and air pipes, etc.).

Experimental studies

An experimental programme [13] was launched to verify the results obtained with the simulations and to measure the effectiveness of the shielding. The programme was divided into two phases.

In the first phase the neutron background was measured with a ^3He detector and the gamma background with two C_6D_6 liquid scintillators to identify the initial conditions. In most of the runs, one C_6D_6 detector was kept at a fixed position, facing the sample, while the other was moved around the experimental area. Figure 6 shows the response of the ^3He detector covered with a polyethylene sphere of $\varnothing 81$ mm as a function of the arrival time of the event, together with the estimation based on the simulation folded with the efficiency of the detector. The small differences between the measurement and the estimated response can be partially related to the moderation time in the polyethylene ball for fast times $t < 100 \mu\text{s}$, and for larger times $t > 1$ ms to an underestimation of the beam related background in the simulation.

Later, a 40 cm thick wall was mounted directly behind the 3.2 m wall separating the experimental area from the second collimator region. From this measurement a strong indication concerning the background mechanism was expected. The aim of the test was to discriminate between the various models of background production, since the attenuation of the background is expected to be different for neutrons and muons. For fast neutrons coming from the target the attenuation with a 40 cm wall is expected to be of about a factor 3, while for muons it is expected to be much lower. Afterwards, a beam stopper was placed inside the first collimator. The purpose was to measure the variation of the background inside the experimental area by removing any contribution from the neutron beam.

The first phase of measurements was stopped in order to mount the shielding as suggested by the simulations. The shielding consisted of a 3.2 m thick iron wall placed in the nTOF tunnel, in between the magnet and the second collimator (Figure 7). Ideally, this wall should have been made entirely of

Figure 6. Background measurement with ^3He +polyethylene sphere and simulation

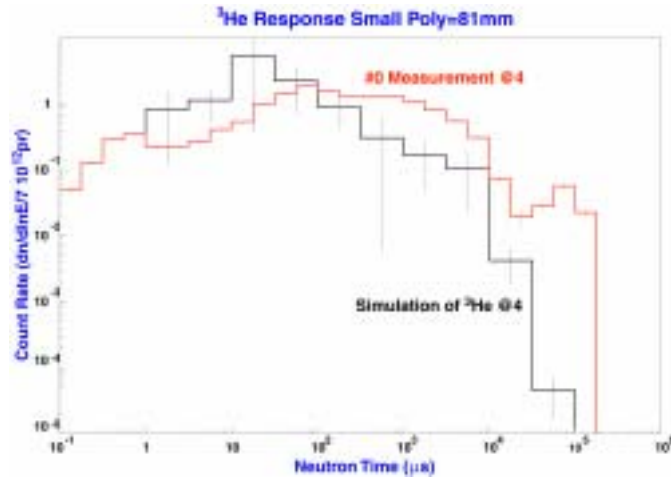


Figure 7. The 3.2 m iron wall, showing the area of concrete, iron and the empty space



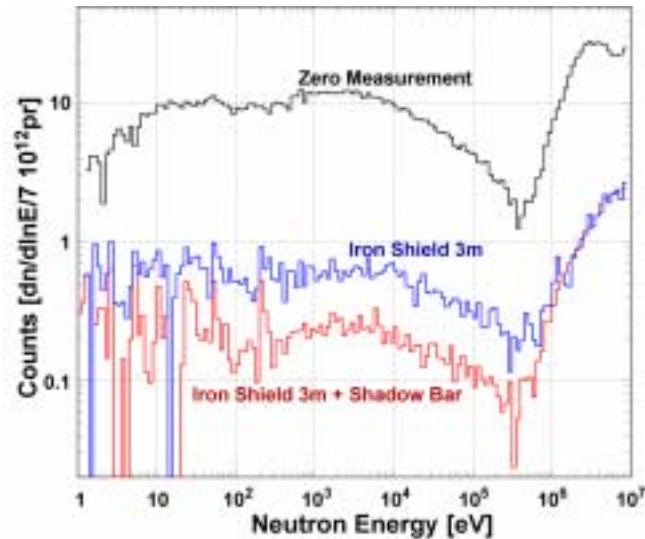
iron, and should have closed the full section of the tunnel. For technical reasons, the wall closed only the right-hand section of the tunnel, covering an area of about $2.8 \text{ m} \times 3.4 \text{ m}$, and the base was made of concrete. As shown in Figure 7, an area of about 3% of the right-hand side of the tunnel is not shielded.

In the second phase of measurements data were taken with and without the 40 cm wall, and the beam stopper (Figure 8). The measurements confirmed the results from the simulations concerning the mechanism of the background production. As a result of the installation of the shielding, a strong reduction of about a factor 30 was achieved on the main background.

Background from air activation

For high-resolution γ spectrometry, we used one HPGe detector. The detector was placed in the experimental room, near the centre, 50 cm below the beam line. The γ -ray peaks present [13,14] are from ^{232}Th decay products (U-Ra radioactive family), ^{40}K , air activation products ^{41}Ar and some spallation products ^7Be and ^{24}Na . The presence of short-lived activation products was evident after

Figure 8. Comparison of the background levels, measured with the C_6D_6 . The top histogram corresponds to the reference measurement. The lower one represents the residual contribution of the muon background, after the installation of the 3.2 m iron wall, and with the beam stopper inserted in the first collimator. The beam-related component is visible in the middle histogram.



subtracting the γ background from the measured spectra, where the 511 keV annihilation peak and the 1 293 keV ^{41}Ar γ line were clearly observed. These measurements have revealed another source of background, which is not directly beam-related. The ^{41}Ar is produced by neutron capture on ^{40}Ar found in the air produced near the target and collimators area where the neutron flux is high. The solution to prevent the ^{41}Ar from arriving at the experimental area and the control room was to make the area as airtight as possible. This has reduced the quantity of argon by a factor 10 in the experimental area; nevertheless, strong fluctuations were observed due to the variation of air circulation from the tunnel.

Due to the incident angle of 10° of the proton beam with respect to the neutron tube, the secondary particle cascade downstream of the nTOF target travels a few meters in the air before reaching the surrounding concrete walls of the tunnel where it produces a considerable amount of ^7Be and ^{24}Na , from spallation in the air. A measurement of the activity made by TIS [15] during the nTOF operation at a distance of 70 m from the lead target with 1/4 of the nominal proton intensity revealed an activity of 240 Bq/m³ for ^7Be and 77 Bq/m³ for ^{24}Na . Thirty-three (33) hours after shutdown neither of these two isotopes was found in the air. The exchange rate of the air in the nTOF tunnel it is estimated to lie between three and eight hours, due to the presence of ^{41}Ar ($t_{1/2} = 1.83$ h) while isotopes with shorter half-lives were not present. Thus, a rough approximation of the monthly release would amount to 240 MBq of ^7Be and 80 MBq of ^{24}Na . A simulation of the air activation was performed with FLUKA [10] assuming a five hour renewal of the air, resulting in an activity of 470 Bq/m³ for ^7Be , and 55 Bq/m³ for ^{24}Na , which is consistent with the measurements carried out, given all the assumptions made and the uncertainty on the used cross-sections.

The solution proposed for reducing the air activation consisted of adding extra concrete shielding around the neutron tube after the lead target, reducing in this way the track length in air of the secondary particles. Two scenarios were simulated adding a 4.8 m and 14.4 m long shield around the tube. The reduction achieved was of the order of 5 and 8, respectively, for both ^7Be and ^{24}Na . The extra shielding is currently being installed at the nTOF target.

Conclusions

Construction of the nTOF ended in April 2001, and the facility is currently operational. The commissioning measurements gave results consistent with the expectations for the neutron flux and energy resolution. The commissioning phase has also shown that radiation levels are acceptable and the target temperature is constant. The rapid energy deposition of the proton beam on the lead target produces sound waves, generating a strong audible signal. Analytic calculations and measurements have shown that possible damages due to the presence of the sound waves can be neglected.

An unexpected neutron background was observed 2 orders of magnitude higher than the calculated one. The main mechanism producing this background has proven to be the negative muon captures in the experimental area. A massive iron shielding was devised to stop the muons, and the background has been reduced by a factor of 30.

The component of the γ background coming from air activation (^{41}Ar) was investigated. Through the installation of a sealing of the wall separating the measuring station from the secondary zone, this component was strongly reduced. An improvement in the shielding, together with the lining of the experimental area with borated polyethylene, could lead to a further reduction of the background. The presence of spallation products (^7Be and ^{24}Na) in the air from the secondary particle cascade led to the addition of extra shielding around the neutron tube, close to the target area.

Acknowledgements

We are grateful to CERN TIS division for the measurements and fruitful discussions concerning the radioprotection aspects of the nTOF installation. We want to thank the CRS4 for performing the calculations for the temperature behaviour and the sound wave studies of the lead target. The participation of the CEA-Saclay and INFN teams with regard to the background measurements and analysis is thankfully acknowledged.

REFERENCES

- [1] Rubbia, C., *et al.*, *A High-resolution Spallation-driven Facility at the CERN-PS to Measure Neutron Cross-sections in the Interval from 1 eV to 250 MeV*, (+add.1), CERN/LHC/98-02.
- [2] The nTOF Collaboration, *Proposal for a Neutron Time-of-flight Facility*, CERN/SPSC 99-8.
- [3] Billinge, R., "The CERN PS Complex: A Multi-purpose Particle Source", *Proc. of XIIth Int. Conf. on High-energy Acc.* (1983).
- [4] The nTOF Collaboration, *Status Report*, CERN/INTC 2001-21.
- [5] The nTOF Facility (PS 213), *Technical Design Report*, CERN/INTC/2000-004.

- [6] Lacoste, V., *et al.*, “Activation Studies and Radiation Safety for the nTOF Experiment”, *Proceedings of SATIF-5* (2000).
- [7] Aragonese, C., *et al.*, *Thermal Analysis of the TOF Lead Target at CERN*, CRS4 technical report 01/27, 22 March 2001.
- [8] Freymann, R., *Acoustic Application in Vehicle Engineering* (1999).
- [9] Kozłowski, T., *et al.*, “Energy Spectra and Asymmetries of Neutrons Emitted after Muon Capture”, *Nucl. Phys.*, A436, 717-732 (1985).
- [10] Fassò, A., *et al.*, “Intermediate Energy Nuclear Data: Models and Codes”, Proceedings of a Specialists Meeting, Issy-les-Moulineaux (France) 30/5-1/6/1994, p. 271, published by OECD.
- [11] Ferrari, A., C. Rubbia, V. Vlachoudis, *A Comprehensive Study of the nTOF Background*, CERN/SL/EET Note 2001-036.
- [12] Vlachoudis, V., *et al.*, *Particle Distribution Entering the Vacuum Tube from a $80 \times 80 \times 60 \text{ cm}^3$ Lead Target*, SL-Note-2000-029 (EET), also in *MC 2000* conference proceedings, Lisbon, 23-26 Oct. 2000, p. 1175 (2000).
- [13] The nTOF Collaboration, *Study of the Background in the Measuring Station at the nTOF Facility at CERN: Sources and Solutions*, CERN/SL/Note 2001-046, CERN/INTC 2001-038.
- [14] Lacoste, V., *Gamma Background Measurement in the nTOF Experimental Area*, Internal Note, CERN/SL/EET 2000-006.
- [15] Otto, T., A. Müller, *Air Activation in the nTOF Target Area*, CERN Idto2001-38m-bis 16/11/2001.

NEUTRON PRODUCTION MEASUREMENTS RELEVANT TO SHIELDING FOR SPACE-RELATED ACTIVITIES

Lawrence Heilbronn

Lawrence Berkeley National Laboratory

Yoshiyuki Iwata, Takeshi Murakami

National Institute of Radiological Studies

Hiroshi Iwase, Takashi Nakamura, Hisaki Sato

Tohoku University

Reginald Ronningen

National Superconducting Cyclotron Laboratory

Abstract

Neutron production cross-sections were measured from 290 MeV/nucleon C and 600 MeV/nucleon Ne interacting in a slab of simulated Martian regolith/polyethylene composite, and from 400 MeV/nucleon Ne interacting in a section of wall materials from the International Space Station. Neutron spectra were measured at seven angles between 5° and 80°, and for neutron energies 5 MeV and greater. Spectra at forward angles are dominated by the break-up of the projectile, whereas spectra at back angles show the typical exponential fall-off with energy that is indicative of decay from the overlap region and the target remnant. The measured total neutron production cross-sections indicate that the regolith/polyethylene composite may be a more effective shielding material than the ISS wall materials, in terms of the number of neutrons produced.

Introduction

One of the primary limiting factors to long-term human space operations is the health risk to the astronaut from exposure to the space ionising radiation environment. The establishment of a permanent human presence on the International Space Station and the exploration and settlement of the moon and Mars are examples of such mission scenarios. The ultimate limitation on long-term operations is maintaining the radiation-induced cancer risks to acceptable levels. The most effective means to reduce radiation exposures is the use of intervening materials to reduce the radiation intensity within an enclosed structure.

The space ionising radiation environment is very complex, consisting of a low-level background of galactic cosmic radiation (GCR), transient solar particle events (SPE) and, while in Earth orbit, the trapped radiation belts. As these radiations traverse shielding materials they interact with the materials through specific atomic and nuclear processes, including breaking up the ions into smaller fragments and producing secondary radiation that can penetrate more deeply into the material. The composition and intensity of these transmitted radiations (secondaries and fragments) depend on the elemental constituents of the specific materials. The radiation-induced injury in biological tissue depends on the composition and intensity of the transmitted particles. An extremely important secondary particle component in this respect is the neutron, which has no charge and is not reduced in atomic interactions but is extremely damaging to biological tissue. Current theoretical models have shown the secondary neutrons to be a major contributor to exposures within lunar habitats and on the Martian surface, and recent studies have shown that neutrons could comprise 30 to 60% of the dose equivalent on the ISS. A recent review of the neutrons in the Earth's atmosphere has raised serious questions about the adequacy on our understanding of the production and propagation of neutrons by GCR in atmospheric components. Any advances on the specification of shielding for habitats on the moon or Mars require measurements on the transmitted neutron component within lunar and Martian shielding materials and improvements on databases and computational procedures.

The National Aeronautics and Space Administration (NASA) of the United States is currently supporting a ground-based research programme to study the effects of Galactic Cosmic Ray (GCR) transport through spacecraft materials and human tissue. The goal of the programme is to provide a reliable database of relevant nuclear cross-sections and thick target yields for the development and verification of transport model calculations used for low-Earth orbit and deep space shielding design. Ions with $Z \geq 2$ make up approximately 12% of the GCR flux; however, previous calculations indicate that neutron production from heavy-ion interactions in shielding materials may contribute at least 30% of the total neutron flux. Our group has measured several neutron production cross-sections that are relevant to heavy-ion GCR transport through shielding materials. In this paper we present cross-sections from two specialised NASA targets: (1) a slab of simulated Martian regolith mixed with polyethylene, referred to herein as "Marsbar", and (2) a section of wall from the International Space Station (ISS).

Experimental details

The experiments were carried out at the Heavy Ion Medical Accelerator in Chiba (HIMAC) facility at the National Institute of Radiological Sciences, Chiba, Japan. HIMAC delivered beams of 290 MeV/nucleon C, 400 MeV/nucleon Ne and 600 MeV/nucleon Ne to targets placed along the PH2 beam course. The 290 AMeV C and 600 AMeV Ne beams were incident upon the Marsbar, and the 400 AMeV Ne was incident upon the ISS wall section. Table 1 summarises the beam-target information from each run, including the beam energy at midpoint in the target. The midpoint energy is used as the relevant beam energy from this point on.

Table 1. Beam and target combinations

Beam	Energy	Target	Thickness
C	265 AMeV	Marsbar	5 g/cm ²
Ne	380 AMeV	ISS wall	3 g/cm ²
Ne	570 AMeV	Marsbar	5 g/cm ²

The Marsbar is comprised of 85% simulated Martian regolith and 15% polyethylene. Table 2 shows the atomic parameters of a representative sampling of Martian regolith. The ISS wall is comprised of 1.89 g/cm² of aluminium, 0.218 g/cm² of Nomex® honeycomb wall, 0.08 g/cm² of Nomex® cloth, 0.06 g/cm² Durette® batting and 0.72 g/cm² silicone rubber.

Table 2. Martian regolith composition

Element	Atomic density (atoms/g)
O	1.67×10^{22}
Mg	1.62×10^{21}
Si	5.83×10^{21}
Ca	7.81×10^{20}
Fe	1.80×10^{21}

Beam was delivered every 3.3 seconds in pulses that lasted between 0.6 and 1 second. Beam intensity was between 10^4 to 10^5 ions per pulse. In general, live time was of the order of 60 to 90%.

Immediately after exiting the beam-line vacuum system, the beam passed through a 0.5 mm thick plastic scintillator, referred to as the trigger detector. The trigger detector was used to count the number of incident ions, as well as reject any pile-up events. The targets were placed approximately 5 cm downstream from the beam scintillator. After passing through the target, the beam travelled about 20 m through the air before stopping in a beam dump.

The neutron detectors used were cylinders (12.7 cm in diameter and 12.7 cm in depth) of liquid scintillator (NE 213). Seven detectors were placed at 5°, 10°, 20°, 30°, 40°, 60° and 80° in the lab. Flight paths from target centre to detector centre varied between 306 and 506 cm. A 5 mm thick, solid plastic scintillator was placed directly in front of each neutron detector. Those scintillators were used to reject any events due to charged particles incident upon the accompanying neutron detector.

Gamma-ray events were distinguished from neutron events by using the pulse shape difference between those two types of events

Neutron energies were measured by time of flight. The time difference between corresponding signals in the trigger detector and neutron detector was recorded for each event. For neutron detectors placed 506 cm from the target, the overall energy resolution was 8%, 11% and 14% for 200, 400 and 600 MeV neutrons, respectively. For the 306 cm flight path, the corresponding energy resolutions were 13%, 18% and 23%, respectively. Background neutrons were measured using the shadow-bar technique. Additional information regarding experimental details may be found in Ref. [1].

Results

Figures 1-3 show the double-differential neutron production cross-sections from the three systems, at the indicated angles. So as to clearly present the data, the spectra have been multiplied by successive factors of 0.1 as the angle increases. At forward angles, the spectra are dominated by neutrons produced in the break-up of the projectile. Because of the kinematical boost from Fermi momentum, neutron energies greater than two times the incoming beam energy per nucleon are detected. The lower threshold on neutron energy is 5 MeV for all the spectra. The error bars show only the statistical uncertainties. The systematic uncertainties are being determined at the time of this writing, and are estimated to be between 20 to 50%. As angle increases from 5° to 30°, the contribution from projectile break-up becomes less significant. At large angles, the spectra exhibit an exponential fall-off with energy. The exponential behaviour indicates that the spectra there are dominated by the decay of the target remnant and the overlap region between the target and projectile.

Figure 1. Double-differential spectra from 380 AMeV Ne + ISS wall (unpublished)

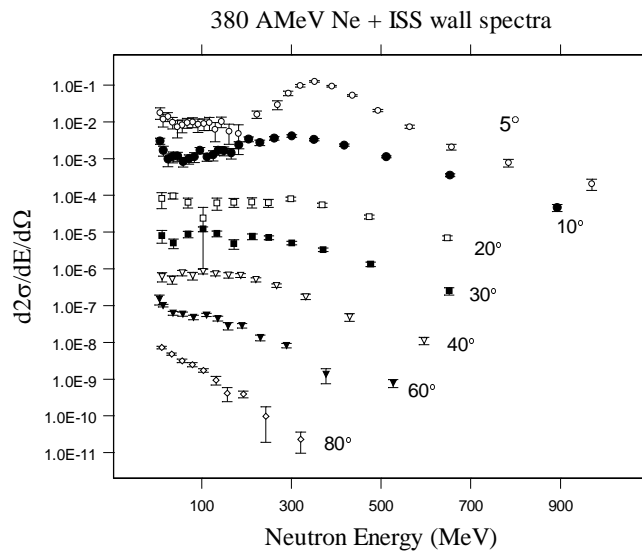


Figure 2. Double-differential spectra from 265 MeV/nucleon C + Marsbar system (unpublished)

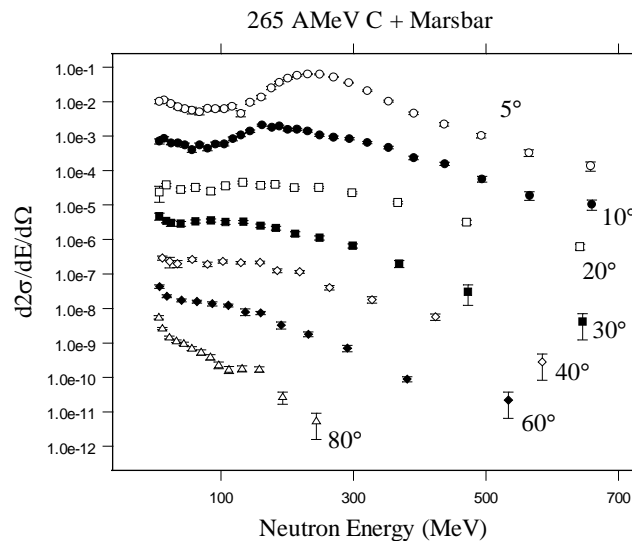
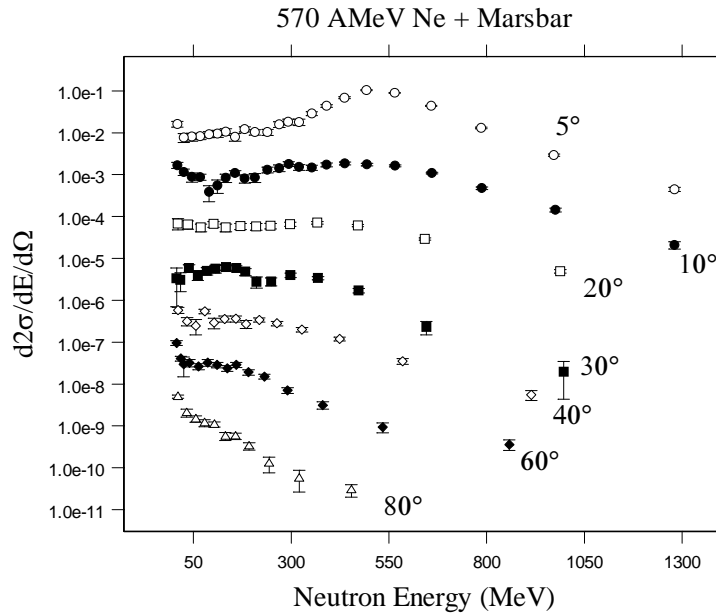


Figure 3. Double-differential neutron spectrum from 600 MeV/nucleon Ne +Marsbar (unpublished)



The double-differential spectra, such as the one in Figures 1-3, can be integrated over energy to yield angular spectra. Figure 4 shows the angular distribution between 5° and 80° from all three systems, for neutron energies 5 MeV and greater. The error bars only indicate statistical uncertainties. The distribution shown in Figure 2 is typical of such neutron angular spectra from heavy-ion interactions [1,2]. The spectra are forward-peaked, and can be fitted with the sum of two exponentials. The point where the contributions from both exponentials are equal is dependent upon the incoming beam momentum per nucleon [2].

Figure 4. Neutron angular distribution from all three systems (unpublished)

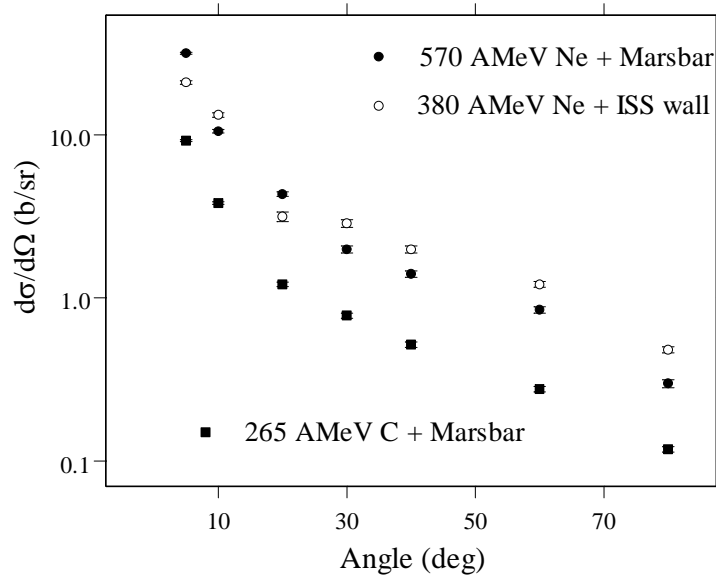
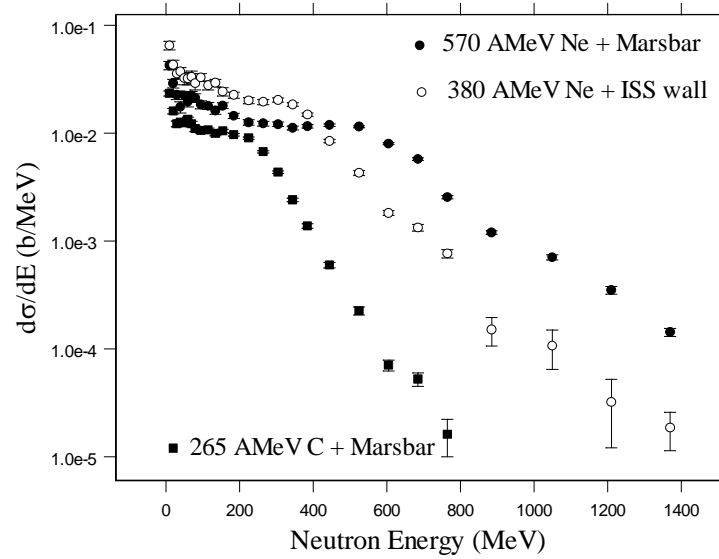


Figure 5 shows the neutron energy distribution from all three systems. To generate this spectrum, the 5° spectrum was assumed to cover the range between 0° and 7.5°, the 10° spectrum ranges between 7.5° and 15°, the 20° spectrum ranges between 15° and 25°, the 30° spectrum ranges between 25° and 35°, the 40° spectrum ranges between 35° and 50°, the 60° spectrum ranges between 50° and 70°, and the 80° spectrum ranges between 70° and 90°. This spectrum can then be integrated over energy to yield the total neutron production cross-section.

Figure 5. Energy spectra from all three indicated systems (unpublished)



The total neutron production cross-section is 3.4 barns for 290 AMeV C + Marsbar, 9.9 barns for 600 AMeV Ne + Marsbar, and 10.5 barns for 400 AMeV Ne + ISS wall. Comparison of these total neutron cross-sections with those reported in Ref. [1] are shown in Table 3, and indicate that the Marsbar and ISS wall materials have an effective elemental mass between C and Cu, at least in terms of neutron production. Assuming a linear relationship between total neutron production cross-section and elemental mass, the Marsbar has an effective mass number of about 30, whereas the ISS wall has an effective mass number of 40. Both the Marsbar and the ISS wall used in the experiments are relatively thick, and as such there may be a need to correct for target thickness in order to extract “true” cross-sections. In any case, this analysis indicates that the Marsbar may be more effective in limiting neutron production than the ISS wall. These preliminary results indicate that building materials with light-mass elemental components may be the most effective for reducing the number of neutrons produced from interactions with the heavy ions present in space radiation.

Table 3. Total neutron production cross-sections (0°-90°), in barns (unpublished)

Beam	Targets				
	Carbon	Marsbar	ISS wall	Cu	Pb
290 AMeV C	1.9 b	3.4 b		6.1 b	22.1 b
400 AMeV Ne	4.4 b		10.5 b	15.8 b	52.8 b
600 AMeV Ne	3.7 b	9.9 b		18.7 b	57.2 b

Acknowledgements

The authors wish to acknowledge the HIMAC staff for their support and efficient operation of the accelerator. This work was supported by the US National Science Foundation under Grant No. 95-28844, NASA Contract No. H-29456D and Grant No. L14230C through the US DOE under Contract No. AC03076SF00098.

REFERENCES

- [1] Iwata, Y., T. Murakami, H. Sato, H. Iwase, T. Nakamura, T. Kurosawa, L. Heilbronn, R.M. Ronningen, K. Ieki, Y. Tozawa, and K. Niita, "Double-differential Cross-sections for the Neutron Production from Heavy-ion Reactions at Energies $E/A = 290-600$ MeV", *Phys. Rev. C*, Volume 64, 054609 (2001).
- [2] Heilbronn, L., R. Madey, M. Elaasar, M. Htun, K. Frankel, W.G. Gong, B.D. Anderson, A.R. Baldwin, J. Jiang, D. Keane, M.A. McMahan, W.H. Rathbun, A. Scott, Y. Shao, J.W. Watson, G.D. Westfall, S. Yennello and W-M. Zhang, "Neutron Yields from 435 MeV/nucleon Nb Stopping in Nb and 272 MeV/nucleon Nb Stopping in Nb and Al", *Phys. Rev. C*, Volume 58, No. 6, pp. 3451-3461 (1998).

RADIATION CALCULATIONS FOR THE NA60 EXPERIMENT

M. Brugger

University of Technology Graz, Austria and CERN TIS/RP-CP, Switzerland

G.R. Stevenson

CERN TIS/RP-CP, Switzerland

Abstract

The study of high-energy heavy ion collisions is presently a very active field in high-energy physics. At the CERN SPS accelerator, the NA60 experiment will be able to study both the production of prompt dimuons and the production of muons originating from the decay of charmed mesons in proton and ion collisions. The major improvement as compared to preceding SPS experiments is the placement of high-resolution detectors directly after the target. The corresponding readout electronics, therefore, will be situated very close to the beam axis, being exposed to a strong radiation field. In this study, radiation damage to electronics due to ionising and non-ionising effects has been investigated using detailed FLUKA simulations. This simulation allows one to choose the best position for sensitive devices in the target region. The configuration of the absorber presented a challenging subject to the set-up of the experiment, since a compromise between the best possible dimuon signal, minimising multiple scattering and a very good suppression of background effects had to be found. Using the FLUKA simulation package, different absorber configurations were tested and an optimum was derived.

Introduction

The NA60 [4] experiment uses proton and ion beams of very high intensity. During the short design phase – of only several months – of the new detector electronics and the optimisation of the set-up of the experiment, radiation effects turned out to be a critical issue.

Radiation damage of the electronics situated in the target region, due to ionising and non-ionising effects has been estimated with detailed computer simulations. This present study was performed to determine the radiation dose to the electronics of the pixel detectors being placed close to the beam axis. The total dose deposited in silicon and the displacement damage induced by neutrons, protons and charged pions were determined. These quantities were calculated using the Monte Carlo code FLUKA [1,2]. Note that single event effects were not considered in this study but could be estimated as described in [3].

A second simulation was performed in order to optimise the configuration of the NA60 hadron absorber. Different absorber configurations were simulated which should fulfil two contradictory requirements: suppression of background particles and minimisation of multiple scattering of muons produced in the target, in order to improve the dimuon mass resolution. This study shows simulations with a proton beam hitting a target, which can be compared to some extent to data collected in the past.

The NA60 experiment

The NA60 collaboration is preparing an experiment to accurately study the production of open charm and of prompt dimuons in collisions induced by proton and heavy ion beams on nuclear targets at the CERN SPS accelerator. The experiment will study the phase transition from confined hadronic matter to deconfined partonic matter by addressing specific questions left open by the past SPS heavy ion physics programme. The present results strongly indicate that a new state of QCD matter, in which the quarks and gluons are no longer confined into hadrons, is formed in head-on collisions of lead nuclei at the top SPS energies.

NA60 will investigate in more detail existing signals of this new state of matter, and will also probe new signals with the aim of converting this evidence into solid proof. The proposal was approved by the CERN Research Board, in the year 2000, for a two-week long commissioning run in October 2001, followed by physics runs in 2002 and 2003, with proton, lead and indium beams.

The NA60 detector complements the muon spectrometer and zero degree calorimeter previously used in NA50 with new state-of-the-art silicon detectors placed in the target region inside a C-shaped dipole magnet. Downstream of the target system and inside a dipole magnetic field of 2.5 T, there is a silicon tracking telescope that tracks the charged particles. During event reconstruction, this allows to identify which one of the detected muons in the target region provides the best match to the muons measured in the muon spectrometer, placed behind a five-meter long hadron absorber.

For proton runs, this telescope will be made of 16 silicon microstrip planes [5], probably complemented by a few pixel planes. For the ion runs, the very high multiplicities of charged particles impose the use of silicon pixel detectors. In this case, the pixel telescope will have 14 pixel planes, the first six having four chips each and the last eight (grouped in four double planes) being made of eight chips. These new detectors will allow the NA60 experiment to separately study the production of prompt dimuons and of muons originating from the decay of charmed mesons in proton and ion collisions. This will help to clarify if the origin of the dimuon excess in the intermediate mass region

in ion collisions, seen by NA38 and NA50, is due to thermal dimuon production or to the enhancement of charm production. NA60 will also measure the absolute yield of charmed mesons and the pattern of J/ψ and ψ' production in collisions of lead and indium nuclei.

The FLUKA calculations

The FLUKA code [1,2] is capable of handling the transport and interactions of hadronic and electromagnetic particles in any material. This can be done over a wide energy range, from thermal neutron to cosmic ray energies. It is intrinsically an analogue code, but can be run in biased mode for a variety of deep penetration applications. Interactions are treated in a theory-driven approach, and model implementations are always guided and checked against experimental data. Hadron-nucleus interaction models are based on resonance production and decay below a few GeV, and on the Dual Parton Model (DPM) above. For momenta below 3-5 GeV/c, the so-called PEANUT program includes a very detailed Generalized Intra-Nuclear Cascade (GINC) and a pre-equilibrium stage. At high energies, a two-step approach is chosen, using first the DPM model, which contains the Regge theory and the Gribov-Glauber multiple collision mechanism. This is then followed by a second step, which includes a less refined GINC. Both modules are followed by equilibrium processes: evaporation, fission, Fermi break-up and γ de-excitation. A specialised multi-group transport, based on a dedicated neutron library, is implemented for low-energy neutrons (<20 MeV). More details on Monte Carlo techniques used, simulated processes and underlying physical models can be found in [1,2] and references therein.

The presented calculations are carried out with the 2001 version of the particle interaction and transport code FLUKA. The program has been used to simulate the electromagnetic and hadronic particle cascade in the NA60 experiment.

The FLUKA NA60 geometry and materials

The complex geometry of a seven metre long section of the experimental set-up was modelled in detail with the ALIFE geometry editor [6]. The geometry is described in a right-handed orthogonal system with its origin centred in the beam axis and 200 cm upstream of the front face of the absorber, x as the vertical axis and z pointing downstream. A three-dimensional view of the FLUKA geometry is shown in Figure 1. The geometry consists of the NA60 target that will be used in the proton run in May 2002, the PT7 magnet, the pre-absorber and the main hadron absorber, as well as the first muon chamber.

For the studies of the different absorber configurations, a cylindrical geometry – symmetrically around the z -axis – was used. A cut through the geometry (c.f. Figure 2) alongside the yz plane shows the different regions and the corresponding materials.

The last part of the inner absorber of 80 cm thickness is sliced into four pieces of 20 cm each, consisting of either carbon, iron or, if absent, air. In order to find the best compromise between little muon scattering and a good suppression of background particles, the number of particles entering the first muon chamber, which is situated ~16 cm after the main absorber, was simulated using the different absorber configurations shown in Table 1.

The Zero Degree Calorimeter (ZDC) is situated in the inner core of the main absorber (c.f. Figure 2) to detect the non-interacting beam particles. However, in proton runs the use of this ZDC is not needed. Hence, it was suggested to use a 20 cm long bar of tungsten to replace the air gap in front of the ZDC and a tungsten bar to replace the ZDC itself. It was thought that the additional tungsten bar would absorb particles more efficiently as it shifts the cascade in the upstream direction.

Figure 1. Three-dimensional representation of the FLUKA geometry created using FlukaCAD [7] and AutoCAD. In this view, the z-axis is pointing from the right to the left.



Figure 2. Geometry cut through the simulated section of the NA60 experiment. The target, the preabsorber and the different layers of the absorber can be seen. In this view, the z-axis is pointing from the left to the right.

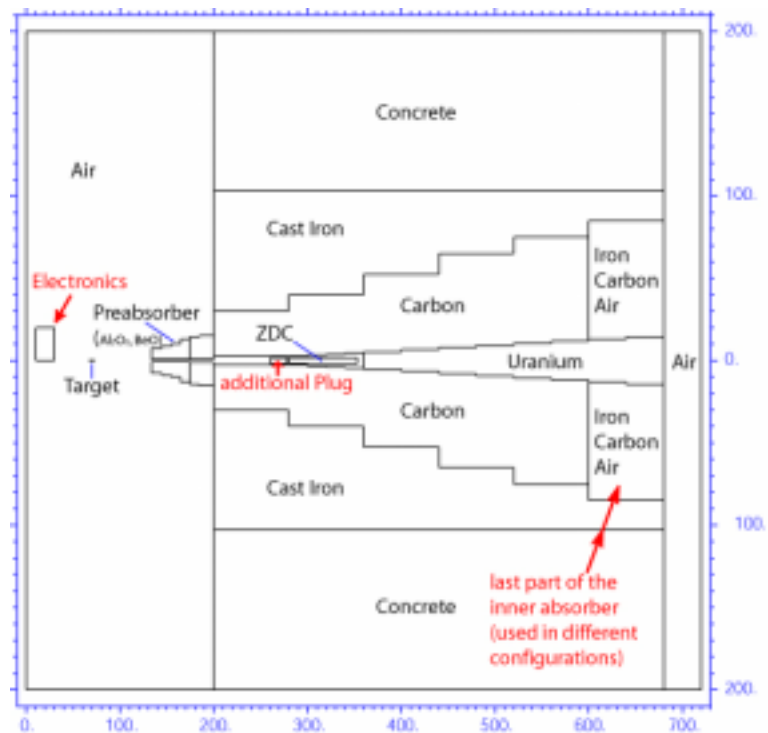


Table 1. Different configurations of the last 80 cm thick part of the inner absorber

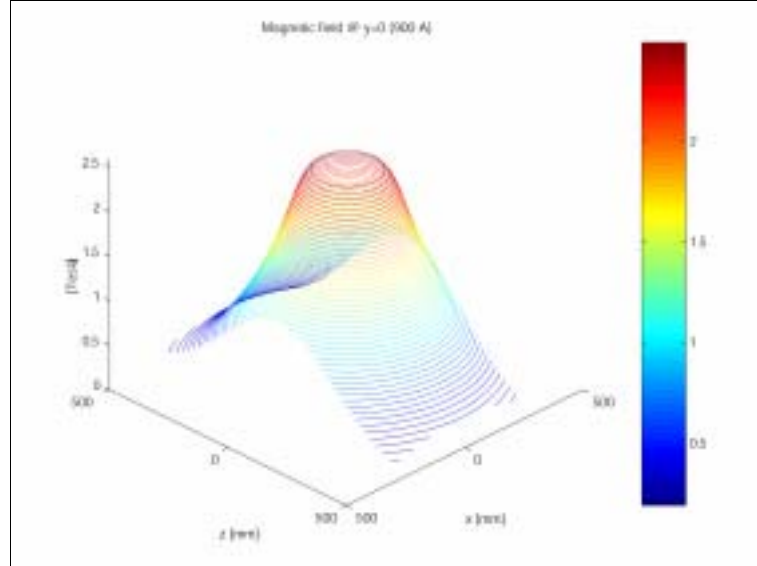
This plug is divided into four 20 cm slices, which can be either made of carbon (C), iron (Fe) or, if absent, of air (A). The slices are subsequently numbered with slice 1 being the innermost one.

Ver	Slice				Ver	Slice			
	1	2	3	4		1	2	3	4
1	Fe	Fe	Fe	Fe	9	Fe	C	A	A
2	Fe	Fe	Fe	C	10	Fe	A	A	A
3	Fe	Fe	Fe	A	11	C	C	C	C
4	Fe	Fe	C	C	12	C	C	C	A
5	Fe	Fe	C	A	13	C	C	A	A
6	Fe	Fe	A	A	14	C	A	A	A
7	Fe	C	C	C	15	A	A	A	A
8	Fe	C	C	A					

The magnetic field of the PT7 magnet

The magnetic field of the PT7 dipole magnet is very homogeneous (c.f. [8] and Figure 3), and reaches a strength of 2.5 T at the longitudinal position of the tracking telescope. The field can be fitted to an analytical function [c.f. Eq. (1) and (2)] and was implemented into the FLUKA calculations.

Figure 3. Three-dimensional representation of the PT7 magnetic field.
Note that in this figure the origin refers to the centre of the magnet.



$$\begin{aligned}
 B_r &= y \cdot \text{tail} \cdot \text{plateau} \\
 \text{tail} &= p_3 \cdot e^{-p_2 \cdot r^2} + p_5 \cdot e^{-p_4 \cdot r^2} \\
 \text{plateau} &= \frac{1}{1 + e^{-p_1 \cdot (r - p_0)}} \\
 r &= \sqrt{x^2 + z^2}
 \end{aligned}
 \tag{1}$$

$$B_y = p_1 \cdot \left((1 - plateau) \cdot tail + plateau \right) + bumps \quad (2)$$

$$tail = \frac{1}{1 + (p_0 \cdot r)^{p_4}}$$

$$plateau = e^{-(p \cdot p_0)^{p_2}}$$

$$\rho = \sqrt{r^2 + y^2 \cdot \frac{p_9 \cdot e^{p_{11}(r-p_{10})}}{1 + e^{p_{11}(r-p_{10})}}}$$

$$bumps = (p_5 \cdot y + p_6) \cdot e^{-(r-p_7)^{p_8}}$$

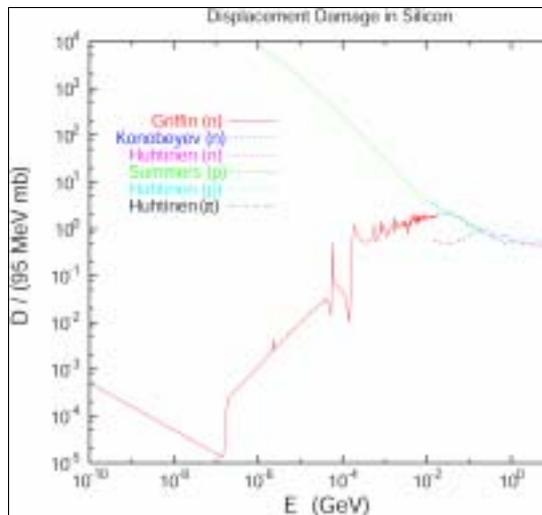
Simulation details and calculated quantities

For the simulation, a proton beam of 400 GeV/c was assumed to interact with the NA60 target, as used during the May 2002 run. In this configuration, the target consists of two millimetre thick slices of different materials. They are placed at six millimetres distance from each other and in the beam direction of the following order: one indium (In), three beryllium (Be), one lead (Pb) and again one beryllium target.

Electronics situated in the NA60 target region

The radiation damage of the electronics by ionising radiation was estimated by calculating the total dose (electromagnetic and hadronic) to silicon at the respective location of the electronic devices. The displacement damage is proportional to the Non-Ionising Energy Loss (NIEL) of a particle in the semiconductor lattice and can be expressed in terms of a displacement damage function $D(E)$, c.f. [9] and references therein. In order to characterise the damage efficiency of a particle for a given energy E , the values of $D(E)$ are normalised to the ones for 1 MeV neutrons (95 mb). Figure 4 (taken from [9]) shows a compilation of damage efficiency functions for silicon [10,11], which are widely used to estimate radiation damage in LHC experiments (e.g. [3]) and which were applied in this study.

Figure 4. Displacement damage functions for neutrons, protons and pions [11] (see also [10] and references therein). All values are normalised to the displacement damage by 1 MeV neutrons (95 MeVmb).



The damage functions are implemented as a FLUKA user subroutine [9], in order to fold the hadron fluence Φ with the 1 MeV neutron displacement damage function.

$$\Phi_{eq}^{1MeV} = \int dE \frac{D(E)}{95 \text{ MeV} \cdot \text{mb}} \Phi(E) \quad (3)$$

The resulting quantity was scored in a three-dimensional mesh for any location in the NA60 target region. Φ_{eq}^{1eV} (in units of $\text{cm}^{-2}\text{s}^{-1}$) can be considered as the equivalent 1 MeV neutron fluence producing the same bulk damage inside the electronic device.

Since the results are averaged over a rather large silicon volume of $8\,000 \text{ cm}^3$ (as compared to the size of the electronics), the real dose value therefore might be underestimated due to self-attenuation inside the silicon. However, this can be corrected for as described later in this paper.

Absorber configuration

In order to calculate the number of charged particles crossing the first muon chamber after the main hadron absorber, a geometrically equivalent model of the muon chamber was implemented in the geometry. In order to estimate the chamber response during one burst of interacting protons (i.e. for a high intensity run 5 s and $1.0 \cdot 10^9$ protons), the total number of charged particles crossing the muon chamber was scored.

The detector is triggered via the muon spectrometer, which demands that two muons be in coincidence. Thus, to get a better understanding of the effect of the different absorber configurations on the number of particles entering the muon chambers, charged particles and muons have been scored separately in a double-differential distribution in angle and energy. Therefore, the spectral distribution could be studied separately for muons and charged particles, which both result in a signal in the muon chamber.

To determine the lateral distribution of the interacting particles, fluence was scored in a regular mesh in x and y . To make a comparison possible between fluence values of different bins, it is necessary to use the same cross-section areas for each of the bins.

Biasing and energy thresholds used within the simulation

Electronics in the NA60 target region

For the calculation of the dose at the location of the electronics, a silicon volume was assumed and the energy deposited therein was scored. The results were corrected for self-attenuation, due to the large size of the silicon volume, as described below. In case of the damage to electronics, which uses fluence estimators, the silicon was replaced by air in order to avoid any self-attenuation at all. In order to save CPU-time, energy thresholds for the transport of electrons and photons in the displacement damage calculations were set higher than in the dose calculations. Since in the former calculations only the hadronic cascade was of interest, the threshold for electron/positron transport was set to 20 MeV and for photon transport to 6 MeV. For the latter case, the thresholds were lowered to 1 MeV and 100 keV for electrons/positrons and photons, respectively. Note that the energy limits for the displacement damage calculations approximately correspond to the lower energy threshold for Giant Dipole Resonance interactions.

Absorber configuration

In the case of the comparison of the different absorber configurations, the particle transport through the six-metre long absorber formed the main point of interest for biasing techniques. Particle splitting by region importance biasing was used in the different parts of the absorber corresponding to the material properties. According to the attenuation of particles inside the absorber, the region importance was increased, in order to enhance the statistical significance of the results.

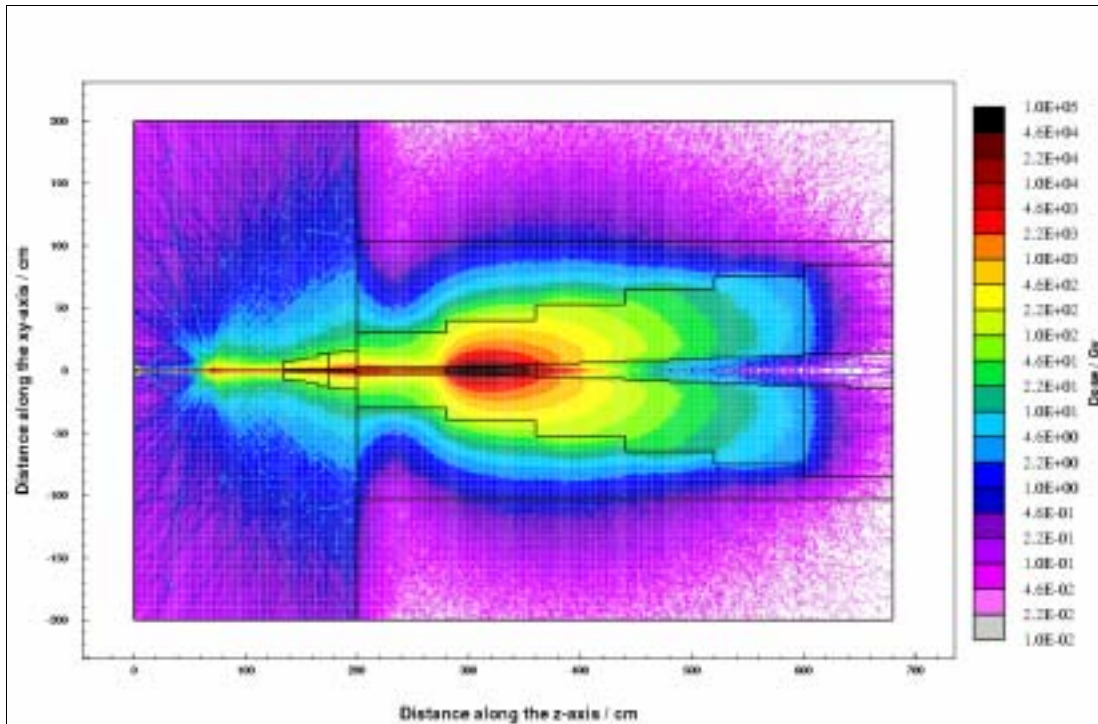
Since the particle cascade upstream of the last part of the absorber is identical for the different configurations – and in fact uses most of the CPU time – the simulation was split in two parts. In a first run the full geometry and interactions from the origin of the geometry downstream shortly before the actual absorber plug of interest was simulated and the particles were dumped into files. A second simulation used these particles as a source to simulate the cascade inside the last part of the geometry. The latter case was then used to compare the different material combinations inside the last part of the absorber.

Simulation results

To get a first impression of the radiation field in the target region and inside the absorber a cylindrical geometry was used. This allowed scoring quantities in an r/z binning (i.e. integrating in the azimuthal angle), which results in a faster statistical convergence. In this way the total dose distribution in the various materials of the experimental set-up was retrieved as shown in Figure 5.

Figure 5. Total dose distribution for the NA60 set-up, approximated by a cylindrical geometry

The dose values are normalised to one month of operation with a beam intensity of $1 \cdot 10^9$ protons per burst and are scored in the various materials of the geometry. The general distribution of the radiation field shows the regions of high and low doses and points already out that a removal of the final part of the absorber most probably would result in a high background rate in the first muon chamber.



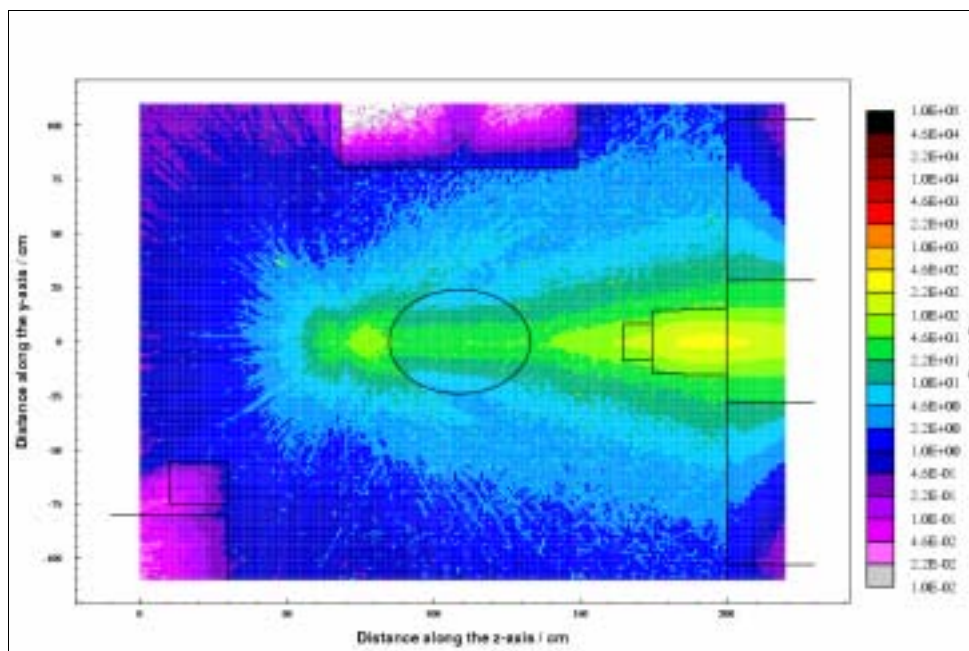
The aim of the following study was to understand the effect of the different possible absorber configurations and to determine the optimum placement of the electronics in the target region. Both results are discussed as follows.

Damage to electronics in the NA60 target region

The total dose deposited in the target region and the various materials was scored in a projection of the target region along the beam axis. Figure 6 shows the dose distribution in the xz plane and the chosen location of the electronics (c.f. rectangle at $x = -65$ cm, $y = 10$ cm, $z = 20$ cm).

Figure 6. Total dose distribution in the NA60 target region shown as an off-axis xz cut at $y = 10$ cm, which corresponds to the lateral location of the electronics

The dose values are normalised to one month of operation with a beam intensity of $1 \cdot 10^9$ protons per burst and are scored in the various materials of the geometry. The rectangle in the lower left corner represents the chosen location of the electronics.

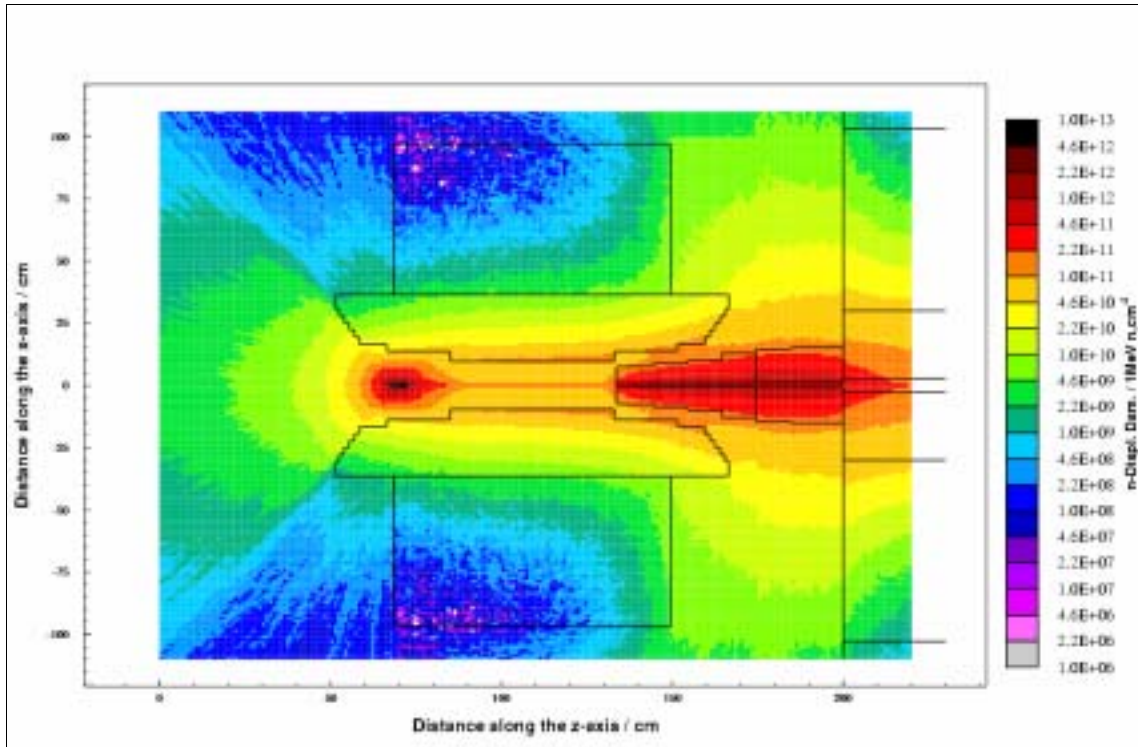


Displacement damage

The equivalent 1 MeV neutron fluence Φ_{eq}^{1MeV} was scored for neutrons, protons and charged pions in a mesh covering the whole NA60 target region with a bin size of $1 \text{ cm} \times 1 \text{ cm}$ in the projected plane and averaged over 10 cm in the perpendicular direction. In the regions of interest the displacement damage due to protons and pions was two orders of magnitude less than that due to neutrons. Hence, only the damage due to neutrons will be discussed. Figure 7 shows a vertical cut through the target region along the x - and z -axes. The values shown correspond to the simulated radiation damage induced by neutrons. The values are averaged over 1 cell volume in xz and 10 cm in the y direction and have to be interpreted as the displacement damage, which a silicon material (e.g. semiconductor device) would experience over one month of operation at high intensity (equal to $1.44 \cdot 10^{14}$ interacting protons).

Figure 7. Displacement damage by neutrons in silicon in a vertical section ($x = 0$) through the NA60 target region

The geometry shows the dipole magnet, the target on the left, the preabsorber and the first part of the main absorber on the right.



For the chosen location of the electronic devices, this results in a 1 MeV equivalent neutron fluence of $(2.0 \pm 0.1) \cdot 10^9 \text{ cm}^{-2}$.

Dose to electronics

From the distribution of the displacement damage the best position for installing the electronics was derived. Initially, the maximal cable length from the detector to the readout electronics was required to be relatively short, i.e. 50 cm. In this case, the electronics would have been close to the beam axis and the target, therefore, exposed to a rather high radiation field. Fortunately, during the last month of detector development, this maximum cable length could be extended to 1.5 m. Due to the field distribution, a placement as upstream as possible seemed to be the best solution. Hence, we chose the location shown in Figure 2.

The result for the total dose deposited in the silicon volume at the chosen location is given as:

$$0.30 \pm 0.02 \text{ Gy}$$

The quoted error reflects the statistical uncertainties of the Monte Carlo simulation only. The intrinsic error introduced due to simplifications is not taken into account. Note that this result is an average value for a rather large silicon volume (as compared to the size of the electronics) and the real dose value therefore, might be underestimated due to self-attenuation in the silicon.

This underestimation can, however, be corrected for silicon, if the attenuation is known. It is assumed that silicon and concrete have similar properties so that the dependence of energy deposition decreases exponentially with depth with a slope of 0.063 cm^{-1} [9]. Assuming furthermore that the location inside the silicon volume that corresponds to the average dose value is shielded by 12 cm of silicon, the resulting correction factor would be $e^{(0.063 \text{ cm}^{-1} \cdot 12 \text{ cm})} = 2.2$. Using this correction factor, the actual dose delivered to an electronic component is $0.66 \pm 0.04 \text{ Gy}$.

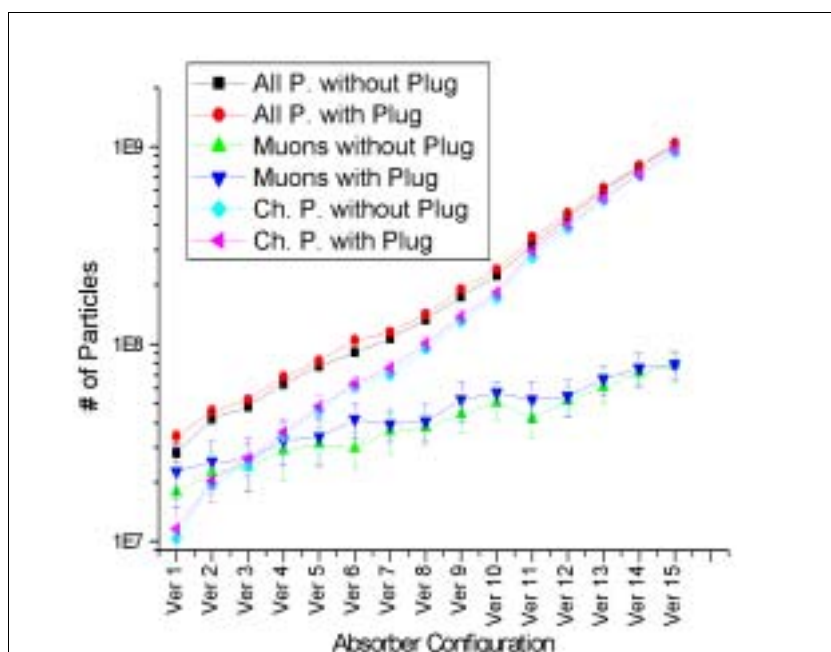
Determination of the optimum absorber configurations

During the October 2001 run the sensitive configuration of the last 80 cm of the absorber and its drastic consequences to the first and even second muon chamber have been recognised. If the last block of the absorber (c.f. Figure 2) is removed completely, a large number of charged particles overwhelm the first muon chamber, therefore making measurements extremely difficult. On that score, we studied different configurations of the main absorber.

In order to compare the different configurations from the simulation point of view, the number of particles entering the first muon chamber was counted. The results were normalised to one burst of protons ($1 \cdot 10^9$) interacting with the target and the downstream absorber. The values compared for the different versions of the absorber (c.f. Table 1) are shown in Figure 8.

Figure 8. Number of charged particles entering the first muon chamber

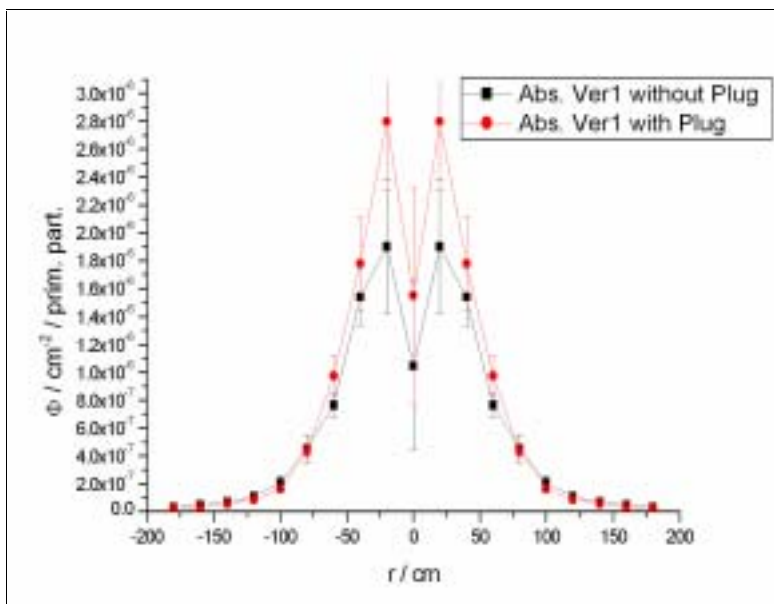
Different absorber configurations are compared; note the effect of the additional plug. The number of particles was normalised to one burst of protons.



Unfortunately, the additional tungsten plug in front of the ZDC does not help to suppress the particles. On the contrary, due to the interaction centre shifted to negative z values and the large radiation length of carbon, more particles are produced and leave the absorber. Plotting the lateral distribution (xy) of the charged particles that enter the first muon chamber shows this unwanted effect (c.f. Figure 9).

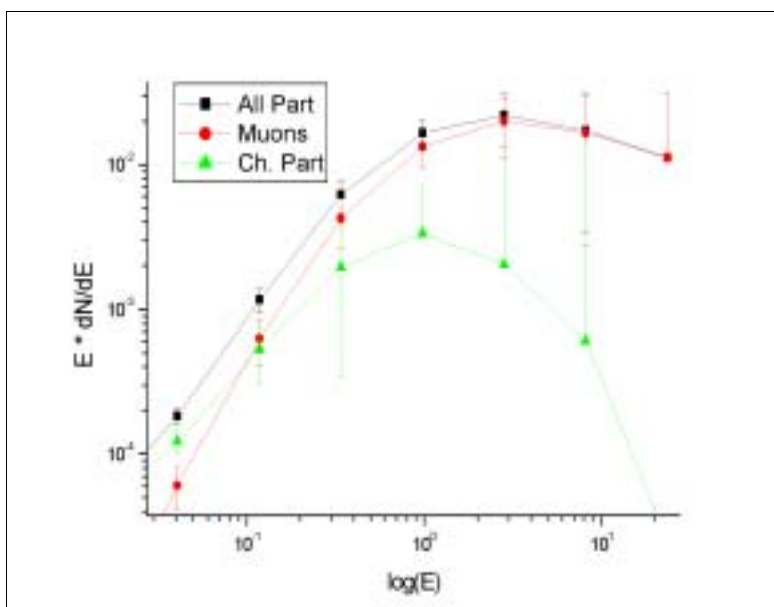
Figure 9. Lateral distribution in xy of the number of particles leaving the absorber and entering the first muon chamber

The version including the additional tungsten plug is compared to the standard NA60 absorber set-up



The energy distribution of the particles interacting with the first muon chamber (i.e. for the absorber configuration “Ver 1”) is shown in Figure 10. It is obvious that the main portion of the interacting charged particles has high energies and will therefore interact in the first muon chamber and will produce a signal in the muon chambers downstream as well.

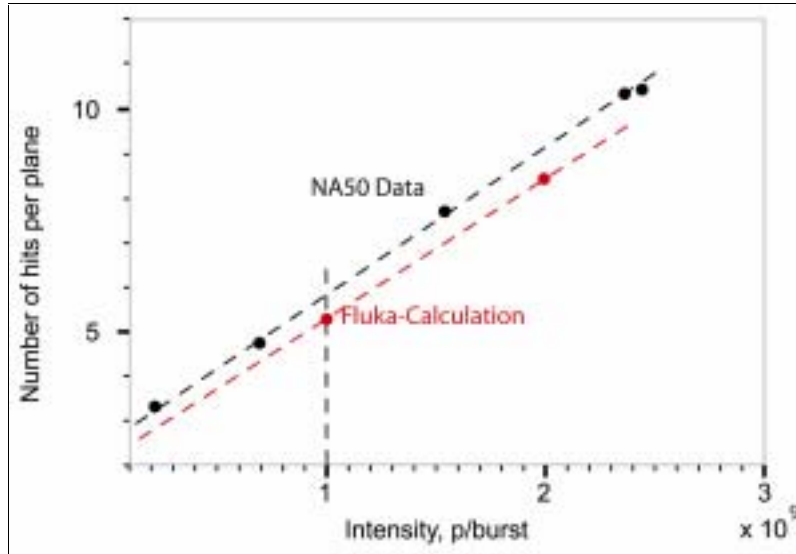
Figure 10. Energy distribution of charged particles and muons for “Ver 1”



A very good agreement was obtained, comparing the FLUKA results with the number of particles interacting with the first muon chamber measured during the NA50 proton runs (c.f. Figure 11).

Figure 11. Number of hits per plane [12] inside the first muon chamber, plotted as a function of the beam intensity

The NA50 data are compared to the results obtained with the FLUKA simulation



During these measurements, an absorber configuration equivalent to “Ver 1” (c.f. Figure 8) was used. This corresponds to a total number of $3.5 \cdot 10^7$ charged particles interacting with the first muon chamber. Since the number of hits in Figure 11 corresponds to a trigger gate of ~ 100 ns and the fact that it is necessary to add the two triggered muons, the equivalent value of Figure 8 in Figure 11 for “Ver 1” is $((3.2 \cdot 10^7 \cdot 10^2) / 1.0 \cdot 10^9) + 2 = 5.2$. This results in a very good agreement at intensity of $1 \cdot 10^9$ protons per burst. However, in this comparison lies a non-negligible uncertainty, since it is not fully known what exact configuration has been used for the “ZDC” during the NA50 runs.

Conclusions

The present study provides estimates for the radiation damage to electronics in the NA60 target region. Total doses delivered to silicon and equivalent 1 MeV neutron fluences were calculated with FLUKA. Due to this calculation, the optimal placement at a given maximal cable length was obtained.

Over one month of operation, the electronics installed at the given location will receive a total dose of 0.66 ± 0.04 Gy. The equivalent 1 MeV neutron fluence is estimated to be about $(2.0 \pm 0.1) \cdot 10^9 \text{ cm}^{-2}$. Therefore, at the given location, the electronic devices should sustain the radiation field without damage. Note that single event effects (c.f. [3]) have not been considered in these calculations.

The study of different absorber configurations resulted in the final configuration of the NA60 main absorber. It was shown that an additional tungsten plug would not help to suppress the charged particles, but results in even more interactions in the first muon chamber. The configuration-dependent result of the number of interacting charged particles and especially of muons allowed the determination of the best compromise between little muon scattering and a good suppression of background particles.

Based on the simulation results, the NA60 collaboration was able to find an optimal position for the electronics. In the case of the absorber configurations, “Ver 7” will be used for the May 2002 proton run.

Acknowledgements

The authors are grateful to Alfredo Ferrari who provided the FLUKA code and to Stefan Roesler for providing the FLUKA implementation of the displacement damage functions as well as for valuable comments on the manuscript. Many thanks go to Heinz Vincke for his constant support and help with the handling and set-up of FLUKA. The CERN TIS-RP/CP group participated in many fruitful discussions, and without the significant support from the whole NA60 collaboration, these studies could not have been performed.

REFERENCES

- [1] Fassò, A., *et al.*, “Electron-photon Transport in FLUKA: Status”, *Proceedings of the International Conference on Advanced Monte Carlo for Radiation Physics, Particle Transport Simulation and Application (Monte Carlo 2000)*, Lisbon, Portugal, 23-26 October 2000, p. 159, A. Kling, *et al.*, eds., Springer-Verlag, Berlin, Heidelberg (2001).
- [2] Fassò, A., *et al.*, “FLUKA: Status and Perspectives for Hadronic Applications”, *Proceedings of the International Conference on Advanced Monte Carlo for Radiation Physics, Particle Transport Simulation and Application (Monte Carlo 2000)*, Lisbon, Portugal, 23-26 October 2000, p. 955, A. Kling, *et al.*, eds., Springer-Verlag, Berlin, Heidelberg (2001).
- [3] Huhtinen, M. and F. Faccio, “Computational Method to Estimate Single Event Upset Rates in an Accelerator Environment”, *Nuclear Instruments and Methods in Physics Research, Section A*, Volume 450, Issue 1, pp. 155-172 (2000).
- [4] <http://na60.web.cern.ch/NA60/>
- [5] Buytaert, J., *et al.*, *The NA60 Silicon Tracking Telescope for Proton Running*, NA60 Note, 2001-5, 1 July 2001.
- [6] Morsch, *ALIFE: A Geometry Editor and Parser for FLUKA*, November 1997.
- [7] Vincke, H., “Flukacad/Pipsicad: Three-dimensional Interfaces Between FLUKA and AutoCAD”, *Proceedings of SATIF-5*, Paris, France, 18-21 July 2000, pp. 361-370 (2001).
- [8] Banicz, K., *et al.*, *The PT7 Magnet*, NA60 Internal Note, CERN, May 2001.
- [9] Roesler, S., *et al.*, “Radiation Damage to Electronics in the Beam Tunnel of the Next Linear Collider”, *Proceedings of SATIF-5*, Paris, France, 18-21 July 2000, pp. 127-137 (2001).
- [10] Lindström, G., *et al.*, “Radiation Hardness of Silicon Detectors – A Challenge from High-energy Physics”, *Nucl. Instrum. Meth.*, A426, 1 (1999).
- [11] Vailescu (INPE Bucharest) and G. Lindström (University of Hamburg), *Displacement Damage in Silicon, On-line Compilation*, <http://sesam.desy.de/~gunnar/Si-dfuncs.html>.
- [12] Shahoian, R., private communication, *NA50 Proton Data Results*, CERN, March 2002.

**EXPERIMENTAL AND CALCULATED NEUTRON PRODUCTION BY DEUTERONS
IMPINGING ON Be, C AND U THICK TARGETS (17, 20, 28, 80, 160 AND 200 MeV)***

N. Pauwels, F. Clapier, J. Proust
Institut de Physique Nucléaire d'Orsay
F-91406 Orsay Cedex, France

M. Mirea
Institute of Physics and Nuclear Engineering Bucarest
P.O. Box MG-6, Romania

Abstract

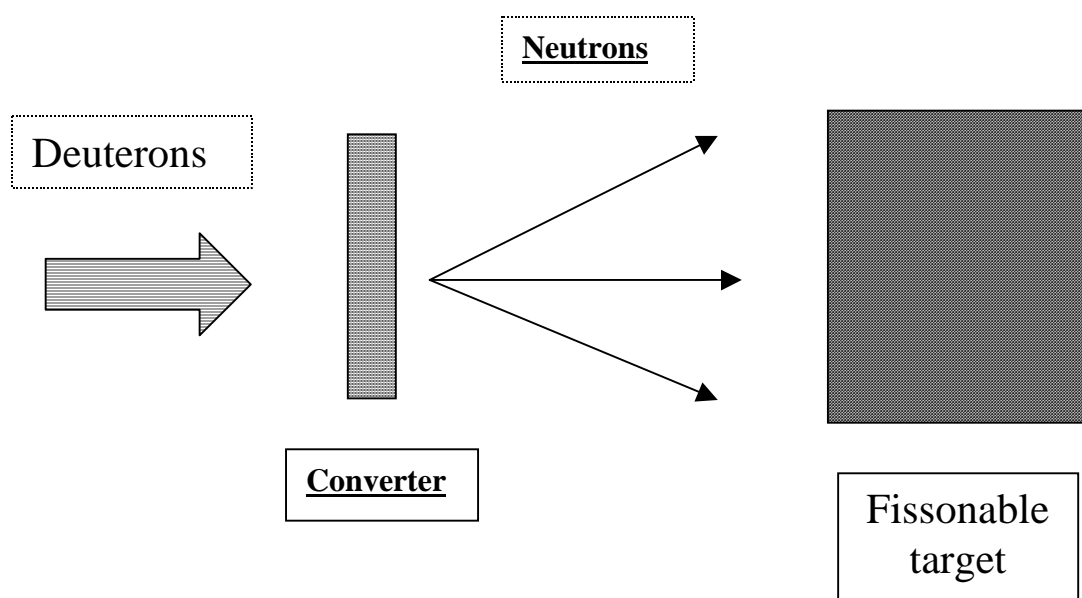
Experimental angular and energy distributions of neutrons secondary to the interaction between deuterons and thick targets of Be, C and U are presented. The incident deuteron beam energies were 17, 20, 28, 80, 160 and 200 MeV and the data were obtained using the time of flight or activation detectors methods. These data are compared with a model based on the stripping formalism extended to thick targets.

* *This paper was erroneously omitted from SATIF-5. Our sincerest apologies to the authors.*

Introduction

The production of neutron rich radioactive beams can be obtained through the fission of ^{238}U induced by fast neutrons [1]. The technique (Figure 1) can be summarised as follows: fast neutrons are produced which then irradiate a thick fissionable target; the resulting fission products are extracted, ionised, mass-selected and accelerated. The main objective of the PARRNe and SPIRAL-II R&D projects is the investigation of the optimum conditions for a neutron rich isotope source [2,3]. One way to produce neutron beams is to break deuterons on a thick target (called a converter). The energy and the angular distributions of the neutrons obtained with this method and used to irradiate the fissionable target are some of the important parameters to study. For this study, one needs experimental data and a theoretical model to predict the characteristics of neutron beams for a large range of incident deuteron energy and for different converters.

Figure 1. Schematic set-up of the technique



The experimental data were obtained with deuteron beams of 17, 20, 28, 80, 160 and 200 MeV stopped in Be, C or U [4,5]. The model developed is based on Serber's theory [6].

Experimental set-up

The measurement of angular and energy distributions of neutrons were performed with the time of flight method for deuteron energies ranging from 17 to 160 MeV and with the activation detectors method at 200 MeV.

For the time of flight technique a set of DEMON and EDEN detectors were displayed around the target. These two kinds of detectors are filled with an organic scintillator liquid and are described in Refs. [7,8]. The activation detectors used for the experiment at 200 MeV were made of Al, Ni, Co and Bi. The characteristics of the neutron cross-sections of Bi were recently determined experimentally and compared with calculated ones [9]. The different experimental configurations (beam energy, converter) and the angles of detection are reported in Table 1. In all cases the deuterons were completely stopped in the converter.

Table 1. Experimental configurations

Deuteron energy (MeV)	Beryllium (deg.)	Carbon (deg.)	Uranium (deg.)
17*	0, 5, 10, 20	–	–
20*	0, 5, 10, 20	0, 5, 10, 20	0, 5, 10, 20
28*	0, 5, 10, 20	0, 5, 10, 20	0, 5, 10, 20
80**	2.4, 3.4, 6, 8.7, 11.1, 15.2, 20.6, 24.5, 30.1, 33.4, 41.4, 50, 70, 90	2.4, 3.4, 6, 8.7, 11.1, 15.2, 20.6, 24.5, 30.1, 33.4, 41.4, 50, 70, 90	–
160**	2.4, 3.4, 6, 8.7, 11.1, 15.2, 20.6, 24.5, 30.1, 33.4, 41.4, 50, 70, 90	2.4, 3.4, 6, 8.7, 11.1, 15.2, 20.6, 24.5, 30.1, 33.4, 41.4, 50, 70, 90	–
200***	0, 11, 36, 60, 84	–	0, 11, 36, 60, 84

* Time of flight (TANDEM, Orsay).

** Time of flight (KVI, Gröningen).

*** Activation detectors (LNS, Saclay).

Model

The model is derived from the semi-classical Serber theory [6]. This theory provides an approximation for the relative neutron energy and angular distribution obtained by the bombardment of a thin target by high-energy deuterons. The relative distributions can be calculated for thick targets and intermediate energies by making averages of the target thickness and selected angles, and by extending the formalism towards low deuteron energies. The target thickness will always be considered as equal to the range of the deuteron as a function of incident energy in the given material. The theoretical relative distribution is normalised using an experimental systematic of neutron yields at 0° for Be targets. These yields are extracted from experimental data available in the literature for deuteron energies between 5 and 50 MeV. The yields between 50 and 200 MeV are taken from our experimental results. Afterwards, a simple formula is used to generalise the results for other kinds of targets.

Results and discussion

The neutron energy and angular distributions are presented in Figures 2-5 for 20, 80, 160 and 200 MeV deuterons and different converters. In all cases the neutron yields delivered by the Be thick targets are about 1.4 greater than those obtained with the C. The neutron yields produced with the U converter are always small in comparison.

The energy distribution clearly shows two well-known regions: the first region corresponding to the low-energy neutrons which are mainly produced by the evaporation of the target and the second region corresponding to high-energy neutrons generated by the break-up of the deuterons.

The angular distribution of neutrons are slightly narrower with the Be than with the C. As expected, for both Be and C targets, the full width at half maximum of the angular distributions decreases when the deuteron energy increases.

The experimental values are well reproduced by the model up to about 15°, whereas large discrepancies appear above that parameter. These differences are due to the neutrons produced by the evaporation and which are not included in our simulation. In the forward direction, the break-up dominates the production, this being why the simulation is in good agreement with the experiment. At higher angles the main process becomes the evaporation.

Conclusion

Given the data made available one can consider that a good basis for Monte Carlo codes benchmarking has been developed at energies above 50 MeV for deuterons impinging on beryllium and carbon thick targets. As for the project we pursue, specifically the choice of the best deuteron energy and neutron production target to produce neutron rich radioactive beams, the work presented here adds precious guidance.

REFERENCES

- [1] Nolen, J., *Third International Conference on Radioactive Nuclear Beam*, D.J. Morrissey, ed., Edition Frontières, Gif-sur-Yvette (1993), 111.
- [2] Clapier, F., A.C. Mueller, J. Obert, O. Bajeat, M. Ducourtieux, A. Ferro, A. Horbowa, L. Kotfila, C. Lau, H. Lefort, S. Kandri-Rody, N. Pauwels, J.C. Potier, J. Proust, J.C. Puteaux, C.F. Liang, P. Paris, A.C.C. Villari, R. Lichtenthäler, L. Maunoury, *J. Lettry. Phys. Rev. Special Topics – Accelerators and Beams*, Vol. 1 (1998), 1-3.
- [3] Kandri-Rody, S., J. Obert, E. Cottureau, O. Bajeat, M. Ducourtieux, C. Lau, H. Lefort, J.C. Potier, J.C. Puteaux, F. Clapier, J. Lettry, A.C. Mueller, N. Pauwels, J. Proust, C.F. Liang, P. Paris, H.L. Ravn, B. Roussière, J. Sauvage, J.A. Scarpaci, F. Leblanc, G. Lalu, I. Lhenry, T. Von Egidy, R. Antoni, *Nucl. Instr. Methods*, B 160 (2000), 1-6.
- [4] Menard, S., M. Mirea, F. Clapier, N. Pauwels, J. Proust, C. Donzaud, D. Guillemaud-Mueller, I. Lhenry, A.C. Mueller, J.A. Scarpaci, O. Sorlin, *Phys. Rev. Special Topics – Accelerators and Beams*, Vol. 2 (1999), 1-14.
- [5] Pauwels, N., F. Clapier, P. Gara, M. Mirea, J. Proust, *Nucl. Instr. Methods*, B 160 (2000), 315-327.
- [6] Serber, R., *Phys. Rev.*, 72 (1947), 1 008-1 016.
- [7] Tilquin, I., Y. El Masri, M. Parlog, Ph. Collon, M. Hadri, Th. Keutgen, J. Lehmann, P. Leleux, P. Lipnik, A. Nimane, F. Hanappe, G. Bizard, D. Durand, P. Mosrin, J. Péter, R. Réggimbart, B. Tamain, *NIM A* 365 (1995), 446-461.
- [8] Laurent, H., H. Lefort, D. Beaumel, Y. Blumenfeld, S. Fortier, S. Galès, J. Guillot, J.C. Roynette, P. Volkov, S. Brandenburg, *NIM A* 326 (1993), 517-525.
- [9] Kim, E., T. Nakamura, A. Konno, Y. Uwamino, N. Nakanishi, M. Imamura, N. Nakao, S. Shibata, S. Tanaka, *Nuc. Sci. Eng.*, 129 (1998), 209-223.

Figure 2. Energy and angular distribution of neutrons produced by 20 MeV deuterons on thick targets

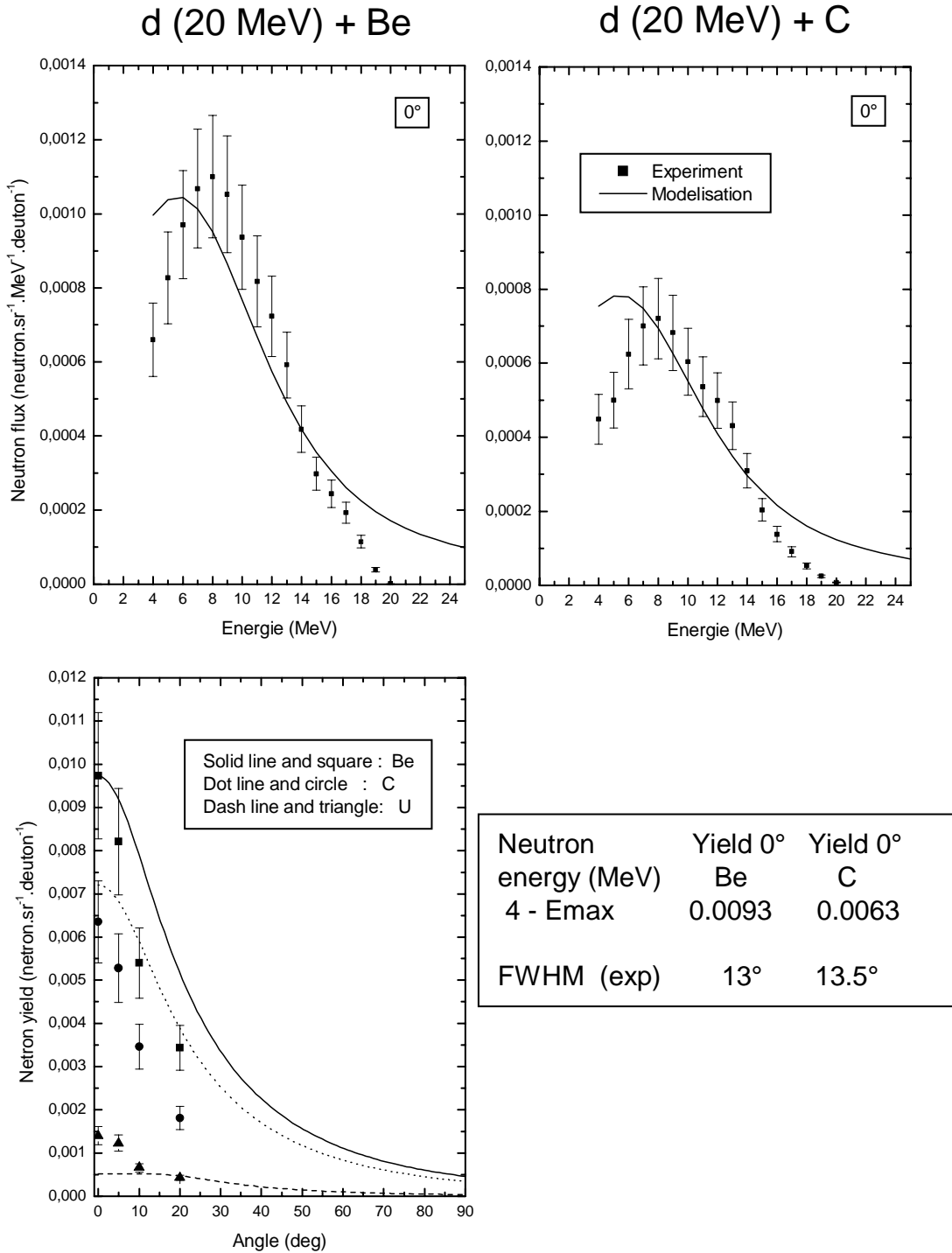


Figure 3. Energy and angular distribution of neutrons produced by 80 MeV deuterons on thick targets

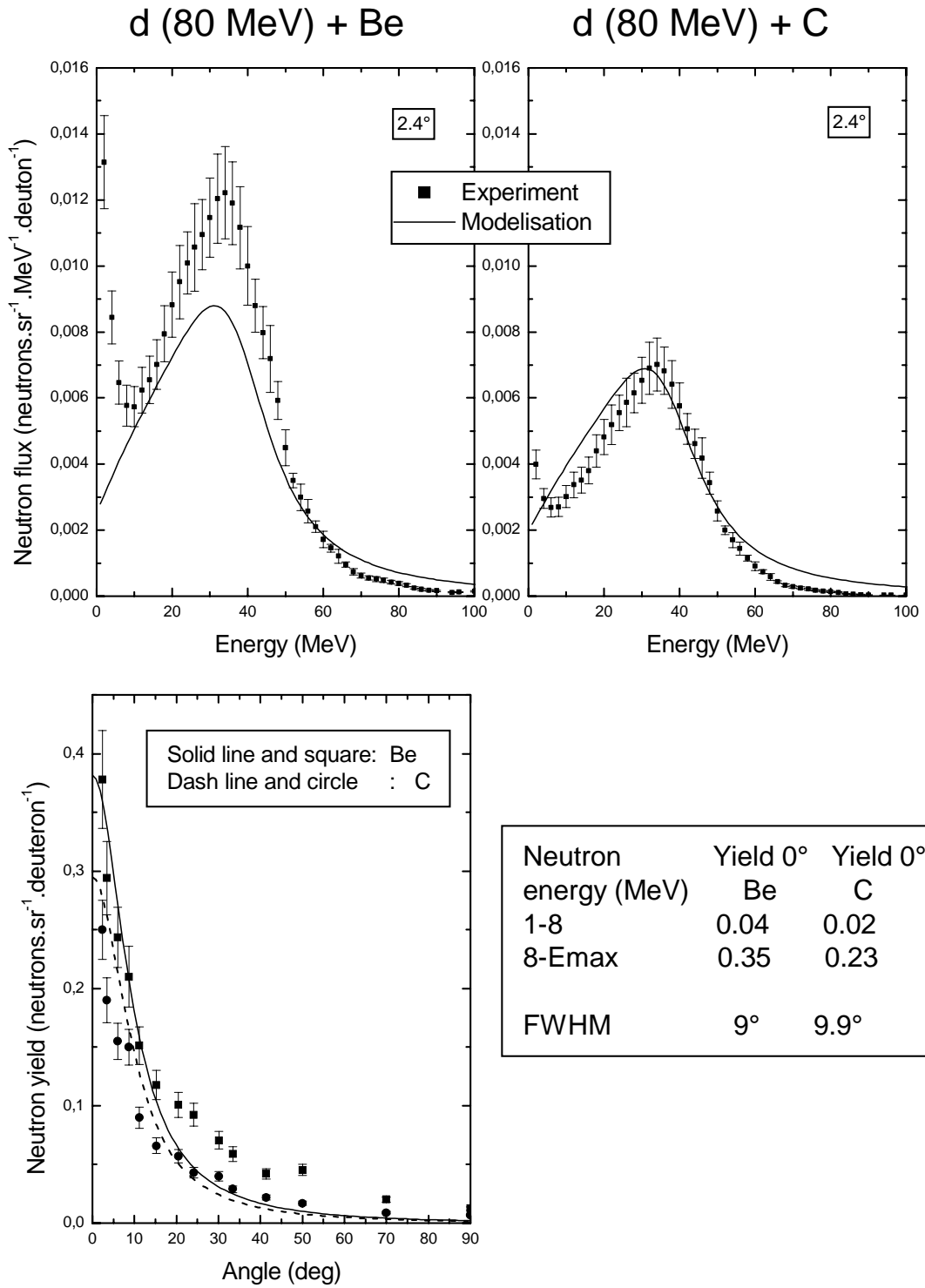


Figure 4. Energy and angular distribution of neutrons produced by 200 MeV deuterons on thick targets

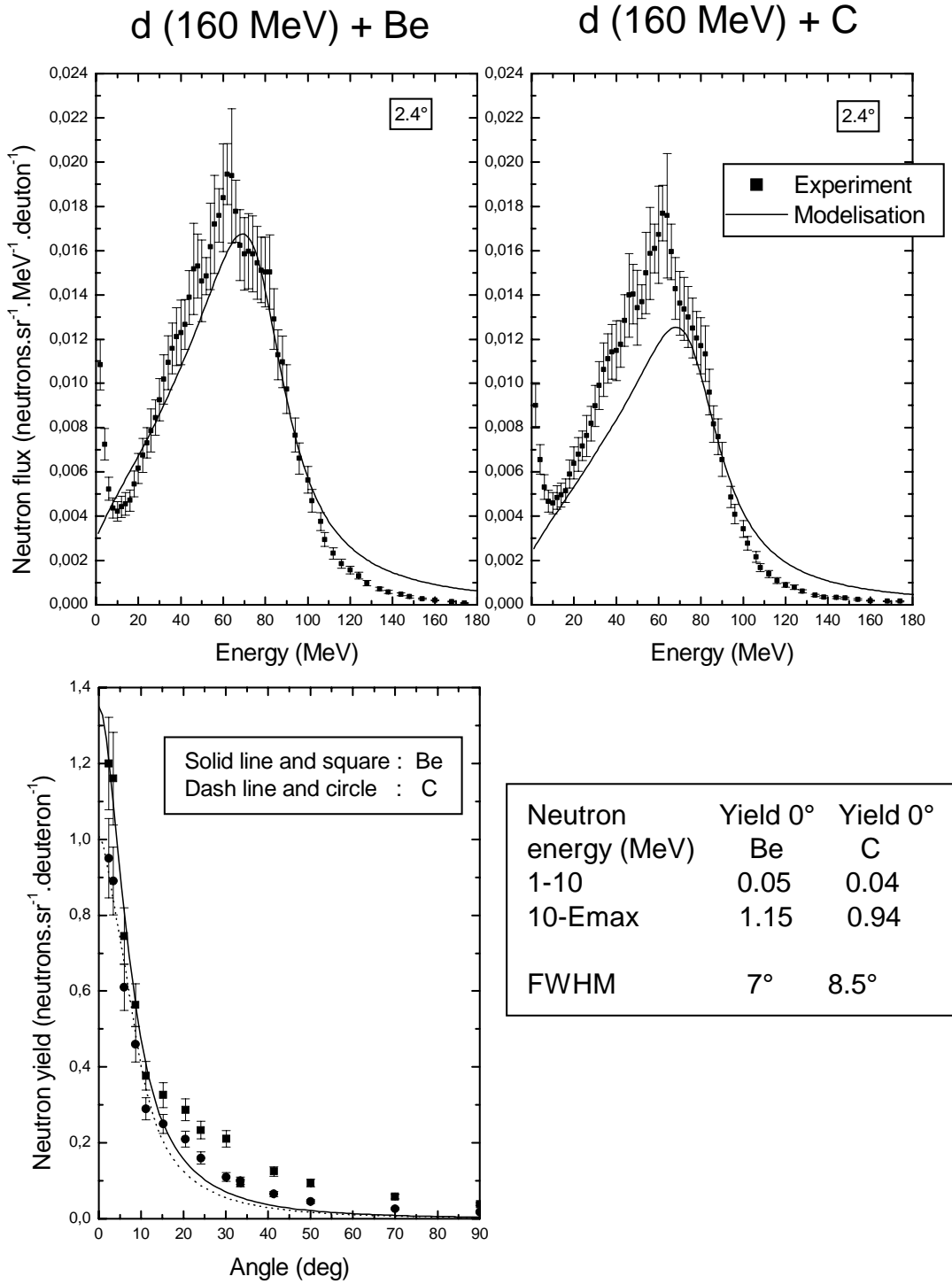
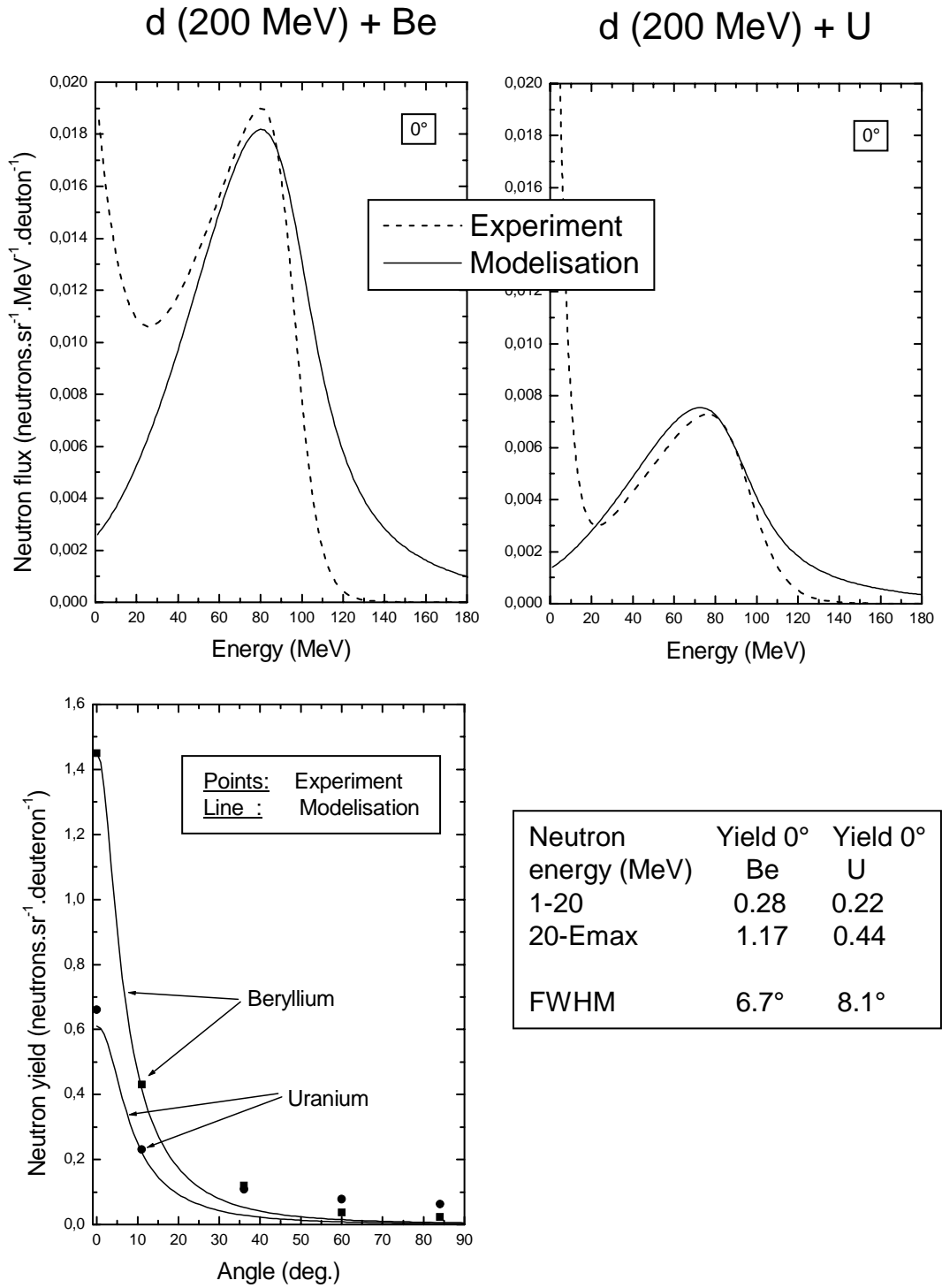


Figure 5. Energy and angular distribution of neutrons produced by 200 MeV deuterons on thick targets



SESSION II

**Measurements and Calculations
of Induced Radioactivity**

Chair: M. Silari

INDUCED RADIOACTIVITY OF MATERIALS BY STRAY RADIATION FIELDS AT AN ELECTRON ACCELERATOR

S.H. Rokni, T. Gwise, J.C. Liu
Stanford Linear Accelerator Center
Menlo Park, California 94025, USA

A. Fassò, S. Roesler
CERN-EP/AIP, CH-1211 Geneva 23, Switzerland

Abstract

Samples of soil, water, aluminium, copper and iron were irradiated in the stray radiation field generated by the interaction of a 28.5 GeV electron beam in a copper dump in the Beam Dump East facility at the Stanford Linear Accelerator Center. The specific activity induced in the samples was measured by gamma spectroscopy and other techniques. In addition, the isotope production in the samples was calculated with detailed Monte Carlo simulations using the FLUKA code. The calculated activities are compared to the experimental values and differences are discussed. Taking the uncertainties in the measurements and simulations into account, the agreement of measured and calculated induced radioactivity within a factor of two, as is the case for half of the identified isotopes in this study, can be considered to be acceptable.

Introduction

One of the main radiation safety issues at high-energy electron accelerators is the personnel exposure from induced radioactivity in beam line components and shielding materials. Additionally, the concentration of induced activity in the groundwater and soil in the environment surrounding the accelerator needs to be carefully evaluated as part of documents required by overseeing agencies. Therefore, an accurate calculation of the induced radioactivity in various materials has become an essential part of the design and operation of high-energy electron accelerators.

The radiation field causing induced radioactivity at electron accelerators is very complex, as it involves both electromagnetic and hadronic cascade processes. Calculation techniques based on analytical methods that are commonly used in predicting the amount of induced activity generally have large uncertainties associated with them [1]. These uncertainties can be at least an order of magnitude [2], for example in situations where multi-material structures are exposed to beam or stray radiation. Additionally, analytical methods require information on production cross-sections of various radionuclides which often does not exist.

Recently, the Monte Carlo particle interaction and transport code FLUKA [3-5] has been used for directly calculating the isotope production by electron-induced particle showers [2,6,7]. In order to estimate the reliability and predictive power of the involved models the results must be benchmarked against experimental data. Unfortunately, such experimental information is still very limited for electron accelerators. A first detailed benchmark study based on an in-beam geometry experiment [8] was discussed in [2]. However, radioactivity in an accelerator environment is often caused by stray radiation which may activate beam line components, cooling water circuits as well as in soil and groundwater. A benchmark study of this aspect can be found in [6] which, however, carried large uncertainties associated with the number of beam particles, the chemical composition of the samples used in the measurement and the correction for self-absorption due to the thickness of the targets.

In order to provide further data on activation of materials by stray radiation fields an experiment was performed in the Beam Dump East facility at the Stanford Linear Accelerator Center. Samples of soil, water, aluminium, copper and iron were exposed to stray radiation from the interaction of 28.5 GeV electrons in a beam dump. This paper describes the measurements and data analysis and compares the specific activities of the different samples with results of detailed FLUKA calculations.

The experiment

The soil sample was taken from an area on the SLAC site and its stones and other debris were removed. It was dried, sieved to 0.208 mm and packaged in a 500 ml plastic bottle. An outside company (Element Analysis Corporation, 101 Ventura Ct., Lexington, KY 40510) determined the chemical composition which is listed in Table 1 using a combination of proton-induced X-ray emission (PIXE), proton-induced gamma-ray emission (PIGE) and fast neutron activation analysis techniques. The density of the soil sample was measured to be 1.3 g/cm^3 . Furthermore, a sample of low conductivity water was also prepared by filling it into a 500 ml bottle. The metallic samples had a diameter of 4.45 cm and a thickness and density that is used for building magnets at SLAC. The composition of the metallic samples was again determined by an outside company (Calcoast Analytical, 4072 Watts Street, Emeryville, CA 94608) using chemical analysis methods.

For the experiment a water-cooled copper dump, 14.4 cm in diameter and 25.2 cm in length, was placed in the Beam Dump East facility upstream of the main beam dump D400. The metallic disks were taped on the soil and water bottles which were placed on an aluminium table 31 cm below the dump.

Table 1. Chemical composition of the soil sample (in % by weight)

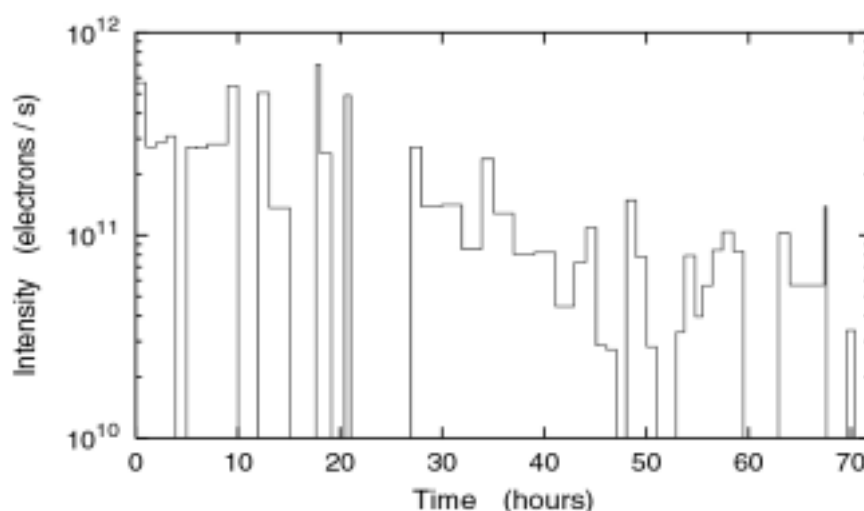
O	54.41	Mn	3.163×10^{-2}
Si	31.98	Zr	1.987×10^{-2}
Al	6.235	Sr	9.705×10^{-3}
Fe	2.106	Ni	6.684×10^{-3}
Na	1.841	Cu	5.108×10^{-3}
K	1.219	Zn	4.694×10^{-3}
Mg	1.045	Rb	4.439×10^{-3}
Ca	6.782×10^{-1}	Pb	2.440×10^{-3}
Ti	3.495×10^{-1}	Br	7.931×10^{-4}
Cr	5.034×10^{-2}	Ga	5.969×10^{-4}

Table 2. Density, thickness and chemical composition (in % by weight) of the metallic samples

Sample	Iron		Aluminium		Copper	
Density (g/cm^3)	7.43		2.67		8.89	
Thickness (mm)	0.9		0.7		1.6	
Composition	Fe	99.15	Al	99.82	Cu	99.415
	Sn	0.5	Fe	0.18	Zn	0.5
	Mn	0.35			Sn	0.05
					Ni	0.025
					Ag	0.01

The irradiation started on 6 February 2000 and lasted for about three days during which a total of 2.88×10^{16} beam electrons of an energy of 28.5 GeV were sent onto the dump. The irradiation profile was monitored with an upstream toroid and is shown in Figure 1.

Figure 1. Beam profile during the experiment



Data analysis

Tritium measurements

A liquid scintillation counter (Packard BioSciences, Canberra Industries, 800 Research Parkway, Meriden, CT 06450) was used to analyse the water sample for tritium. Two 5 ml aliquots of the sample were dispensed into 20 ml plastic scintillation vials with 15 ml of cocktails. The samples with similarly prepared background and quality control samples were counted as a batch three times. Each batch was counted for 300 minutes per cycle. The minimum detectable activity was approximately 4.7 Bq/l.

The tritium in the soil was measured by an outside company (Thermo Retec Nuclear Service, 7030 Wright Ave., Richmond, VA 94804) which heated a small amount of the irradiated soil (0.05-0.2 g) to ignition. The combustion gases were condensed, collected in a liquid scintillation vial and counted.

Gamma spectroscopy

The gamma rays from the irradiated soil and water samples as well as the metallic disks were measured with a high-purity Ge detector. The spectroscopy of the samples was performed using the EG&G ORTEC Gammavision data acquisition and analysis package (EG&G Ortec, 100 Midland Road, Oak Ridge, TN 37831). The Gammavision package is comprised of a set of complete algorithms for nuclide identification, background subtraction, efficiency corrections and the determination of the activity for each radionuclide. A sample of the irradiated soil of a weight of 579.9 g was counted for 12 hours. The background was determined by counting an un-irradiated sample of the soil, weighing 582.2 g, in the same geometry. The activity of 40 K was measured at 0.42 Bq/g. The activities of ^{232}Th and ^{382}U were estimated from their progenies to be 0.013 and 0.27 Bq/g. The same detector was used to measure the activity of a 480 ml sample of the irradiated water and the metallic disks. The water and the metallic samples were counted for 12 and 4 hours, respectively. A traceable source of the National Institute of Standards and Technology (NIST) was used to create the efficiency and energy calibrations. In addition, a post-measurement comparison of the calibration files to the source was performed as a quality control check.

The FLUKA calculations

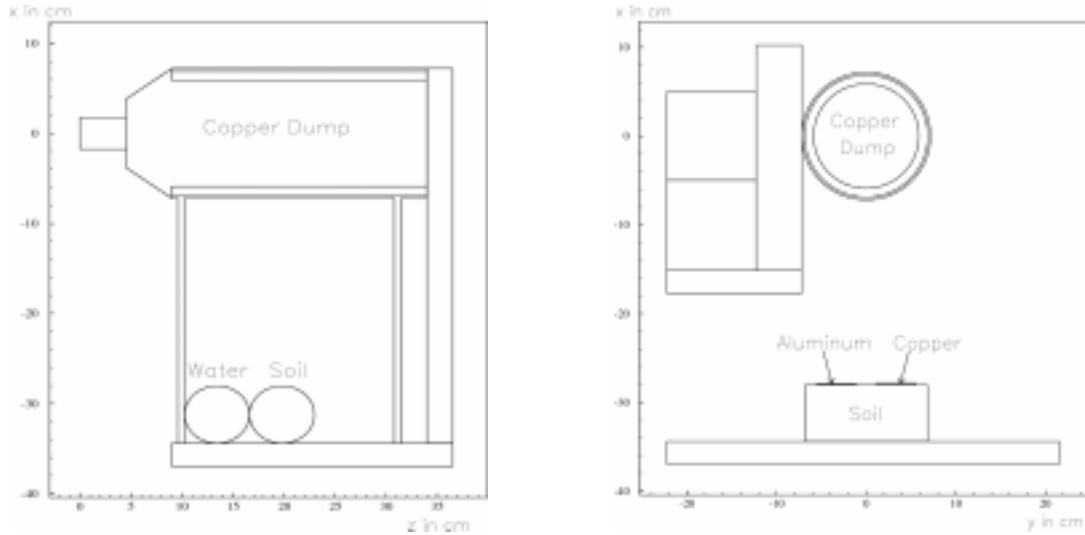
The concentration of different radionuclides in the samples was calculated with FLUKA based on a detailed description of the experimental set-up. A 13 m long section of the beam tunnel was modelled containing the copper dump and its support structure, the samples, local lead shielding along one side and downstream of the dump and the main beam dump D400 which is a big cylindrical water tank. Figure 2 shows longitudinal and transverse sections through the geometry of the copper dump and the samples. The D400 dump is downstream of the copper dump and is not shown in the figure.

The small object in front of the copper dump [see Figure 2(a)] is a strontium-ferrite probe which was installed as part of a material damage study. The bodies to the left of the dump in Figure 2(b) are lead and copper shielding blocks, respectively. The geometry also contained the metallic samples in their true size. The aluminium and copper disks were taped on top of the soil bottle [see Figure 2(b)] and the iron disk on top of the water bottle. The origin of the co-ordinate frame of the FLUKA geometry was chosen to be in the centre of the front face of the SrFe probe, the z -axis coinciding with the beam axis and the x -axis pointing up.

Figure 2. Sections through the geometry used in the simulations

(a) Longitudinal section containing the beam axis ($y = 0$)

(b) Transverse section through the soil bottle and the aluminium and copper disks ($z = 20$ cm)



The elemental compositions of the samples were defined in the simulations according to the elemental analyses as listed in Tables 1 and 2. The full electromagnetic and hadronic cascades were simulated in the dump, the samples and the shielding items including particles backscattered from the main dump and the beam tunnel walls. Electrons and photons were transported down to a kinetic energy of 12 MeV and 10 MeV, respectively, and neutrons down to thermal energies. The former limits are below the threshold for the production of the Giant Resonance neutrons in most of the materials. It should be noted that the present FLUKA version uses fits to evaluated experimental cross-section data for Giant Resonance interactions up to the mass of copper [9]. In order to increase the statistical significance of the results for the samples (in particular for the thin disks) importance biasing was applied to a region containing both bottles and the three disks. Further biasing techniques used in the simulations include leading particle biasing and inelastic interaction length biasing for photons. The cascades initiated by 3.608×10^8 primary electrons were simulated in a total of 164 FLUKA runs and the average yield of radionuclides was calculated.

Figures 3 and 4 show the neutron and photon fluence per beam electron for a longitudinal section through the experimental set-up containing the beam axis. They illustrate the spatial development of the particle cascades and supplement energy spectra as given below. In addition, they allow to optimise the experimental arrangement. Benchmark calculations demonstrating the good performances of FLUKA in simulating the lateral shower development and particle fluences around dumps can be found in the literature (see, for example, [10-12]). As can be seen the samples are located in the lateral maximum of the neutron fluence.

On the other hand, the electromagnetic cascade is forward-peaked, having its lateral maximum downstream of the samples. Note that the fluence scales are different in Figures 3 and 4, the photon fluence at the sample locations being about a factor of ten lower than the neutron fluence.

The average neutron energy spectra in the two bottles are shown in Figure 5. Both spectra are dominated by neutrons of about 1 MeV, the high-energy neutron fluence ($E > 20$ MeV) being almost a factor of 100 lower. The high-energy fluence in the soil is somewhat harder than the one in the water,

Figure 3. Neutron fluence per beam electron shown for a longitudinal section through the geometry containing the beam axis. Units are particles/cm²/electron.

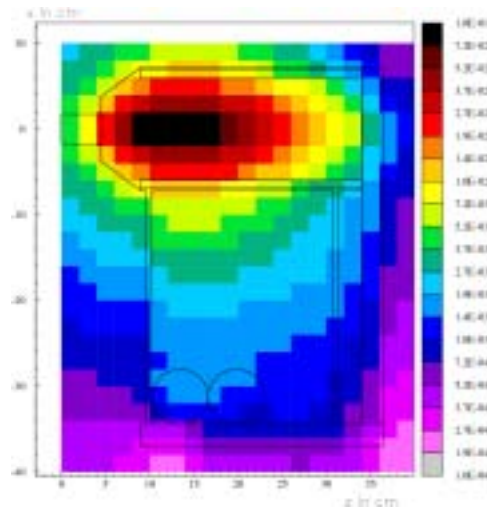


Figure 4. Photon fluence per beam electron shown for a longitudinal section through the geometry containing the beam axis. Units are particles/cm²/electron.

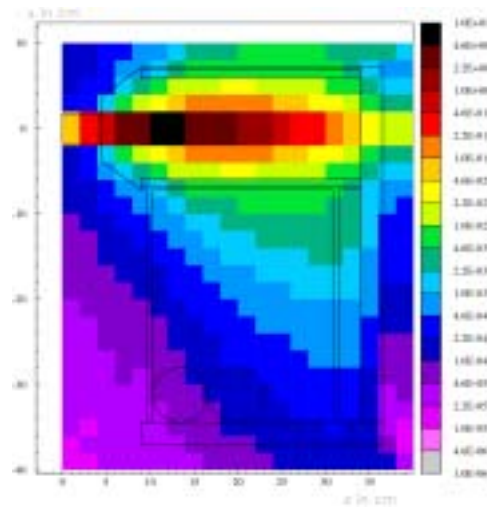
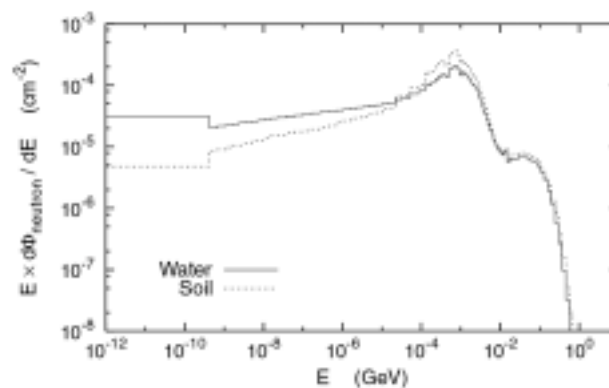


Figure 5. Average neutron energy spectrum in the water and soil bottles normalised per electron



as the soil bottle is located downstream of the water bottle. At low energy the hydrogen content of water clearly moderates the neutrons resulting in a lower peak at 1 MeV, a less steep decrease with energy and a higher thermal neutron fluence than in the soil bottle. The latter implies that the iron sample which was taped on top of the water bottle was exposed to a much higher thermal neutron fluence than are the other two samples.

In the simulations the total yield of radionuclides and the yield produced by low-energy neutrons (i.e. below the threshold for the multi-group treatment, $E < 19.6$ MeV) was scored for all samples and the results written into output .les. The output from the 164 FLUKA runs was then combined in a post-processing step and the standard deviation calculated for each isotope. Based on these results the specific activity for each isotope was calculated for the time of the data analysis. For example, the metallic samples were analysed at the end of September, i.e. almost eight months after the irradiation, and the water and soil samples were analysed in March and April, respectively. For the decay corrections the actual irradiation profile (see Figure 1) and the decay channels up to the third generation were taken into account. (The decay correction was calculated with a modified version of the usrsuw-routine by A. Ferrari.)

Results

The results for the soil sample at the time of the radionuclide analysis are summarised in Table 3. The isotopes listed are only those which were identified in the experiment. The experimental errors contain both the statistical and systematic uncertainties of the spectroscopy analysis. In case of the calculations the errors represent the standard deviation as mentioned above. However, they do not include the errors on the half-lives used for the decay corrections since they are negligible as compared to the statistical uncertainties. In addition to the measured and calculated specific activities, their ratio and the percentage contribution of low-energy neutron interactions to the total yield of a particular isotope are given.

Table 3. Results of experiment and calculations for the specific activity in the soil sample. In the last column the calculated contribution of low-energy neutron interactions to the total isotope production (*Flow*) is given.

Isotope	$t_{1/2}$	Experiment (Bq/g)	FLUKA (Bq/g)	Ratio FLUKA/Exp.	Flow (%)
³ H	12.3	0.313±6.0%	0.108±6.0%	0.35±16.1%	0.0
⁷ Be	53.3 d	2.06±6.0%	1.23±3.6%	0.60±7.0%	0.0
²² Na	2.6	0.562±5.9%	0.315±3.7%	0.56±7.0%	4.4
⁴⁶ Sc	83.8	0.294±6.0%	0.06±8.1%	0.20±10.1%	0.0
⁴⁸ V	16.0	0.0279±6.1%	0.019±20.2%	0.68±21.1%	0.0
⁵¹ Cr	27.7	0.872±6.1%	0.571±8.7%	0.65±10.6%	44.5
⁵⁴ Mn	312.1	0.549±6.0%	0.436±5.4%	2.1±20.0%	30.4
⁵⁹ Fe	44.5	0.0652±6.3%	0.139±19.0%	2.1±20.0%	100.0
⁵⁸ Co	70.8	0.0443±6.1%	0.047±16.8%	1.1±17.9%	100.0
⁶⁰ Co	5.3	0.0226±6.1%	9.53×10^{-7}	$4.2 \times 10^{-5} \pm 17.2\%$	0.0
¹³⁴ Cs	2.1	2.06±6.0%	—	—	—

More than half of the isotope yields are predicted by FLUKA within 50%. The presence of ^{134}Cs in the measurements indicates that the soil contained elements which were not identified by the elemental analysis. The same argument might also apply to the ^{60}Co activity which is predicted to be very small, in contrast to the experimental value. As can be seen from the last column in Table 3, ^{59}Fe and ^{58}Co are exclusively produced in low-energy neutron interactions. The specific activities of ^3H and ^7Be in the water sample are compared to the FLUKA results in Table 4. The calculated activity of tritium is again significantly lower than the measured value whereas one would expect a much better agreement as tritium production from light targets is well predicted in other cases [13].

Table 4. As in Table 3, here for the water sample

Isotope	$t_{1/2}$	Experiment (Bq/g)	FLUKA (Bq/g)	Ratio FLUKA/Exp.	Flow (%)
^3H	12.3	0.659±3.1%	0.121±2.1%	0.18±3.7%	
^7Be	53.3 d	5.67±6.9%	4.0±4.0%	0.71±8.0%	

The specific activities in the metallic samples at the time of the gamma spectroscopy analysis are summarised in Tables 5 to 7. The presence of the Co isotopes in the measurements for the iron sample is most likely due to an element which was present in the alloy but not identified in the chemical analysis (such as nickel). Similar arguments may also explain the presence of ^{54}Mn in the analysis of the irradiated aluminium disk. On the other hand, the absence of that isotope in the calculations could also be due to a lack of statistics taking into account the small thickness of the disk and the small amount of iron in the elemental composition (see Table 2) as well as the small fraction of ^{54}Fe in the natural iron composition (5.8%). All other isotopes are predicted within about a factor of 2-3 and are mostly underestimated. A normalisation uncertainty as reason for the latter can be excluded since the number of electrons on the dump is relatively well known (to within a few %). All calculated values with statistical errors larger than about 15%, such as ^{22}Na in the aluminium disk and ^{59}Fe and ^{65}Zn in the copper disk, should be taken with caution as the true uncertainty might be larger than the errors quoted.

Table 5. As in Table 3, here for the iron sample

Isotope	$t_{1/2}$	Experiment (Bq/g)	FLUKA (Bq/g)	Ratio FLUKA/Exp.	Flow (%)
^{46}Sc	83.8 d	0.282±7.1%	0.527±8.4%	1.9±11.0%	0.0
^{51}Cr	27.7 d	0.443±32.1%	0.170±8.4%	0.38±33.2%	0.0
^{54}Mn	312.1 d	32.9±6.0%	17.2±6.2%	0.52±8.6%	27.00
^{59}Fe	44.5 d	0.550±6.9%	0.777±14.8%	1.4±16.3%	100.0
^{58}Co	70.8 d	0.0663±24.4%	–	–	–
^{60}Co	5.3 y	0.225±7.2%	–	–	–

Table 6. As in Table 3, here for the aluminium sample

Isotope	$t_{1/2}$	Experiment (Bq/g)	FLUKA (Bq/g)	Ratio FLUKA/Exp.	Flow (%)
^{22}Na	2.6 y	1.24±6.6%	0.27±19.7%	0.22±20.8%	0.0
^{54}Mn	312.1 d	0.11±20.3%	–	–	

Table 7. As in Table 3, here for the copper sample

Isotope	$t_{1/2}$	Experiment (Bq/g)	FLUKA (Bq/g)	Ratio FLUKA/Exp.	Flow (%)
⁴⁶ Sc	83.8 d	0.044±10.9%	0.106±7.0%	2.4±12.9%	0.0
⁵⁴ Mn	312.1 d	0.964±6.1%	0.498±15.1%	0.52±16.3%	0.0
⁵⁹ Fe	44.5 d	0.124±10.6%	0.034±24.4%	0.27±26.6%	0.0
⁵⁶ Co	77.3 d	0.324±6.5%	0.116±18.7%	0.36±19.8%	0.0
⁵⁷ Co	271.8 d	2.02±6.0%	1.29±8.7%	0.36±19.8%	0.0
⁵⁸ Co	70.8 d	3.59±6.0%	1.93±4.8%	0.54±7.7%	10.5
⁶⁰ Co	5.3 y	1.41±6.0%	0.514±5.6%	0.36±8.2%	63.0
⁶⁵ Zn	244.3 d	0.094±12.0%	0.041±53.5%	0.44±54.8%	10.5

Discussion and conclusions

An activation experiment has been performed in the Beam Dump East facility at SLAC during which samples of soil, water, aluminium, copper and iron were irradiated in stray radiation fields generated by interactions of 28.5 GeV electrons in a copper dump. Prior to the experiment the chemical composition of the samples was determined. The specific activities were measured using various techniques, such as gamma spectroscopy. In addition, the experiment was simulated in detail using the FLUKA code. The comparison of measured and calculated activities showed that the isotope yields are underestimated by the calculations, in most cases by about a factor of 2, in some cases by up to a factor of 3-5. In order to understand and evaluate these results it must be noted that the radiation field causing induced radioactivity at electron accelerators is very complex, as it involves both electromagnetic and hadronic processes – a situation which is different from that found at proton accelerators. Therefore, the reasons for the discrepancies between measured and calculated activities are also of complex nature. The experimental uncertainties include the following:

- There are statistical and systematic uncertainties in the spectroscopy methods used to analyse the irradiated samples. These include calibration uncertainties, such as possible differences in self-absorption in the samples with respect to calibration sources (self-absorption corrections become large in relatively thick samples) and uncertainties in energy calibration. In addition, uncertainties associated with background subtraction could cause significant difficulties in correctly identifying the radionuclides and their intensities in different samples. All these uncertainties are reflected in the errors quoted for the measured activities in Tables 3 to 7.
- The overall normalisation of the measured activation depends on the total number of beam particles on the target. Any uncertainty leads to an offset between the measured and calculated yields. In addition, for long irradiations and/or relatively short-lived isotopes an accurate consideration of the beam pattern is essential. In the present experiment both uncertainties are relatively small.
- In order to simulate the experiment with a Monte Carlo code the elemental composition of the samples has to be determined. The presence of trace amounts of some elements not identified in the elemental analysis may cause significant discrepancies between measured and calculated activities of certain isotopes. For example, the presence of ¹³⁴Cs in the spectroscopy results for soil, the presence of the cobalt isotopes in the results for iron and of ⁵⁴Mn in the results for

aluminium suggests deficiencies in the elemental analysis determining the composition of the samples. On the other hand, the following uncertainties in the Monte Carlo simulations and models may contribute to the observed discrepancies:

- Predictions for isotopes produced by thermal neutron capture depend strongly on the accurate description of moderating materials in the vicinity of the experiment, such as concrete walls, the huge water dump or the water bottle in the present study. If these factors are neglected or modelled incompletely the predictions for those isotopes can well be off by large factors. However, in the present study the material distribution around the experiment has been modelled rather accurately. In addition, these isotopes are not produced at all if the code does not contain the corresponding cross-section information, such is the case for Zn, Ga, Br and Sr in FLUKA.
- The small size of the metallic samples causes large statistical uncertainties which can not be compensated for by increasing the computing time. Calculated activities carrying statistical uncertainties larger than about 20% cannot be considered to be reliable. Unfortunately, the size effect on the theoretical uncertainties is opposite to the one on the experimental uncertainties, in which thick samples result in large self-absorption corrections (see above). It would be desirable to have the option of biasing the production of residual nuclei in the Monte Carlo code, such as repeated sampling of an inelastic interaction and adjusting (reducing) the weight of the interaction correspondingly.
- The description of isotope production by integrated Monte Carlo transport codes is based on many different models for both transport and interactions of particles. The particle which eventually creates the isotope is often of high generation in the “tree” of the cascade (especially in activation by stray radiation fields). Small inaccuracies at each interaction or transport step can thus add up to sizeable uncertainties in the predictions for a certain isotope and it is often difficult to trace back the reason to a specific model. For example, the simulation of Giant Dipole Resonance (GDR) interactions is based on evaluated experimental cross-sections. These cross-sections often carry up to a factor of two uncertainty. Therefore, the neutron field produced by GDR interactions and the isotopes produced in re-interactions of these neutrons (or produced directly in the GDR interaction) are modelled only within the same uncertainty. In this respect, integrated codes such as FLUKA should be preferred to multi-step simulations where the output of one code (such as photon track lengths) is used as input for a second code (for example to simulate the photonuclear interaction) as those interfaces often cause additional uncertainties. Taking these uncertainties into account, the agreement of measured and calculated induced radioactivity within a factor of two, as is the case for half of the identified isotopes in this study, can be considered to be acceptable. However, the uncertainties together with the scarcity of experimental information on induced radioactivity at electron accelerators clearly calls for further measurements as benchmark for Monte Carlo transport codes.

Acknowledgements

We would like to thank Ronald Seefred and Roger Sit for their assistance during the measurements and Paola Sala for valuable comments on the manuscript. This work was supported by the Department of Energy contract DE-AC03-76SF00515.

REFERENCES

- [1] Swanson, P., *Radiological Safety Aspects of the Operation of Electron Linear Accelerators*, Technical Report Series No. 188, IAEA, ed., Vienna (1979).
- [2] Fassò, A., M. Silari and L. Ulrici, “Predicting Induced Radioactivity at High-energy Electron Accelerators”, *Proceedings of the 9th International Conference on Radiation Shielding, ICRS-9*, Tsukuba, Japan, 1999, *Journal of Nuclear Science and Technology*, Suppl. 1, 827 (2000).
- [3] Fassò, A., A. Ferrari, J. Ranft and P.R. Sala, “New Developments in FLUKA Modeling of Hadronic and EM Interactions”, *Proceedings of the 3rd Workshop on Simulating Accelerator Radiation Environments (SARE-3)*, H. Hirayama, ed., pp. 32-43, Proceedings 97-5, KEK, Tsukuba, Japan (1997).
- [4] Fassò, A., A. Ferrari and P.R. Sala, “Electron-photon Transport in FLUKA: Status”, *Proceedings of the International Conference on Advanced Monte Carlo for Radiation Physics, Particle Transport Simulation and Applications (Monte Carlo 2000)*, Lisbon, 23-26 October 2000, A. Kling, F. Barao, M. Nakagawa, L. Tavora and P. Vaz, eds., Springer-Verlag, Berlin, Heidelberg, pp. 159-164 (2001).
- [5] Fassò, A., A. Ferrari, J. Ranft and P.R. Sala, “FLUKA: Status and Perspectives for Hadronic Applications”, *Proceedings of the International Conference on Advanced Monte Carlo for Radiation Physics, Particle Transport Simulation and Applications (Monte Carlo 2000)*, Lisbon, 23-26 October 2000, A. Kling, F. Barao, M. Nakagawa, L. Tavora and P. Vaz, eds., Springer-Verlag, Berlin, Heidelberg, pp. 955-960 (2001).
- [6] Silari, M., L. Ulrici and S. Ye, *On the Estimation of Low Levels of Induced Radioactivity in LEP*, CERN Internal Report, TIS-RP/IR/99-13 (1999).
- [7] Rokni, S., J.C. Liu and S. Roesler, “Initial Estimates of the Activation Concentration of the Soil and Groundwater Around the NLC Beam Delivery System Tunnel”, *Proceedings of the 5th Specialists Meeting on Shielding Aspects of Accelerators, Targets and Irradiation Facilities (SATIF-5)*, Paris, France, 2000, Proceedings OECD/NEA, p. 115 (2001).
- [8] Ban, S., H. Nakamura, T. Sato and K. Shin, *Radiat. Prot. Dosim.*, 93, 231 (2000).
- [9] Fassò, A., A. Ferrari and P.R. Sala, “Total Giant Resonance Photonuclear Cross-sections for Light Nuclei: A Database for the FLUKA Monte Carlo Transport Code”, *Proceedings of the 3rd Specialists Meeting on Shielding Aspects of Accelerators, Targets and Irradiation Facilities (SATIF-3)*, Tohoku University, Sendai, Japan, 1997, Proceedings OECD/NEA, pp. 61-74 (1998).
- [10] Fassò, A., A. Ferrari, J. Ranft, P.R. Sala, G.R. Stevenson and J.M. Zazula, *Nucl. Instr. and Meth.*, A 332, 459 (1993).

- [11] Fassò, A., A. Ferrari, J. Ranft and P.R. Sala, “FLUKA: Present Status and Future Developments”, *Proceedings of the 4th International Conference on Calorimetry in High-energy Physics*, La Biodola, Italy, 1993, A. Menzione and A. Scribano, eds., World Scientific, p. 493 (1993).
- [12] Ferrari, A. and P.R. Sala, “Physics Processes in Hadronic Showers”, *Proceedings of the 9th International Conference on Calorimetry in High-energy Physics*, Annecy, France, 2000. Currently available from <http://fluka.web.cern.ch/fluka/talks/calp-1.html>.
- [13] Ferrari, A. and P.R. Sala, “Intermediate and High-energy Models in FLUKA: Improvements, Benchmarks and Applications”, *Proceedings of the International Conference on Nuclear Data for Science and Technology (NDST-97)*, Trieste, Italy, 1997, G. Re.o, A. Ventura and C. Grandi, eds., p. 247 (1997).

**PRODUCTION OF RADIOACTIVE ISOTOPES IN Al, Fe AND Cu
SAMPLES BY STRAY RADIATION FIELDS AT A PROTON ACCELERATOR**

H. Vincke, I. Brunner, M. Huhtinen

Abstract

This paper describes the production of induced radioactivity in samples of aluminium, iron and copper exposed to high-energy hadronic radiation. The samples were irradiated in a stray radiation field generated by the interaction of 24 GeV/c protons in the beam dump of the PS IRRAD2 facility at CERN. The specific radioactivity induced in the samples was measured by gamma spectrometry. The Monte Carlo particle transport code FLUKA was used to simulate the irradiation experiment in order to predict the production of radioactive isotopes in the samples. These predictions are compared with the experimental measurements.

Introduction

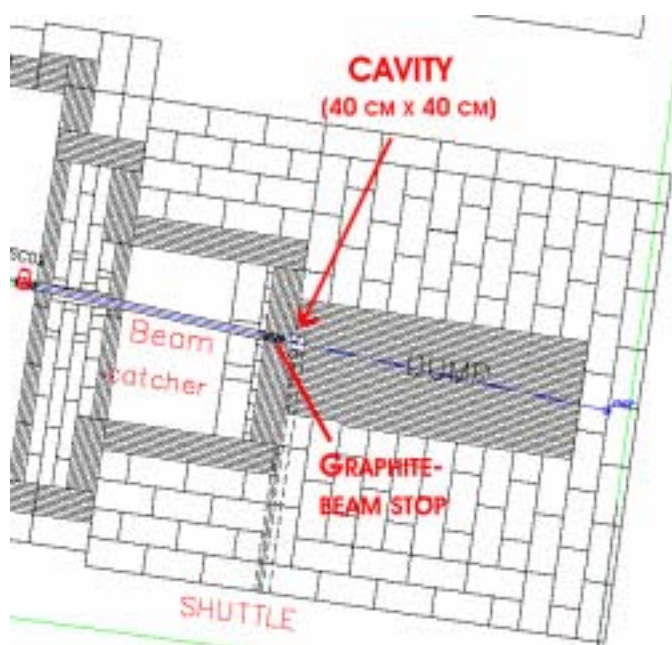
Personal exposure from radioactivity induced in construction and shielding materials around accelerators is one of the main radiation safety issues that require careful surveillance and control during maintenance activities. Most of this activity is contained within irradiated solid materials. Thus, detailed knowledge of the production of induced radioactivity, especially of gamma emitters, in various structural and shielding materials is an important issue at high-energy accelerators.

Samples of aluminium, iron and copper were irradiated in a stray radiation field generated by interaction of 24 GeV/c protons in the beam dump of the CERN Proton Synchrotron (PS) IRRAD2 facility at CERN. Measurements of the induced radioactivity in these samples were performed by detailed gamma spectrometry. The experiment was also simulated using the Monte Carlo particle transport code FLUKA [1,2]. This paper compares the experimentally obtained activities in the different samples with the results of detailed FLUKA calculations.

Experimental set-up

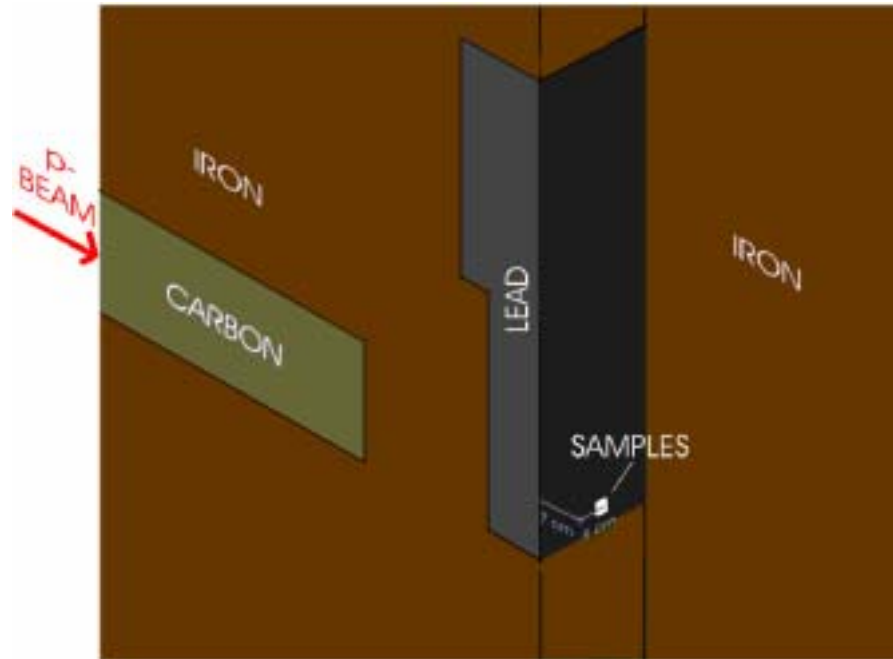
The IRRAD2 irradiation facility (see Figure 1) at CERN has been operational at the PS since 1999. It is located in the PS East hall complex and allows one to perform irradiation tests of electronics and other items with a high hadron flux. A remotely controlled shuttle can be used at the IRRAD2 facility to bring the samples into the irradiation position within a small cavity of $40 \times 40 \text{ cm}^2$ cross-section.

Figure 1. The IRRAD2 area at the PS



The irradiation cavity is located behind a carbon beam stop followed by an 18.2 cm thick steel wall and a 10-15 cm thick lead slab, see Figure 2. A proton beam with a beam spread (FWHM) of 5.6 cm horizontal and 3.4 cm vertical and with a momentum of 24 GeV/c hit the centre of the carbon beam stop. The samples were placed inside the cavity and were irradiated for a total of 34 hours and 13 min.

Figure 2. Details of the IRRAD2 area. Half of the shielding is removed to show the inner details of the experimental set-up.



Samples

For the purpose of this study, sheets of aluminium, iron, copper and lead were cut into pieces of $20 \times 20 \times 2 \text{ mm}^3$, were stacked next to each other and were placed at the irradiation position in the cavity as shown in Figure 2 and Figure 3. Due to technical problems with the analysis of the complex gamma spectrum of the Pb samples (99.98% pure lead), results of induced radioisotopes in lead are not given. Details for the other samples are given in Table 1.

Figure 3. Samples irradiated at IRRAD2

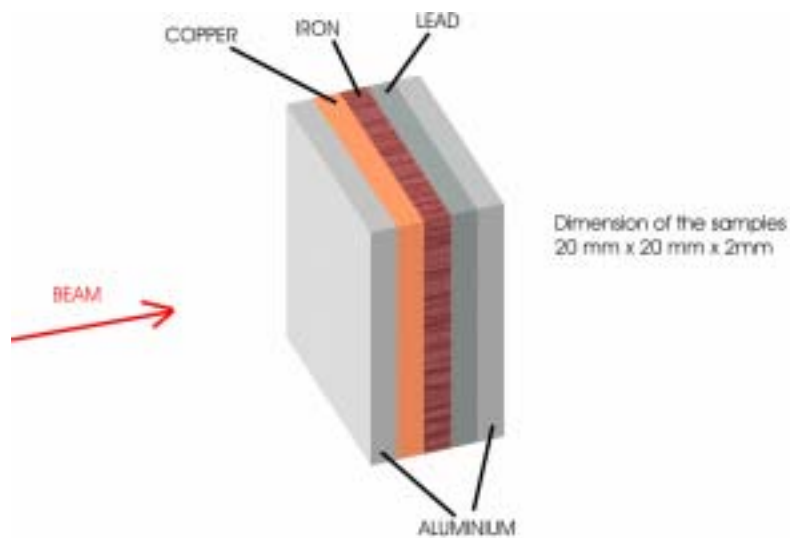


Table 1. Details of the irradiated materials

Aluminium	Iron	Copper
CERN number: 44.01.30 <i>Alloy symbol:</i> <i>ISO Al 99, 5 EN AW-1050 A</i> Density: 2.7 g cm ⁻³ Dimension: 20 × 20 × 2 mm ³	CERN number: 44.39.02 <i>Alloy symbol:</i> <i>S235JR (DIN St 37-2K)</i> Density: 7.8 cm ⁻³ Dimension: 20 × 20 × 2 mm ³	CERN number: 44.09.56.A <i>Alloy symbol:</i> <i>Cu-OF</i> Density: 8.9 cm ⁻³ Dimension: 20 × 20 × 2 mm ³
Chemical composition:	Chemical composition:	Chemical composition:
Al = 99.5% Traces: Cu, Zn, Si, Fe, Mn, Ti, Mg	Fe = 99.5% Traces: C, P, S and N	Cu = 99.95% Traces: O

Details of the FLUKA simulations

The production of radionuclides in the samples was calculated using FLUKA based on a detailed description of the experimental set-up. The following section defines the essential parameters for the simulation.

- *Material assignments.* The aluminium, iron, copper and lead samples were defined as pure elements. Small impurities – see Table 1 – were neglected. The carbon beam stop had a density of 2.0 g cm⁻³. The iron shielding around the shaft was assumed to have a density of 7.87 g cm⁻³ and a chemical composition as follows (wt.%): Fe 98.6%, C 0.1%, Si 0.1%, Ni 1% and Cu 0.2%. Further, the lead slabs of the shielding in front of the cavity were composed of pure lead with a density of 11.35 g cm⁻³.
- *Scoring.* The RESNUCLE option of FLUKA was used to score the residual nuclides from inelastic interactions directly. In order to enhance the statistical significance of the results, the simulation was split into two parts. In the first part the impact of the beam on the carbon beam stop was simulated and all particles reaching the region of the samples were stored in a file. In order to prevent double counting each stored particle was killed at the point where it reached the area of interest (set to black hole). A total of six primary runs were submitted, with each run transporting 50 000 primary protons. For the second part the stored particles (obtained from the runs of the first part) were used as source particles and were transported one hundred times through the samples. A total number for the primary protons of 3.0×10^7 was achieved. All results are presented as averages of these six secondary runs. The standard deviation of the mean of the residual nuclei production was calculated and used as an estimate of the statistical uncertainty.

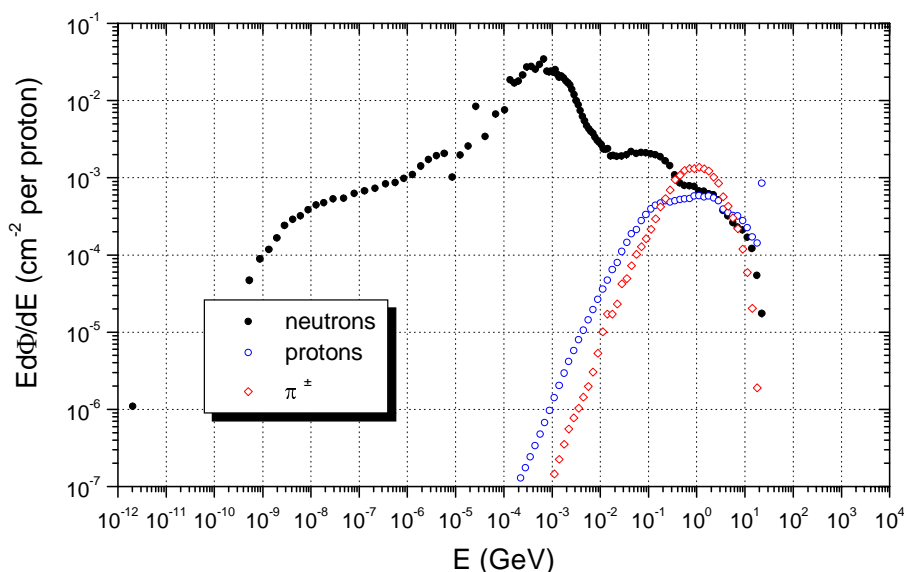
Results

Proton intensity

Unfortunately, the IRRAD2 facility does not accurately monitor incident proton intensity. Therefore it was estimated by using the calculated (with FLUKA) energy spectra of neutrons, protons

and pions at the place of the samples and folding these spectra with semi-experimental cross-sections¹ for ²⁴Na production. The calculated energy spectra are given in Figure 4 for neutrons, protons and π^{\pm} respectively. Based on a measured ²⁴Na activity of 16 400 Bq in the aluminium sample after 123 180 s of irradiation and 197 967 s cooling time, the total number of protons incident on the carbon stop was calculated as 1.62×10^{15} protons. It should be noted that the intensity of the proton beam was stable during the irradiation.

Figure 4. Energy spectra at the position of the samples; errors are below 5%



Gamma spectrometry

The gamma spectra emitted by the irradiated samples were measured with the HPGe detector called Ge1. The detector was calibrated in energy with a ²²⁸Th certified source and in efficiency with a ¹⁵²Eu certified point source, which produces the geometry of the samples. The uncertainty due to slight differences in the diameter of the different samples was assessed to be within the overall statistical uncertainty. The data acquisition and analysis were carried out via the Genie2000 (version 1.4) software package by Canberra running on a personal computer. Genie2000 is a comprehensive set of capabilities for acquiring and analysing spectra from Multichannel Analysers (MCAs). Its functions include MCA control, spectral display and manipulation and comprehensive spectrum analysis. The aluminium samples were analysed five times after the irradiation with progressively longer cooling times starting from 10 000 s up to 2.3 days and increasing acquisition times (1 000 s up to 7 h). The iron and copper samples were analysed seven times with cooling times varying from 5 360 s to 67 days and acquisition times from 1 000 s for the first measurement up to 2.66 days for the last analysis. Results of these measurements are given in comparison with FLUKA simulations for Al, Fe and Cu in Tables 2-4. Experimental values are given for the cooling time that had the smallest error in analysis. Note that only isotopes reliably identified by the Genie2000 software are listed in these tables.

¹ Experimental production cross-sections for ²⁴Na are well known for protons but for pion and neutrons only for a limited energy range. Thus, an effort has been made to extend the energy range of these cross-sections in order to cover the broad hadron spectra at the IRRAD2 facility. Details are described in [3].

Table 2. Results of experiment and calculations for the activity in the Al sample

Isotope	Half-life	Experiment (Bq/sample)	FLUKA (Bq/sample)	Ratio FLUKA/Exp.
⁷ Be	53.3 d	1.23E+02±1%	2.00E+02±21.7%	1.63
²² Na	2.6 y	1.57E+02±1%	7.95E+01±5.6%	0.51
²⁴ Na	15 h	5.51E+01±2%	4.69E+01±1.8%	0.85

Table 3. Results of experiment and calculations for the activity in the Fe sample

Isotope	Half-life	Experiment (Bq/sample)	FLUKA (Bq/sample)	Ratio FLUKA/Exp.
⁷ Be	53.3 d	8.22E+01±1.0%	1.73E+01±25.4%	0.21
²² Na	2.6 y	2.59E+01±2.3%	2.71E+00±26.8%	0.10
²⁴ Na	15 h	5.75E+02±1.0%	7.10E+01±9.4%	0.12
³⁸ Cl	37.3 m	4.00E+03±9.9%	1.54E+03±9.4%	0.38
³⁹ Cl	55.6 m	1.45E+03±9.8%	5.07E+02±28.5%	0.35
⁴¹ Ar	1.82 h	1.31E+03±7.7%	4.92E+02±35.6%	0.38
⁴² K	12.4 h	4.28E+02±2.8%	1.28E+02±12.0%	0.30
⁴³ K	22.3 h	8.27E+02±1.3%	9.19E+02±10.3%	1.11
⁴³ Sc	3.9 h	2.63E+04±3.3%	2.23E+04±6.0%	0.85
^{m44} Sc	2.44 d	7.08E+01±2%	2.84E+01±6.2%	0.40
⁴⁶ Sc	83.8 d	8.74E+02±1.1%	3.35E+02±2.3%	0.38
⁴⁷ Sc	3.4 d	1.53E+02±1.3%	9.45E+01±7.5%	0.62
⁴⁸ Sc	1.8 d	1.14E+03±1.1%	7.16E+02±19.3%	0.63
⁴⁸ V	16.0 d	1.14E+03±0.9%	9.45E+02±4.0%	0.83
⁴⁸ Cr	21.6 h	4.16E+02±1.8%	3.44E+02±18.8%	0.83
⁴⁹ Cr	42.3 m	9.62E+02±7.7%	1.08E+03±6.6%	1.13
⁵¹ Cr	27.7 d	5.70E+03±0.8%	4.53E+03±1.8%	0.79
^{m52} Mn	5.6 d	1.76E+01±1.6%	1.47E+01±2.5%	0.84
⁵⁴ Mn	312.0 d	3.26E+03±1%	2.51E+03±0.9%	0.77
⁵⁶ Mn	2.6 h	1.62E+05±1.3%	1.76E+05±1.7%	1.08
⁵² Fe	8.3 h	7.59E+02±4.7%	5.34E+02±8.4%	0.70
⁵⁹ Fe	44.5 d	3.06E+01±3.2%	2.93E+01±1.6%	0.96
⁵⁵ Co	17.5 h	3.32E+02±1.6%	2.91E+02±11.4%	0.88
⁵⁶ Co	77.3 d	2.94E+02±0.8%	2.39E+02±7.5%	0.81
⁵⁷ Co	272.0 d	3.54E+01±1.2%	3.30E+00±41.7%	0.09
⁵⁸ Co	70.9 d	2.39E+01±2.4%	2.47E+00±21.2%	0.10

Table 4. Results of experiment and calculations for the activity in the Cu sample

Isotope	Half-life	Experiment (Bq/sample)	FLUKA (Bq/sample)	Ratio FLUKA/Exp.
⁷ Be	53.3 d	1.36E+02±0.8%	2.89E+00±71.1%	0.02
²² Na	2.6 y	1.97E+01±2.5%	1.46E+00±37.7%	0.07
²⁴ Na	15 h	1.83E+04±1.1%	1.95E+03±20.5%	0.11
⁴¹ Ar	1.82 h	4.44E+03±4.5%	2.66E+02±34.9%	0.06
⁴² K	12.4 h	6.24E+03±2.9%	1.70E+03±22.3%	0.27
⁴³ K	22.3 h	2.03E+03±1.6%	1.32E+03±20.8%	0.65
⁴³ Sc	3.9 h	1.31E+04±6.8%	9.84E+03±10.2%	0.75
^{m44} Sc	2.44 d	5.51E+03±0.7%	1.43E+03±6.1%	0.26
⁴⁶ Sc	83.8 d	5.70E+02±0.9%	2.12E+02±6.6%	0.37
⁴⁷ Sc	3.4 d	2.00E+02±1.4%	1.26E+02±9.8%	0.63
⁴⁸ Sc	1.8 d	6.58E+02±1.3%	4.22E+02±9.6%	0.64
⁴⁸ V	16.0 d	3.38E+03±0.6%	2.04E+03±4.3%	0.60
⁴⁸ Cr	21.6 h	7.54E+01±3%	6.99E+01±33.8%	0.93
⁴⁹ Cr	42.3 m	3.66E+03±5.6%	4.32E+03±7.2%	1.18
⁵¹ Cr	27.7 d	1.87E+03±0.8%	1.14E+03±4.8%	0.61
^{m52} Mn	5.6 d	1.60E+03±0.7%	7.08E+02±6.6%	0.44
⁵⁴ Mn	312.0 d	8.35E+02±1%	5.46E+02±4.5%	0.65
⁵⁶ Mn	2.6 h	1.55E+04±0.9%	1.09E+04±13.1%	0.70
⁵² Fe	8.3 h	2.93E+02±29.8%	6.53E+02±15.4%	2.23
⁵⁹ Fe	44.5 d	2.95E+02±2.3%	2.46E+02±7.9%	0.83
⁵⁵ Co	17.5 h	1.69E+03±1.5%	1.11E+03±12.5%	0.66
⁵⁶ Co	77.3 d	1.27E+03±0.5%	8.63E+02±8%	0.68
⁵⁷ Co	272.0 d	1.26E+03±0.7%	8.52E+02±2.5%	0.68
⁵⁸ Co	70.9 d	6.79E+03±0.6%	4.21E+03±0.8%	0.62
⁶¹ Co	1.65 h	4.79E+03±4.5%	1.10E+04±3.1%	2.30
⁶¹ Cu	3.3 h	1.21E+05±0.8%	1.40E+05±1.3%	1.16
⁶⁴ Cu	12.7 h	2.25E+05±0.9%	1.91E+05±0.9%	0.85
⁵⁷ Ni	35.6 h	7.43E+02±1.9%	6.71E+02±13.5%	0.90
⁶⁵ Ni	2.52 h	4.57E+03±4%	8.28E+03±6.2%	1.81

Residual nuclei

The RESNUCLE option of FLUKA gives only the production rate of an isotope per primary particle. Hence, the activity at the beginning of the gamma spectrometry was calculated in a post-processing step by taking into account the number of protons, decay channels, the irradiation time and the cooling time². This post-processing program analytically solves the set of coupled differential equations governing the production and the radioactive decay channels up to the third generation. Nuclides with several isomeric states are somewhat problematic, because in general the relative production rates of these states are not known. In these cases – except for some special neutron activation reactions – equal sharing between all states has been assumed.

² Activity was calculated with a modified version of the *usrsuw*-routine by A. Ferrari and P. Sala.

Al sample

Results of the activities in the “upstream” aluminium sample (see Figure 3) obtained from the experiment and the calculation are given in Table 2. In addition to the measured and the calculated activity the ratios are also given. From Table 2 it can be seen that three radioactive isotopes have been identified by the gamma spectrometry, namely ^7Be , ^{22}Na and ^{24}Na . Compared to the results from the simulation it can be concluded that the calculated activity from ^7Be was overestimated by a factor of 1.6. ^{24}Na and ^{22}Na were slightly underestimated, but still within about a factor of two. A comparison of the activities between the two aluminium samples, the one placed at the beginning and the one at the end of the sample stack, showed no difference. Thus it can be assumed that all samples were exposed to similar particle spectra.

It is to be emphasised here that the total number of protons on the target was determined from ^{24}Na production in aluminium, by using semi-experimental production cross-sections and the hadron spectra predicted by FLUKA. Thus, the yield estimate obtained from FLUKA residual nuclide scoring for ^{24}Na can differ from unity. This difference shows that the residual nuclide production in FLUKA is not fully consistent with the semi-experimental cross-sections used for the normalisation.

Fe sample

The results of the activities in the iron sample are given in Table 3. In total 26 radioisotopes were found by the gamma spectrometry. Due to the fact that the first measurement of the samples was carried out 90 minutes after the end of the irradiation, isotopes with half-lives less than one hour were also identified. In general, good agreement was found between the experiment and the simulation for most of the isotopes close to the target mass ($\pm 20\%$). Nevertheless, both sodium isotopes were underestimated by about a factor of ten due to a missing multi-fragmentation model in FLUKA. The short-lived isotopes ^{38}Cl and ^{39}Cl were underestimated by a factor of three for the same reason. It can be concluded that the activities of most of the isotopes are predicted within a factor of 2.

Cu sample

Table 4 shows the experimental and the calculated results of the activities in the copper sample. Again, ^{22}Na and ^{24}Na are considerably underestimated. We have identified 29 radioisotopes through gamma ray analysis. Two isotopes, ^{52}Fe and ^{61}Co , were overestimated by a factor greater than two but, especially for ^{52}Fe , it should be noted that the statistical uncertainty of the measurement is already 30%. As for aluminium and iron, it can be emphasised that most of the isotopes were predicted within about a factor of 2.

Conclusion

The ^7Be production from the aluminium sample is slightly overestimated by FLUKA, whereas the underestimate of this isotope is significant for iron and copper. The missing multi-fragmentation model in the FLUKA code can explain this. In general multi-fragmentation has a small cross-section, but it is important when considering the distribution of residual nuclei far from the target mass. In the case of aluminium the pre-fragment, i.e. the nucleus before evaporation/fragmentation is usually in the range of the Fermi break-up model of FLUKA. Thus the ^7Be yield is reasonably reproduced. For the

heavier elements the pre-fragment is too heavy for the Fermi break-up and thus only sequential evaporation of light nuclei is possible in the simulation. The severe underestimate of ^{22}Na and ^{24}Na in the case of iron and copper is also caused due to the lack of a multi-fragmentation model.

Nevertheless, in general FLUKA reproduces rather well the yield of isotopes close to the target mass – mostly within $\pm 30\%$. Most other isotopes are predicted to within a factor two.

REFERENCES

- [1] Fassò, A., A. Ferrari, P.R. Sala, “Electron-photon Transport in FLUKA: Status”, *Proc. of the Monte Carlo 2000 Conference, Lisbon, 23-26 October 2000*, A. Kling, F. Barao, M. Nakagawa, L. Tavora, P. Vaz, eds., Springer-Verlag, Berlin, pp. 159-164 (2001).
- [2] Fassò, A., A. Ferrari, J. Ranft and P.R. Sala, “FLUKA: Status and Prospective for Hadronic Applications”, *Proceedings of the Monte Carlo 2000 Conference, Lisbon, 23-26 October 2000*, A. Kling, F. Barao, M. Nakagawa, L. Tavora, P. Vaz, eds., Springer-Verlag, Berlin, pp. 955-960 (2001).
- [3] Huhtinen, M., *Recommendations for Irradiations of CMS Components in the IRRAD2 Facility at PS*, CMS internal note, CMS IN 2001/012.

FLUKA CALCULATIONS OF RADIONUCLIDES, STAR AND NEUTRON FLUENCE IN SOIL AROUND HIGH-ENERGY ELECTRON AND PROTON LINEAR ACCELERATORS

Andrew Puryear

Texas A&M University, College Station, Texas 77841

James C. Liu, Sayed Rokni

Stanford Linear Accelerator Center, California, 94025

Abstract

Information concerning radionuclide production and the attenuation of high-energy neutrons in the soil shielding around accelerators is important for environmental impact assessment. The radionuclide concentration of ^3H , ^7Be , ^{22}Na , ^{24}Na , ^{45}Ca , ^{54}Mn and ^{55}Fe in the soil outside the cylindrical concrete tunnel from a uniform beam loss along a copper linac was calculated using FLUKA. The atom concentration and the number of atoms per star for radionuclides were given as a function of soil depth. The attenuation length of star density, as well as the neutron fluence spectra, was calculated. Studies for electron and proton beams at 500 GeV were made and their results were compared to examine the common understanding that the radiation and radioactivity patterns outside a certain thickness of shielding are the same between high-energy electron and proton beams. The effects of star-scoring threshold (20 or 50 MeV) by neutrons or by all particles on the results were also investigated.

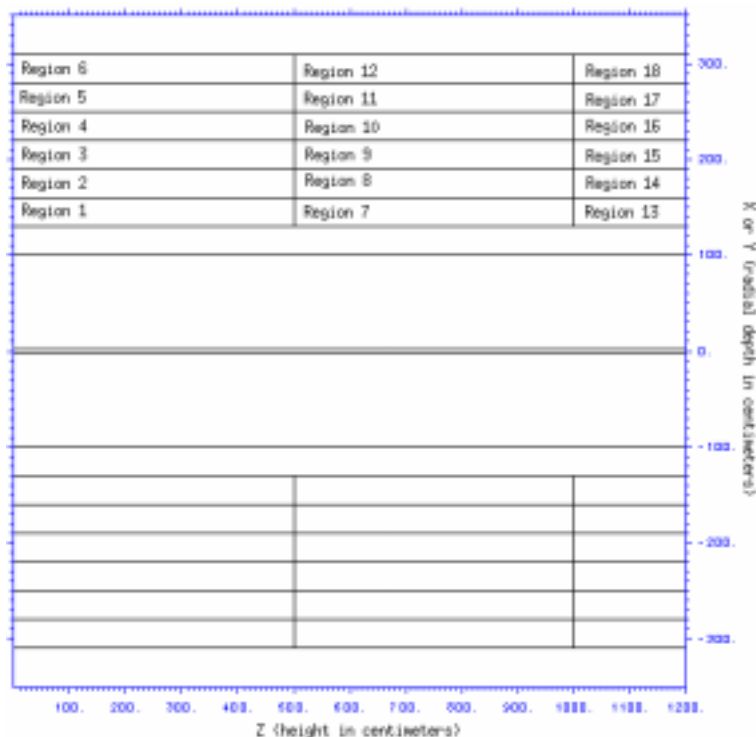
Introduction

To evaluate environmental impact, the information concerning radionuclide yields and the attenuation of radiation (mainly the high-energy neutrons, which propagate the cascade) in the soil shielding around a high-energy accelerator is important. In this study, the atomic concentration of some important radionuclides (^3H , ^7Be , ^{22}Na , ^{24}Na , ^{45}Ca , ^{54}Mn and ^{55}Fe) in the soil surrounding the cylindrical linac tunnel was calculated using FLUKA [1,2] for the case of a uniform beam loss. The attenuation length of star density in soil and the neutron fluence spectra in soil were also calculated. The effects of scoring threshold (20 or 50 MeV) for star production on the results were investigated. Studies for a 500 GeV electron beam and a 500 GeV proton beam were made to examine the understanding [3] that the radiation and radioactivity patterns outside a certain thickness of shielding are the same between high-energy electron and proton machines.

FLUKA calculations

A cylindrical geometry (see Figure 1), symmetric about the Z-axis, was used in FLUKA to simulate the concrete tunnel and the soil surrounding of a linac. The origin was at the centre of the tunnel front face. The concrete tunnel is coaxial with the Z-axis (inner radius 100 cm, outer radius 130 cm, a length of 1 200 cm). The linac is simulated as a copper rod (radius 2.5 cm and a length of 1 200 cm) in the centre of the concrete cylinder. Six layers of soil, each layer having a radial thickness of 30 cm, surround the concrete cylinder. All soil layers are divided into three sections along the Z-axis: the front section from 0 to 500 cm, the middle section from 500 to 1 000 cm, and the back section from 1 000 to 1 200 cm. The main focus is on the middle section because it represents a “uniform” region for a line source, as shown below. Each soil region is numbered (1-18) for future reference.

Figure 1. FLUKA cylindrical geometry for the linac and tunnel



The concrete had a density of 2.35 g/cm³ with a composition (by weight) of O (50.0%), Ca (19.5%), C (3.0%), Al (3.0%), Fe (1.4%), Na (1.0%), K (1.0%), H (0.6%) and Mg (0.5%). The SLAC soil used in this study had a density of 2.1 g/cm³ with a composition of O (54.6%), Si (30.7%), Al (4.2%), K (2.5%), Fe (1.8%), Mg (1.7%), H (1.6%), Na (1.3%), Ca (1.2%), Mn (0.003%) and the remaining fraction from B, Ti, V, Cr, Co, Ni, Cu, Zr and Ba. Based on the hydrogen content of the SLAC soil, the water content of the SLAC soil is 29.4% by volume (14.2% by weight).

The new evaporation module was activated. All photonuclear reactions were activated in all materials. The interaction length of nuclear inelastic interactions of photons is biased by a factor of 50 in all materials to increase photoneutron production. Full leading particle biasing was activated for all electromagnetic processes in all regions. The region importance biasing for all particles is activated in the soil regions. Neutrons were transported down to thermal while other hadrons had a transport cut-off at 10 keV. The transport cut-off was 5 MeV for electrons, positrons and photons. Muon was discarded.

Simulations were made for 500 GeV electron (250 000 × 7 particles) and 500 GeV proton (5 000 × 7 particles) beams with the star-scoring threshold at either 20 MeV (default) or 50 MeV. The beam particles hit the copper linac uniformly between Z = 0 to Z = 1 200 cm. The star density profiles (star/cm³/beam particle) with the 50 MeV threshold for both the electron and proton beams were found to be constant within 6.4% in the first layer of soil for Z = 500-1 000 cm. Thus, the FLUKA results in the middle section of soil regions (7-12) can be used for a line source situation.

The radionuclide of ³H, ⁷Be, ²²Na, ²⁴Na, ⁴⁵Ca, ⁵⁴Mn and ⁵⁵Fe were scored directly in soil regions 7-12 using the RESNUCLE card and the results were post-processed using the program *rusrsw*. The star densities produced by neutrons and by all particles (hereafter called neutron star and all star, respectively) in the soil regions were scored using SCORE. The atom/star values were then calculated using the radionuclide concentration and star density values. The spatial distributions of neutron star density and all star density in regions 7-12 were scored using USRBIN for radius from 130 to 310 cm (12 bins) and for Z from 500 to 1 000 cm (25 bins). Attenuation lengths of star in soil were calculated based on the star profiles. Finally, the neutron fluence spectra were scored in regions 7-12 using the USRTRACK card.

Results

Figure 2(a) (electron beam) and Figure 2(b) (proton beam) show the atom concentration of each radionuclide as it varies radially for regions 7-12. There appear to be two distinct slopes for ²⁴Na, ⁴⁵Ca and ⁵⁵Fe (in particular, for the electron beam case), while the rest have only one slope. The star density (dominated by neutron star at all depths) decreases radially, resembling the pattern of most radionuclides. The neutron star density approaches the all star density in outer soil regions meaning that, in deep soil, neutron will eventually become the only contributing particle to stars. This can also be clearly seen in Figure 3.

The star profiles in soil regions for electron and proton beams with 50 and 20 MeV star-scoring thresholds are summarised in Figure 3 (left). Proton beam produces a star density that is a factor of 123-153 higher than the corresponding case of electron beam. The ratios of star density, normalised to the all star density with 50 MeV threshold, for either the electron or proton beam are shown in Figure 3 (right). In any case, the neutron star density is over 80% of the all star density at all depths. The star density for 20 MeV threshold is ~1.5 times higher than that for 50 MeV threshold. It is clear that, at region 11 (i.e. 30 cm concrete plus 120 cm soil ≈ 150 cm soil), the “equilibrium” state was reached. Note that the equilibrium state is reached earlier for electron beam than for proton beam and also earlier for the 50 MeV than for the 20 MeV threshold.

Figure 2(a). Radionuclide concentration and star density in soil regions 7-12 for electron beam with 50 (top) and 20 MeV (bottom) star-scoring thresholds

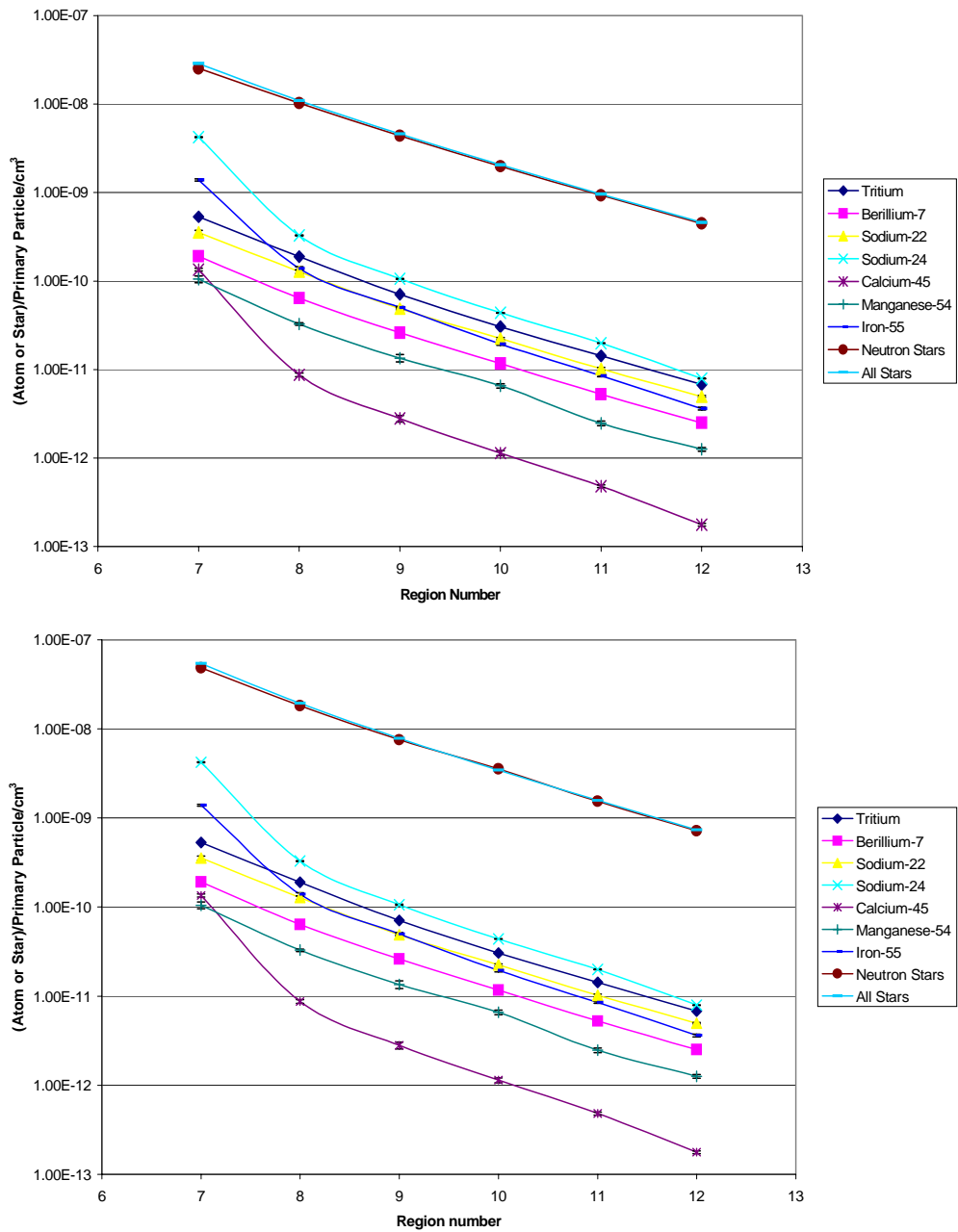


Figure 2(b). Radionuclide concentration and star density in soil regions 7-12 for proton beam with 50 (top) and 20 MeV (bottom) star-scoring thresholds

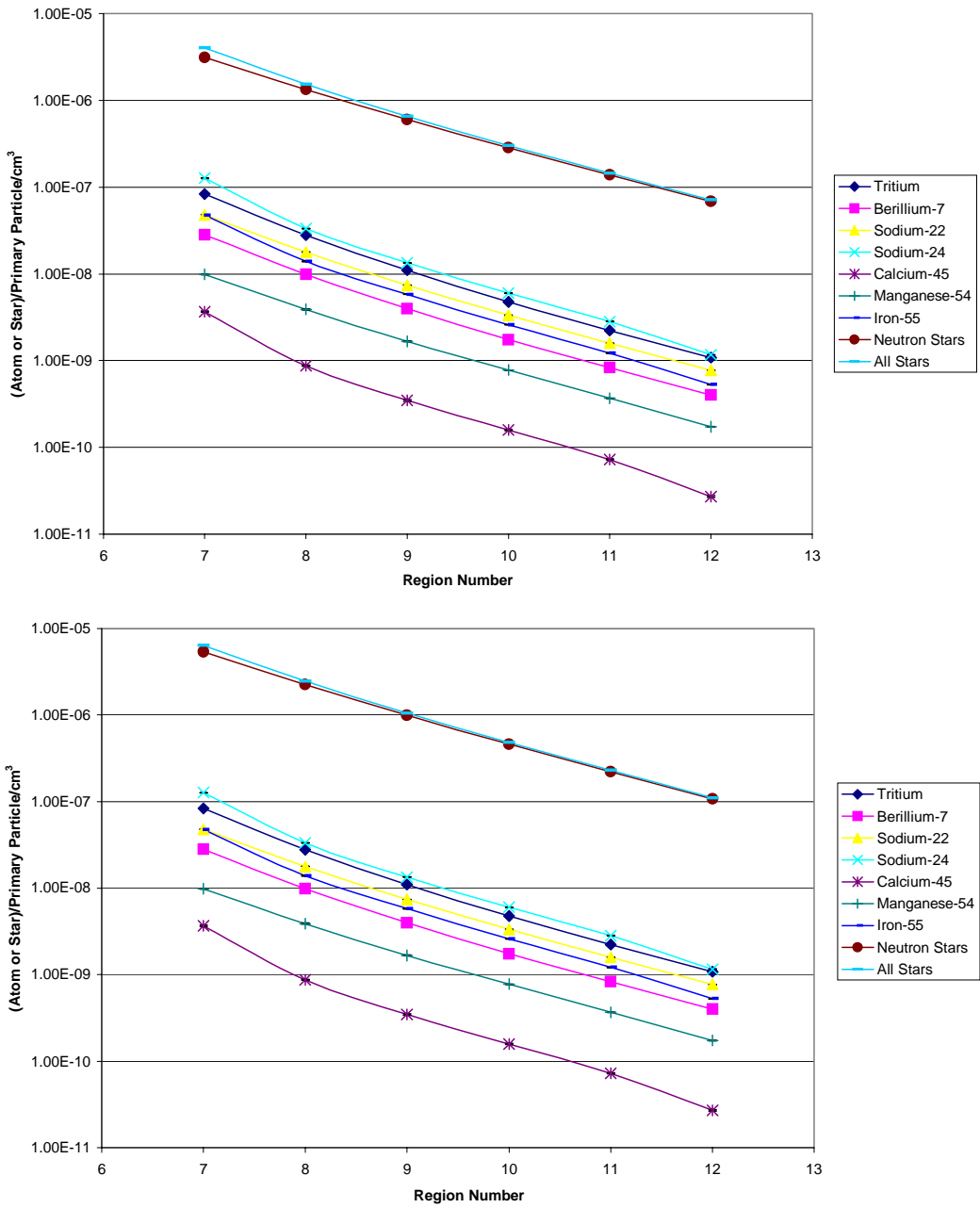
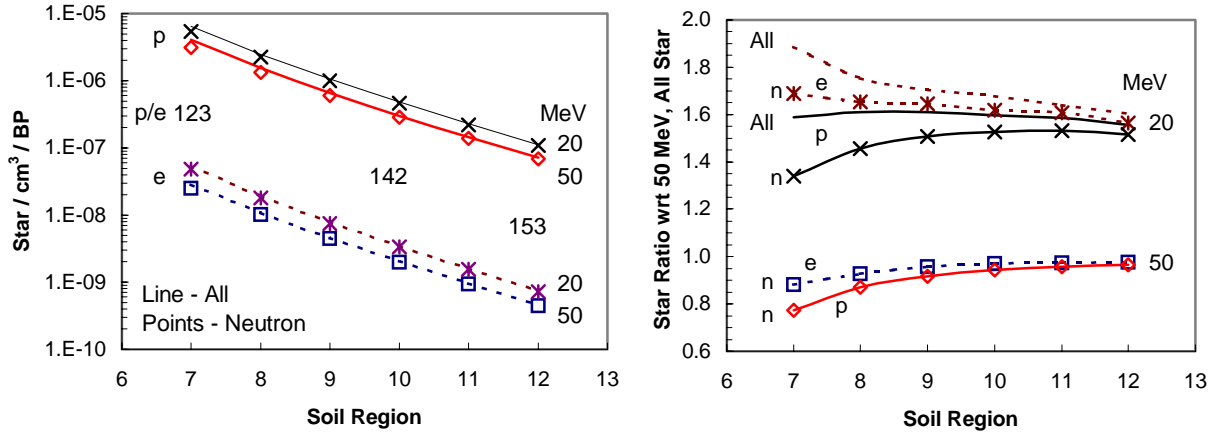
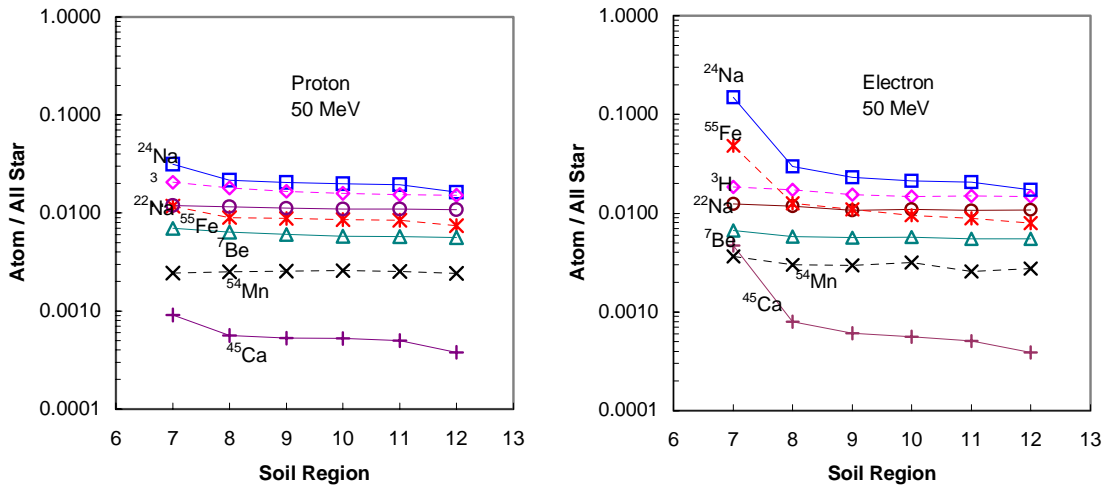


Figure 3. Comparison of star density profiles in soil regions 7-12 between electron and proton beams and with 50 and 20 MeV star-scoring thresholds (left) and the ratio of star density when normalised to the all star density with the 50 MeV threshold (right)



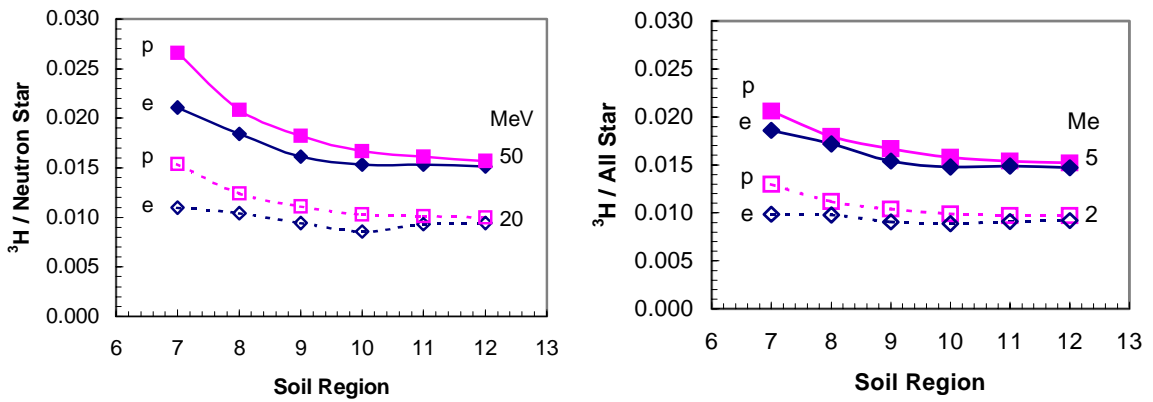
Dividing the radionuclide concentration by the all star density in the same soil region led to the result seen in Figure 4. For most radionuclides, the results of atom per star are different for electron and proton beams within region 8 (< 90 cm soil). However, the atoms per star are similar beyond region 9 (> 120 cm soil). At these equilibrium depths, a number of 0.01 atoms per all star can be used for the estimations of the yield for most radionuclides (within a factor of 3), except for ⁵⁴Mn and ⁴⁵Ca.

Figure 4. Number of radionuclides per all star in soil regions 7-12 for electron and proton beams with 50 MeV star-scoring threshold



Using ³H as an example, a close examination of the characteristics of the atom per star profiles is given in Figure 5. Again, electron and proton beams have different atom/star values within shallow regions, but the difference is < 10% beyond region 9. Note that the difference between electron and proton beams is smaller in the case of atom per all star. This is likely due to the fact that the proton beam produces many types of hadrons while the electron beam produces mainly neutrons. The proton beam has higher atom/star values than the electron beam. However, at deep regions the atom per star approaches an asymptotic value (0.015 ³H/star at 50 MeV threshold and 0.01 ³H/star at 20 MeV threshold), which is independent of beam type as well as the type of star (all star or neutron star). This

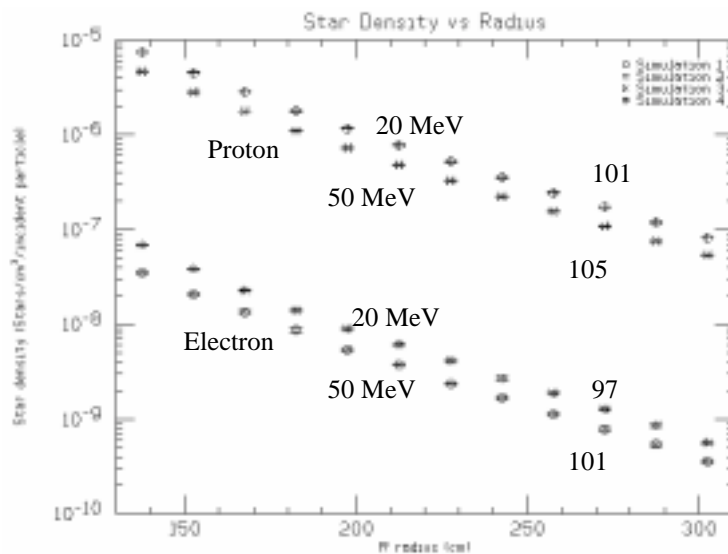
Figure 5. Number of ^3H atom per neutron star (left) and per all star (right) in soil regions 7-12 for electron and proton beams with 20 MeV and 50 MeV star-scoring thresholds



indicates that neutrons are the only particles that produce stars and radionuclides at deep regions. Again, the equilibrium state was reached at region 10 (> 120 cm soil) for the electron beam and region 11 (> 150 cm soil) for the proton beam.

The attenuation length of all star density in soil was obtained from its profile as a function of radius in the soil. The all star density is plotted in Figure 6 as a function of radius (130 to 310 cm) at $Z = 800$ cm. It appears that, beyond radius $r = 220$ cm (i.e. beyond region 9), the slopes become constant. Thus, after corrected with $1/r$ for the line source geometry, attenuation lengths can be calculated by performing a least square exponential fit to the last five points of the curves (the equilibrium part) in Figure 6. The calculated attenuation length at equilibrium depth ranges from 97 g/cm^2 (for electron beam with 20 MeV threshold) to 105 g/cm^2 (for proton beam with 50 MeV threshold). The attenuation length for proton beam is higher (~4%) than that of electron beam, and the attenuation length at 50 MeV threshold is also 4% higher than that at 20 MeV threshold. The errors associated with attenuation lengths were < 2%, estimated using different number of points in fitting.

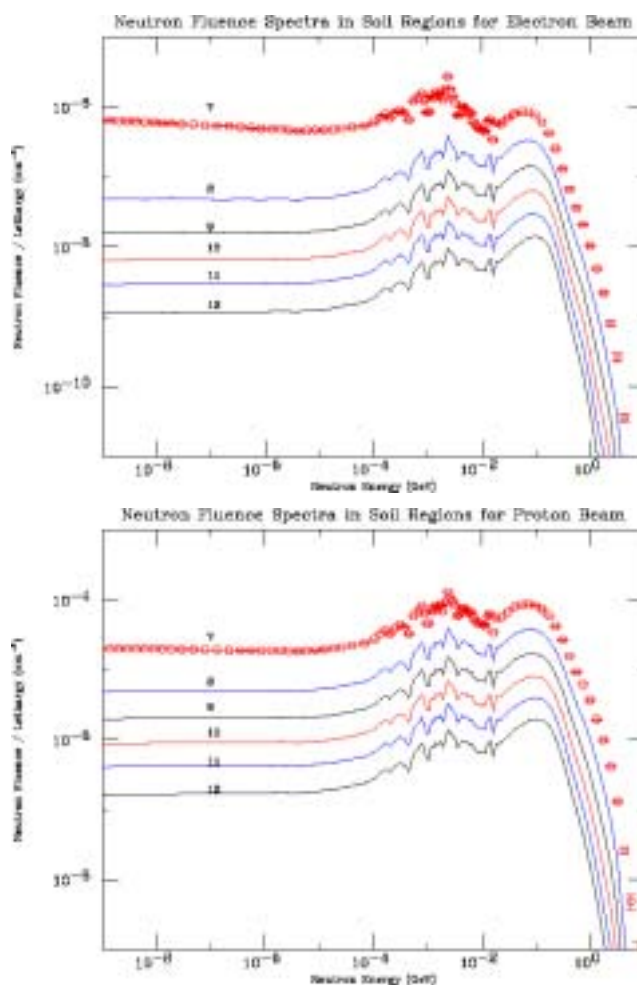
Figure 6. The all star density as a function of radius (130 to 310 cm) at $Z = 800$ cm for electron and proton beam with 50 MeV and 20 MeV thresholds. The numbers shown on the right are attenuation lengths in soil (g/cm^2), calculated using the last five points of the curve.



It is known [4,5] that the attenuation length varies as a function of angle; the larger the angle, the smaller the attenuation length. Fassò [4] found that, for GeV electron beams, the attenuation length varied from 73 gm/cm² at 90° to 125 gm/cm² at 30°, and he recommended a conservative value of 100 gm/cm² for the lateral shield of high-energy electron accelerators. Dinter [5] found similar dependence with 95 gm/cm² at 90° to 110 gm/cm² at 30° for electron beam, as well as 110 gm/cm² at 90° to 140 gm/cm² at 30° for proton beam. The attenuation length results (at equilibrium depth for a line source) in this study are consistent with others (at any depth for a point source) [4,5].

The neutron fluence spectra in soil regions can provide insight and support conclusions for radionuclide production, as well as radionuclide per star. The neutron spectra in soil regions 7-12 are shown in Figure 7 for electron beam (top) and proton (bottom) beam. Both plots are lethargy plots of neutron fluence (neutron/cm²/beam particle) vs. neutron energy (GeV). The two-peak feature (one at 1-2 MeV and the other at 100 MeV) is clearly seen. At shallow regions, the ratio between low-energy peak to high-energy peak is higher for the electron beam than for the proton beam. At deep regions, the spectral shapes for electron and proton beams are similar. Actually, beyond region 10, the spectrum reaches the equilibrium state for both electron and proton beams, and the neutron spectrum of the proton beam is a factor of ~135 higher than that of the electron beam.

Figure 7. Neutron spectra (in lethargy plot per unit beam particle) in soil regions 7-12 for electron beam (top) and proton (bottom) beams



Conclusions

The accurate prediction of induced radioactivity using FLUKA or another Monte Carlo code is not yet perfected, and a factor of 2-3 agreement is common for most radionuclides [6,7]. Thus, the absolute radionuclide yields in this study should not be paid special attention. The relative results between the electron and proton beams between 50 MeV and 20 MeV star-scoring thresholds or between neutron star and all star are of more interests, particularly at the equilibrium depth.

There are several main conclusions which emerge from this study:

- As expected, the radionuclide profiles in the soil resemble the star profile beyond the shallow layer, which forms the basis of estimating the induced radioactivity using the star density.
- Neutrons dominate the star production (> 80% at all depths). At deep regions, the star and radionuclide production is due almost entirely to neutrons, with all other particles contributing to less than a few % of the all star density.
- Equilibrium state was reached beyond 120 cm thick soil for the electron beam and 150 cm for the proton beam.
- The atom/star factors for radionuclides are comparable for electron and proton beams, particularly at equilibrium depth. At equilibrium, a value of 0.01 atom/star can be used to estimate the yields of five radionuclides in this study for both electron and proton beams within a factor of 3.
- At equilibrium, the attenuation length λ of star (contributed by neutrons only) is 100 g/cm², with λ for proton beam being 4% higher than λ for electron beam.
- At equilibrium, the star density ratio between proton and electron beams is ~150, while the corresponding neutron fluence ratio is 135 (the spectral shape is the same). The star density at the 20 MeV threshold is 1.5 times more than that at the 50 MeV threshold.

Acknowledgements

The authors wish to acknowledge Alberto Fassò, Ralph Nelson, and Stefan Roesler for their help with this study. The work was supported by Department of Energy contract DE-AC03-76SF00515.

REFERENCES

- [1] Fassò, A., A. Ferrari and P.R. Sala, "Electron-photon Transport in FLUKA: Status", *Proc. of the Monte Carlo 2000 Conference*, Lisbon, 23-26 October 2000, A. Kling, F. Barao, M. Nakagawa, L. Tavora, P. Vaz, eds., Springer-Verlag, Berlin, pp. 159-164 (2001).
- [2] Fassò, A., A. Ferrari, J. Ranft and P.R. Sala, "FLUKA: Status and Prospective for Hadronic Applications", *Proc. of the Monte Carlo 2000 Conference*, Lisbon, 23-26 October 2000, A. Kling, F. Barao, M. Nakagawa, L. Tavora, P. Vaz, eds., Springer-Verlag, Berlin, pp. 955-960 (2001).
- [3] Nelson, W.R. and T.M. Jenkins, "Similarities Among the Radiation Fields at Different Types of High-energy Accelerators", *IEEE Transactions on Nuclear Science*, NS-23, No. 4, August 1976.
- [4] Fassò, A., M Hofert and A. Ioannidou, "On the Shielding of Electron Accelerators in the GeV Energy Range", *Radiat. Prot. Dosim.* 38(4), pp. 301-305 (1991).
- [5] Dinter, H., A. Leuschner, K. Tesch, D. Dworak and J. Loskiewicz, "Calculations of Hadron Yields Around Thick Targets and Doses Behind Concrete Shielding of High-energy Electron Accelerators", *Nucl. Instru. Methods in Phys. Res.*, A455, pp. 460-469 (2000).
- [6] Fassò, A., M. Silari and L. Ulrici, "Predicting Induced Radioactivity at High-energy Electron Accelerators", *Proceedings of the 9th International Conference on Radiation Shielding (ICRS-9)*, Tsukuba, Japan, 1999, *Nucl. Sci. Tech.*, 1 (Suppl.), p. 827 (2000).
- [7] Rokni, S.H., J.C. Liu and S. Roesler, "Induced Radioactivity of Materials by Stray Radiation Fields at an Electron Accelerator", *these proceedings*.

INDUCED RADIOACTIVITIES OF SPALLATION PRODUCTS BY VARIOUS PROJECTILE IONS

Hiroshi Yashima, Hiroshi Sugita, Takashi Nakamura

Department of Quantum Science and Energy Engineering, Tohoku University, Japan

Yoshitomo Uwamino

The Institute of Physical and Chemical Research, Japan

Akifumi Fukumura

National Institute of Radiological Sciences, Japan

Abstract

The radioactivities of spallation products in a Cu target were obtained by bombarding 230 and 100 MeV/nucleon Ne, C, He, p and 230 MeV/nucleon Ar ions. Irradiation experiments were performed at the Heavy Ion Medical Accelerator in Chiba (HIMAC) facility, National Institute of Radiological Sciences. The gamma-ray spectra from the irradiated samples inserted into the Cu target were measured with a HPGe detector. From the gamma-ray spectra, we obtained the variation of radioactivities of nuclides produced in the samples with the depth of the Cu target and the mass-yield distribution of nuclides produced in the samples on the surface of the Cu target. The results showed that the dependence of the cross-sections on the projectile mass strongly depends on the mass number difference between Cu and the produced nuclide.

We have also applied the semi-empirical formula to the heavy-ion-induced spallation cross-section calculation by using the obtained projectile dependency of mass-yield distribution.

Introduction

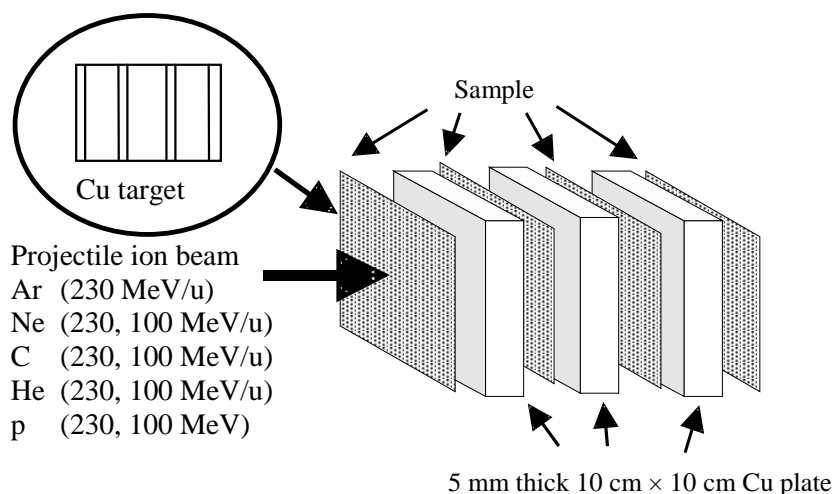
High-energy and high-intensity ion accelerators are being increasingly used for nuclear physics, solid-state physics, radiotherapy, material damage study and so on. Safety design considerations with regard to the accelerator facilities require the reaction cross-section data for high-energy ions to estimate the radioactivities induced in the accelerator components and in the shielding materials. The reaction cross-section data for heavy ions, however, are quite poor.

We therefore performed measurements of these data by irradiating 230 and 100 MeV/nucleon Ne, C, He, p and 230 MeV/nucleon Ar ions onto a Cu target, which is a main element of accelerator components, and investigated the projectile dependency of induced radioactivities of spallation products. We applied the semi-empirical formula given by Silberberg and Tsao [1,2] to the heavy-ion-induced spallation cross-section calculation by using the measured data in order to investigate the accuracy of this formula to heavy-ion reactions.

Experiment and analysis

Irradiation experiments were performed at the Heavy Ion Medical Accelerator in Chiba (HIMAC) facility, National Institute of Radiological Sciences. A schematic view of the experimental set-up is shown in Figure 1. The Cu target was composed of a stack of 100 mm × 100 mm × 5 mm Cu plates, and Cu samples were inserted between the Cu plates. The samples put on the front surface of the Cu target are for measurement of the reaction cross-section and the mass-yield distribution of produced nuclides. The samples inserted between the Cu plates are for the measurement of the variations of residual activities with the Cu target depth. The thickness of the Cu target is longer than the beam range of the projectile beam.

Figure 1. Schematic view of the experimental geometry



After irradiation, we measured the gamma-ray spectra from samples with a HPGe detector. The reaction rates of radionuclides produced in samples which were identified from the gamma-ray spectra and the decay curves were estimated after being corrected for the peak efficiency of the HPGe detector and the coincidence-summing effect.

Results

Nuclides produced in Cu

From reaction rates, we obtained the variation of the residual activities [Bq per g/cm² for one projectile ion] of nuclides produced in Cu samples with the Cu target depth and the mass-yield distribution of nuclides produced in the Cu sample set on the surface of the Cu target by 230 and 100 MeV/nucleon Ne, C, He, p and 230 MeV/nucleon Ar ions.

We identified various nuclides from ⁷Be to ⁶⁵Zn. The maximum number of 44 nuclides was obtained for 230 MeV/nucleon Ne irradiation. The list of the nuclides produced in Cu is given in Table 1. The half-lives of these nuclides range from 7 minutes to 5 years.

Table 1. Nuclides produced in Cu

Residual nuclides	Gamma-ray energy [keV]	half-life*	Residual nuclides	Gamma-ray energy [keV]	half-life*
⁷ Be	477.61	53.29 D	⁵² Mn	935.54	5.591 D
²² Na	1 274.53	2.6019 Y	^{52m} Mn	1 434.06	21.1 M
²⁴ Na	1 368.63	14.9590 H	⁵⁴ Mn	834.85	312.12 D
²⁷ Mg	843.76	9.458 M	⁵⁶ Mn	1 810.72	2.5785 H
²⁸ Mg	400.69	20.91 H	⁵² Fe	168.69	8.275 H
²⁹ Al	1 273.3	6.56 M	⁵³ Fe	377.9	8.51 M
^{34m} Cl	146.36	32 M	⁵⁹ Fe	1 291.6	44.503 D
³⁸ Cl	1 642.71	37.24 M	⁵⁵ Co	931.1	17.53 H
³⁹ Cl	1 267.18	55.6 M	⁵⁶ Co	1 238.28	77.27 D
⁴¹ Ar	1 293.59	109.34 M	⁵⁷ Co	122.06	271.79 D
⁴² K	1 524.7	12.36 H	⁵⁸ Co	810.77	70.82 D
⁴³ K	617.49	22.3 H	⁶⁰ Co	1 173.24	5.2714 Y
⁴³ Sc	372.76	3.891 H	⁶¹ Co	67.42	1.65 H
⁴⁴ Sc	1 157.03	3.927 H	^{62m} Co	1 163.5	13.91 M
^{44m} Sc	271.13	58.6 H	⁵⁷ Ni	1 377.63	35.6 H
⁴⁶ Sc	889.28	83.79 D	⁶⁵ Ni	1 481.84	2.5172 H
⁴⁷ Sc	159.38	3.3492 D	⁶⁰ Cu	1 791.6	23.7 M
⁴⁸ Sc	1 037.52	43.67 H	⁶¹ Cu	282.96	3.333 H
⁴⁸ V	983.52	15.9735 D	⁶⁴ Cu	1 345.77	12.7 H
⁴⁸ Cr	308.24	21.56 H	⁶² Zn	596.56	9.186 H
⁴⁹ Cr	90.64	42.3 M	⁶³ Zn	669.62	38.47 M
⁵¹ Cr	320.08	27.702 D	⁶⁵ Zn	1 115.55	244.26 D

* Y: year, D: day, H: hour, M: minute

Variation of residual activities with Cu target depth

The variations of residual activities of ³⁸Cl, ⁴⁹Cr, ⁶¹Cu produced in the Cu samples with the Cu target depth are shown in Figures 2 to 4, respectively. The target depth is expressed as the unit of the beam range. The vertical dashed lines give the range of the projectile beam. The lozenge points are for Ar, square points are for Ne, the circle points are for C, the triangle points are for He, the inverse triangle points are for p. The black points are 230 MeV/nucleon, the white points are 100 MeV/nucleon.

Figure 2. Variation of residual activities of ^{38}Cl produced in the Cu samples with Cu target depth

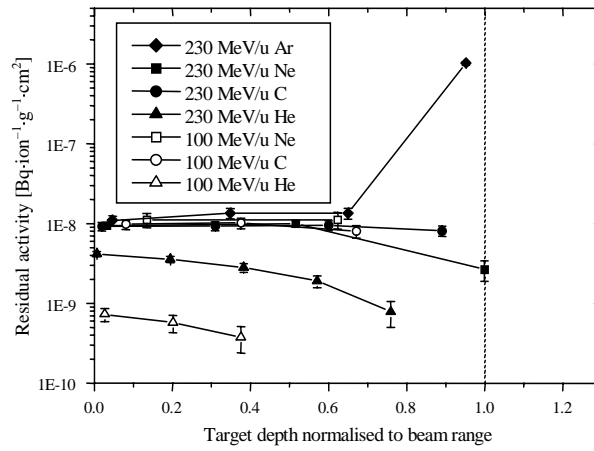


Figure 3. Variation of residual activities of ^{49}Cr produced in the Cu samples with Cu target depth

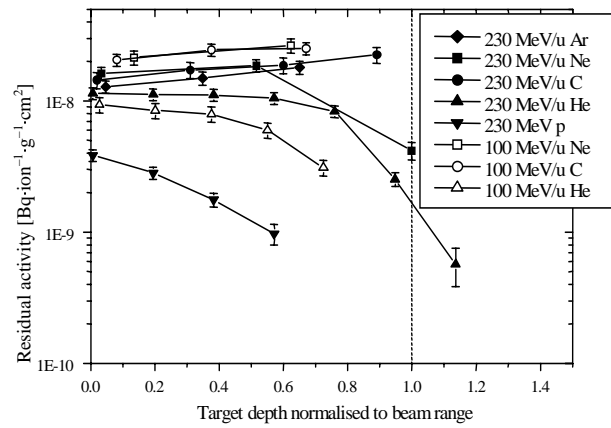
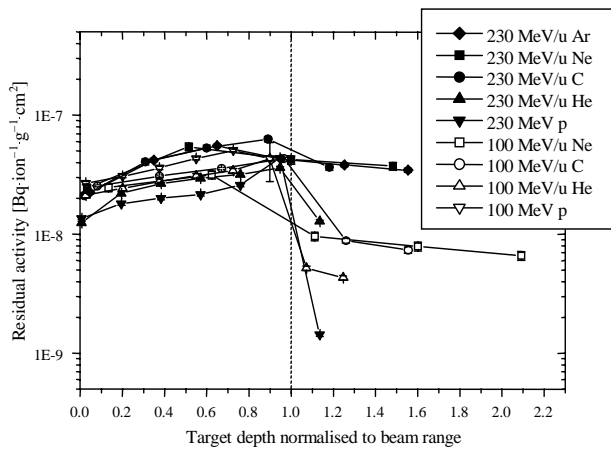


Figure 4. Variation of residual activities of ^{61}Cu produced in the Cu samples with Cu target depth



In Figure 2, the residual activities of ^{38}Cl are almost constant down to the beam range and rapidly decrease beyond it in the case of the C and Ne ion (230,100 MeV/nucleon) irradiations, while it gradually decreases with the target depth in the case of 230,100 MeV/nucleon He ion. Since the mass number difference between Cu and ^{38}Cl is large, ^{38}Cl is produced dominantly by a primary projectile beam. Only for 230 MeV/nucleon Ar, the residual activities of ^{38}Cl are almost constant down to the beam range, but rapidly increase near the beam range.

In Figure 3, the residual activities of ^{49}Cr increase down to the beam range and decrease beyond it in the case of C, Ne and Ar ion (230,100 MeV/nucleon) irradiations. It is almost constant down to the beam range and rapidly decreases beyond it in the case of 230,100 MeV/nucleon He, and it monotonously decreases with the target depth in the case of 230 MeV/nucleon p ion. Since the mass number of ^{49}Cr becomes closer to Cu than that of ^{38}Cl , the fraction of ^{49}Cr produced by secondary particles increases.

In Figure 4, the residual activities of ^{61}Cu show the a similar tendency to that of ^{49}Cr . In this case, the ^{61}Cu production also increases with the target depth for 230 and 100 MeV proton irradiation. The increasing rate of residual activities with the target depth is much larger for spallation products of which the mass number is closer to Cu.

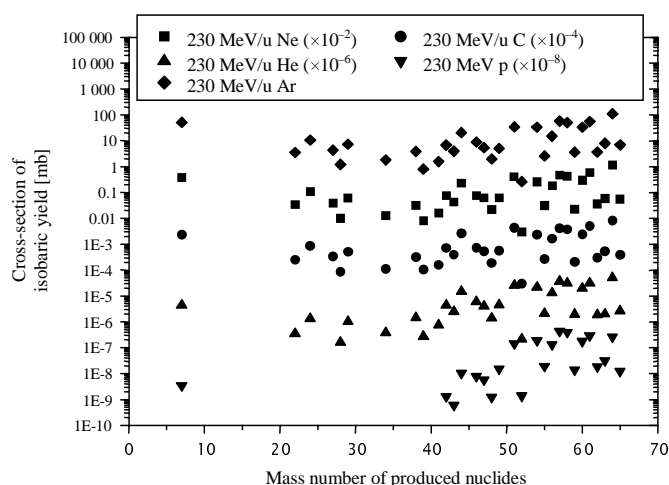
When the mass number difference between Cu and the produced nuclide is large, nuclides are produced dominantly by a primary projectile beam. The reaction cross-sections are almost constant down to the beam range or gradually decrease with the target depth. When the mass number difference between Cu and produced nuclide is small, the fraction of nuclides produced by secondary particle is large. When the projectile mass number and energy increases, the reaction cross-section increases toward the inner part of the Cu target due to the increasing number of secondary particles.

Mass-yield distribution of nuclides produced in Cu

From the reaction cross-sections obtained, we extracted the mass-yield distribution of nuclides produced in a Cu sample.

The mass-yield (isobaric yield) distributions of nuclides produced in a Cu sample set on the surface of a Cu target irradiated by 230 MeV/nucleon Ar, Ne, C, He and p ions are shown in Figure 5.

Figure 5. Mass-yield distribution of nuclides produced in Cu

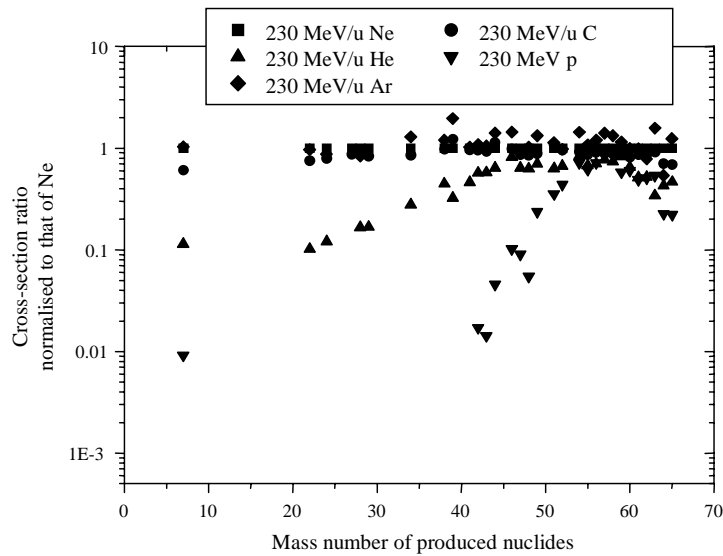


In Figure 5, the cross-section of isobaric yield decreases with an increase in the mass number difference between Cu and the produced nuclide, but the ${}^7\text{Be}$ production cross-section again increases except for 230 MeV protons, since a light nuclide of ${}^7\text{Be}$ is mainly produced by projectile fragmentation. When the projectile energy is 100 MeV/nucleon, the mass-yield distribution shows a similar tendency.

Projectile dependency of nuclides produced in Cu

The projectile dependency of nuclides produced on the front surface of the Cu target bombarded by 230 MeV/nucleon Ar, Ne, C, He and p ions is shown in Figure 6. The vertical axis is the ratio of cross-sections produced by Ar, C, He and p ions normalised to those for Ne ions.

Figure 6. Mass-yield distribution of nuclides produced in Cu



From Figure 6, it is clear that the heavier projectile having a higher total energy produces lighter spallation products. The projectile dependency is thus larger for 100 MeV/nucleon than for 230 MeV/nucleon.

Application of semi-empirical formula to the heavy-ion-induced spallation cross-section estimation

We have also applied the semi-empirical formula given by Silberberg and Tsao [1,2], which was originally developed for proton spallation reactions, to the heavy-ion-induced spallation cross-section calculation by using the projectile dependency of mass-yield distribution obtained in this work. The semi-empirical formula given by Silberberg and Tsao is:

$$\sigma = \sigma_0 f(A) f(E) e^{-P\Delta A} e^{-R|Z-SA+TA^2|^\nu} \Omega \eta \xi \quad (1)$$

This formula is applicable for cross-sections (in units of mbarn) of targets having mass numbers in the range $9 \leq A_t \leq 209$ and products with $6 \leq A \leq 200$, except for peripheral interactions with small values of ΔA .

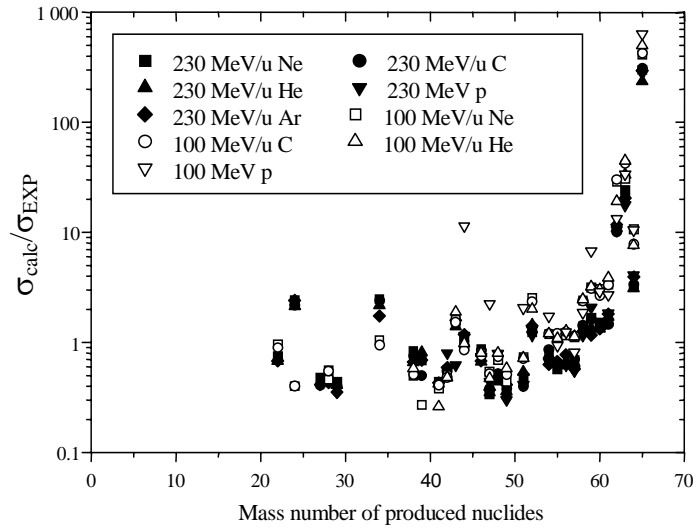
We applied this formula for the calculation of the heavy-ion-induced spallation cross-section by scaling Eq. (1). The equation for calculating the heavy-ion-induced spallation cross-section (σ_{HI}) is:

$$\sigma_{HI} = S_C \sigma_p \quad (2)$$

where σ_p is the spallation cross-section induced by a proton which has the same projectile energy per nucleon as a heavy-ion to be calculated and the scaling factor S_C is the ratio of heavy-ion-induced cross-section to proton-induced cross-section (shown in Figure 6) fitted to an exponential function with a third-order polynomial of A .

The ratios of calculated cross-section (σ_{calc}) to experimental cross-section (σ_{EXP}) are shown in Figure 7.

Figure 7. Ratios of experimental cross-section (σ_{EXP}) to calculated cross-section (σ_{calc})



In Figure 7, the calculated results generally agree with experimental results within a factor 3 margin of accuracy except for peripheral interactions with small values of ΔA .

Conclusions

We performed the irradiation experiments by 230 and 100 MeV/nucleon Ne, C, He, p and 230 MeV/nucleon Ar ions, and obtained the spatial distribution of residual activities of nuclides produced in Cu sample with the Cu target depth and mass-yield distribution of nuclides produced in Cu sample on the surface of Cu target.

We also applied the semi-empirical formula to the heavy-ion-induced spallation cross-section calculation by using the obtained projectile dependency of mass-yield distribution. The calculated results generally agree with experimental results within a factor of 3 margin of accuracy except for peripheral interactions with small values of ΔA . It is strongly needed to have more accurate formula to estimate the heavy-ion-induced spallation cross-sections.

This systematic study will be useful for designing the high-energy heavy-ion accelerator facility and benchmark test of the nuclear reaction simulation codes.

Acknowledgements

We gratefully acknowledge the support and assistance of the accelerator operation staff at HIMAC. We wish to thank the members of the Nakamura Laboratory of Department of Quantum Science and Energy Engineering, Tohoku University. This work was supported in part by the research project with heavy-ions at NIRS-HIMAC.

REFERENCES

- [1] Silberberg, R. and C.H. Tsao, "Partial Cross-sections in High-energy Nuclear Reactions and Astrophysical Applications. I. Targets with $Z \leq 28$ ", *The Astrophysical Journal Supplement Series*, No. 220 (I), 25, 315-333 (1973).
- [2] Silberberg, R. and C.H. Tsao, "Partial Cross-sections in High-energy Nuclear Reactions and Astrophysical Applications. II. Targets Heavier than Nickel", *The Astrophysical Journal Supplement Series*, No. 220 (II), 25, 335-368 (1973)

SESSION III

Benchmarking – Calculations and Results

Chair: H. Hirayama, R. Prael

**INTERCOMPARISON OF MEDIUM-ENERGY
NEUTRON ATTENUATION IN IRON AND CONCRETE (4)**

Hideo Hirayama

KEK, High Energy Accelerator Research Organisation
1-1 Oho, Tsukuba, Ibaraki, 305-0801 Japan
E-mail: hideo.hirayama@kek.jp

Attenuation Length Sub-working Group in Japan

Abstract

From the results presented at SATIF-5, revised problems to be calculated were prepared by the Japanese Working Group and sent to the participants of this action. Then, 5 and 10 GeV neutrons were added as the source neutrons to determine their energy dependence. From the results presented at a previous meeting, it became clear that the attenuation length of secondary neutrons depended strongly on their spectra. Considering this situation, secondary neutron spectra for various angles, produced by 3 GeV protons on a Hg target and calculated by F. Maekawa using MCNPX, were added as the secondary neutron problems.

This paper presents a comparison of the neutron attenuation length of iron and concrete sent from four groups to the organiser by the end of February, including results presented at previous SATIF meetings and future themes which result from this intercomparison.

Introduction

Neutron attenuation at high energies (above a few GeVs) is not supposed to depend on the energy. Its energy dependence below this energy, especially below 1 GeV, has not been well understood. It is desired to obtain common agreements concerning the behaviours of neutrons inside various materials. This is necessary in order to agree on definitions of the attenuation length, which is very important for shielding calculations involving high-energy accelerators. As one attempt, it was proposed by Japanese attendants of SATIF-2 to compare the attenuation of medium-energy neutrons inside iron and concrete shields between various computer codes and data, and was cited as a suitable action for SATIF. From the results for neutrons below 400 MeV presented at SATIF-3 [1], it has become clear that neutrons above 20 MeV are important for understanding that the attenuation length and the geometry, planar or spherical, does not greatly affect the results. The attenuation length of neutrons above 20 MeV was compared for the planer geometry included for secondary neutrons produced by medium-energy protons at SATIF-4 [2]. Though the attenuation lengths were slightly different, all of the results showed the same tendency for an attenuation length increase along with an increase in the neutron energy up to 500 MeV. The same tendency was presented at SATIF-5 [3] for higher neutron energies of 1, 1.5 and 3 GeV. From the results presented at SATIF-4 and SATIF-5, it is clear that the attenuation length of secondary neutrons strongly depends on their spectra.

Considering these results, revised problems to be calculated were prepared by the Japanese Working Group and sent to the participants of this action. Then, 5 and 10 GeV neutrons were added as source neutrons to determine their energy dependence. The secondary neutrons emitted in several directions from a Hg target bombarded by 3 GeV protons, calculated by F. Maekawa [4] using MCNPX [5], were also added as source neutrons.

The results from four groups were sent to the organiser by the end of February. This paper presents a comparison of the neutron attenuation lengths of iron and concrete, including the results presented at previous meetings and the future themes which result from this intercomparison.

Problems for an intercomparison (4)

Considering the results presented at SATIF-5 [3], the following revised problems were proposed to be calculated by various codes with their own databases. Secondary neutrons produced from a Hg target by 3 GeV protons toward various directions were also added, and were calculated by F. Maekawa using MCNPX [5].

Attenuation calculation

Source neutron energy

- Source neutrons are uniformly distributed within the following energy regions:

40-50 MeV	1 GeV
90-100 MeV	1.5 GeV
180-200 MeV	3 GeV
375-400 MeV	5 GeV
	10 GeV

- Secondary neutrons to 90° from Fe target (5 cm diameter, 5 cm length, see Figure1):

From 200 MeV protons.	From 1 GeV protons.
From 500 MeV protons.	From 3 GeV protons.
From 5 GeV protons.	

- Secondary neutrons in various directions from a Hg target with a Pb moderator (120 cm diameter and 120 cm length) shown in Figure 2 with 3 GeV protons (Figure 3).

Geometry

Plane (6 m thick) with normal-incident parallel beams.

Shielding material

As typical shielding materials, iron and concrete were selected. The densities of the two materials and the composition of concrete are also shown (Table 1).

- Iron (density 7.87 g cm⁻³).
- Concrete (density 2.27 g cm⁻³) [Type 02-a, ANL-5800, 660 (1963)].

Energy group and fluence to the dose-equivalent conversion factor

The energy group in Table 2 is presented as the standard one; it is required that the neutron spectra be presented in this energy group, if possible.

In dose calculations, it is recommended to use the neutron flux-to-dose equivalent conversion factor (Table 3), so as to avoid any ambiguity due to the conversion factor used. The values given in Table 3 are conversion factors to the neutron energy corresponding to that given in Table 2.

Figure 1. Secondary neutron at 90° from an iron target bombarded by protons (FLUKA calculations)

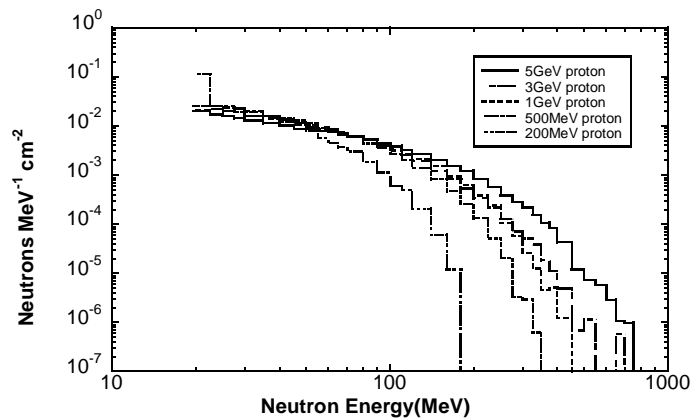


Figure 2. Calculation geometry of secondary neutrons from a Hg target with 3 GeV protons

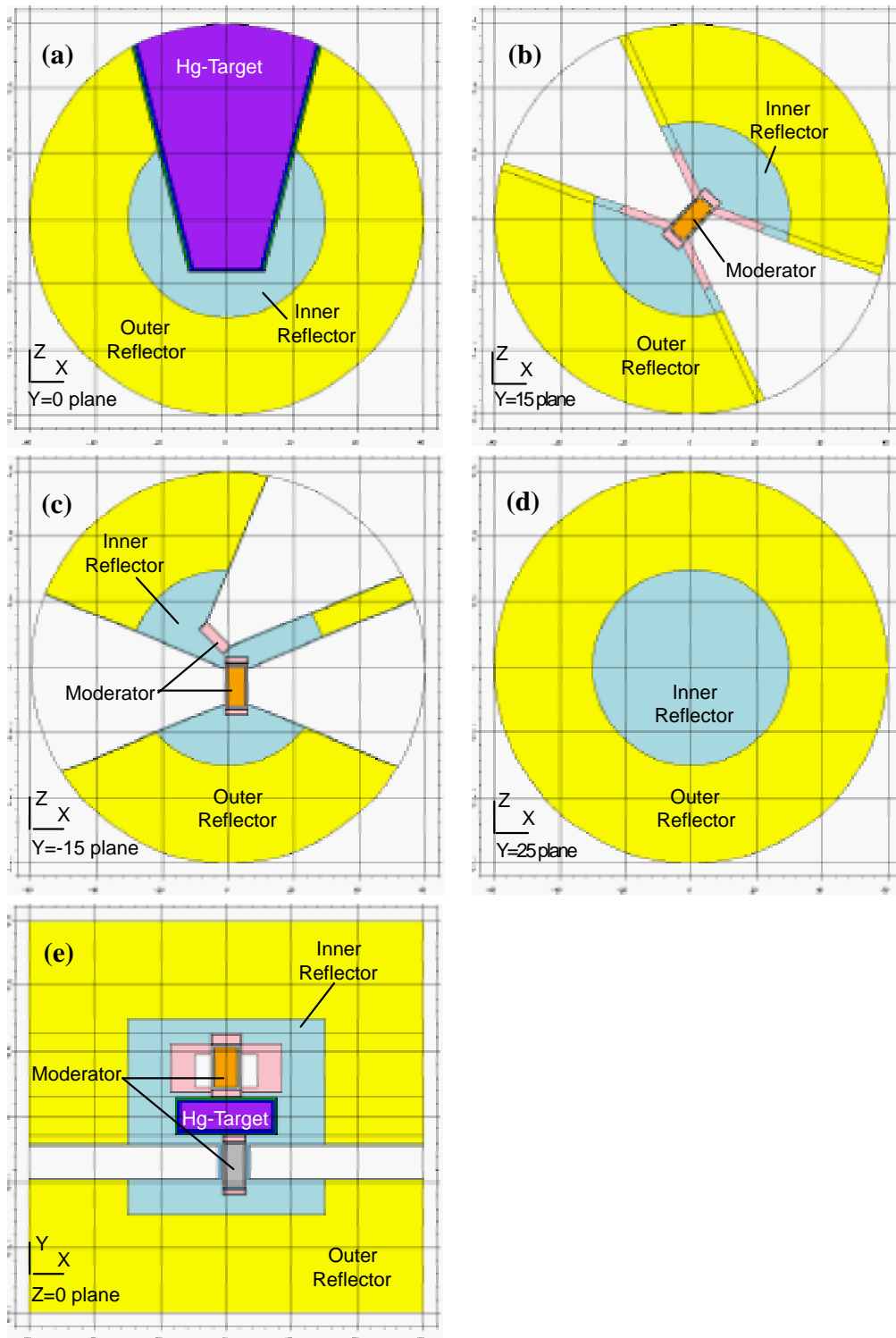


Figure 3. Secondary neutron spectrum from a Hg target bombarded by 3 GeV protons (MCNPX calculations)

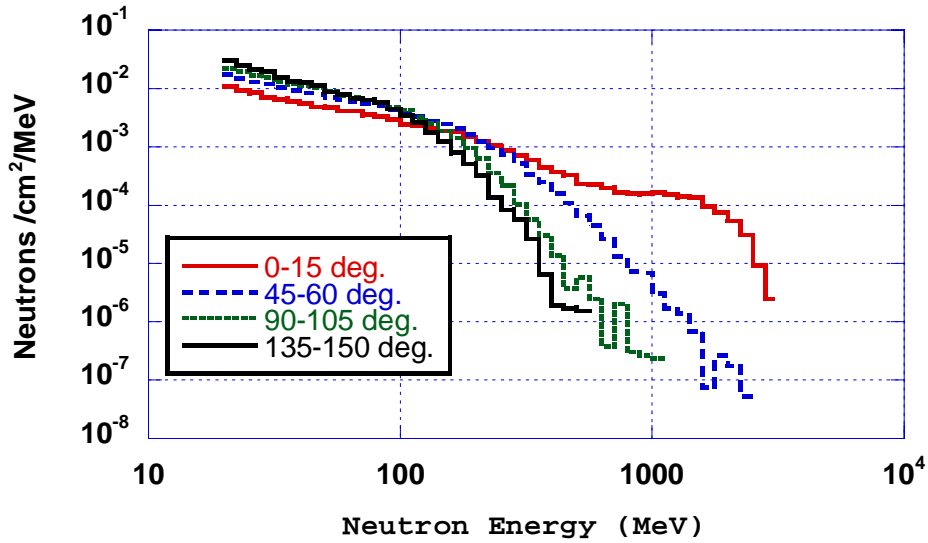


Table 1. Composition of concrete

Element	Atomic no. density (10 ²⁴ /cm ³)	wt.%	Element	Atomic no. density (10 ²⁴ /cm ³)	wt.%
H	1.3851E-2	1.02	Si	1.6621E-2	34.21
C	1.1542E-4	1.00	K	4.6205E-4	1.32
O	4.5921E-2	53.85	Ca	1.5025E-3	4.41
Mg	1.2388E-4	0.22	Fe	3.4510E-4	1.41
Al	1.7409E-3	3.44			

Table 2. Upper energy of 66 neutron energy groups (MeV)

1.00E+4	9.00E+3	8.00E+3	7.00E+3	6.00E+3	5.00E+3	4.50E+3	4.00E+3	3.50E+3	3.00E+3
2.50E+3	2.00E+3	1.90E+3	1.80E+3	1.70E+3	1.60E+3	1.50E+3	1.40E+3	1.30E+3	1.20E+3
1.10E+3	1.00E+3	9.00E+2	8.00E+2	7.00E+2	6.00E+2	5.00E+2	4.00E+2	3.75E+2	3.50E+2
3.25E+2	3.00E+2	2.75E+2	2.50E+2	2.25E+2	2.00E+2	1.80E+2	1.60E+2	1.40E+2	1.20E+2
1.10E+2	1.00E+2	9.00E+1	8.00E+1	7.00E+1	6.50E+1	6.00E+1	5.50E+1	5.00E+1	4.50E+1
4.00E+1	3.50E+1	3.00E+1	2.75E+1	2.50E+1	2.25E+1	2.00E+1			

Table 3. Neutron flux-to-dose conversion factor [(Sv/hr)/(n/sec/cm²)]

(ICRP51 [6], Maximum Dose Equivalent, Table 23)

1.09E-5	1.05E-5	1.00E-5	9.55E-6	9.01E-6	8.42E-6	8.11E-6	6.77E-6	7.41E-6	7.02E-6
6.72E-6	6.32E-6	6.22E-6	6.11E-6	5.98E-6	5.84E-6	5.69E-6	5.52E-6	5.34E-6	5.14E-6
4.94E-6	4.72E-6	4.47E-6	4.18E-6	3.78E-6	3.26E-6	2.72E-6	2.25E-6	2.20E-6	2.15E-6
2.10E-6	2.05E-6	1.99E-6	1.93E-6	1.86E-6	1.82E-6	1.79E-6	1.77E-6	1.74E-6	1.72E-6
1.70E-6	1.68E-6	1.65E-6	1.64E-6	1.63E-6	1.62E-6	1.61E-6	1.60E-6	1.59E-6	1.58E-6
1.57E-6	1.56E-6	1.55E-6	1.54E-6	1.53E-6	1.52E-6				

Quantities to be calculated

The following quantities must be calculated for intercomparisons:

- Dose equivalent due to neutrons above 20 MeV at 50, 100, 150, 200, 250, 300, 350, 400, 450 and 500 cm.
- Neutron spectrum in n/cm²/MeV/source neutron at 100, 200, 300, 400 and 500 cm.

Summary of contributors

Neutron attenuation calculation

Four groups sent their results to Hideo Hirayama at KEK before the end of February. Table 4 lists the participants, the names of the computer codes used and the names of databases used in the computer codes.

Table 4. Summary of contributors

Name of participants and organisation	Name of computer code	Name of database used in the computer code
S. Roesler (CERN)	FLUKA	Library data in FLUKA
H. Nakashima (JAERI) T. Abe (Start Com Co. Ltd.)	NMTC/JAM	JAM
Y. Uwamino (Riken)	HETC-3STEP	Library data in HETC
Y. Sakamoto (JAERI)	ANISN-JR	HILO-86R(≤ 400 MeV) P ₅ S ₆₄

Results and discussion

Attenuation length

The attenuation length (λ ; g cm⁻²) for each case was obtained by a least-squares fitting at the region where the dose decreased exponentially. The thus-obtained neutron attenuation lengths of iron and concrete are shown in Figures 4 and 5, respectively. In the case of iron, the results of JAM were calculated for a 300 cm slab, not a 600 cm one. In these figures, the results presented at previous SATIF meetings are also plotted. The attenuation lengths for iron are scattered around each other below 500 MeV, but are relatively close above 1 GeV. Although the value itself still increases with an increase of the source neutrons, even at 10 000 MeV, the increase rate decreases compared with the area below 500 MeV. It is supposed that the attenuation length reaches a constant value at several tens of GeVs. On the other hand, the difference in the attenuation length between each code does not depend on the source neutron energy in the case of concrete. The attenuation length still increases with an increase of the source neutrons, even at 10 000 MeV.

The attenuation lengths of iron and concrete for secondary neutrons from a Hg target with 3 GeV protons are shown as a function of the emission angle in Figures 6 and 7, respectively. Neutrons above 400 MeV were replaced on 400 MeV neutrons in the ANISN calculation. This portion is 27%, 2.7%, 0.3% and 0.03% at 0-15, 45-60, 90-105 and 135-150 degrees, respectively. The relatively small values

Figure 4. Comparison of the attenuation length of iron

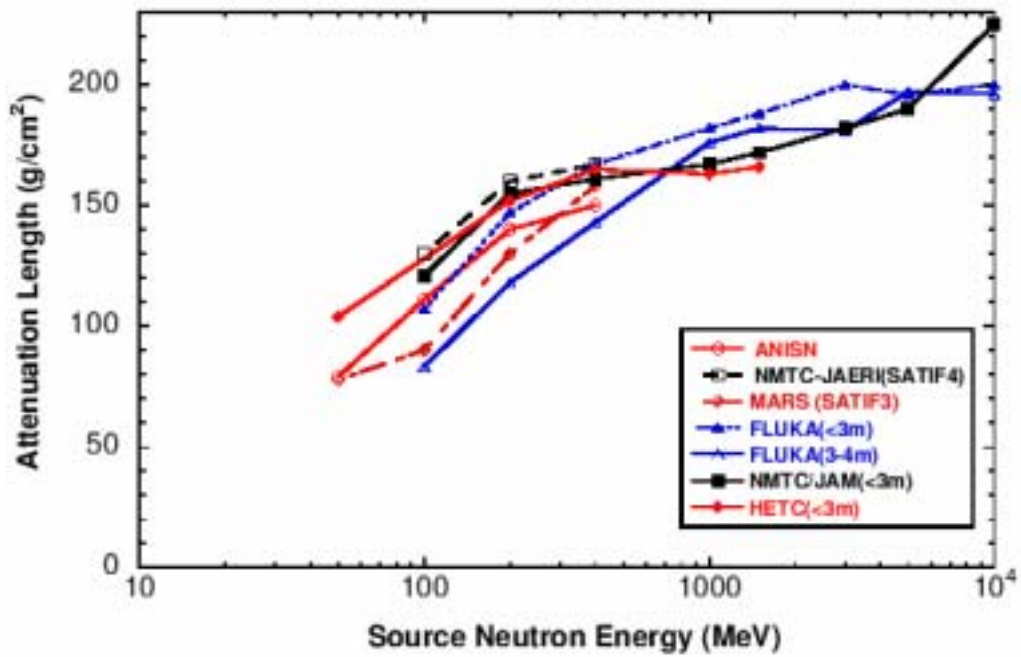


Figure 5. Comparison of the attenuation length of concrete

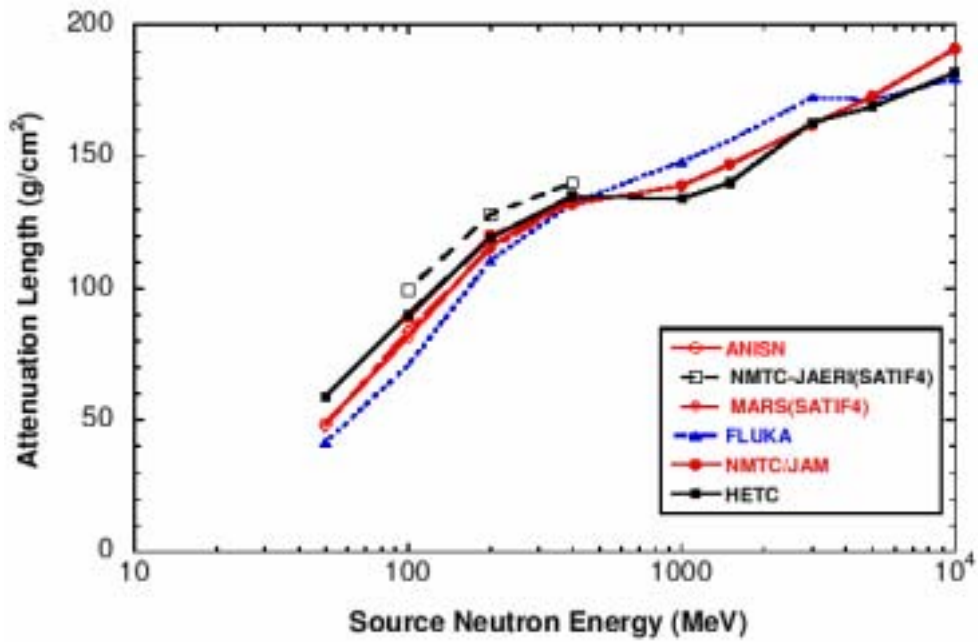


Figure 6. Comparison of the neutron attenuation length of iron for secondary neutrons from 3 GeV protons on Hg target

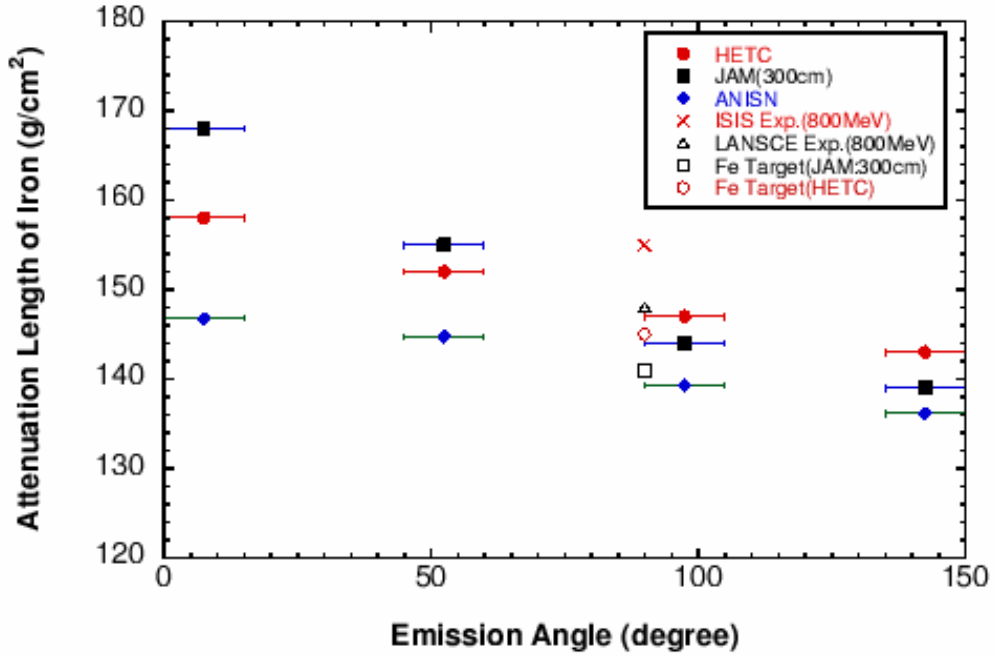
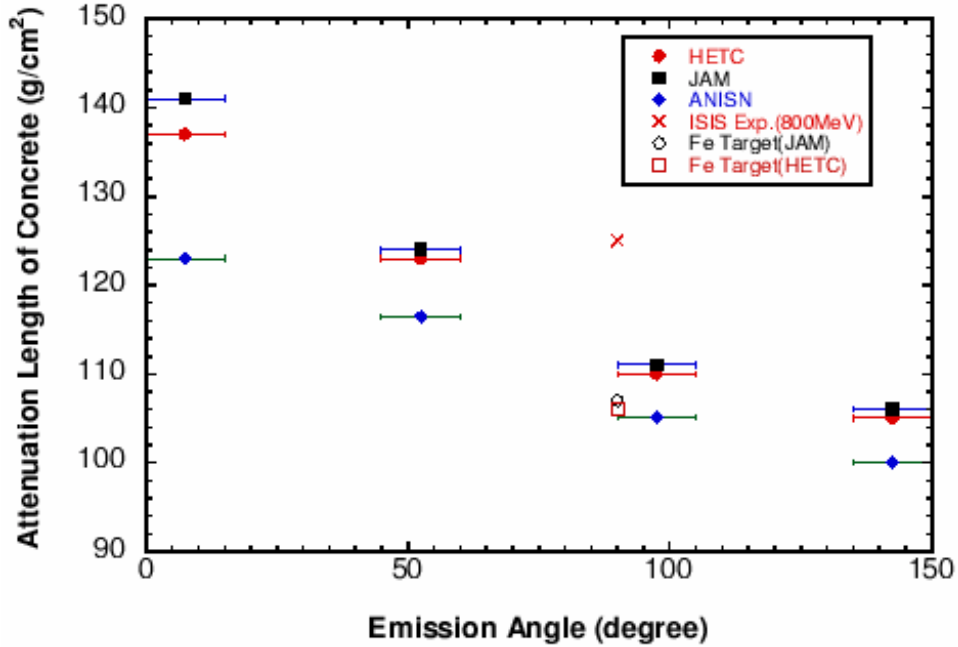


Figure 7. Comparison of the neutron attenuation length of concrete for secondary neutrons from 3 GeV protons



of ANISN at small angles are supposed to be due to this treatment. In these figures, the results for secondary neutrons from a Fe target with 3 GeV protons and the experimental results at ISIS [7] and LANSCE [8] for 800 MeV protons are also plotted. The attenuation lengths of both iron and concrete decrease with an increase in the emission angle. This tendency comes from the difference in the shape of the spectrum shown in Figure 2. The higher-energy neutrons may increase the attenuation length. The attenuation length for a Hg target is larger than that for a Fe target around 90 degrees, reflecting the thickness of the target. Although more secondary neutrons are emitted in the forward direction, they are not scattered to a lateral direction in the case of a thin target. Some parts of neutrons will be reflected in the lateral direction in the case of a thick target. This may be the reason for the differences between two targets.

Future themes

From the comparisons given above, it is necessary to discuss and perform the following actions as the next step:

- Compare with the results of other codes to confirm the tendency shown above. It is desired to receive the results from other groups.
- Neutron dose equivalent attenuation up to 100 GeVs in order to confirm whether the attenuation length reaches a constant value or not.
- Select suitable experiments to compare for understanding the attenuation length of secondary neutrons from high-energy protons. The results of AGS shielding experiments presented by H. Nakashima, *et al.* will be suitable for this purpose.

REFERENCES

- [1] Hirayama, H., *et al.*, “Intercomparison of the Medium-energy Neutron Attenuation in Iron and Concrete”, *Proceedings of the Workshop on Shielding Aspects of Accelerators, Targets and Irradiation Facilities (SATIF-3)*, Tohoku University, 12-13 May 1997, pp. 185-195 (1998).
- [2] Hirayama, H., *et al.*, “Intercomparison of the Medium-energy Neutron Attenuation in Iron and Concrete (2)”, *Proceedings of the Workshop on Shielding Aspects of Accelerators, Targets and Irradiation Facilities (SATIF-4)*, Knoxville, Tennessee, USA, 17-18 September 1998, pp. 143-154 (1999).
- [3] Hirayama, H., *et al.*, “Intercomparison of the Medium-energy Neutron Attenuation in Iron and Concrete (3)”, *Proceedings of the Workshop on Shielding Aspects of Accelerators, Targets and Irradiation Facilities (SATIF-5)*, Paris, France, 18-21 July 2000, pp. 189-201 (2001).
- [4] Maekawa, F., private communication.

- [5] Hughes, H.G., R.E. Prael and R.C. Little, *MCNPX – The LAHET/MCNP Code Merger*, Los Alamos National Laboratory Report XTM-RN(U)97-012 (1997).
- [6] ICRP Publication 51, *Data for Use in Protection Against External Radiation*, Annals of the ICRP 17(2/3) (1987).
- [7] Nunomiya, T., *et al.*, “Measurement of Deep Penetration of Neutrons Produced by 800 MeV Proton Beam through Concrete and Iron at ISIS”, *Nucl. Instr. And Meth.*, B179, pp. 89-102 (2001).
- [8] Bull, J.S., J.B. Donahue and R.L. Burman, “Measurement of Neutron Attenuation Through Thick Shields and Comparison with Calculation”, *Proceedings of the 4th Workshop on Simulating Accelerator Radiation Environments (SARE-4)*, Knoxville, Tennessee, 14-16 September 1998, pp. 201-208 (1999).

CODE AND DATA BENCHMARKING WITH THE NEW IAEA PHOTONUCLEAR DATA LIBRARY

Danas Ridikas

DSM/DAPNIA/SPhN, CEA Saclay
F-91191 Gif-sur-Yvette, France

Peter Vertes

KFKI Atomic Energy Research Institute
H-1525 Budapest, Hungary

Abstract

As a result of an international co-operative activity, a recommended file of photonuclear reactions of 164 isotopes became available. The formal and practical quality of these data are examined by using them for the calculation of photoneutron production in thick targets bombarded by photons and electrons. The Monte Carlo calculations are accomplished with a recent version of the MCNP code enhanced with a photonuclear capability. The energy range of our investigations is from the photonuclear threshold up to 150 MeV. In some cases, a comparison between our calculations and a new version of the MCNPX code, recently updated with the LANL photonuclear data files (12 isotopes) is established. Our results are also compared with the experimental data when available. These data include early measurements of the total neutron yields from thick targets bombarded by electrons as a function of energy, target thickness and atomic number, as well as recent measurements of ^{238}U photofission yields. We show that in general the agreement between the experimental and calculated results is satisfactory. However, a number of particular examples where this is not the case seem to exist. Most of these cases are identified.

Introduction

In recent times, the world-wide interest in photonuclear processes has steadily grown. For a long time these processes were neglected by particle transport codes mainly due to the lack of the evaluated photonuclear data files. The presently growing interest is motivated by a number of different applications such as shielding problems of medical or fundamental research accelerators, the need for new cost-effective neutron sources, transmutation of nuclear waste either directly by photons [1] or by neutrons created from photonuclear reactions [2], radioactive nuclear beam factories based on photofission process [3], etc.

In 1996, in order to make up this backlog, IAEA started a co-ordinated research programme for the compilation and evaluation of photonuclear data for applications. As a result of this effort, a photonuclear data file in ENDF format for 164 isotopes became available in 2000 [4]. Five different laboratories provided these files. Mainly for this reason the representation of data, in spite of earlier recommendations, is not unified.

One of the first efforts to include the photonuclear transport option into the MCNP code [5] was made by Gallmeier [6] in 1995. As the photonuclear effects might also be important for energies higher than 20 MeV, this task has been left to the high-energy extension of the MCNP code, i.e. MCNPX [7]. The first version of MCNPX being enhanced with photonuclear capability is the beta version 2.2.3 [8]. Presently, this is distributed with 12 photonuclear tables containing data for the following isotopes [8]: ^{12}C , ^{16}O , ^{27}Al , ^{28}Si , ^{40}Ca , ^{56}Fe , ^{63}Cu , ^{181}Ta , ^{184}W , ^{206}Pb , ^{207}Pb and ^{208}Pb . For nine of these isotopes the evaluated data files are taken from LANL as recommended by the IAEA [4]. Presumably, the photonuclear tables are also prepared from these evaluations. For ^{56}Fe , ^{181}Ta and ^{28}Si , however, the IAEA recommends the data files from JAERI.

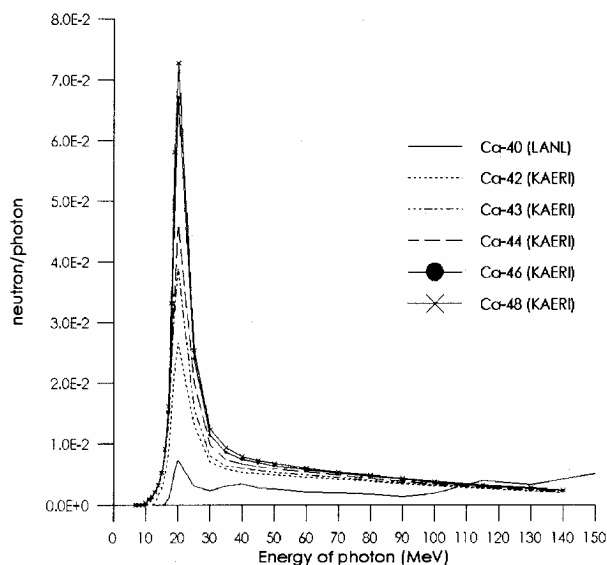
It seems that because of many open reaction channels the construction of photonuclear transport tables within MCNPX is a complicated procedure and it will take some time to convert all recommended photonuclear data into such a form. Therefore, there is an urgent need to try and use all available data by other means. In this context, if one can be satisfied only with neutron secondaries and in some cases with poor accuracy in energy-angular distribution, then an enhancing patch of MCNP provided by Vertes [9] can be applied to all 164 available photonuclear data files. This enhancement is based on adding the regular photon tables with photonuclear data, rather than on creating new tables as is done in the new beta version of MCNPX. This addition is accomplished by a special program which can process the entire IAEA Photonuclear Data Files while disregarding some of their formal errors. By means of this enhancement all data could be tested as far as their applicability in transport calculations is concerned. Our benchmarking results include testing of evaluated files with monoenergetic gammas interacting with thick targets, verification with experimental data when available and comparison with the MCNPX 2.2.3 results [8].

Test calculation with monoenergetic photons

Some interesting features of the photonuclear data supplied by different laboratories can be highlighted if the photoneutron production as a function of gamma energy is investigated. In our calculations with MCNP, large targets (50 cm diameter and 100 cm thick) were irradiated with monoenergetic photons of different energies. In order to exclude neutron production by multiply scattered photons, a cut-off energy for photons, less by 0.5 MeV than the source energy, was applied. The nucleus density was taken as that of natural Pb for all 164 isotopes. Here only the most important findings are quoted.

We found interesting to compare the yields of different isotopes of the same element, and the case of Ca is taken as an example. In the evaluation of this particular data, ^{40}Ca (abundance 96.94%) experimental cross-sections are used. For other isotopes corresponding evaluated data tables are the result of model calculations. Perhaps due to this fact, for all isotopes except ^{40}Ca , one observes a rather regular energy dependence and neutron yields increase with mass number (see Figure 1). On the other hand, the energy dependence of ^{40}Ca curve is of somewhat different character.

Figure 1. Photoneutron production with monoenergetic gammas for a thick target of different Ca isotopes



The difference in neutron yields of two isotopes of C, namely ^{12}C and ^{13}C , is remarkable, as shown in Figure 2. Again there are non-negligible deviations in energy dependence, presumably partly due to the same reason as for Ca, and partly due to the direct reaction ($\gamma, n0$) included in the ^{12}C evaluation. The same conclusions are valid for two isotopes of O (^{15}O and ^{16}O) as shown in Figure 3.

Figure 2. Same as Figure 1 but for different isotopes of C

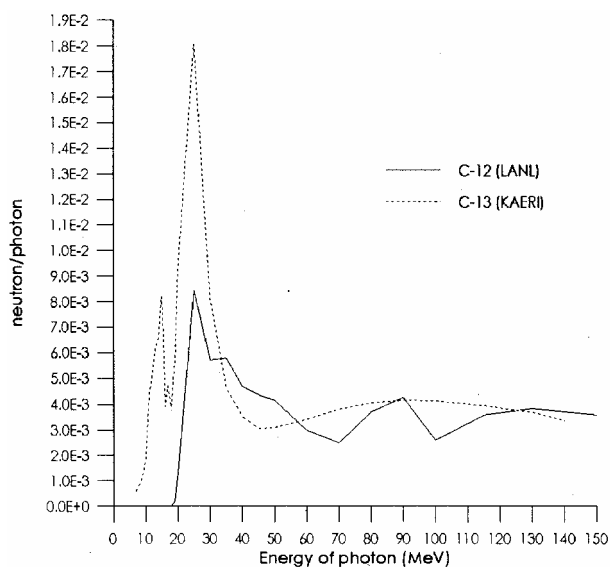
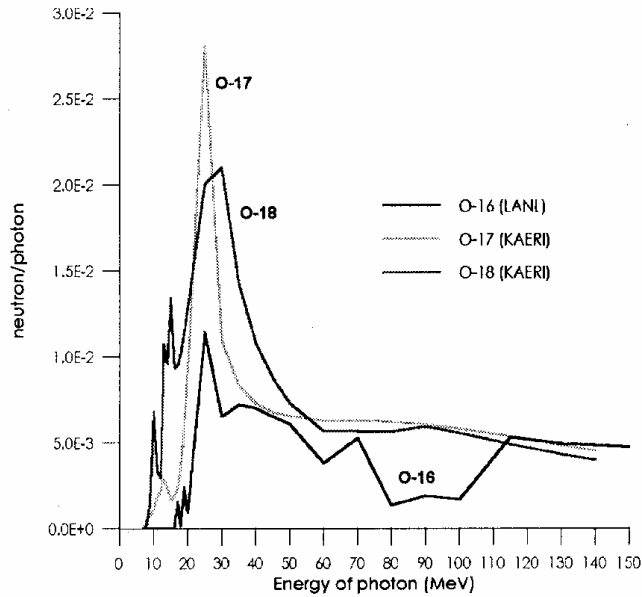


Figure 3. Same as Figure 1 but for different isotopes of O



For comparison, the above-described calculations have also been performed with the new beta version of MCNPX for all 12 isotopes, for which photonuclear tables are presently included in the code package [8]. For the isotopes that the IAEA recommends the use of the LANL evaluations, the results for the weight and energy agree within statistical errors with only small deviations observed for ^{181}Ta . On the other hand, for nuclei such as ^{56}Fe and ^{28}Si in particular (see Figures 4 and 5) the differences are non-negligible. These large deviations might be attributed to the different data evaluation approach for energies higher than 20 MeV [10].

Figure 4. Same as Figure 1 but for ^{28}Si taken from different data evaluations

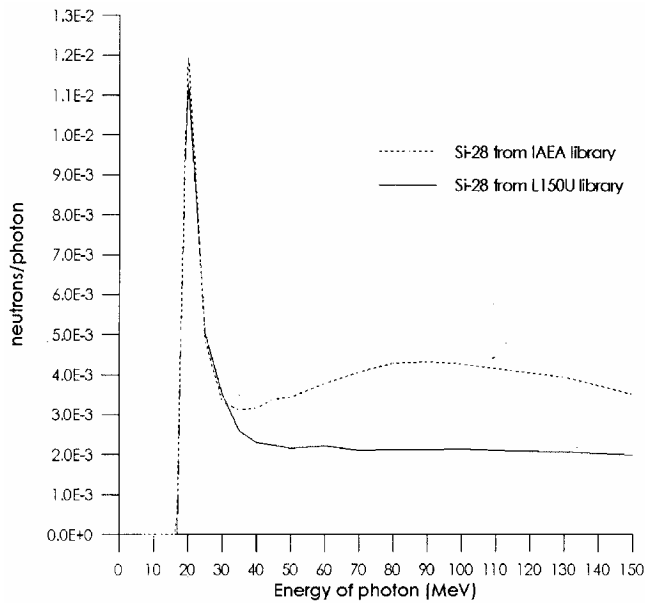
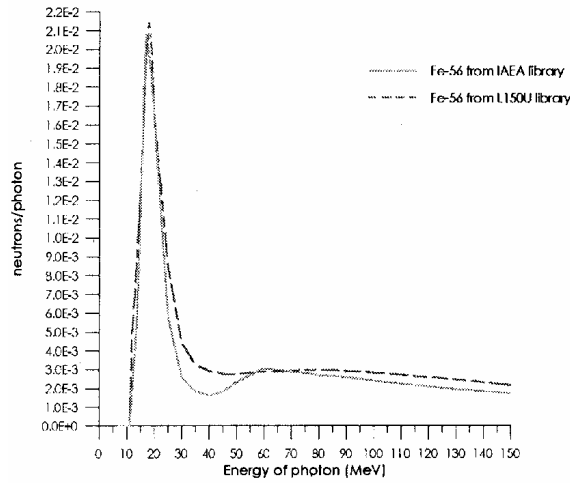


Figure 5. Same as Figure 4 but for ^{56}Fe



Validation with experimental data

Neutron yields from targets bombarded by electrons

Although photons from electron bremsstrahlung have been used for a long time for neutron production, a number of published experiments on photoneutron yields are very limited. The only set of data useful for validation purposes is the old paper of Barber and George [11] (also referred to by White [8]), where neutron yields per incident electron as a function of a target material, thickness and incident electron energy in the range of 10-36 MeV were reported. All experimental targets were squares of $11.5 \times 11.5 \text{ cm}^2$. With the MCNP code, enhanced with a photonuclear capability [9], we have attempted to reproduce the yield dependence on electron energy for natural materials as C, Al, Cu, Ta, Pb and U. Both target isotopic compositions, geometry and beam spot of 1.27 cm diameter were taken explicitly into account during our calculations.

Our results and experimental data, estimated from the curves of Barber's paper [11], are given in Tables 1 to 5. In general, the comparative agreement between the calculation and experimental data for all targets is rather good. One should not forget that all experimental data points are uncertain within 15% [11]. We note that in nearly all cases calculated values and experimental data agree within 10-30%. In some cases, e.g. Cu and Ta, the agreement is even better than 10% for nearly all energies considered. On the other hand, we have to admit that in general the predictions are poor at the photonuclear threshold (see Table 4 in particular). This problem has already been identified by White [8] and has yet to be understood.

Table 1 Experimental neutron yield compared to calculation (both with KFKI and LANL enhanced codes presented by the cal./exp. and MCNPX/exp. ratios respectively) for various electron energies incident on 19.46 cm thick C

Energy (MeV)	Exp. yield (10^{-5} n/e)	Ratio (calc./exp.)	Ratio (MCNPX/exp.)
22	0.5	0.70	0.17
28	6.0	0.70	0.60
34	17.4	0.86	0.80

Table 2. Same as Table 1 but for 8.96 cm thick Al

Energy (MeV)	Exp. yield (10^{-4} n/e)	Ratio (calc./exp.)	Ratio (MCNPX/exp.)
22	0.5	0.67	0.71
28	2.1	0.74	0.76
34	4.3	0.75	0.74

Table 3. Same as Table 1 but for 1.48, 2.96 and 4.45 cm thick Cu, respectively

Energy (MeV)	Exp. yield (10^{-4} n/e)	Ratio (calc./exp.)	Ratio (MCNPX/exp.)
16	0.6, 0.9, 1.1	0.74, 0.90, 0.93	0.63, 0.77, 0.85
20	2.8, 4.5, 5.5	0.92, 0.98, 1.00	0.92, 0.94, 0.96
28	8.3, 14.0, 17.9	0.91, 0.97, 0.97	0.86, 0.91, 0.91
34	13.0, 23.8, 29.4	0.88, 0.91, 0.95	0.84, 0.86, 0.91

Table 4. Same as Table 1 but for 0.37 cm thick Ta

Energy (MeV)	Exp. yield (10^{-4} n/e)	Ratio (calc./exp.)	Ratio (MCNPX/exp.)
10	0.8	0.08	0.07
19	5.2	1.04	1.02
28	13.5	1.04	1.03
34	17.8	0.95	0.94

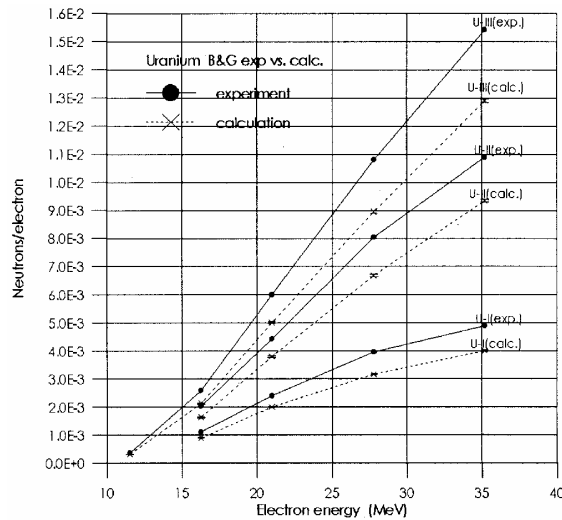
Table 5. Same as Table 1 but for 0.52, 1.52, and 3.03 cm thick Pb, respectively

Energy (MeV)	Exp. yield (10^{-4} n/e)	Ratio (calc./exp.)	Ratio (MCNPX/exp.)
18	7.5, 17.5, 24.5	0.69, 0.71, 0.70	0.70, 0.71, 0.70
28	16.5, 46.0, 66.0	0.77, 0.78, 0.76	0.81, 0.78, 0.76
34	20.5, 63.5, 88.5	0.75, 0.77, 0.79	0.73, 0.77, 0.78

Tables 1 to 5 also include calculations with the recent MCNPX version enhanced by a photonuclear capability. As one could expect, both calculations agree very well. However, in the case of C and Cu (see Tables 1 and 3) our model predictions give slightly higher neutron yields, which is actually closer to the measured values. This is due to a more precise definition of natural C (^{12}C and ^{13}C) and Cu (^{63}Cu and ^{65}Cu) compositions. In LANL photonuclear data files, distributed with the MCNPX code, only ^{12}C and ^{63}Cu are included. In addition, the energy threshold of photoneutron production is around 19 MeV for ^{12}C and only 5 MeV for ^{13}C , which can be seen from Figure 2. Precisely for this reason, neutron production at 22 MeV is strongly underestimated by MCNPX, while our calculation gives a similar deviation of 30% as for other energies (see Table 1). We note separately that in the case of Pb, both calculations agree very well since the LANL photonuclear data files include all isotopes of the natural lead.

In Figure 6 we compare the data and our calculations for the U targets of different thickness. In this particular case neutrons may also originate from gamma-induced fissions. A systematic underestimation of the experimental data is observed for all targets and all energies considered. On the

Figure 6. Neutron yields as a function of electron energy for natural uranium of variable thickness (I – 0.33 cm, II – 0.66 cm, III – 0.99 cm)



other hand, this underestimation never exceeds 25%, which is also valid for nearly all non-fissile targets. We note separately that LANL data files do not yet include fissile materials; thus, with the present version of MCNPX gamma-induced fission cannot be simulated.

Photofission fragments from UCx target bombarded by electrons

Another set of data we found useful for our benchmarking is related to the measurements of gaseous photofission fragments in the projects related to the radioactive nuclear beam (RNB) production [3]. Recently a new experiment was performed at CERN (Switzerland) with 50 MeV electrons [12]. Three different experimental set-ups were considered: t8 electrons hit the W target converter (4 mm thick) placed at 80 mm from the secondary UCx target, t4 electrons hit the W target converter placed at 40 mm from the same UCx target and t0 electrons hit directly the same UCx target, i.e. W is omitted. The mass of ^{238}U in UCx was ~ 30 g with an effective target density of 3.3 g/cm^3 . The gaseous fission products, which leave the UCx target, were transported to the cold finger and their intensities could be measured via corresponding gamma lines with a Ge detector (see Ref. [12] for more details on the experimental procedure).

Table 6 presents the relative ratios of experimentally observed photofission fragment yields (isotopes of Kr and Xe) in the case of three different experimental set-ups as explained above. For comparison we simulated the exact experimental conditions in order to calculate the fission rates in UCx. In this way we estimated a number of fissions due to both gamma- and secondary-neutron-induced reactions for the “t0”, “t4” and “t8” experiments respectively. Again, a rather good agreement (within 25%) between experimental and theoretical ratios is obtained as shown in the same table. We note separately that the fission events due to the secondary neutrons did not contribute more than 2% to the total number of fissions in this particular case.

Conclusions

Testing of the evaluated photonuclear data for a large range of isotopes is necessary before generalised problems based on photonuclear reactions can be simulated. Such data became available in

Table 6. Relative ratios of experimentally observed photofission fragment yields (isotopes of Xe) in the case of three different experimental set-ups (see text for details) compared to the calculated ratios of corresponding fission events

Meas. yield ratio	(t0/t4)	(t0/t8)	(t4/t8)
⁸⁹ Kr	3.67	5.79	1.58
⁹⁰ Kr	4.94	7.18	1.46
⁹¹ Kr	3.94	5.00	1.27
⁹² Kr	4.17	5.25	1.20
¹³⁷ Xe	3.01	4.91	1.63
¹³⁸ Xe	3.17	5.01	1.58
¹³⁹ Xe	4.38	6.51	1.48
¹⁴⁰ Xe	3.68	5.90	1.60
Meas. average	3.87	5.70	1.48
Calc. fission ratio	4.35	7.14	1.64

the ENDF format from IAEA thanks to an international co-operative effort. In this paper the formal and practical quality of these data was examined in the simulations of photoneutron production by the use of the recent versions of MCNP and MCNPX codes enhanced with a photonuclear capability.

From the series of calculations with monoenergetic photons the following conclusions could be drawn:

- The regularity of a neutron yield dependence on isotope mass of the same element is perturbed when the available experimental data, in addition to the theoretical model evaluations, is taken into account, e.g. C, O and Ca.
- There are some non-negligible differences between the photonuclear data tables provided by LANL and IAEA, and the origin of these differences is attributed to the different evaluation approach for photon energies higher than 20 MeV, e.g. ²⁸Si and ⁵⁶Fe.

From the comparison of the experimental data for neutron yields with calculated ones a number of important findings should be mentioned:

- The calculated values, with a few exceptions (e.g. Ta), are smaller than the experimental ones, but the deviations rarely exceed 20%; larger deviations are at smaller energies, which is due to the threshold effects.
- The observed deviations do not depend on the target thickness; this fact refers to the correctness of the transport calculation of all particles considered.
- At lower energies ¹³C, in spite of the small amount existent in natural C, must be taken into account explicitly; this is because of much higher threshold of ¹²C than ¹³C. On the contrary, in the case of the calculations with natural Cu, it was not crucial to take into account its precise isotopic composition.

In the case of calculations with fissile materials, e.g. U, in the data tables presently used the upper energy limit of 20 MeV may become problematic. At higher energies a horizontal extrapolation of the evaluated data tables seems to be more realistic than one which linearly decreases to zero when compared to the experimental cross-sections. This was confirmed by the comparison of the experimental data for neutron yields with calculated ones.

Finally, we conclude that there is much left to be done before proper reliability estimates can be set for these newly evaluated data files. Indeed, additional experimental data are needed to benchmark the present evaluations and model calculations. These include total photoneutron measurements similar to those reported by Barber [11], but of better quality and with corresponding angular and energy distributions for both non-fissile and fissile elements in particular. Establishing an international data file from these newly measured photoneutron yields would be highly recommended.

Acknowledgement

We are grateful to Dr. Lee of Korean Atomic Energy Research Institute for his comments concerning the evaluated data libraries.

REFERENCES

- [1] Matsumoto, T., "Calculation of Gamma Ray Incineration of ^{90}Sr and ^{137}Cs ", *Nucl. Instr. and Methods in Phys. Res.*, A 268, 234 (1988).
- [2] Bernardin, B, D. Ridikas, H. Safa, "A Prototype Sub-critical Reactor Driven by Electron Accelerator", *Proceedings of the Int. Conf. on Accelerator Applications/Accelerator Driven Transmutation Technology and Applications (AccApp/ADTTA'01)*, 12-15 November 2001, Reno, Nevada, USA.
- [3] Oganessian, Yu.Ts., *et al.*, "RIB Production with Photofission of Uranium", *Proc. of the 5th Int. Conf. on Radioactive Nuclear Beams (RNB 2000)*, 2-8 April 2000, Divonne, France; in print by *Nucl. Phys. A*, Safa, H., D. Ridikas, *et al.*, "Photofission for the SPIRAL-2 Project", *Proc. of the Int. Conference on Isotope Separation On Line (ISOL'01)*, 11-14 March 2001, Oak Ridge, USA.
- [4] *Handbook on Photonuclear Data for Applications*, IAEA TECDOC Draft No. 3, March 2000.
- [5] Briesmeister, J.F., *MCNP – A General Monte Carlo N-particle Code*, Technical Report LA-12625-M, Los Alamos National Laboratory (1997).
- [6] Gallmeier, F.X., *Description of the Photonuclear Option of MCNP4A*, ORNL-TM-13073, Oak Ridge National Laboratory (1995).
- [7] Waters, L.S., *MCNPXTM User's Manual*, Los Alamos National Laboratory, pre-print TPO-E83-G-UG-X-00001 (November 1999); see also <http://mcnpx.lanl.gov/>.
- [8] White, M.C., R.C. Little and M.B. Chadwick, "Photonuclear Physics in MCNP(X)", *Proceedings of the 3rd International Topic Meeting on Nuclear Applications of Technology*, Long Beach, California, 14-18 November 1999, American Nuclear Society, 515 (1999).

- [9] Vertes, P. and D. Ridikas, “Some Test Calculations with the IAEA Photonuclear Data Library”, *Proceedings of the Int. Conference on Nuclear Data for Science and Technology (ND2001)*, 7-12 October 2001, Tsukuba, Ibaraki, Japan; in print by *Nuclear Science and Technology*.
- [10] Dr. Lee, private communication.
- [11] Barber, W.C., W.D. George, “Neutron Yields from Targets Bombarded by Electrons”, *Phys. Rev.*, 116, 1551 (1959).
- [12] Ibrahim, F., *et al.*, “Photofission...”, in print by *European Physical Journal* (2001); F. Ibrahim, private communication.

EVENT GENERATOR BENCHMARKING FOR PROTON RADIOGRAPHY APPLICATIONS

Stepan G. Mashnik, Richard E. Prael, Arnold J. Sierk
Los Alamos National Laboratory, Los Alamos, NM 87545, USA

Konstantin K. Gudima
Institute of Applied Physics
Academy of Science of Moldova, Kishinev, MD-2028, Moldova

Nikolai V. Mokhov
Fermi National Accelerator Laboratory, Batavia, IL 60510, USA

Abstract

We have benchmarked the QGSM code and event generators of the MARS and LAHET3 codes as potential candidates for high-energy programs to be used in simulations for the Proton Radiography (PRad) Project. We have compiled from the literature experimental data on spectra of particles emitted from proton-induced reactions at incident energies from 30 GeV to 70 GeV on different nuclei and have performed calculations for all reactions for which we found data with these three codes without any modifications and using only default parameters and standard inputs. Our results (514 plots) show that all three codes reasonably describe most of the studied reactions, though all of them should be further improved before becoming reliable tools for PRad. We present here our conclusions concerning the relative roles of different reaction mechanisms in the production of specific secondary particles. We comment on the strengths and weaknesses of QGSM, MARS and LAHET3 and suggest further improvements to these codes and to other models.

Introduction

The process of determining the feasibility of Proton Radiography (PRad) [1-3] as the radiographic probe for the Advanced Hydrotest Facility as well as its design and operation require information about spectra of secondary particles produced by high-energy protons interacting in the target and structural materials. Reliable models and codes are needed to provide such data. We studied the literature and chose three potential candidates for high-energy codes that may be used in simulations for PRad, namely the Quark-gluon String Model (QGSM) as developed by Amelin, Gudima and Toneev [4], the MARS code by Mokhov, *et al.* [5], and a version of the Los Alamos National Laboratory (LANL) transport code LAHET [6], known as LAHET3 [7].

The energy of the proton beam at PRad is supposed to be about 50 GeV. Unfortunately, there are very few measurements of particle spectra for proton-induced reactions exactly at 50 GeV or very close energies. In fact, we found only one published work at 50 GeV, namely spectra of π^- and π^+ measured at 159° from $p(50 \text{ GeV}) + W$ published in Russian together with pion spectra for other energies and targets, in a Joint Institute for Nuclear Research (Dubna) Communication by Belyaev, *et al.* [8].

With only a few data available at 50 GeV, we benchmarked QGSM, MARS and LAHET3 against measured spectra of particles emitted from interaction of protons with energies $50 \pm 20 \text{ GeV}$, *i.e.* from 30 to 70 GeV, with all targets for which we found experimental data. Independently of how many spectra were measured in an experiment, we performed calculations with the standard versions of QGSM, MARS and LAHET3 without any modifications or adjustments, using only default parameters in the input of codes, and calculated double-differential cross-sections at 0, 4.75, 9, 13, 20, 45, 60, 90 and 159 degrees, angle-integrated energy spectra, and mean multiplicities for emission of n, p, d, t, ^3He , ^4He , π^+ , π^- , K^+ , K^- and \bar{p} for all cases listed in Table 1. The next section presents a brief description of the benchmarked codes, followed by results, discussion and conclusions in the last two sections.

Benchmarked codes

QGSM

The core of the QGSM is built on a time-dependent version of the intranuclear cascade model developed at Dubna to describe both particle- and nuclei-induced reactions, often referred in the literature simply as the Dubna Intranuclear Cascade Model (DCM) (see [9] and references therein). The DCM models interactions of fast cascade particles (“participants”) with nucleon spectators of both the target and projectile nuclei and includes interactions of two participants (cascade particles) as well. It uses experimental cross-sections (or those calculated by the Quark-gluon String Model for energies above 4.5 GeV/nucleon) for these elementary interactions to simulate angular and energy distributions of cascade particles, also considering the Pauli exclusion principle. When the cascade stage of a reaction is completed, QGSM uses the coalescence model described in [9] to “create” high-energy d, t, ^3He and ^4He by final state interactions among emitted cascade nucleons, already outside of the colliding nuclei. After calculating the coalescence stage of a reaction, the QGSM moves to the description of the last slow stages of the interaction, namely to pre-equilibrium decay and evaporation, with a possible competition of fission using the standard version of the Cascade Exciton Model (CEM) [10]. But if the residual nuclei have atomic numbers with $A \leq 13$, QGSM uses the Fermi break-up model to calculate their further disintegration instead of using the pre-equilibrium and evaporation models.

MARS

The MARS Monte Carlo code system, developed over 29 years ago, allows fast and reliable inclusive and exclusive simulation of three-dimensional hadronic and electromagnetic cascades in shielding, accelerator and detector components in the energy range from a fraction of an electron volt up to about 100 TeV [5]. It is under continuous development. The reliable performance of the code has been demonstrated in numerous applications at Fermilab, CERN, KEK and other centres as well as in special benchmarking studies. Description of elastic and inelastic hN , hA , γA and νA cross-sections is based on the newest compilations and parameterisations [11]. At high energies ($5 \text{ GeV} < E < 100 \text{ TeV}$), σ_{tot} , σ_{in} , σ_{prod} and σ_{el} are calculated in the framework of the Glauber multiple scattering theory with σ_{hN} as an input. The nucleon density distribution in nuclei is represented as the symmetrised Fermi function with the parameters of [12] for medium and heavy nuclei ($Z > 10$) and the ones of [13] for $Z < 10$. Modern evaluated nuclear data as well as fitting formulae are used to simulate hadron-nucleus elastic scattering. For protons, nuclear, Coulomb elastic scattering and their interference is taken into account. At $E > 5 \text{ GeV}$, a simple analytical description used in the code for both coherent and incoherent components of $d\sigma/dt$ is quite consistent with experiment. A version of the Cascade Exciton Model of nuclear reactions [10] as realised in the code CEM95 [14] and also containing several recent refinements [15] has now been implemented in the 1998 version of MARS [11] as default for $1\text{-}10 \text{ MeV} < E < 3\text{-}5 \text{ GeV}$. A set of phenomenological models, as described in Refs. [5,16,17], is used for inclusive production of secondary particles in hA , dA , γA and νA interactions at projectile energies from 5 GeV to 100 TeV. The 2001 version [11] of the MARS code was employed in the present benchmark.

LAHET3

LAHET is a Monte Carlo code for the transport and interaction of nucleons, pions, muons, light ions and antinucleons in complex geometry [6]; it may also be used without particle transport to generate particle production cross-sections. LAHET allows to choose one of several options for the Intranuclear Cascade (INC) and fission models to be employed in calculations; it is widely used and well known in the applied nuclear physics community; therefore, we do not describe it here (a comprehensive description of LAHET may be found in [6] and references therein). The version of LAHET realised in the code LAHET3 [7] uses a version of the code FLUKA, known in the literature as FLUKA96 [19] to describe the first, INC stage of reactions, and its own Multi-stage Pre-equilibrium Model (MPM) [20] to describe the following intermediate pre-equilibrium stage, followed by evaporation/fission slow processes (or by the Fermi break-up model after the cascade instead of pre-equilibrium and evaporation/fission, if the residual nuclei have atomic numbers with $A \leq 13$ and for $14 \leq A \leq 20$ with excitation energy below 44 MeV), as described in [6,7]. We mention again that only the high-energy event generator from FLUKA96 is employed here, as implemented in LAHET3; the default pre-equilibrium, evaporation and Fermi break-up models of LAHET3 are used for low-energy nucleon and complex particle emission. More details and further references on LAHET3 with FLUKA96 can be found in [21].

Results and discussion

Table 1 lists the cases we calculated with QGSM, MARS and LAHET3, and provides references to experimental works where at least one spectrum of a secondary particle (from the ones listed in the introduction) was measured. A detailed report of the study containing 514 plots with spectra and multiplicities of secondary particles from reactions listed in Table 1 is now in preparation. Here, we present only our main conclusions and several examples of results from the study.

Table 1. Proton energy and target list covered by the present benchmark

T_p (GeV)	Nuclei	Measurements
30	^9Be , ^{27}Al	[8,22-24]
47	^{12}C	[8,25]
50	^{184}W	[8,25]
51	^9Be , ^{48}Ti	[8,25]
53	^{27}Al	[8,25]
54	^{96}Mo	[8,25]
70	^{12}C , ^{27}Al , ^{64}Cu , ^{118}Sn , ^{208}Pb	[26-30]

Our analyses have shown that all three codes tested here reasonably describe most of the secondary particle spectra. As a rule the higher the incident proton energy, the better the calculated spectra agree with experimental data. Several reaction mechanisms participate in the production of secondary nucleons and complex particles. These mechanisms are:

- Fast INC processes.
- Pre-equilibrium emission from residual nuclei after the cascade stage of reactions.
- Evaporation of particles from compound nuclei after the pre-equilibrium stage, or from fission fragments if the compound nucleus was heavy enough to undergo fission.
- Fermi break-up of light excited nuclei formed after the cascade stage of reactions.
- Coalescence of complex particles by final state interactions among emitted cascade nucleons.
- Fast complex particle emission via knock out and pick up processes.
- Multi-fragmentation of highly-excited residual nuclei after the INC.

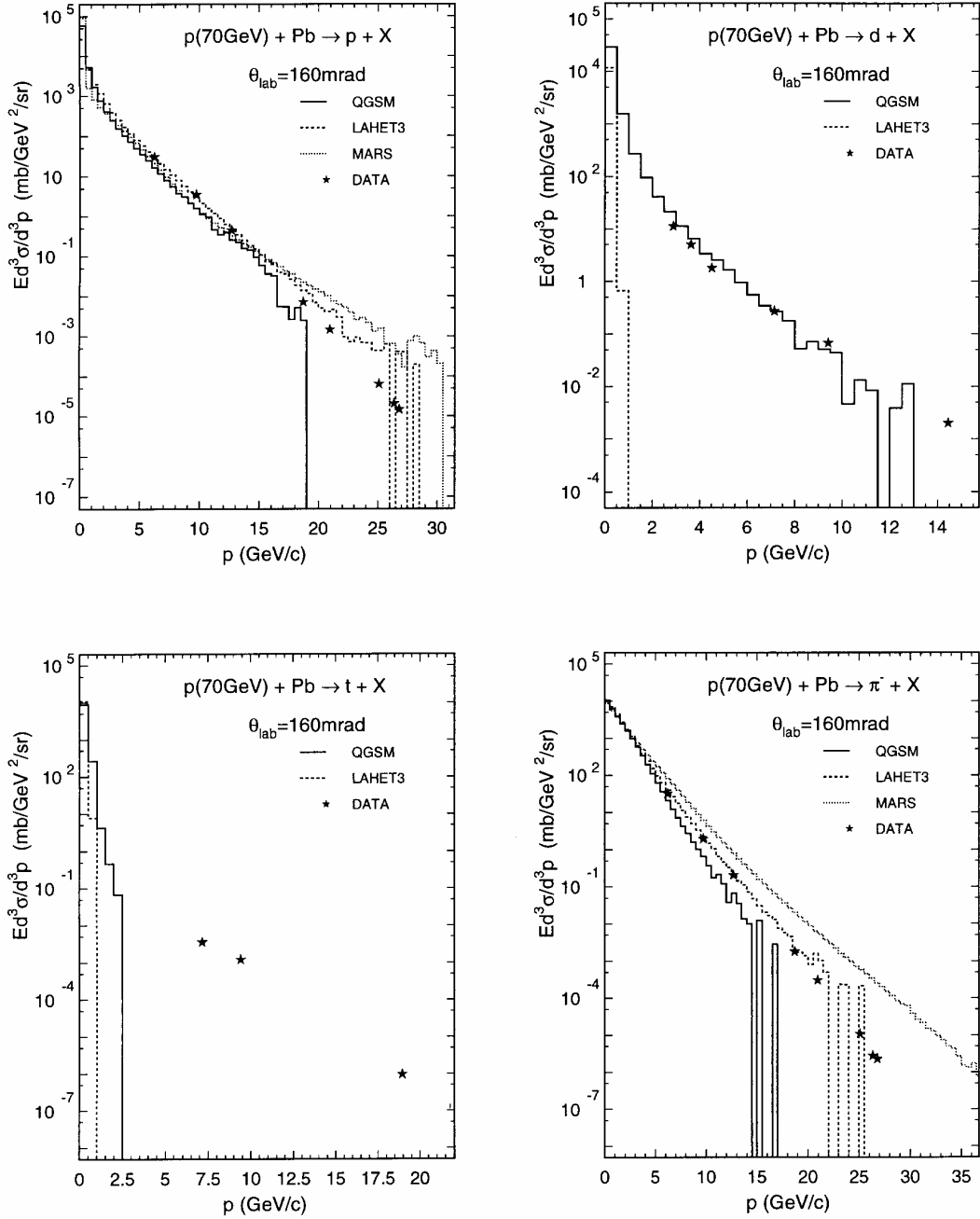
Their relative roles change significantly with the changing atomic mass number of the targets, and are different for different energies and angles of emission of secondary particles. Different codes describe these spectra better, worse, or do not describe them at all, depending of how these reaction mechanisms are (or are not) implemented into a specific code.

As an example, Figure 1 shows spectra of p, d, t and π^- emitted at 9.17° from the reaction $p(70 \text{ GeV}) + ^{208}\text{Pb}$. Results for other reactions at 70 GeV are similar. One can see that all three codes describe the proton spectra well. The agreement for the pion spectra is not so good but is still reasonable, with some underestimation of the high-energy tails of spectra by QGSM and some overestimation by MARS. Note that as the angle of pion emission changes the situation is reversed: we observe that most of the high-energy tails of pion spectra at 159° , and to a lesser extent at 90° , are over-predicted by LAHET3 and underestimated by MARS.

The situation with the deuteron and tritium spectra is quite different. We see that deuterons with momentum of up to about 15 GeV/c and tritium with momenta up to 19 GeV/c are emitted and measured in this particular reaction. Utilising the coalescence mechanism for complex particle emission, QGSM is able to describe high-energy deuteron production, and agrees well with the measurement. LAHET3 does not consider the coalescence of complex particles and therefore describes emission of only evaporative and pre-equilibrium deuterons with momenta not higher than 1 GeV/c. MARS does not consider emission of complex particles at such high incident proton energies, therefore no d and t spectra by MARS are shown in Figure 1.

Figure 1. Invariant cross-sections $Ed^3\sigma/d^3p$ for forward production of p, d, t and π^- at 160 mrad (9.17°) as functions of particle momentum p from 70 GeV protons on ^{208}Pb

*Experimental data for p and π^- are from Table 1 of Ref. [29] and for d and t, from Ref. [30].
Calculations by QGSM, LAHET3 and MARS are shown as indicated in the legends.*



For tritium, the situation is worse since LAHET3, as is the case of deuterons, describes only pre-equilibrium emission and evaporation of tritons with momenta not higher than 1 GeV/c and QGSM, even taking into account coalescence of tritium, describes emission of t from this reaction up to only 2.5 GeV/c while the experimental spectrum of t extends to 19 GeV/c. This deficiency can be understood by considering the coalescence mechanism; it is much more probable to emit two cascade

nucleons with very similar momenta that can coalesce into a deuteron than to get three INC nucleons with very similar momenta that can coalesce into a triton. The experimental values of high-energy triton spectra are several orders of magnitude below the corresponding values of the deuteron spectra, and the statistics of our present QGSM simulation could be simply too small to get such high-energy tritium via coalescence. There is also a possibility that knock-out processes of pre-formed clusters (or fluctuations of nuclear density, leading to “fluctons”) by bombarding protons are seen in these experimental d and t spectra, but are not taken into account by any of the tested codes, providing the observed difference in the t spectrum and, less pronounced, in the d spectrum. A third possible mechanism of complex particle emission with greater than 1 GeV/c momenta would be multi-fragmentation of highly-excited residual nuclei after the INC. This mechanism is not taken into account by any of the tested codes and we cannot estimate its contribution.

Figure 2 shows examples of π^+ spectra at 159° from 51 GeV proton collisions with ^9Be and ^{48}Ti . As already mentioned above for π^- , we see that LAHET3 overestimates the high-energy tails of pion spectra and MARS slightly underestimates them. Similar results were obtained for other targets and incident proton energies.

Figure 2. Invariant cross-sections $E d^3\sigma/d^3p$ for forward production of π^+ at 159° as functions of pion momentum p from 51 GeV protons on ^9Be and ^{48}Ti

Experimental data are by Belyaev, et al. [8].

Calculations by QGSM, LAHET3 and MARS are shown as indicated in the legends.

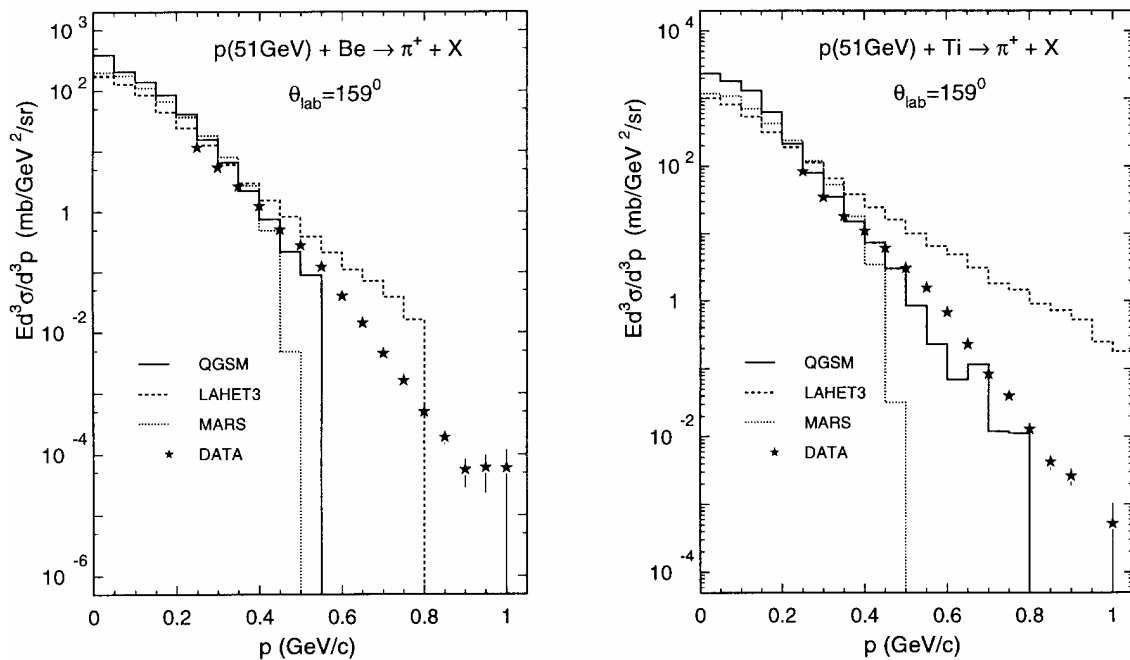


Figure 3 shows an example of how calculated proton spectra depend on the angle of emission, for the reaction $p(30\text{ GeV}) + ^9\text{Be}$. We see that at 30 GeV, the agreement of calculated proton spectra with the data is not as good as that obtained in Figure 1 for 70 GeV. The shapes and absolute values of proton spectra predicted by different codes depend significantly on the angle of detection, as does the agreement with the data. Similar results were obtained for other secondary particles and for other targets and incident energies.

Figure 3. Momentum spectra of secondary protons from 30 GeV protons on Be

Experimental data at 9° and 20° are taken from Figure 1 of Baker, et al. [22],
at 30° from Figure 5 of Ref. [23] and at 90° from Figure 2 of Ref. [24].
Calculations by QGSM, LAHET3 and MARS are shown as indicated in the legends.

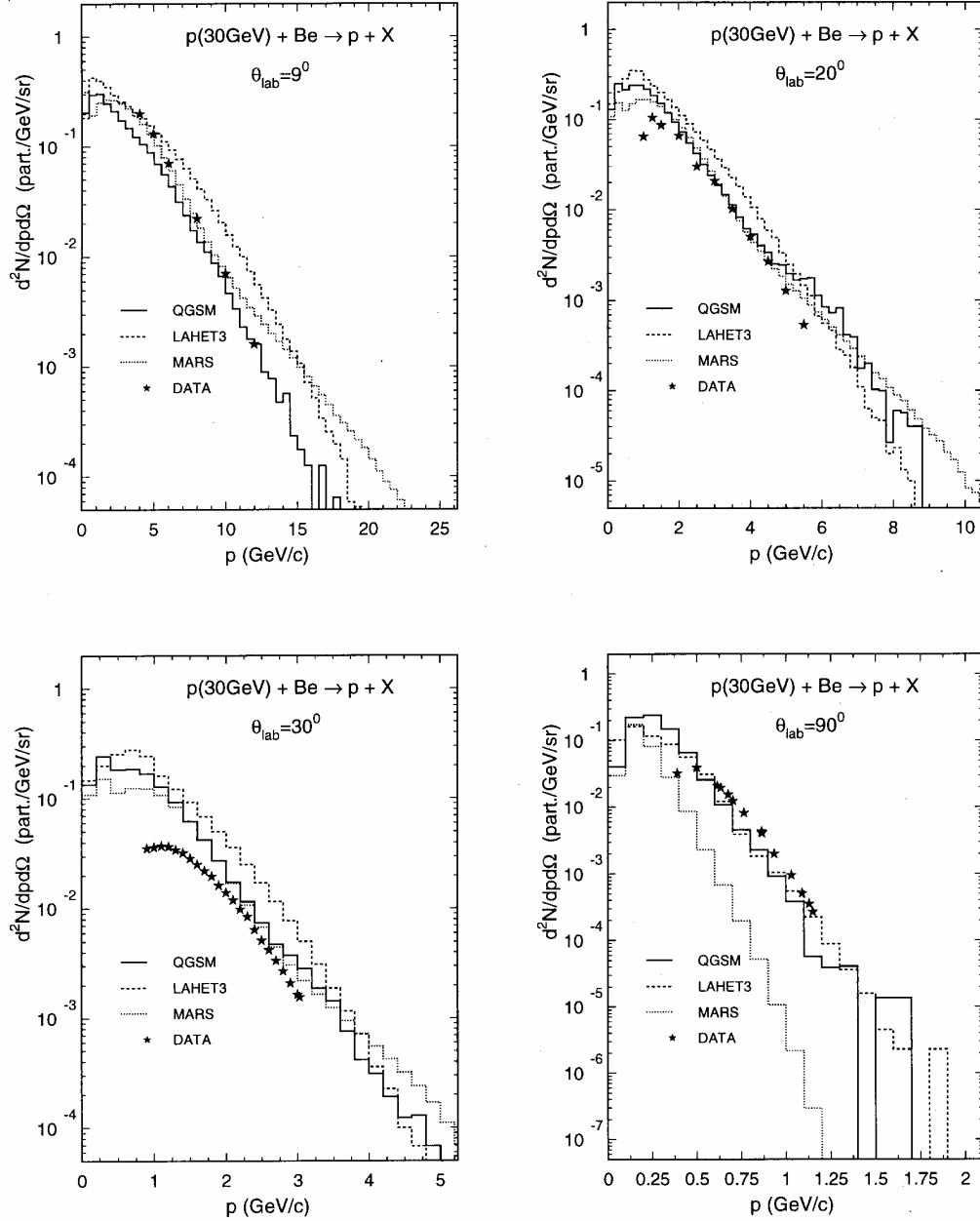
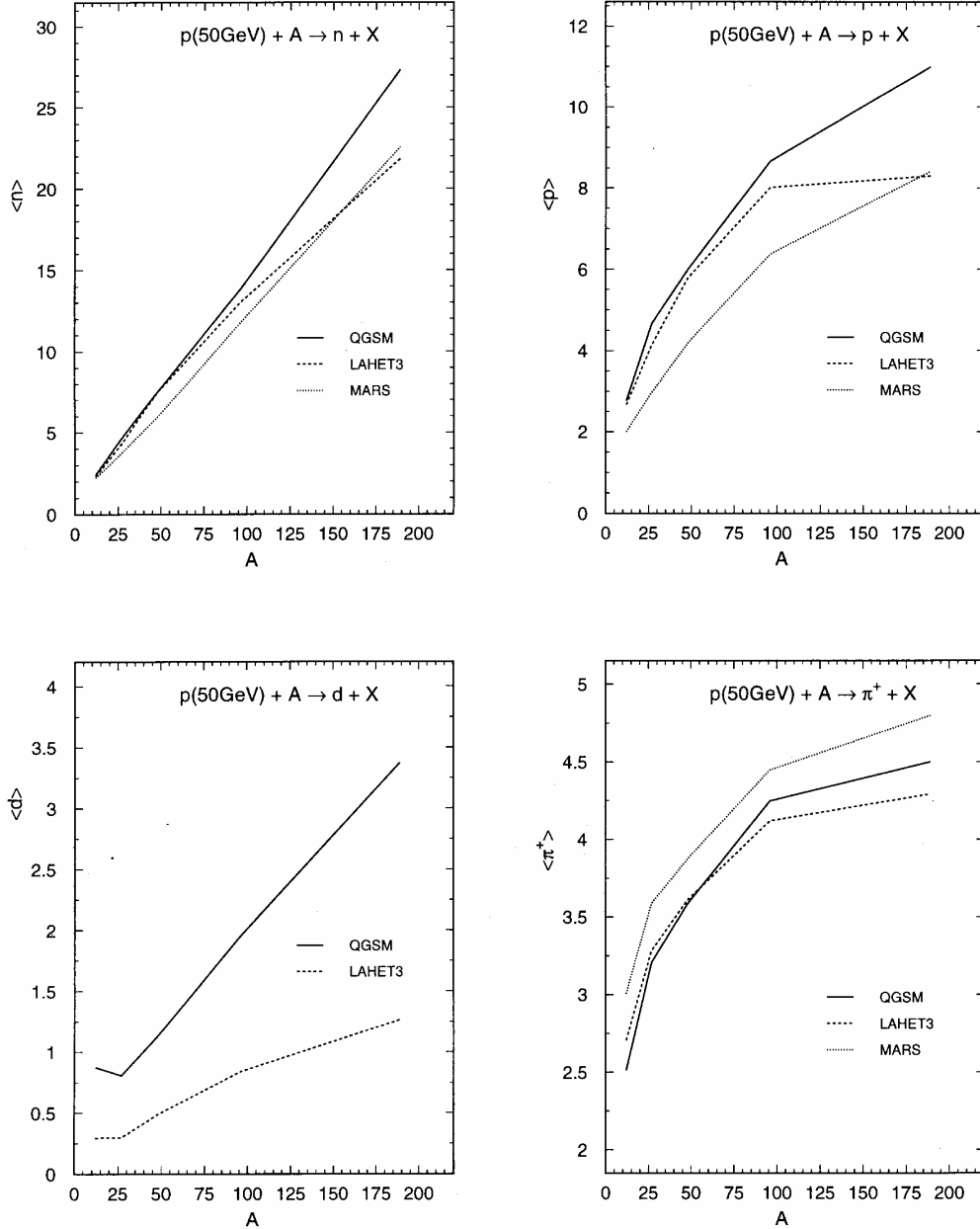


Figure 4 shows an example of mean multiplicity of secondary n , p , d and π^+ predicted by the tested codes for interaction of protons of about 50 GeV with different nuclei as functions of the mass number of targets. We see that predicted particle multiplicities differ significantly from each other, and the differences increase with increasing mass number of the target. The observed differences point to a quite significant difference in the treatment by the codes of the cascade stage of reactions (pions are emitted only at the cascade stage of reactions) and of the subsequent pre-equilibrium, evaporation and

Figure 4. Predicted by QGSM, LAHET3 and MARS mean multiplicities of secondary n, p, d and π^+ emitted from 50 GeV proton-induced reactions as functions of the mass number of targets

Note that actual energies of incident protons in our calculations were 47 GeV for ^{12}C , 50 GeV for ^{184}W , 51 GeV for ^9Be and ^{48}Ti , 53 GeV for ^{27}Al and 54 GeV for ^{96}Mo . (MARS does not calculate production of deuterons at these incident energies.)



Fermi break-up stages as well (we recall that at these incident energies MARS uses its own approximations for the total particle spectra without separately considering contributions from different mechanisms of nuclear reactions). These differences indicate that further experimental data are necessary at these incident proton energies and further development and improvement of the codes is required.

Further work

Our study shows that all three codes describe reasonably well many of the secondary particle spectra analysed here, though all of them should be further improved before becoming reliable tools for PRad.

For instance, we find that QGSM has some problems in a correct description of several pion spectra and does not sufficiently describe the high-energy tails of measured t and ${}^3\text{He}$ spectra. Nevertheless, QGSM is the only code tested here that accounts for coalescence of complex particles from cascade nucleons and provides production of high-energy complex particles.

MARS overestimates the high-energy tails of some pion, kaon and proton spectra at small angles (4.75° , 9° and 13°) and slightly underestimates them at large angles (90° and 159°). At these incident energies, MARS does not calculate complex particle production. However, MARS has one significant advantage in comparison with the two other codes: It is several orders of magnitude faster and requires almost no computing time, meanwhile providing reliable results for many applications.

LAHET3 overestimates the high-energy tails of practically all pion spectra at 159° and some nucleon and complex particle spectra in the pre-equilibrium energy region. It does not consider coalescence of complex particles and does not describe production of high-energy complex particles.

We also observe big differences between predicted high-energy tails of both neutron and proton spectra at 0° and for the mean multiplicities of almost all secondary particles, though no experimental data for these quantities are available at present for the reactions studied here.

We note that many of the problems we observe in our study for particular codes have already been solved, since all benchmarked event generators are under continuous development and improvement and all of them have been further improved in comparison with the versions we use in this study.

On the basis of QGSM, we have developed the Los Alamos version of the Quark-gluon String Model code, LAQGSM [31]. LAQGSM differs from QGSM by replacing the pre-equilibrium and evaporation parts of QGSM described according to the standard CEM [10] with the new physics from CEM2k [32] and has a number of improvements and refinements in the cascade and Fermi break-up models. Originally, both QGSM and LAQGSM were not able to describe fission reactions and production of light fragments heavier than ${}^4\text{He}$, as they had neither a high-energy-fission nor a fragmentation model. Recently, we addressed these problems [33] by further improving CEM2k and LAQGSM and by merging them with the Generalized Evaporation Model code GEM2 developed by Furihata [34]. The improved LAQGSM+GEM2 code describes both spectra of secondary particles and yields of produced nuclides much better than QGSM does; exemplary results by LAQGSM and further references may be found in [35].

The MARS code system is being continuously developed and improved. For instance, a new version of the code, MARS14(2002) was completed after we started the present work. It contains a large number of improvements and refinements and provides better results in comparison with the version used here. Recently, the authors of MARS started to develop new and better approximations for the double-differential cross-sections of inelastic hN and hA interactions. The new systematics allow to solve the above-mentioned problems with the pion, kaon and proton spectra at forward and large angles and describe the experimental data much better.

The FLUKA code has also been updated very significantly (see e.g., [36] and references therein) since the version FLUKA96 was incorporated into LAHET3 as used here; no updated version is yet incorporated into LAHET.

Our study points to the importance of taking into account coalescence in high-energy complex-particles production. We find it appropriate and easy to implement these processes into MARS and LAHET, as well as into other codes that do not now consider coalescence.

We think that at such high incident energies, multi-fragmentation of highly-excited heavy nuclei may also be of significance and should be taken into account in these event generators and in other codes.

Acknowledgements

The study was supported by the US Department of Energy and by the Moldovan-US Bilateral Grants Program, CRDF Project MP2-3025.

REFERENCES

- [1] Morris, Christopher L., *Proton Radiography for an Advanced Hybrotest Facility*, Los Alamos National Report LA-UR-00-5716, 2000; <http://lib-www.lanl.gov/la-pubs/00357005.pdf>.
- [2] Ziock, H-J., *et al.*, *The Proton Radiography Concept*, Los Alamos National Report LA-UR-98-1368 (1998); <http://lib-www.lanl.gov/la-pubs/00460235.pdf>; Amann, J.F., *et al.*, *High-energy Test of Proton Radiography Concepts*, Los Alamos National Report LA-UR-97-1520 (1997); <http://lib-www.lanl.gov/cgi-bin/getfile?00366878.pdf>.
- [3] King, N.S.P., *et al.*, “An 800-MeV Proton Radiography Facility for Dynamic Experiments”, *Nucl. Instr. Meth.*, A424, 84-91 (1999).
- [4] Amelin, N.S., K.K. Gudima and V.D. Toneev, “Ultrarelativistic Nucleus-nucleus Collisions in a Dynamical Model of Independent Quark-gluon Strings”, *Sov. J. Nucl. Phys.*, 51, 1093-1101 (1990) [*Yad. Fiz.*, 51, 1730-1743 (199)]; Amelin, N.S., K.K. Gudima and V.D. Toneev, “Further Development of the Model of Quark-gluon Strings for the Description of High-energy Collisions with a Target Nucleus”, *Sov. J. Nucl. Phys.*, 52, 172-178 (1990) [*Yad. Fiz.*, 52, 272-282 (1990)]; Amelin, N.S., *Simulation of Nuclear Collisions at High Energy in the Framework of the Quark-gluon String Model*, Joint Institute for Nuclear Research Report JINR-86-802, Dubna (1986).
- [5] Mokhov, N.V., *The MARS Code System User’s Guide*, Fermilab-FN-628 (1995); Mokhov, N.V. and O.E. Krivosheev, *MARS Code Status*, Fermilab-Conf-00/181 (2000); see also the site <http://www-ap.fnal.gov/MARS/>.

- [6] Prael, R.E. and H. Lichtenstein, *User Guide to LCS: The LAHET Code System*, LANL Report No. LA-UR-89-3014, Los Alamos (1989); <http://www-xdiv.lanl.gov/XTM/lcs/lahet-doc.html>.
- [7] Prael, R.E., *Release of LAHETTM Version 3.00*, Los Alamos National Laboratory Research Note XCI-RN 98-10 (U), 14 Jan. 1998; LA-UR-00-2116; Prael, R.E., *Release Notes for LAHET Code System with LAHETTM Version 3.16*, LANL Report LA-UR-01-1655, Los Alamos (2001); <http://lib-www.lanl.gov/la-pubs/00795117.pdf>.
- [8] Belyaev, I.M., *et al.*, *The Cross-sections of π^+ - and π^- Production at an Angle 159° l.s. in Proton-nuclear Interactions at the Energy of the Incident Protons from 15 to 65 GeV*, JINR Communication P1-89-112, Dubna, Russia (1989); part of the Be data from this report are available from the HEPDATA: REACTION DATA Database at the following web page: <http://cpt19.dur.ac.uk/hepdata/reac2.html>.
- [9] Toneev, V.D. and K.K. Gudima, "Particle Emission in Light and Heavy-ion Reactions", *Nucl. Phys.*, A400, 173c-190c (1983).
- [10] Gudima, K.K., S.G. Mashnik and V.D. Toneev, "Cascade-exciton Model of Nuclear Reactions", *Nucl. Phys.*, A401, 329-361 (1983).
- [11] Mokhov, N.V., S.I. Striganov, A. Van Ginneken, S.G. Mashnik, A.J. Sierk and J. Ranft, *MARS Code Development*, Fermilab-Conf-98/379 (1998); LANL Report LA-UR-98-5716 (1998); Eprint: nucl-th/9812038; *Proceedings 4th Int. Workshop on Simulating Accelerator Radiation Environments (SARE-4)*, Hyatt Regency, Knoxville, TN, 13-16 September 1998, T.A. Gabriel, ed., ORNL, pp. 87-99 (1999).
- [12] Alkhasov, G.D., S.L. Belostotsky and A.A. Vorobyov, "Scattering of 1 GeV Protons on Nuclei", *Phys. Rep.*, 42, 89-144 (1978); see also de Veries, H., C.W. de Jager and C. de Vries, "Nuclear Charge-density-distribution Parameters from Elastic Electron Scattering", *Atomic Data and Nuclear Data Tables*, 36, 495-536 (1997).
- [13] Burov, V.V., D.N. Kadrev, V.K. Lukianov and Yu.S. Pol, "Analysis of Charge-density Distributions in Nuclei", *Phys. At. Nucl.*, 61, 525-532 (1998) [*Yad. Fiz.*, 61, 595-602 (1998)].
- [14] Mashnik, S.G., *User Manual for the Code CEM95*, JINR, Dubna (1995); OECD/NEA Data Bank, Paris, France (1995); <http://www.nea.fr/abs/html/iaea1247.html>; RSIC-PSR-357, Oak Ridge (1995).
- [15] Mashnik, S.G. and A.J. Sierk, "Improved Cascade-exciton Model of Nuclear Reactions", Eprint: nucl-th/9812069; *Proc. 4th Int. Workshop on Simulating Accelerator Radiation Environments (SARE-4)*, Hyatt Regency, Knoxville, TN, 13-16 September 1998, T.A. Gabriel, ed., ORNL, pp. 29-51 (1999).
- [16] Kalinovskii, A.N., N.V. Mokhov, Yu.P. Nikitin, *Passage of High-energy Particles through Matter*, AIP, NY (1989).
- [17] Mokhov, N.V. and S.I. Striganov, "Model for Pion Production in Proton-nucleus Interactions", *Proc. of the Workshop on Physics at the First Muon Collider*, Fermilab, November 1997, AIP Conf. Proc. No. 435, pp. 453-459; Fermilab-Conf-98/053 (1998).
- [18] Ranft, J., *Dual Parton Model at Cosmic Ray Energies*, *Phys. Rev.*, D51, 64-85 (1995); Gran Sasso Report INFN/AE-97/45 (1997).

- [19] Fassò, A., A. Ferrari, J. Ranft and P.R. Sala, “An Update About FLUKA”, *Proceedings of the 2nd Workshop on Simulating Accelerator Radiation Environments (SARE-2)*, CERN, Geneva, 9-11 October 1996, G.R. Stevenson, ed., Geneva, Switzerland, pp. 158-170 (1997); more references and many details on FLUKA may be found at the web page <http://pcuka.mi.infn.it/>.
- [20] Prael, R.E. and M. Bozoian, *Adaptation of the Multistage Preequilibrium Model for the Monte Carlo Method (I)*, LANL Report LA-UR-88-3238, Los Alamos (1988).
- [21] Prael, R.E., A. Ferrari, R.K. Tripathi and A. Polanski, “Comparison of Nucleon Cross-section Parametrization Methods for Medium and High Energies”, LANL Report LA-UR-98-5813 (1998); <http://www-xdiv.lanl.gov/XCI/PEOPLE/rep/>; *Proc. 4th Int. Workshop on Simulating Accelerator Radiation Environments (SARE-4)*, Hyatt Regency, Knoxville, TN, 13-16 Sept. 1998, T.A. Gabriel, ed., ORNL, pp. 171-181 (1999).
- [22] Baker, W.F., *et al.*, “Particle Production by 10-30 BeV Protons Incident on Al and Be”, *Phys. Rev. Let.*, 7, 101-104 (1961).
- [23] Schwarzschild, A. and Č. Zupančič, “Production of Tritons, Deuterons, Nucleons, and Mesons by 30-GeV Protons on Al, Be, and Fe Targets”, *Phys. Rev.*, 129, 854-862 (1962).
- [24] Fitch, V.L., S.L. Meyer and P.A. Piroué, “Particle Production at Large Angles by 30- and 33-BeV Protons Incident on Aluminum and Beryllium”, *Phys. Rev.*, 126, 1849-1851 (1962).
- [25] Gavrishchuk, O.P., *et al.*, “Charged Pion Backward Production in 15-65 GeV Proton-nucleus Collisions”, *Nucl. Phys.*, A523, 589-596 (1991); the Be data from this paper are available from the HEPDATA: REACTION DATA Database which can be found at the web page <http://cpt19.dur.ac.uk/hepdata/reac2.html>.
- [26] Barkov, L.M., *et al.*, “Production of Low-energy Hadrons at Zero Angle in Proton-nucleus Collisions at Energy 70 GeV”, *Sov. J. Nucl. Phys.*, 35, 694-698 (1982) [*Yad. Fiz.*, 35, 1186-1193 (1982)].
- [27] Barkov, L.M., *et al.*, “Measurement of the Cross-sections for Production of Hadrons with Momentum Up to 2 GeV/c in Proton-nucleus Collisions at Energy 70 GeV”, *Sov. J. Nucl. Phys.*, 37, 732-737 (1983) [*Yad. Fiz.*, 37, 1232-1240 (1983)].
- [28] Abramov, V.V., *et al.*, “High P_{\perp} Hadron Production of Nuclei at 70 GeV”, *Z. Phys.*, C24, 205-215 (1984).
- [29] Abramov, V.V., *et al.*, “Production of Hadrons with Large P_{\perp} in Nuclei at 70 GeV”, *Sov. J. Nucl. Phys.*, 41, 227-236 (1985) [*Yad. Fiz.*, 41, 357-370 (1985)]; Pre-print IFVE-84-26, Serpukhov (1984); tabulated values are available in the HEPDATA: REACTION DATA Database at the web page <http://cpt19.dur.ac.uk/hepdata/reac2.html>.
- [30] Abramov, V.V., *et al.*, “Production of Deuterons and Antideuterons with Large p_{\perp} in pp and pA Collisions at 70 GeV”, *Sov. J. Nucl. Phys.*, 45, 845-851 (1987) [*Yad. Fiz.*, 45, 1362-1372 (1987)]; Pre-print IFVE-86-56, Serpukhov (1986); tabulated values are available in the HEPDATA: REACTION DATA Database which can be found at the following web page: <http://cpt19.dur.ac.uk/hepdata/reac2.html>.

- [31] Gudima, K.K., S.G. Mashnik and A.J. Sierk, *User Manual for the Code LAQGSM*, Los Alamos National Report LA-UR-01-6804 (2001).
- [32] Mashnik, S.G. and A.J. Sierk, “CEM2k – Recent Developments in CEM”, *Proc. AccApp00*, Washington, DC, USA, pp. 328-341, La Grange Park, IL, USA (2001) (nuclth/00116); Mashnik, S.G. and A.J. Sierk, “Recent Developments of the Cascade-exciton Model of Nuclear Reactions”, *Proc. ND2001*, Tsukuba, Japan, *J. Nucl. Sci. Techn.*, Supplement 2, 720-725 (2002); Eprint: nucl-th/0208074.
- [33] Mashnik, S.G., K.K. Gudima and A.J. Sierk, “Merging the CEM2k and LAQGSM Codes with GEM2 to Describe Fission and Light-fragment Production”, *these proceedings*; LANL Report LA-UR-02-0608, Los Alamos (2002); see also Mashnik, S.G., A.J. Sierk and K.K. Gudima, “Complex-particle and Light-fragment Emission in the Cascade-exciton Model of Nuclear Reactions”, *Proc. RPSD 2002*, Santa Fe, NM; LANL Report LA-UR-02-5185, Los Alamos (2002); Eprint: nuclth/0208048.
- [34] Furihata, S., “Statistical Analysis of Light Fragment Production from Medium Energy Proton-induced Reactions”, *Nucl. Instr. Meth.*, B171, 252-258 (2000); Furihata, S., *The Gem Code Version 2 Users Manual*, Mitsubishi Research Institute, Inc., Tokyo, Japan (2001).
- [35] Mashnik, S.G., K.K. Gudima, I.V. Moskalenko, R.E. Prael and A.J. Sierk, “CEM2k and LAQGSM as Event Generators for Space-radiation-shielding and Cosmic-ray-propagation Applications”, *Proceedings 2nd World Space Congress, COSPAR 2002*, Houston, TX, USA, 10-19 October 2002; LA-UR-02-6558, Los Alamos (2002); Eprint: nucl-th/0210065; to be published in the journal *Advances in Space Research*.
- [36] Fassò, A., A. Ferrari, J. Ranft and P.R. Sala, “FLUKA: Status and Prospective for Hadronic Applications”, *Proc. Monte Carlo 2000 Conf.*, Lisbon, 23-26 October 2000, A. Kling, F. Barao, M. Nakagawa, L. Tavora, P. Vaz, eds., Springer-Verlag, Berlin pp. 955-960 (2001); more references and many details on FLUKA may be found on the web page <http://www.uka.org/>.

**CALCULATION OF NEUTRON TIME-OF-FLIGHT AND ENERGY
SPECTRA BEHIND THICK SHIELDING OF AN ELECTRON
ACCELERATOR AND COMPARISON TO EXPERIMENTAL DATA**

S. Roesler

CERN

CH-1211 Geneva 23, Switzerland

J.C. Liu, S.H. Rokni

Stanford Linear Accelerator Center

Stanford, CA 94309, USA

Abstract

Energy spectra of high-energy neutrons and neutron time-of-flight spectra were calculated for the set-up of experiment T-454 performed with a NE213 liquid scintillator at the Final Focus Test Beam (FFTB) facility at the Stanford Linear Accelerator Center. The neutrons were created by the interaction of a 28.7 GeV electron beam in the aluminium beam dump of the FFTB which is housed inside a thick steel and concrete shielding. To determine the attenuation length of high-energy neutrons, additional concrete shielding of various thicknesses was placed outside the existing shielding. The calculations were performed using the FLUKA interaction and transport code. The energy and time-of-flight were recorded for the location of the detector allowing a detailed comparison with the experimental data. A generally good description of the data is achieved, adding confidence in the use of FLUKA for the shielding design of high-energy electron accelerators.

Introduction

The radiation environment outside lateral, thick shielding at high-energy electron accelerators, e.g. as can be found around beam dumps or collimators, is characterised by neutrons and photons of a wide energy range. Dose to personnel is dominated by the neutrons, of which those with high energies ($E > \text{MeV}$) contribute a significant fraction.

High-energy neutrons are produced in inelastic hadronic interactions of secondary (bremsstrahlung) photons in the beam line elements or dumps. Depending on the energy of the photon different models are commonly used to describe the interaction process. In the energy range between approximately 30 MeV and 200 MeV the process can be understood as a quasi-deuteron absorption of the photon followed by an intranuclear cascade and a de-excitation of the target nucleus. At energies between 200 MeV and a few GeV delta resonance production and decay, again accompanied by an intranuclear cascade and nuclear de-excitation, governs neutron production. At even higher energies the photon is assumed to fluctuate into a hadronic state (vector meson) which subsequently interacts hadronically, similarly to a pion.

As result of such interactions hadrons (neutrons, protons, pions) are emitted which may re-interact in the dump or beam line components. If emitted under a sufficiently large angle these secondary hadrons may also hit the lateral shielding where they are depleted in energy and attenuated in further particle cascades. Thus, the neutrons which are eventually emitted on the outer shield surface are of high generation in the “tree” of the electromagnetic and hadronic cascade. Any simulation attempting to predict the high-energy neutron spectra outside thick shields is therefore very sensitive to even small inaccuracies at each interaction or transport step as they may add up to sizeable uncertainties.

This fact underlines the importance of benchmarking calculations of high-energy neutron spectra with experimental data. Unfortunately, only a very few experiments have performed high-energy neutron measurements outside thick shields at electron accelerators [1,2]. One of these measurements was performed by experiment T-454 outside the steel and concrete shield of the dump cavern of the Final Focus Test Beam (FFTB) at the Stanford Linear Accelerator Center (SLAC) at an electron beam energy of 28.7 GeV. In this experiment high-energy neutron and time-of-flight (TOF) spectra were measured behind shielding of different thicknesses with a NE213 organic liquid scintillator. Details of the measurements and data analysis can be found in [2]. The present paper discusses the Monte Carlo (MC) simulations of the experiment performed with the FLUKA particle interaction and transport code [3,4].

The FLUKA calculations

The calculations were carried out with the year 2000 version of the particle interaction and transport code FLUKA. The program has been used to simulate the electromagnetic and hadronic particle cascade in the FFTB dump and the surrounding shielding. In the following, details of the calculations are discussed which are of importance to the present study.

Description of the geometry

The geometry is described in a right-handed orthogonal system with its origin centred on the front face of the FFTB dump, x pointing up, and z coinciding with the beam axis. Horizontal and vertical sections through the geometry are shown in Figures 1 and 2.

Figure 1. Horizontal section through the geometry used in the simulations

The beam axis runs vertically through the centre of the aluminium dump. The origin of the co-ordinate frame is at the impact point of the beam on the dump. The beam pipe through the upstream part of the shield (bottom part in the figure) was omitted in the simulations.

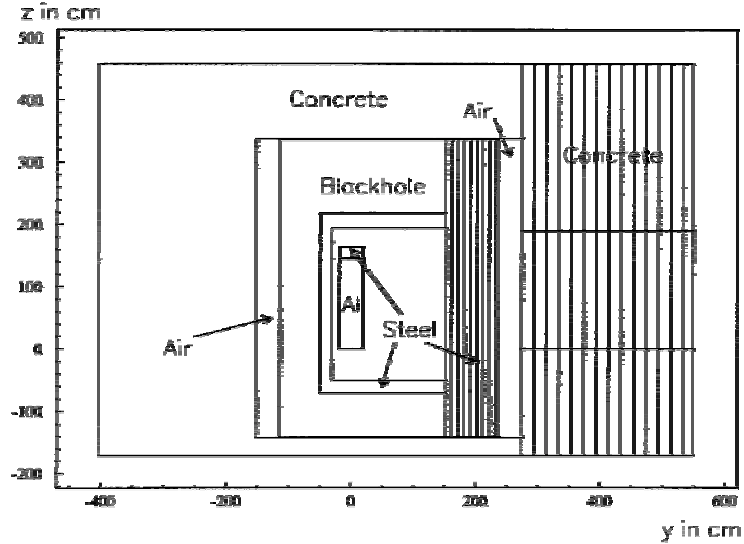
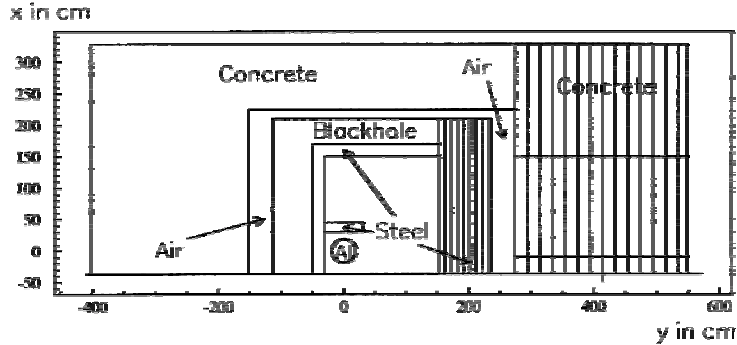


Figure 2. Vertical section through the geometry used in the simulations ($z = 100$ cm)



The dump consists of an aluminium cylinder with a radius of 19 cm and a length of 145 cm followed by an 18 cm long steel cylinder of the same radius. Any support structures of the dump were omitted in the FLUKA geometry. The centre of the dump is at 37.12 cm above the concrete floor. A steel plate of a thickness of 15.24 cm is located directly above the dump.

The dump shielding consists of an inner steel and an outer concrete enclosure separated by an air gap. The lateral steel enclosure has a thickness of 83.82 cm (2 feet and 9 inches) and the lateral concrete enclosure of 182.88 cm (6 feet). For the experiment additional concrete shielding blocks were placed outside the southern, longitudinal side of the shield (i.e. in positive y-direction) allowing to measure the neutron spectra at three different concrete shield thicknesses: 274.32 cm (9 feet), 335.28 cm (11 feet) and 396.24 cm (13 feet). No measurements were taken with the default thickness of 182.88 cm in order to avoid pulse pile-up in the detector. Figures 1 and 2 show the geometry for the 274.32 cm thick shield.

As the measurements were performed on the south side of the shield only the particle cascade in that direction was of interest in the simulation. Therefore, the outer part of the steel shield in the other

directions was assumed to be “Blackhole” (see Figures 1 and 2) – a pseudo-material in FLUKA terminating the particle cascade. Only an inner steel layer of about 20 cm was kept in order to correctly simulate particles scattered back into the dump cavern.

Materials and simulation parameters

The concrete shield was assumed to have a density of 2.35 g/cm³ and the following chemical composition (the values in brackets give the corresponding mass fractions): oxygen (50.0%), silicon (20.0%), calcium (19.5%), aluminium (3.0%), carbon (3.0%), iron (1.4%), sodium (1.0%), potassium (1.0%), hydrogen (0.6%) and magnesium (0.5%). All steel shielding components including the back-end of the dump were assumed to consist of iron, nickel and chromium with an atom relative content of 0.7, 0.2 and 0.1, respectively, and a density of 7.5 g/cm³.

In order to obtain the neutron spectrum outside the shield over the whole energy range transport cut-offs were set to much lower energies than would have been required for the calculation of only the high-energy neutron spectrum. Photons and electrons were transported down to 100 keV and 1 MeV (kinetic energy), respectively, neutron interactions were simulated for all but thermal neutrons, and charged hadrons were followed until they were captured or decayed. For simplicity, the primary electron beam was assumed to be a pencil beam.

The use of several variance reduction (biasing) techniques was essential to obtain results with reasonable statistical significance. They included leading particle biasing at each electromagnetic interaction, biasing of the photon mean-free-path with respect to photonuclear interactions and particle splitting during transport through the shield. To enable the latter the steel shield was split into layers (regions) of 10 cm thickness and the concrete shield into layers of 20 cm thickness. Each layer was assigned a different region-importance factor increasing in value toward the outside of the shield. The boundaries between the layers are shown in Figures 1 and 2.

Calculated quantities

Dedicated simulations were performed for the three different concrete shield thicknesses. In each case the following information on neutrons with an energy greater than 5 MeV and on photons of any energy emitted from the outer shield surface was recorded in a file for later analysis:

- Number of the primary electron.
- Generation of the particle. The generation of a particle increases with each sampled discrete interaction (electromagnetic or hadronic), i.e. the primary electron is generation “1”, the generation of the photon after the first bremsstrahlung process would be “2”, etc. Interactions which preserve the incoming particle, e.g. elastic neutron scattering, do not increase the generation.
- Age (time-of-flight) of the particle with respect to the time at which the beam electron hits the dump.
- Weight of the particle.
- Kinetic energy.
- Co-ordinates (x and z) and direction cosines at the shield surface.

In order to restrict the analysis to approximately the area where the detectors were placed during the measurements and to still achieve reasonable statistical significance only those neutrons and photons were recorded which were emitted from a limited area. This area extended longitudinally over the length of the dump and vertically from about the beam axis to 150 cm above that axis. The area is marked in Figures 1 and 2 by transverse lines through the concrete shield. In addition, one of the simulations also recorded neutrons and photons crossing the inner boundary of the southern part of the steel shield ($y = 152.4$ cm, referred to as “source” below).

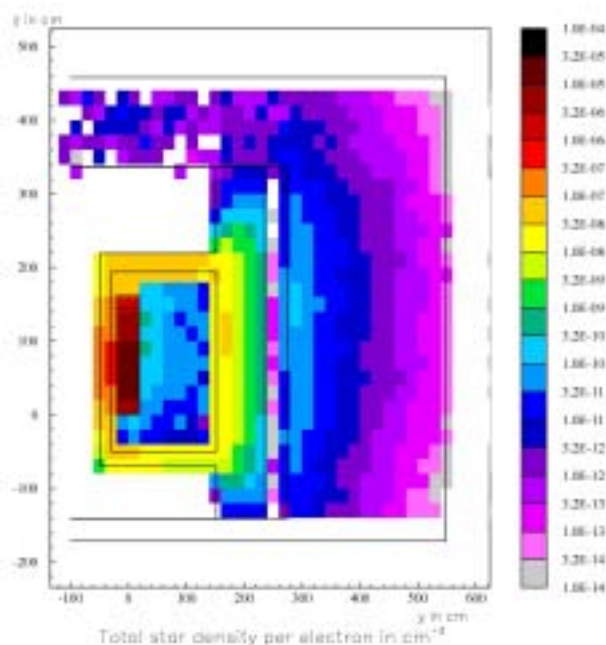
Furthermore, standard scoring capabilities of FLUKA were used to obtain the following quantities and spectra: the neutron energy spectrum outside the shield in the whole energy range including low-energy neutrons, the density of inelastic interactions with energies above 20 MeV (“stars”) in the dump and shielding components, and ambient dose equivalent rate throughout the whole geometry. The latter was calculated by folding particle fluence with energy-dependent conversion coefficients [5].

Results of the simulations

Inelastic interaction density

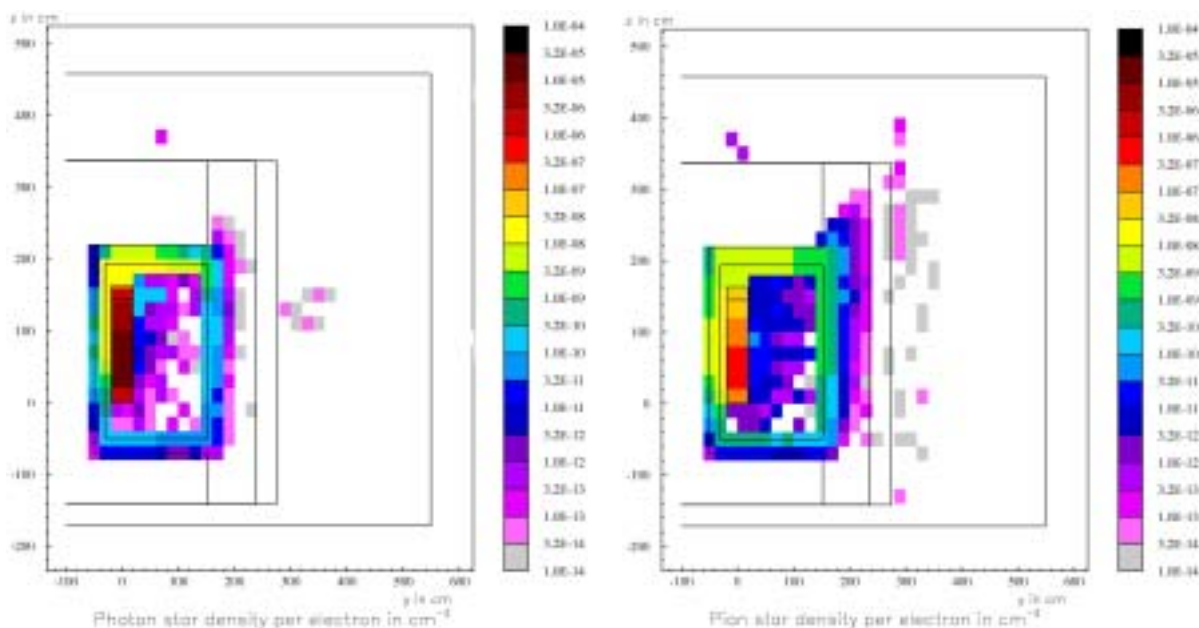
The high-energy neutrons reaching the outside of the shield are produced in hadronic interactions of photons or in inelastic re-interactions of secondary hadrons inside the dump or in the shield. Figure 3 shows the density profile of interactions at energies larger than 20 MeV for a horizontal slice through the geometry centred at the beam axis. The values are averaged in the vertical (x -) direction over 40 cm. As expected, the interaction density is highest in the dump and in the steel shield. Only relatively few particles interact in the concrete shield (about two orders of magnitude less than in the steel shield).

Figure 3. Total density of inelastic interactions (“stars”) at energies greater than 20 MeV. The figure shows a horizontal section through the dump cavern and the lateral shield at the height of the beam axis.



The interaction density of photons and charged pions above 20 MeV is shown in Figure 4. In the dump photons clearly dominate the total interaction density and contribute significantly to the interactions in the forward (transverse) steel shield. On the other hand, there are practically no high-energy photoproduction interactions in the lateral shield. Similarly, photoproduced pions interact mainly in the dump and forward shield and only a few high-energy pions are emitted at larger angles and interact the steel shield.

Figure 4. As in Figure 3, here the hadronic interaction density of photons (left) and of charged pions (right)



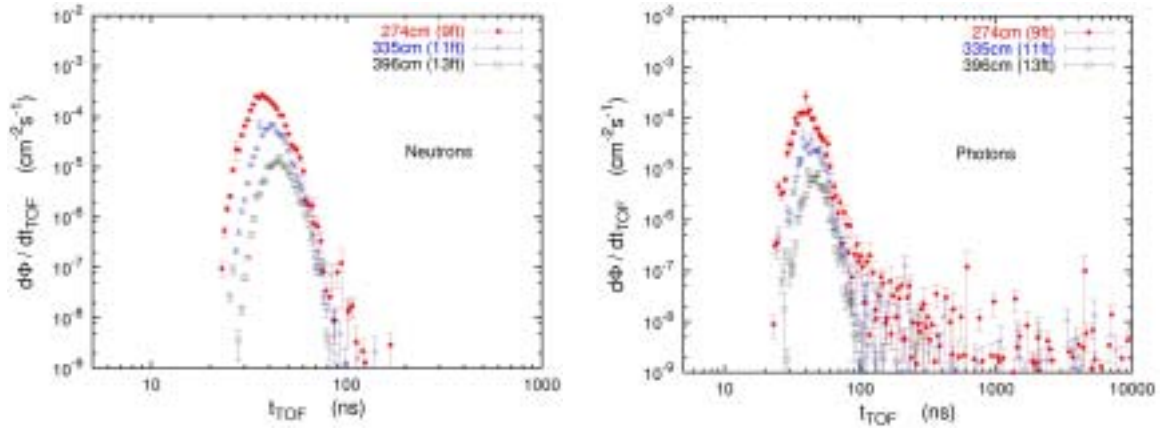
Consequently, most of the high-energy inelastic interactions in the steel and concrete shields (see Figure 3) are caused by neutrons with a minor contribution by protons. High-energy neutrons which reach the outside of the shield are either produced directly in the dump or are secondary products of interacting neutrons.

Time-of-flight spectra

As mentioned above, neutrons with kinetic energies greater than 5 MeV and photons of all energies crossing the outer shield boundary were recorded in files. This allowed a detailed analysis of the distributions in the various variables by applying cut-offs, calculating correlations, or by the off-line folding with detector response functions. The comparison of calculated and measured TOF spectra is particularly important as it provides a benchmark of the Monte Carlo code which is independent from the uncertainties involved in the unfolding of the experimental count rates.

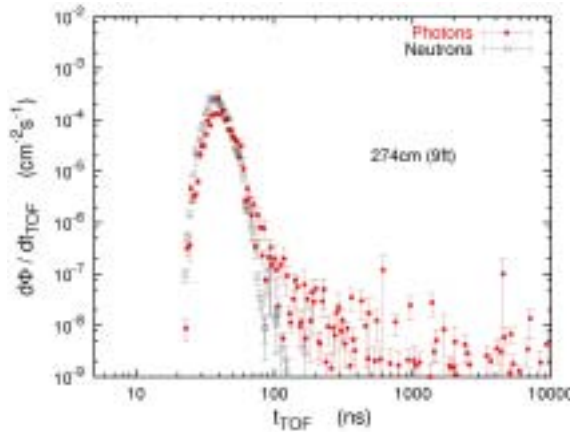
TOF spectra of neutrons and photons are shown for the different shield thicknesses in Figure 5. All distributions are normalised per beam electron. Despite having recorded all neutrons down to 5 MeV, only those with energies larger than 20 MeV were included in the TOF spectra as this is the energy range of main interest for the experiment. The neutron spectra peak at about 37.3 ns, 41.6 ns and 45.2 ns, respectively. The shift between the peaks of 3.6-4.3 ns reflects the increase in shield thickness of 60.96 cm. Using relativistic kinematics this shift corresponds to neutron energies between 120 MeV and 200 MeV.

Figure 5. Time-of-flight spectra of neutrons with energies greater than 20 MeV (left) and photons (right) behind different concrete shield thicknesses



The neutron and photon TOF spectra for the 274 cm thick shield are compared to each other in Figure 6. As can be seen, photons and neutrons reach the outside of the shield at the same time. Taking into account that, in case of the 274 cm concrete shield, a photon would need only about 18 ns for the 549 cm distance between the centre of the dump and the outside of the shield (i.e. less than half of the peak TOF) it can be concluded that these photons are secondary products of neutron interactions in the shield.

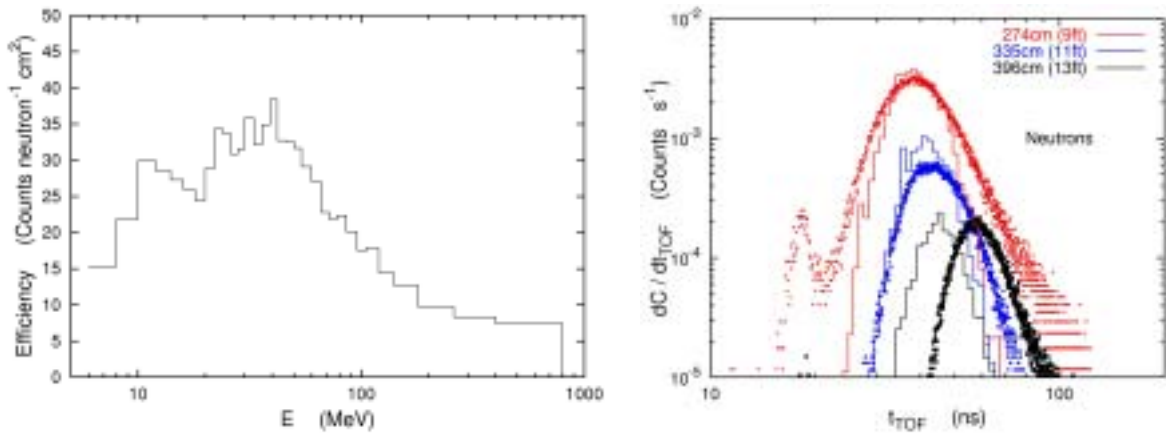
Figure 6. Comparison of time-of-flight spectra of neutrons and photons behind a concrete shield thickness of 274 cm



The calculated time-of-flight spectra can be directly compared to the count rates measured with the NE213 detector if they are folded with the energy efficiency function of the scintillator. This function is shown in Figure 7 (left) for a light output threshold of 3 MeVee [2]. As the detector responds to the number of neutrons the calculated *current* of neutrons above 5 MeV was used in the folding procedure. The resulting calculated count rates are compared to the measured count rates in Figure 7 (right).

There is generally a good agreement in the centre of the distributions for the 274 cm and 335 cm shield thicknesses. The measured tails of the distributions are overestimated in both cases, which could be due to uncertainties in the response function at high energies (low TOF) and to uncertainties in the subtraction of the photon-induced signal. In addition, the measured TOF spectrum for the 274 cm

Figure 7. Left: Efficiency of the NE213 detector for a light output threshold of 3 MeVee. Right: The calculated time-of-flight spectra for the different shield thicknesses obtained by folding the current of neutrons crossing the outer shield boundary with the detector efficiency function (histograms) are compared to experimental data (points) [2].



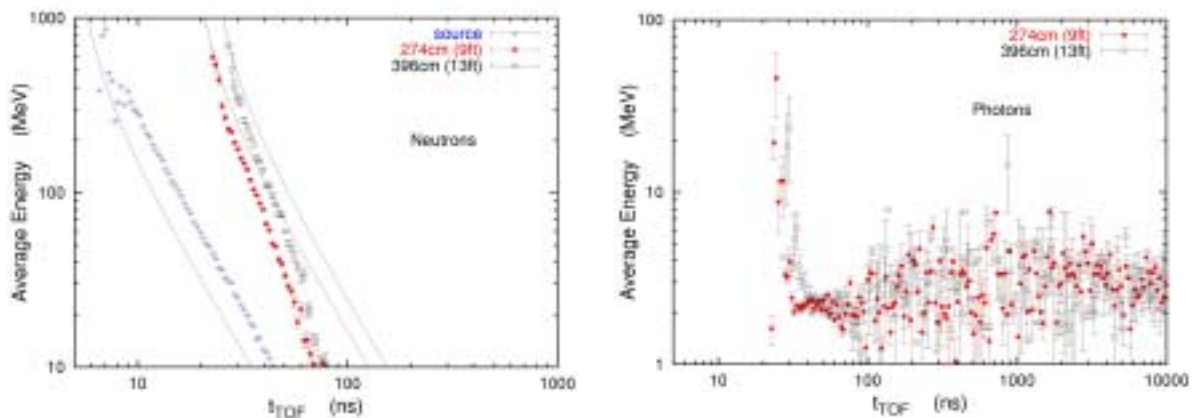
shield shows a small peak at very low TOF which is not seen in the calculations. The calculated and measured TOF spectra for the 396 cm shield agree in shape and absolute value but the measured distribution is shifted with respect to the calculated one by about 15 ns, a phenomenon which is not yet understood.

Correlation between time-of-flight and energy

From simple kinematic considerations it can be expected that there is a strong correlation between the energy of a neutron and its TOF. Figure 8 shows the average energy of neutrons and photons outside the 274 cm and 396 cm thick concrete shields as a function of the TOF.

Figure 8. Average energy of neutrons (left) and photons (right) as a function of time-of-flight behind concrete shield thicknesses of 274 cm and 396 cm (symbols)

In addition, the average energy of neutrons at the inner boundary of the steel shield (“source”) is shown. See text for a discussion of the solid lines.

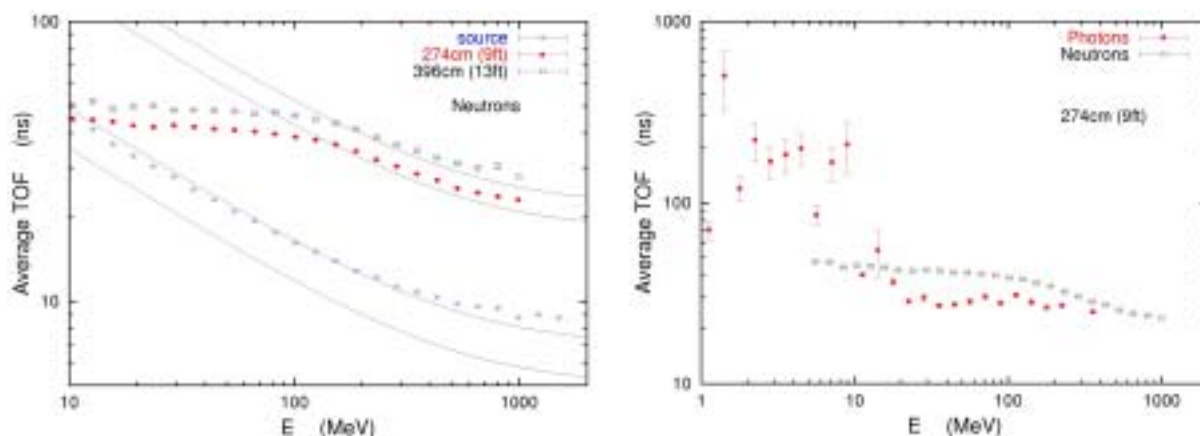


The average neutron energy (Figure 8, left) steeply decreases with TOF. In addition, the average energy of the high-energy neutrons entering the steel shield (“source”) is shown. Solid lines indicate the maximum possible neutron energy entering at the three boundaries assuming the neutron being emitted from the beam axis in a horizontal plane at 90°. For the source neutrons this line is to the left of the calculated dependency since most high-energy neutrons are emitted from the dump under smaller angles with regard to the beam axis, thus having a longer path and flight time to the steel shield. At the outer boundary of the concrete shield the situation is reversed. For pure geometrical reasons, neutrons reaching the scoring area at that boundary are caused by source neutrons emitted under larger angles. The 90° curve should therefore be a good approximation for the maximum energy. The calculated average energies are lower than the maximum value since the shield degrades the neutron energy. In addition, at large TOF the neutrons are produced in the concrete shield and have therefore much lower average energies.

The average photon energy (Figure 8, right) also rapidly decreases up to a TOF of about 40 ns (the maximum in the TOF spectrum) from where it stays approximately constant at around a few MeV, an energy typical for de-excitation photons after nuclear interactions in concrete.

The inverse correlation, i.e. the average TOF as function of energy, is shown in Figure 9. In the left figure (neutrons) the top two solid lines indicate the minimum TOF required for a neutron to reach the outside boundary of the respective concrete shield if it was emitted from the beam axis in a horizontal plane at 90°. At high energy ($E > \text{MeV}$) the actual TOF is somewhat larger since the neutron path is longer due to smaller emission angles and scattering. At lower energies neutrons are secondary products of high-energy neutron interactions in the shield and therefore reach the outside shield boundary earlier than if they started their path with the same energy from the beam axis. The bottom solid line represents the minimum TOF for a neutron to reach the inner steel shield boundary, again assuming a 90° emission angle. The actual average TOF (symbols labelled “source”) is clearly larger because of the smaller emission angle and therefore larger flight paths. It is well fitted with an average TOF curve based on a 45° emission angle (second solid line from the bottom).

Figure 9. Average time-of-flight of neutrons (left) as a function of energy behind concrete shield thicknesses of 274 cm and 396 cm and at the inner boundary of the steel shield (symbols). See text for an explanation of the solid lines. The right figure shows a comparison of the average time-of-flight of neutrons and photons behind a concrete shield of 274 cm as function of energy (note the different scales).

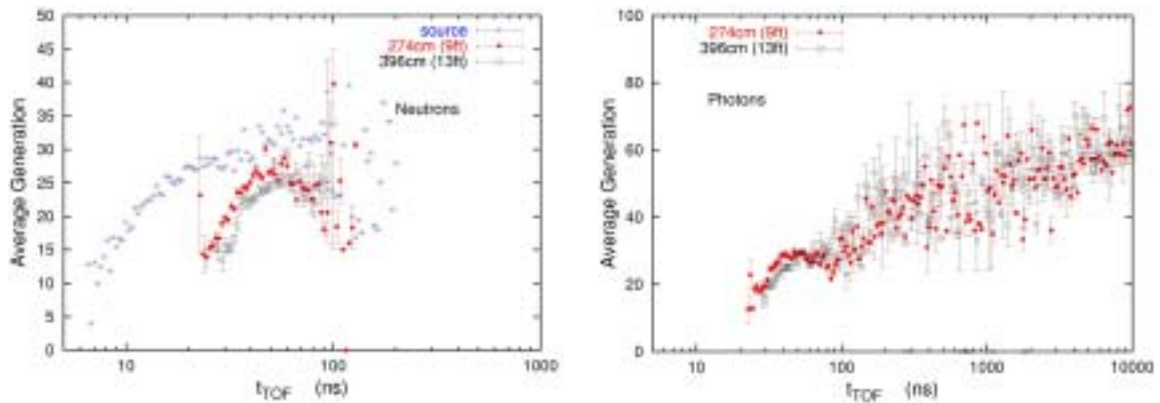


As expected, high-energy photons ($E > \text{MeV}$) produced in neutron interactions in the shield arrive at the outer shield boundary earlier than neutrons of the same energy. This is shown in Figure 9 (right) for the 274 cm concrete shield. Photons of lower energies accompany low-energy neutron interactions and therefore reach the outer shield boundary at larger TOF.

Average particle generation

As mentioned above, FLUKA keeps track of the particle generation in the tree of the cascade. Figure 10 shows this generation as function of the TOF for neutrons (left) and for photons (right). Up to about 60 ns the average generation rises as the average energy decreases (c.f. Figure 8). At larger TOF it stays approximately constant due to attenuation and possibly also due to effects of the 5 MeV threshold in recording the neutrons. Most of the increase in generation is caused in the strong electromagnetic cascade of the primary electron in the dump. The average generation of the neutrons at the inner steel boundary (symbols labelled “source” in Figure 10, left) is already relatively high and almost comparable that of the neutrons at the outside of the shield.

Figure 10. Average generation of neutrons (left) and of photons (right) as a function of time-of-flight behind concrete shield thicknesses of 274 cm and 396 cm. For neutrons the average generation is also given for the inner boundary of the steel shield.



Photons, being secondary products of neutron interactions, show a similar dependence of generation on TOF as the neutrons up to a few hundred nanoseconds (Figure 10, right). At higher TOF the average generation increases rapidly as these photons are produced in low-energy neutron interactions.

Energy spectra

Energy spectra of neutrons and photons outside the shield are shown for the three concrete shield thicknesses in Figure 11. As mentioned above, neutrons were scored in the whole energy range (including low-energy neutrons) with standard scoring capabilities of FLUKA. The spectra are presented in units of lethargy, i.e. differential fluence $d\Phi/dE$ multiplied by energy E . The spectra are typical equilibrium spectra with a shape which is independent of the shield thickness. The area under the spectra corresponds to the number of particles indicating a significant contribution of high-energy neutrons (left).

The calculated high-energy neutron spectra are compared to the spectra measured with the NE213 organic liquid scintillator [2] in Figure 12. Here, symbols represent the experimental data and histograms the FLUKA results. Except for very high energies ($E > \text{MeV}$) there is generally a good agreement

Figure 11. Energy spectra of neutrons (left) and photons (right) behind concrete shield thicknesses of 274 cm, 335 cm and 396 cm

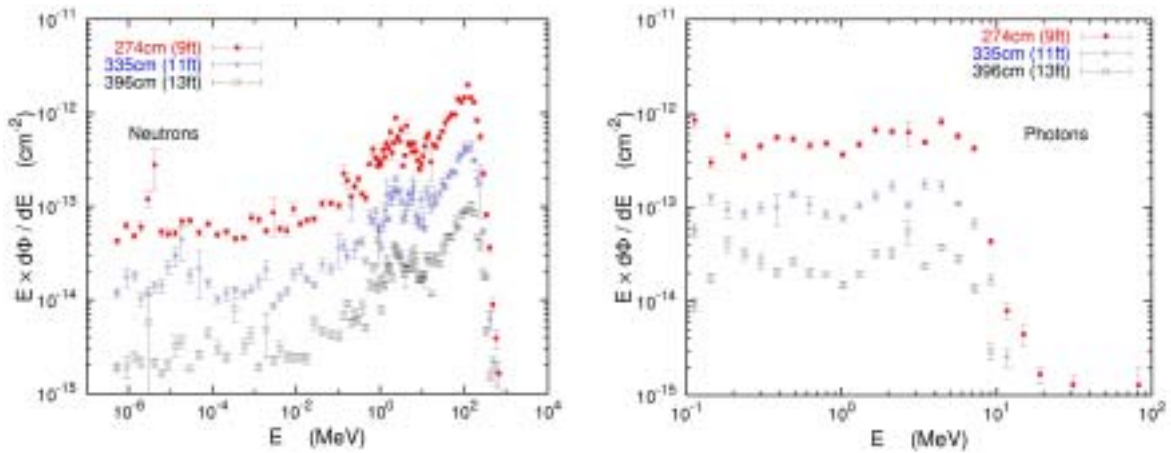
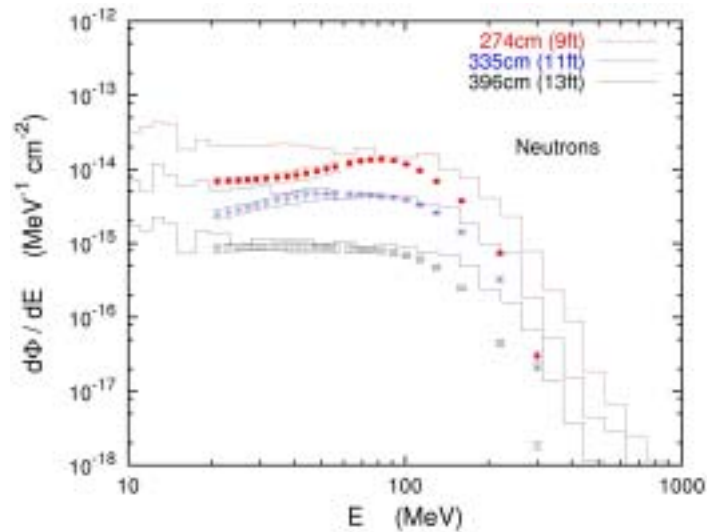


Figure 12. Energy spectra of high-energy neutrons behind concrete shield thicknesses of 274 cm, 335 cm and 396 cm. Calculated spectra are shown as histogram and measured spectra [2] as symbols.

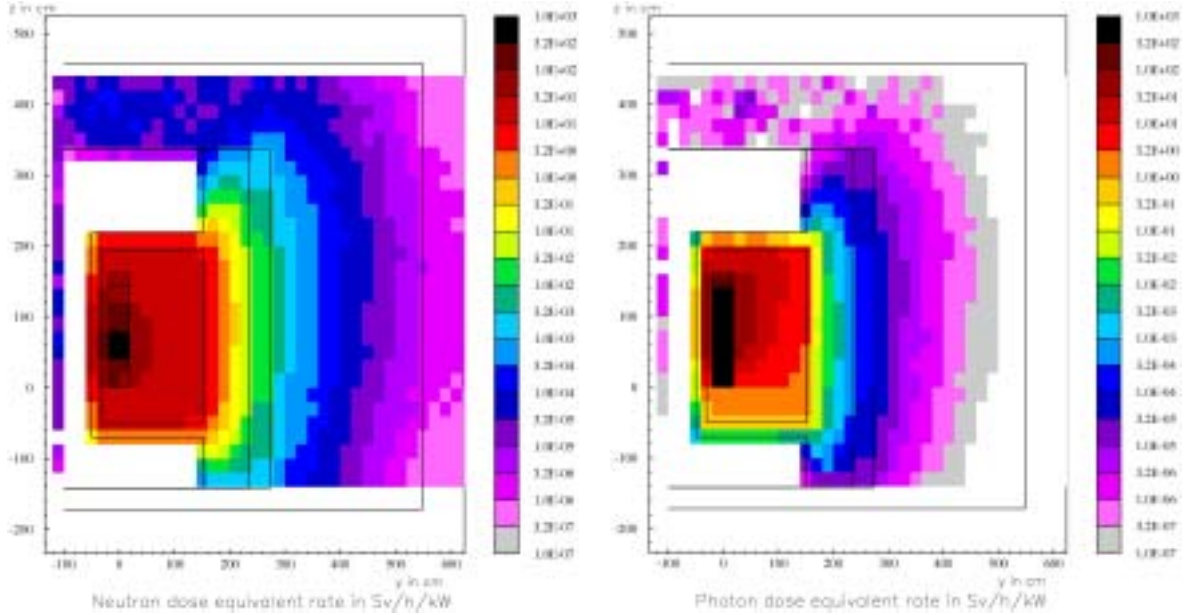


between measured and calculated spectra for the 335 cm and 396 cm shields. For the smallest thickness (274 cm) the calculated spectrum overestimates the measured one by about a factor of two. It is interesting to note that the shape of the measured spectra varies slightly with shield thickness at lower energies whereas the shape of the calculated spectra is almost constant. This effect is not yet fully understood but could be due to uncertainties in the detector response function at low energy [2].

Dose attenuation

As mentioned above, the ambient dose equivalent rate was calculated by folding particle fluence with energy-dependent conversion coefficients [5]. Figure 13 shows the dose rate from neutrons and photons for a horizontal slice through the geometry centred at the beam axis for the 274 cm concrete

Figure 13. Neutron (left) and photon ambient dose equivalent rate (right) shown for a horizontal section through the dump cavern and the lateral shield (steel and 274 cm of concrete) at the height of the beam axis



shield. The values are averaged in the vertical (x -) direction over 40 cm. It should again be mentioned that thermal neutrons were not simulated. Therefore, the dose rates neither include dose from thermal neutrons nor dose due to photons from thermal neutron capture. The figure clearly shows that the dose rate in and outside the shield is dominated by neutrons.

Table 1 gives the ambient dose equivalent rate obtained by folding the measured and calculated neutron energy spectra (Figures 11 and 12) with the conversion coefficients. All values are normalised to a beam power of 1 kW. As the low-energy cut-off in the experimental spectra is at 20 MeV the values can be directly compared to the FLUKA results for high-energy neutrons (third column). The calculated values are generally higher by about a factor of 1.2-2.0. The contribution of high-energy neutrons to the total dose rate (ratio of the last two columns in Table 1) is independent of the shield thickness and is about 57%. The attenuation coefficient for the high-energy neutron dose in concrete obtained from the three calculated values is 116 g/cm^2 .

Table 1. Neutron ambient dose equivalent rate outside the FFTB dump shield for different concrete shield thicknesses. Experimental values are compared to FLUKA predictions for the high-energy neutron dose rate. In addition, the calculated total neutron dose rate is given.

Thickness (cm)	Experiment ($\mu\text{Sv/h/kW}$)	FLUKA ($E > \text{MeV}$) ($\mu\text{Sv/h/kW}$)	FLUKA (all energies) ($\mu\text{Sv/h/kW}$)
274	0.38	0.72	1.29
335	0.15	0.18	0.32
396	0.029	0.041	0.070

Similarly, the photon dose rate can be calculated by folding the spectra of Figure 11 (right) with energy-dependent conversion coefficients. The resulting values are 10.4, 2.3 and 0.54 nSv/h/kW for the three shield thicknesses, respectively.

Summary and conclusions

Energy and time-of-flight spectra of high-energy neutrons and of photons outside the dump shield of the Final Focus Test Beam at SLAC were calculated with the FLUKA Monte Carlo code. The aim of this study was to benchmark FLUKA with experimental data obtained with a NE213 organic liquid scintillator.

The aluminium beam dump as well as the steel and concrete shielding was simulated in detail. According to the experimental set-up calculations were performed for three different thicknesses of the concrete shield between 270 cm and 400 cm. High-energy neutrons and photons crossing the outer boundary of the concrete shield were recorded in files for later analysis. In addition, the density of inelastic interactions and ambient dose equivalent rate were scored for a horizontal slice through the centre of the geometry.

High-energy neutrons are created in hadronic interactions of photons and secondary hadrons in the dump and in interactions of neutrons and protons in the lateral shielding. There are practically no high-energy photoproduction interactions in the shielding. Photons reaching the outside of the shield are mainly produced in interactions of neutrons in the shield. The steel and concrete shield absorbs almost all photons produced in the dump.

The TOF spectra of neutrons and photons show a broad peak at about 35-50 ns. There is generally a good agreement between calculated and measured TOF spectra except for the tails of the distributions and for the thickest shield. The comparison of the TOF spectra is particularly important as it provides a benchmark of the Monte Carlo code which is independent from the uncertainties involved in the unfolding of the experimental count rates. Various correlations between the energy and the TOF as well as between the generation of a particle and its TOF were studied, confirming the origin of the components contributing to the TOF spectra.

Furthermore, energy spectra of neutrons (at all energies) and photons outside the shield were calculated and high-energy neutron spectra were compared to experimental data. The calculated spectra generally agree with the measured spectra within a factor of two. The reason for the discrepancy is still under investigation. It might be partially caused by uncertainties in the response function of the NE213 detector at high energies.

Finally, the ambient dose equivalent rate was calculated by folding neutron and photon fluence with energy-dependent conversion factors. The dose outside the shield is mainly caused by neutrons of which those above 20 MeV contribute about 57%. Dose rates were also derived from the measured spectra by folding with the conversion factors. As observed for the energy spectra, the calculated dose rate of high-energy neutrons is about a factor of two higher than the measured one.

Acknowledgements

The authors are grateful to Alberto Fassò, Alfredo Ferrari, Ken Kase, Takashi Nakamura and Shingo Taniguchi for the stimulating discussions and to Shingo Taniguchi for providing the experimental data. This work was supported by the Department of Energy under contract DE-AC03-76SF00515.

REFERENCES

- [1] Vylet, V., J.C. Liu, S.H. Rokni and L-X. Thai, "Measurements of Neutron Spectra at the Stanford Linear Accelerator Center", *Radiat. Prot. Dosim.*, 70, 425-428 (1997).
- [2] Taniguchi, S., *et al.*, "Shielding Experiment of Neutrons Through Concrete Outside the Beam Dump of 28.4 GeV Electron Linear Accelerator", *these proceedings*.
- [3] Fassò, A., A. Ferrari and P.R. Sala, "Electron-photon Transport in FLUKA: Status", *Proc. of the International Conference on Advanced Monte Carlo for Radiation Physics, Particle Transport Simulation and Applications (Monte Carlo 2000)*, Lisbon, Portugal, 23-26 October 2000, A. Kling, F. Barao, M. Nakagawa, L. Tavora and P. Vaz, eds., Springer-Verlag, Berlin, Heidelberg, pp. 159-164 (2001).
- [4] Fassò, A., A. Ferrari, J. Ranft and P.R. Sala, "FLUKA: Status and Prospective for Hadronic Applications", *Proc. of the International Conference on Advanced Monte Carlo for Radiation Physics, Particle Transport Simulation and Applications (Monte Carlo 2000)*, Lisbon, Portugal, 23-26 October 2000, A. Kling, F. Barao, M. Nakagawa, L. Tavora and P. Vaz, eds., Springer-Verlag, Berlin, Heidelberg, pp. 955-960 (2001).
- [5] Pelliccioni, M., "Overview of Fluence-to-effective Dose and Fluence-to-ambient Dose Equivalent Conversion Coefficients for High-energy Radiation Calculated Using the FLUKA Code", *Radiat. Prot. Dosim.*, 88, 279-297 (2000).

MEASUREMENT OF NEUTRON ENERGY SPECTRA BEHIND THE LATERAL SHIELD OF A HIGH-ENERGY ELECTRON BEAM DUMP

S. Taniguchi,^{1,2} M. Sasaki,² T. Nunomiya,² H. Iwase,² S. Yonai,²
T. Nakamura,² K. Kase,³ J.C. Liu,³ S.H. Rokni,³ S. Roesler⁴

¹Japan Synchrotron Radiation Research Institute

Koto 1-1-1, Mikazuki-cho, Sayo-gun, Hyogo, 679-5198, Japan

²Tohoku University, Sendai, Japan

³Stanford Linear Accelerator Center, Stanford, CA 94309, USA

⁴CERN, CH-1211 Geneva 23, Switzerland

Abstract

Neutron spectra behind the lateral shield of the 28.7 GeV electron beam dump at the Final Focus Test Beam (FFTB) facility at the Stanford Linear Accelerator Center (SLAC) were measured with a NE213 organic liquid scintillator and the unfolding technique. The measurements were performed with three additional concrete thicknesses of 91, 152 and 213 cm, which were added to the existing shield of 84 cm of iron and 183 cm of concrete. The neutron spectra were also calculated with the FLUKA Monte Carlo simulation code. The calculated and measured results are in agreement.

Introduction

Electron accelerators have been widely used for high-energy physics, synchrotron radiation and various other purposes. They produce high-energy (> 20 MeV) neutrons through the photonuclear reactions from the bremsstrahlung photons generated in targets, beam stops and other beam line components. The information on neutron spectra due to high-energy electron beams is indispensable for radiation safety and shielding design at high-energy electron accelerator facilities. However there are few experimental data on neutron energy spectra from high-energy electron beams [1]. Therefore, neutron spectra behind the lateral shield of a 28.7 GeV electron beam dump were measured in this study.

Experiment

The measurements were performed at the Final Focus Test Beam (FFTB) electron linear accelerator of the Stanford Linear Accelerator Center (SLAC). The 28.7 GeV electron beam was extracted from the linear accelerator at a 10 to 30 Hz repetition rate. The beam intensity of each pulse was monitored with the Toroid Charge Monitor (TCM) and beam intensity was limited to 2×10^9 to 5×10^9 e/pulse in order to avoid the pulse pile-up problem of the detector.

Figure 1 is the schematic view of the experimental set-up. The aluminium beam dump (145 cm length, 38 cm diameter) is shielded on the side with 84 cm of iron and 183 cm of concrete laterally to the beam dump. Iron blocks for muon shielding are placed outside the dump room in the forward direction with respect to the beam line. To measure the energy spectra of neutrons generated in the beam dump, two NE213 detectors (12.7 cm diameter, 12.7 cm thickness) were placed at 90° to the beam axis in a hutch outside the shield. The measurements were performed by adding the extra concrete shielding of three different thicknesses of 91, 152 and 213 cm between the wall and the detectors in order to investigate the attenuation profile. The average electron beam intensity was 2×10^9 , 5×10^9 and 5×10^9 electrons per pulse for the three thicknesses, respectively.

Figure 1. Neutron spectra measurement experimental set-up at FFTB of SLAC

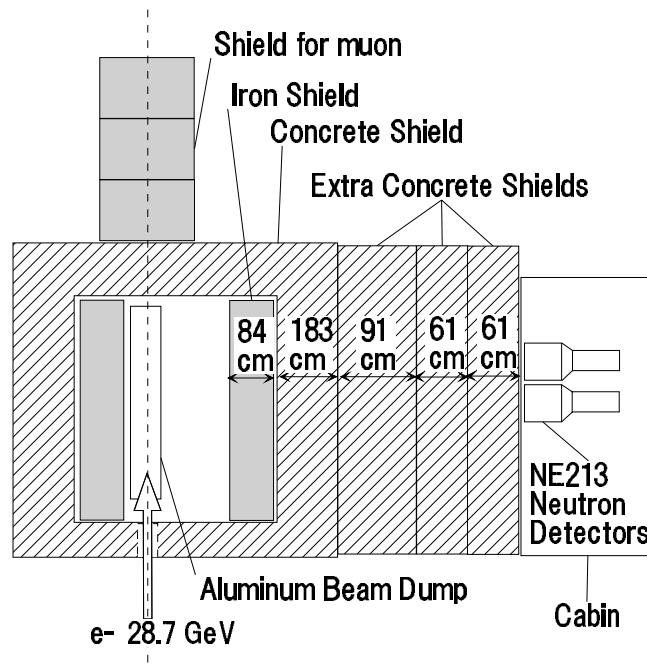
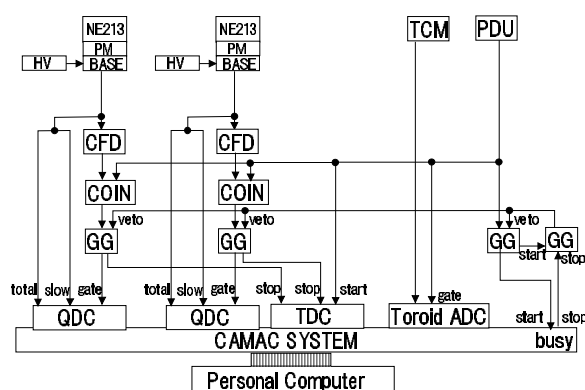


Figure 2 shows a simplified block diagram of the electronic circuit. The output signal from the muon counter was adjusted in time with the programmable delay unit (PDU) signal from the accelerator used as the event trigger. The integrated charges of total component and slow (decay) component of the signals from the NE213 detector were measured by the charge analogue-to-digital converter (QDC) for particle identification between neutrons and gamma rays (i.e. neutron-gamma discrimination using pulse-shape differentiation). The time difference between the PDU signal and the particle detection, which represents the difference between the time that the beam strikes the dump and the time that the particle is detected by NE213, was also measured as the TOF spectra. These processes were controlled by the Kakuken Online Data Acquisition System (KODAQ) [2]. The TOF spectra and neutron spectra can then be compared with those calculated using the FLUKA Monte Carlo code [3,4].

Figure 2. Simplified block diagram of electronic circuit for the measurements using two NE213 scintillation detectors

PM: photomultiplier, HV: high voltage power supply, CFD: constant fraction discriminator, COIN: coincidence unit, GG: gate and delay generator, ADC: analogue-to-digital converter, QDC: charge analogue-to-digital converter, TDC: time-to-digital converter, TCM: toroid charge monitor, PDU: programmable delay unit



Data analysis

The neutron events were separated from the gamma-ray events by using two-dimensional graphical plots of the total and slow pulse height components of the NE213 detectors, as shown in Figure 3. The pile-up events were also eliminated using Figure 3. The neutron events can be clearly discriminated from the gamma-ray events, though a small fraction of pile-up events are also seen in the figure.

The light outputs from the NE213 detectors were calibrated using the Compton edges from the 1.17 MeV and 1.33 MeV gamma rays, and from the 4.43 MeV gamma ray in the spectra of ^{60}Co gamma-ray source and a $^{241}\text{Am-Be}$ source, respectively.

The neutron energy spectrum was obtained with the unfolding technique using the FORIST code [5]. The response function of the NE213 detector for neutrons up to 800 MeV was measured by Sasaki, *et al.* [6].

Results and discussion

Figure 4 shows the measured neutron energy spectra compared with the spectra calculated with FLUKA [7]. The measured and calculated spectra are in general agreement both in the spectral shapes

Figure 3. Two-dimensional plot of the total and slow components of pulse charges of NE213 detector for neutron-gamma discrimination

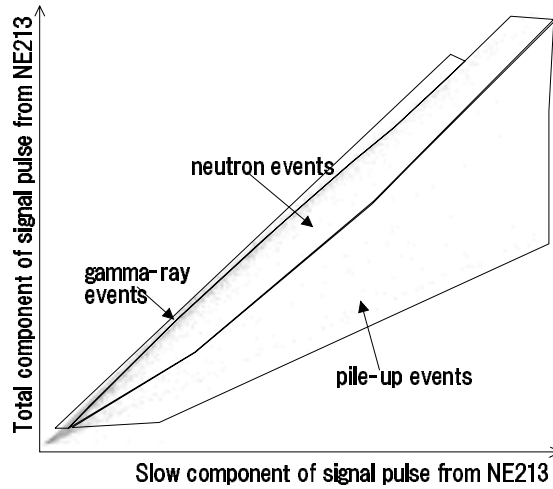
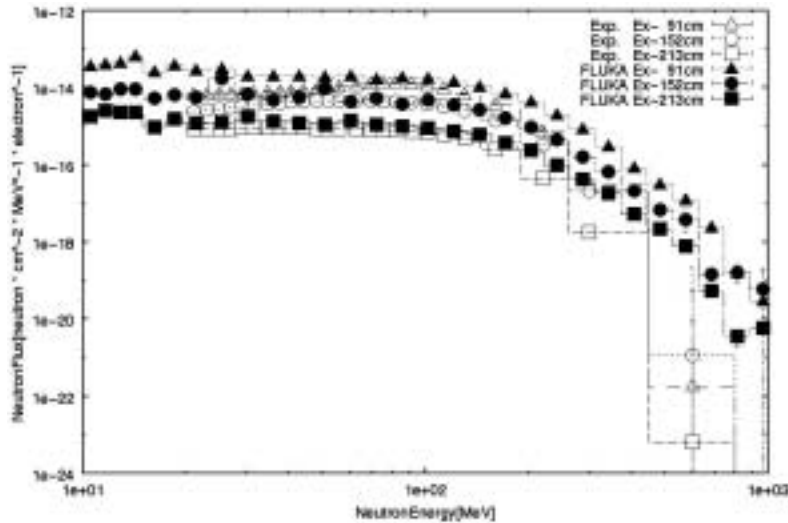


Figure 4. The measured neutron energy spectra behind the three different shields, along with the FLUKA calculated spectra



and in absolute values in the energy region from 5 to 200 MeV. In the energy region above 200 MeV, the measured spectra are lower than the calculated spectra. This could be due to the poor accuracy of the response function of NE213, caused by low neutron detection efficiency, and in part due to poor statistics.

Conclusions

The neutron energy spectra behind the concrete shield at 90° to the 28.7 GeV electron beam dump were measured by using the NE213 organic liquid scintillator and the unfolding technique using the FORIST code. Those were also calculated with the FLUKA Monte Carlo particle transport code. The measured neutron spectra show good agreement with the calculated spectra.

Acknowledgements

The authors are grateful to the staff of the Accelerator Operation and the Experimental Facility Departments at SLAC. This work was supported in part by the US Department of Energy under contract DE-AC03-76SF00515.

REFERENCES

- [1] Vylet, V., J.C. Liu, S.H. Rokni, L.X Thai, "Measurements of Neutron Spectra at the Stanford Linear Accelerator Center", *Radiat. Prot. Dosim.*, 70, 425-428 (1997).
- [2] Omata, K., Y. Fujita, N. Yoshikawa, M. Sekiguchi, Y. Shida, *A Data Acquisition System Based on a Personal Computer*, INS-Rep.-884, Institute for Nuclear Study, University of Tokyo (1991).
- [3] Fassò, A., A. Ferrari, P.R. Sala, "Electron-photon Transport in FLUKA: Status", *Proc. of the Monte Carlo 2000 Conference*, Lisbon, 23-26 October 2000, A. Kling, F. Barao, M. Nakagawa, L. Tavora, P. Vaz, eds., Springer-Verlag, Berlin, pp. 159-164 (2001).
- [4] Fassò, A., A. Ferrari, J. Ranft, P.R. Sala, "FLUKA: Status and Prospective for Hadronic Applications", *Proc. of the Monte Carlo 2000 Conference*, Lisbon, 23-26 October 2000, A. Kling, F. Barao, M. Nakagawa, L. Tavora, P. Vaz, eds., Springer-Verlag, Berlin, pp. 955-960 (2001).
- [5] Johnson, R.H., B.W. Wehring, ORNL/RSIC-40, Oak Ridge National Laboratory (1976).
- [6] Sasaki, M., N. Nakao, T. Nakamura, T. Shibata and A. Fukumura, "Measurements of the Response Functions of an NE213 Organic Liquid Scintillator to Neutrons Up to 800 MeV", *Nucl. Instrum. and Methods*, A480, 2-3, 188 (2002).
- [7] Roesler, S., J. Liu, S. Rokni and S. Taniguchi, "Calculation of Neutron Time-of-flight and Energy Spectra Behind Thick Shielding of an Electron Accelerator and Comparison to Experimental Data", *these proceedings*.

DEEP-PENETRATION CALCULATION WITH AN 800 MeV PROTON BEAM COMPARED WITH THE SHIELDING EXPERIMENT AT ISIS

Tomoya Nunomiya, Hiroshi Iwase, Takashi Nakamura
Tohoku University, Aramaki, Aoba-ku, Sendai, 980-8579, Japan

Noriaki Nakao
High Energy Accelerator Research Organization (KEK)
Oho 1-1, Tsukuba, Ibaraki, 305-0801, Japan

Abstract

A calculation of neutron penetration through a thick shield was performed with a three-dimensional multi-layer technique using the MARS14 Monte Carlo code to compare with the existing experimental data for the ISIS spallation neutron source facility shielding.

In the calculation, secondary neutrons from a tantalum target bombarded by 800 MeV protons were transmitted through a bulk shield of approximately 3 m thick iron and 1 m thick concrete. The geometry of the bulk shield was divided into several layers about 50 cm thick, and a step-by-step calculation was carried out to multiply the particles at the boundaries between the layers. Finally, the energy spectra of high-energy neutrons behind the bulk shield were obtained with good statistics. Corresponding $^{12}\text{C}(n,2n)$ reaction rates which agree with the experimental data within 30% were also obtained.

Introduction

Although steady progress in computer technologies makes calculations faster, reliable calculations of the neutron transmission through a very thick shield remain quite difficult. This is because a long computing time and sophisticated variance reduction techniques are needed to obtain particle fluxes and energy spectra with good statistics. Moreover, corresponding experimental data are rather scarce.

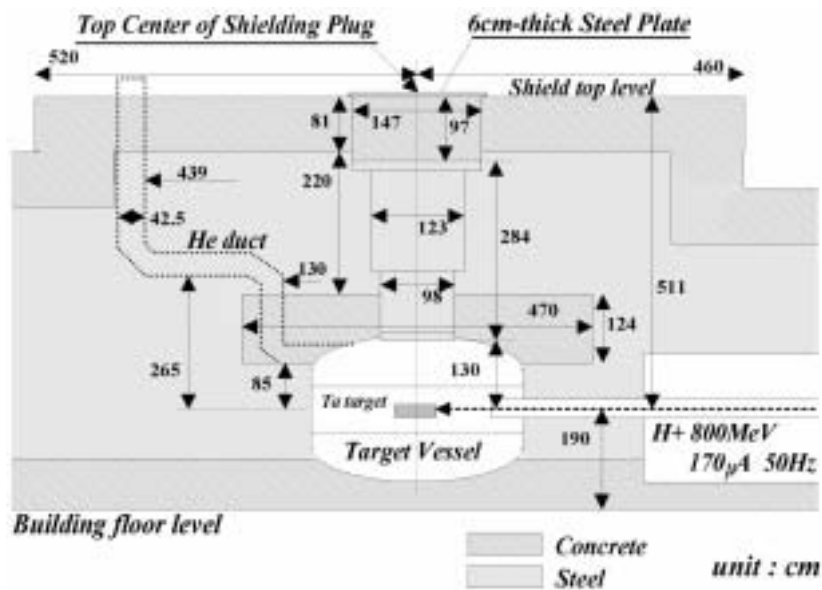
Measurements of neutron deep penetration through a thick bulk shielding have been performed to obtain benchmark experimental data at the intense spallation neutron source facility (ISIS) of the Rutherford Appleton Laboratory (RAL) since 1992 [1,2]. In a 1998 experiment, concrete and iron shields were additionally installed on the shield top floor of the target station to measure the neutron energy spectra and reaction rates behind shields of various thickness using activation detectors [3-5].

One-dimensional equivalent geometry Monte Carlo [6] and two-dimensional discrete ordinate calculations [7] had been performed earlier to analyse this ISIS shielding experiment; they were, however, inadequate to obtain the particle flux distributions, since a calculation with three-dimensional geometry based on the actual shield structure could hardly be accomplished. In this work, a deep-penetration calculation was performed with a three-dimensional multi-layer technique using the MARS14 Monte Carlo code [8] to analyse the ISIS shielding experiment [5]. The spatial distributions of the neutron flux and the energy spectra were thus obtained.

Shielding geometry of the ISIS target station

A cross-sectional view of the target station at ISIS is shown in Figure 1. A 130 cm void representing the inside of the target vessel is followed on the top by a bulk shield consisting of a 284 cm thick steel (7.35 g/cm³), 97 cm thick concrete (2.3 g/cm³) and a 6 cm thick steel vacuum plate. The shield top surface is located 528 cm above the beam line. In the 1998 experiment, an iron igloo was equipped for background neutron reduction and 119 cm diameter additional shields of 20 to 120 cm thick concrete (2.36 g/cm³) and 10 to 60 cm iron (7.8 g/cm³) were assembled at the shield top centre inside the iron igloo to measure the attenuation profiles of the neutron flux through the additional shields.

Figure 1. Cross-sectional view of the ISIS target station



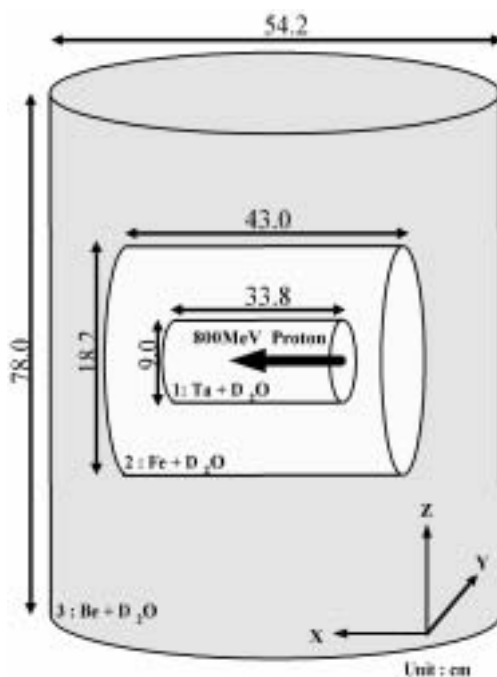
Calculation

A calculation employing a three-dimensional multi-layer technique was carried out using the MARS14 Monte Carlo code.

Target system and geometry

The calculation model of the target system includes a target, a container and a reflector, as shown in Figure 2. All of these are of cylindrical shape and have a common centre of (0, 0, 0). Two small cylinders are parallel to the X-axis, and the largest cylinder is perpendicular to it. The axes are defined as follows: X is a proton beam axis, Y is a horizontal axis perpendicular to the proton beam and Z is a vertical axis. An 800 MeV proton beam is injected from the bottom of the cylindrical target, as shown in Figure 2.

Figure 2. Target system geometry, consisting of: 1) a target, 2) a container and 3) a reflector. All cylinders have a common centre of (0, 0, 0).

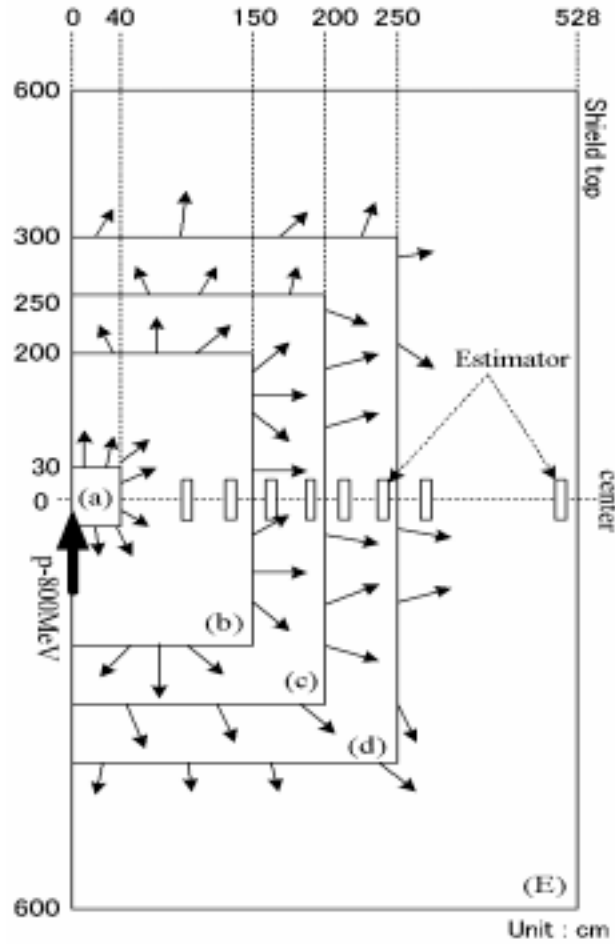


MARS multi-layer calculation

The shielding geometry is divided into several layers, as shown in Figure 3. The energy, co-ordinate, direction cosines and weights of the neutrons, protons and pions crossing the layer boundaries toward the outside were recorded and used as source terms for the next-layer calculation.

At the first stage, the information on the secondary particles leaked from the first layer (a), a 30 cm radius by 40 cm high cylinder which completely includes half of the target system, as shown in Figure 2, is stored. Since the geometry of the target system is symmetrical with respect to the $Z = 0$ plane, particles leaked in the region $Z < 0$ are also stored as those having an absolute value of Z co-ordinate and reversed Z vector. The weights of these particles are multiplied by 0.5.

Figure 3. Calculation geometry used in a three-dimensional multi-layer calculation using the MARS14 code. Neutrons leaked from region (a) were used as the source for region (b). The estimator indicates a track-length estimator as a neutron flux detector.



In this step-by-step calculation, the number of particles at the layer boundaries were multiplied by a factor of 5 to 10, similar to a splitting method. Track-length estimators (10 cm diameter and 5 cm thick) were located in the bulk shield and above the shield top to obtain the neutron energy spectra.

To save computing time, the cut-off energies of all particles were set to 20 MeV, up to about 1 m below the shield top floor; above that, those of neutrons and charged hadrons were set to be thermal and 0.2 MeV, respectively. This was done because the neutron attenuation in the lower-energy region is much faster than that in the high-energy region, and the contribution of the lower-energy neutron penetration behind a 1 m thick shield is negligible compared with the newly-generated lower-energy neutrons due to the high-energy hadron cascade.

Dose equivalent and reaction rates

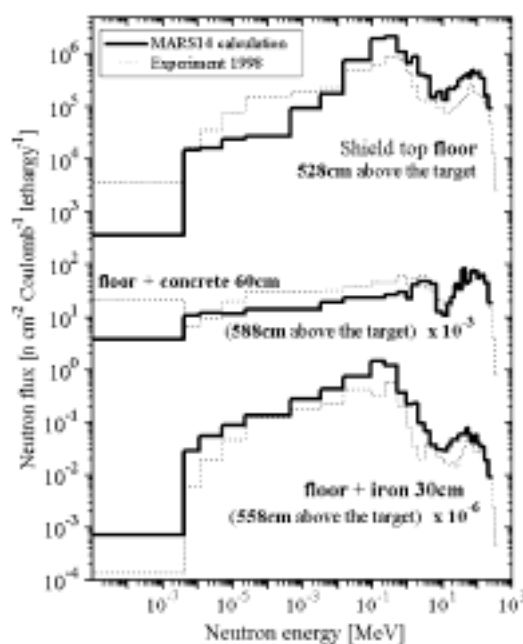
The neutron dose equivalent and $^{12}\text{C}(n,2n)^{11}\text{C}$ reaction rate inside and behind the bulk shield were estimated using the calculated neutron energy spectra. The neutron flux-to-dose conversion factor of 1 cm depth dose equivalent of ICRP Publication 74 [9] was used, and was assumed to be constant at $E > 200$ MeV.

Results and discussion

Neutron energy spectra

Figure 4 shows the calculated neutron energy spectra on the shield top floor, after adding 60 cm thick concrete and 30 cm thick iron, in comparison with the experimental data. Note that the calculated energy spectrum above 20 MeV on the additional concrete shield is in a good agreement within about 30%. On the shield top floor and on the additional iron shield, on the other hand, the calculated spectra agreed within a factor of 2 above 20 MeV and within a factor of 3 below 20 MeV.

Figure 4. Calculated neutron energy spectra at the shield top floor, behind a 60 cm thick concrete and a 30 cm thick iron additional shield, compared with the experimental data



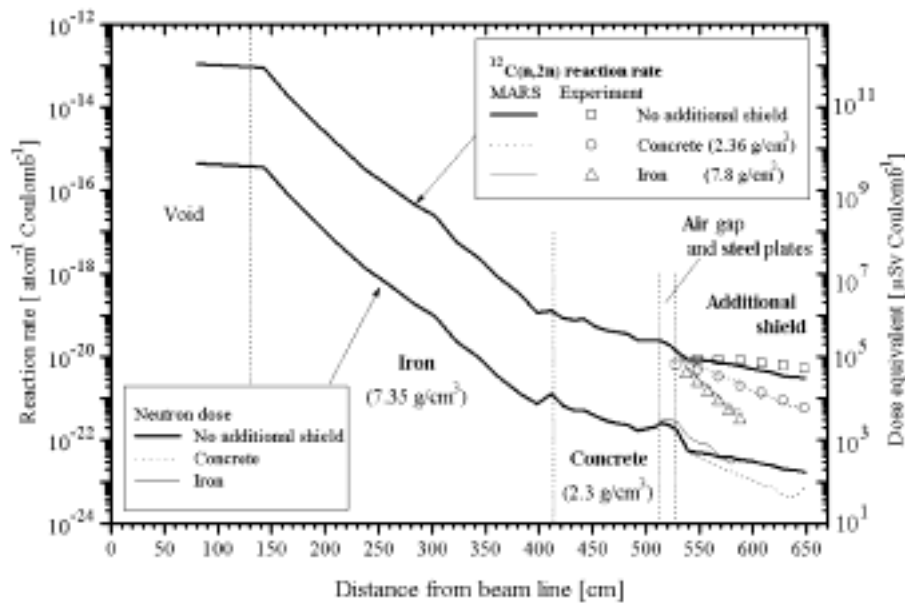
Reaction rate and dose equivalent

Attenuation profiles of the calculated neutron dose equivalent and $^{12}\text{C}(n,2n)$ reaction rate are shown in Figure 5. The measured reaction rates are also shown in the figure. Above the shield top floor without an additional shield, the attenuation profiles of the calculated and measured reaction rates show a slight difference, and the discrepancy of the reaction rate is a factor of 2 in the maximum case. On the other hand, the calculated reaction rates for additional concrete and iron generally agreed very well with the experimental data within 30%. It can be said that this calculation gave much more accurate values than the earlier simple calculations [1,6,7] which resulted in large underestimations of about one order.

Neutron attenuation length

The attenuation lengths of neutrons with additional shielding were also estimated from the attenuation profiles of the $^{12}\text{C}(n,2n)^{11}\text{C}$ reaction rates obtained in this manner, and are 116.7 and 150.3 g/cm³ for concrete and iron, respectively. These values are about 7% shorter than those estimated from the experiment.

Figure 5. Comparison of the calculated and measured attenuation profiles of the $^{12}\text{C}(n,2n)^{11}\text{C}$ reaction rate and the dose-equivalent rate through the bulk shield and the additional shield



Conclusion

An analysis of an ISIS shielding experiment with an 800 MeV proton beam on a tantalum target has been performed via a deep-penetration calculation with a three-dimensional multi-layer technique using the MARS14 Monte Carlo code. The neutron energy spectra behind a very thick shield of approximately 3 m iron and 1 m concrete were calculated in the energy range from thermal to 400 MeV, and agreed with the measurements within a factor of 3 in the high-energy region. The $^{12}\text{C}(n,2n)^{11}\text{C}$ reaction rates were also estimated from the calculated neutron energy spectra, and agreed within 20% and 30% behind the concrete and iron additional shields, respectively. The neutron attenuation lengths were also estimated in the additional shield, and are about 7% shorter than the experimental data.

Acknowledgements

We would like to thank Dr. Nikolai Mokhov of Fermi National Accelerator Laboratory for his great help with the MARS code system and useful comments on this paper.

REFERENCES

- [1] Uwamino, Y., T. Shibata, T. Ohkubo, S. Sato and D. Perry, "Study on Bulk Shielding of an 800 MeV Proton Accelerator", *OECD/NEA/NSC Specialists Meeting on Shielding Aspects of Accelerators, Targets and Irradiation Facilities (SATIF-1)*, Arlington, Texas, 185 (1994).
- [2] Nakao, N., T. Shibata, T. Ohkubo, S. Sato, Y. Uwamino, Y. Sakamoto and D.R. Perry, "Shielding Experiment at 800 MeV Proton Accelerator Facility", *Proc. 1998 ANS Radiation Protection and Shielding Division Topical Conference*, Nashville, Tennessee, Vol. 2, pp. 192-199 (1998).
- [3] Nunomiya, T., N. Nakao, P. Wright, T. Nakamura, E. Kim, T. Kurosawa, S. Taniguchi, M. Sasaki, H. Iwase, T. Shibata, Y. Uwamino, S. Ito and D.R. Perry, "Measurement of Deep Penetration of Neutron Produced by 800 MeV Proton Beam Through Concrete and Iron", *Nuclear Instrument and Methods B*, 179, 89-102 (2001).
- [4] Nakao, N., T. Shibata, T. Nunomiya, T. Nakamura, E. Kim, T. Kurosawa, S. Taniguchi, M. Sasaki, H. Iwase, Y. Uwamino, S. Ito, P. Wright and D.R. Perry "Deep Penetration Experiment at ISIS", *OECD/Nuclear Energy Agency, Specialists Meeting on Shielding Aspects of Accelerators, Targets and Irradiation Facilities (SATIF-5)*, Paris, France, 18 (2000).
- [5] Nunomiya, T., N. Nakao, P. Wright, T. Nakamura, E. Kim, T. Kurosawa, S. Taniguchi, M. Sasaki, H. Iwase, T. Shibata, Y. Uwamino, S. Ito and D.R. Perry, *Experimental Data of Deep-penetration Neutrons Through a Concrete and Iron Shield at the ISIS Spallation Neutron Source Facility Using an 800 MeV Proton Beam*, KEK Report 2001-24, February 2002.
- [6] Nakao, N. and Y. Uwamino, "Deep Penetration Calculation Compared with the Shielding Experiments at ISIS", *Proceedings of 9th International Conference on Radiation Shielding, J. Nucl. Sci. Technol.*, Supplement 1, 162 (March 2000).
- [7] Handa, H., M. Saitoh, K. Hayashi, K. Yamada, T. Abe and Y. Uwamino, "Analysis on High-energy Neutron Shielding Experiments in ISIS", *SARE-3*, KEK Proceedings 97-5, Vol. 97-5, 300 (1997).
- [8] Mokhov, N.V., *The Mars Code System User's Guide*, Fermilab-FN-628 (1995); also "MARS Code Status", Fermilab-Conf-00/181 (2000); <http://www-ap.fnal.gov/MARS>.
- [9] *Conversion Coefficients for Use in Radiological Protection Against External Radiation*, ICRP Publication 74, Oxford, Elsevier Science (1995).

**NUCLEAR PHOTOREACTIONS IN THE CONTEXT OF A NUCLEAR DATA REVIEW
FOR RADIATION SHIELDING IN ADVANCED TECHNOLOGY APPLICATIONS**

Giuseppe Maino, Enzo Menapace
ENEA, Applied Physics Division
via Fiammelli, 2, I-40129 Bologna, Italy

Abstract

Following the discussions at ICRS-9 and contributions on the matter at the SATIF-5 Workshop and at the International Conference on Nuclear Data for Science and Technology in Tsukuba (October 2001), recent advances are presented concerning evaluation activities at ENEA-FIS on photonuclear reaction data for radiation shielding within the framework of international co-operation initiatives. To this aim, specific model calculations are compared with the existing measured values concerning photon-induced reactions for Ti natural isotopes and the stable element, as a complement to the previously presented results. Relevant aspects of the present algebraic model approach are discussed, referring to the present reaction data, with special care to the extended model parameterisation features and to a critical comparison with the commonly adopted formulas and systematics.

Introduction

Needs and corresponding priorities for accurate and reliable photonuclear data, mainly in the giant dipole resonance energy region, originate both from the renewed interest in advanced technological solutions in new-concept power plants and from shielding aspects in accelerator applications, including the reliability of the computational simulations and the relevant software, based on nuclear data within the requested accuracy level.

In this context, many co-ordinated activities have recently been performed within the SATIF (Shielding Aspects of Accelerators, Targets and Irradiation Facilities) initiative, according to the NEA Nuclear Science Committee (NSC) and the derivative Working Party on Evaluation Co-operation (WPEC), referring to the national and regional OECD projects (mainly ENDF, JEFF and JENDL) on the evaluated nuclear data libraries, in co-operation with the IAEA.

A generally expressed concern has been that evaluated covariance data should be provided and included in the produced nuclear data files, both ENDF/B, JEFF and JENDL. These evaluated data uncertainties and the related methodology are of utmost importance for the deduction of the confidence interval of transport calculation results and, therefore, the impact on shielding design aspects, including the estimate of the overall costs of plants and facilities, according to radiation protection exigencies and constraints.

As a contribution to provide nuclear data for radiation shielding purposes within the framework of the international co-operations, research activities performed at ENEA were aimed to the development of valuable yet computationally simple nuclear models, the relevant computing codes and to their validation and parameterisation with respect to reliable experimental values and selected benchmarks. In particular, inelastic scattering reactions, energy and angular distributions of the emitted particles and gamma-rays, photonuclear reactions were considered.

Since then, a number of benchmark calculations have been performed aimed to validate the methodology and the relevant parameterisation, namely for photoabsorption and (γ,n) reactions of Ti natural isotopes.

Moreover, an in-depth discussion has taken place on the model features, as improved and validated at ENEA-FIS, for producing reference and physically meaningful calculations, in comparison with different available methods and recipes, considering that the present algebraic approach allows us to emphasise the main characteristics of collective motions and drastically simplify the problem from a computational point of view.

Needs for photonuclear data

The present interest of the international scientific community deals mainly with nuclear applications of the accelerators, chiefly including:

- i) *ADS systems for transmutation* of minor actinides (MA) and of long-lived fission products (LLFP), with applications concerning R&D on ADS under the KEK-JAERI Joint Project in Japan, the Advanced Accelerator Application (AAA) initiative in the United States and the European ADS programme, according to its road-map planning.
- ii) *Spallation neutron sources of the new generation*, where the most important programmes in the field are the development of SNS and LANSCE sources in the USA, that of the Japanese KEK-JAERI Joint Project, the SINQ and the planned ESS in Europe.

- iii) Accelerators for *advanced diagnostics systems* (such as electron accelerators for positron factories, photon and photoneutron sources, light-ion sources and FEL) and for *medical applications* in radiotherapy by means of beams of neutrons, protons and heavy ions.

General research exigencies for all those applications concern the shielding design and the related estimate of radiation dose distributions and significant activation rates. As a matter of fact, the topics relevant to shielding design are rather similar for accelerators with different purposes, especially referring to neutron and other radiation emission by the accelerator itself and the surrounding equipments, and to radiation transport and activation calculations and to their validation with respect to integral benchmarks.

Starting from these considerations, the NEA Nuclear Science Committee promoted the initiative called SATIF (Shielding Aspects of Accelerators, Targets and Irradiation Facilities). The results produced a number of workshop and meetings – this one is the sixth general conference – and published by the NEA represent the state of art in this research and application area of growing interest for both basic and technological studies.

The nuclides whose cross-sections and nuclear data have to be considered cover a wide range, including those relevant to human body, structural as well as shield materials, coolants, airborne and soil materials.

The corresponding nuclear data mainly deal with transport cross-sections (in particular double-differential distributions for particle and gamma-ray emissions) and activation cross-sections, including covariance data needed in order to deduce the confidence intervals in estimating the overall shielding parameters and costs.

Specific needs concern photonuclear reaction data, mainly regarding the electron accelerator applications mentioned above. As pointed out in the JEF/DOC-812 report, main exigencies concern measurements and evaluations of nuclear photoabsorption and (γ,n) reactions, thus including photoneutron yields for thin and thick targets and photoneutron angular distributions.

In recent years the IAEA Photonuclear Data Library has been produced, resulting from an *ad hoc* CRP on the matter, for incident photon energies basically up to 25 MeV. Therefore, a compilation of photoneutron production data (including thin and thick target yields and neutron angular distributions) has been produced and made available for high-photon energies, aimed at problems for shielding of new generation light sources and free-electron laser (FEL) facilities.

An important part of this work concerns development, updating and validation (with respect to the available measurements) of reliable model codes, including intranuclear cascade, pre-equilibrium and evaporation aspects, aimed to support new evaluations at both intermediate and high energies or, alternatively, to improve the existing computing modules for calculating nuclear data internally in the Monte Carlo transport codes.

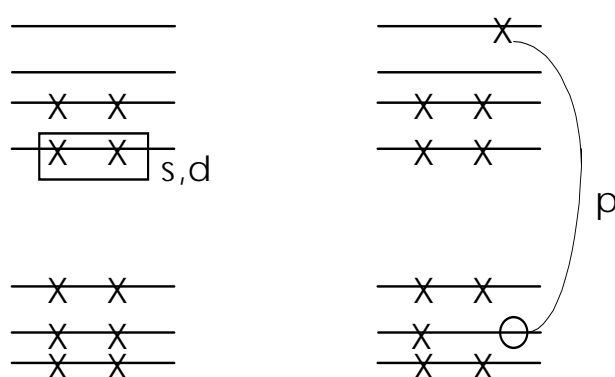
In this paper, we improve our algebraic model of nuclear structure in the energy range of giant resonances, based on versions 3 and 4 of the well-known Interacting Boson Model (IBM) of Arima and Iachello, and apply the relevant results to the evaluation of photonuclear data for isotopes and elemental titanium, where experimental data are scarce or lacking.

Theoretical model and photonuclear cross-section calculations

Our approach is based on a suitable extension of the Interacting Boson-Fermion Model (IBFM), in which the nuclear structure properties are described by means of a semi-phenomenological Hamiltonian consisting of interacting bosons and fermions, corresponding to neutron and proton pairs and unpaired nucleons, respectively, in the valence shells.

Thus, the present model includes the usual s- and d-bosons of the standard IBFM approach (as they are bosons with $L=0$ and 2 angular momenta and positive parity) and a further degree of freedom, a p boson with quantum numbers $L=1$ and negative parity, allowing for nuclear excitations across a major shell closure. In this way, it is possible to describe high-energy collective modes in nuclei, such as those relevant to giant dipole resonance (GDR) excitations.

Figure 1. Structure of s,d and p interacting bosons



In order to evaluate the nuclear photoreaction cross-sections in the MeV energy region, one has therefore to diagonalise a suitable IBFM Hamiltonian in a truncated shell-model space, with typical dimensions of a few hundred eigenvectors, and then to calculate the dipole transition elements which are provided by the expectation values of the p-boson creation and annihilation operators.

Finally, each GDR theoretical component must be folded with an intrinsic width, physically corresponding to the coupling to continuum 2p-2h levels, while the coupling to discrete low-lying states is already provided by the p-boson model. More technical details on the model and the relevant calculations can be found in the literature quoted at the end of this paper.

Moreover, it should be pointed out that, as for light- and medium-mass isotopes, where neutrons and protons occupy the same major shells, isospin is a useful quantum number and it has to be explicitly included in the IBFM calculations. Our p-boson IBFM Hamiltonian – in order to deal with Ti nuclides – must be consequently generalised by including isospin degree of freedom and a further splitting of GDR components arise because of different isospin values. In this article, we present results obtained in a very simple analytical limit, $SU(3)^*$, of the IBFM, where the existence of a (near) exact dynamical symmetry – corresponding to a stable triaxial shape of the nuclear ground state in all the considered isotopes – allows us to apply closed-form expressions for the various photonuclear reactions. Detailed, more refined calculations will be presented in a forthcoming, more lengthy, paper.

By means of many remarkable results (see the enclosed reference list), the capability of the present algebraic approach is shown in reproducing the experimental pronounced broad structure – from dipole, quadrupole and octupole component contributions – which could not be predicted by the simple cross-section shape resulting by the commonly adopted dipole approach and the related systematics or

even more sophisticated microscopic models. In the present cases, shown in the following figures, the weak-coupling limit gives satisfactory results as far as comparisons between measured and calculated photoabsorption cross-sections are concerned, when the former is available. If experimental data are not available, the present results represent a useful source of information for compiling reliable sets of photonuclear data.

Figure 2. (γ,n) cross-section for ^{46}Ti

Experimental data are taken from R.E. Pywell and M.N. Thompson, *Nucl. Phys.*, A318 (1979) 461.

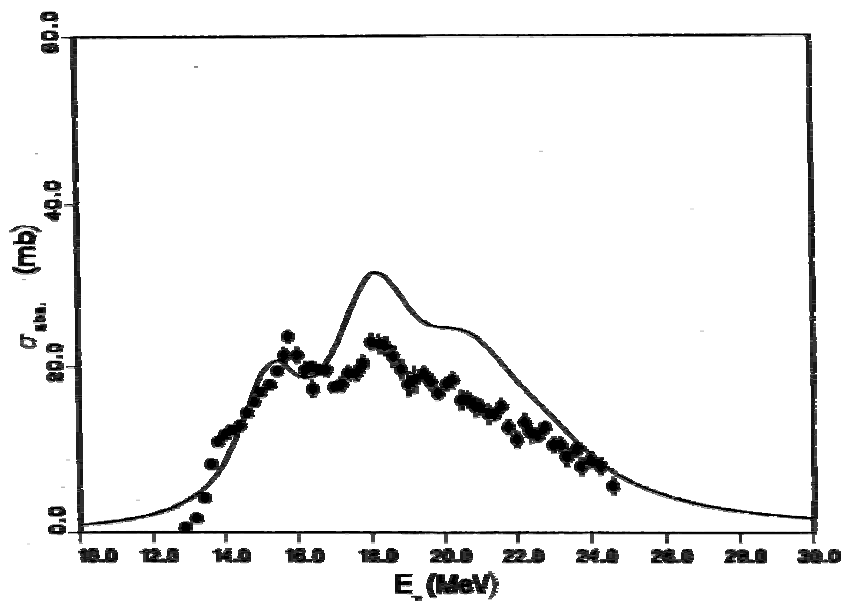


Figure 3. (γ,p) cross-section for ^{46}Ti

Experimental data are taken from S. Oikawa and K. Shoda, *Nucl. Phys.*, A277 (1977) 301.

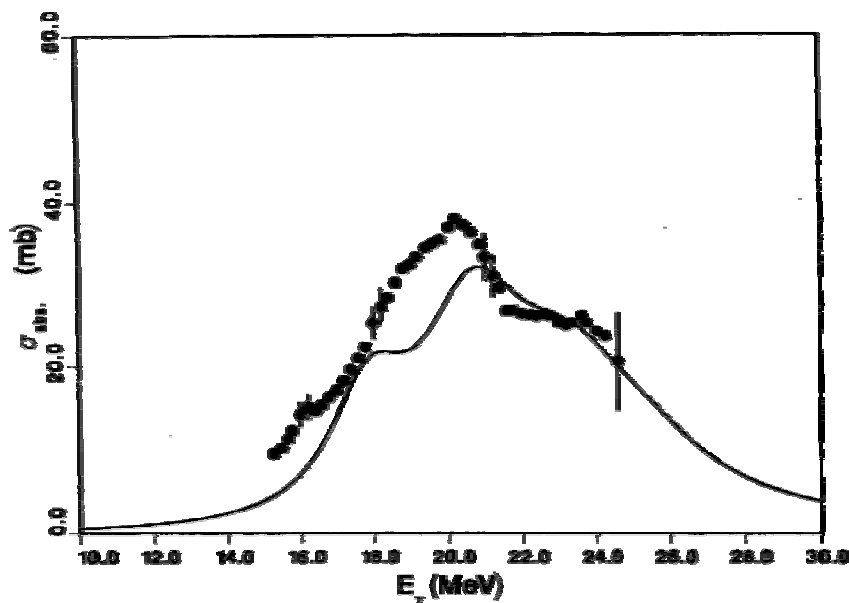


Figure 4. Total photoabsorption cross-section for ^{46}Ti

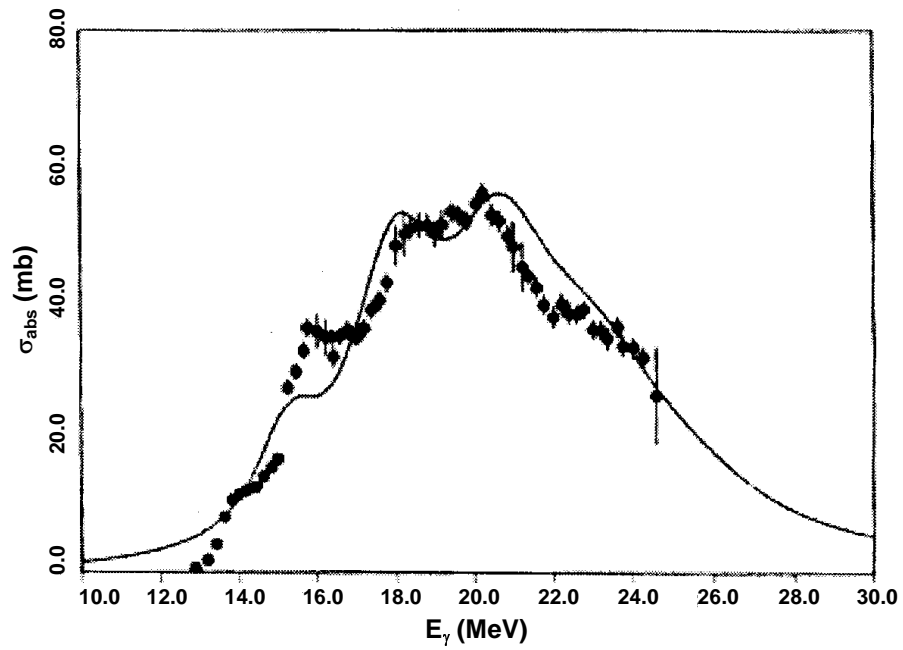


Figure 5. (γ, n) cross-section for ^{48}Ti

Experimental data are taken from R. Sutton, M.N. Thompson, M. Sugawara, K. Shoda, T. Saito and H. Tsubota, *Nucl. Phys.*, A339 (1980) 125.

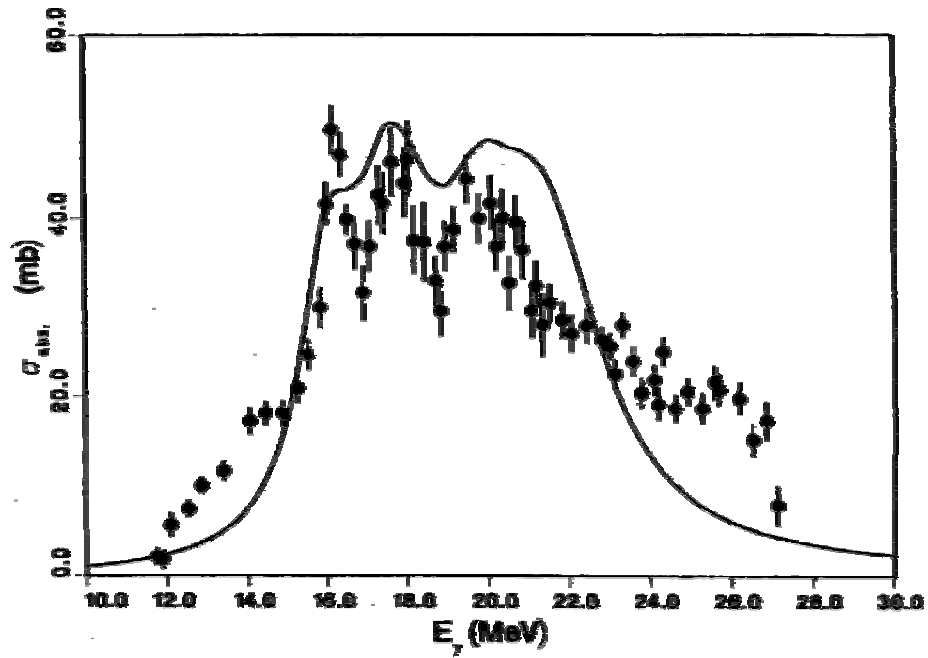


Figure 6. (γ,p) cross-section for ^{48}Ti

Experimental data are taken from J. Weise, *et al.*, Research Report of Lab. of Nucl. Sci., University of Tohoku, 11 (1978) 43.

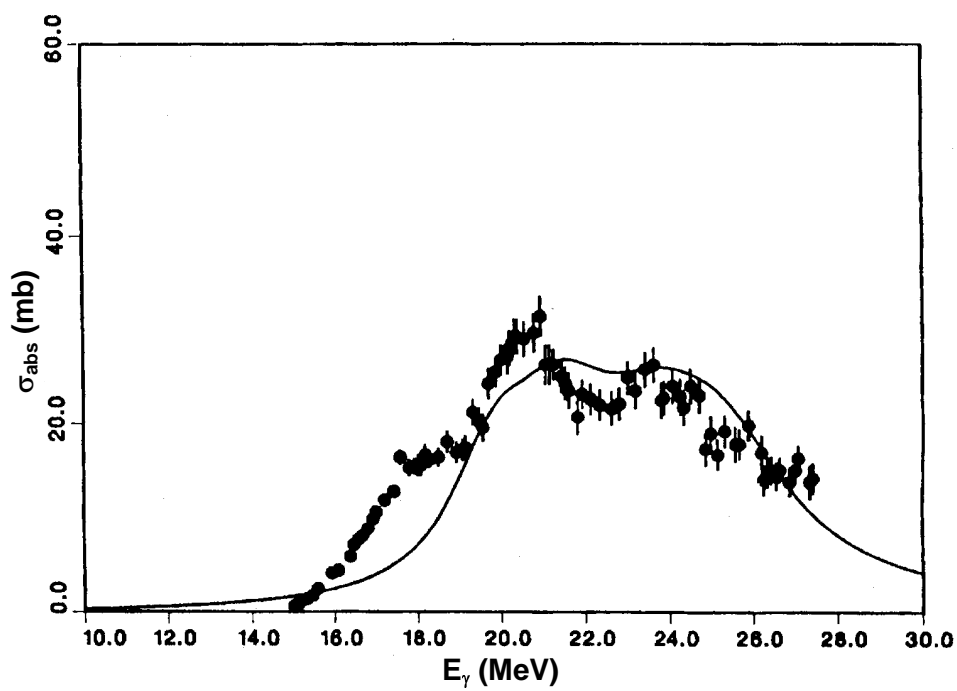


Figure 7. Total photoabsorption cross-section for ^{48}Ti

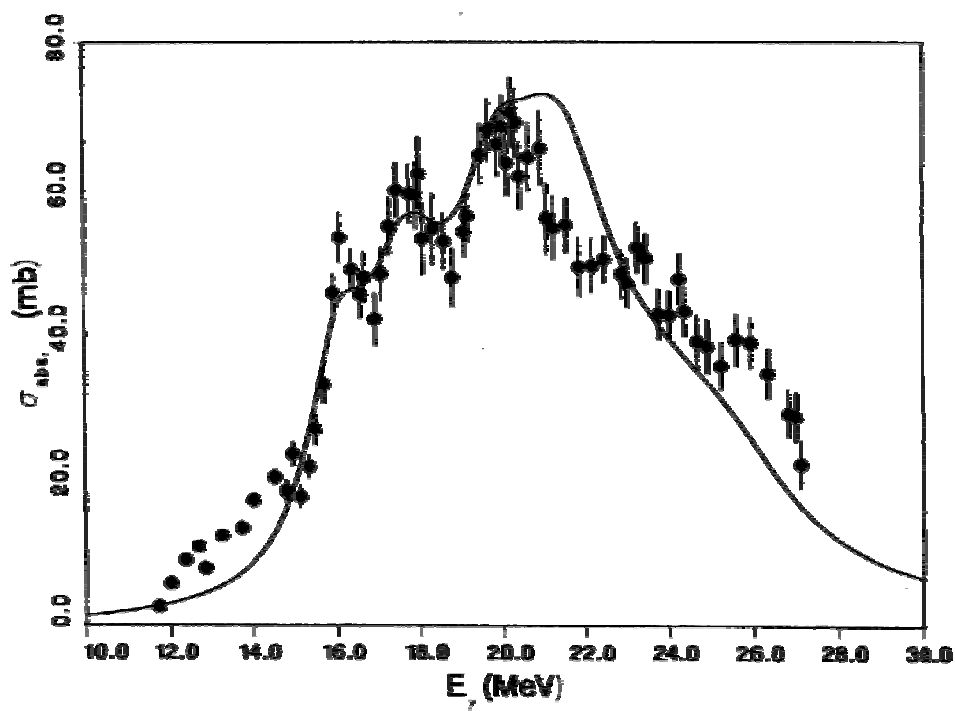


Figure 8. (γ, n) cross-section for ^{nat}Ti

Experimental data are taken from: S. Costa, F. Ferrero, C. Manfredotti,
L. Pasqualini, G. Piragino and H. Arenhovel, *Nuovo Cim.*, B48, 460 (1967).

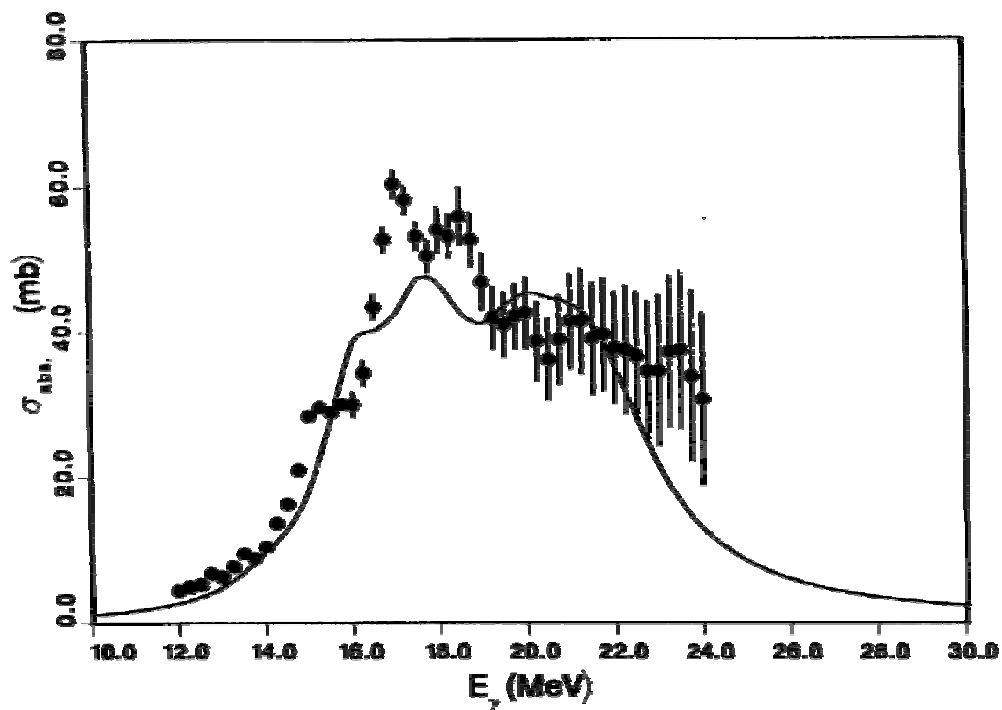


Figure 9. (γ, p) cross-section for ^{nat}Ti

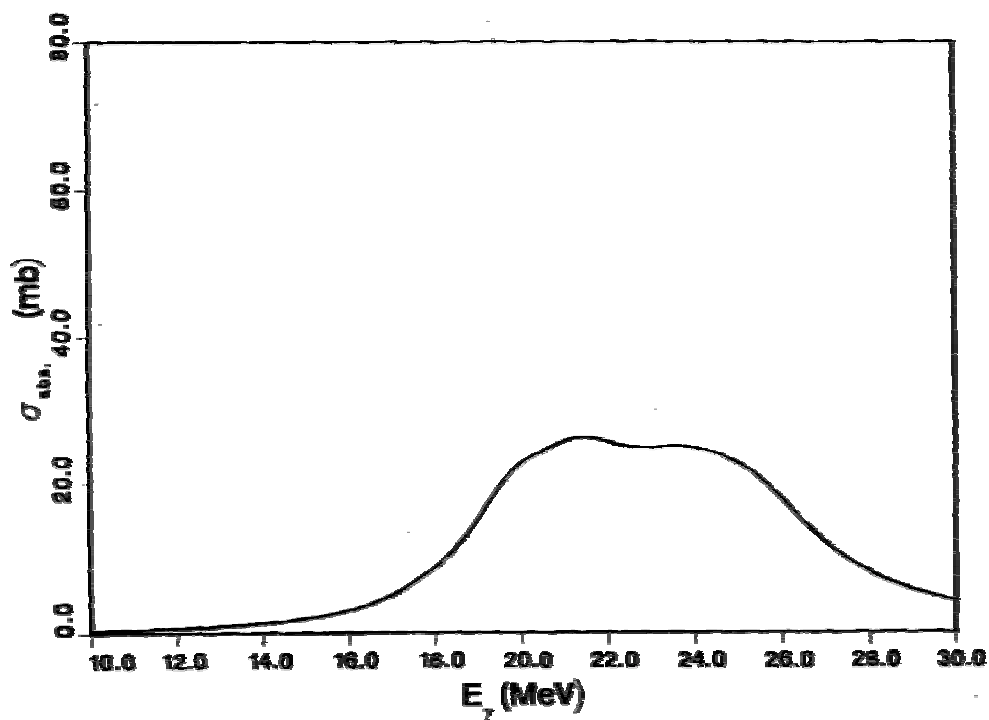
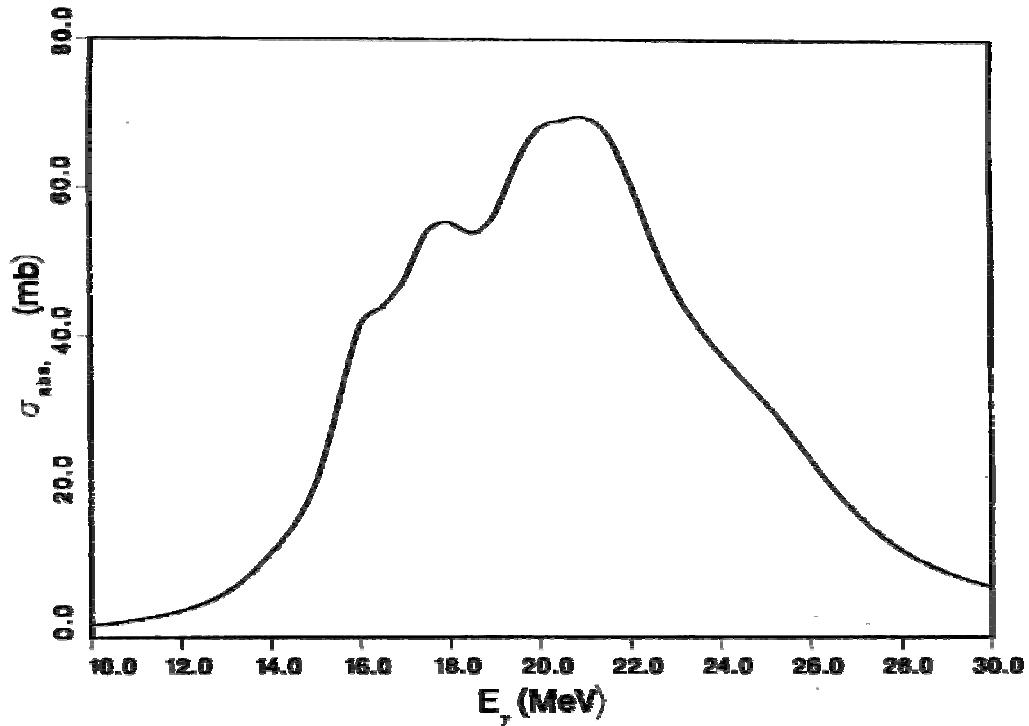


Figure 10. Total photoabsorption cross-section for ^{nat}Ti



Conclusions

In the context of model calculations performed at the ENEA Applied Physics Division on nuclear reaction data relevant to radiation shielding for accelerator applications, the main features of the algebraic model approach to giant resonances within the IBFM framework have been briefly reviewed. This model can provide us with a simple, efficient tool to investigate nuclear structure properties and to predict nuclear photoreaction data in the energy region above 10 MeV, as shown by the presented results, taking into account that the p-boson model can be easily related to a geometrical interpretation. The obvious drawback is that, being semi-phenomenological, the present algebraic description of giant resonances requires adjustable parameters (however, constant or slightly varying with the mass number) determined on the basis of the available experimental information.

On the whole, the present IBFM algebraic approach allows a physically consistent framework to deal with nuclei in transitional-shape regions. Then, it can be used to draw out reasonable theoretical predictions of the form and strength of the GDR excitation functions even where experimental data are not available or show large discrepancies.

REFERENCES

- [1] Menapace, E., *Proc. ICRS-9 Conference, Journal of Nuclear Science and Technology*, Supplement 1, pp. 68-72 (2000).
- [2] Menapace, E., *et al.*, *Proc. ANS Meeting on Applications of Accelerator Technology*, Albuquerque, p. 190 (1997).
- [3] Nakamura, T., T. Fukahori, E. Menapace, “Relevant Nuclear Data Topics Related to Shielding Aspects of Accelerators and Irradiation Facilities”, *Proc. Int. Conference on Nucl. Data for Sci. and Tech.*, Trieste, p. 1478 (1997).
- [4] Menapace, E., *Proc. Int. Conf. on Nucl. Data for Sci. and Tech.*, Gatlinburg, p. 18 (1994).
- [5] Frisoni, M. and E. Menapace, “Needs and Advances on Nuclear Data for Medical Radioisotope Production”, *Proc. Int. Conf. on Nucl. Data for Sci. and Tech.*, Trieste, p.1713 (1997).
- [6] Iachello, F. and P. Van Isacker, *The Interacting Boson-Fermion Model*, Cambridge University Press (1991).
- [7] Maino, G., “Algebraic Methods for Many-body Systems”, *The Physics of Complex Systems*, IOS Press, Amsterdam, p. 637 (1997).
- [8] Bortolani, E. and G. Maino, “Photon Absorption and Scattering Cross-sections by Triaxial Nuclei”, *Computer Physics Communications*, 70, 207-218 (1992).
- [9] Bortolani, E. and G. Maino, “Isospin and Deformation Splittings of the Giant Dipole Resonance for Triaxial Nuclei”, *Physical Review*, C43, 353-356 (1991).
- [10] Canetta, E. and G. Maino, “On the Different Forms of the IBM-2 Hamiltonian”, *Int. Journal of Modern Physics*, E8, 321-335 (1999).
- [11] Maino, G. and E. Menapace, “Nuclear Photoreactions in the Context of a Nuclear Data Review for Radiation Shielding in Advanced Technology Applications”, *Journal of Nuclear Science and Technology* (in press).
- [12] Canetta, E., G. Maino and E. Menapace, “Evaluation of Nuclear Data for Radiation Shielding by Model Calculations and International Co-operation Aspects”, *Proc. of the Workshop on Shielding Aspects of Accelerators, Targets and Irradiation Facilities (SATIF-5)*, Paris, 17-21 July 2000, OECD/NEA, Paris, pp. 405-415 (2001).
- [13] Maino, G. and E. Menapace, “Nuclear Photoreactions for Applications in Industrial and Technological Fields”, *Proc. Int. Conference on Nucl. Data for Sci. and Tech. (ND2001)*, Tsukuba, Ibaraki, Japan, 7-12 October 2001.
- [14] Maino, G. and E. Menapace, *Photonuclear Reaction Data for Multi-purpose Applications*, report JEF/DOC-888 (2001) (in press).

SESSION IV

Dose and Related Issues

Chairs: M. Pelliccioni, A. Leuschner

CONVERSION COEFFICIENTS: AN ADDITION TO EXISTING DATA

Maurizio Pelliccioni

Istituto Nazionale di Fisica Nucleare, Italy

Abstract

Calculations of fluence-to-effective dose conversion coefficients have typically been limited to the standard irradiation geometries of the human body: anterior-to-posterior (AP), posterior-to-anterior (PA), lateral from the right side to the left side (RLAT), lateral from the left side to the right side (LLAT), rotational around the vertical axis (ROT), isotropic incidence from all directions (ISO). However, in some locations at the accelerators, radiation may impinge predominantly from either above or below. Therefore, it was considered useful to extend the calculations to these geometries, at least in the case of photons (from 10 keV to 10 GeV) and neutrons (from thermal energies to 10 GeV). The calculated results are presented.

Introduction

Although the number of conceivable geometries in which the human body might be irradiated is virtually limitless, calculations of effective dose have typically been limited to the standard irradiation geometries: anterior-to-posterior (AP), posterior-to-anterior (PA), lateral from the right side to the left side (RLAT), lateral from the left side to the right side (LLAT), rotational around the vertical axis (ROT), isotropic incidence from all directions (ISO). The conversion coefficients recommended by the international bodies refer to the standard geometries and monoenergetic radiation [1,2].

The geometries defined above are idealised. However, they may be taken as approximations to actual conditions of exposure. When a precise calculation of effective dose is needed for a particular realistic geometry and source, a case-specific calculation would normally have to be computed [3].

In certain environments, like accelerators or nuclear power stations, irradiation geometries that accurately describe practical situations, other than those previously described, may be defined. In some places radiation may impinge predominantly from either above or below. In literature, conversion coefficients in terms of effective dose for these irradiation geometries can be found only for neutrons up to 20 MeV, unfortunately in graphical presentation [4].

Therefore, it was considered useful to extend the calculation of effective dose to these geometries at least in the cases of photons and neutrons. Calculations have been carried out by the most recent version of the FLUKA code [5-8].

An energy range from thermal energies to 10 GeV was considered for neutrons, and from 10 keV to 10 GeV for photons.

Details of the method of calculation have been described to some extent in a previous paper dealing with conversion coefficients for high-energy radiation calculated using the FLUKA code [9]. In particular, readers are referred to this review for details about the mathematical model of the human body used for the simulations.

Results and discussion

Tables 1 and 2 show the calculated conversion coefficients as a function of neutron energy in the case of the irradiation of the mathematical phantom from above and from below, respectively. Since in Publication 60 the ICRP recommended two different sets of radiation weighting factors for neutrons (see Table 1 of paragraph 26 and as an approximation the continuous function given in paragraph A12), the corresponding two sets of conversion coefficients are reported in Tables 1 and 2. As a consequence of the discrepancies between the two sets of recommended radiation weighting factors, the calculated conversion coefficients are diverging up to several tens per cent in the energy range between $5.0E-6$ GeV and 0.05 GeV.

In the opinion of the present author the continuous approximation should not have been used in the calculation of conversion coefficients. It is not clear why people who work, for example, with 100 keV neutrons should use conversion coefficients corresponding to a radiation weighting factor of 16 instead of 10. Unfortunately, it must be taken into account that this was the case for the official coefficients recommended by ICRP (Publication 74) and ICRU (Report 57).

Figures 1 and 2 provide a graphical presentation of the data in Tables 1 and 2. In particular, Figure 1 shows both sets of conversion coefficients from above and from below calculated using the discrete values recommended for the radiation weighing factors. In Figure 2, these sets of conversion

Table 1. Conversion coefficients fluence to effective dose as a function of neutron energy for the irradiation from above

Neutron energy (GeV)	Effective dose per unit fluence (Sv·cm ²)	Effective dose per unit fluence (w _R appr.) (Sv·cm ²)	St. dev. (%)
1.0E-12	7.81E-13	7.81E-13	2.4
1.0E-11	7.81E-13	7.81E-13	2.4
1.0E-10	7.81E-13	7.81E-13	2.4
1.0E-09	1.19E-12	1.19E-12	1.9
1.0E-08	1.27E-12	1.27E-12	3.0
1.0E-07	1.25E-12	1.25E-12	3.7
1.0E-06	1.20E-12	1.21E-12	2.3
5.0E-06	1.18E-12	1.30E-12	2.3
1.0E-05	2.49E-12	1.58E-12	2.1
5.0E-05	3.09E-12	3.71E-12	1.8
1.0E-04	4.23E-12	6.79E-12	2.1
2.0E-04	1.20E-11	1.18E-11	1.5
5.0E-04	2.23E-11	2.45E-11	1.0
1.0E-03	3.53E-11	3.66E-11	1.0
2.0E-03	6.48E-11	5.62E-11	0.8
5.0E-03	7.11E-11	8.54E-11	0.7
1.0E-02	1.21E-10	1.06E-10	0.5
1.9E-02	1.84E-10	1.27E-10	0.8
2.0E-02	1.88E-10	1.27E-10	0.8
2.1E-02	9.62E-11	1.28E-10	0.9
5.0E-02	1.65E-10	1.82E-10	0.7
1.0E-01	2.87E-10	2.96E-10	2.0
1.5E-01	3.78E-10	3.84E-10	0.6
2.0E-01	4.55E-10	4.59E-10	0.9
5.0E-01	6.33E-10	6.34E-10	1.3
1.0E+00	8.54E-10	8.55E-10	1.8
5.0E+00	2.25E-09	2.25E-09	0.9
1.0E+01	3.84E-09	3.84E-09	0.8

Table 2. Conversion coefficients fluence to effective dose as a function of neutron energy for the irradiation from below

Neutron energy (GeV)	Effective dose per unit fluence (Sv·cm ²)	Effective dose per unit fluence (w _R appr.) (Sv·cm ²)	St. dev. (%)
1.0E-12	1.37E-12	1.37E-12	5.3
1.0E-11	1.37E-12	1.37E-12	5.3
1.0E-10	1.37E-12	1.37E-12	5.3
1.0E-09	2.12E-12	2.12E-12	1.3
1.0E-08	2.13E-12	2.13E-12	2.8
1.0E-07	1.80E-12	1.80E-12	2.8
1.0E-06	1.74E-12	1.75E-12	1.7
5.0E-06	1.58E-12	1.73E-12	3.4
1.0E-05	3.63E-12	5.83E-12	1.1
5.0E-05	5.54E-12	6.66E-12	1.1
1.0E-04	9.10E-12	1.46E-11	0.9
2.0E-04	2.99E-11	2.96E-11	0.9
5.0E-04	6.00E-11	6.60E-11	1.0
1.0E-03	9.47E-11	9.79E-11	0.2
2.0E-03	1.51E-10	1.31E-10	0.7
5.0E-03	1.22E-10	1.46E-10	1.1
1.0E-02	1.77E-10	1.56E-10	1.5
1.9E-02	2.43E-10	1.67E-10	0.4
2.0E-02	2.41E-10	1.63E-10	1.2
2.1E-02	1.23E-10	1.63E-10	1.1
5.0E-02	1.58E-10	1.74E-10	1.8
1.0E-01	2.35E-10	2.43E-10	0.9
1.5E-01	3.07E-10	3.12E-10	0.8
2.0E-01	3.78E-10	3.81E-10	1.2
5.0E-01	5.66E-10	5.67E-10	1.1
1.0E+00	7.86E-10	7.86E-10	1.2
5.0E+00	2.37E-09	2.37E-09	1.7
1.0E+01	4.29E-09	4.29E-09	0.5

Figure 1. Conversion coefficients fluence to effective dose from above and from below, calculated using the discrete values recommended for the radiation weighting factors in the ICRP Publication 60, as a function of neutron energy. The ambient dose equivalent per unit of fluence as a function of neutron energy is also shown.

● – from above, ○ – from below, * – ambient dose equivalent

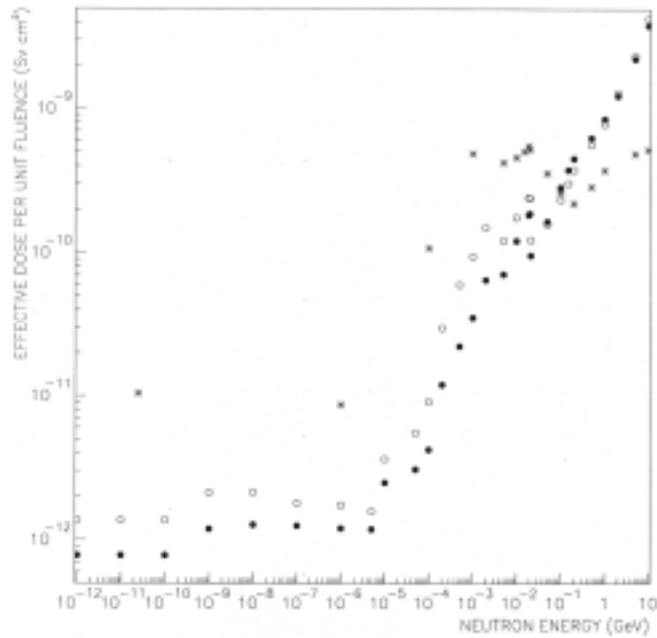
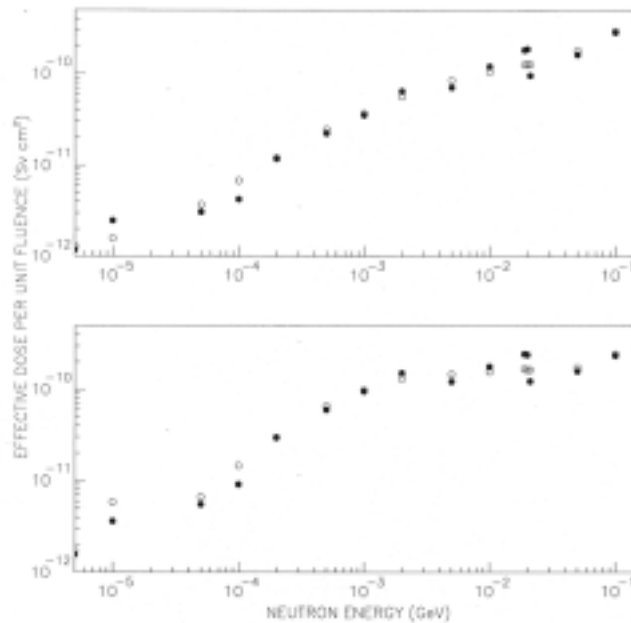


Figure 2. Comparison of the neutron conversion coefficients fluence to effective dose calculated using both the sets of radiation weighting factors recommended in the ICRP Publication 60

Top panel – irradiation from above, Bottom panel – irradiation from below

● – w_R according to Table 1 of ICRP Publication 60

○ – w_R according to the continuous function recommended in paragraph A12 of ICRP Publication 60



coefficients are compared to those calculated according to the continuous approximation of the radiation weighting factors. The ambient dose equivalent per unit of fluence as a function of neutron energy, according to previous calculations [9], is also shown in Figure 1.

The irradiation from below provides effective doses greater than those from above up to about 50 MeV. The reason for this is the higher doses received by the colon and, initially, the gonads. Above 1 GeV the irradiation from below is again more hazardous than that from above, due to the higher doses received in practically all the main organs and tissues.

Both geometries usually originate conversion coefficients lower than the standard geometries.

As shown in Figure 1, the ambient dose equivalent is a conservative predictor of the effective dose for neutron energy up to about 50 MeV.

Note that calculations have been performed at three very close neutron energies (19, 20, 21 MeV) in that they are very significant. Below 19.6 MeV FLUKA uses the kerma factors in order to estimate energy depositions, while above this energy a nuclear model applies. The coherence between the results at 19 and 20 MeV proved the reliability of the code in predicting energy deposition in both energy regions. The effective dose strongly declines from 20 to 21 MeV as an effect of the rude change of the radiation weighting factor from 10 to 5. Of course, the effect disappears when using continuous approximation for the radiation weighting factors.

Tables 3 and 4 show the calculated conversion coefficients as a function of photon energy in the case of irradiation of the mathematical phantom from above and from below, respectively. A graphical presentation of the data is provided in Figure 3, where both sets of conversion coefficients are shown along with the ambient dose equivalent according to previous calculations [9].

Table 3. Conversion coefficients fluence to effective dose as a function of photon energy for the irradiation from above

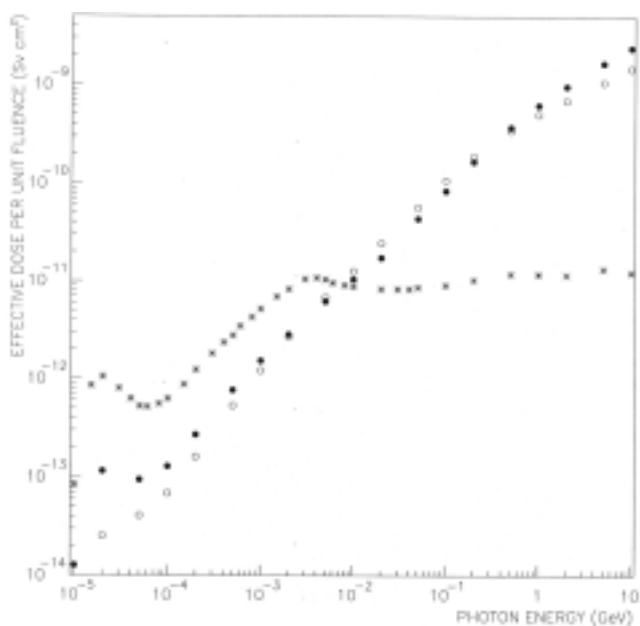
Photon energy (GeV)	Effective dose per unit fluence (Sv·cm ²)	St. dev. (%)
1.0E-05	6.03E-15	1.1
2.0E-05	2.53E-14	2.8
5.0E-05	4.09E-14	1.5
1.0E-04	6.88E-14	1.0
2.0E-04	1.61E-13	0.7
5.0E-04	5.29E-13	1.3
1.0E-03	1.21E-12	0.8
2.0E-03	2.67E-12	0.7
5.0E-03	6.79E-12	0.8
1.0E-02	1.26E-11	0.9
2.0E-02	2.44E-11	1.7
5.0E-02	5.70E-11	1.5
1.0E-01	1.08E-10	0.6
2.0E-01	1.89E-10	0.9
5.0E-01	3.45E-10	1.2
1.0E+00	5.03E-10	1.8
2.0E+00	6.95E-10	1.1
5.0E+00	1.07E-09	1.1
1.0E+01	1.48E-09	2.1

Table 4. Conversion coefficients fluence to effective dose as a function of photon energy for the irradiation from below

Photon energy (GeV)	Effective dose per unit fluence (Sv.cm ²)	St. dev. (%)
1.0E-05	1.27E-14	1.8
2.0E-05	1.15E-13	1.2
5.0E-05	9.43E-14	1.4
1.0E-04	1.29E-13	1.9
2.0E-04	2.70E-13	1.9
5.0E-04	7.61E-13	1.2
1.0E-03	1.52E-12	1.4
2.0E-03	2.84E-12	1.4
5.0E-03	6.18E-12	1.1
1.0E-02	1.04E-11	1.2
2.0E-02	1.73E-11	2.0
5.0E-02	4.38E-11	0.8
1.0E-01	8.45E-11	0.6
2.0E-01	1.68E-10	0.8
5.0E-01	3.71E-10	1.3
1.0E+00	6.24E-10	0.9
2.0E+00	9.72E-10	0.9
5.0E+00	1.67E-09	1.1
1.0E+01	2.38E-09	1.0

Figure 3. Conversion coefficients fluence to effective dose from above and from below as a function of photon energy. The ambient dose equivalent per unit of fluence as a function of photon energy is also shown

● – from above, ○ – from below, * – ambient dose equivalent



The irradiation from below gives effective doses greater than those from above up to about 2 MeV, predominantly due to the gonadal dose, and from 500 MeV, due to slightly greater doses to practically all the main organs and tissues. In the energy range between 2 MeV and 500 MeV, doses received by thyroid and lung make the irradiation from the top slightly more important than that from bottom.

Both the geometries generate conversion coefficients usually higher than the standard geometries, from 100 MeV in the case of the irradiation from the top and from 200 MeV in the case of the irradiation from the bottom.

As shown in Figure 3, the ambient dose equivalent is a conservative predictor of the effective dose for photon energy up to about 50 MeV.

Conclusions

The present results can be considered as an addition to existing data on conversion coefficients from fluence to effective dose. They could be of help when radiation may impinge predominantly from above or from below, which is a condition that sometimes occurs in certain environments at accelerators.

REFERENCES

- [1] International Commission on Radiological Protection, *Conversion Coefficients for Use in Radiological Protection Against External Radiation*, ICRP Publication 74, Annals of ICRP, 26, No. 3/4 (1996).
- [2] International Commission on Radiation Units and Measurements, *Conversion Coefficients for Use in Radiological Protection Against External Radiation*, ICRU Report 57 (Bethesda, MD, ICRU Publications) (1998).
- [3] See for example Pelliccioni, M., M. Silari and L. Ulrici, "Narrow Beam Dosimetry for High-energy Hadrons and Electrons", *Radiation Protection Dosimetry*, 95, 323-332 (2001).
- [4] Hollnagel, R.A., "Conversion Function of Effective Dose E and Effective Dose Equivalent H_E for Neutrons with Energies from Thermal to 20 MeV", *Radiat. Prot. Dos.*, 54, 209-212 (1994).
- [5] Fassò, A., A. Ferrari, J. Ranft, P.R. Sala and G.R. Stevenson, "FLUKA: Hadronic Benchmarks and Applications", *Proc. MC93 Monte Carlo Conference*, Tallahassee, Florida, 22-26 Feb. 1993, 88 (1994).
- [6] A. Fassò, A. Ferrari, J. Ranft and P.R. Sala, "An Update about FLUKA", *Proc. 2nd Workshop on Simulating Accelerator Radiation Environments (SARE-2)*, CERN, 8-11 October 1995, pp. 158-170 (1997).

- [7] Fassò, A., A. Ferrari, J. Ranft and P.R. Sala, “New Developments in FLUKA Modelling of Hadronic and EM Interactions”, *Proc. 3rd Workshop on Simulating Accelerator Radiation Environment (SARE-3)*, KEK-Tsukuba, H. Hirayama, ed., KEK Report 97-5, 7-9 May 1997, p. 32 (1997).
- [8] Ferrari, A. and P.R. Sala, “The Physics of High-energy Reactions”, *Proceedings of the Workshop on Nuclear Reaction Data and Nuclear Reactors Physics, Design and Safety*, ITCP, Miramare-Trieste, Italy, 15 April-17 May 1996, *World Scientific*, Vol. 2, p. 424 (1998).
- [9] Pelliccioni, M., “Overview of Fluence-to-effective Dose and Fluence-to-ambient Dose Equivalent Conversion Coefficients for High-energy Radiation Calculated Using the FLUKA Code”, *Radiat. Prot. Dos.*, 88, 279-298 (2000).

**THE EFFECT OF THE FLUENCE-TO-DOSE CONVERSION COEFFICIENTS
UPON THE DOSE ESTIMATION TO COSMIC RADIATION**

Vladimir Mares

University of Munich, Institute of Radiobiology
Schillerstraße 42, D-80336 München

Hans Schraube

GSF – National Research Center for Environment and Health, Institute of Radiation Protection
Ingolstädter Landstraße 1, D-85764 Neuherberg

Abstract

The MCNPX Monte Carlo code of Los Alamos National Laboratory was employed to calculate the organ doses in the anthropomorphic phantoms ADAM and EVA irradiated by monoenergetic fields of neutrons, protons, electrons, photons, charged pions and muons especially in the energy range of practical interest for air crew dose assessment. From the weighted organ doses the fluence-to-effective dose conversion coefficients were calculated according to ICRP recommendations. Using this consistent set of conversion coefficients along with the particle spectra for the specific geographic position and altitude the dose components can be determined to which an individual is exposed along an aviation route. The effect of the different fluence-to-dose conversion coefficients used for the dose estimation to cosmic radiations is discussed.

Introduction

The cosmic radiation field in the Earth's atmosphere is a complex environment consisting of neutrons, protons, photons, electrons, positrons, pions, muons and heavy ions. Its spectral and particle composition depends on the primary galactic cosmic rays which enter the atmosphere, collide with atomic nuclei in air, and create cascades of the secondary charged and uncharged particles.

The primary spectrum is modulated by solar activity and influenced by the magnetic field of the Earth. The geomagnetic field deflects the low-energy charged particles back into space and prevents them from entering the atmosphere. The third parameter that affects the strength of the cosmic radiation is the altitude, i.e. height above the sea level. Namely, the mass thickness of the air above the altitude provides a shielding effect of the atmospheric layer. Consequently, the intensity and energy distribution of cosmic radiation vary with altitude, location in the geomagnetic field and the point of time in the solar activity cycle.

So as to be able to calculate the effective dose from the particle fluences in the atmosphere, the fluence-to-effective dose conversion coefficients of all particle types produced by the galactic cosmic rays have to be determined by radiation transport calculation in anthropomorphic phantoms. Using this set of conversion coefficients along with the specific particle spectra, one can determine the particle dose components obtained by persons at any point in the atmosphere. Fluence rates and energy distributions for neutrons, protons, charged pions, photons, electrons and muons calculated by the FLUKA Monte Carlo transport code for the different civil flight conditions can be found in [1,2].

The fluence-to-effective dose conversion coefficients for energies below approximately 20 MeV can be found in ICRP Publication 74 [3] or in ICRU Report 57 [4], or for neutrons in [5] and for photons in [6]. In the high-energy range a limited number of data is available [7-14]. Only the *Istituto Nazionale di Fisica Nucleare* (INFN) in Italy has published a consistent set of fluence-to-effective dose and fluence-to-ambient dose equivalent conversion coefficients for all kinds of radiation and incident energies up to 10 TeV, calculated by the FLUKA transport code [9]. In Japan the dose conversion coefficients for neutrons, protons, electrons and photons were calculated using the HERMES and EGS4 codes [10-13], respectively. The conversion coefficients for neutrons and photons calculated with the MCNPX Monte Carlo code of Los Alamos with energies up to 2 GeV are reported in [14].

When comparing the published data, we realised the need for additional computations, as the agreement among the different published data is unsatisfactory and the source of disagreements is often unknown. The differences may be attributed to differences in the transport codes, cross-section tables and physical models used in the calculations. The choice of specific anthropomorphic phantoms used by the different groups influences significantly the organ doses, and, herewith, the effective dose conversion coefficients.

We have calculated the organ doses in the anthropomorphic phantoms ADAM and EVA, which appear to be the models of the human body accepted for general radiation protection purposes [3]. As irradiation geometry, broad monoenergetic particle fields incident in isotropic geometry were used, what appears to be a good approximation of the irradiation conditions expected in aeroplanes. From the weighted organ doses the fluence-to-effective dose conversion coefficients were calculated according to ICRP recommendations [15].

The essential aim of this paper is to validate the earlier calculations of the specific high-energy FLUKA transport code with the results obtained with the code MCNPX. This code is a high-energy extension of MCNP which is well established in the lower-energy range, e.g. for neutrons below 20 MeV, with experimentally proven accuracies. This feature is important because essential spectral

components of the cosmic radiation may be met in this energy range. The data presented here comprise a consistent set of the effective dose conversion coefficients for different radiation components in the Earth's atmosphere calculated using the same code, same geometry and same phantoms. In this way, gaps in the conversion coefficients as a function of particle energy are also filled in and the uncertainties in the energy integration procedures reduced. Finally, the data are used to estimate the effect of the different conversion coefficients on the total effective dose due to cosmic rays at different altitudes.

Dosimetric quantities

The basic dosimetric quantity in radiological protection is the absorbed dose, D , defined as the energy absorbed per unit mass. In radiological protection, the average dose over a tissue or organ is of main interest, since it serves as an indicator of the probability of causing a late health effect. The probability of such stochastic effects not only depends on the magnitude of the dose, but also on the type and energy of the ionising radiation and the distribution of the dose in the body.

ICRP-60 [15] introduced the effective dose, E , for the quantification of the risk from a given radiation exposure and limiting quantity in occupational radiation protection. E is defined as the sum of the weighted equivalent doses in all the tissues and organs of the body:

$$E = \sum_T w_T \cdot H_T \quad (1)$$

where H_T is the equivalent dose in tissue or organ T and w_T is the tissue-weighting factor for tissue T . The recommended values for tissue-weighting factors for 11 tissues and organs, and a remainder (nine additional organs), are given in [15]. The equivalent dose in tissue is the absorbed dose in an organ or tissue multiplied by the appropriate radiation-weighting factor. It is given by the expression:

$$H_T = \sum_R w_R \cdot D_{T,R} \quad (2)$$

where $D_{T,R}$ is the absorbed dose averaged over the tissue or organ T , due to radiation R , and w_R is the radiation-weighting factor for the type and energy of radiation R incident on the body. The specified values of w_R and the smooth w_R function for neutrons is taken from ICRP-60 [15].

Combining Eqs. (1) and (2) one obtains for E the following equation expressed as the sum of double-weighted absorbed doses $D_{T,R}$:

$$E = \sum_R w_R \cdot \sum_T w_T \cdot D_{T,R} \quad (3)$$

Because of the non-physical origin of the weighting factors, w_R and w_T , the effective dose, E , is not directly measurable. Furthermore, the effective dose depends on the specific radiation incidence conditions, for instance, frontal (A-P) or isotropic (ISO) incidence, and on the phantom used to model the human body. Consequently, the coefficients to convert fluence into effective dose have to be calculated for a sufficiently large number of energy points of the energy range and particle type considered, employing Monte Carlo radiation transport codes. The resulting data set may be used to calculate an energy-averaged effective dose by scalar multiplication with the conversion coefficients and the spectral fluence of each particle type.

There is some discussion concerning the question of how the sex-specific phantom topology should be treated. Either to use an anthropomorphic hermaphrodite phantom based on the male size that includes female-specific organs, or to use the real sex-specific phantoms. Several authors [16-20] warn against trying to construct some male-female mixture and they even recommend using the set of sex-specific tissue weighting factors. They argue that the total risk is higher for females than for males. In the present work, the recommendation of ICRP Publication 74 [3] was followed, and the absorbed dose was calculated in each organ for both the male and female phantom, separately. The effective dose was then determined from the combination of male and female equivalent doses using the relation:

$$E = w_{breast} \cdot H_{breast}^f + \sum_{T \neq breast} w_T \cdot \left(\frac{H_T^m + H_T^f}{2} \right) \quad (4)$$

where superscripts m and f denote male and female, respectively.

Actually, the present calculations were conducted by the modified Eq. (4):

$$E_R = \frac{w_R}{2} \cdot \left(2 \cdot w_{breast} \cdot D_{breast,R}^f + \sum_{T \neq breast} w_T \cdot (D_{T,R}^m + D_{T,R}^f) \right) \quad (5)$$

to determine the effective dose, E_R , for each type of radiation R , separately. The statistical variance of the calculated results is derived from the physical model given in Eq. (5) by common error propagation rules.

Anthropomorphic phantoms

The male (ADAM) and female (EVA) mathematical anthropomorphic phantoms applied in this work represent a modified version of the mathematical hermaphrodite MIRD-5 phantom as developed by Kramer, *et al.* [21]. ADAM represents the reference adult man weighing 70 kg and being 170 cm tall, and EVA the woman weighing 60 kg and being 160 cm tall, respectively. The body and internal organs of ADAM and EVA are defined by equations of surfaces of cylinders, cones, ellipsoids, hyperboloids and torus. The oesophagus was added to the phantoms using the model reported by Zankl, *et al.* [22]. The skin is represented by a 2 mm layer covering the whole phantom's body. Muscle, one of the remainder organs, was taken as the volume of the phantom, other than the specified organs, within the phantom boundary.

The phantoms, ADAM and EVA, contain all the organs of interest according to the ICRP recommendations [15]. In the calculations performed the internal organs were considered to be homogeneous in composition and density. Four different compositions and densities were used for lung tissue, skeleton, skin and the bulk of the body considered to be the soft tissue. The composition description of these four tissues were limited to 14 elements: H, C, N, O, Na, Mg, P, S, Cl, K, Ca, Fe, Zr and Pb. Other elements accounting for less than $2 \cdot 10^{-4}$ percentage by weight were neglected in this work. The elemental compositions and the densities can be found in [5].

Due to the complicated geometry of some organs, the volumes of the organs were calculated stochastically by the MCNP code itself using the ray-tracing method. The resulting volumes and masses of ADAM and EVA can also be found in [5]. On the whole the stochastically estimated volumes agree with organ volumes published by Kramer, *et al.* [21]. Only in a few cases do the volumes and masses differ from those. These are thyroid (ADAM and EVA), liver (EVA), breasts (EVA) and colon (EVA). Nevertheless, all these differences are less than 16%, except for thyroid,

which was 25%. The reason is in the slightly different geometrical definition of organ volumes required by the cell description in the Monte Carlo code. The special case is breast size of the reference female, which was already several times discussed by Cristy [27] and Kramer [25,26]. We have used the volume of 450 cm³ for both breasts, which is in reasonable agreement with the volume of about 190-200 cm³ as representative volume of one breast in the young adult female, recommended by Cristy [27] and based on the data of Katch, *et al.* [28]. Kramer, *et al.* [26] has reported a decrease of the average dose equivalent for photons in breast tissue with increasing breast volume or mass. The secondary effect of the variation of the breast volume is a shielding effect for the lungs. The lung dose equivalent increases with decreasing breast volume. A single breast volume of about 260-270 cm³ was suggested in [26].

Special attention was paid to the active bone marrow, which is in reality localised in the small cavities of almost all the bones in the body. The skeletal tissue in ADAM and EVA phantoms consists of a homogeneous mixture of mineralised bone and active bone marrow. Consequently, the energies deposited separately in bone surface and bone marrow (red) could not be determined directly by the Monte Carlo code. To estimate the dose to the bone marrow the method described by Kramer [23] was applied. The energy absorbed in the bone marrow was calculated from the energy absorbed in each bone corrected by the actual bone marrow mass distribution. According to the investigation performed by M. Cristy [24], the mass of bone marrow is 1 120 g for the adult. Cristy has also established the percentage distribution and masses of the active bone marrow in the human skeleton. These values were used in the present calculations.

Monte Carlo simulations

The calculations were performed using the MCNPX [29,30] Monte Carlo code of the Los Alamos National Laboratory. MCNPX is the merged code combining the major capabilities of the LAHET [31] and MCNP [32] Monte Carlo codes.

MCNPX expands the capabilities of MCNP (version 4B) by increasing the set of transportable particles and their energies, using newly-evaluated high-energy nuclear data tables for neutrons, protons and photons, and by applying the physics models where tabular data are not available. LAHET, the main code in the Lahet Code System (LCS) is a very useful tool for transport calculations involving high-energy particles. LAHET not only transports the high-energy incident particles, but also all particles emitted from the resulting nuclear interactions. MCNPX includes all of the LAHET nuclear physics modules. These are Bertini and ISABEL intranuclear cascade models, the multi-stage pre-equilibrium exciton model, the evaporation model, the FLUKA high-energy generator, Fermi break-up model, the nucleon elastic scattering model, the gamma production models and the high-energy fission models (ORNL model and Rutherford Appleton Laboratory (RAL) model). On the other hand, MCNPX expands the capabilities of LAHET through the availability of many of the variance reduction methods of MCNP, through the incorporation of MCNP's geometry, sources, and tally syntax, and through flexible use of both physical models and evaluated nuclear data.

We used the beta-test version of the MCNPX code (version 2.1.5 and 2.2.3) with the options of the Bertini cascade model for nucleons and pions, and the pre-equilibrium model after intranuclear cascade. The nuclear cross-section data derived from the Evaluated Nuclear Data File B-6 (ENDF/B-6) [33] and expanded continuous-energy neutron cross-section tables LA150N [34] were used with MCNPX. All possible secondary particles were transported to avoid that part of the primary particle energy be deposited locally.

Method and results of calculation

The effective dose was calculated using Eq. (5). The energy deposited in the 60 regions of ADAM and 62 regions of EVA, representing the various organs and tissues of the human body were determined for monoenergetic fields of neutrons, protons, electrons, photons, positive pions and negative muons in ISO geometry. The isotropic irradiation (ISO) was modelled using an inward-directed source on a spherical surface around the whole phantom. The space between source and phantoms was assumed to be in a vacuum.

The cross-sections of the main constituents, i.e. H, C, N, O, P, Ca, Fe and Pb, were available up to 150 MeV from the LA150N library [34]. The elements not included in LA150N, i.e. Na, Mg, S, Cl, K and Zr, were omitted to avoid the influence of a “mix and match” problem. It should be stressed that the sum of these six elements only accounts for less than 0.9 percentage by weight.

In these calculations the following changes of the ICRP 60 recommendations were employed as recommended by ICRP 67 [35]: i) the remainder dose was evaluated as an arithmetic mean of nine organs and tissues, the upper large intestine was not included in the remainder tissues, ii) the higher value of doses to the ovaries and to testes was applied to estimate dose to gonads. The absorbed dose to organs and tissues consisting of two or more regions were calculated as the mass-weighted average of the doses to each regions. Finally, due to the uniform whole-body irradiation, the footnote 3 of Table 2 – “Tissue-weighting factors” in ICRP Publication 60 could be ignored.

To obtain the fluence-to-effective dose conversion coefficients the resulting effective dose was then divided by the total fluence of the radiation incident on body. The organ and effective doses per unit fluence for each particle type of the cosmic radiation field in ISO geometry are given in Tables A1-A6. The standard deviation of the mean stands for uncertainties due to the Monte Carlo counting statistics. Any other sources of uncertainties are not included. The number of histories in the Monte Carlo calculations was always large enough to keep the statistical uncertainties below a few per cent. No variation reduction technique was used. However, because of the whole body irradiation geometry, the relatively higher uncertainties for the small volume organs do not strongly influence the uncertainty of the final result.

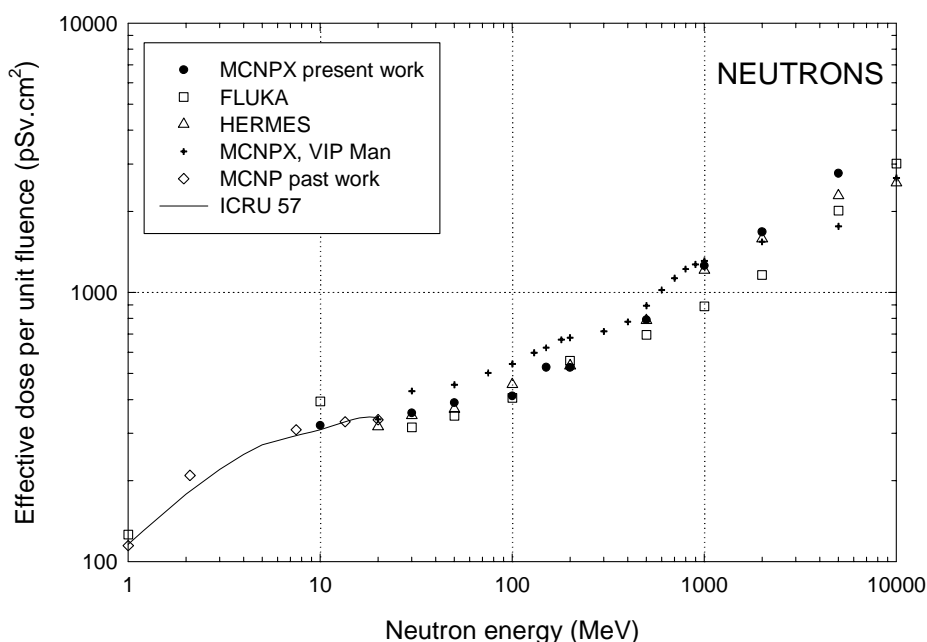
The fluence-to-effective dose conversion coefficients are compared with published data for ISO irradiation geometry in Figures 1 through 6.

Neutrons

Figure 1 shows the calculated effective dose per unit of fluence as a function of neutron energy for ISO irradiation along with data available in literature. The conversion coefficients calculated using MCNPX are in good agreement with those calculated using the HERMES code [12]. This is not that surprising, because LAHET and HERMES are based on the same code, i.e. HETC [40], originally developed at Oak Ridge National Laboratory. Our MCNPX data are systematically higher than those calculated with FLUKA from [9] in the energy range from 30 MeV to 100 MeV and then for energies higher than 200 MeV. The source of these differences is unknown, though it may be attributed to the different transport models used in the Monte Carlo codes.

It should be emphasised that the effective dose at 100 MeV and 150 MeV in Figure 1 was calculated using the LAHET physics models instead of tabular data from the LA150N library (i.e. cross-over energy of 20 MeV). Using the LA150N tabular data (i.e. cross-over energy of 150 MeV) the values of

Figure 1. Comparison of neutron fluence-to-effective dose conversion coefficients for ISO irradiation



effective dose at 100 MeV and 150 MeV were about 20% and 15% higher, respectively. The source of this difference has not yet been satisfactorily explained, but could be attributed to the “double counting” problem reported in [41]. This problem is expected to be eliminated in subsequent versions of MCNPX.

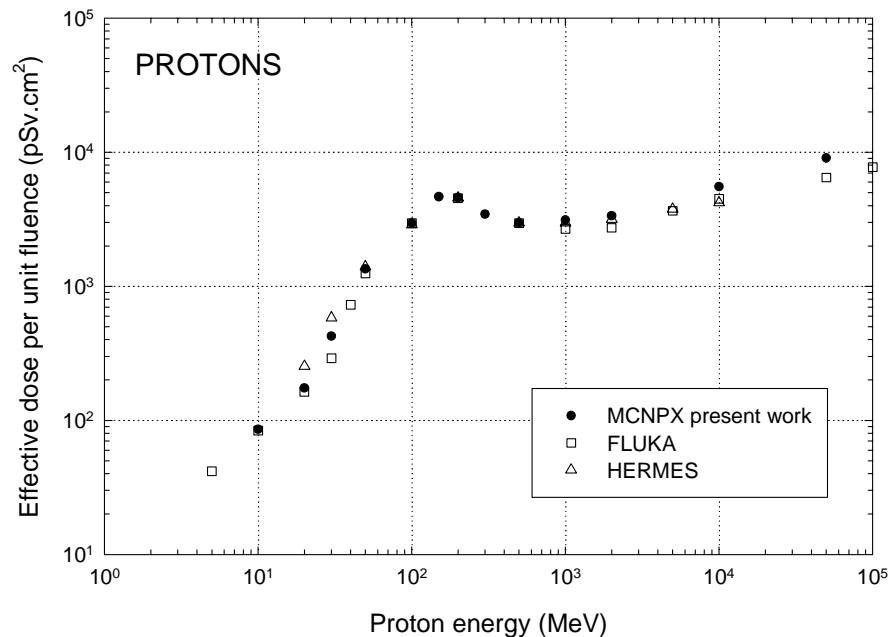
The solid line in Figure 1 shows the neutron conversion coefficients recommended by ICRU 57 [4] up to 20 MeV. Points are omitted for clearness. In the same figure we also show our conversion coefficients from [5] calculated with MCNP in the past and which were included in the averages of ICRP 57. The FLUKA result at 10 MeV is considerably higher.

Fluence-to-effective dose conversion coefficients based on the VIP-Man anatomical model calculated with MCNPX [42] are also shown in the figure for interest. The VIP-Man represents a human anatomical model based on CT-images of a considerably taller and athletic male person, 186 cm in height and 103 kg in weight and is not directly comparable with ADAM and EVA. The resulting coefficients are systematically higher than all other available data.

Protons

According to the recommendation of ICRP Publication 60 and international regulations, e.g. European Basic Safety Standards, the radiation weighting factor w_R for protons was assumed to be 5 for the entire energy range considered in this study. However, we are aware of the discussions to revise w_R for protons. Figure 2 shows a comparison of the conversion coefficients calculated using three different codes. FLUKA data are from [9] and HERMES data from [12]. The effective dose increases steeply with energy to its local maximum around 150 MeV, then it decreases to a local minimum around 1 GeV. The steep increase can be explained by increasing the skin and breast doses with energy, which are dominant components of the effective dose for energies below approximately 100 MeV. As the Bragg peak is shifted deeper into the phantom with rising proton energy, other organ doses are also increasing, reaching the maximum at 150 MeV. It is observed that in the energy range

Figure 2. Comparison of proton fluence-to-effective dose conversion coefficients for ISO irradiation



from 10 to 50 MeV the data of FLUKA are slightly lower and those of the HERMES calculations are slightly higher than the present data. In the rest of the energy region concerned here, agreement with the published data is satisfactory.

Photons

The photon fluence-to-effective dose conversion coefficients are shown in Figure 3 for ISO irradiation compared with the only published data [9] available, calculated in the energy range from 50 keV to 10 GeV. The results of the present work are also compared with the photon conversion coefficients recommended by ICRU 57 [4] up to 10 MeV. The solid line connects the ICRU data points (points are omitted) as a guide to the eye. The agreement of all data is remarkable. Differences occur only in the low energy range below 100 keV for which the present values are higher. This observation may be due to the concept of the higher value of doses to ovaries and testes adopted in this work (see third paragraph of this section).

Electrons

The cut-off energy of electrons was chosen far below the energy of primary electrons, i.e. 10 keV. Below this threshold the remaining energy of electrons was deposited locally. At energies below approximately 1 MeV, more than 95% of the effective dose is due to the exposed skin. For the skin dose a total skin thickness of 2 mm is considered. It should be stressed, however, that the top layer of the skin equal to 70 μm is insensitive to radiation. Therefore, the dose to skin must be related to the sensitive layer only, and the total skin dose has to be multiplied by a correction factor. Appropriate skin correction factors for electrons below 10 MeV can be found in [37,38]. We have used the value of 0.4 at 0.1 MeV, 0.9 at 0.2 MeV and 1.0 at energies higher or equal to 0.5 MeV. The effective dose per unit fluence of electrons as a function of incident electron energy for ISO irradiation is shown in Figure 4.

Unfortunately, the electron conversion coefficients in [37,38] do not include the data for ISO irradiation and we can make a comparison only with data from [9] calculated by FLUKA and [39] by EGS4, respectively.

Figure 3. Comparison of photon fluence-to-effective dose conversion coefficients for ISO irradiation

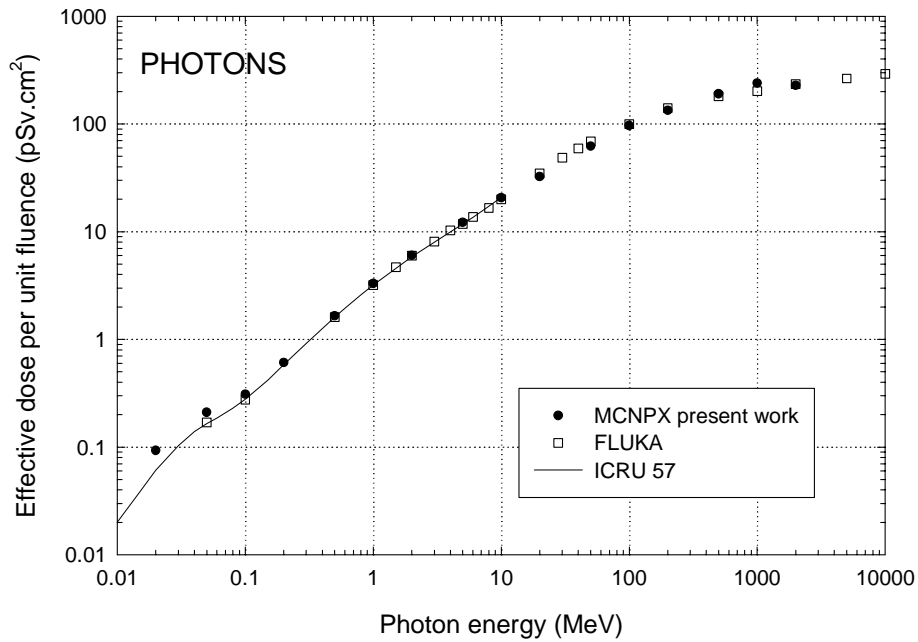
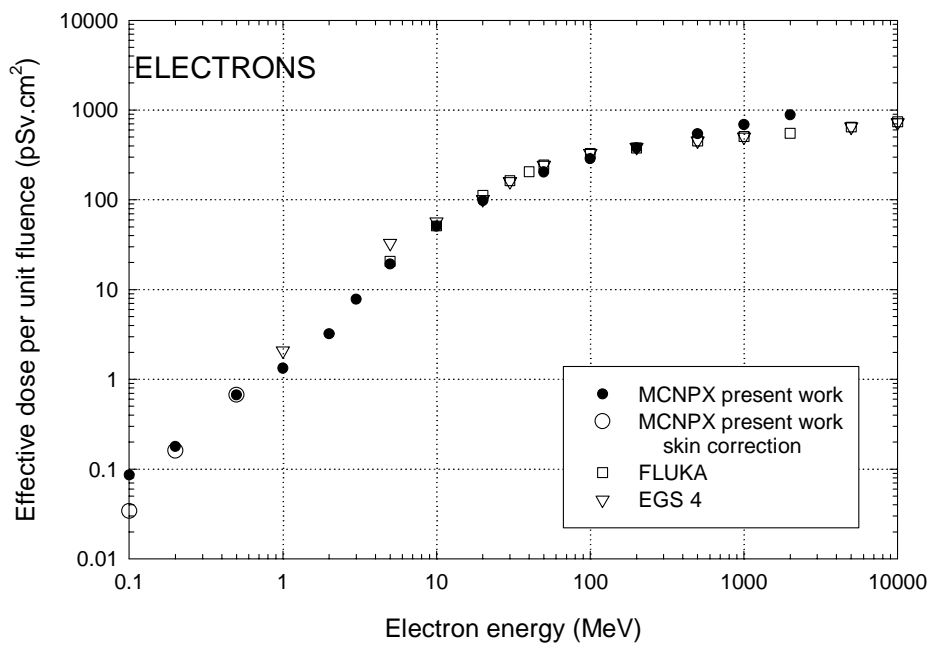


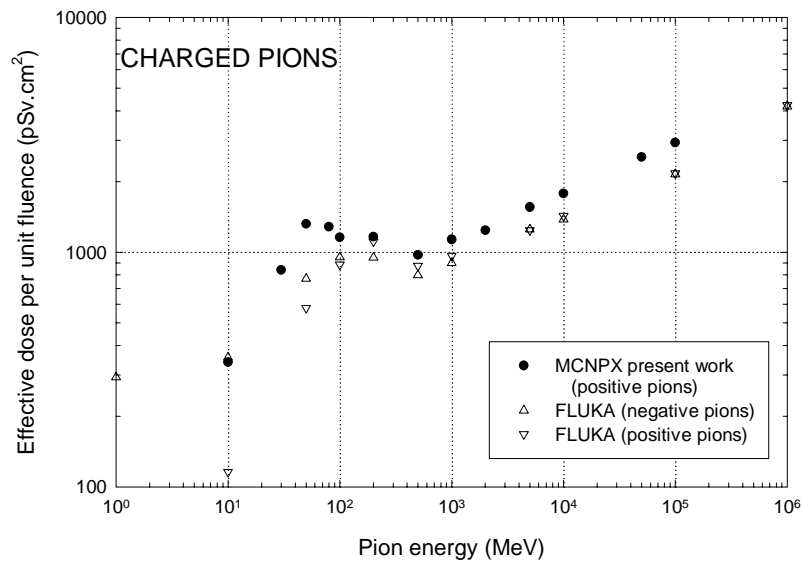
Figure 4. Comparison of electron fluence-to-effective dose conversion coefficients for ISO irradiation



Pions

The radiation weighting factor w_R for pions is not explicitly given in ICRP Publication 60 and could be approximated by the values of effective quality factors at 10 mm depth in the ICRU sphere. In the present paper we calculated effective dose conversion coefficients for positive pions and for them we have adopted the effective quality factors as published in [36]. In Figure 5 we compare our results with FLUKA data published in [9] for ISO irradiation. It can be seen that for pion energies greater than 100 MeV the effective doses for positive pions are very close to those of negative ones. Below 100 MeV the data for negative pions are higher.

Figure 5. Comparison of pion fluence-to-effective dose conversion coefficients for ISO irradiation (preliminary)



Large differences observed between the present work and FLUKA results for positive pions have not yet been explained. The most recent results calculated with MCNPX version 2.2.6, which became available this year, show considerable improvement. For positive pions with energies of 10 MeV and 50 MeV the resulting effective dose per unit fluence is equal to $134.4 \pm 0.7\%$ pSv·cm² and $577.1 \pm 0.6\%$ pSv·cm², respectively.

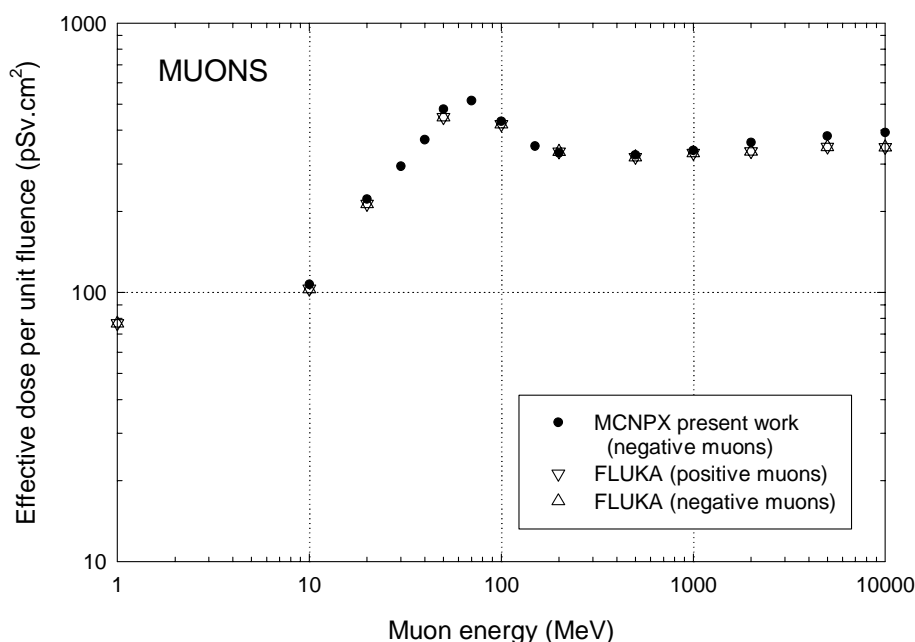
Muons

Calculations were performed for negative muons. They can decay into electrons or be captured by nuclei if they come to rest. Radiation weighting factors were assumed to be equal to 1. Figure 6 shows the effective dose per unit fluence of muons for ISO geometry in the comparison with the only data found in literature [9] and calculated using the FLUKA code. The agreement between both data sets is very good.

Comparison of energy averaged conversion factors

The influence of the conversion coefficients of each single radiation component to the total effective dose at any point in the atmosphere depends strongly on the relative fluence contribution of the radiation considered and the absolute values of the coefficients.

Figure 6. Comparison of muon fluence-to-effective dose conversion coefficients for ISO irradiation



In the literature we found only one complete and consistent set of fluence-to-effective dose conversion coefficients for all kinds of cosmic radiation in special ISO geometry. We used this FLUKA data from [9] for a detailed comparison. This data are also employed in the EPCARD code [43], which permits the calculation of effective dose to aircrews along any flight route at any time period of the solar cycle.

The fluence-to-effective dose conversion coefficients, (E/Φ) , as function of the particle energy, E_p , of both FLUKA and MCNPX data sets were used to calculate the energy averaged conversion factors by the relation:

$$\overline{(E_p/\Phi)} = \frac{\int (E_p/\Phi) \cdot \Phi_E dE_p}{\int \Phi_E dE_p} \quad (6)$$

The specific cosmic particle spectra, $\Phi_E = d\Phi/dE_p$, were taken from [1]. For neutrons between thermal and 20 MeV we used the effective dose conversion coefficients given in ICRU 57 [4]. The resulting values of the conversion factors are given in Table 1. Taking into account the differences between the FLUKA and MCNPX conversion coefficients, as depicted in Figures 1-6 for all particles, the conversion factors are in very good agreement. Particularly for neutrons, which dominate the effective dose at aircraft altitudes, the agreement is very satisfactory. On the whole, the differences are less than 8%, with exception of the positive pions. However, the charged pions contribute less than 1% to the total effective dose at all altitudes up to 25 km.

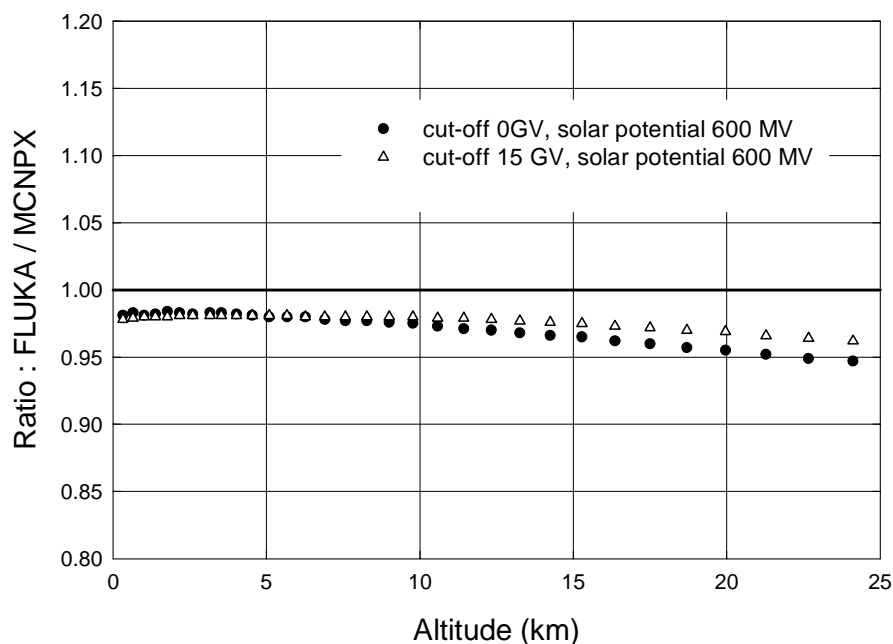
We then applied these conversion factors to particle fluence rates for altitudes from 0 to 25 km for two extreme civil flight conditions: First, in case of cut-off rigidity equal to 0 GV (no geomagnetic shielding), and secondly, 15 GV (which is approximately the highest geomagnetic shielding). A solar deceleration potential of 600 MV was assumed for both energies, i.e. approximately at the time of solar

Table 1. Averaged fluence-to-effective dose conversion factors, (E/Φ) , calculated with FLUKA and MCNPX conversion coefficients respectively

Particle	Conversion factor E/Φ (pSv·cm ²)		Percentage difference
	FLUKA	MCNPX	
Neutrons	207	206	+0.5
Protons	3 000	3 241	+8.0
Photons	6.02	6.01	-0.2
Electrons	116	113	-2.6
Positive pions	1 043	1 281	+22.8
Negative muons	338	351	+3.9

minimum. The total effective dose during a certain exposure time at the given altitude was determined by summing up all particle contributions. In Figure 7 the ratio of total effective dose is shown in dependence of the altitude calculated with the FLUKA and MCNPX conversion factors, respectively. It can be stated that the differences are smaller than 6% in whole altitude region considered. Between 5 and 14 km, which is the usual range of civil flight altitudes, the differences are even less than 3%.

Figure 7. The ratio of the total effective dose per hour in altitude dependence calculated with FLUKA and MCNPX conversion factors for conditions near solar minimum activity (solar deceleration potential 600 MV)



The particle spectra, Φ_E , employed are those for an altitude of 12 km and are assumed to be unchanged for the other altitudes, in order to receive information on the effect of varying the data set of the conversion factors. This assumption is also used in the current version of EPCARD. In fact, there are some systematic changes in the spectral shapes with altitude and cut-off rigidity [2], which may change the averaged conversion factors up to approximately $\pm 10\%$. This figure is generally acceptable for radiation protection purposes, but may easily be allowed for.

Summary and conclusions

This paper presents a full data set of fluence-to-dose conversion coefficients for the determination of effective dose due to cosmic ray particles in the Earth's atmosphere, i.e. for neutrons, protons, pions, electrons, muons and photons. The data are derived with the Monte Carlo code MCNPX in its most recent version of program and data. The energy range studied covers more than that where particles may create an absorbed or effective dose. The data provide a link to generally proven and adopted radiation protection data obtained by MCNP in the energy range of man-made sources.

The data essentially verify the findings of published calculations which were conducted with the specific high-energy radiation transport code FLUKA. The differences observed may be attributed to differences in physical models and in the transport codes, cross-section tables and anthropomorphic phantoms, and in the procedures to calculate effective dose from the organ doses. The data are sufficiently dense with respect to the energy points, which facilitates integration procedures and reduces respective calculation uncertainties.

The data set presented here and the published FLUKA data were used to calculate total effective doses for all particles at civil flight altitudes. The differences were smaller than about 3% in the range from 5 to 14 km and are, thus, smaller than changes in the conversion coefficients caused by the – also small – changes in spectral shape of the cosmic ray particles.

Acknowledgements

The authors are grateful to the MCNPX development crew at Los Alamos National Laboratory for providing the most recent versions of the Monte Carlo code and the data library, especially to Drs. Laurie Waters and Dick Prael. The authors also acknowledge the help of Professor Wolfgang Heinrich for making available the data of cosmic radiation spectra.

REFERENCES

- [1] Schraube, H., W. Heinrich, G. Leuthold, V. Mares and S. Roesler, "Aviation Route Dose Calculations and its Numerical Basis", *Proc. 10th International Congress of the International Radiation Protection Association*, Hiroshima, Japan. T-4-4, P-1a-45, 1-9 (2000). Full document available at: (<http://www.oita-nhs.ac.jp/%7Eirpa10/CD-ROM/Full/topical.html>).
- [2] Roesler, S., W. Heinrich, H. Schraube, "Monte Carlo Calculation of the Radiation Field at Aircraft Altitudes", *Radiat. Prot. Dosim.* (2002) in print.
- [3] ICRP, *Conversion Coefficients for Use in Radiological Protection Against External Radiation*, Publication 74 (Oxford: Pergamon Press) (1997).
- [4] ICRU, *Conversion Coefficients for Use in Radiological Protection Against External Radiation*, Report 57, Bethesda, Maryland (1998).

- [5] Leuthold, G., V. Mares and H. Schraube, *Monte Carlo Calculations of Dose Equivalents for Neutrons in Anthropomorphic Phantoms Using the ICRP 60 – Recommendations and the Stopping Power Data of ICRU 49*, GSF-Report, Neuherberg (2002).
- [6] Zankl, M., G. Drexler, N. Petoussi-Henß and K. Saito, *The Calculation of Dose from External Photon Exposures Using Reference Human Phantoms and Monte Carlo Methods*, GSF-Report 8/97, Neuherberg (1997).
- [7] Nabelssi, B.K. and N.E. Hertel, “Effective Dose Equivalents and Effective Doses for Neutrons from 30 to 180 MeV”, *Radiat. Prot. Dosim.*, 48, 227-243 (1993).
- [8] Mares, V., G. Leuthold and H. Schraube, “Organ Doses and Dose Equivalent for Neutrons Above 20 MeV”, *Radiat. Prot. Dosim.*, 70, 391-394 (1997).
- [9] Pelliccioni, M., “Overview of Fluence-to-effective Dose and Fluence-to-ambient Dose Equivalent Conversion Coefficients for High-energy Radiation Calculated Using the FLUKA Code”, *Radiat. Prot. Dosim.*, 88, 279-297 (2000).
- [10] Iwai, S., T. Uehara, O. Sato, N. Yoshizawa, S. Furihata, S. Takagi, S. Tanaka and Y. Sakamoto, “Overview of Fluence-to-dose Equivalent Conversion Coefficients for High-energy Radiations: Calculational Methods and Results of Effective Dose Equivalent and Effective Dose per Unit Particle Fluence”, *Proc. of the 3rd Specialists Meeting on Shielding Aspects of Accelerators, Irradiation and Target Facilities (SATIF-3)*, 12-13 May 1997, Tohoku University, Sendai, Japan (1998).
- [11] Yoshizawa, N., O. Sato, S. Takagi, S. Furihata, S. Iwai, T. Uehara, S. Tanaka and Y. Sakamoto, “External Radiation Conversion Coefficients Using Radiation Weighting Factor and Quality Factor for Neutron and Proton from 20 MeV to 10 GeV”, *Nucl. Sci. Tech.*, 35, 928-942 (1998).
- [12] Iwai, S., T. Uehara, O. Sato, N. Yoshizawa, S. Furihata, S. Takagi, S. Tanaka and Y. Sakamoto, “Overview of Fluence to Dose Equivalent Conversion Coefficients for High-energy Radiations: Calculational Methods and Results of Two Kinds of Effective Doses per Unit Particle Influence”, *Proc. of the 4th Specialists Meeting on Shielding Aspects of Accelerators, Irradiation and Target Facilities (SATIF-4)*, Knoxville, Tennessee, USA, 17-18 September 1998 (1999).
- [13] Sakamoto, Y., S. Tsuda, O. Sato and N. Yoshizawa, “Evaluation of Dose Conversion Coefficients for High-energy Radiation in Japan after SATIF-4”, *Proc. of the 5th Specialists Meeting on Shielding Aspects of Accelerators, Irradiation and Target Facilities (SATIF-5)*, Paris, France, 18-21 July 2000 (2001).
- [14] Sutton, M.R., N.E. Hertel and L.S. Waters, “Fluence-to-effective Dose Conversion Coefficients for High-energy Radiations Calculated with MCNPX”, *Proc. of the 4th Specialists Meeting on Shielding Aspects of Accelerators, Irradiation and Target Facilities (SATIF-5)*, Paris, France, 20-21 July 2000 (2001).
- [15] ICRP, *1990 Recommendations of the International Commission on Radiological Protection*, Publication 60 (Oxford: Pergamon Press) (1991).
- [16] Austerlitz, C., B. Kahn, G. Eichholz, M. Zankl and G. Drexler, “Calculation of the Effective Male Dose Equivalent Relative to the Personal Dose at Nine Locations with a Free-arm Model”, *Radiat. Prot. Dosim.*, 36, 13-21 (1991).

- [17] Stewart, R.D., J.E. Tanner and J.A. Leonowich, “An Extended Tabulation of Effective Dose Equivalent from Neutrons Incident on a Male Anthropomorphic Phantom”, *Health Physics*, 65, 405-413 (1993).
- [18] Xu, X.G. and W.D. Reece, “Sex-specific Tissue Weighting Factors for Effective Dose Equivalent Calculations”, *Health Physics*, 70, 81-86 (1996).
- [19] Zankl, M. and G. Drexler, “Some Critical Remarks on the Use of Sex-specific Tissue Weighting Factors for Effective Dose Equivalent Calculations”, *Health Physics*, 72, 486-487 (1997).
- [20] Xu, X.G., “Response to Zankl and Drexler”, *Health Physics*, 72, 488 (1997).
- [21] Kramer, R., M. Zankl, G. Williams and G. Drexler, *The Calculation of Dose from External Photon Exposures Using Reference Human Phantoms and Monte Carlo Methods, Part I: The Male (Adam) and Female (Eva) Adult Mathematical Phantoms*, GSF-Bericht S-885 (1982).
- [22] Zankl, M., N. Petoussi and G. Drexler, “Effective Dose and Effective Dose Equivalent – The Impact of the New ICRP Definition for External Photon Irradiation”, *Health Physics*, 62(5), 395-399 (1992).
- [23] Kramer, R., *Ermittlung von Konversionsfaktoren zwischen Körperdosen und relevanten Strahlungskenngrößen bei externer Röntgen- und Gamma-bestrahlung*, GSF-Bericht-S-556, Neuherberg, München (1979).
- [24] Cristy, M., *Mathematical Phantoms Representing Children of Various Ages for Use in Estimates of Internal Dose*, Oak Ridge National Laboratory, ORNL/NUREG/TM-367 (1980).
- [25] Kramer, R. and G. Drexler, “Representative Breast Size of Reference Female”, *Health Physics*, 40(June), 913-914 (1981).
- [26] Kramer, R., G. Williams and G. Drexler, “Reply to M. Cristy”, *Health Physics*, 43(6), 932-935, (1982).
- [27] Cristy, M., “Representative Breast Size of Reference Female”, *Health Physics*, 43(6), 930-932, (1982).
- [28] Katch, V.L., B. Campaigne, P. Freedson, S. Sady, F.I. Katch and A.R. Behnke, “Contribution of Breast Volume and Weight to Body Fat Distribution in Females”, *Am. J. Phys. Anthropol.*, 53, 93-100 (1980).
- [29] Hughes, H.G., R.E. Prael and R.C. Little, “MCNPX – The LAHET/MCNP Code Merger”, LA-UR-97-4891, Los Alamos National Laboratory (1997).
- [30] *MCNPX User’s Manual, Version 2.1.5*, TPO-E83-G-UG-X-00001, Revision 0, L.S. Waters, ed., Los Alamos National Laboratory (1999).
- [31] Prael, R.E. and H. Lichtenstein, “User Guide to LCS: The LAHET Code System”, LA-UR-89-3014, Los Alamos National Laboratory (1989).
- [32] *MCNP – A General Monte Carlo N-particle Transport Code, Version 4B*, LA-12625-M, J.F. Briesmeister, ed., Los Alamos National Laboratory (1997).

- [33] Hendricks, J.S., S.C. Frankle and J.D. Court, *ENDF/B-IV Data for MCNP*, LA-12891, Los Alamos National Laboratory (1994).
- [34] Chadwick, M.B., P.G. Young, S. Chiba, S.C. Frankle, G.M. Hale, H.G. Hughes, A.J. Koning, R.C. Little, R.E. MacFarlane, R.E. Prael and L.S. Waters, “Cross-section Evaluations to 150 MeV for Accelerator-driven Systems and Implementation in MCNPX”, *Nuclear Science and Engineering*, 131(3), 293 (1999).
- [35] ICRP, *Age-dependent Doses to Members of the Public from Intakes of Radionuclides: Part 2 Ingestion Dose Coefficients*, ICRP Publication 67, *Ann. ICRP*, 23(3/4), Oxford Pergamon, (1993).
- [36] Ferrari, A., M. Pelliccioni and M. Pillon, “Fluence to Effective Dose Conversion Coefficients for Negatively and Positively Charged Pions”, *Radiat. Prot. Dosim.*, 80(4), 361-370 (1998).
- [37] Schultz, F.W. and J. Zoetelief, “Organ and Effective Doses in the Male Phantom ADAM Exposed in AP Direction to Broad Unidirectional Beams of Monoenergetic Electrons”, *Health Physics*, 70(4), (1996).
- [38] Katagiri, M., M. Hikoji, M. Kitaichi, M. Sawamura and Y. Aoki, “Effective Doses and Organ Doses per Unit Fluence Calculated for Monoenergetic 0.1 MeV to 100 MeV Electrons by the MIRD-5 Phantom”, *Radiat. Prot. Dosim.*, 90 (4), 393-401 (2000).
- [39] Tsuda, S., A. Endo, Y. Yamaguchi and O. Sato, “Fluence to Effective Dose Conversion Coefficients for Electrons with Energy from 1 MeV to 100 GeV”, *Radiat. Prot. Dosim.*, 95(1), 5-16, (2001).
- [40] Radiation Shielding Information Center, *HETC Monte Carlo High-energy Nucleon-meson Transport Code*, Report CCC-178, ORNL (1977).
- [41] Sutton, M.R., N.E. Hertel and L.S. Waters, “Fluence-to-effective Dose Conversion Coefficients for Neutrons up to 2 GeV”, *American Nuclear Society Radiation Protection and Shielding Division Topical Meeting*, Spokane, Washington (September 2000).
- [42] Bozkurt, A., T.C. Chao and X.G. Xu, “Fluence-to-dose Conversion Coefficients Based on the VIP-Man Anatomical Model and MCNPX Code for Monoenergetic Neutrons above 20 MeV”, *Health Physics*, 81(2), 184-202, (2001).
- [43] Schraube, H., G. Leuthold, W. Heinrich, S. Roesler and V. Mares, *EPCARD – European Program Package for the Calculation of Aviation Route Doses*, GSF-Neuherberg and European Commission, Luxembourg (2002).

Table A1. Organ doses and effective doses per unit neutron fluence incident in ISO geometry in pGy·cm² and pSv·cm² respectively

NEUTRONS - ISO					
Energy(MeV)	10	30	50	100	150
Gonads	39.8	60.7	75.3	82.9	131.7
RBM	29.1	49.3	59.5	81.2	100.6
Colon	33.1	57.9	70.0	85.9	106.1
Lungs	39.5	61.6	71.5	79.6	92.9
Stomach	35.3	59.4	70.2	75.7	99.2
Bladder	33.0	57.6	74.0	81.7	93.0
Breast	42.7	62.3	72.4	67.9	79.0
Liver	36.1	60.3	71.8	81.8	100.9
Oesophagus	34.5	62.4	69.4	78.9	98.4
Thyroid	41.0	64.2	78.5	79.3	92.0
Skin	45.5	65.1	70.1	52.5	63.5
Bone	30.5	50.3	60.6	69.6	85.3
Remainders					
Adrenals	33.8	56.9	74.8	69.3	106.0
Brain	43.7	65.7	75.4	78.7	88.7
Small intestines	32.3	58.3	69.3	81.4	108.7
Kidneys	36.0	60.2	72.6	78.8	93.5
Soft tissue	39.4	62.0	71.8	74.3	89.4
Pancreas	32.6	59.2	69.2	79.7	115.7
Spleen	36.1	58.0	69.0	80.3	103.9
Thymus	37.3	59.1	66.8	69.6	84.0
Uterus	32.5	60.4	71.2	91.1	103.7
Effective Dose	320.0±0.5%	356.4±0.9%	389.3±1.4%	412.1±2.1%	526.9±2.1%

Energy(MeV)	200	500	1000	2000	5000
Gonads	109.3	200.8	317.6	374.7	643.9
RBM	106.2	153.3	252.0	346.6	553.6
Colon	114.3	158.9	255.4	340.1	592.4
Lungs	96.8	133.9	214.2	288.2	483.5
Stomach	106.8	146.3	246.0	343.4	543.8
Bladder	98.1	157.9	248.8	359.4	577.1
Breast	78.6	118.2	181.7	258.3	417.1
Liver	105.6	154.6	247.3	329.9	540.1
Oesophagus	127.6	162.9	262.9	362.5	535.2
Thyroid	85.1	140.6	175.8	296.0	515.1
Skin	67.1	98.5	157.4	210.2	357.7
Bone	88.8	129.5	210.2	287.8	458.8
Remainders					
Adrenals	98.4	146.8	241.0	335.2	517.1
Brain	86.6	120.9	193.6	261.1	422.0
Small intestines	111.8	157.2	263.1	357.3	603.6
Kidneys	109.8	155.5	239.9	340.8	545.1
Soft tissue	93.1	133.9	215.4	291.5	485.7
Pancreas	133.2	166.3	251.1	346.5	606.8
Spleen	109.3	161.5	251.0	370.2	539.2
Thymus	107.5	163.2	235.2	330.9	450.1
Uterus	98.4	161.9	240.6	349.9	575.0
Effective Dose	525.9±1.9%	790.8±1.9%	1255.1±1.6%	1675.1±1.7%	2766.6±1.4%

Table A2. Organ doses and effective doses per unit proton fluence incident in ISO geometry in pGy·cm² and pSv·cm² respectively

PROTONS - ISO							
Energy(MeV)	10	20	30	50	100	150	200
Gonads	7.79E-03	1.24E+01	1.49E+02	7.20E+02	665.3	998.6	951.8
RBM	2.11E-02	1.67E+01	1.03E+02	2.69E+02	603.1	821.9	970.7
Colon	4.25E-02	1.13E-01	2.78E-01	1.79E+00	201.5	948.5	887.8
Lungs	3.71E-03	1.40E-02	3.32E-02	2.93E+01	930.7	945.5	889.8
Stomach	4.00E-03	1.27E-02	3.61E-02	4.49E+01	564.6	903.0	893.0
Bladder	2.83E-03	8.74E-03	4.40E-02	2.13E+01	459.7	809.0	935.7
Breast	5.26E-03	1.86E+02	5.05E+02	9.43E+02	908.1	807.3	838.4
Liver	3.17E-03	1.32E-02	2.80E-02	2.67E+00	595.2	915.4	886.8
Oesophagus	3.54E-03	2.40E-03	1.40E-02	1.33E-01	85.7	1147.8	934.0
Thyroid	1.43E-03	6.47E-05	3.53E-02	3.61E+02	758.3	964.0	949.9
Skin	1.71E+03	2.03E+03	1.49E+03	1.04E+03	803.0	819.4	811.5
Bone	1.91E-01	1.70E+01	1.14E+02	3.18E+02	705.3	891.3	818.8
Remainders							
Adrenals	1.75E-03	2.16E-02	2.74E-02	1.35E-01	524.5	850.2	874.0
Brain	3.31E-03	8.71E-03	3.32E-02	8.43E+01	1065.0	1129.8	860.7
Small intestines	2.72E-03	7.90E-03	2.82E-02	1.50E-01	210.7	917.5	913.9
Kidneys	3.23E-03	1.46E-02	3.42E-02	3.59E+01	649.6	836.6	892.8
Soft tissue	2.38E-01	8.54E+01	2.09E+02	4.08E+02	732.2	900.0	864.6
Pancreas	1.62E-03	8.51E-03	3.19E-02	2.10E-01	86.3	984.4	954.1
Spleen	5.15E-03	1.41E-02	2.52E-02	2.03E-01	616.1	938.4	864.7
Thymus	8.69E-04	1.98E-02	3.07E-02	1.67E+02	640.6	848.9	873.7
Uterus	1.85E-03	6.23E-03	2.53E-02	1.32E-01	205.6	948.8	932.9
Effective Dose	85.6±0.1%	173.9±0.3%	423.8±0.6%	1346.0±1.0%	2953.8±0.5%	4648.4±0.5%	4577.4±0.6%

Energy(MeV)	300	500	1000	2000	10000	50000
Gonads	696.8	673.0	683.5	772.1	1231.8	2063.4
RBM	656.1	549.5	579.9	701.3	1148.2	1869.1
Colon	708.2	590.5	629.2	664.1	1143.3	1882.7
Lungs	677.7	571.7	594.9	617.3	1032.1	1607.4
Stomach	701.4	586.6	623.8	658.7	1082.0	1809.3
Bladder	701.7	582.2	649.7	648.4	1073.9	1792.3
Breast	669.3	549.3	552.9	549.2	921.3	1487.1
Liver	697.1	582.6	620.5	646.5	1078.4	1758.7
Oesophagus	707.4	569.2	605.1	653.5	1108.2	1826.3
Thyroid	682.7	573.2	634.6	595.6	1015.4	1478.1
Skin	653.4	537.9	524.7	527.1	817.3	1247.3
Bone	648.5	543.1	569.6	588.6	965.7	1553.2
Remainders						
Adrenals	665.8	570.1	577.4	673.2	1118.9	1871.8
Brain	676.2	564.7	576.0	607.5	950.2	1420.4
Small intestines	709.7	591.3	636.8	668.2	1144.4	1910.5
Kidneys	693.4	589.2	622.9	664.8	1073.8	1758.5
Soft tissue	681.3	568.5	590.1	606.5	995.7	1586.9
Pancreas	727.5	605.3	645.8	668.5	1155.3	1925.4
Spleen	705.3	579.3	605.6	641.8	1089.0	1785.8
Thymus	665.2	566.0	603.1	597.2	900.9	1547.7
Uterus	708.0	599.5	646.0	698.4	1160.2	1876.6
Effective Dose	3445.6±0.5%	2965.6±0.7%	3113.4±0.9%	3347.9±1.0%	5530.0±1.0%	9025.8±0.7%

Table A3. Organ doses and effective doses per unit photon fluence incident in ISO geometry in pGy·cm² and pSv·cm² respectively

PHOTONS - ISO								
Energy(MeV)	0.02	0.05	0.1	0.2	0.5	1	2	5
Gonads	1.89E-01	0.205	0.294	0.638	1.72	3.46	6.41	12.68
RBM	1.49E-01	0.456	0.496	0.714	1.67	3.23	5.84	12.00
Colon	3.50E-03	0.126	0.247	0.527	1.47	2.96	5.62	11.30
Lungs	2.46E-02	0.189	0.300	0.624	1.73	3.48	6.23	12.49
Stomach	2.84E-02	0.156	0.271	0.556	1.56	3.14	5.69	11.73
Bladder	2.50E-02	0.143	0.258	0.550	1.51	3.02	5.53	11.46
Breast	2.89E-01	0.231	0.324	0.690	1.89	3.79	6.67	13.15
Liver	1.64E-02	0.161	0.274	0.572	1.60	3.17	5.78	11.81
Oesophagus	6.75E-04	0.111	0.233	0.531	1.49	3.03	5.62	11.31
Thyroid	8.40E-02	0.183	0.288	0.628	1.80	3.69	6.57	13.52
Skin	6.34E-01	0.237	0.329	0.728	2.00	3.85	6.75	13.12
Bone	1.51E-01	0.469	0.495	0.723	1.73	3.34	6.01	12.24
Remainders								
Adrenals	3.70E-03	0.130	0.246	0.516	1.57	3.02	5.43	10.99
Brain	4.50E-03	0.177	0.306	0.682	1.90	3.79	6.84	13.38
Small intestines	3.83E-03	0.122	0.243	0.516	1.43	2.89	5.43	11.27
Kidneys	4.43E-02	0.162	0.272	0.576	1.58	3.13	5.73	11.73
Soft tissue	1.30E-01	0.185	0.289	0.625	1.73	3.42	6.17	12.34
Pancreas	1.09E-03	0.127	0.248	0.517	1.45	3.10	5.64	11.79
Spleen	1.34E-02	0.169	0.275	0.580	1.60	3.12	5.83	11.75
Thymus	4.28E-02	0.174	0.280	0.576	1.65	3.39	6.26	11.90
Uterus	1.97E-03	0.124	0.251	0.547	1.53	3.09	5.91	12.25
Effective Dose	0.093±1.6%	0.21±0.7%	0.31±0.5%	0.61±0.6%	1.65±0.6%	3.30±0.8%	6.02±0.8%	12.15±0.8%

Energy(MeV)	10	20	50	100	200	500	1000	2000
Gonads	26.0	36.2	72.6	121.1	162.1	232.5	298.1	262.5
RBM	18.9	31.0	57.1	85.6	119.1	173.0	221.3	232.6
Colon	20.1	33.2	66.3	101.6	142.8	208.3	252.5	252.4
Lungs	20.6	33.4	61.7	88.8	118.8	166.2	203.1	186.8
Stomach	18.9	31.2	63.4	95.2	136.2	189.2	242.4	232.3
Bladder	20.1	32.1	64.0	96.7	137.1	198.5	247.1	228.0
Breast	18.5	25.5	39.1	58.4	81.8	127.2	165.9	154.4
Liver	20.0	33.2	61.4	90.8	127.1	186.3	235.0	210.8
Oesophagus	18.1	36.8	71.9	110.8	153.0	210.1	260.9	247.5
Thyroid	17.8	24.2	40.9	83.0	116.4	141.7	176.1	206.8
Skin	10.3	15.9	30.4	47.7	69.4	105.0	137.8	146.0
Bone	18.9	30.8	55.5	80.6	111.2	157.2	200.1	187.3
Remainders								
Adrenals	22.0	38.3	60.3	96.3	136.5	230.2	254.5	246.7
Brain	21.0	33.1	56.0	74.9	97.4	129.7	153.0	146.0
Small intestines	18.9	32.1	67.1	103.2	147.9	215.4	267.7	250.9
Kidneys	18.5	30.4	59.1	87.6	127.5	190.0	244.5	230.3
Soft tissue	18.5	29.6	53.0	78.2	109.1	155.1	199.1	189.3
Pancreas	22.3	33.5	68.0	109.1	159.0	225.2	191.1	237.4
Spleen	19.0	31.3	66.5	97.5	133.9	186.9	238.5	231.4
Thymus	20.3	30.2	57.5	76.8	115.0	161.4	204.6	205.9
Uterus	19.2	38.0	69.2	105.3	141.1	220.2	281.7	242.5
Effective Dose	20.63±2.9%	32.40±2.4%	62.16±1.3%	96.63±1.2%	133.5±1.0%	190.2±1.5%	238.9±1.4%	227.7±1.3%

Table A4. Organ doses and effective doses per unit electron fluence incident in ISO geometry in pGy·cm² and pSv·cm² respectively

ELECTRONS - ISO								
Energy(MeV)	0.1	0.2	0.5	1	2	3	5	10
Gonads	5.64E-04	0.00E+00	9.35E-03	3.60E-02	2.30E+00	1.21E+01	5.02E+01	1.27E+02
RBM	3.96E-04	1.72E-03	1.12E-02	9.17E-02	2.05E+00	1.33E+01	1.95E+01	4.58E+01
Colon	9.07E-04	7.21E-03	2.14E-02	4.90E-02	1.33E-01	3.32E-01	8.78E-01	3.92E+00
Lungs	1.10E-04	2.74E-04	5.93E-03	2.35E-02	1.08E-01	2.78E-01	1.09E+00	1.69E+01
Stomach	0.00E+00	6.66E-04	3.87E-03	2.13E-02	1.01E-01	2.47E-01	1.11E+00	2.09E+01
Bladder	0.00E+00	2.43E-04	5.20E-03	2.35E-02	8.91E-02	2.48E-01	8.03E-01	1.50E+01
Breast	1.30E-03	2.43E-03	1.07E-02	7.78E-01	1.75E+01	3.79E+01	7.63E+01	1.44E+02
Liver	5.46E-06	4.70E-04	4.77E-03	1.95E-02	9.85E-02	2.53E-01	8.01E-01	1.07E+01
Oesophagus	3.13E-05	1.63E-04	2.67E-03	1.84E-02	7.63E-02	2.28E-01	7.69E-01	2.96E+00
Thyroid	0.00E+00	6.03E-04	4.74E-03	2.99E-02	1.08E-01	8.19E-01	9.86E+00	5.76E+01
Skin	8.56E+00	1.77E+01	6.62E+01	1.25E+02	1.51E+02	1.55E+02	1.57E+02	1.65E+02
Bone	1.22E-03	2.83E-03	1.76E-02	9.65E-02	2.33E+00	7.78E+00	2.20E+01	5.22E+01
Remainders								
Adrenals	0.00E+00	1.40E-03	3.99E-03	3.62E-02	6.70E-02	2.33E-01	7.11E-01	2.97E+00
Brain	0.00E+00	2.00E-04	4.84E-03	2.20E-02	1.06E-01	2.88E-01	1.20E+00	3.11E+01
Small intestines	3.56E-05	8.43E-04	3.98E-03	1.81E-02	8.72E-02	2.19E-01	7.19E-01	3.32E+00
Kidneys	0.00E+00	5.65E-04	6.00E-03	2.15E-02	9.98E-02	2.95E-01	9.89E-01	3.19E+01
Soft tissue	1.25E-03	3.26E-03	1.61E-02	5.84E-01	7.66E+00	1.56E+01	3.12E+01	6.65E+01
Pancreas	0.00E+00	3.34E-04	2.13E-03	1.38E-02	7.80E-02	2.06E-01	7.50E-01	3.39E+00
Spleen	0.00E+00	6.78E-04	2.22E-03	2.34E-02	9.35E-02	2.86E-01	8.98E-01	6.51E+00
Thymus	0.00E+00	1.38E-04	3.51E-03	1.45E-02	1.01E-01	2.72E-01	2.82E+00	6.09E+01
Uterus	0.00E+00	0.00E+00	1.58E-03	2.76E-02	9.05E-02	2.84E-01	6.59E-01	2.37E+00
Effective Dose	0.086±0.3%	0.178±0.4%	0.671±0.3%	1.33±0.4%	3.22±1.8%	7.81±2.2%	19.20±2.4%	50.81±2.2%

Energy(MeV)	20	50	100	200	500	1000	2000
Gonads	167.9	218.0	266.2	354.4	562.3	724.4	1030.5
RBM	92.9	195.7	272.8	363.0	510.8	647.4	819.2
Colon	24.0	173.5	290.9	403.7	573.8	740.5	926.3
Lungs	98.4	250.1	328.2	409.2	536.7	644.0	786.6
Stomach	70.5	183.1	270.6	378.6	541.1	681.9	886.8
Bladder	62.3	169.1	275.6	385.4	516.8	717.9	912.7
Breast	197.8	248.9	290.9	353.7	449.5	540.3	670.7
Liver	69.3	196.7	285.0	387.8	543.6	697.0	860.1
Oesophagus	16.1	161.0	292.9	398.8	591.0	706.8	883.5
Thyroid	118.5	216.7	318.5	389.9	595.7	723.9	856.4
Skin	177.5	221.9	263.5	317.1	408.3	494.6	603.2
Bone	104.2	215.7	283.3	365.4	490.4	615.0	762.7
Remainders							
Adrenals	63.0	172.8	284.8	406.3	567.5	712.9	998.3
Brain	123.2	284.7	344.8	406.0	490.5	582.4	669.9
Small intestines	26.5	155.2	272.8	391.1	577.5	748.5	948.5
Kidneys	105.5	191.4	283.0	377.5	540.2	701.2	862.3
Soft tissue	120.2	216.8	285.7	367.6	495.9	621.0	767.8
Pancreas	16.5	156.1	270.1	417.4	621.4	745.6	976.5
Spleen	67.9	213.2	304.2	381.2	518.0	658.1	842.5
Thymus	116.6	191.5	271.6	360.4	507.2	651.9	804.2
Uterus	23.3	168.8	259.7	423.1	560.5	819.2	929.8
Effective Dose	97.57±1.4%	203.6±1.1%	285.7±1.2%	379.7±1.1%	542.9±1.3%	685.6±1.2%	882.5±1.2%

Table A5. Organ doses and effective doses per unit pion fluence incident in ISO geometry in pGy-cm² and pSv-cm² respectively (preliminary)

PIONS - ISO							
Energy(MeV)	10	30	50	80	100	200	500
Gonads	493.8	1036.3	1234.4	867.6	737.7	643.8	565.2
RBM	528.1	983.8	1026.6	914.5	726.0	652.1	547.8
Colon	62.9	135.2	1127.7	820.7	686.8	627.3	503.3
Lungs	99.3	921.5	1397.5	828.5	620.2	600.9	496.5
Stomach	87.9	690.6	847.5	807.1	698.5	599.6	490.7
Bladder	79.5	530.8	756.3	962.8	657.5	594.7	487.0
Breast	1757.2	1412.1	711.5	655.8	646.4	531.0	454.9
Liver	79.9	622.3	1070.6	795.1	667.1	613.0	500.5
Oesophagus	59.9	131.2	1453.8	978.8	609.4	609.9	494.1
Thyroid	123.2	848.8	1126.3	974.1	648.5	563.6	465.2
Skin	2922.0	758.9	687.3	670.5	572.2	508.7	434.6
Bone	450.4	844.3	1062.5	727.3	596.4	556.5	464.7
Remainders							
Adrenals	70.2	440.3	829.8	901.1	618.6	577.2	491.9
Brain	118.5	1619.3	1946.1	672.1	591.5	594.8	482.8
Small intestines	57.7	156.6	894.5	902.2	679.7	617.9	508.6
Kidneys	98.3	1209.7	689.3	813.7	696.3	601.7	500.4
Soft tissue	765.1	966.6	930.7	775.1	629.2	577.4	480.8
Pancreas	58.3	113.1	958.9	1027.6	664.6	644.1	530.1
Spleen	74.8	508.9	1197.8	751.4	676.8	616.0	489.0
Thymus	187.8	1222.3	634.2	1073.8	579.9	568.0	466.6
Uterus	58.6	126.4	831.7	1024.9	666.6	635.3	473.8
Effective Dose	339.1±1.9%	840.0±1.0%	1317.3±1.2%	1281.7±1.1%	1157.2±1.1%	1164.3±0.8%	971.5±0.9%

Energy(MeV)	1000	2000	5000	10000	50000	100000
Gonads	591.4	772.3	967.8	1110.2	1552.0	1747.1
RBM	661.2	730.2	910.6	664.8	1574.4	1835.8
Colon	823.4	693.5	876.9	1073.0	1577.7	1866.6
Lungs	605.0	651.1	816.8	987.1	1351.6	1568.1
Stomach	594.1	666.9	821.5	1012.6	1454.6	1731.7
Bladder	603.4	691.6	870.5	1081.7	1521.8	1851.3
Breast	523.1	579.7	732.0	853.6	1172.7	1359.7
Liver	610.8	671.8	836.3	1025.9	1464.7	1723.3
Oesophagus	603.2	665.0	790.5	1037.6	1503.2	1786.4
Thyroid	608.2	604.7	821.4	954.1	1314.6	1614.8
Skin	505.6	546.6	674.1	793.1	1077.2	1245.4
Bone	561.1	614.7	768.1	922.3	1314.3	1540.0
Remainders						
Adrenals	643.3	666.4	831.0	1017.9	1470.4	1744.2
Brain	582.4	619.5	770.6	899.0	1188.6	1373.5
Small intestines	628.3	702.7	867.1	1078.5	1568.3	1862.6
Kidneys	605.8	669.3	839.4	1028.5	1454.9	1734.5
Soft tissue	579.7	630.9	791.0	952.8	1338.8	1559.8
Pancreas	640.4	677.2	859.5	1069.2	1545.7	1816.3
Spleen	616.3	660.4	852.9	1011.5	1460.3	1665.0
Thymus	594.5	616.1	879.8	1073.6	1335.2	1686.7
Uterus	609.7	745.5	901.0	1033.1	1576.1	1835.2
Effective Dose	1132.2±0.9%	1240.2±0.9%	1554.9±1.1%	1775.3±0.9%	2543.2±0.8%	2922.6±1.8%

Table A6. Organ doses and effective doses per unit muon fluence incident in ISO geometry in pGy·cm² and pSv·cm² respectively

MUONS - ISO								
Energy(MeV)	10	20	30	40	50	70	100	150
Gonads	161.8	474.9	435.6	350.0	501.9	554.7	455.3	455.3
RBM	106.8	212.7	291.5	373.5	422.3	468.6	399.7	399.7
Colon	42.5	58.9	101.2	236.2	519.5	526.8	449.3	449.3
Lungs	80.5	121.9	321.6	551.9	586.0	499.9	408.9	408.9
Stomach	61.9	124.0	254.0	365.3	437.8	482.2	432.5	432.5
Bladder	55.5	93.1	210.4	313.0	369.2	548.6	439.2	439.2
Breast	303.4	528.7	533.7	447.3	406.8	411.0	411.2	411.2
Liver	64.1	89.5	244.2	397.8	485.6	494.6	430.4	430.4
Oesophagus	40.5	53.9	89.7	198.2	471.0	631.1	445.8	445.8
Thyroid	83.9	257.5	326.9	431.3	474.8	532.2	447.8	447.8
Skin	756.1	494.9	423.2	400.3	399.8	424.7	392.5	392.5
Bone	117.5	242.4	324.1	429.5	482.8	454.3	388.3	388.3
Remainders								
Adrenals	54.1	69.0	203.7	360.8	366.3	579.1	446.3	446.3
Brain	90.6	179.9	436.3	636.6	694.6	484.9	392.2	392.2
Small intestines	40.4	54.1	99.9	219.8	429.1	540.3	434.3	434.3
Kidneys	71.4	126.6	374.9	379.7	369.5	502.0	432.9	432.9
Soft tissue	164.0	283.4	370.0	421.9	458.1	477.9	409.9	409.9
Pancreas	37.7	52.0	81.1	178.3	481.7	596.6	459.8	459.8
Spleen	64.9	87.3	232.2	423.5	554.2	476.4	437.2	437.2
Thymus	80.6	236.8	385.7	353.6	339.1	598.5	382.8	382.8
Uterus	38.8	49.0	88.7	227.3	427.3	623.0	443.2	443.2
Effective Dose	107.1±1.0%	221.9±1.1%	293.7±0.8%	368.7±0.6%	478.4±0.7%	515.0±0.7%	431.8±0.8%	348.6±0.5%

Energy(MeV)	200	500	1000	2000	5000	10000	20000	50000
Gonads	345.5	337.8	342.8	365.6	391.4	399.4	410.9	426.1
RBM	312.0	306.5	320.7	343.2	378.5	374.9	387.9	403.2
Colon	324.9	316.9	329.6	353.5	370.4	387.5	401.3	416.8
Lungs	328.0	330.6	348.1	374.8	392.8	407.6	421.1	436.8
Stomach	329.2	324.1	338.0	360.7	377.1	392.6	406.6	421.7
Bladder	327.2	317.4	330.8	355.1	370.3	387.3	400.6	417.0
Breast	323.6	319.7	337.9	362.1	374.0	394.0	408.3	424.4
Liver	328.6	323.0	335.6	359.8	378.4	391.6	405.3	421.4
Oesophagus	323.4	316.2	329.9	354.8	371.0	388.0	401.2	415.4
Thyroid	329.8	332.1	346.3	372.7	383.7	391.9	405.3	421.5
Skin	325.8	321.8	335.9	359.4	375.7	390.6	404.0	419.7
Bone	310.0	306.2	320.8	343.5	359.4	374.6	387.6	403.2
Remainders								
Adrenals	320.3	315.8	327.2	346.3	368.8	376.6	389.5	402.3
Brain	325.6	325.6	338.3	362.6	380.0	392.5	406.5	422.1
Small intestines	327.4	319.2	333.9	357.6	373.5	387.6	401.1	416.2
Kidneys	332.8	325.4	337.6	362.1	378.6	393.9	407.8	423.7
Soft tissue	326.2	321.4	336.3	360.4	376.2	391.6	405.0	420.6
Pancreas	335.5	325.0	339.3	363.9	378.3	391.3	404.5	419.8
Spleen	332.8	326.6	339.9	364.3	383.0	399.2	411.4	428.1
Thymus	323.1	314.6	329.9	353.5	367.1	390.9	403.9	419.8
Uterus	329.3	322.8	334.0	358.4	376.4	387.5	398.4	414.2
Effective Dose	328.8±0.5%	323.7±0.5%	336.3±0.4%	360.2±0.4%	380.5±0.5%	392.2±0.4%	405.3±0.4%	420.8±0.4%

FEASIBILITY STUDY ON AN ACTIVE NEUTRON DOSEMETER BASED ON CARBON ACTIVATION FOR THE LINEAR COLLIDER TESLA

A. Leuschner

Deutsches Elektronen-Synchrotron DESY, Germany

Abstract

The linear collider TESLA will be operated with a radio frequency (rf) pulse length of almost 1 ms at a repetition rate not higher than 5 Hz. From the point of dosimetry 1 ms of radiation is followed by at least 200 ms rest. The measurement of neutron fluences for radiation protection of persons behind the shielding and that of the electronics inside the tunnel is desirable. The time structure of the radiation opens up the opportunity to use methods where the information is released delayed to the rf-pulse such as activation methods. Therefore an active dosimeter on the basis of a simple plastic scintillator is proposed which uses the activation reaction $^{12}\text{C}(n,p)^{12}\text{B}$ due to neutrons above 13 MeV. The subsequent β decay of ^{12}B with a half-life of 20 ms leads to an exponential signal pattern right after the rf-pulse. Thermal neutrons also appear in the time spectrum with a lifetime of less than 2 ms clearly separated from the ^{12}B decay pattern as well as from the prompt peak. These three indications allow the setting-up of a dose equivalent for persons and a neutron displacement equivalent for electronics. Furthermore the dosimeter could be applied as a beam loss monitor capable of separating dark current and beam.

Introduction

At the linear collider TESLA the dosimetry of high-energy neutrons is one of the main issues of radiation protection. Behind thick shielding high-energy neutrons are the largest contributor to total dose [1]. The challenge for an active dosimeter is the time structure of the accelerator: 1 ms long bunch trains with a repetition rate of 5 Hz. Only fast scintillation counters can withstand the high rates within the duty time. Pulse height measurement as well as n- γ discrimination are not suitable due to dead time effects.

An active dosimeter is proposed that adopts the ^{11}C method. The underlying principle is the transfer of information of the prompt neutron field in residual activity decaying delayed. What is the ^{11}C method? It is described and compared to other dosimeters in [2]. A naked plastic scintillator is exposed in a neutron field for about 20 min. Neutrons with energies above 20 MeV produce residual activity by the reaction $^{12}\text{C}(n,2n)^{11}\text{C}$. After irradiation the scintillator is brought to a measuring station to count the induced ^{11}C activity. This discontinuous procedure can only be used in a very few cases and is not suitable for monitoring purposes.

To adopt the ^{11}C method implies finding another endoenergetic nuclear reaction leading to a radioactive nuclide with a half-life between 5 ms and 50 ms. The data of the activation reactions and of their decays are listed in Table 1. Details of the production cross-sections are displayed in Figure 1 along with a typical neutron spectrum (30 GeV electrons on a thick target behind 80 cm of lateral concrete shielding). Finally, the reaction product ^{12}B looks very promising. A special advantage is the high energy of the β particle emitted by the ^{12}B decay allowing the suppression of low-energy interactions. The time structure for a 5 Hz operation is shown in Figure 2.

The nuclides ^9C and ^9Li are produced with a lower cross-section starting from higher thresholds compared to ^{10}C and ^8Li . Thus a competitive signal at 0.1...0.2 s half-life is not expected. The situation is completely different for ^8Li and ^6He , which certainly compete to the ^{12}B signal but with 40 times longer half-life. Their signal could be exploited at repetition rates smaller than 1 Hz.

Table 1. Data of activation of ^{12}C and the decay of the residual nuclei

*Only short-lived but not prompt decaying nuclides are listed.
The cross-section values are taken at a neutron energy of 100 MeV (ENDF library).*

Activation				Decay			
Nuclear reaction	Product	Energy threshold [MeV]	Cross-section [mb]	Type	Daughter nuclide	Half-life [s]	Highest β energy [MeV]
(n,2n)	^{11}C	19	14	β^+	^{11}B	1 200	1.0
(n,3n)	^{10}C	32	1.7	β^+	^{10}B	19	1.9
(n,4n)	^9C	53	–	EC, p	^8B	0.13	8.2
(n,p)	^{12}B	13	18	β^-	^{12}C	0.02	13.4
(n,4np)	^8B	55	1.6	EC, β^+	2α	0.77	14.0
(n,2p)	^{11}Be	27	0.7	β^-	^{11}Be	14	11.5
(n,n3p)	^9Li	47	–	β^-	^9Be	0.18	13.6
(n,p α)	^8Li	23	13	β^-	2α	0.84	13.0
(n,n2p α)	^6He	32	16	β^-	^6Li	0.81	3.5

Figure 1. Production yield cross-sections of neutrons on ^{12}C (solid) and a typical neutron fluence spectrum (dashed) of 30 GeV electrons on a thick target behind 80 cm lateral concrete shielding

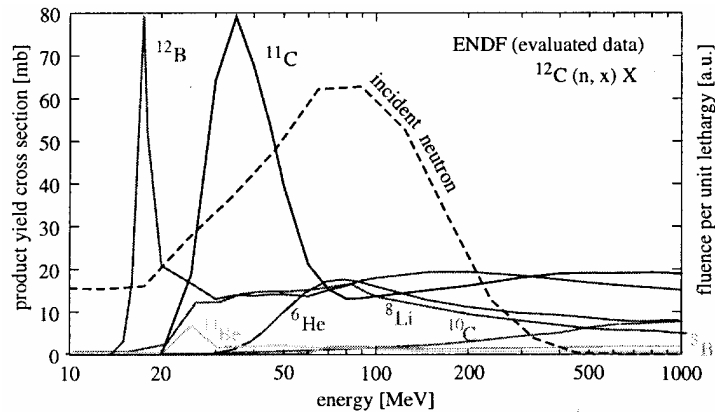
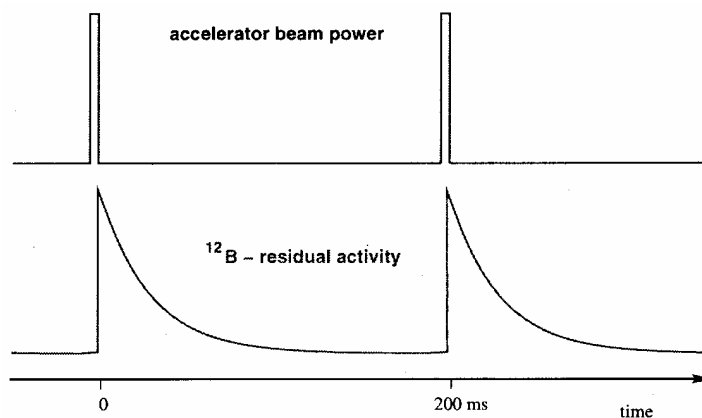


Figure 2. Decay of the ^{12}B activity at a pulse repetition rate of 5 Hz

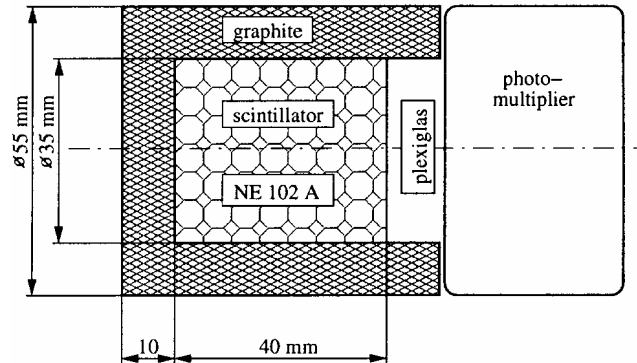


In 1967 the cross-section $^{12}\text{C}(n,p)^{12}\text{B}$ was measured [3] with a plastic scintillator in a pulsed neutron beam where the ^{12}B decay pattern was used. Although the experimental data differ from the evaluated ones (ENDF) an active dosimeter on the basis of ^{12}B activation is worth being investigated.

Dosimeter design

A sketch of the detector is shown in Figure 3. A plastic scintillator (38.5 cm^3) of type NE 102A is surrounded by a graphite cylinder and read out by a photomultiplier. The graphite shell contributes to the wanted signal and acts as a certain shield against low-energy background radiation. The analogue signal is fed into a discriminator. A 200 MHz counter (STRUCK STR-7201), the clock of which is not synchronised to that of the accelerator, counts the out-coming pulses. Thus, the counting is independent of any accelerator operation mode. With a counting time of 1 ms one obtains 60 000 numbers per detector and minute. This amount of data can well be compressed by replacing a chain of zeros by just the number of zeros as a negative value. Finally, an array of 2 000 integers is passed to an archive that is accessible via Internet. This limits the background count rate to 10 cps (counts per second) already allocating $10 \cdot 60 \cdot 2 = 1\,200$ integers.

Figure 3. Sketch of the detector cross-section. The cylindrical detector is housed in an aluminium cylinder. The photomultiplier is longer than shown here.



Data analysis

The stored data are analysed in order to convert them into dose equivalent. First, the correlated count rate caused by accelerator operation and the uncorrelated count rate due to background radiation have to be separated. Second, the different contributions of the radiation field inducing the correlated count rate should be determined.

Count rate separation

The separation of correlated and uncorrelated count rate is simple and fast. It is based on the Poisson distribution of the uncorrelated count rate. The one-minute reading of a counter leads to a set of $N = 60\,000$ numbers n_i . Let n be their mean in the order of 0.01 corresponding to a count rate of 10 cps. So any non-zero bin is followed by 100 zeros on average. The probability of finding $c = 0, 1, 2, \dots$ counts in any bin is then:

$$f(c) = \frac{1}{c!} \cdot n^c \cdot e^{-n}$$

For this example the total number of counts is set up to 99% from bins containing one count, 0.99% from bins with two counts and so on. So, just counting all time bins containing one count is a good estimation of the uncorrelated count rate within a few per cent error. An accelerator correlated signal shows up at higher bin contents not compatible with this distribution.

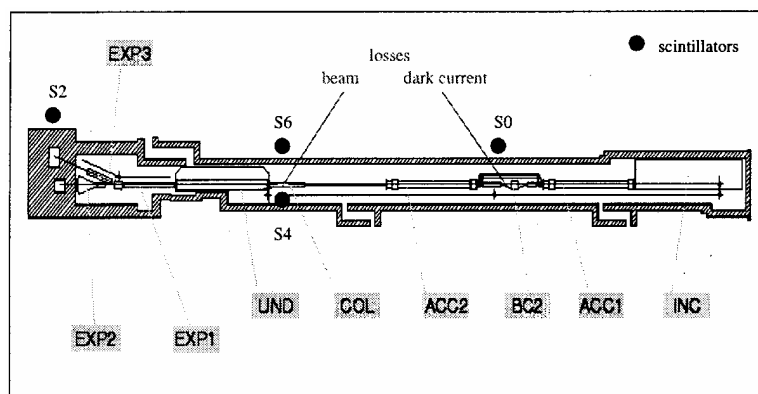
Evaluation of the correlated counts rate

The separation of correlated and uncorrelated count rate is performed for every data set. But the evaluation of the correlated count rate is only performed for events with a minimum quality as the desired ^{12}B signal is expected to be 4 orders of magnitude smaller than the prompt signal. The statistical method could be called “coherent superposition”. It acts like a scope. A trigger threshold is applied such that if a cluster of counts contains more than 10 counts it is regarded as an event. The event is a 2 500 ms wide time window starting 100 ms before the cluster centre. These events are averaged over longer time periods (1 min, 1 hour, 1 day).

Measurements

The four scintillators S0, S2, S4 and S6 were positioned around the TTF 1 as shown in Figure 4. S0, S2 and S6 were outside the heavy concrete shielding and S4 inside the tunnel.

Figure 4. Positions of beam and dark current losses and detectors at TTF



Prompt signal

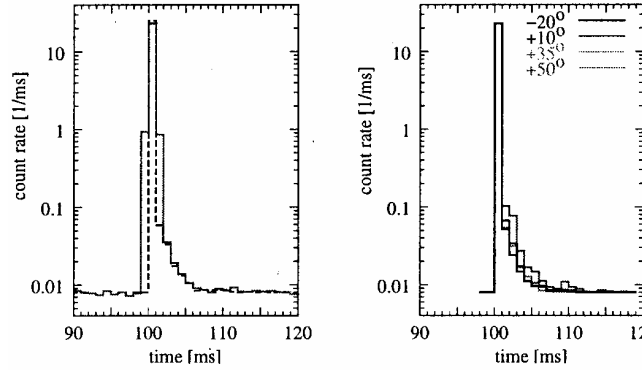
The comparison of the S0 counter history with different accelerator parameters shows a correlation to the accelerator gradient in module 2 but not to the bunch charge of the beam. Thus S0 sees the dark current of the module 2 coming upstream and being deflected by the most downstream dipole of the bunch compressor 2. This is in agreement with measurements of residual activity in the wall of the beam pipe.

Thermal neutrons

The first set of measurements was performed with the counter S0 near the dark current loss point but outside the shielding (Figure 4). These electrons with energies around 100 MeV are not capable of producing high-energy neutrons but low-energy ones (giant resonance). The time spectrum is therefore expected to show none of the desirable decay patterns. In spite of this, a tail follows the prompt peak as is shown in Figure 5 (left). The only secondary particles capable of time-of-flights (TOF) in the ms range are thermal neutrons. But the thermalisation even in large detectors takes much less time than 1 ms [4]. Thus only thermal neutrons arriving from longer paths with a speed of 2.2 m/ms can cause such a tail. In Figure 5 (left) the tail is about 4 ms long, i.e. a path length up to 10 m.

To verify this explanation a Monte Carlo simulation with FLUKA [5,6,7] was performed with a pure cylindrical geometry. The aluminium target is 70 cm long with a radius of 12 cm. It is surrounded by an 80 cm thick heavy concrete shielding starting at radius 250 cm. Outside the shielding, 3 cm thick and 200 cm long scintillator rings are located. They are defined by their angle with respect to the target, 0° meaning lateral, $< 0^\circ$ backward and $> 0^\circ$ forward geometry. The energy deposited in a scintillator ring "RULL" was scored as a function of the delay time "ATRACK" counted from the start of the primary electron. The results are shown in Figure 5 (right). The normalisation of the time spectra was done at the prompt peak of the measured spectrum of S0. The S0 background was added, as well. All time spectra show almost the same shape independent of the angle/distance.

Figure 5. Right: FLUKA simulation of the time spectrum (RULL vs. ATRACK) for different angles. 0° means lateral geometry describing the position of counter S0 relative to the bunch compressor 2 (BC 2) as shown in Figure 4. Left: Comparison of the simulated time spectrum (dashed) with the measured one (solid) from counter S0.



To understand the mechanism by which thermal neutrons are counted, the detector was surrounded by a 0.5 mm thick cadmium cover. The TOF tail does not disappear with the Cd cover but collects more counts. So the γ radiation from neutron capture (n,γ) in the environment of the detector (mainly shielding) is measured. The characteristic time of the TOF tail can be regarded as the lifetime of thermal neutrons in the vicinity of the counter and therefore the signal might be geometry and/or material dependent.

High-energy neutrons

Model

The time spectra must be analysed quantitatively. They show five different contributions: prompt peak, thermal neutrons, ^{12}B decay, ^8Li decay and background. For the rf-pulse at $t = 0$ the spectrum is fitted to:

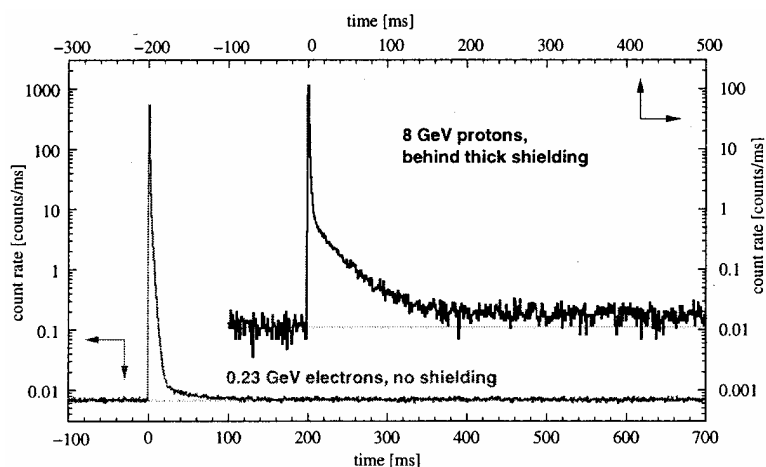
$$A(t) = \underbrace{A_p \cdot \delta(t)}_{\text{prompt peak}} + \underbrace{A_1 \cdot \exp(-t/\tau_1)}_{\text{thermal neutrons}} + \underbrace{A_{12} \cdot \exp(-t/\tau_{12})}_{^{12}\text{B decay}} + \underbrace{A_8 \cdot \exp(-t/\tau_8)}_{^8\text{Li decay}} + \underbrace{A_b}_{\text{back ground}}$$

where the A_x are the amplitudes and τ_x the lifetimes. $\tau_{12} = 20 \text{ ms} / \ln(2)$ and $\tau_8 = 840 \text{ ms} / \ln(2)$ are kept fixed. In practice the prompt peak consists of three bins. They are added to get the number of counts per pulse. While the exponential function exactly describes the decay patterns, it is just taken for the thermal neutrons as a first approximation. The counts per pulse are calculated by the products $\tau_x A_x$.

Measurements inside the TTF 1 tunnel

Because of its low electron energy of about 230 MeV the TTF 1 is not well suited for measuring high-energy neutrons. Nevertheless an experiment with the linac was performed for which the beam was dumped in the collimator where the counter S4 is located (see Figure 4). Figure 6 displays the corresponding time spectrum (left). The ^{12}B decay pattern is clearly seen. But the desirable signal is about 4 orders of magnitude smaller than the prompt peak, and much smaller than the TOF signal, is well. Unfortunately, the neutron fluences for this parasitic measurement are unknown. Therefore a calibration must be undertaken at higher beam energies.

Figure 6. Time spectra from a mainly e- γ radiation field in the TTF tunnel (left) and a neutron radiation field in the PETRA southeast hall near the DESY 3 to PETRA transfer line



Measurements near the DESY 3 to PETRA transfer line

The radiation field in the TTF 1 tunnel is mainly dominated by the e- γ component. Neutrons or even high-energetic neutrons hardly contribute to the dose. That is why one counter has been operated in a neutron-dominated radiation field caused by 8 GeV protons being transferred from the DESY 3 synchrotron to the PETRA ring at a repetition rate of $\frac{1}{4}$ Hz or less. The counter is located in the PETRA southeast hall. It is laterally shielded by 2 m of soil and concrete from a line source of 8 GeV proton losses. The time spectrum of the counter in Figure 6 (right) shows very clearly the ^{12}B and ^8Li decay patterns. The fit gives $A_{12} = 0.49$ and $A_8 = 0.0075$ counts/ms leading to 14 and 9 counts per rf-pulse, respectively. The count ratio is in agreement with the cross-sections of both processes being on the same level (see Figure 1).

The whole spectrum is an average of 1 300 rf-pulses corresponding to 600 μSv neutron dose. A first estimate of the counter's sensitivity gives 30 detected ^{12}B decays per μSv . Doses lower than 10 μSv can hardly be detected because of bad statistics.

Summary

In an e- γ radiation field at TTF 1 and in a neutron radiation field at the DESY 3 to PETRA transfer line active dosimeters on plastic scintillator basis were tested in parasitic mode. Their time spectra show the expected ^{12}B decay pattern as well as a time-of-flight part. The first is a clear signature of high-energy neutrons. The latter is caused by thermal neutrons.

The size of the dosimeter has to be optimised according to the application. A simple calibration and functionality check as well as robust pattern recognition have to be developed using test beams.

The dosimeter can only be applied in pulsed radiation fields with repetition rates less than 10 Hz at TESLA. Here it could be also used inside the tunnel to discriminate dark current from beam losses.

In terms of the primary electron energy the discrimination threshold is between 100 MeV and 200 MeV.

REFERENCES

- [1] Dinter, H., A. Leuschner, K. Tesch, D. Dworak and J. Łoskiewicz, “Calculation of Hadron Yields Around Thick Targets and Doses Behind Concrete Shielding of High-energy Electron Accelerators”, *NIM*, A 455:460-469 (2000).
- [2] Dinter, H., B. Racky and K. Tesch, “Neutron Dosimetry at High-energy Accelerators”, *NIM*, A 376:104-114 (1996).
- [3] Rimmer, E.M. and P.S. Fisher, “Resonances in the (n,p) Reaction on ^{12}C ”, *Nuclear Physics*, A108:567-576 (1968).
- [4] Dinter, H. and K. Tesch, “Moderated REM Meters in Pulsed Neutron Fields”, *NIM*, 136:389-392 (1976).
- [5] Fassò, A., A. Ferrari, J. Ranft and P.R. Sala, “New Developments in FLUKA Modelling of Hadronic and EM Interactions”, *Workshop on Simulating Accelerator Radiation Environments (SARE-3)* (1997).
- [6] Fassò, A., A. Ferrari and P.R. Sala, “Designing Electron Accelerator Shielding with FLUKA”, *8th Int. Conf. on Radiation Shielding*, Arlington (1994).
- [7] Ferrari, A., T. Rancati and P.R. Sala, “FLUKA Applications in High-energy Problems: From LHC to ICARUS and Atmospheric Showers”, *Workshop on Simulating Accelerator Radiation Environments (SARE-3)* (1997).

**BENCHMARK CALCULATIONS WITH
SIMPLE PHANTOM FOR NEUTRON DOSIMETRY (2)**

Yukio Sakamoto, Shuichi Tsuda, Tatsuhiko Sato
JAERI, Japan Atomic Energy Research Institute, Japan

Nobuaki Yoshizawa
MRI, Mitsubishi Research Institute, Japan

Hideo Hirayama
KEK, High-energy Accelerator Research Organisation, Japan

Abstract

Benchmark calculations for high-energy neutron dosimetry were undertaken after SATIF-5. Energy deposition in a cylindrical phantom with 100 cm radius and 30 cm depth was calculated for the irradiation of neutrons from 100 MeV to 10 GeV. Using the ICRU four-element soft tissue phantom and four single-element (hydrogen, carbon, nitrogen and oxygen) phantoms, the depth distributions of deposition energy and those total at the central region of phantoms within 1 cm radius and at the whole region of phantoms within 100 cm radius were calculated. The calculated results of FLUKA, MCNPX, MARS, HETC-3STEP and NMTC/JAM codes were compared. It was found that FLUKA, MARS and NMTC/JAM showed almost the same results. For the high-energy neutron incident, the MCNP-X results showed the largest ones in the total deposition energy and the HETC-3STEP results showed smallest ones.

Introduction

Subsequent to the recommendations of ICRP Publication 60 [1], effective doses for high-energy neutrons were calculated using several computer codes. Unfortunately, above 20 MeV there are few cross-section libraries due to a lack of experimental data. Consequently, computer codes that do not need cross-section data were used for effective dose calculation for high-energy neutrons. In those computer codes, theoretical models or empirical formulae are used to calculate cross-sections.

The dose conversion coefficients from neutron fluence to effective dose evaluated with FLUKA, HERMES (HETC-3STEP) and MCNPX codes were reviewed in previous SATIF meetings [2-9]. From the comparison of neutron effective dose conversion coefficients for AP, PA and ISO irradiations, the maximum ratio of maximum to minimum value of effective dose was about 1.8 at 2 GeV for AP irradiations [10]. The difference was caused by the variations in anthropomorphic computational models and cross-section model.

Two neutron dosimetry experiments were also reviewed during the SATIF-5 meeting. One was a high-energy depth-dose experiment performed at LANCE/WNR (USA) using filtered beams of neutrons with energies up to 800 MeV [11] and the other was TIARA plastic phantom experiments in Japan using 40 and 65 MeV quasi-mono-energetic neutrons [12].

To investigate the performance of computer codes for high-energy neutron dosimetry calculations, simple benchmark calculations were planned and calculation results for neutron dose were compared. During the SATIF-4 meeting, neutron dose distributions in the ICRU four-element soft tissue phantom having semi-infinite geometry were presented with HETC-3STEP and MARS calculations [13]. For the SATIF-5 meeting, neutron dose distributions in ICRU four-element soft tissue phantom and single-element phantoms having finite geometry were compared among FLUKA, MCNPX and HETC-3STEP calculations [10]. There were large differences among calculated results, especially for the single-element phantom (up to a factor of seven).

During this meeting, SATIF-5 results were revised and the results calculated with the MARS and NMTC/JAM codes were added.

Benchmark calculations

Figure 1 shows the geometry of the simple cylindrical phantom with 100 cm radius and 30 cm depth having a density of 1.0 g cm^{-3} . Energy deposition distributions in phantoms irradiated by neutrons were calculated for the ICRU four-element soft tissue phantom and four single-element (hydrogen, carbon, nitrogen and oxygen) phantoms. The depth distributions at the central region within 1 cm radius from the beam line and at the whole region within 100 cm radius were evaluated for 100 MeV, 1 GeV, 3 GeV and 10 GeV neutrons irradiated with pencil beam. Requested results were deposition energy per unit volume or deposition energy per region.

Computer codes

Five computer codes were used in this benchmark calculation. The names of the participants are shown in Table 1.

Table 1. Participants and the codes used

Participant	Organisation	Code	Additional information
M. Pelliccioni	INFN (Italy)	FLUKA [14-17]	
M. Sutton	Georgia Institute of Tech. (USA)	MCNPX [18]	LA150 library [25]
N. Yoshizawa S. Tsuda	MRI (Japan) JAERI (Japan)	HETC-3STEP [19] MORSE-CG/KFA [20]	JENDL-3.1 library [26]
N. Mokhov	Fermi Laboratory (USA)	MARS [21,22]	
T. Sato	JAERI (USA)	NMTC/JAM [23] MCNP [24]	

Results of calculations*Energy deposition distribution*

Figures 2-4 show the results of energy deposition distributions in ICRU four-element soft tissue, hydrogen and oxygen cylindrical phantom for 10 GeV neutron irradiations. For the soft tissue phantom, maximum differences at the central region and at the whole region are within factors of six and three at 10 GeV neutron irradiation, respectively. For the hydrogen phantom, calculated results agree well with each other up to 1 GeV, except for 0-3 cm depth at 100 MeV. Above 3 GeV neutron irradiation, systematic differences appear. For the carbon, nitrogen and oxygen phantoms, results are very similar. For almost all energy regions, maximum results emerge from the HETC-3STEP calculations and minimum results from the FLUKA calculations for both the central and the whole region of the phantom. The overestimation of HETC-3STEP ones was caused by the mismatch of number densities in carbon, nitrogen and oxygen phantoms. Figure 5 shows the revised results of energy deposition distribution in the oxygen phantom for 10 GeV neutron irradiation. The overestimation of the HETC-3STEP calculation disappeared.

Figure 6 shows the energy deposition distribution in the semi-infinite ICRU four-element soft tissue for 100 MeV, 1 GeV and 10 GeV neutron irradiations calculated with MARS and HETC-3STEP. For 1 GeV neutron irradiation, the two results are very similar. The HETC-3STEP result is larger than that of MARS for 100 MeV neutron irradiation and smaller than that of MARS for 10 GeV neutron irradiation. The latter behaviour is the same as that shown in Figure 2.

Figure 7 shows the energy deposition distribution in the infinite ICRU four-element soft tissue at the central region and at the whole region for 10 GeV neutron irradiations calculated with FLUKA and NMTC/JAM codes. The difference between the two results is very small. Figure 8 shows the energy deposition distribution in the finite ICRU four-element soft tissue phantom at the whole region for 10 GeV neutron irradiation calculated with FLUKA and NMTC/JAM, and in semi-infinite soft tissue phantom calculated with MARS. The results of the three codes are in fairly good agreement.

Total deposition energy

Total deposition energies in the whole region of each phantom were calculated by the integration of energy deposition distributions over the depth. Figures 9-11 show the total deposition energy at the whole region of the phantoms as a function of incident neutron energy for the ICRU four-element soft tissue, hydrogen and oxygen phantoms, respectively. In the case of the soft tissue, the FLUKA result

for 1 GeV is smaller than the other code results. For 10 GeV neutron irradiation, MARS, NMTC/JAM and FLUKA results agree well. The HETC-3STEP result is smaller than the other three code results, whereas the MCNP result is larger. For the hydrogen phantom, the results agree well up to 1 GeV and differences become greater with increasing neutron energy above 3 GeV. MCNPX results show the largest values and HETC-3STEP results show the smallest values. For the oxygen phantom, there are large differences between three code results above 1 GeV and the order of size in the three code results is the same as that in the hydrogen phantom.

Summary

A simple benchmark for high-energy neutron dosimetry was set up. Calculated neutron doses in the simple cylinder phantom were compared in the energy range from 100 MeV to 10 GeV. It was found that FLUKA, MARS and NMTC/JAM results were almost the same. For the high-energy neutron incident, the MCNP-X results showed the largest results and the HETC-3STEP results showed the smallest ones in the total deposition energy calculations.

As a result of this benchmark, it is recommended to perform further studies so as to better predict the accuracy of the computer codes for high-energy neutron dosimetry calculations. Some studies listed below are needed in the future:

- Comparison of energy deposition distribution for neutrons up to 100 GeV.
- Comparison of partial energy deposition by p, d, t, ^3He , alpha and other particles.
- Experimental approach is also needed (ex. Refs. [11,12]).

Acknowledgements

We wish to thank Dr. M. Pelliccioni, Dr. M. Sutton and Dr. N. Mokhof for their contribution to this benchmark.

REFERENCES

- [1] International Commission on Radiological Protection (ICRP), *1990 Recommendations of the International Commission on Radiological Protection*, Publication 60, Pergamon Press, Oxford (1991).
- [2] Iwai, S., T. Uehara, O. Sato, N. Yoshizawa, S. Furihata, S. Tanaka and Y. Sakamoto, "Evaluation of Effective Dose Irradiated by High-energy Radiation", *Proc. of the Specialists Meeting on Shielding Aspects of Accelerators, Targets and Irradiation Facilities*, Arlington, Texas (USA), 28-29 April 1994, OECD Documents, pp.305-322 (1995).

- [3] Iwai, S., T. Uehara, O. Sato, N. Yoshizawa, S. Furihata, S. Takagi, S. Tanaka and Y. Sakamoto, “Evaluation of Fluence to Dose Equivalent Conversion Coefficients for High-energy Neutrons – Calculation of Effective Dose Equivalent and Effective Dose”, *Proc. of 2nd Specialists Meeting on Shielding Aspects of Accelerators, Targets and Irradiation Facilities*, CERN, Geneva, Switzerland, 12-13 October 1995, OECD Documents, pp. 233-253 (1996).
- [4] Pelliccioni, M., “Conversion Coefficients for High-energy Radiation”, *Proc. of 3rd Specialists Meeting on Shielding Aspects of Accelerators, Targets and Irradiation Facilities*, Tohoku University, Sendai, Japan, 12-13 May 1997, OECD Documents, pp. 289-298 (1998).
- [5] Iwai, S., T. Uehara, O. Sato, N. Yoshizawa, S. Furihata, S. Takagi, S. Tanaka and Y. Sakamoto, “Overview of Fluence to Dose Equivalent Conversion Coefficients for High-energy Radiations – Calculational Methods and Results of Effective Dose Equivalent and Effective Dose Per Unit Particle Fluence”, *Proc. of 3rd Specialists Meeting on Shielding Aspects of Accelerators, Targets and Irradiation Facilities*, Tohoku University, Sendai, Japan, 12-13 May 1997, OECD Documents, pp. 299-331 (1998).
- [6] Pelliccioni, M., “Radiation Weighting Factors and Conversion Coefficients for High-energy Radiation”, *Proc. of 4th Specialists Meeting on Shielding Aspects of Accelerators, Targets and Irradiation Facilities*, Knoxville, Tennessee, USA, 17-18 September 1998, OECD Documents, pp. 179-191 (1999).
- [7] Iwai, S., T. Uehara, O. Sato, N. Yoshizawa, S. Furihata, S. Takagi, S. Tanaka and Y. Sakamoto, “Overview of Fluence to Dose Equivalent Conversion Coefficients for High-energy Radiations: Calculational Methods and Results of Two Kind of Effective Doses Per Unit Particle Fluence”, *Proc. of 4th Specialists Meeting on Shielding Aspects of Accelerators, Targets and Irradiation Facilities*, Knoxville, Tennessee, USA, 17-18 September 1998, OECD Documents, pp. 193-220 (1999).
- [8] Sutton, M.R., N.E. Hertel and L.S. Waters, “Fluence-to-effective Dose Conversion Coefficients for High-energy Radiations Calculated with MCNPX”, *Proc. 5th Specialists Meeting on Shielding Aspects of Accelerators, Targets and Irradiation Facilities*, Paris, France, 18-21 July 2000, OECD Documents, pp. 297-311 (2001).
- [9] Sakamoto, Y., S. Tsuda, O. Sato and N. Yoshizawa, “Evaluation of Dose Conversion Coefficients for High-energy Radiation in Japan after SATIF-4”, *Proc. of 5th Specialists Meeting on Shielding Aspects of Accelerators, Targets and Irradiation Facilities*, Paris, France, 18-21 July 2000, OECD Documents, pp. 313-324 (2001).
- [10] Yoshizawa, N., Y. Sakamoto, S. Iwai and H. Hirayama, “Benchmark Calculation with Simple Phantom for Neutron Dosimetry”, *Proc. of 5th Specialists Meeting on Shielding Aspects of Accelerators, Targets and Irradiation Facilities*, Paris, France, 18-21 July 2000, OECD Documents, pp. 253-264 (2001).
- [11] Sutton, M.R., N.E. Hertel and L.S. Waters, “A High-energy Neutron Depth-dose Experiment Performed at the LANCE/WNR Facility”, *Proc. of 5th Specialists Meeting on Shielding Aspects of Accelerators, Targets and Irradiation Facilities*, Paris, France, 18-21 July 2000, OECD Documents, pp. 231-240 (2001).

- [12] Nakane, Y. and Y. Sakamoto, “Benchmark Experiments of Absorbed Doses in a Slab Phantom for Several Tens MeV Neutrons at the TIARA Facility”, *Proc. 5th Specialists Meeting on Shielding Aspects of Accelerators, Targets and Irradiation Facilities*, Paris, France, 18-21 July 2000, OECD Documents, pp. 241-252 (2001).
- [13] Yoshizawa, N., N. Nakao, Y. Sakamoto and S. Iwai, “Comparison of Computer Code Calculations for the ICRU Slab Phantom”, *Proc. of 4th Specialists Meeting on Shielding Aspects of Accelerators, Targets and Irradiation Facilities*, Knoxville, Tennessee, USA, 17-18 Sept. 1998, OECD Documents, pp. 231-238 (1999).
- [14] Fassò, A., *et al.*, “FLUKA: Hadronic Benchmarks and Applications”, *Proc. MC93 Monte Carlo Conference*, 22-26 February 1993, Tallahassee (Florida), P. Dragovitsch, S.L. Linn, M. Burbank (eds.), p. 88 (1994).
- [15] Fassò, A., *et al.*, “An Update about FLUKA”, *Proc. 2nd Workshop on Simulating Accelerator Radiation Environments*, CERN, Geneva, Switzerland, 9-11 Oct. 1995, G.R. Stevenson (ed.), CERN Report TIS-RP/97-05, pp. 158-170 (1995).
- [16] Fassò, A., *et al.*, “New Developments in FLUKA Modelling Hadronic and EM Interactions”, *Proc. 3rd Workshop on Simulating Accelerator Radiation Environments*, KEK, Tsukuba, Japan, 7-9 May 1997, H. Hirayama (ed.), KEK Proceedings 97-5, pp. 32-43 (1997).
- [17] Ferrari, A., *et al.*, “The Physics of High-energy Reactions”, *Proc. of the Workshop on Nuclear Reaction Data and Nuclear Reactors Physics, Design and Safety*, International Centre for Theoretical Physics, Miramare-Trieste, Italy, 15 April-17 May 1996, A. Gandini and G. Reffo (eds.), *World Scientific* (1998).
- [18] Hughes, H.G., *et al.*, “MCNPX – The LAHET/MCNP Code Merger”, XTM-RN(U) 97-012 (1997).
- [19] Yoshizawa, N., K. Ishibashi, H. Takada, *J. Nucl. Sci. and Technol.*, 32, 601 (1995).
- [20] Cloth, P., *et al.*, KFA-IFLE-EAN 12/88 (1988).
- [21] Mokhov, N.V., *The MARS Code System User’s Guide*, Fermilab-FN-628 (1995).
- [22] Krivosheev, O.E. and N. V. Mokhov, *A New MARS and its Applications*, Fermilab-Conf-98/43 (1998).
- [23] Niita, K., “High-energy Nuclear Reaction Code JAM”, *Proc. of the 1999 Symposium on Nuclear Data*, JAERI-Conf-2000-005, pp. 98-103 (2000).
- [24] Biesmeister, J.F. (ed.), *MCNP – A General Monte Carlo N-particle Transport Code, Version 4A*, LA-12625-M (1993).
- [25] Chadwick, M.B., *et al.*, *Nucl. Sci. Eng.*, 131, 293 (1999).
- [26] Nakagawa, T., *et al.*, *J. Nucl. Sci. and Technol.*, 32, 1259 (1995).

Figure 1. Geometry of simple phantom for the benchmark calculations

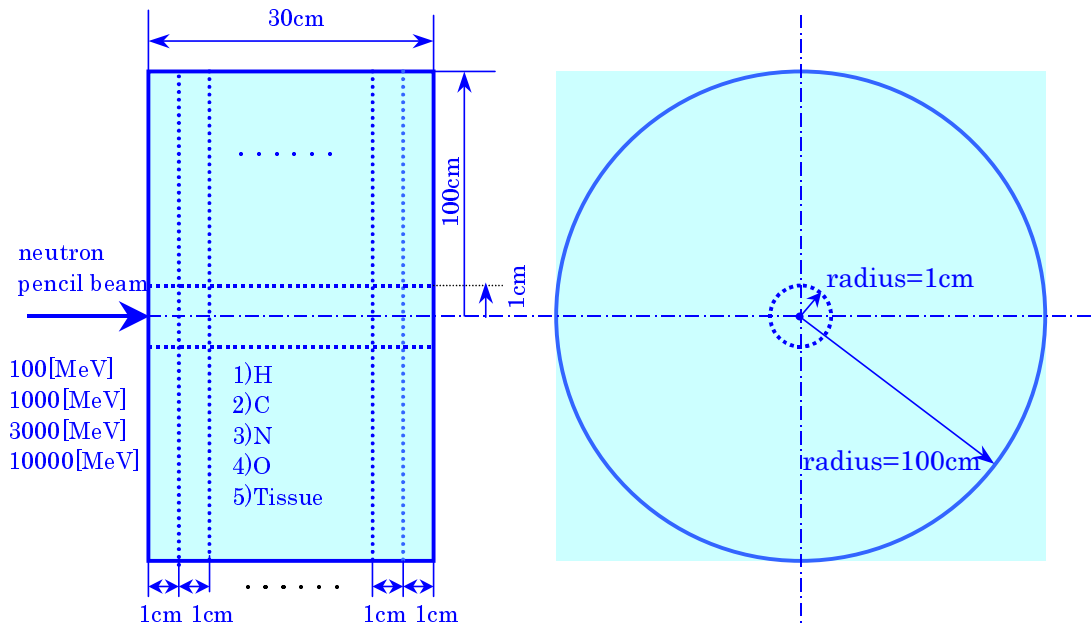


Figure 2. Comparison of energy deposition distribution in ICRU soft tissue phantom for 10 GeV neutron irradiation

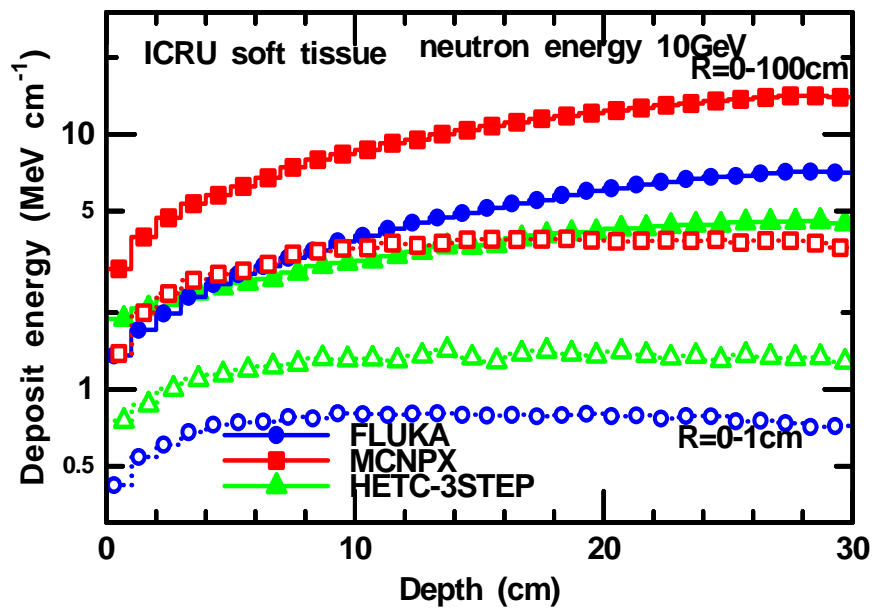


Figure 3. Comparison of energy deposition distribution in hydrogen phantom for 10 GeV neutron irradiation

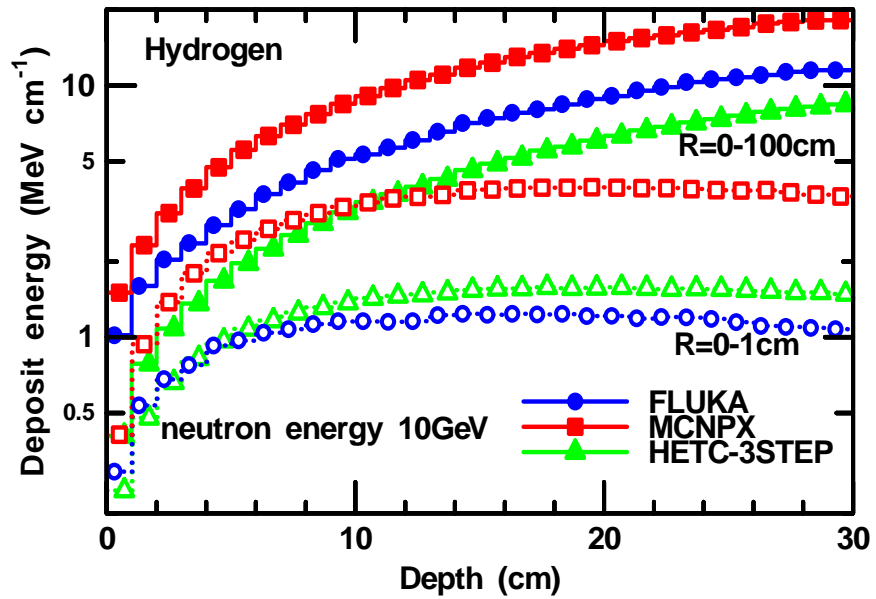


Figure 4. Comparison of energy deposition distribution in oxygen phantom for 10 GeV neutron irradiation (old results)

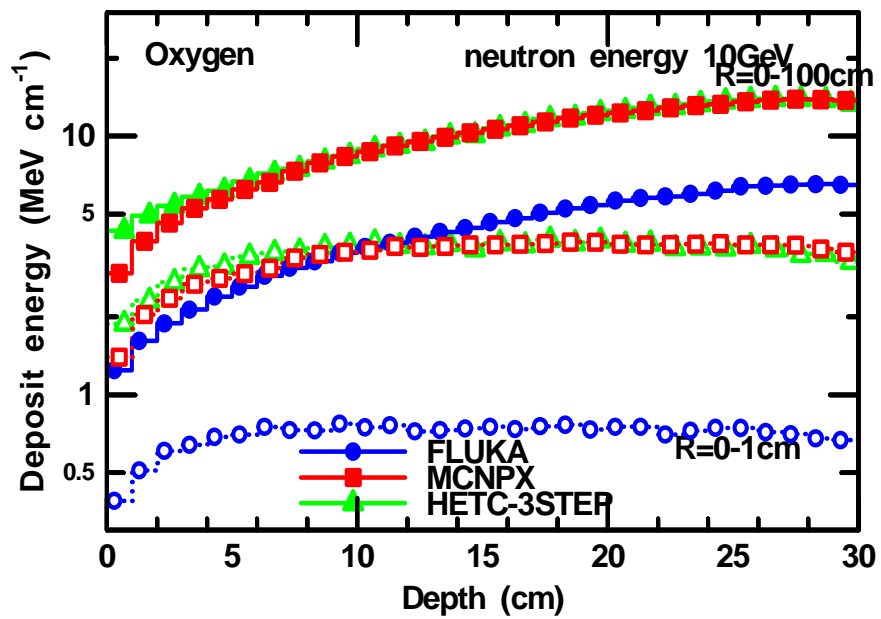


Figure 5. Comparison of energy deposition distribution in oxygen phantom for 10 GeV neutron irradiation (revised results)

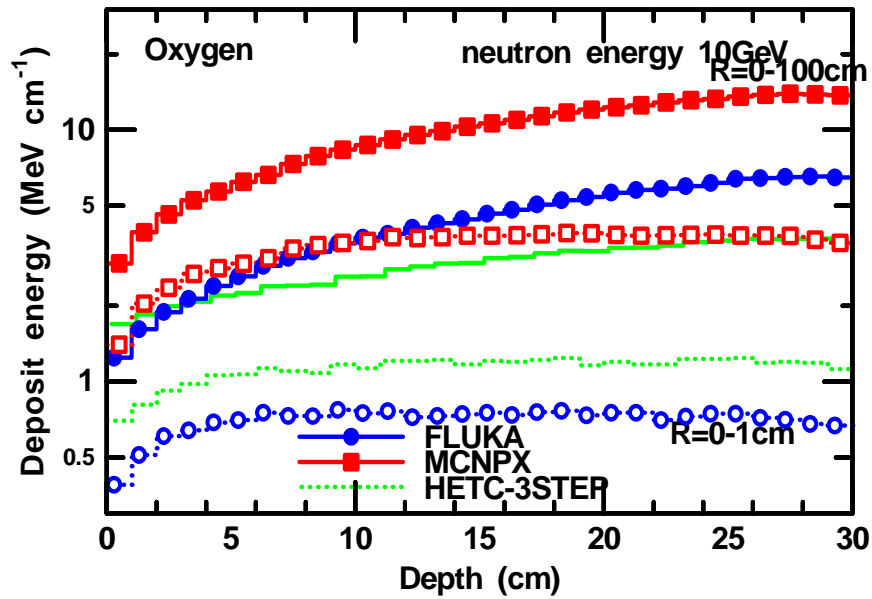


Figure 6. Comparison of energy deposition distribution in ICRU soft tissue semi-infinite phantom for 10 GeV neutron irradiation

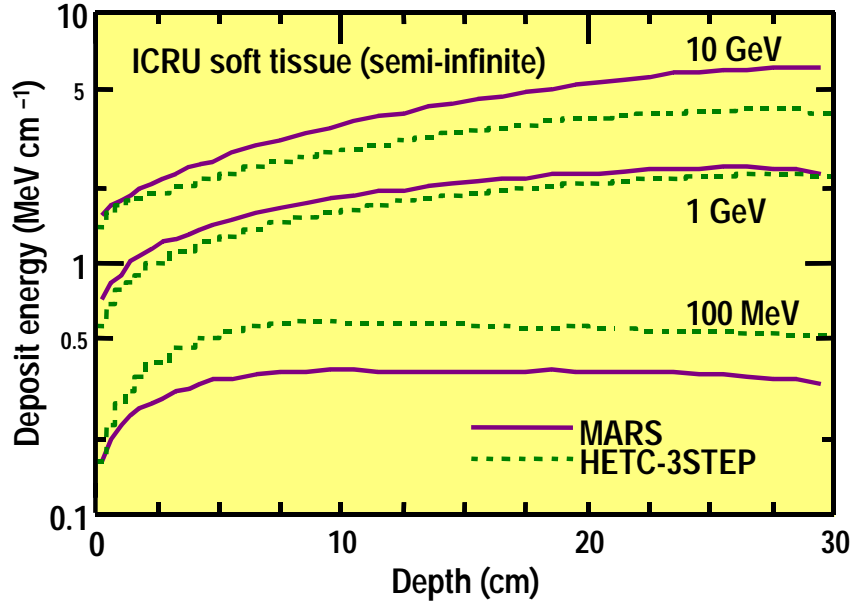


Figure 7. Comparison of energy deposition distribution at the central and at the whole regions of ICRU soft tissue for 10 GeV neutron irradiation

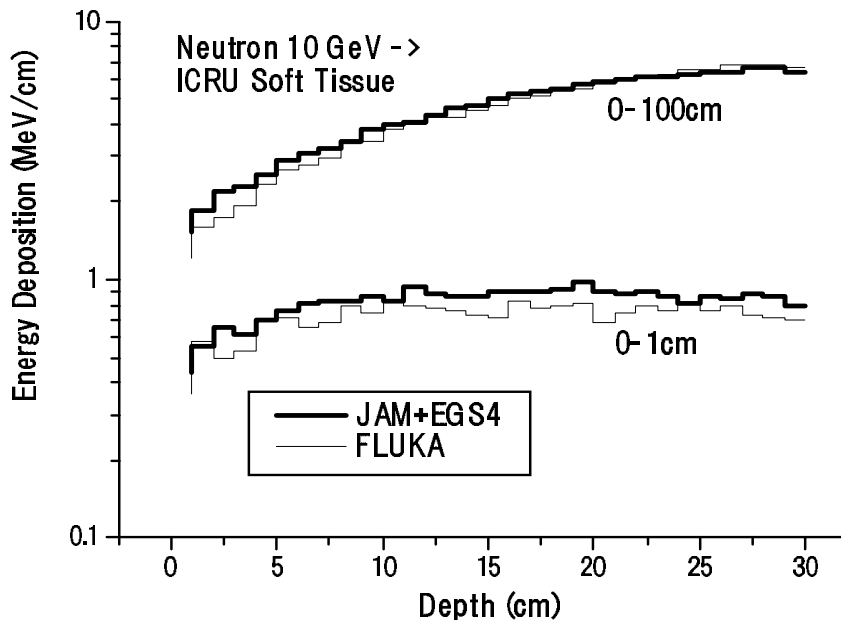


Figure 8. Comparison of energy deposition distribution at the whole region of ICRU soft tissue for 10 GeV neutron irradiation

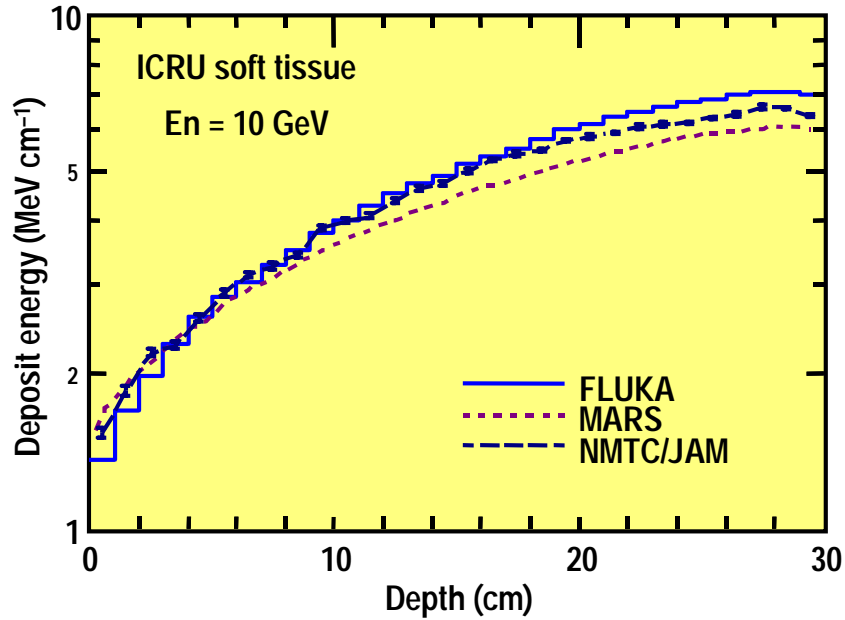


Figure 9. Comparison of total deposition energy at the whole region of ICRU soft tissue for 10 GeV neutron irradiation

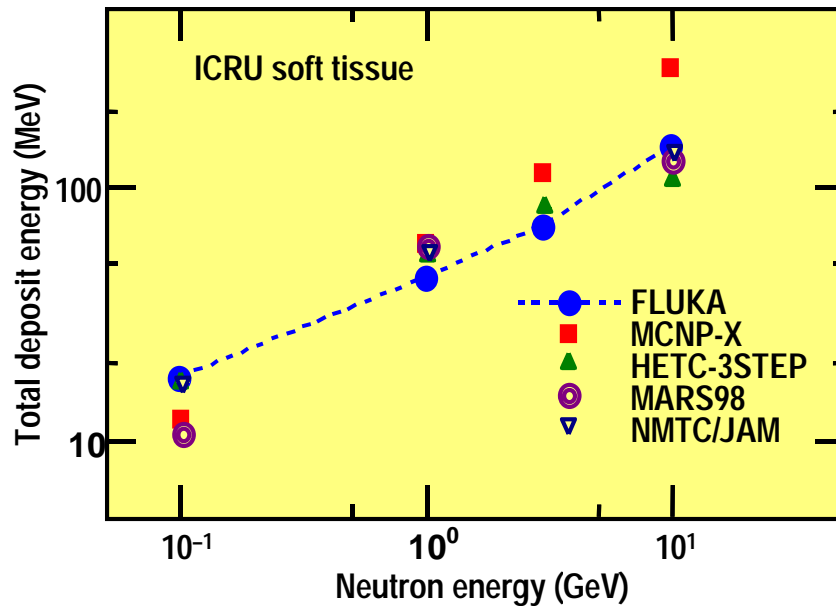


Figure 10. Comparison of total deposition energy at the whole region of hydrogen phantom for 10 GeV neutron irradiation

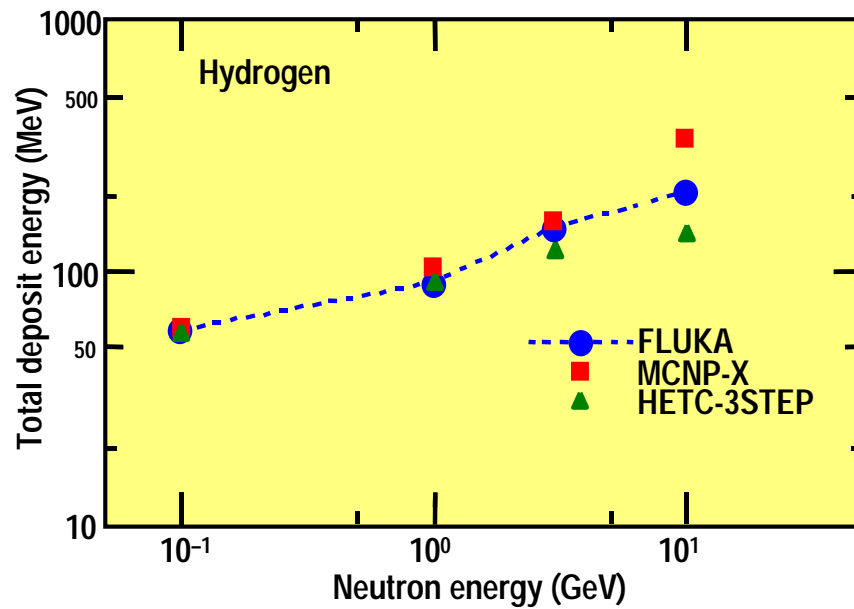
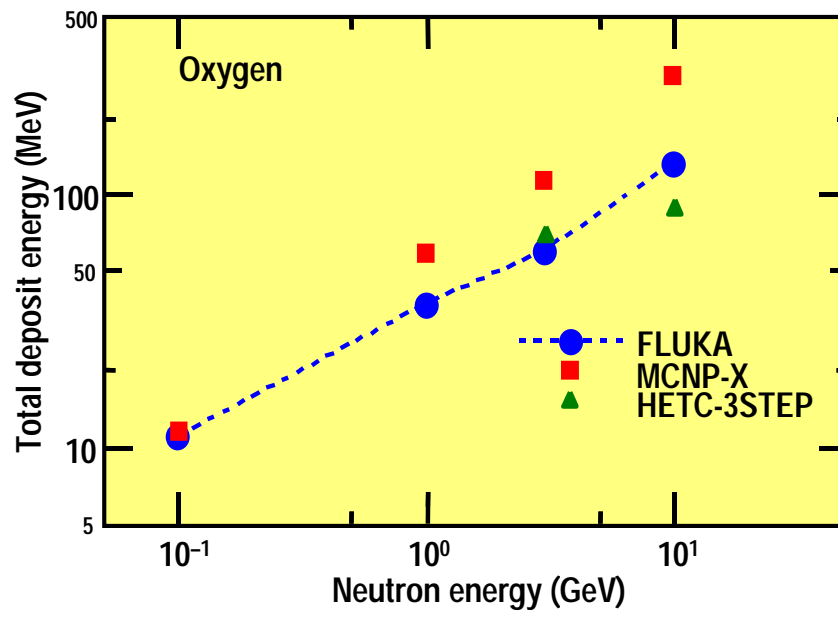


Figure 11. Comparison of total deposition energy at the whole region of oxygen phantom for 10 GeV neutron irradiation



RADIATION LEVELS EXPERIENCED BY THE INSERTION DEVICES OF THE THIRD-GENERATION SYNCHROTRON RADIATION SOURCES

P.K. Job, J. Alderman
Advanced Photon Source
Argonne National Laboratory

Abstract

Third-generation synchrotron radiation sources like the Advanced Photon Source (APS) use insertion devices made of Nd-Fe-B permanent magnets to produce X-rays for scientific research. The concern of radiation-induced demagnetisation of these insertion devices spurred a project aimed to measure and analyse the radiation levels experienced by these insertion devices during the operation of synchrotron radiation sources. The project required a reliable photon high-dose dosimetry technique capable of measuring high integrated dose levels during one operational cycle. Radiachromic dosimeters were considered for this purpose. In collaboration with the National Institute of Standards and Technology (NIST) these dosimeters were tested, calibrated and used at the Advanced Photon Source. Prior to each run radiachromic dosimeters are placed on the upstream and downstream edges of the 2.5 m long insertion devices. Following each operational cycle these dosimeters are retrieved from the storage ring and optical density changes are analysed. The measurements are compared with previous estimates. The results show that the previous predictions grossly underestimate the radiation levels received by the insertion devices.

Introduction

The Advanced Photon Source (APS) uses Nd-Fe-B permanent magnets in the insertion devices to produce X-rays [1,2]. Earlier investigations have exhibited varying degrees of demagnetisation of these magnets [3] due to irradiation from electron beams [4,5,6], ^{60}Co γ -rays [5] and neutrons [7,8]. A growing concern for the APS insertion devices, as well as for the permanent magnets that will be used in next generation high-power light sources, resulted from the radiachromic dosimeter measurements and also from the partial demagnetisation observed in some of the devices at the European Synchrotron Radiation Facility [4,6]. This concern in relation to radiation-induced demagnetisation spurred a long-term project aimed to measure and analyse the total absorbed doses received by the APS insertion devices. The project required a reliable photon high-dose dosimetry technique capable of measuring absorbed doses greater than 10^6 rad, which was not readily available at the APS. In collaboration with the National Institute of Standards and Technology (NIST), one such technique using radiachromic dosimeters was considered, tested and calibrated at the APS. This consequently led to the implementation of radiachromic dosimeters as the technique of choice for measuring the total absorbed doses received by the insertion devices for each of the APS runs.

Dose measurements with radiachromic dosimeters

Radiachromic dosimeters are nylon-based aminotriphenyl methane dye derivatives [9,10]. Upon exposure to ultraviolet light or ionising radiation, these films undergo radiation-induced coloration by photoionisation [9,11]. The change from a clear or colourless state to a deep blue-coloured state occurs gradually as a direct function of the radiation exposure received [9,12]. The change in colour intensity, or optical density, is measured using an optical reader, or a spectrophotometer. The radiachromic dosimeters used at the APS have a linear response to ionising radiation over a dose range of approximately 0.1 Mrad to 10 Mrad [9,12,13]. They have an equivalent response to X-rays, γ -rays and electrons from ultraviolet energies up to approximately 1 MeV [14-16].

Results and discussion

Figure 1 gives the absorbed dose received by the APS insertion devices for a particular run, as registered by the radiachromic dosimeters placed on the upstream and the downstream end of the devices. The results show that, on average, each insertion device receives approximately 1 Mrad of absorbed dose during a typical run period of 6-8 weeks. It is evident that doses on the downstream end of the insertion devices are typically higher than doses on the upstream end of the devices. This may be explained by the greater amount of synchrotron radiation present, and consequently the higher absolute number of scattered photons at the downstream end of an insertion device. It may also be explained by the greater possibility of a bremsstrahlung shower, produced just in front of the insertion device, to strike the downstream end rather than the upstream end due to the larger dimensions of the shower at the downstream end.

The results shown in Figure 2 provide the measured absorbed dose results as shown in Figure 1, normalised to the total beam current for a particular run period of eight weeks at the Advanced Photon Source. These results can be compared with earlier estimates [17] of unshielded radiation levels outside the vacuum chamber, at the centre of long straight section at the APS. These estimates project the total dose as 2.6×10^7 rad for 20 years of APS operation. Present results from radiachromic dosimeters project an average absorbed dose of greater than 10^8 rad for 500 Amp-h operation per year during a 20 year operation period. The EGS4 estimates of the photon radiation levels at the ALS

Figure 1. Absorbed dose per insertion device during a typical run of eight weeks

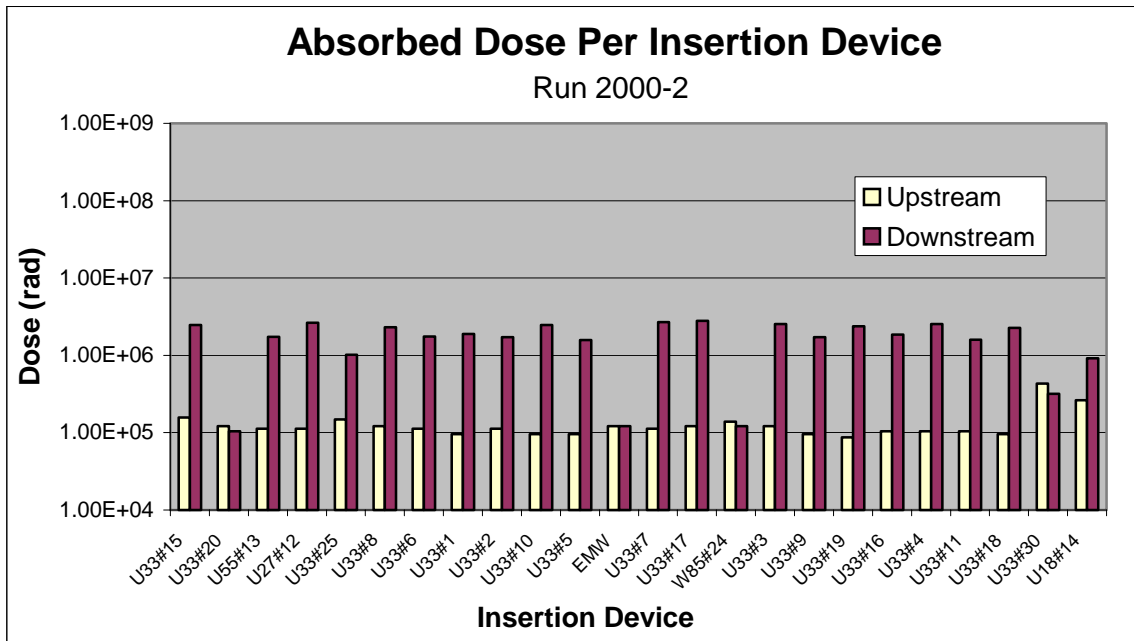
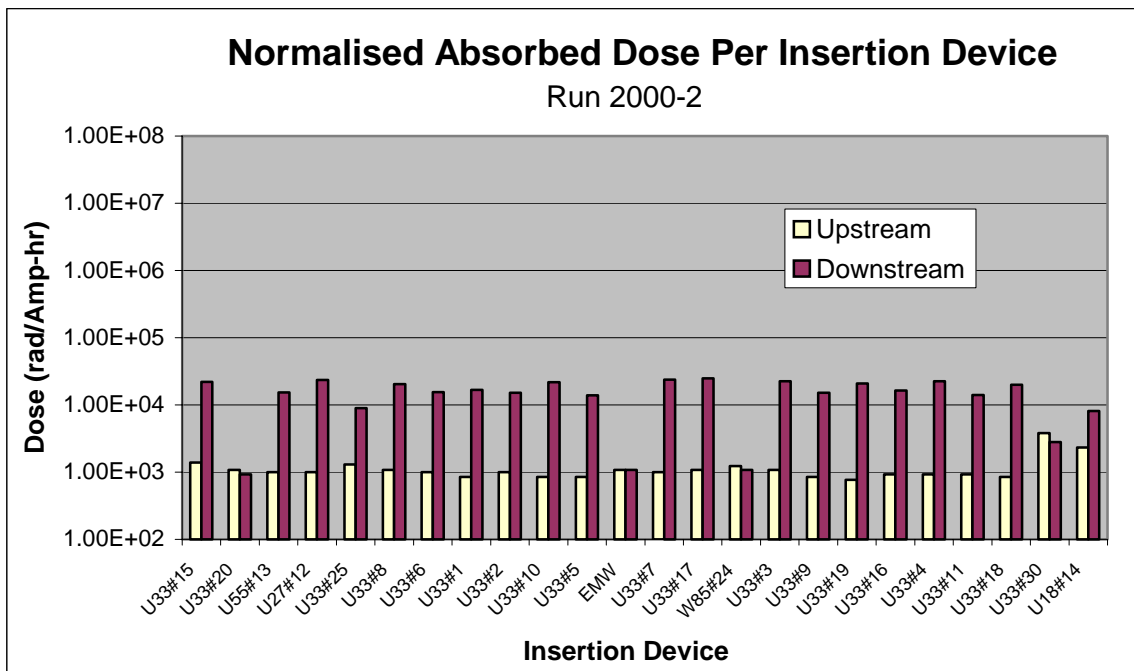


Figure 2. Normalised absorbed dose per insertion device during a typical run



insertion devices [18] provides 3×10^6 rad for 20 year operation at a beam current of 400 mA. This number scales to approximately 10^5 rad for 20 years of APS operation at 100 mA. The comparisons show that the estimates are non-conservative and the measured photon dose rates are even higher than the conservative estimates.

Absorbed dose measurements at the PETRA (17-23 GeV) storage ring [19,20] showed considerably higher radiation levels, typically 10^4 to 10^5 rad/Amp-h in the PETRA tunnel with a 3 mm lead-shielded vacuum chamber, and 4.8×10^8 rad/Amp-h with unshielded vacuum chambers, which is at least four orders of magnitude larger than the measured doses in the APS storage ring. This discrepancy cannot be explained only by the higher particle energy in the PETRA ring. It may be accounted for, however, by the fact that in the modern machines like the APS, the beam losses are better controlled by active feedback mechanisms during injection and operation.

Over the three-year period beginning with Run 1996-6 and ending with Run 1999-5, the highest dose received by an APS insertion device was approximately $2.0\text{E}+07$ rad. This worst-case scenario is important because we are ultimately interested in the total doses received by each insertion device in relation to the radiation-induced demagnetisation of the insertion devices over time. A dose rate of $2.0\text{E}+07$ rad every three years could be projected to a dose between $1.3\text{E}+08$ rad and $1.4\text{E}+08$ rad after twenty years, which is the desired life span of the insertion devices.

Conclusions

The results of this series of measurements show that the earlier estimates of the radiation doses received by the insertion devices of third-generation light sources were not conservative. Better control of beam loss mechanisms due to an active feedback system have helped to reduce the dose received by the insertion devices to a considerable extent. As the insertion devices become more sophisticated (like in-vacuum insertion devices) better understanding of dose levels at the vicinity of the beam is essential. It is also important to be aware of the threshold radiation levels that cause the deterioration of the magnetic materials, so as to develop better radiation-resistant magnets.

Acknowledgements

This work is supported by the US Department of Energy, BES-Material Sciences, under contract no. W-31-109-ENG-38.

REFERENCES

- [1] *The Advanced Photon Source, A National Synchrotron Radiation Research Facility at Argonne National Laboratory*, ANL/APS/TB-25-Rev., Argonne National Laboratory (1997).
- [2] Lai, B., A. Khounsary, R. Savoy, L. Moog and E. Gluskin, *Undulator A Characteristics and Specifications*, ANL/APS/TB-3, Argonne National Laboratory (1993).
- [3] Brown, R.D. and J.R. Cost, "Radiation-induced Changes in Magnetic Properties of Nd-Fe-B Permanent Magnets", *IEEE Trans. Magn.*, 25, 3117 (1989).
- [4] Colomp, P., T. Oddolaye and P. Elleaume, *Demagnetization of Permanent Magnets to 180 MeV Electron Beam*, ESRF/MACH/93-09 (1993).
- [5] Okuda, S., K. Ohashi and N. Kobayashi, "Effects of Electron-beam and γ -ray Irradiation on the Magnetic Flux of Nd-Fe-B and Sm-Co Permanent Magnets", *Nucl. Instr. and Meth., B* 94, 227 (1994).
- [6] Chavanne, J., P. Elleaume and P. Van Vaerenbergh, *Partial Demagnetization of ID6 and Dose Measurements on Certain IDs*, ESRF Machine Technical Note 1-1996/ID (1996).
- [7] Cost, J.R., R.D. Brown, A.L. Giorgi and J.T. Stanley, "Effects of Neutron Irradiation on Nd-Fe-B Magnetic Properties", *IEEE Trans. Magn.* 24, 2016 (1988).
- [8] Brown, R.D., J.R. Cost, G.P. Meisner and E.G. Brewer, "Neutron Irradiation Study of Nd-Fe-B Permanent Magnets made from Melt-spun Ribbons", *J. Appl. Phys.*, 64, 5305 (1988).
- [9] Humpherys, K.C. and A.D. Kantz, "Radiachromic: A Radiation Monitoring System", *Radiat. Phys. Chem.*, 9, 737 (1977).
- [10] Humpherys, K.C., J.D. Rickey and R.L. Wilcox, "Humidity Effects on the Dose Response of Radiachromic Nylon Film Dosimeters", *Radiat. Phys. Chem.*, 35, 713 (1990).
- [11] O'Donnell, J.H., "Chemistry of Radiation Degradation of Polymers", *Proc. of ACS Symposium Series*, 475, 402 (1990).
- [12] McLaughlin, W.L., J.C. Humphreys, D. Hocken and W.J. Chappas, "Radiochromic Dosimetry for Validation and Commissioning of Industrial Radiation Processes", *Radiat. Phys. Chem.*, 31, 505 (1988).
- [13] McLaughlin, W.L., A. Miller, F. Abdel-Rahim and T. Preisinger, "Plastic Film Materials for Dosimetry of Very Large Absorbed Doses", *Radiat. Phys. Chem.*, 25, 729 (1985).
- [14] McLaughlin, W.L., *National Institute of Standards and Technology*, Gaithersburg, MD, private communication (1997).

- [15] McLaughlin, W.L., A. Miller, R.M. Uribe, S. Kronenberg, C.R. Siebentritt, "Energy Dependence of Radiochromic Dosimeter Response to X- and γ -rays", *Proc. of an International Symposium on High-dose Dosimetry*, Vienna, 397 (1985).
- [16] McLaughlin, W.L., J.C. Humphreys, B.B. Radak, A. Miller and T.A. Olejnik, "The Response of Plastic Dosimeters to Gamma Rays and Electrons at High Absorbed Dose Rates", *Radiat. Phys. Chem.*, 14, 535-550 (1979).
- [17] Dejus, R.J., *Estimates of Unshielded Radiation Levels Outside the Vacuum Chamber at the APS Storage Ring*, intra-laboratory memo, September (1992).
- [18] Hassenzahl, W.V., T.M. Jenkins, Y. Namito, W.R. Nelson and W.P Swanson, "An Assessment of the Effects of Radiation on Permanent Magnet Material in the ALS Insertion Devices", *Nucl. Instr. and Meth.*, A 291, 378 (1990).
- [19] Dinter, H., "Absorbed Doses Due to Synchrotron Radiation in the Tunnel of the Storage Ring PETRA", *Nucl. Instr. and Meth.*, A239, 597 (1985).
- [20] Dinter, H., K. Tesch and C. Yamaguchi, "Absorbed Radiation Dose Due to Synchrotron Radiation in the Storage Ring PETRA", *Nucl. Instr. and Meth.*, 200, 437 (1982).

SESSION V

Status of Computer Codes, Cross-sections and Shielding Data Libraries

Chairs: H. Hunter, N. Mokhov

PROGRESS REPORT ON THE AVAILABLE ANALYTICAL TOOLS FOR ACCELERATOR SHIELDING ANALYSIS 2002

Hamilton T. Hunter, Jennifer B. Manneschildt, Bernadette L. Kirk, Maurice Greene

Radiation Safety Information Computational Center (RSICC)

Oak Ridge National Laboratory (ORNL)¹

Oak Ridge, TN 37831-6362, USA

cdc@ornl.gov, <http://www-rsicc.ornl.gov/rsic.html>

Enrico Sartori

OECD/NEA Data Bank

12, Boulevard des Iles

92130 Issy-les-Moulineaux, France

sartori@nea.fr • <http://www.nea.fr/html/databank/welcome.html>

Tadakazu Suzuki

Research Organisation for Information Science and Technology (RIST)

2-4, Shirane shirakata, Tokaimura Nakagun,

Ibaraki-ken, 319-1106 Japan

tadakazu@hero.tokai.jaeri.go.jp • <http://www.rist.or.jp/nucis>

Pedro Vaz

Instituto Tecnológico e Nuclear

Estrada Nacional 10

P-2686-953 Sacavém, Portugal

pedrovaz@itn.pt

Abstract

Given the new developments in accelerators, especially spallation neutron sources, new analytical tools and applications have recently been developed, tested and used. An ongoing need exists to distribute the codes, their data and the benchmarks used in validating the design parameters for shielding energies and particles involved in the applications. What is presented is the fruit of the efforts of the data centres that identify, collect, test and disseminate the tools necessary for proper accelerator shielding analysis around the world. The OECD Nuclear Energy Agency Data Bank (NEA DB), the ORNL Radiation Safety Information Computational Center (RSICC) and the Research Organisation for Information Science and Technology (RIST) have continued to lead the European, American and Japanese nuclear communities, respectively, to state-of-the-art software and data that fit their needs. The following contains a listing of those tools that are available and most applicable to today's accelerator shielding analyses.

¹ Managed by UT-Battelle, LLC, under contract DE-AC05-00OR22725 with the US Department of Energy.

Introduction

Over the past decade, SATIF meetings have been held about every two years, and updates from NEA DB and RSICC analytical tool centres [1,2] have provided information on the data centres' activities [3-6] to the experts in accelerator radiation analysis. At the last SATIF-5 meeting in July 2000, Sartori, *et al.* [7] displayed useful tables that outlined information available from NEA DB and RSICC. This paper will augment those fifteen (15) tables (see Appendix 1) [7] as they are excellent visual guides as to where computational and data growth has occurred since the SATIF-5 meeting.

The three main areas of accelerator application tools at the centres include:

1. Basic nuclear data, derived application data libraries, group constants, continuous energy data.
2. Computer codes for different accelerator system modelling aspects.
3. Integral experiments database.

An excellent flow chart showing the interaction and relationship between the above three areas is shown in Figure 1(b) of Appendix 2 [7].

Software use and distribution goals

Issues surrounding the existence of analytical tool centres in the world constantly re-emerge that require the centres to validate their existence and costs. The value added of the centres' role as middleman allows the necessary third-party review and processing before the software tool hits the world market. Each centre has well-practised procedures for software quality assurance when issuing an available analytical tool to the recipient. A centre's quality assurance issues pertain to:

- Complete tool documentation and testing for specified platforms, hardware and data.
- Proper code storage, handling and delivery.
- Tool version control and notable errors and issues lists.
- Proper code installation and use.
- Feedback to authors and customers on errors discovered or new development needs.
- Maintenance of export control and sensitivities related to certain software and entities.
- Development of educational and dissemination information to encourage modelling uses with the best available data and analytical tools.
- Promulgating the information, data and tools to the public, via World Wide Web (WWW), file transfer protocol (ftp), e-mail, conferences, workshops and postal services.

The growth of the international accelerator community has recently ballooned, necessitating more of the strict data and software quality assurance (SQA) that the reactor and nuclear safety community has required for some time. As power levels and the energy/nucleon of these new international accelerators increase, better benchmark data and higher quality cross-sections are exponentially more important due to the need for increased accuracy of final dose estimates at shutdown, minimisation of construction costs and decreased limits on absorbed dose for facility personnel.

Other areas of SQA involve the accurate prediction of limiting dose to accelerator materials. As experiments become larger and more powerful, this has been an emerging problem, as particle energies and currents are sufficient to cause catastrophic heating and failure of a wide array of accelerator (plasma) components such as vacuum boundaries, shutters and source targets. These accidents would cause irreparable damage to experiments and operations, in addition to threatening the safety of facility personnel.

SATIF-5 summary

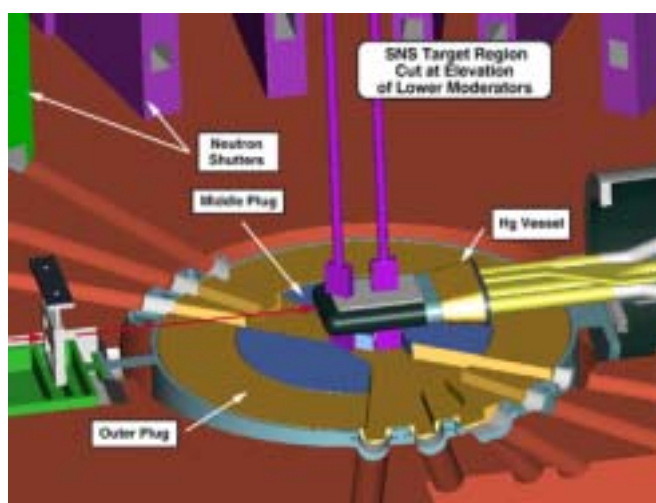
Many of the computational areas specified in the SATIF-5 Executive Summary [8] have undergone improvements in recent years due to more strict radiation transport, transfer and transformation modelling requirements. Using codes from the Monte Carlo methods, and/or deterministic codes, a better understanding of the fluence of particles at deep penetrations has emerged. The same is true of the data collection and analysis that forms the basis of generation rates for various reactions. Covariance analyses allow one to determine the effects of uncertainties in cross-section evaluations on calculated results.² At some time in the future, these codes will merge into a seamless operation on parallel systems to best predict the true 3-D fluence within the accelerator structure and for all surrounding materials (e.g. dirt).

Recent accelerator applications

The Spallation Neutron Source (SNS, 2 MW of 1 GeV protons on a mercury target) will be operational in 2006. It is being built as a co-operative effort between six US national laboratories. The responsibility for the design of the target and surrounding shielding was assigned to ORNL. Since the neutrons emerging from the target are thermalised by scattering through cells filled with water (to produce room-temperature neutrons) or through containers of liquid hydrogen at a temperature of 20 K (to produce cold neutrons), spallation neutrons must lose at least 10-12 orders of magnitude in

Figure 1. SNS target area and beam lines

(Ref. ORNL WWW site <http://www.sns.gov/partnerlabs/ornl.gov/partnerlabs/ornl.htm>)



² SAMMY M6B (Beta Version: code system for multi-level R-matrix fits to neutron and charged-particle cross-section data using Bayes' equations).

energy before entering the beam lines. The use of codes and data based upon improvements to older transport developments, and the merging of two methods, stochastic and deterministic, was necessary to accurately describe and analyse the necessary shielding areas. Newly developed codes (soon to be released) M2T, M2D and M2A (standing for Monte Carlo-to-TORT, Monte Carlo-to-DORT and Monte Carlo-to-ANISN) have been useful for providing source terms to insert into the one-, two- and three-dimensional deterministic computations at various depths into the target and beam dump or shutter areas.

The SNS target project development team used a robust, well-defined benchmark-validated “tool box” of software to design and analyse the SNS target and surrounding shielding areas. The primary codes and data that have been (or are being) used are:

- MCNPX and MCNP and their associated libraries.
- DOORS v3.2 (ANISN, DORT, TORT, and associated utility codes, GRTUNCL, GIP, etc.).
- Monte Carlo to ANISN (MTA), Monte Carlo to DORT (MTD), and Monte Carlo to TORT (MTT) interface codes (locally developed at ORNL and eventually to be packaged with DOORS).³
- ORIHET95 – build-up and decay code, originally part of HERMES code system (similar to ORIGEN).
- Activation Analysis Sequence (AAS), locally written code to link the MCNPX and MCNP transport codes to the ORIHET95 code.
- HILO2K, DABL69, BUGLE96 broad group data libraries.
- VITAMIN B6 fine group library.
- FENDL neutron cross-section activation data library.

Note: HETC (from the latest version of CALOR), LAHET 2.8 and HILO86 were used initially, however, the MCNPX code proved to be a more user-friendly tool for analysis.

Updated codes and data libraries released since SATIF-5

NEA DB and RSICC accelerator analytical tools released for the period of July-March 2002 follow. Some of these tools are not specific to accelerator applications but could be useful in lower-energy transport analysis of particles generated from primary and secondary reactions within the accelerator target or shield.

In Japan, the Research Organisation for Information Science and Technology (RIST) has a collection of analytical tools that are useful for various accelerator applications in Japan. Of the codes available at RIST, three are mentioned below that neither RSICC nor the NEA DB offers as packages at this time. Acquisition of codes for public use are a very important function of centres, such that improvements and widespread knowledge of their availability can be supplied in the future.

³ Professor Ron Pevey of the University of Tennessee, Knoxville, TN is directing the final computational changes to the merger of the Monte Carlo and deterministic codes with proper documentation for future public use of these new codes (release expected FY02).

A total of thirty-two (32) new or updated accelerator analytical tools have been added to the public collection via the NEA DB or RSICC centres since the last SATIF meeting (July 2000). These are listed below with underlined html links to their respective WWW abstracts at the NEA DB and RSICC organisations.

- [C00693/MNYCP/00 \(NEA 1638\)](#) ANITA-2000
Code system to calculate isotope inventories from neutron irradiation for fusion applications.
Contributed by: ENEA, Centro Ricerche, Energia “E. Clementel”, INN-FIS-MACO (Bologna, Italy) through the NEA Data Bank (Issy-les-Moulineaux, France).
- [P00513/MNYWS/00 \(NEA 1627\)](#) BOT3P1.0
Code system for 2-D and 3-D mesh generation and graphical display of geometry and results for the DOORS deterministic transport codes.
Contributed by: ENEA Nuclear Data Centre (Bologna, Italy), through the OECD Nuclear Energy Agency Data Bank (Issy-les-Moulineaux, France).
- [P00333/MNYCP/03](#) CHENDF 6.12
Codes for handling ENDF/B-V and ENDF/B-VI data.
Contributed by: National Nuclear Data Center, Brookhaven National Laboratory (Upton, New York).
- DCHAINSP2001 (RIST Japan)
High-energy particle-induced radioactivity calculation code.
Computer: OS:HP, Sun ,DEC/UNIX, Linux.
Programming language: FORTRAN77.
Author: Fujio Maekawa, Centre for Neutron Science, Japan Atomic Energy Research Institute (JAERI).
References: “DCHAIN-SP2001: High-energy Particle-induced Radioactivity Calculation Code”, Tetsuya Kai, Fujio Maekawa, *et al.*, JAERI-Data Code (2000).
- [D00213/MNYCP/00 \(NEA DB – NEA1644\)](#) DECDC 1.0
Nuclear decay data files for radiation dosimetry calculations.
Contributed by: Department of Health Physics, Tokai Research Establishment, JAERI (Tokai, Ibaraki, Japan).
- [NEA 1564](#) EASY-99
The European Activation System.
EASY-99 is a complete tool for the calculation of activation in materials exposed to neutrons. It can be used for any application (fusion, transmutation, fission and accelerator) for which the neutron energy does not exceed 20 MeV. EASY-99 consists of the inventory code FISPACT-99 and the EAF-99 file, which contains various libraries of nuclear data.
- [P00497/PC586/00 \(NEA DB – IAEA1169\)](#) EMPIRE-II
Statistical model code system for nuclear reaction calculations, version 2.13.
Contributed by: IAEA (Vienna, Austria) through the OECD Nuclear Energy Agency Data Bank (Issy-les-Moulineaux, France).

- [C00581/IBMPC/02](#) ([NEA DB - IAEA1388/01](#)) FOTELP-2KG
Photons, electrons and positrons transport in 3-D by Monte Carlo techniques.
 FOTELP-2KG is a new compact version of the previous FOTELP/EM code designed to compute the transport of photons, electrons and positrons through three-dimensional material and sources geometry by Monte Carlo techniques.
Contributed by: Institute of Nuclear Sciences “Vinca”, Physics Laboratory (090) (Belgrade, Yugoslavia) through the NEA Data Bank (Issy-les-Moulineaux, France).
- [C00697/PC586/01](#) ([NEA DB](#)) GUI2QAD-3D
Point kernel code system for neutron and gamma-ray shielding calculations in complex geometry, including a graphical user interface.
Contributed by: Safety Research Institute (Kalpakkam, Tamilnadu, India).
- [M00000/MNYCP/00](#) HIMAC
 Recent experimental data are summarised in this paper on differential neutron yields in energy and angle produced by 100, 155 and 180 MeV/nucleon He, 100, 155, 180 and 400 MeV/nucleon C, 100, 180, 400 MeV/nucleon Ne, 400 MeV/nucleon Ar, Xe and Fe, 272 and 435 MeV/nucleon Nb and 800 MeV/nucleon Si ions stopping in thick targets of C, Al, Cu, Pb and Nb.
Contributed by: Quantum Radiation Division, Electrotechnical Laboratory (Japan), Department of Quantum Science and Energy Engineering, Tohoku University (Japan), Lawrence Berkeley National Laboratory (Berkeley, CA 94720, USA).
- [NEA-1656/01](#) ZZ IAEA-2001
Intermediate energy activation file.
 The Intermediate Energy Activation File (IEAF-2001) is a compilation of neutron-induced activation cross-sections in ENDF-6 data format for activation analyses in fusion technology and intermediate energy applications. The IEAF-2001 data library contains neutron-induced activation cross-sections in the energy range 10^{-5} eV to 150 MeV for 679 target nuclides from Z=1 (hydrogen) to 84 (polonium). The total number of reaction channels with activation cross-section data is 134 431. The European Activation File (EAF-99) served as basis for the activation data below 20 MeV neutron energy. Threshold reaction cross-sections were evaluated on the basis of geometry dependent hybrid exciton and evaporation models using a modified version of the ALICE code. The IEAF-2001 data library can be processed with standard ENDF processing tools such as NJOY. A group-wise IEAF-2001 data library has been prepared for 256 energy groups in GENDF data format. The IEAF-2001 CD-ROM contains both the point-wise ENDF and the group-wise GENDF data files.
Contributed by: U. Fischer, D. Leichte, U.V. Möllendorff and I. Schmuck, Association FZK-Euratom Institut fuer Reaktorsicherheit (IRS) (Forschungszentrum Karlsruhe Postfach 3640, 76021 Karlsruhe, Germany) and Yu. Konobeyev, Yu.A. Korovin, P.E. Pereslavytsev, Obninsk Institute of Nuclear Power Engineering (INPE, Studgorodok 1, 249020 Obninsk, Russian Federation).
- INTEL-BERMUDA (RIST)
Radiation shielding calculation for fusion reactor, accelerator and reprocessing facility.
Computer: OS: FACOM-M780, SUN/MSP, UNIX.
Programming language: FORTRAN77, C++.
Authors: Akira Hasegawa, Dept. of Nuclear Energy System, Japan Atomic Energy Research Institute (JAERI).

- [C00696/MFMWS/00 \(NEA DB\)](#) LAHET 2.8
Code system for high-energy particle transport calculations.
Contributed by: Los Alamos National Laboratory (Los Alamos, New Mexico).
- [P00137/MNYCP/06 \(NEA DB\)](#) MARLOWE
Computer simulation of atomic collisions in crystalline solids version 15a.
Contributed by: Oak Ridge National Laboratory (Oak Ridge, Tennessee).
- [NEA-\(to be determined\)](#) MCB
A continuous energy Monte Carlo burn-up simulation code.
A code for integrated simulation of neutronics and burn-up based upon continuous energy Monte Carlo techniques and transmutation trajectory analysis has been developed. Being especially well suited for studies of nuclear waste transmutation systems, the code is an extension of the well-validated MCNP transport program of Los Alamos National Laboratory. Among the advantages of the code is a fully integrated data treatment combined with a time-stepping routine that automatically corrects for burn-up dependent changes in reaction rates, neutron multiplication, material composition and self-shielding. Fission product yields are treated as continuous functions of incident neutron energy, using a non-equilibrium thermodynamical model of the fission process. In the present paper a brief description of the code and applied methods are given.
Contributed by: Jerzy Cetnar, Jan Wallenius and Waclaw Gudowski, Department of Nuclear and Reactor Physics, Royal Institute of Technology through the NEA Data Bank (Issy-les-Moulineaux, France).
- [P00500/MNYCP/00 \(NEA DB\)](#) MCNP-UISED 4C2
Visual editor for creating MCNP4C2 input files.
Contributed by: Visual Editor Consultants (Richland, Washington).
- [C00701/ALLCP/00 \(NEA DB\)](#) MCNP4C2
Monte Carlo N-particle transport code system.
A new LA150U photonuclear library of particle emission data for nuclear events from incident neutrons, protons and photons with energies up to 150 MeV is included in the MCNP4C2 package.
Contributed by: Los Alamos National Laboratory (Los Alamos, New Mexico).
- [D00200/ALLCP/00 \(NEA DB\)](#) MCNPDATA
Standard neutron, photon and electron data libraries for MCNP4C.
Contributed by: Los Alamos National Laboratory (Los Alamos, New Mexico).
- [C00705/MNYCP/00 \(NEA DB\)](#) MCNPX2.1.5 (new 2.3.0 release expected in a few weeks)
Monte Carlo N-particle transport code system for multi-particle and high-energy applications.
MCNPX extends the CCC-660/MCNP4B code to all particles and all energies. Neutron tabular data are used as in MCNP4B; above the table energy limits, physics modules are used. Current physics modules include the Bertini and ISABEL models taken from the LAHET Code System (LCS) and CEM. An old version of FLUKA is available for calculations above the range of INC physics applicability. MCNPX eliminates the need now present in LCS to transfer large files between separate codes. MCNPX is released with the LA150N library, and further 150 MeV libraries will follow shortly for protons and photonuclear interactions. In addition, variance reduction schemes (such as secondary particle biasing), and new tallies have been created specific to the intermediate and high-energy physics ranges. The “mesh”

and “radiography” tallies have been included for two and three-dimensional imaging purposes. Energy deposition has received a substantial reworking based on the demands of charged-particle high-energy physics. An auxiliary program, GRIDCONV, converts the mesh and radiography tally results for viewing by independent graphics packages.

Contributed by: Los Alamos National Laboratory (Los Alamos, New Mexico).

- [D00205/ALLCP/01 \(NEA DB\)](#) MCNPXDATA
Standard neutron, photon and electron data libraries for MCNPX.
This release includes LA150N, the photon libraries MCPLIB1 and MCPLIB02, the electron library EL, and MCNP4A libraries used with the MCNP4C and 4C2 transport codes.
Contributed by: Los Alamos National Laboratory (Los Alamos, New Mexico).
- [CCC-0156/01 \(NEA DB\)](#) MECC-7
Medium-energy intranuclear cascade code system, modified for modern computer systems.
MECC-7 calculates the results of nuclear reactions caused by a medium-high energy particle colliding with a nucleus. The incident particles may be protons or neutrons with energies from about 100 to 2 500 MeV or charged pions with energies from about 100 to 1 500 MeV. Target nuclei may be any element heavier than carbon. MECC-7 writes a history tape containing data regarding the properties of the particles escaping from the nucleus as a result of the particle-nucleus collision. The data consist of the type of escaping particles, their energies, and angles of emission. I4C utilises the data on the MECC-7 history tape to calculate particle multiplicities and various cross-sections, such as the inelastic cross-section or the doubly differential cross-section for energy-angle correlated distributions. I4C also carries the nuclear reaction through an additional phase, that of evaporation, and calculates evaporation residual nuclei (radiochemical) cross-sections and the particle multiplicities and energy spectra of particles “boiled off” from the nucleus after the cascade has stopped.
Contributed by: OECD/NEA Data Bank (Issy-les-Moulineaux, France).
- [D00207/MNYCP/00 \(NEA IAEA 1376\)](#) MENDL-2P
The library includes proton cross-sections for 504 nuclei with atomic numbers from 13 to 84 at energies up to 200 MeV. The total number of reactions is equal to 87 196. This version has been converted to ENDF-6 format and verified through the ENDF-6 format utility codes. MENDL-2 proton cross-sections are calculated on the basis of ALICE-IPPE, which differs from the ALICE-91 as follows.
The algorithm for the level density calculation according to the generalised super-fluid model was tested, corrected and improved. The pre-equilibrium cluster emission calculation is included in the code. Calculation of the alpha particle spectra is performed taking into account the pick-up and knock-out processes. The phenomenological approach is used to describe direct channel for the deuteron emission. The triton and ³He spectra are calculated according to the coalescence pick-up model of Sato, Iwamoto, Harada.
Contributed by: Yu.N. Shubin, V.P. Lunev, A.Yu. Konobeyev, A.I. Dityuk, Institute of Physics and Power Engineering (249020 Bondarenko Sq. 1 Obninsk, Kaluga Region, Russian Federation) and Dr. Arjan Koning, NRG Nuclear Research and Consultancy Group (Building 34.333 Westerduinweg 3, P.O. Box 25 NL-1755 ZG Petten, The Netherlands) through the OECD/NEA Data Bank (Issy-les-Moulineaux, France).
- [C00694/SUN05/00 \(NEA 0974\)](#) NMTC-JAERI97
Monte Carlo nucleon-meson transport code system.
Contributed by: Centre for Neutron Science, Japan Atomic Energy Research Institute, (Tokai-mura, Naka-gun, Japan) through the OECD/NEA Data Bank (Issy-les-Moulineaux, France).

- **OSCAR (RIST Japan)**
Calculation of yields of nuclear reaction products for particle accelerator.
Computer: OS:FACOM M780/ MSP.
Programming language: FORTRAN77.
Author: Kentaro Hata, Dept. of Material Science, Japan Atomic Energy Research Institute (JAERI).
References: "OSCAR, A Code for Calculation of the Yield of Radioisotopes Produced by Charged-particle Induced Reactions", K. Hata, H. Baba, JAERI-M 88-184 (1988).
- [C00682/MNYCP/02 \(NEA-1525/05\)](#) **PENELOPE-2001**
A code system for Monte Carlo simulation of electron and photon transport.
 PENELOPE performs Monte Carlo simulations of coupled electron-photon transport in arbitrary materials and complex quadric geometries. A mixed procedure is used for the simulation of electron and positron interactions (elastic scattering, inelastic scattering and bremsstrahlung emission), in which "hard" events (i.e. those with deflection angle and/or energy loss larger than pre-selected cut-offs) are simulated in a detailed way, while "soft" interactions are calculated from multiple scattering approaches. Photon interactions (Rayleigh scattering, Compton scattering, photoelectric effect and electron-positron pair production) and positron annihilation are simulated in a detailed way.
Contributed by: Universitat de Barcelona and Institut de Tècniques Energètiques, Universitat Politècnica de Catalunya (Barcelona, Spain) and Universidad Nacional de Cordoba (Argentina), through the Nuclear Energy Agency Data Bank (Issy-les-Moulineaux, France).
- [D00212/MNYCP/00](#) **POINT-2000**
Temperature-dependent, linearly interpolable, tabulated cross-section library based on ENDF/B-VI, release 7.
Contributed by: Lawrence Livermore National Laboratory (Livermore, California).
- [P00226/IBMPC/01](#) **PRECO2000**
Exciton model pre-equilibrium code system with direct reactions.
 PRECO-2000, also known as PRECOM (M for Millennium), is a two-component exciton model code for the calculation of double-differential cross-sections of light particle nuclear reactions. PRECO calculates the emission of light particles ($A = 1$ to 4) from nuclear reactions induced by light particles on a wide variety of target nuclei. Their distribution in both energy and angle is calculated. Since it currently only considers the emission of up to two particles in any given reaction, it is most useful for incident energies of 14 to 30 MeV, however the pre-equilibrium calculations are valid up to 100 MeV.
Contributed by: Triangle Universities Nuclear Laboratory, Duke University (Durham, North Carolina).
- [P00158/IRISC/07 \(NEA DB\)](#) **SAMMY-M6B**
Beta version: Code system for multi-level R-matrix fits to neutron and charged-particle cross-section data using Bayes' equations.
 The SAMMY code is used for analyses of neutron-induced cross-section measurements, primarily for experiments performed on time-of-flight facilities such as the Oak Ridge Electron Linear Accelerator. Analysis of neutron cross-section data in the resolved-resonance region has three distinct aspects, each of which must be included in any analysis code: First, an appropriate formalism is needed for generating theoretical cross-sections. Second, a plausible mathematical description must be provided for every experimental condition that affects the values of the quantities being measured. Third, a fitting procedure must be available to determine the parameter values which provide the "best" fit of theoretical to experimental

numbers. SAMMY incorporates state-of-the-art treatments for each of these three requirements: Reich-Moore R-matrix theory for the first, Bayes' method for the third and a wide variety of techniques for the second (including Doppler and resolution-broadening, finite-size corrections, etc.). Recent enhancements in the code include the extension to charged particles (so that, for example, proton or alpha-particle scattering experiments can be analysed in addition to neutron-induced reactions) and additional options for treatment of resolution broadening.
Contributed by: Oak Ridge National Laboratory (Oak Ridge, TN).

- [P00294/MNYCP/02 \(NEA 0829\)](#) SCAT-2B
Code system for calculating total and elastic scattering cross-sections based on an optical model of the spherical nucleus, versions SCAT-2 and SCAT-2B.
Contributed by: Centre d'Etudes de Bruyeres-le-Chatel (France) and Bucharest University, Faculty of Physics (Bucharest Magurele, Romania), through the NEA Data Bank (Issy-les-Moulineaux, France).
- [C00667/SUN05/00](#) SHIELD
Monte Carlo transport code for simulating interaction of high-energy hadrons with complex macroscopic targets.
 The SHIELD code considers interaction of high-energy particles with condensed matter, including hadron-nucleus interactions inside the target, generation and transportation of secondary particles, deposition of energy and production of radionuclides in the target. The modern version of the SHIELD code allows simulation of the transfer of nucleons (including low energy neutrons), pions, kaons, anti-nucleons and muons in an energy range up to 1 TeV. Recently, the transfer of ions (arbitrary A,Z-nuclei) was added. The ionisation loss and straggling (optionally) are taken into account as well as the main modes of the mesons decay. The transfer of neutrons ($E_n < 14.5$ MeV) is simulated on the basis of the 28-group neutron data system BNAB.
Contributed by: Institute for Nuclear Research of the Russian Academy of Science (RAS) (Moscow, Russia).
- [CCC-646/IBMPC/03 \(NEA DB\)](#) SKYSHINE-KSU
Code system to calculate neutron and gamma-ray skyshine doses using the integral line-beam method.
Contributed by: Kansas State University (Manhattan, Kansas).
- [NEA DB IAEA1382/01](#) SRNA-2KG
Proton transport using 3-D by Monte Carlo techniques.
 SRNA-2KG performs Monte Carlo transport simulation of protons in 3-D source and 3-D geometry of arbitrary materials. The proton transport is based on a condensed history model, and on a model of the compound nuclei decay that is created in non-elastic nuclear interactions by proton absorption.
Contributed by: Institute of Nuclear Sciences VINCA Physics Laboratory (Belgrade, Yugoslavia), through the NEA Data Bank (Issy-les-Moulineaux, France).
- [P00498/PC586/00 \(NEA 0461\)](#) STAPREF
Code system to calculate nuclear reaction cross-sections by the Evaporation Model.
Contributed by: Radiation Physics and Chemistry Problems Institute (Minsk-Sosny, Belarus) and the Institut für Radiumforschung und Kerphysik der Österreichischen, Akademie der Wissenschaften (Vienna, Austria), through the OECD/NEA Data Bank (Issy-les-Moulineaux, France).

- [C00638/MNYCP/04](#) TART2000
Coupled neutron-photon, 3-D, combinatorial geometry, time-dependent, Monte Carlo transport code system.
Contributed by: Lawrence Livermore National Laboratory (Livermore, California).
- [CCC-709/MNYWS/00](#) TDTORT
Time-dependent, three-dimensional, discrete ordinates, neutron transport code system.
Contributed by: Oak Ridge National Laboratory (Oak Ridge, Tennessee).

SINBAD Integral Accelerator Benchmark Additions since SATIF-5

The SINBAD 2002 collection due to be released this summer (2002) from RSICC and NEA DB have added data sets for comparing accelerator radiation transport computational analysis with the experimental benchmark data. In particular, five (5) sets of benchmark analysis have been added to SINBAD and were performed as part of the SQA on the MCNPX⁴ high-energy transport code. A total of ten sets of benchmarks have been performed by Georgia Tech and all will be added to the SINBAD collection.

Table 15(a) in Appendix 1 lists the updated SINBAD information on fission, fusion and accelerator benchmarks that have been added (or are in the process of being added) since the SATIF-5 meeting. A recent paper on SINBAD development is due to be published soon [9] that describes the details of progress with integral shielding benchmarks.

Current collections at RSICC and NEA DB

High-energy (>20 MeV) data libraries

Listed below in Table 1 are the currently available high-energy (>20 MeV) data libraries that have recently been analysed for content and characteristics and are available at the NEA Data Bank and the RSICC data centre. Associated with the package name (DLC---) are the particles in the reactions with the relative upper energies measured or computed for the target materials specified.

A valuable comprehensive list of the available data libraries at the NEA Data Bank can be viewed via the <http://www.nea.fr/html/dbprog/appldatlib.htm> area on the WWW.

In addition to these data collections, there are almost one hundred (100) multi-group neutron and/or neutron-photon libraries that can be used for shielding analyses for energies below 20 MeV. There are also another fifty (50) or so point-continuous energy libraries of cross-sections, dose factors and other functions with utility for other kinds of analyses that may be needed. These lower energy data collections are very useful since many “accelerators” produce neutrons and photons that must be shielded to < 1 mrem/hr levels. Therefore, data for accelerator shielding analyses must be available for all energies.

⁴ The major capabilities of LAHETTM and MCNPTM have now been combined into merged code MCNPXTM.

Table 1. Identified data collections with possible utility in accelerator applications

DLC	Name	Particles	Upper energy (MeV)	Materials
001	LEP	Pi-mesons, protons, neutrons	400	¹² C, ¹⁶ O, ²⁷ Al, ⁵² Cr, ⁶⁵ Cu, ¹⁰⁰ Ru, ¹⁴⁰ Ce, ¹⁸⁴ W, ²⁰⁷ Pb, ²³⁸ U
022	FLEP	Protons, neutrons	400	C, O, Al, Cr, Cu, Ru, Ce, W, Pb, U
084	MENSLIB	Neutrons	60	H, B, C, N, O, Si, Fe, W
119	HILO86	Neutrons, photons	400	H, ¹⁰ B, ¹¹ B, C, N, O, Na, Mg, Al, Si, S, K, Ca, Cr, Fe, Ni, W, Pb
128	LAHIMACK	Neutrons, photons	800	¹ H, C, O, Al, Si, Fe, Pb
166	PNESD	Protons	1 000	² H, ³ He, Li, Be, ⁹ Be, ¹¹ B, C, ¹² C, Al, ²⁷ Al, Si, ²⁸ Si, S, Ar, Ca, ⁴⁰ Ca, ⁴² Ca, ⁴⁴ Ca, ⁴⁸ Ca, Ti, ⁴⁸ Ti, ⁴⁹ Ti, ⁵⁰ Ti, V, ⁵¹ V, Cr, ⁵² Cr, ⁵³ Cr, Mn, Fe, ⁵⁴ Fe, ⁵⁶ Fe, ⁵⁷ Fe, ⁵⁸ Fe, Co, ⁵⁹ Co, Ni, ⁵⁸ Ni, ⁶⁰ Ni, ⁶² Ni, ⁶⁴ Ni, Cu, ⁶³ Cu, ⁶⁵ Cu, Zn, ⁶⁴ Zn, ⁶⁶ Zn, ⁶⁸ Zn, ⁷⁰ Zn, Kr, ⁸⁹ Y, Zr, ⁹⁰ Zr, ⁹¹ Zr, ⁹² Zr, ⁹⁴ Zr, ⁹⁶ Zr, Nb, Mo, Rh, Pd, Ag, Cd, In, Sn, ¹¹⁶ Sn, ¹¹⁷ Sn, ¹¹⁸ Sn, ¹¹⁹ Sn, ¹²⁰ Sn, ¹⁴⁸ Sm, Ta, ¹⁸¹ Ta, Au, ²⁰⁸ Pb, ²⁰⁹ Bi, Th, U
187	HILO86R	Neutrons, photons	400	H, C, N, O, Mg, Al, Si, K, Ca, Fe
189	MCNPXS*	Neutrons, photons, electrons	Varied	Z = 1-94 for photons and electrons, large list of nuclides for neutrons
200	MCNPDATA*	Neutrons, photons, electrons	Varied	Z = 1-94 for photons and electrons, large list of nuclides for neutrons
205	MCNPXDATA*	Neutrons, photons, electrons	Varied	Z = 1-94 for photons and electrons, large list of nuclides for neutrons
208	ELAST2	Electrons, positrons	100	Z = 1 100

* The three MCNP libraries have different limits for different particles. For neutrons, the limit may be as low as 20 or 30 MeV. Some libraries have photon data that extend to 100 GeV. Other data collections go up to 100 MeV. There is a library called LA150 that extends ENDF/B-VI to 150 MeV. See M.B. Chadwick, *et al.*, *NSE*, 131, 293-328 (1999).

Accelerator analytical tools

The following thirteen codes have possible application to accelerator shielding and contain links to their respective abstracts at RSICC.

- [BISON-C](#)

Forty-two (42) group neutron cross-section set for 60 nuclides obtained from JENDL-3.

BISON-C calculates time-dependent functions and parameters of a nuclear system with external source including burn-up, k-effective, neutron and gamma-ray flux, neutron reaction rates, and system power in complex heterogeneous blanket structures. It is applicable for research of transmutations in accelerator driven subcritical systems.

Auxiliary codes or data: BIS60.XSV, AC22.IX – burn-up library, BIS60.RSC – response function file.

Contributed by: Faculty of Physics and Nuclear Techniques, University of Mining and Metallurgy (Cracow, Poland).

- [CALOR95](#)

Monte Carlo code system for design and analysis of calorimeter systems, spallation neutron source (SNS) target systems, etc.

Auxiliary codes or data: HETC, MORSE, EGS4.

Contributed by: Oak Ridge National Laboratory (Oak Ridge, Tennessee).

- [CASIM](#)
Monte Carlo simulation of transport of hadron cascades in bulk matter.
Contributed by: Fermi National Accelerator Laboratory (Batavia, Illinois).
- [EASY-97](#)
A multi-purpose activation and transmutation code system.
Contributed by: UKAEA/EURATOM Fusion Association (Oxfordshire, United Kingdom).
- [E-DEP-1](#)
Heavy-ion energy deposition code system.
Version P5.00, packaged by RSIC December 1986, employs improved stopping powers and includes several minor corrections and improvements from the previous CDC version.
Contributed by: Naval Research Laboratory (Washington, DC).
- [EGS4](#)
Monte Carlo simulation of the coupled transport of electrons and photons.
Auxiliary codes or data: MORTRAN 3 – macroprocessor to convert MORTRAN to ANSI Fortran, PEGS 4 – data processor for EGS, EGS_Windows – graphical tool for displaying acceleration and geometry data files.
Contributed by: Radiation Physics Group, Stanford Linear Accelerator Center (Stanford University, Stanford, California), National Laboratory for High Energy Physics (KEK, Oho-machi, Tsu-kuba-gun, Ibaraki-ken, Japan), National Research Council of Canada (Ottawa, Canada), Institute for Applied Physiology and Medicine (Seattle, Washington).
- [FLUKA-TRANKA](#)
Three-dimensional high-energy extranuclear hadron cascade Monte Carlo system for cylindrical backstop geometries.
Auxiliary codes or data: CASCA – core of cascade calculator (cylindrical geometries).
Contributed by: Radiation Group, European Organization for Nuclear Research (CERN), (Geneva, Switzerland).
- [HERAD](#)
Three-dimensional Monte Carlo computer code system for calculating radiation damage from ion beams.
Auxiliary codes or data: POTEN – preparation of binary files for input.
Contributed by: University of Wisconsin, Madison, Wisconsin.
- [HERMES-KFA](#)
Monte Carlo code system for high-energy radiation transport calculations.
Contributed by: Forschungszentrum Jülich GmbH (Germany) through the NEA Data Bank (Issy-les-Moulineaux, France).
- [HIC-1](#)
Monte Carlo code system for calculating heavy-ion reactions at energies > 50 MeV/nucleon.
Auxiliary codes or data: CONVERSION – cross-section and evaporation data BCD-to-binary converter code, NUCLEAR CONFIGURATION – cross-section data generator, CASCADE – intranuclear cascade code, EVAPORATION – intermediate-to-final history data processor, ANALYSIS – final history data analysis spectral data tables generation, FLTRAN, FLOTR, FLTRN – random number generators.
Contributed by: Oak Ridge National Laboratory (Oak Ridge, Tennessee).

- [MAGIK](#)
A Monte Carlo code system for computing-induced residual activation dose rates.
Contributed by: Oak Ridge National Laboratory (Oak Ridge, Tennessee).
- [RACC-PULSE](#)
RACC code system for computing radioactivity-related parameters for fusion reactor systems modified for pulsed/intermittent activation analysis.
Auxiliary codes or data: CONVERTFLUX – routine to convert ONEDANT and TWODANT flux data, RACCDLIB – decay constant data, RACCXLIB – transmutation cross-section data.
Contributed by: University of Wisconsin (Madison, Wisconsin).
- [TRANSPORT](#)
Charged particle beam transport systems design code system (first- and second-order matrix multiplication).
The original first-order TRANSPORT computer program was written in BALGOL at Stanford Linear Accelerator Center (SLAC). The BALGOL version was translated into FORTRAN by Massachusetts Institute of Technology (MIT) and later debugged and improved at SLAC. In 1971-72, National Accelerator Laboratory (NAL) completely rewrote the program and developed an efficient second-order fitting routine using the coupling coefficients (partial derivatives) of multipole components to the optics. This version was implemented at SLAC in 1972 and subsequently carried to CERN in 1972. CERN made further contributions to the program structure and improved the convergence capabilities of the first-order fitting routines. A standard version of the resulting program has now been adopted at SLAC, NAL and CERN.
Auxiliary codes or data: CSECT – utility routine.
Contributed by: Fermi National Accelerator Laboratory (NAL, Batavia, Illinois), Stanford Linear Accelerator Center (SLAC, Stanford, California), CERN (Geneva, Switzerland).

Future work on collections

RSICC DLC group libraries

In scanning almost 200 data collections at RSICC, information has been gathered about each collection by reviewing the previously scanned and archived Adobe Acrobat® PDF documents describing the collections. An Access® database was constructed to mirror key information for intelligent searching of the DLC collections. The Access® database contains the following fields:

- 1) DLC number.
- 2) Name of the collection.
- 3) Title of the collection.
- 4) References for the collection.
- 5) Date for the collection.
- 6) Data contributors.
- 7) Particle types.

8) Number of neutron groups (if applicable).

9) Number of photon groups (if applicable).

Additionally, five more fields were recently added to more fully describe each collection:

10) Applications for the collections.

11) Nuclides in the collection.

12) Brief descriptions of just what the collection is and what it is intended for.

13) Upper energy of the data in the collection (if applicable).

14) Energy group structures associated with the collection.

The reasoning for the above field additions are to help people do focused searches over the collections and allow ease of tracking the progress for updates to each former set of data.

The Access® database was used to create a text file that can be searched by a FORTRAN or Cold Fusion® program. This could be expanded to allow customers to search all of the files simultaneously to locate data collections of interest on the WWW.

Identified analytical tools for public distribution

A very important function of the centres is to find and acquire, test and process, package and disseminate software analytical tools that have been designed around the nuclear science of accelerator particles and energies. With the long-term focused effort of the SATIF working groups, there will be a continuing need to identify tools that have been/are being developed in all parts of the world community in support of the science and engineering behind new accelerator applications and upgrades.

The following packages have been/are being requested for submission by the parent organisation to the centres for packaging and public distribution:

SINBAD integral accelerator benchmark experiments for SQA

SINBAD has many new accelerator benchmarks from the Japanese, European, FSR and American experimental facilities. For a cursory look at upcoming accelerator benchmarks to be added this coming year or two, see Table 2. Further information on the SINBAD international database efforts can be found on the respective home pages of the NEA DB (<http://www.nea.fr/abs/html/nea-1552.html>) and the RSICC (<http://www-rsicc.ornl.gov/BENCHMARKS/SINBAD.html>).

Table 2. SINBAD future accelerator benchmarks

Accelerator applications	Facility
ROSTI data & target yield series	CERN
RIKEN (quasi-monoenergetic neutron field using the $7\text{Li}(p,n)7\text{Be}$ reaction 70-210 MeV)	RIKEN
High-energy neutron spectra generated by 590-MeV protons on a thick lead target	PSI
Transmission of medium-energy neutrons through concrete shields	AVF Osaka-U.
Neutron production from thick targets of carbon, iron, copper and lead by 30- and 52-MeV protons	INS Tokyo-U.
The nucleon-meson cascade in iron induced by 1- and 3-GeV protons	ORNL
68 MeV proton on thick Cu target	JAERI
113 MeV proton on thick Fe target	LANL
Shielding experiments through concrete and iron with high-energy proton and heavy ion accelerators (100-800 MeV protons, 20-120 cm concrete and 20-60 cm iron)	HIMAC, KEK
MCNPX benchmark computation #6, TRIUMF – 492-MeV protons on graphite	Georgia Tech; Jeremy Sweezy; Nolan Hertel
MCNPX benchmark computation #7, neutron spectra from 0.5-1.5 GeV protons on thick lead target	Georgia Tech; Jeremy Sweezy; Nolan Hertel
MCNPX benchmark computation #8, transmission of quasi-monoenergetic neutrons generated by 43-MeV and 68-MeV protons through iron and concrete	Georgia Tech; Jeremy Sweezy; Nolan Hertel
MCNPX benchmark computation #9, total neutron yields from 100-MeV protons on Pb, Li, Cu, Fe and Th	Georgia Tech; Jeremy Sweezy; Nolan Hertel
MCNPX benchmark computation #10, neutron fluxes in and around iron beam stop irradiated by 500-MeV protons	Georgia Tech; Jeremy Sweezy; Nolan Hertel

Acknowledgements

The authors wish to thank the NEA Data Bank (Paris) and the Research Organisation for Information Science and Technology (Japan) for their help in putting this paper together and the arduous task of collecting and dissemination responsibilities in their respective communities. Also to be recognised as extremely helpful contributors to this paper are Jeff O. Johnson of the SNS project, ORNL, and Nancy Larson of the Nuclear Data Information Analysis group in ORNL.

REFERENCES

- [1] Nuclear Energy Agency Data Bank (NEA DB) within the Organisation for Economic Co-operation and Development (OECD), Paris, France, <http://www.nea.fr/welcome.html>.
- [2] Radiation Safety Information Computational Center (RSICC) within the Oak Ridge National Laboratory (ORNL), Oak Ridge, TN, USA, <http://www-rsicc.ornl.gov/rsic.html>.
- [3] Roussin, R.W., E. Sartori, "Sharing of Computer Codes and Data for Accelerator Shield Modelling", *Proceedings of the Specialists Meeting on Shielding Aspects of Accelerators, Targets and Irradiation Facilities*, Arlington, Texas (USA), 28-29 April 1994, OECD document ISBN 92-64-14327-0 (1995).
- [4] Roussin, R.W., E. Sartori and P. Vaz, "Status Report on the Collection of Computer Codes and Data Libraries for Accelerator Shielding Modelling", *Proceedings of the 2nd Specialists Meeting on Shielding Aspects of Accelerators, Targets and Irradiation Facilities*, CERN, Geneva (Switzerland), 12-13 October 1995, OECD document ISBN 92-64-15287-3 (1996).
- [5] Kirk, B.L., E. Sartori and P. Vaz, "Progress Report on the Collection of Computer Codes and Data Sets for Accelerator Shielding Analysis", *Proceedings of the 3rd Specialists Meeting on Shielding Aspects of Accelerators, Targets and Irradiation Facilities (SATIF-3)*, Tohoku University, Sendai, Japan, 12-13 May 1997, OECD document ISBN 92-64-16071 (1998).
- [6] Manneschildt, J.B., B.L. Kirk, H.T. Hunter, E. Sartori and P. Vaz, "Progress Report on the Collection of Computer Codes and Data Sets for Accelerator Shielding Analysis", *Proceedings of the 4th Specialists Meeting on Shielding Aspects of Accelerators, Targets and Irradiation Facilities (SATIF-4)*, Gatlinburg, TN (USA), 17-18 September 1998, OECD document ISBN 92-64-17044-8 (1999).
- [7] Sartori, E., P. Vaz, H.T. Hunter, B.L. Kirk and J.B. Manneschildt, "Progress Report on the Collection of Computer Codes and Data Sets for Accelerator Shielding Analysis", *Proceedings of the 5th Specialists Meeting on Shielding Aspects of Accelerators, Targets and Irradiation Facilities (SATIF-5)*, Château de la Muette, Paris, France, 18-21 July 2000, OECD document ISBN 92-64-18691-3 (2001)
- [8] *Executive Summary of the Fifth Meeting of the Task Force on Shielding Aspects of Accelerators, Targets, and Irradiation Facilities*, unpublished report OECD/NEA DB (2000).
- [9] Hunter, H.T., E. Sartori and I. Kodeli, "SINBAD Benchmark Mission and Recent Activities", American Nuclear Society, *Proceedings of the ANS Radiation Protection and Shielding Division Topical Meeting*, Santa Fe, NM, 14-17 April 2002.

Appendix 1

Table 1(a). List of NEADB and RSICC programs and data in alphabetical order

Name	
<blank>	<i>Programs available</i>
(**)	<i>Programs known but not publicly available</i>
(***)	<i>Additions/updates since the SATIF5 meeting</i>
Identification	
CCC-,PSR-,DLC-M00	<i>: original packaging by RSICC</i>
RIST	<i>: located at the Research Organization for Information Science and Technology</i>
NESC	<i>: original packaging by NESC (now ESTSC)</i>
USCD	<i>: originated in US/Canada, packaged by NEA DB</i>
NEA, IAEA	<i>: original packaging by NEA DB</i>
<blank>	<i>: acquisition sought</i>

Name	Identification	Function
ABAREX	PSR-248	optical statistical model to calculate energy-averaged neutron-induced reaction x-sections
ACTIV-87	IAEA1275	library with fast neutron activation x-sections
AIRSCAT	CCC-0341	dose rate from gamma air scattering, single scat. approx.
ALBEDO	NEA 1353	gamma, neutron attenuation in air ducts
ALDOSE	CCC-0577	calculates absorbed dose and dose equivalent rates as function of depth in water irradiated by alpha source
ALICE91	PSR-0146	pre-compound/compound nuclear decay model
ALPHN	CCC-0612	calculates the (alpha, n) production rate in a mixture receiving alpha particles from emitting actinides
AMALTHEE	NEA 0675	emission spectra for n, p, d, h3, he3, alpha reaction
ANISN	CCC-0650	1-D Sn, n, gamma transport in slab, cylinder, sphere
ANITA2000 ***	NEA 1638	code system to calculate isotope inventories from neutron irradiation for fusion applications
ASOP	CCC-0126	1-D Sn shield calculation (new version for AIX and Linux)
ASTAR	IAEA1282	calculates stopping power and range for alphas
ASTROS	CCC-0073	primary/secondary proton dose in sphere/slab tissue
AUJP	IAEA0906	optical potential parameters search by chi*2 method
BALTORO	NEA 0675	n, gamma transport perturbation from MORSE, ANISN calculation
BASACF	IAEA0953	integral neutron adjustment and dosimetry
BERMUDA	NEA 0949	1-D, 2-D, 3-D, n, gamma transport for shielding
BETA-2B	CCC-0117	MC time-dependent bremsstrahlung, electron transport
BETA-S3.1	CCC-657	calculates beta decay source terms and energy spectra
BOT3P 1.0***	NEA 1627	code system for 2-D and 3-D mesh generation and graphical display of geometry and results for the DOORS deterministic transport codes
BREESE	PSR-0143	distribution function for MORSE from albedo data
BREM RAD	CCC-0031	external/internal bremsstrahlung
BRHGAM	CCC-0350	MC absorbed dose from X-rays in phantom
CADE	NEA 1020	multiple particle emission x-sections by Weisskopf-Ewing
CALOR95	CCC-0610	MC system for design, analysis of calorimeter system
CAMERA	CCC-0240	radiation transport and computerised man model
CARP-82	PSR-0131	multi-group albedo data using DOT angular flux results
CASCADE	CCC-0176	high-energy electron-photon transport in matter
CASIM	NESC0742	MC high-energy cascades in complex shields
CCRMN	PSR-355	computation of reactions of a medium-heavy nucleus with six light particles
CEM95	IAEA1247	MC calculation of nuclear reactions (cascade exciton model)
CENDL	IAEA1256	Chinese evaluated nuclear data library (neutron, proton, deuteron, triton, He3 and He4)
CEPXS/ONELD	CCC-0544	1-D coupled electron photon multi-group transport
CFUPI	IAEA1266	n, charged-particle reaction of fissile nuclei E < 33 MeV
CHARGE-2/C	CCC-0070	electron, p, heavy particle flux/dose behind shield
CHEMENGL	NEA-1561	chemical and physical properties of elements
CHENDF 6.1 ***	PSR-333	codes for handling ENDF/B-V and ENDF/B-VI data
CHUCK	USCD1021	n, charged particle x-sections, coupled channel model
CMUP2	IAEA1265	reaction x-sections for n, p, d, t, he3, he4, E < 50 MeV
COLLI-PTB	NEA 1126	MC n fluence spectra for 3-D collimator system
COMNUC3B	PSR-0302	compound nucleus interaction in n reactions
COVFILES	DLC-0091	library of neutron x-sections covariance data, useful to estimate radiation damage or heating

Table 1(a). List of programs and data in alphabetical order (cont.)

Name	Identification	Function
DANTSYS	CCC-0547	1-D, 2-D, 3-D Sn neutron, photon transport
DASH	CCC-0366	void tracing Sn-MC coupling with fluxes from DOT
DCTDOS	CCC-0520	n, gamma penetration in composite duct system
DCHAINSP2000**	RIST	high-energy particle-induced radioactivity calculation code
DDCS	IAEA1290	neutron, proton, deuteron, triton, He3, and alpha-induced reactions of medium heavy nuclei up to 50 MeV
DECDC 1.0***	NEA 1644	nuclear decay data files for radiation dosimetry calculations
DISDOS	CCC-0170	dose from external photons in phantom
DOORS3.2	CCC-0650	discrete ordinates system for deep penetration neutron and gamma transport
DORT	CCC-0543	1-D, 2-D, Sn, n, photon transport with deep penetration
DOSDAT-2	DLC-0079	gamma, electron dose factors data library for body organs
DOSEDAT-DOE	DLC-0144	dose rate factors for external photon, electron exposure
DUST	CCC-0453	albedo MC simulation of n streaming inducts
DWBA98	NEA 1209	distorted wave born approximation nuclear model
DWUCK-4	NESC9872	distorted wave born approximation nuclear model
E-DEP-1	CCC-0275	heavy ion energy deposition
EADL	DLC-0179	library of atomic subshell and relaxation data
EAF99	NEA-1609	x-section library for neutron induced activation materials
EASY-97	NEA-1564	European neutron activation system
ECIS-95	NEA 0850	Schroedinger/Dirac nuclear model with experimental fit
ECPL-86	DLC-0106	evaluated charged particle x-sections
EDMULT	NEA 0969	electron depth dose in multi-layer slab absorbers
EEDL	DLC-179	electron interaction x-section from 10 eV to 100 GeV
EGS4	CCC-0331	MC electron photon shower simulation
ELBA	CCC-0119	bremsstrahlung dose from electron flux on Al shield
ELPHIC-PC	IAEA1223	statistical model MC simulation of heavy ion reaction
ELPHO	CCC-0301	MC muon, electron, positron generation from pions
ELTRAN	CCC-0155	MC 1-D electron transport
EMPIRE-MSC	IAEA1169	multi-step compound nucleus/pre-equilibrium x-sections
EMPIRE-II v 2.13***	IAEA1169	statistical model code system for nuclear reaction calculations, version 2.13
ENLOSS	PSR-0047	energy loss of charged particles
ENDLIB-97	DLC-0179	coupled electron & photon transport library (in LLL ENDF format)
EPDL-97	DLC-0179	photon interaction x-sections library (10 eV to 100 GeV)
EPICSHOW-96.1	IAEA1285	interactive viewing of the electron-photon interaction (10 eV < E < 1 GeV)
ERINNI	NEA 0815	multiple cascades emission spectra by optical model
ESTAR	IAEA1282	calculates stopping power and range for electrons
ETRAN	CCC-0107	MC electron, gamma transport with secondary radiation
EVA		codes performing the nuclear evaporation processes (working on the output from ISABEL)
EVALPLOT	IAEA0852	plots x-sections in ENDF/B format, angular and energy distributions
EVAP_F **		modified version of the Dresner evaporation code
EXIFONGAMMA	IAEA1211	n, alpha, proton, gamma emission spectra model
FALSTF	CCC-0351	n, gamma flux detector response outside cylindrical shields
FEM-RZ	NEA 0566	2-D multi-group n transport in r-z geometry
FGR-DOSE	DLC-0167	library of dose coefficients for intake and exposure to radionuclides
FLEP	DLC-0022	neutron, proton non-elastic x-sections and spectra E < 400 MeV
FLUKA	CCC-0207	MC high energy extranuclear hadron cascades
FOTELP/EM	CCC-0581	MC photons, electrons and positron transport
FOTELP/2KG***	IAEA 1388/01	photons, electrons and positrons transport in 3-D by Monte Carlo techniques
FRITIOF **		hadronic cascades in high-energy heavy ion collisions
FSMN	IAEA1264	fission spectra by compound-nucleus optical model
FSXLIB-J3R2	NEA 1424	JENDL-3 Evaluated Nuclear Data File, fusion neutronics
G33-GP	CCC-0494	multi-group gamma scattering using gp build-up-factor
GAMMONE	NEA 0268	MC gamma penetration from various geometrical sources
GBANISN	CCC-0628	1-D neutron & gamma fluxes with group band fluxes
GCASCAD	IAEA1362	gamma production x-sections from statistical model
GEANT-CERN		
GGG-GP	CCC-0564	multi-group gamma-ray scattering – build-up factors
GMA	PSR-367	generalised least squares evaluation of related x-sections
GNASH-FKK	PSR-0125	multi-step direct and compound and Hauser Feshbach models
GNASH-LANL	PSR-0125	pre-equilibrium/statistical x-sections, emission spectra
GRACE-1	NESC0045	multi-group gamma attenuation, dose in slab
GRAPE	NEA 1043	pre-compound/compound nuclear reaction models
GRPANL	PSR-0321	germanium gamma and alpha detector spectra unfolding
GUI2QAD 3D***	CCC-697/01	point kernel code system for neutron and gamma-ray shielding calculations in complex geometry, including a graphical user interface
HELLO	DLC-0058	47 n, 21 gamma group coupled x-sections from VITAMIN-C library
HERMES-KFA	NEA 1265	MC high-energy radiation transport
HERMES96b	NEA 1265	MC high-energy radiation transport
HETC NMTC	CCC-0178	MC high-energy nucleon meson cascade transport
HETC-KFA	CCC-0496	MC high-energy nucleon-meson cascades
HETC95 **		MC high-energy nucleon-meson cascades and transport

Table 1(a). List of programs and data in alphabetical order (cont.)

Name	Identification	Function
HFMOD	IAEA1317	elastic and inelastic x-section calculation by Hauser-Feshbach and Moldauer
HFTT	IAEA0954	n x-sections by compound-nucleus evaporation model
HIC-1	CCC-0249	MC heavy ion reactions at $E > 50$ MeV/nucleon
HIJET **		hadronic cascades in high-energy heavy-ion collisions
HILO86	DLC-0119	66 n, 22 gamma group x-section lib. for ANISN-ORNL, DORT, MORSE-CGA
HILO86R	DLC-0187	66 n, 22 gamma group x-section, up to 400 MeV (neutron) and 20 MeV (gamma)
HIMAC***	M00000	differential neutron yields in energy and angle produced by high-energy Ar, C, Fe, He, Ne, Nb, Si, on thick Al, C, Cu, Nb, and Pb
HOMO	IAEA1253	program for mixing/converting libraries in ANISN format
HUGO-VI	DLC-0146	photon interaction evaluated data library ENDF-6 format
IAEF-2001***	NEA 1656/01	Intermediate Energy Activation File IEAF-2001
ICOM	CCC-651	calculate transport characteristics of ion radiation
IDC	CCC-0384	ICRP dosimetric calculational system
IHEAS-BENCH	NEA 1468	high-energy accelerator shielding benchmarks
IMPACTS	ESTS0005	radiological assessment code
INFLTB	PSR-0313	dosimetric mass energy transfer and absorption coefficients
INTEL-BERMUDA**	RIST	radiation shielding calculation for fusion reactor, accelerator and reprocessing facility
ISABEL	NEA 1413	intranuclear cascade model allowing hydrogen and helium ions and antiprotons as projectiles
ISAJET **		hadronic cascades in high-energy heavy-ion collisions
ISO-PC	CCC-0636	kernel integration code system for general purpose isotope shielding
ITS-3.0	CCC-0467	MC system of coupled electron photon transport, photon, neutron dose in electron accelerator
K009	CCC-0062	charged particle penetration – phantom quantum mechanical multi-step direct model
LA100	DLC-0168	evaluated data library for n, p up to 100 MeV, ENDF-6 format
LAHET 2.8 ***	CCC-696	code system for high-energy particle transport calculations
LAHIMAC	DLC-0128	neutron, gamma x-sections – response functions, $E < 800$ MeV
LEP	DLC-0001	results from intranuclear cascade and evaporation
LIMES	NEA 1337	intermediate mass fragments in heavy ion nuclear reactions
LPPC	CCC-0051	proton penetration, slab
LPSC	CCC-0064	p, n flux, spectra behind slab shield from p irradiation
LRSPC	CCC-0050	range and stopping power calculator for ions
MAGIK	CCC-0359	MC for computing induced residual activation dose rates
MAGNA	NEA 0163	dose rates from gamma source in slab or cylindrical shell shields
MARLOWE15a***	PSR-0137/06	atomic displacement cascades in solids
MARMER	NEA 1307	point-kernel shielding, ORIGEN-S nuclide inventories
MATXS10	DLC-0176	library with 30n-12gamma energy groups for particle transport codes
MATXS11	DLC-0177	library with 80n-24gamma energy groups for particle transport codes
MCB***	NEA 1656	continuous energy Monte Carlo burn-up simulation code
MCNP-4B2	CCC-0660	MC 3-D time-dependent coupled n, photon, electron transport
MCNP-4C2***	CCC-0701/00	MC 3-D time-dependent coupled n, photon, electron transport
MCNPDATA***	DLC-0200	x-section data library for the MCNP-4C2 transport code
MCNP-VISED 4C2***	PSR-500/00	visual editor for MCNP 4C2 input
MCNPXDATA***	DLC-205/01	x-section data library for the MCNPX 2.1.5
MCNPXS	DLC-0189	x-section data for MCNP4B2
MCNPX 2.1.5***	CCC-705/00	The LAHET/MCNP code merger
MECC-7***	CCC-0156/01	medium-energy intranuclear cascade model
MENDL-2P***	IAEA 1376	proton x-sections for 504 nuclei with atomic number from 13 to 84 at the energies up to 200 MeV
MENSLIB	DLC-0084	neutron 60 group x-sections, $E < 60$ MeV
MERCURE-4	NEA 0351	MC 3-D gamma heating/gamma dose rate, fast flux
MEVDP	CCC-0157	radiation transport in computerised anatomical man
MICAP	PSR-0261	MC ionisation chamber responses
MIRDOSE3.1	CCC-0528	calculate internal dose estimates by the MIRD technique
MORSE-CGA	CCC-0474	MC n, gamma multi-group transport
MRIPP 1.0	CCC-0655	magnetic resonance image phantom for <i>in vivo</i> measurements
MSM-SOURCE	PSR-0369	estimate stopping characteristics of proton transmissions
MUONLM	NEA 1475	calorimeter interaction of muons
MUP-2	IAEA0907	fast n reaction x-sections of medium-heavy nuclei
MUTIL	NEA-1451	calculates the asymmetry factor of the Mott scattering of electrons and positrons by point nuclei
NDEM**		generates a gamma-ray source from the de-excitation of residual nuclei
NESKA	NEA 1422	electron, positron scattering from point nuclei
NFCLIST	ESTS0352	radionuclide decay data tabulations (240 radionuclides)
NJOY-94.61	PSR-0171	n, p, photon evaluated data processing system
NJOY97.0	PSR-355	n, p, photon evaluated data processing system
NJOY99.0	PSR-0480	data processing system of evaluated nuclear data files ENDF format
NMTC/JAERI	NEA 0974	MC high-energy p, n, pion reactions
NMTC/JAERI-97***	NEA-0974	high-energy neutron, proton, pion reaction Monte Carlo simulation
NMF-90	IAEA1279	database for neutron spectra unfolding
NUCDECAY	DLC-0172	nuclear decay data for radiation dosimetry calculations
NucDecayCalc	DLC-0202	nuclear decay data for radiation dosimetry and retrieval program
NUCHART	IAEA1320	nuclear properties and decay data chart
NUCLEUS		nuclear spallation simulation and primary products

Table 1(a). List of programs and data in alphabetical order (cont.)

Name	Identification	Function
NUCLEUS-CHART	NEA-1492	interactive chart of nuclides
OPTMOD	IAEA1316	elastic & total x-section, polarisation calculations using the optical model
OSCAR **	RIST	calculation of yields of nuclear reaction products for particle accelerator
PACE2 **		codes performing the nuclear evaporation processes (working on the output from ISABEL)
PALLAS-2DY	NEA 0702	2-D n ,gamma transport for fixed source
PCROSS	IAEA1220	pre-equilibrium emission spectra in neutron reaction
PCNUDAT32.2.8	USCD1205	nuclear properties database & retrieval system
PEGAS	IAEA1261	unified model of particle and gamma emission reactions
PENELOPE 2001***	NEA 1525	Monte Carlo code for electron-photon transport
PEQAG-2	IAEA1185	pre-equilibrium model nucleon, gamma spectra, x-sections
PEREGRINE **		used to model dose to humans from radiation therapy
PHENOM/BCS-COLL	IAEA1327	nuclear level density of excited nuclei
PHOTX	DLC-0136	photon interaction x-section library for 100 elements
PICA	CCC-0160	MC nuclear cascade reactions by the collision of photons (30 < E < 400 MeV) with nuclei
PIPE	NEA 0416	1-D gamma transport for slab, spherical shields
PLACID	CCC-0381	MC gamma streaming in cylindrical duct shields
PNESD	IAEA1235	elastic x-sections of 3 MeV to 1 000 MeV p on natural isotopes
POINT2000 ***		temperature-dependent, linearly interpolable, tabulated x-section library based on ENDF/B-VI, Release 7
POTAUS	IAEA1249	H through U ion ranges, stopping power for various materials
PREANG	NEA 0809	nuclear model particle spectra, angular distribution
PRECO-2000***	PSR-0226/01	pre-equilibrium, direct reaction double-differential x-sections
PREM	NEA 0888	nucleon emission pre-equilibrium energy spectra, x-sections
PREPRO-96	CCC-351	pre-processing code system for data in ENDF/B format
PSTAR	IAEA1282	calculates stopping power and range for protons
PTRAN	CCC-0618	MC proton transport for 50 to 250 MeV
PUTZ	CCC-0595	point-kernel 3-D gamma shielding
QAD-CGGP-A	CCC-0645	fast neutron and gamma-ray penetration in shields
QMD		intranuclear cascade and classical molecular dynamics
GUIZQAD 3D***	CCC-697/01	point kernel code system for neutron and gamma-ray shielding calculations in complex geometry, including a graphical user interface
RADCOMPT	PSR-0348	sample analysis for alpha and beta dual channel detect
RADDECAY	DLC-0134	decay data library for radiological assessment
RADHEAT-V3	NEA 0467	transport, heat, radiation damage x-sections in reactor, shield
RAID	CCC-0083	gamma, n scattering into cylindrical or multi-bend duct
RAF	IAEA1350	neutron and proton radiative capture differential and integrated x-section
REAC	CCC-0443	activation and transmutation
REAC-2	NESC9554	nuclide activation, transmutation
REAC*3	CCC-0443	isotope activation & transmutation in fusion reactors
REBEL-3	IAEA0846	MC radiation dose to human organs
RECOIL/B	DLC-0055	heavy charged particle recoil spectra library for radiation damage
REMIT	ESTS0579	radiation exposure monitoring and inf. transmittal system
REPC	PSR-0195	dose from protons in tissue
RESRAD5.82	CCC-0552	calculation of residual radioactive material guidelines, site specific radiation doses and risks
SAM-CE	CCC-0187	MC time-dependent 3-D n ,gamma transport in complex geometry
SAMMY M6B***	PSR158/07	code system for multi-level r-matrix fits to neutron and charged-particle x-section data using Bayes' equations
SAMSY	IAEA0837	N, gamma dose rates, heat source for multi-layer shields
SAND-II	PSR-0345	determines neutron energy spectra using multiple experimental activation detector data
SANDYL	CCC-0361	MC 3-D time-dependent gamma electron cascade transport
SCAP-82	CCC-0418	scattering, albedo, point-kernel anal. in complex geometry
SCAT-2B***	NEA-0829	spherical optical model for light particles and heavy ions
SCINFUL	PSR-0267	MC response of scintillation neutron detector (incident neutron energies from 0.1 to 75 MeV)
SEECAL	CCC-0620	age-dependent effective energies for 54 and 32 target regions in the human body (825 radionuclides)
SFERXS	NEA 1239	photon absorption, coherent, incoherent x-sections for shielding
SHIELD***	CCC-667	universal code for exclusive simulation of hadron cascades in complex macroscopic targets
SIGMA-A	DLC-0139	photon interaction and absorption data 1 KeV-100 MeV
SINBAD97	DLC-191	Shielding INtegral Benchmark Archive DataBase
SINBAD2000		Shielding INtegral Benchmark Archive DataBase
SITHA **	IAEA1179	Simulation Transport HAdron, calculates hadron transport
SKYIII-PC	CCC-0289	PC version of program SKYSHINE-III
SKYPORT	DLC-0093	importance of n, photon skyshine dose from accelerators
SKYSHINE-KSU***	CCC-0646/03	computation of gamma skyshine doses by different methods
SNLRML	DLC-0178	dosimetry library compendium
SNL/SAND-II	PSR-0345	enhanced version of SAND-II
SOURCE **		description of the proton transmission and generation of n source
SOURCESA4	CCC-661	(α ,n), spontaneous fission and (β ,n) delayed neutron sources and spectra due to decay in homog. media
SPACETRAN	CCC-0120	radiation leakage from cylinder with ANISN flux
SPAR	CCC-0228	stopping power and ranges from muons, pions, protons ions
SPARES	CCC-0148	space radiation environment and shielding evaluation

Table 1(a). List of programs and data in alphabetical order (cont.)

Name	Identification	Function
SPEC	IAEA1332	computation of neutron and charged particle reactions using optical and evaporation models
SPCHAIN **		calculates accumulation and decay of nuclides
SPECTER-ANL	PSR-0263	n damage for material irradiation
SRIM-2000	NEA 0919	stopping power and ranges of ions (10 ev-2 GeV/amu)
SRNA-2KG***	IAEA 1382/01	proton transport using 3-D by Monte Carlo techniques
STAC-8		transmitted, absorbed power/spectrum – synchrotron radiation
STAPRE-H95	IAEA0971	evaporation, pre-equilibrium model reaction x-sections
STAPREF***	NEA-0461	nuclear reactions x-sections by evaporation model, gamma-cascades
STARCODES	PSR-0330	stopping power, ranges for electrons, protons, alpha
STOPOW	IAEA0970	stopping power of fast ions in matter
STR92	ESTS1041	energy deposition in accelerator ring components
STRAGL	CCC-0201	energy loss straggling of heavy charged particles
SWIMS	ESTS0682	angular dispersion of ion beams at small-angle incoherent multiple scattering by gaseous or solid media
TART2000***	CCC-638/01	3-D MC transport program for neutrons and photons
TDTORT***	CCC-709/00	time-dependent, three-dimensional, discrete ordinates, neutron transport code system
TNG1	PSR-0298	n multi-step statistical model
TORT	CCC-0543	3-D Sn n, photon transport with deep penetration
TPASGAM	DLC-0088	library with gamma-ray decay data for 1438 radionuclides
TRANSX2.15	PSR-0317	code to produce neutron, photon transport tables for discrete ordinates and diffusion codes
TRAPP	CCC-0205	proton and alpha transport, reaction products neglected
TRIPOLI-3		MC time-dependent 3-D N, gamma transport
TRIPOS	CCC-0537	MC ion transport
TWODANT-SYS	CCC-0547	1-D, 2-D multi-group Sn n, photon transport
UNGER	DLC-0164	effective dose equivalent data for selected isotopes
UNIFY	IAEA1177	fast n x-sections, spectrum calculation for structural materials
UNSPEC	ESTS0827	X-ray spectrum unfolding using an iterative technique
VEGAS **		intranuclear cascade code (from which ISABEL is derived)
VIRGIN	IAEA0932	uncollided neutron flux and neutron reactions due through a neutron beam through any thickness of material
VITAMIN-E	DLC-0113	x-section data library with 174n-38gamma energy groups
VITAMIN-B6	DLC-0184	x-section data library with 199n-42gamma energy groups from ENDF/B-VI Release 3
XCOM	DLC-0174	photon x-sections from 1 KeV to 100 GeV
ZOTT99***	IAEA1371	data evaluation using partitioned least squares

**Table 2(a). Evaluated and processed data
(cross-sections, co-variance, dose conversion, ranges, stopping powers)**

Name	Identification	Function
ACTIV-87	IAEA1275	library with fast neutron activation x-sections
CENDL	IAEA1256	Chinese evaluated nuclear data library (neutron, proton, deuteron, triton, He3 and He4)
CHENDF 6.1***	PSR-333	codes for handling ENDF/B-V and ENDF/B-VI data
COVFILES	DLC-0091	library of neutron x-sections covariance data, useful to estimate radiation damage or heating
DECDC 1.0***	NEA 1644	nuclear decay data files for radiation dosimetry calculations
DOSDAT-2	DLC-0079	gamma, electron dose factors data library for body organs
DOSEDAT-DOE	DLC-0144	dose rate factors for external photon, electron exposure
EADL	USCD1192	library of atomic sub-shell and relaxation data
EAFF99	NEA-1609	x-section library for neutron induced activation materials
EASY-97	NEA-1564	European neutron activation system
ECPL-86	DLC-0106	evaluated charged particle x-sections
EEDL	USCD1193	electron interaction x-section from 10 eV to 100 GeV
ENDLIB-94	DLC-0179	coupled electron & photon transport library (in LLL ENDL format)
ENDLIB-97	DLC-0179	coupled electron & photon transport library (in LLL ENDL format)
EPDL-VI/MOD	USCD1187	photon interaction x-sections library (10 eV to 100 GeV)
FGR-DOSE	DLC-0167	library of dose coefficients for intake and exposure to radionuclides
FLEP	DLC-0022	neutron, proton non-elastic x-sections and spectra E < 400 MeV
FSXLIB-J3R2	NEA 1424	JENDL-3 Evaluated Nuclear Data File, fusion neutronics
HIL086	DLC-0119	66 N, 22 gamma group x-section library for ANISN-ORNL, DORT, MORSE-CGA
HIL086R	DLC-0187	66 N, 22 gamma group x-sections, up to 400 MeV (neutron) and 20 MeV (gamma)
HIMAC***	M00000	differential neutron yields from high-energy Ar, C, Fe, He, Ne, Nb, Si, on thick Al, C, Cu, Nb, and Pb
HELLO	DLC-0058	47 n, 21 gamma group coupled x-section from VITAMIN-C library
HUGO-VI	DLC-0146	photon interaction evaluated data library ENDF-6 format
IAEF-2001***	NEA 1656/01	Intermediate Energy Activation File IAEF-2001
IDC	CCC-0384	ICRP dosimetric calculational system
IHEAS-BENCH	NEA 1468	high-energy accelerator shielding benchmarks
JENDL-3.2	NEA-1470	x-section data library and plots for neutrons up to 70 MeV
JENDL/D-99	NEA-1624	dosimetry x-section data library and plots for neutrons
LA100	DLC-0168	evaluated data library for n, p up to 100 MeV, ENDF-6 format
LAHIMACK	DLC-0128	multi-group neutron and gamma x-sections up to 800 MeV
LEP	DLC-0001	results from intranuclear cascade and evaporation
LRSPC	CCC-0050	range and stopping power calculator
MATXS10	DLC-0176	library with 30 n-12 gamma energy groups for particle transport codes
MATXS11	DLC-0177	library with 30 n-12 gamma energy groups
MCNPDATA***	DLC-0200	x-section data library for the MCNP-4C2 transport code
MCNPXS	DLC-0189	x-section data for MCNP-4B2
MCNPXDATA***	DLC-205/01	x-section data library for the MCNPX 2.1.5
MENDL-2P***	IAEA 1376	proton x-sections for 504 nuclei with atomic number from 13 to 84 at the energies up to 200 MeV
MENSLIB	DLC-0084	neutron 60 group x-sections, E < 60 MeV
NJOY97.0	PSR-355	n, p, photon evaluated data processing system
NJOY99.0	PSR-480	data processing system of evaluated nuclear data files ENDF format
NMF-90	IAEA1279	database for neutron spectra unfolding
NUCDECAY	DLC-0172	nuclear decay data for radiation dosimetry calculations
NucDecayCalc	DLC-0202	nuclear decay data for radiation dosimetry and retrieval program
NUCHART	IAEA1320	nuclear properties and decay data chart
PCNUDAT32.2.8	USCD1205	nuclear properties database & retrieval system
PHOTX	DLC-0136	photon interaction x-section library for 100 elements
PNESD	IAEA1235	elastic x-sections of 3 MeV to 1 000 MeV p on natural isotopes
POINT97	DLC-0192	combination of resonance parameters and/or tabulated energy dependent evaluated x-sections
POINT2000 ***	DLC-212	temperature-dependent, linearly interpolable, tabulated x-section library based on ENDF/B-VI, Release 7
RADDECAY	DLC-0134	decay data library for radiological assessment
RECOIL/B	DLC-0055	heavy charged particle recoil spectra library for radiation damage
SAMMY M6B***	PSR158/07	code system for multilevel r-matrix fits to neutron and charged-particle x-section data using Bayes' equations
SFERXS	NEA 1239	photon absorption, coherent, incoherent x-sections for shielding
SIGMA-A	DLC-0139	photon interaction and absorption data 1 KeV-100 MeV
SINBAD2000	DLC-191/02	shielding integral benchmark archive database
SINBAD2002***	DLC-191/03	shielding integral benchmark archive database
SKYIII-PC	CCC-0289	PC version of program SKYSHINE-III
SKYPORT	DLC-0093	importance of n, photon skyshine dose from accelerator
SKYSHINE-KSU***	CCC-0646/03	computation of gamma skyshine doses by different methods
SNLRML	DLC-0178	dosimetry library compendium
SPAR	CCC-0228	stopping power and ranges from muons, pions, protons, ions
SRIM-2000	NEA 0919	stopping power and ranges of ions (10 eV-2 GeV/amu) in matter
STARCODES	PSR-0330	stopping power, ranges for electrons, protons, alpha
STOPOW	IAEA0970	stopping power of fast ions in matter
TPASGAM	DLC-0088	library with gamma-ray decay data for 1438 radionuclides
UNGER	DLC-0164	effective dose equivalent data for selected isotopes
VITAMIN-E	DLC-0113	x-section data library with 174 n-38 gamma energy groups
VITAMIN-B6	DLC-0184	x-section data library with 199 n-42 gamma energy groups derived from ENDF/B-VI Release 3
XCOM	DLC-0174	photon x-sections from 1 KeV to 100 GeV

Table 3(a). Generating cross-sections – spectra from nuclear models (for E > 20 MeV)

Name	Identification	Function
ALICE91	PSR-0146	pre-compound/compound nuclear decay model
AMALTHEE	NEA 0675	emission spectra for n, p, d, h3, he3, alpha reaction
ASOP	CCC-0126	1-D Sn shield calculation
AUJP	IAEA0906	optical potential parameters search by chi**2 method
CADE	NEA 1020	multiple particle emission x-sections by Weisskopf-Ewing
CCRMN	IAEA1347	computation of reactions of a medium-heavy nucleus with six light particles
CEM95	IAEA1247	MC calculation of nuclear reactions (Cascade Exciton Model)
CFUP1	IAEA1266	n, charged-particle reaction of fissile nuclei E < 33 MeV
CHUCK	USCD1021	n, charged particle x-sections, coupled channel model
CMUP2	IAEA1265	reaction x-sections for n ,p, d, t, he3, he4, E < 50 MeV
COMNUC3B	PSR-0302	compound nucleus interaction in n reactions
DWBA82	NEA 1209	distorted wave born approximation nuclear model
DWUCK-4	NESC9872	distorted wave born approximation nuclear model
ECIS-95	NEA 0850	Schroedinger/Dirac nuclear model with experimental fit
ELPHIC-PC	IAEA1223	statistical model MC simulation of heavy ion reaction
EMPIRE-MSC	IAEA1169	multi-step compound nucleus/pre-equilibrium x-sections
EMPIRE-II	IAEA1169	comprehensive nuclear model code, nucleon-, ion-induced x-sections
EMPIRE-II v 2.13***	IAEA1169	statistical model code system for nuclear reaction calculations, Version 2.13
ERINNI	NEA 0815	multiple cascades emission spectra by optical model
EVA		codes performing the nuclear evaporation processes
EVAP_F**		modified version of the Dresdner evaporation code
EXIFONGAMMA	IAEA1211	n, alpha, proton, gamma emission spectra model
FRITIOF **		MC high-energy heavy ion collisions
GCASCAD	IAEA1362	gamma production x-sections from statistical model
GNASH-FKK	PSR-0125	multi-step direct and compound and Hauser-Feshbach models
GNASH-LANL	PSR-0125	pre-equilibrium/statistical x-sections, emission spectra
GRAPE	NEA 1043	pre-compound/compound nuclear reaction models
HETC NMTC	CCC-0178	MC high energy nucleon meson cascade transport
HETC-KFA	CCC-0496	MC high energy nucleon-meson cascades
HETC95 **		MC high energy nucleon-meson cascades and transport
HFMOD	IAEA1317	elastic and inelastic x-section calculation by Hauser-Feshbach and Moldauer
HFTT	IAEA0954	n x-section by compound-nucleus evaporation model
HJET **		MC high-energy heavy ion collisions
ISABEL	NEA 1413	intra-nuclear cascade model allowing hydrogen and helium ions and antiprotons as projectiles
ISAJET **		MC high-energy heavy ion collisions
KAPSIES		quantum mechanical multi-step direct model
LIMES	NEA 1337	intermediate mass fragments in heavy ion nuclear reactions
MARLOWE15a***	PSR-0137	atomic displacement cascades in solids
MECC-7***	CCC-0156/01	medium energy intra-nuclear cascade model
MUP-2	IAEA0907	fast n reaction x-section of medium-heavy nuclei
MUTIL	NEA 1451	calculates the asymmetry factor of the Mott scattering of electrons and positrons by point nuclei
NDEM**		generates a gamma-ray source from the de-excitation of residual nuclei
NJOY-94.61	PSR-0171	n, p, photon evaluated data processing system
NJOY97.0	PSR-355	n, p, photon evaluated data processing system
NJOY99.0	PSR-0480	data processing system of evaluated nuclear data files ENDF format
NMTC/JAERI-97***	NEA 0974	MC high-energy p, n, pion reactions
NUCLEUS		nuclear spallation simulation and primary products
OPTMOD	IAEA1316	elastic & total x-section, polarisation calculations using the optical model
PACE2 **		codes performing the nuclear evaporation processes
PCROSS	IAEA1220	pre-equilibrium emission spectra in neutron reaction
PEGAS	IAEA1261	unified model of particle and gamma emission reactions
PEQAG-2	IAEA1185	pre-equilibrium model nucleon, gamma spectra, x-section
PHENOM/BCS-COLL	IAEA1327	nuclear level density of excited nuclei
PREANG	NEA 0809	nuclear model particle spectra, angular distribution
PRECO-D2	PSR-0226	pre-equilibrium, direct reaction double differential x-section
PRECO-2000***	PSR-0226/01	pre-equilibrium, direct reaction double differential x-sections
PREM	NEA 0888	nucleon emission pre-equilibrium energy spectra, x-section
QMD		intranuclear cascade and classical molecular dynamics
RAF	IAEA1350	neutron and proton radiative capture differential and integrated x-section
REAC	CCC-0443	activation and transmutation
REAC-2	NESC9554	nuclide activation, transmutation
REAC*3	CCC-0443	isotope activation & transmutation in fusion reactors
SCAT-2B***	NEA-0829	spherical optical model for light particles and heavy ions
SOURCES4A	CCC-661	determine (α ,n), spontaneous fission and (β ,n) delayed
SPEC	IAEA1332	computation of neutron and charged particle reactions using optical and evaporation models
STAPRE-H95	IAEA0971	evaporation, pre-equilibrium model reaction x-sections
STAPREF***	NEA-0461	nuclear reactions x-sections by evaporation model, gamma-cascades
TNG1	PSR-0298	n multi-step statistical model
UNIFY	IAEA1177	fast n x-section, spectrum calculation for structural materials

Table 4(a). Monte Carlo (MC) and deterministic radiation transport (neutron/photon)

Name	Identification	Function
ALBEDO	NEA 1353	gamma, neutron attenuation in air ducts
ANISN	CCC-0254	1-D Sn, n, gamma transport in slab, cylinder, sphere
ASOP	CCC-0126	1-D Sn shield calculation
BALTORO	NEA 0675	n, gamma transport perturbation from MORSE, ANISN calculation
BASACF	IAEA0953	integral neutron adjustment and dosimetry
BERMUDA	NEA 0949	1-D,2-D,3-D n gamma transport for shielding
BREESE	PSR-0143	distribution function for MORSE from albedo data
CARP-82	PSR-0131	Multi-group albedo data using DOT angular flux results
COLLI-PTB	NEA 1126	MC n fluence spectra for 3-D collimator system
DANTSYS	CCC-0547	1-D, 2-D, 3-D Sn neutron, photon transport
DASH	CCC-0366	void tracing Sn-MC coupling with fluxes from DOT
DCTDOS	CCC-0520	n, gamma penetration in composite duct system
DOORS3.2	CCC-0650	discrete ordinates system for deep penetration neutron and gamma transport
DORT	CCC-0543	1-D, 2-D, Sn, n, photon transport with deep penetration
DOMINO	PSR-0064	coupling of Sn DOT with MC MORSE
DOT	CCC-0276	2-D Sn, n photon transport with deep penetration
DUST	CCC-0453	albedo MC simulation of n streaming inducts
FALSTF	CCC-0351	n, gamma flux detector response outside cylindrical shields
FEM-RZ	NEA 0566	FEM 2-D multi-group n transport in r-z geometry
GBANISN	CCC-0628	1-D neutron & gamma fluxes with group band fluxes
GEANT-CERN		MC hadron shower simulation
LAHET 2.8 ***	CCC-696	code system for high-energy particle transport calculations
MAGIK	CCC-0359	MC-induced residual activation dose rates
MCB***	NEA ????	Continuous-energy Monte Carlo burn-up simulation code
MCNP-4A	CCC-0200	MC 3-D time-dependent coupled n, photon, electron transport
MCNP-4B	CCC-0660	MC 3-D time-dependent coupled n, photon, electron transport
MCNP-4B2	CCC-0660	MC 3-D time-dependent coupled n, photon, electron transport
MCNP-4C2***	CCC-0701/00	MC 3-D time-dependent coupled n, photon, electron transport
MCNPX 2.1.5***	CCC-705/00	LAHET/MCNP code merger
MICAP	PSR-0261	MC ionisation chamber responses
MORSE-CGA	CCC-0474	MC n, gamma multi-group transport
PALLAS-2DY	NEA 0702	2-D n ,gamma transport for fixed source
RADHEAT-V3	NEA 0467	transport, heat, radiation damage x-sections in reactor, shield
QAD-CGGP-A	CCC-0645	fast neutron and gamma-ray penetration in shields
RAID	CCC-0083	gamma, n scattering into cylindrical or multi-bend duct
SAMSY	IAEA0837	n, gamma dose rates, heat source for multi-layer shields
SAM-CE	CCC-0187	MC time-dependent 3-D n ,gamma transport in complex geometry
SCINFUL	PSR-0267	MC response of scintillation neutron detector (incident neutron energies from 0.1 to 75 MeV)
SCAP-82	CCC-0418	scattering, albedo, point-kernel anal. in complex geometry
SNL/SAND-II	PSR-0345	enhanced version of SAND-II
SPACETRAN	CCC-0120	radiation leakage from cylinder with ANISN flux
SPECTER-ANL	PSR-0263	n damage for material irradiation
STAPREF***	NEA-0461	nuclear reactions x-sections by evaporation model, gamma-cascades
STARCODE S	PSR-0330	stopping power, ranges for electrons, protons, alpha
TART2000***	CCC-638/01	3-D MC transport program for neutrons and photons
TDTORT***	CCC-709/00	time-dependent, three-dimensional, discrete ordinates, neutron transport code system
TORT	CCC-0543	3-D Sn, n photon transport with deep penetration
TRANSX	PSR-0317	code to produce neutron, photon transport tables for discrete ordinates and diffusion codes
TRIPOLI-2	NEA 0874	MC time-dependent 3-D n, gamma transport
TWODANT-SYS	CCC-0547	1-D,2-D multi-group Sn, n, photon transport
VIRGIN	IAEA0932	uncollided neutron flux and neutron reactions due through a neutron beam through any thickness of material

Table 5(a). Monte Carlo (MC) and deterministic radiation transport (photon)

Name	Identification	Function
AIRSCAT	CCC-0341	dose rate from gamma air scattering, single scat. approx.
GAMMONE	NEA 0268	MC gamma penetration from various geometrical sources
MERCURE-4	NEA 0351	MC 3-D gamma heating/gamma dose rate, fast flux
PLACID	CCC-0381	MC gamma streaming in cylindrical duct shields
BRHGAM	CCC-0350	MC absorbed dose from X-rays in phantom
BREM RAD	CCC-0031	external/internal bremsstrahlung
GRPANL	PSR-0321	germanium gamma and alpha detector spectra unfolding
G33-GP	CCC-0494	multi-group gamma scattering using gp build-up factor
ISO-PC	CCC-0636	kernel integration code system for general purpose isotope shielding
MAGNA	NEA 0163	dose rates from gamma source in slab or cylindrical shell shields
MARMER	NEA 1307	point-kernel shielding, ORIGEN-S nuclide inventories
PELSHIE	IAEA0855	dose rates from gamma source, point-kernel method
PIPE	NEA 0416	1-D gamma transport for slab, spherical shields
PUTZ	CCC-0595	point-kernel 3-D gamma shielding
SKYSHINE-KSU***	CCC-0646/03	computation of gamma skyshine doses by different methods
STAC-8		transmitted, absorbed power/spectrum – synchrotron radiation
UNSPEC	ESTS0827	X-ray spectrum unfolding using an iterative technique

Table 6(a). Monte Carlo (MC) and deterministic radiation transport (electron/photon)

Name	Identification	Function
BETA-2B	CCC-0117	MC time-dependent bremsstrahlung, electron transport
BETA-S3.1	CCC-0657	calculates beta decay source terms and energy spectra
CASCADE	CCC-0176	high-energy electron-photon transport in matter
CEPXS ONELD	CCC-0544	1-D coupled electron photon multi-group transport
DOSDAT-2	DLC-0079	gamma, electron dose factors data library for body organs
EDMULT	NEA 0969	electron depth dose in multi-layer slab absorbers
EGS4	CCC-0331	MC electron photon shower simulation
ELBA	CCC-0119	bremsstrahlung dose from electron flux on Al shield
EPICSHOW-96.1	IAEA1285	interactive viewing of the electron-photon interaction (10 eV < E < 1 GeV)
ESTAR	IAEA1282	calculates stopping power and range for electrons
ETRAN	CCC-0107	MC electron, gamma transport with secondary radiation
ELTRAN	CCC-0155	MC 1-D electron transport
FOTELP	CCC-0581	MC photons, electrons and positron transport
FOTELP/EM	CCC-0581	MC photons, electrons and positron transport
FOTELP/2KG***	IAEA 1388/01	Photons, electrons and positrons transport in 3-D by Monte Carlo techniques
INFLTB	PSR-0313	dosimetric mass energy transfer and absorption coefficients
ITS-3.0	CCC-0467	MC tiger system of coupled electron photon transport
MCNP-4A	CCC-0200	MC 3-D time-dependent coupled n, photon, electron transport
MCNP-4B	CCC-0660	MC 3-D time-dependent coupled n, photon, electron transport
MCNP-4C2***	CCC-0701	MC 3-D time-dependent coupled n, photon, electron transport
PENELOPE 2001***	NEA 1525	Monte Carlo code for electron-photon transport
SANDYL	CCC-0361	MC 3-D time-dependent gamma electron cascade transport

Table 7(a). Monte Carlo (MC) and deterministic radiation transport (proton)

Name	Identification	Function
ASTROS	CCC-0073	primary/secondary proton dose in sphere/slab tissue
LPPC	CCC-0051	proton penetration, slab
PSTAR	IAEA1282	calculates stopping power and range for protons
PTRAN	CCC-0618	MC proton transport for 50 to 250 MeV
SOURCE **		description of the proton transmission and generation of n source
SRNA-2KG***	IAEA 1382/01	proton transport using 3-D by Monte Carlo techniques
TRAPP	CCC-0205	proton and alpha transport, reaction products neglected

Table 8(a). Monte Carlo (MC) and deterministic radiation transport (alpha)

Name	Identification	Function
ALDOSE	CCC-0577	absorbed dose and dose equivalent rates as function of depth in water irradiated by alpha source
ALPHN	CCC-0612	(alpha,n) production rate in a mixture from alpha emitting actinides
ASTAR	IAEA1282	calculates stopping power and range for alphas
GRPANL	PSR-0321	germanium gamma and alpha detector spectra unfolding
RADCOMPT	PSR-0348	sample analysis for alpha and beta dual channel detectors

Table 9(a). Monte Carlo (MC) and deterministic radiation transport (nucleons/hadrons/cascades)

Name	Identification	Function
CALOR95		MC system for design, analysis of calorimeter system
CASIM	NESC0742	MC high-energy cascades in complex shields
FLUKA	CCC-0207	MC high-energy extranuclear hadron cascades
GEANT-CERN		MC hadron shower simulation
HERMES-KFA	NEA 1265	MC high-energy radiation transport
HERMES96b		idem
HETCNMTC-97	CCC-0178	MC high-energy nucleon meson cascade transport
HETC-KFA	CCC-0496	MC high-energy nucleon-meson cascade transport
LAHET 2.8 ***	CCC-696	code system for high-energy particle transport calculations
LPSC	CCC-0064	p, n flux, spectra behind slab shield from p irradiation
NMTC/JAERI97***	NEA 0974	MC high-energy p, n, pion reactions
SITHA **	IAEA1179	simulation transport hadron, used to calculate hadron transport
SHIELD ***	IAEA1287	hadron cascades in complex macroscopic targets

Table 10(a). Monte Carlo (MC) and deterministic radiation transport (heavy ions)

Name	Identification	Function
E-DEP-1	CCC-0275	heavy-ion energy deposition
ELPHIC-PC	IAEA1223	statistical model MC simulation of heavy ion reaction
HIC-1	CCC-0249	MC heavy-ion reactions at $E > 50$ MeV/nucleon
STRAGL	CCC-0201	energy loss straggling of heavy charged particles
SWIMS	ESTS0682	angular dispersion of ion beams at small-angle incoherent multiple scattering by gaseous or solid media
TRIPOS	CCC-0537	MC ion transport

Table 11(a). Monte Carlo (MC) and deterministic radiation transport (muons)

Name	Identification	Function
MUONLM	NEA 1475	calorimeter interaction of muons

Table 12(a). Monte Carlo (MC) and deterministic radiation transport (other cascades)

Name	Identification	Function
CHARGE-2/C	CCC-0070	electron, p, heavy particle flux/dose behind shield
DDCS	IAEA1290	neutron, proton, deuteron, triton, He3, and alpha induced reactions of medium heavy nuclei in the energy range up to 50 MeV
ELPHO	CCC-0301	MC muon, electron, positron generation from pions
IMPACTS-BRC	ESTS0005	radiological assessment code
JENKINS		photon, neutron dose in electron accelerator
PICA	CCC-0160	MC nuclear cascade reactions by the collision of photons ($30 < E < 400$ MeV) with nuclei
SPARES	CCC-0148	space radiation environment and shielding evaluation

Table 13(a). Monte Carlo (MC) and deterministic radiation transport (anthropomorphic phantom modelling)

Name	Identification	Function
BRHGAM	CCC-0350	MC absorbed dose from X-rays in phantom
CAMERA	CCC-0240	radiation transport and computerised man model
DISDOS	CCC-0170	dose from external photons in phantom
K009	CCC-0062	charged particle penetration – phantom
MEVDP	CCC-0157	radiation transport in computerised anatomical man
MIRDOSE3.1	CCC-0528	calculate internal dose estimates by the MIRD technique
MRIPP 1.0	CCC-0655	magnetic resonance image phantom for <i>in vivo</i> measurements
PENELOPE 2001***	NEA 1525	Monte Carlo code for electron-photon transport
PEREGRINE **		used to model dose to humans from radiation therapy
REBEL-3	IAEA0846	MC radiation dose to human organs
REPC	PSR-0195	dose from protons in tissue
SEECAL	CCC-0620	computes age-dependent effective energies for 54 and 32 target regions in the human body (825 radionuclides)

Table 14(a). Benchmark data relative to reactor shields* sets included in the SINBAD database

Name	Description
ASPIS-FE	Winfrith Iron Benchmark Experiment (ASPIS)
ASPIS-FE88	Winfrith Iron 88 Benchmark Experiment (ASPIS)
ASPIS-GRAPHITE	Winfrith Graphite Benchmark Experiment (ASPIS)
IPPE- BTiH	IPPE Fast n/γ through BTiH Prism
Winfrith H2O	Winfrith Water Benchmark Experiment
Winfrith PCA-REPLICA	Winfrith Water/Iron Benchmark Experiment
Winfrith NESDIP-2	Radial Shield of a PWR
Winfrith NESDIP-3	Radial Shield w/Cavity and Backing Shield of a PWR
Winfrith Water/Steel	Winfrith Neutron-Gamma Ray Transport through Water/Steel Arrays (ASPIS)
EURACOS-FE	Ispra Iron Benchmark Experiment (EURACOS)
EURACOS-NA	Ispra Sodium Benchmark Experiment (EURACOS)
HARMONIE-NA	Cadarache Sodium Benchmark Experiment (HARMONIE)
HB Robinson II	HB Robinson-2, Cycle 9 (US NRC PV Benchmark)
JANUS-I	Fast Reactor w/Mild Steel, SS, and Concrete -Phase I
JANUS-VIII	Fast Reactor w/ Mild Steel, SS, Sodium, Polyethylene, Lead
KFK-FE	Karlsruhe Iron Sphere Benchmark Experiment
PROTEUS-FE	Wuerenlingen Iron Benchmark Experiment
PCA-PV	Pool Critical Assembly – Pressure Vessel Experiment (PCA)
SDT1	Iron Broomstick Benchmark Experiment (TSF-ORNL)
SDT2	Oxygen Broomstick Benchmark Experiment (TSF-ORNL)
SDT3	Nitrogen Broomstick Benchmark Experiment (TSF-ORNL)
SDT4	Sodium Broomstick Benchmark Experiment (TSF-ORNL)
SDT5	Stainless Steel Broomstick Benchmark Experiment (TSF-ORNL)
SDT 11	ORNL Neutron Transport in Iron and SS
SDT 12	ORNL Neutron Transport in Thick Sodium
SB2	Gamma Production Cross-Sections from Thermal Neutrons
SB3	Gamma Production Cross-Sections from Fast Neutron in 14 elements and SS
JASPER Axial Shield	Fast Reactor w/SS, B4C
JASPER Radial Shield	Fast Reactor w/SS, Graphite, B4C, and Sodium
JASPER Int. Heat Exch.	Fast Reactor w/Sodium, Spent Fuel, and B4C
Illinois Iron Sphere	Univ. of Illinois Iron Sphere

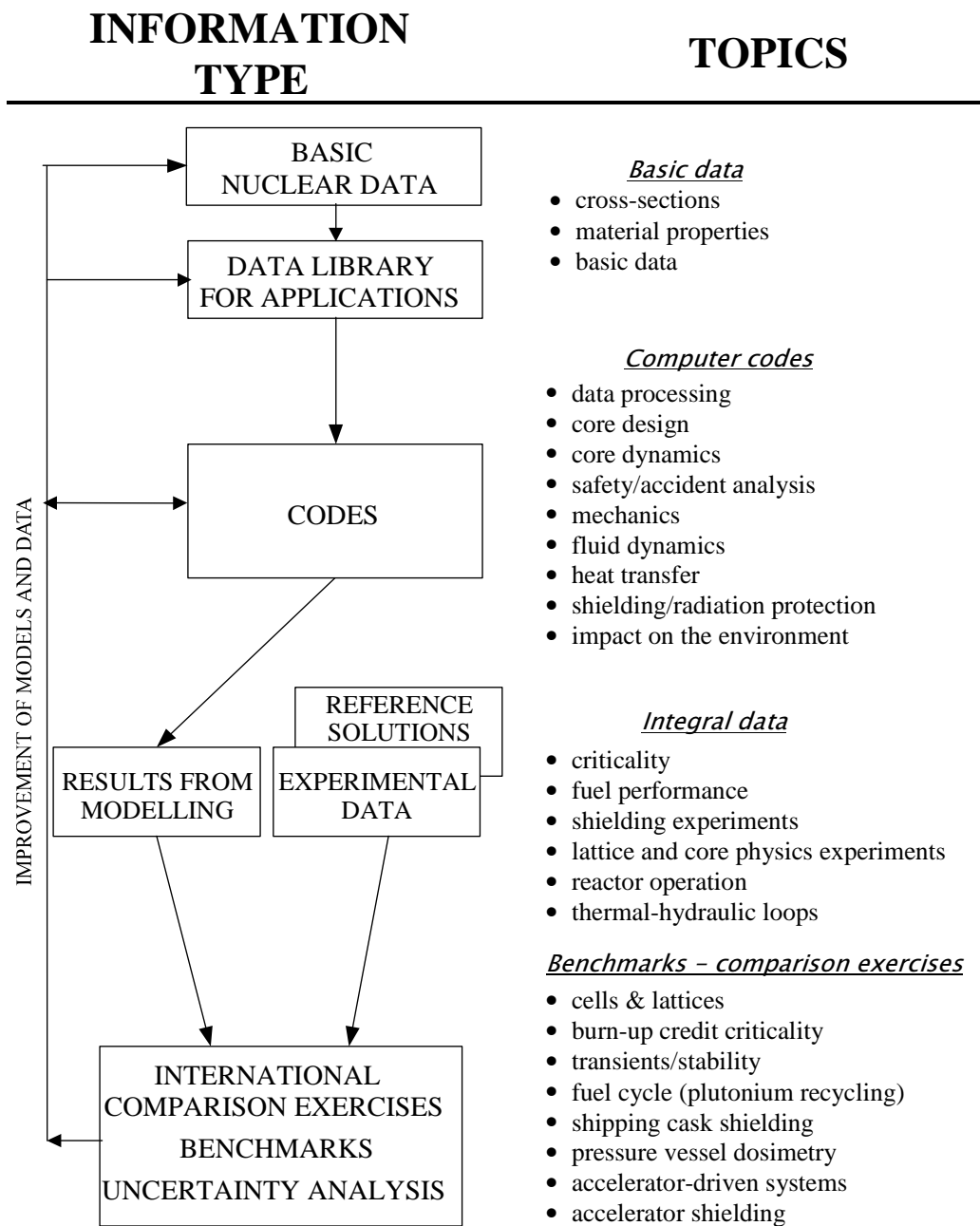
* *Bold indicates new SINBAD additions since the SATIF-5 meeting, July 2000.*

Table 15(a). Benchmark data sets relative to fusion shielding and accelerator shielding included in the SINBAD database

Name	Description
FNS-Graphite	FNS Graphite Cylindrical Assembly
FNS-Vanadium	FNS Vanadium block
OKTAVIAN-Fe	Osaka Iron Sphere Benchmark Experiment
OKTAVIAN-Ni	Osaka Nickel Benchmark Experiment
OKTAVIAN-Al	Osaka Leakage Neutron and Gamma Spectra from Aluminum Sphere Pile
OKTAVIAN-Si	Osaka Silicon Sphere Experiment
TUD Iron Slab	TU Dresden Iron Slab
TUD FNG Bulk Shield	TU Dresden FNG Bulk Shield
SB5	ORNL 14-MeV Neutron Stainless-Steel/Borated Polyethylene Slab Experiment
ENEA Bulk SS	FNG SS Bulk Shield Benchmark Experiment (Frascati)
ENEA Blanket	FNG ITER Blanket (VV+First Wall+Shield+TF Coil) (Frascati)
<i>Accelerators:*</i>	
U. of Tokyo INS	Intermediate Energy Neutrons and Gamma-rays on Shielding Materials – 52 MeV and 65 MeV Protons MCNPX Benchmark Calculation Number 4 Rev. 0.0.1 Penetration Through Shielding Materials of Secondary Neutrons and Photons Generated by 52-MeV Protons
Osaka U. AVF	Penetration of Secondary Neutrons and Photons through Concrete, Fe, Pb, and C MCNPX Benchmark Calculation Number 2 Rev. 0.0.1 Transmission Through Shielding Materials of Neutron and Photons Generated by 65-MeV Protons
Osaka U. AVF	MCNPX Benchmark Experiment Number 3 Rev. 0.0.1 (75 MeV protons) Transmission of Medium Energy Neutrons Through Concrete Shields (1991)
TIARA	TIARA 40 and 65 MeV Neutron Transmission Through Iron, Concrete and Polyethylene
U. of Tokyo, INS	MCNPX Benchmark Experiment Number 5 Rev. 0.0.1 Neutron Production from Thick Targets of Carbon, Iron, Copper, and Lead by 30- and 52-MeV Protons(1982)
Swiss SINR	MCNPX Benchmark Experiment Number 1 Rev. 0.0.1 -High Energy Neutron Spectra Generated by 590-MeV Protons on a Thick Lead Target (1979)

* *Bold indicates new SINBAD additions since the SATIF-5 meeting, July 2000.*

Figure 1(b). Procedures, data and computer codes for model validation and improvement [7]



MERGING THE CEM2k AND LAQGSM CODES WITH GEM2 TO DESCRIBE FISSION AND LIGHT-FRAGMENT PRODUCTION

S.G. Mashnik,¹ K.K. Gudima,² and A.J. Sierk¹

¹Los Alamos National Laboratory, Los Alamos, NM 87545, USA

²Institute of Applied Physics, Academy of Science of Moldova, Kishinev, MD-2028, Moldova

Abstract

We present the current status of the improved Cascade-exciton Model (CEM) code CEM2k and of the Los Alamos version of the Quark-gluon String Model code LAQGSM. To describe fission and light-fragment (heavier than ^4He) production, both CEM2k and LAQGSM have been merged with the GEM2 code of Furihata. We present some results on proton- and deuteron-induced spallation, fission and fragmentation reactions predicted by these extended versions of CEM2k and LAQGSM. We show that merging CEM2k and LAQGSM with GEM2 allows us to describe many fission and fragmentation reactions in addition to the spallation reactions, which are already relatively well described. Nevertheless, the standard version of GEM2 does not provide a completely satisfactory description of complex particle spectra, heavy-fragment emission and spallation yields, and is not yet a reliable tool for applications. We conclude that we may choose to use a model similar to the GEM2 approach in our codes, but it must be significantly extended and further improved. We observe that it is not sufficient to analyse only A and Z distributions of the product yields when evaluating this type of model, as is often done in the literature; instead it is important to study all the separate isotopic yields as well as the spectra of light particles and fragments.

Introduction

In recent years, for a number of applications such as Accelerator Transmutation of Nuclear Wastes (ATW), Accelerator Production of Tritium (APT), Rare Isotope Accelerator (RIA), Proton Radiography (PRAD), and other projects, we at the Los Alamos National Laboratory have been developing an improved version of the Cascade-exciton Model (CEM), contained in the code CEM2k, to describe nucleon-induced reactions at incident energies up to 5 GeV [1] and the Los Alamos version of the Quark-Gluon String Model, realised in the high-energy code LAQGSM [2], able to describe both particle- and nucleus-induced reactions at energies up to about 1 TeV/nucleon.

In our original motivation, different versions of the CEM and LAQGSM codes were developed to reliably describe the yields of spallation products and spectra of secondary particles, without a special emphasis on complex-particle and light-fragment emission or on fission fragments in reactions with heavy targets. In fact, the initial versions of the CEM2k and LAQGSM codes only simulate spallation, and do not calculate the process of fission, nor do they provide fission fragments and a further possible evaporation of particles from them. Thus, in simulating the compound stage of a reaction, when these codes encounter a fission, they simply tabulate this event (permitting the calculation of fission cross-sections and fissility) and finish the calculation without a subsequent treatment of fission fragments. To be able to describe nuclide production in the fission region, these codes have to be extended by incorporating a model of high-energy fission (e.g. in the transport code MCNPX [3], where CEM2k and, initially, its precursor, CEM97 [4], are used, they are supplemented by Atchison's fission model [5,6]).

Since many nuclear and astrophysical applications also require reliable data on complex particles (gas production) and light and/or fission fragment production, we addressed these questions by further developing the CEM2k and LAQGSM codes. We tried different ways of solving these problems; as a first attempt to describe both emission of intermediate-mass fragments heavier than ^4He and production of heavy fragments from fission, we merged CEM2k and LAQGSM with Furihata's Generalized Evaporation Model (GEM) code [7,8]. We have benchmarked our codes on all proton-nucleus and nucleus-nucleus reactions measured recently at GSI (Darmstadt, Germany) and on many other different reactions at lower and higher energies measured earlier at other laboratories. The size of the present paper allows us to present only a few results here, which we choose to be for the GSI measurements on interaction of ^{208}Pb beams with p [9] and d [10] targets. Results for other reactions may be found in [11,12].

CEM2k and LAQGSM codes

A detailed description of the initial version of the CEM may be found in Ref. [13], therefore we outline here only its basic assumptions. The CEM assumes that reactions occur in three stages. The first stage is the IntraNuclear Cascade (INC) in which primary particles can be re-scattered and produce secondary particles several times prior to absorption by or escape from the nucleus. The excited residual nucleus remaining after the cascade determines the particle-hole configuration that is the starting point for the pre-equilibrium stage of the reaction. The subsequent relaxation of the nuclear excitation is treated in terms of an improved Modified Exciton Model (MEM) of pre-equilibrium decay followed by the equilibrium evaporative final stage of the reaction. Generally, all three stages contribute to experimentally measured outcomes.

The improved Cascade-exciton Model in the code CEM2k differs from the older CEM95 version (which is available free from the NEA/OECD, Paris) [14] by incorporating new approximations for the elementary cross-sections used in the cascade, using more precise values for nuclear masses and pairing energies, employing a corrected systematics for the level-density parameters, adjusting the

cross-sections for pion absorption on quasi-deuteron pairs inside a nucleus (including the Pauli principle in the pre-equilibrium calculation) and improving the calculation of the fission widths. Implementation of significant refinements and improvements in the algorithms of many subroutines led to a decrease of the computing time by up to a factor of 6 for heavy nuclei, which is very important when performing simulations with transport codes. Essentially, CEM2k [1] has a longer cascade stage, less pre-equilibrium emission, and a longer evaporation stage with a higher excitation energy, as compared to its precursors CEM97 [4] and CEM95 [14]. Besides the changes to CEM97 and CEM95 mentioned above, we also made a number of other improvements and refinements, such as:

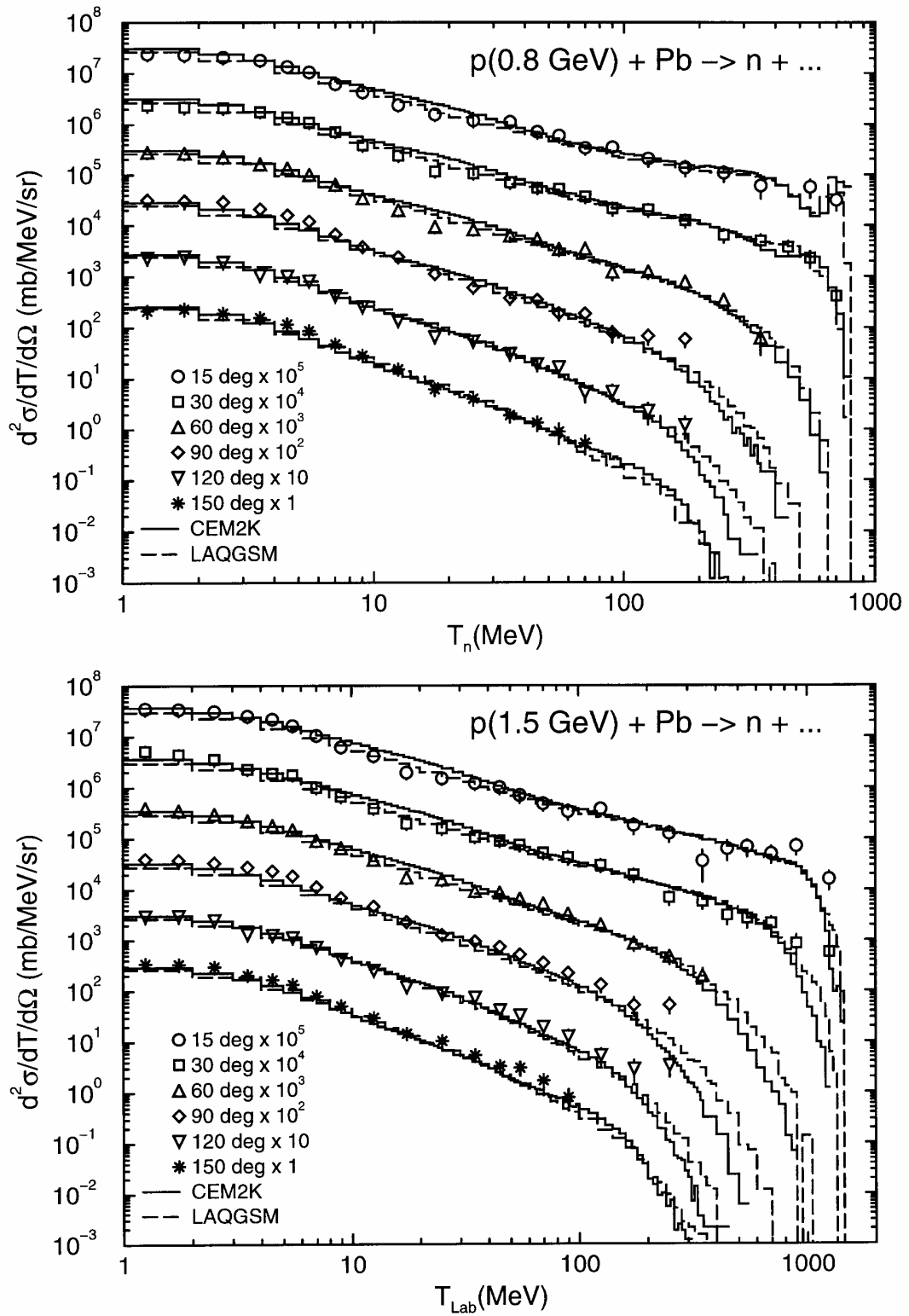
- Imposing momentum-energy conservation for each simulated event (the Monte Carlo algorithm previously used in CEM provides momentum-energy conservation only statistically, on the average, but not exactly for the cascade stage of each event).
- Using real binding energies for nucleons at the cascade stage instead of the approximation of a constant separation energy of 7 MeV used in previous versions of the CEM.
- Using reduced masses of particles in the calculation of their emission widths instead of using the approximation of no recoil used previously.
- A better approximation of the total reaction cross-sections.

On the whole, this set of improvements leads to a much better description of particle spectra and yields of residual nuclei and a better agreement with available data for a variety of reactions. Details, examples, and further references may be found in Refs. [1,15].

The Los Alamos version of the Quark-gluon String Model (LAQGSM) [2] is the next generation of the Quark-gluon String Model (QGSM) by Amelin, *et al.* (see [16] and references therein) and is intended to describe both particle- and nucleus-induced reactions at energies up to about 1 TeV/nucleon. The core of the QGSM is built on a time-dependent version of the intranuclear cascade model developed at Dubna, often referred in the literature simply as the Dubna Intranuclear Cascade Model (DCM) (see [17] and references therein). The DCM models interactions of fast cascade particles (“participants”) with nucleon spectators of both the target and projectile nuclei and includes interactions of two participants (cascade particles) as well. It uses experimental cross-sections (or those calculated by the Quark-gluon String Model for energies above 4.5 GeV/nucleon) for these elementary interactions to simulate angular and energy distributions of cascade particles, also considering the Pauli exclusion principle. When the cascade stage of a reaction is completed, QGSM uses the coalescence model described in [17] to “create” high-energy d, t, ^3He and ^4He by final state interactions among emitted cascade nucleons, already outside of the colliding nuclei. After calculating the coalescence stage of a reaction, QGSM moves to the description of the last slow stages of the interaction, namely to pre-equilibrium decay and evaporation, with a possible competition of fission using the standard version of the CEM [13]. But if the residual nuclei have atomic numbers with $A \leq 13$, QGSM uses the Fermi break-up model to calculate their further disintegration instead of using the pre-equilibrium and evaporation models. LAQGSM differs from QGSM by replacing the pre-equilibrium and evaporation parts of QGSM described according to the standard CEM [13] with the new physics from CEM2k [1] and has a number of improvements and refinements in the cascade and Fermi break-up models (in the current version of LAQGSM, we use the Fermi break-up model only for $A \leq 12$). A detailed description of LAQGSM and further references may be found in [2].

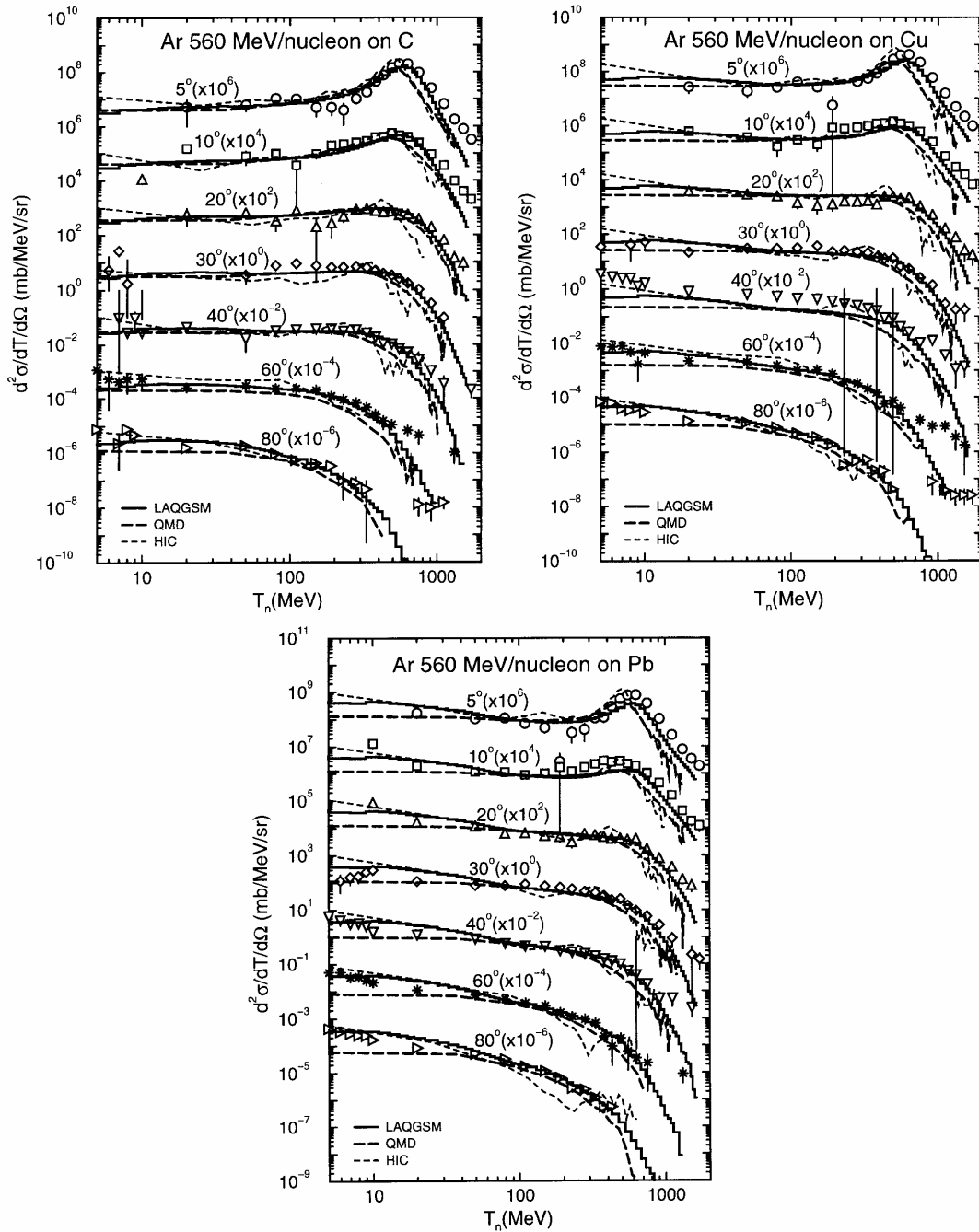
We have benchmarked CEM2k and LAQGSM against most available experimental data and have compared our results with predictions of other current models used by the nuclear community. Figure 1 shows examples of calculated neutron spectra from the interaction of protons with ^{208}Pb at 0.8 and

Figure 1. Comparison of measured [18] double-differential cross-sections of neutrons from 0.8 and 1.5 GeV protons on Pb with CEM2k and LAQGSM calculations



1.5 GeV compared with experimental data [18], while Figure 2 gives examples of neutron spectra measured by Nakamura's group (see [19] and references therein) from 560 MeV/nucleon Ar beams on C, Cu and Pb targets compared with our LAQGSM results and predictions by QMD [20] and HIC [21] from Iwata, *et al.* [19]. It can be seen that our codes describe neutron spectra both for proton- and nucleus-nucleus reactions rather well, and agree with the data no worse than other models do. Similar results are obtained for other reactions for which we found measured data.

Figure 2. Comparison of measured [19] double-differential cross-sections of neutrons from 560 MeV/nucleon Ar beams on C, Cu and Pb with our LAQGSM results and calculations by QMD [20] and HIC [21] from Iwata, *et al.* [19]



Merging CEM2k and LAQGSM with GEM2

The Generalised Evaporation Model (GEM) [7,8] is an extension by Furihata of the Dostrovsky, *et al.* [22] evaporation model as implemented in LAHET [23] to include up to 66 types of particles and fragments that can be evaporated from an excited compound nucleus plus a modification of the version of Atchison's fission model [5,6] used in LAHET. Many of the parameters were adjusted for a better description of fission reactions when using it in conjunction with the extended evaporation model. GEM2 (the last update of the GEM code) was merged with CEM2k and LAQGSM as follows. The cascade and pre-equilibrium stages of a reaction are calculated with CEM2k or LAQGSM, then the subsequent evaporation of particles and fragments and fission from the remaining excited compound nuclei are described using GEM2. To understand the role of pre-equilibrium particle emission, we performed calculations of all the reactions we tested both with emission of pre-equilibrium particles and without them, i.e. going directly to GEM2 after the intranuclear cascade stage of a reaction described by CEM2k or LAQGSM.

A very detailed description of GEM, together with a large amount of results obtained for many reactions using GEM coupled either with the Bertini or ISABEL INC models in LAHET are published by Furihata [7,8,24]; many useful details of GEM2 may also be found in our paper [11]. Therefore, only the main features of GEM are briefly listed below, and for more details, interested readers are directed to Refs. [7,8,11,24]. Furihata did not change in GEM the general algorithms used in LAHET to simulate evaporation and fission. The decay widths of evaporated particles and fragments are estimated using the classical Weisskopf-Ewing statistical theory [25].

The new ingredient in GEM in comparison with LAHET (which considers evaporation of only six particles – n, p, d, t, ^3He and ^4He) is that Furihata included the possibility of evaporation of up to 66 types of particles and fragments (both in the ground and excited states) and incorporated into GEM several sets of parameters used to calculate inverse cross-sections and Coulomb barriers for each ejectile (only the default parameters of GEM2 are used here). The 66 ejectiles considered by GEM are: n, p, d, t, $^{3,4,6,8}\text{He}$, ^{6-9}Li , $^{7,9-12}\text{Be}$, $^{8,10-13}\text{B}$, $^{10-16}\text{C}$, $^{12-17}\text{N}$, $^{14-20}\text{O}$, $^{17-21}\text{F}$, $^{18-24}\text{Ne}$, $^{21-25}\text{Na}$ and $^{22-28}\text{Mg}$.

The fission model used in GEM is based on Atchison's model [5,6] as implemented in LAHET [23], often referred to in the literature as the Rutherford Appleton Laboratory (RAL) model, that being where it was developed. There are two choices of parameters for the fission model: one is the original parameter set by Atchison [5,6] as implemented in LAHET [23], and the other is a parameter set evaluated by Furihata [7,8], used here as a default of GEM2.

The Atchison fission model is designed only to describe fission of nuclei with $Z \geq 70$. It assumes that fission competes only with neutron emission, i.e. from the widths Γ_j of n, p, d, t, ^3He and ^4He , the RAL code calculates the probability of evaporation of any particle. When a charged particle is selected for evaporation, no fission competition is taken into account. When a neutron is selected for evaporation, the code does not actually simulate its evaporation, instead it considers that fission may compete, and chooses either fission or evaporation of a neutron according to the fission probability P_f . This quantity is treated differently by the RAL code for the elements above and below $Z = 89$. The reasons Atchison split the calculation of the fission probability P_f are: (1) there is very little experimental information on fission in the region $Z = 85$ to 88, (2) the marked rise in the fission barrier for nuclei with Z^2/A below about 34 (see Figure 2 in [6]) together with the disappearance of asymmetric mass splitting indicates that a change in the character of the fission process occurs. If experimental information were available, a split between regions about $Z^2/A \approx 34$ would more sensible [6].

$70 \leq Z_j \leq 88$

For fissioning nuclei with $70 \leq Z_j \leq 88$, GEM uses the original Atchison calculation of the neutron emission width Γ_n and fission width Γ_f to estimate the fission probability as:

$$P_f = \frac{\Gamma_f}{\Gamma_f + \Gamma_n} = \frac{1}{1 + \Gamma_n/\Gamma_f} \quad (1)$$

Atchison uses [5,6] the Weisskopf and Ewing statistical model [25] with an energy-independent pre-exponential factor for the level density (see Eq. (6) in [11]) and Dostrovsky's [22] inverse cross-section for neutrons and estimates the neutron width Γ_n as:

$$\Gamma_n = 0.352 \left(1.68J_0 + 1.93A_i^{1/3}J_1 + A_i^{2/3}(0.76J_1 - 0.05J_0) \right) \quad (2)$$

where J_0 and J_1 are functions of the level density parameter a_n and $s_n (= 2\sqrt{a_n(E - Q_n - \delta)})$ as

$$J_0 = \frac{(s_n - 1)e^{s_n} + 1}{2a_n} \quad \text{and} \quad J_1 = \frac{(2s_n^2 - 6s_n + 6)e^{s_n} + s_n^2 - 6}{8a_n^2}.$$

Note that the RAL model uses a fixed value for the level density parameter a_n , namely:

$$a_n = (A_i - 1)/8 \quad (3)$$

and this approximation is kept in GEM when calculating the fission probability according to Eq. (1), though it differs from the Gilbert-Cameron-Cook-Ignatyuk (GCCCI) parameterisation (see Eq. (7) in [11]) used in GEM to calculate particle evaporation widths. The fission width for nuclei with $70 \leq Z_j \leq 88$ is calculated in the RAL model and in GEM as:

$$\Gamma_f = \frac{(s_f - 1)e^{s_f} + 1}{a_f} \quad (4)$$

where $s_f = 2\sqrt{a_f(E - B_f - \delta)}$ and the level density parameter in the fission mode a_f is fitted by Atchison [6] to describe the measured Γ_f/Γ_n as:

$$a_f = a_n \left(1.08926 + 0.01098(\chi - 31.08551)^2 \right) \quad (5)$$

and $\chi = Z^2/A$. The fission barriers B_f [MeV] are estimated as:

$$B_f = Q_n + 321.2 - 16.7 \frac{Z_i^2}{A} + 0.218 \left(\frac{Z_i^2}{A_i} \right)^2 \quad (6)$$

Note that neither the angular momentum nor the excitation energy of the nucleus are taken into account in the estimate of the fission barriers.

$Z_j \geq 89$

For heavy fissioning nuclei with $Z_j \geq 89$ GEM follows the RAL model [5,6] and does not calculate at all the fission width Γ_f and does not use Eq. (1) to estimate the fission probability P_f . Instead, the following semi-empirical expression obtained by Atchison [5,6] by approximating the experimental values of Γ_n/Γ_f published by Vandenbosch and Huizenga [26] is used to calculate the fission probability:

$$\log(\Gamma_n/\Gamma_f) = C(Z_i)(A_i - A_0(Z_i)) \quad (7)$$

where $C(Z)$ and $A_0(Z)$ are constants dependent on the nuclear charge Z only. The values of these constants are those used in the current version of LAHET [23] and are tabulated in Table 5 of Ref. [11] (note that some adjustments of these values have been made since Atchison's papers [5,6] were published).

The selection of the mass of the fission fragments depends on whether the fission is symmetric or asymmetric. For a pre-fission nucleus with $Z_i^2/A_i \leq 35$, only symmetric fission is allowed. Both symmetric and asymmetric fission are allowed for $Z_i^2/A_i > 35$, depending on the excitation energy E of the fissioning nucleus. No new parameters were determined for asymmetric fission in GEM.

For nuclei with $Z_i^2/A_i > 35$, whether the fission is symmetric or not is determined by the asymmetric fission probability P_{asy} :

$$P_{asy} = \frac{4870e^{-0.36E}}{1 + 4870e^{-0.36E}} \quad (8)$$

For asymmetric fission, the mass of one of the post-fission fragments A_1 is selected from the Gaussian distribution of mean $A_f = 140$ and width $\sigma_M = 6.5$. The mass of the second fragment is $A_2 = A_i - A_1$.

For symmetric fission, A_1 is selected from the Gaussian distribution of mean $A_f = A_i/2$ and two options for the width σ_M as described in [7,8,11].

The charge distribution of fission fragments is assumed to be a Gaussian distribution of mean Z_f and width σ_Z . Z_f is expressed as:

$$Z_f = \frac{Z_i + Z'_1 - Z'_2}{2}$$

where $Z'_l = \frac{65.5A_l}{131 + A_l^{2/3}}$, and $l = 1$ or 2 .

The original Atchison model uses $\sigma_Z = 2.0$. An investigation by Furihata [8] suggests that $\sigma_Z = 0.75$ provides a better agreement with data; therefore $\sigma_Z = 0.75$ is used in GEM2 and in all our calculations.

The kinetic energy of fission fragments [MeV] is determined by a Gaussian distribution with mean ε_f and width σ_{ε_f} . The original parameters in the Atchison model are:

$$\varepsilon_f = 0.133Z_i^2/A_i^{1/3} - 11.4, \text{ and } \sigma_{\varepsilon_f} = 0.084\varepsilon_f$$

Furihata's parameters in GEM2, which we also use, are:

$$\varepsilon_f = \begin{cases} 0.131Z_i^2/A_i^{1/3}, & \text{for } Z_i^2/A_i^{1/3} \leq 900 \\ 0.104Z_i^2/A_i^{1/3} + 24.3, & \text{for } 900 < Z_i^2/A_i^{1/3} \leq 1800 \end{cases}$$

and:

$$\sigma_{\varepsilon_f} = \begin{cases} C_1(Z_i^2/A_i^{1/3} - 1000) + C_2, & \text{for } Z_i^2/A_i^{1/3} > 1000 \\ C_2, & \text{for } Z_i^2/A_i^{1/3} \leq 1000 \end{cases}$$

where $C_1 = 5.70 \times 10^{-4}$ and $C_2 = 86.5$. More details may be found in [8].

We note that Atchison has also modified his original version using recent data and published [27] an improved (and more complicated) parameterisation for many quantities and distributions in his model; these modifications [27] are not yet included in either LAHET or in GEM2.

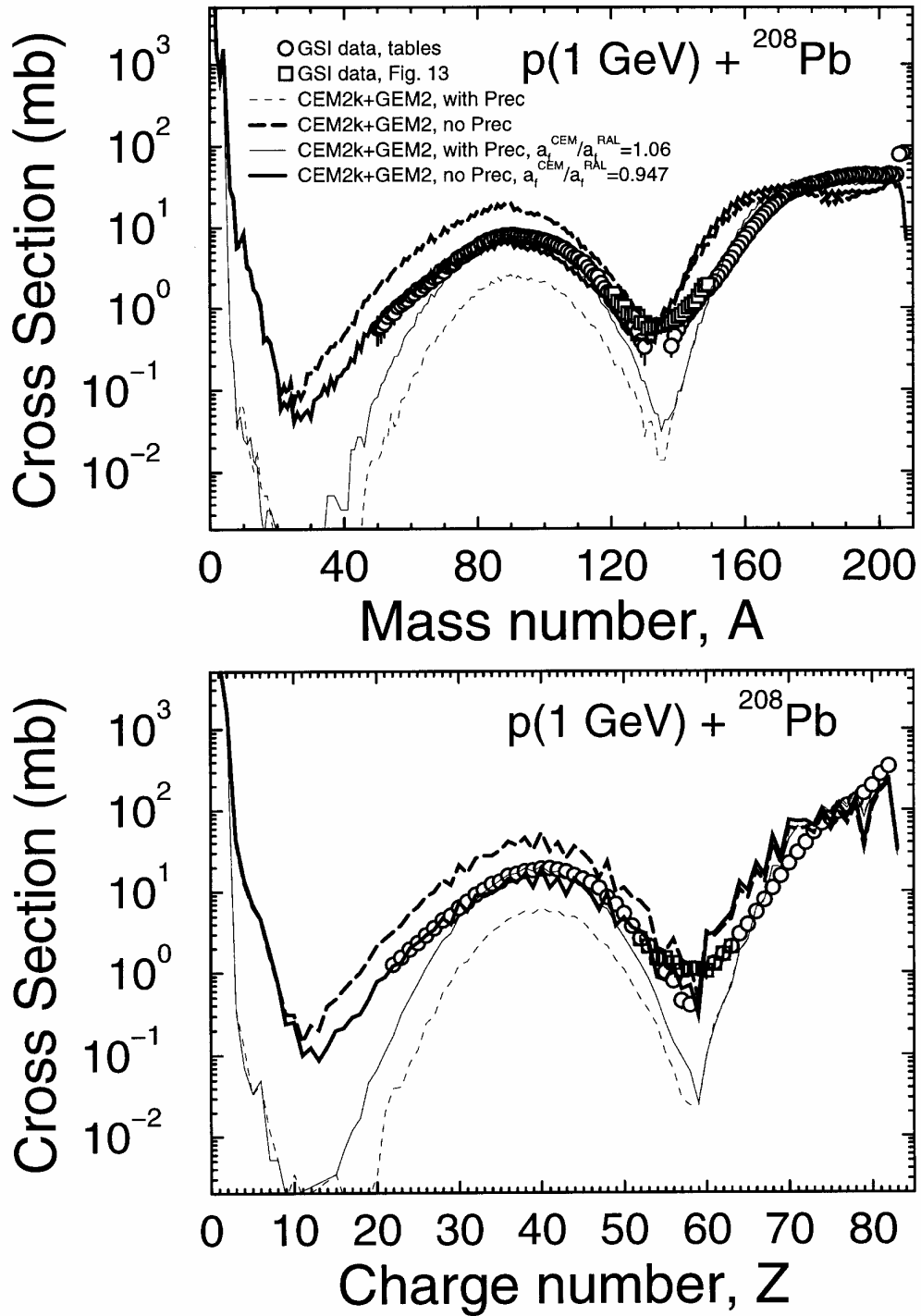
We have merged the GEM2 code with CEM2k and LAQGSM, initially keeping all the default options in GEM2. We began by concentrating on an analysis of the recent GSI measurements in inverse kinematics as the richest and best data set for testing this kind of model. As mentioned above, to understand the role of pre-equilibrium particle emission, we performed calculations of all the reactions we tested both taking into account pre-equilibrium particle emission and ignoring it, i.e. going directly to GEM2 after the intranuclear cascade stage of a reaction described by CEM2k or LAQGSM.

If we merge GEM2 with CEM2k without any modifications, the new code does not correctly describe the fission cross-section (and the yields of fission fragments) whether we take into account pre-equilibrium emission (see the short-dashed line in Figure 3) or not (see the long-dashed line in Figure 3). Such results were anticipated, as Atchison fitted the parameters of his RAL fission model when it was coupled with the Bertini INC [28] (which differs from our INC). In addition, he did not model pre-equilibrium emission. Therefore, the distributions of fissioning nuclei in A , Z and excitation energy E^* simulated by Atchison differ significantly from the distributions we get; as a consequence, all the fission characteristics are also different.

Furihata used GEM2 coupled either with the Bertini INC [28] or with the ISABEL [29] INC code (which also differs from our INC) and did not include pre-equilibrium particle emission. Therefore the real fissioning nuclei simulated by Furihata differ from those in our simulations, and the parameters adjusted by Furihata to work the best with her INC should not be the best for ours. To obtain a good description of the fission cross-section (and fission-fragment yields) at least one parameter in GEM2 should be modified, specifically the level density parameter a_f should be adjusted to get the correct fission cross-section [see Eq. (5)], in the case of fissioning nuclei with $Z \leq 88$ (pre-actinides), and the parameter $C(Z)$ [see Eq. (7)] for fissioning nuclei with $Z > 88$ (actinides). From the dashed lines in Figure 5 we see that we need to enlarge a_f in our code to get a proper fission cross-section when we include pre-equilibrium emission (the excitation energy of our fissioning nuclei and their A and Z are

Figure 3. Comparison of the experimental mass and charge distributions of the nuclides produced in the reaction $p(1 \text{ GeV}) + \text{Pb}$ with different calculations

Circles show data from Tables 3 and 4 of Ref. [9] and squares from Figure 13 of Ref. [10]. The dashed lines show results found by merging CEM2k with GEM2 without any modifications when pre-equilibrium emission is (thin lines) or is not (thick lines) included. Solid lines show results from CEM2k+GEM2 with a modified a_f : thin lines are for the case with pre-equilibrium emission ($a_f^{\text{CEM}}/a_f^{\text{RAL}} = 1.06$) and thick lines show the results without pre-equilibrium emission ($a_f^{\text{CEM}}/a_f^{\text{RAL}} = 0.947$).



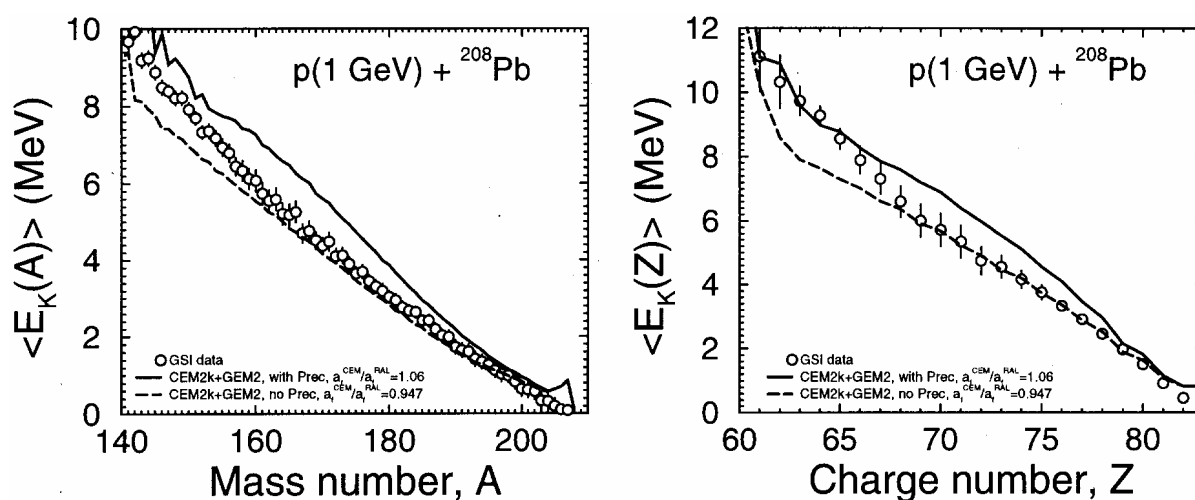
smaller than provided by the Bertini or ISABEL INC without pre-equilibrium), and we need to decrease a_f in the case without pre-equilibrium. By increasing a_f by 1.06 compared with the original RAL and GEM2 value ($a_f^{CEM} / a_f^{RAL} = 1.06$) we are able to correctly reproduce the fission cross-section for this reaction with CEM2k+GEM2 when we take into account pre-equilibrium emission (below, such results are labelled “with Prec”). In the case with no pre-equilibrium emission, a proper fission cross-section is obtained for $a_f^{CEM} / a_f^{RAL} = 0.947$ (such results are labelled “no Prec”). We choose these values for a_f for all our further CEM2k+GEM2 calculations of this reaction and do not change any other parameters.

The solid lines in Figure 3 show results with these values of a_f . One can see that the “no Prec” version provides a good description of both the mass and charge distributions and agrees better with the data for these characteristics than the “with Prec” version (this is not true for isotopic distributions of individual elements, as we show below). The “with Prec” version correctly reproduces the position of the maximum in both A and Z distributions and the yields of fission fragments not too far from these maximums, but the calculated distributions are narrower than the experimental ones. This is again because both Atchison and Furihata fitted their A and Z distributions using models without pre-equilibrium emission, which provide higher values for the excitation energy, A , and Z of fissioning nuclei. This means that to obtain a good description of A and Z distributions for fission fragments using GEM2 in CEM2k “with Prec”, we would need to modify the A and Z distributions of fission fragments in GEM2, making them wider. This would take us beyond the scope of the present work and here we do not vary any more parameters than we have already discussed.

Figure 4 shows the GSI measurements [9] of the A and Z distributions of the kinetic energy of products from the same reaction compared with our CEM2k+GEM2 calculations, both with and without pre-equilibrium emission. Both versions of our calculations are in reasonable agreement with the data.

Figure 4. Comparison of the experimental [9] mass and charge distributions of the spallation-residue kinetic energies of the nuclides produced in the reaction $p(1 \text{ GeV}) + \text{Pb}$ (circles) with our CEM2k+GEM2 calculations

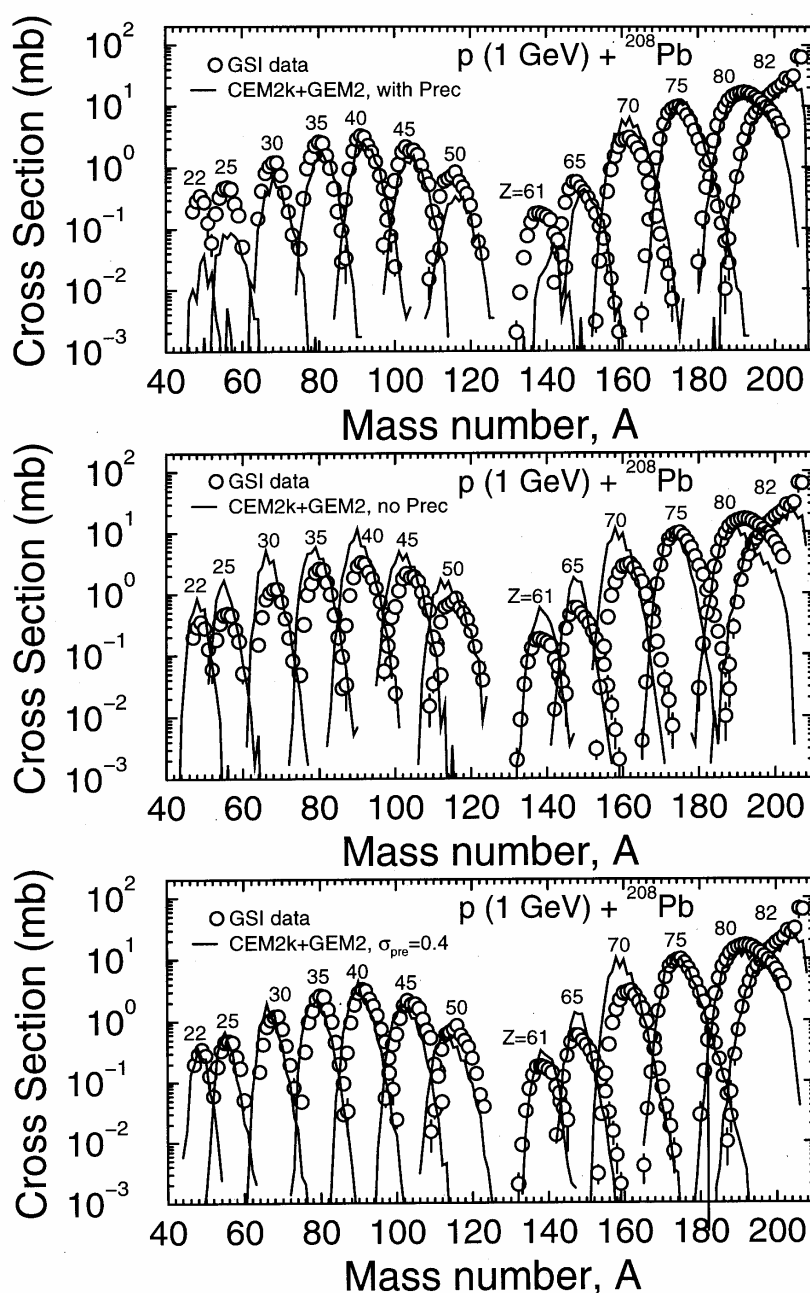
“with Prec” results are shown by solid lines, “no Prec” results are shown by dashed lines



Mass and charge distributions of the yields or kinetic energies of the nuclides produced show only general trends and are not sensitive enough to the details of a reaction. It is much more informative to study the characteristics of individual nuclides and particles produced in a reaction. Figure 5 shows a comparison of the experimental data on production yields of thirteen separate isotopes with Z lying from 22 to 82 from the same reaction measured at GSI [9] with our calculations using both the “with Prec” (upper plot) and “no Prec” (middle plot) versions.

Figure 5. Experimental [9] mass distributions of the cross-sections of thirteen isotopes with the charge Z from 22 to 82 compared with our CEM2k+GEM2 calculations

“with Prec” results are shown on the upper plot, “no Prec” results are shown in the middle, results with reduced pre-equilibrium emission according to Eq. (9), are shown at bottom



The agreement (or disagreement) of our calculations with these data is different from what we have for the integral A or Z distributions in Figures 3 and 4. It can be seen that for the isotopes produced in the spallation region (not too far from the target) and for fission fragments in the region with the maximum yield, the “with Prec” version agrees much better with the data than the “no Prec” version. Only for production of isotopes at the border between spallation and fission and between fission and fragmentation does the “with Prec” version underestimate the data, due to too-narrow A and Z distributions in the simulation of fission fragments, as previously discussed. The “no Prec” version agrees better with the data in these transition regions but is in worse agreement for isotopes both in the spallation region and in the middle of the fission region. We conclude that if a model agrees well with some A or Z distributions this does not necessarily mean that it also describes production of separate isotopes well. In other words, integral A and Z distributions are not sensitive enough to develop and test such models, a practice which is often used in the literature.

The lower plot in Figure 5 shows results of calculations with a version of CEM2k+GEM2 with reduced pre-equilibrium emission. We prefer to discuss this version along with results by LAQGSM+GEM2, and will return to this plot later.

It is more difficult for any model to correctly describe the energy dependence for the production cross-sections of different isotopes, i.e. excitation functions. We calculated all the excitation functions for the same reaction, $p + \text{Pb}$, for proton energies from 10 MeV to 3 GeV using both the “with Prec” and “no Prec” versions of CEM2k+GEM2 and compared our results with all available data from our compilation (referred to here as T-16 Library – “T16 Lib”) [30]. Only several typical examples from our comparison are shown below.

Figure 6 shows two examples of excitation functions for the production of several isotopes in the spallation (first two columns of plots) and fission (the last two columns of plots regions). One can see a not-too-good, but still reasonable, agreement of both calculations with many data (note that most of the data were measured for $^{\text{nat}}\text{Pb}$ targets, while our calculations were done for ^{208}Pb). We see that merging CEM2k with GEM2 allows to reasonably describe yields of fission fragments, while in the old standard CEM2k there are no fission fragments and such reactions cannot be described at all. We see that, as shown in Figure 5 for a single proton energy of 1 GeV, the “with Prec” version agrees better with the data in the whole energy region both for spallation products and for the production of most of the fission fragments. Only on the border between fission and fragmentation regions (^{46}Sc and ^{60}Co) does the “no Prec” version agree much better with the data than the “with Prec” version; the reason for this we have already discussed. Similar results were obtained for excitation functions of many other isotopes in the spallation and fission regions. On the whole, the “with Prec” version reproduces most of the experimental excitation functions better than the “no Prec” version.

In Figure 7 we show examples of excitation functions for the production of light fragments (the first two columns of plots) in the fragmentation region that are produced in CEM2k+GEM2 only via evaporation (the contribution to the yield of these isotopes from fission or deep spallation is negligible), and of nucleons and complex particles up to α (the last two columns of plots). We see that with the “no Prec” version, GEM2 correctly reproduces the yields of light fragments ^6He , ^9Li , ^7Be , ^{13}N and ^{18}F , and not so well the excitation functions for heavier fragments like ^{22}Na . As the mass of the fragment increases, the calculations progressively underestimate their yields. Note that in [11], very similar results for excitation functions of the $p + \text{Au}$ reaction were obtained. The “with Prec” version strongly underestimates the yields of all these fragments, and this is again not surprising, as Furihata developed her model and fitted all parameters without taking into account pre-equilibrium processes.

Figure 6. Excitation functions for the production of ^{203}Bi , ^{200}Tl , ^{196}Au , ^{194}Au , ^{192}Ir , ^{148}Eu , ^{124}Sb , ^{95}Nb , ^{86}Rb , ^{82}Br , ^{60}Co and ^{46}Sc from $p + ^{208}\text{Pb}$

Results by CEM2k+GEM2 “with Prec” are shown by solid lines and “no Prec” by dashed lines. Experimental data (filled circles for ^{208}Pb targets and opaque circles for natPb) are from our LANL compilation (“T16 Lib”) [30] and are available from the authors upon request.

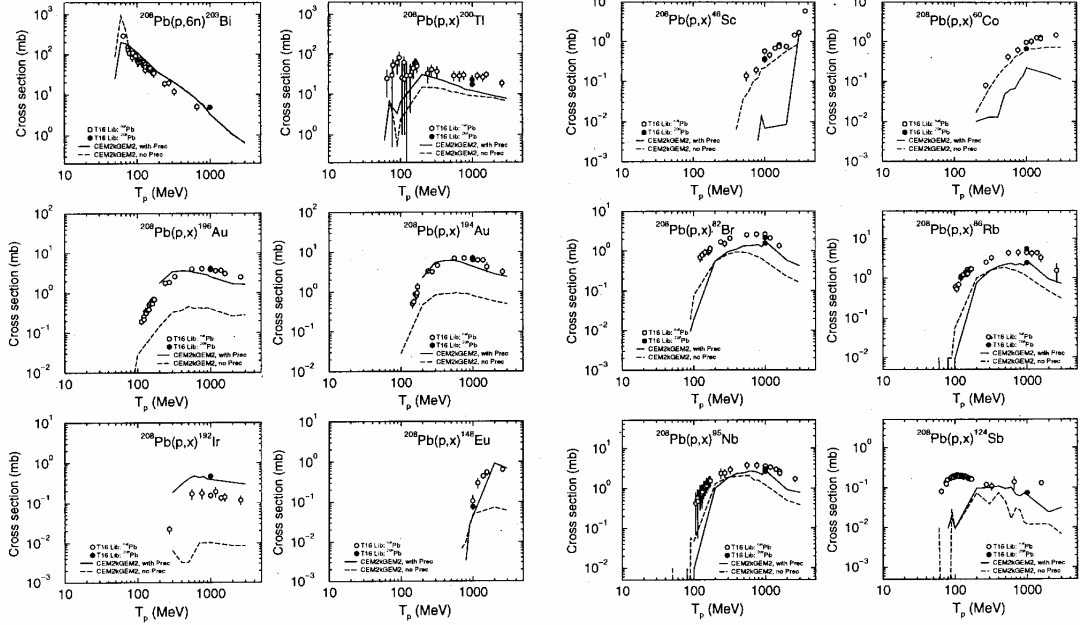
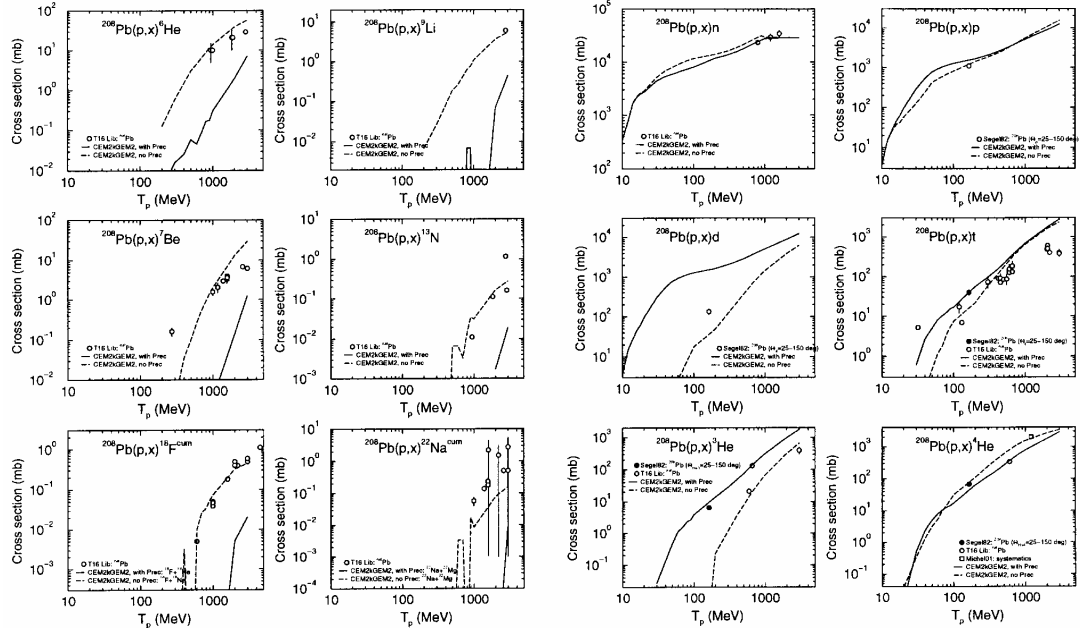


Figure 7. The same as Figure 6 but for the production of ^{22}Na , ^{18}F , ^{13}N , ^7Be , ^9Li , ^6He , ^4He , ^3He , t, d, p and n

The complex particles up to ^4He are produced in CEM2k+GEM2 via evaporation and pre-equilibrium emission; n and p are also produced during the cascade stage; fragments heavier than ^4He are produced only via evaporation. Data labelled as “Segel82” are from Ref. [31].



Undeniably, the parameters determining the yields of evaporated fragments in GEM (inverse cross-sections and Coulomb barriers) could be adjusted to get a good agreement with the data for the yields of light fragments with the “with Prec” version (see, e.g. how Furihata and Nakamura addressed this problem in [24] for their version of a code without pre-equilibrium emission). This is not the aim of the present work and we will not do this here. Even if we were to do this, we expect in advance to obtain results similar to those for the “no Prec” version: it would be possible to correctly describe the yields and spectra of light fragments but not of heavy fragments like ^{24}Na and ^{28}Mg . To describe such heavy fragments (not only their yields, but also their spectra) the model would need to be further improved, by considering other mechanisms for heavy fragment production in addition to the evaporation process taken into account by GEM2.

Finally, the two last columns of plots in Figure 7 show excitation functions for emission of nucleons and complex particles up to α for this reaction. Note that the data for these excitation functions are not as extensive and precise as those for heavier products: many data points were obtained by integration (plus extrapolation) of the spectra of particles measured only at several angles and only for a limited range of energy. But even from a comparison with these sparse and imprecise data we see that the “with Prec” version describes these excitation function better than the “no Prec” version, just as was found in [11] for the $p + \text{Au}$ reaction. This is an expected result, as the high Coulomb barriers for heavy nuclear targets oppose evaporation of low-energy charged particles and the main contribution to their yields comes from pre-equilibrium emission from highly-excited pre-compound nuclei.

For completeness sake, we also show here an example of results from a calculation with the merged CEM2k+GEM2 code of a reaction on an actinide, $p(100 \text{ MeV}) + ^{238}\text{U}$. Generally, to obtain a proper fission cross-section for actinides, we need to adjust in GEM2 the parameters $C(Z)$ [or, also $A_0(Z)$] in Eq. (7), as they were fitted by Atchison to work the best with Bertini’s INC and we have in CEM2k our own INC. As mentioned above for actinides, Eq. (1) is not used in GEM2 and a_f is not used in any calculations, therefore we do not need to adjust a_f/a_n for fissioning nuclei with $Z > 88$. We found that for this particular reaction, $p(100 \text{ MeV}) + ^{238}\text{U}$, we get with CEM2k+GEM2 a fission cross-section in agreement with the data without any adjustments of the parameter $C(Z)$ in GEM2, i.e. we can use just the default parameters of GEM2. Nevertheless, our results for other reactions show that for higher energies of the incident protons or for other target nuclei, the parameter $C(Z)$ has to be fitted to obtain a correct fission cross-section when GEM2 is coupled either with CEM2k or with LAQGSM. In addition, we should mention that for reactions on actinides at intermediate or high energies, the parameter a_f^{CEM}/a_f^{RAL} should also be fitted along with $C(Z)$. In some simulated events several protons can be emitted at the cascade and pre-equilibrium stages of the reaction, as well as at the evaporation stage, before the compound nucleus actually fissions (complex particles can also be emitted before fission), and the charge of the fissioning nucleus can have $Z \leq 88$, even when the initial charge of the target has $Z > 88$. At the same time, for $Z \leq 88$, due to charge exchange reactions, the charge of the fissioning nucleus may exceed 88, so that we would also need to fit $C(Z)^{CEM}/C(Z)^{RAL}$. This is a peculiarity of treating the fission probability P_f differently for the elements above and below $Z = 89$ in the Atchison model.

Figure 8 shows mass distributions of products from $p(100 \text{ MeV}) + ^{238}\text{U}$ calculated with both versions of CEM2k+GEM2 compared to the available experimental data [32] and with results by the phenomenological code CYF of Wahl [33] (short dashed lines). We need to mention that these data are not as good for testing and developing models as are the GSI data measured in inverse kinematics for the $p + \text{Pb}$ reaction discussed above; all the data shown in Figure 8 were obtained using the γ -spectrometry method. Only some of the produced isotopes were measured, and most of the data were measured for the cumulative yields. To get the “experimental” A distribution, we summed for each A the available data taking care to not sum the individual cross-sections already included in some

**INTERACTION OF ION BEAMS WITH TISSUE-LIKE MEDIA:
SIMULATIONS WITH THE SHIELD-HIT MONTE CARLO TRANSPORT CODE**

Nikolai Sobolevsky

Institute for Nuclear Research of Russian Academy of Sciences, Russia

Irena Gudowska, Pedro Andreo, Dzevad Belkic, Anders Brahme

Dept. of Medical Radiation Physics, Stockholm University-Karolinska Institutet, Sweden

Abstract

The development of the Monte Carlo code SHIELD-HIT (Heavy Ion Transport) for the transport of protons and light ions ($Z \leq 10$) in tissue-like media is described. SHIELD-HIT, a spin-off of SHIELD (available as RSIC CCC-667), extends the transport of hadron cascades in shielding materials to that of ions in tissue-like materials, and includes ionisation energy-loss straggling (Gaussian or Vavilov) and multiple scattering (Gaussian) effects. The consistency with experimental data and other existing Monte Carlo codes for ion transport (PTRAN, PETRA) has been verified by comparing depth energy depositions of protons and ^{12}C ions impinging on water, up to depths well beyond the Bragg peak. SHIELD-HIT yields profiles consistent with a proper treatment of nuclear inelastic collisions. Energy depositions up to and beyond the Bragg peak due to nuclear fragmentation are also well predicted. Good agreement is equally found with experimental determinations of the number of fragments of given type as a function of depth in water produced by ^{12}C ions of 670 MeV/u.

Introduction

The SHIELD Monte-Carlo transport code [1-4] (available as RSIC CCC-667) simulates the interactions of hadrons and atomic nuclei of arbitrary charge and mass number (Z, A) with complex extended targets in a wide energy range, from 1 TeV/u down to 1 MeV/u or thermal energies in the case of neutrons. SHIELD is used for solving the same type of problems as other well-known Monte Carlo codes, e.g. LAHET, HERMES, FLUKA, GEANT or MCNPX. Nuclear reactions are taken into account in an exclusive approach (using “Russian-models”) where all stages of hadron-nucleus and nucleus-nucleus interactions are described. Thus, SHIELD can be used to simulate interactions of heavy ions with complex macroscopic targets. The version of SHIELD [4] extended to simulate heavy-ion transport is called SHIELD-HIT.

This work describes the application of the SHIELD-HIT Monte Carlo code to oncology and the simulation of the interactions of proton and light-ion ($Z \leq 10$) beams with tissue-like media in the context of hadron therapy. SHIELD-HIT not only extends the transport of hadron cascades in shielding materials to that of ions in tissue-like materials, but also includes ion energy-loss straggling (using Gaussian or Vavilov distributions) and angular multiple scattering (Gaussian distribution). The results presented in this work stem from a co-operative research project between the Department of Medical Radiation Physics, Karolinska Institutet (Stockholm) and the Institute for Nuclear Research of the Russian Academy of Science (Moscow).

The interactions with tissue-like media of projectiles ranging from proton (H^{+1}) to neon ($^{20}Ne^{+10}$) ions with incident energies in the interval 10-670 MeV/u have been studied so far. Spatial distributions of the energy deposition to the target, due to the primary beam particles and their secondaries, generated by nuclear reactions (fragmentation), have been computed for narrow (pencil) beams impinging on a water phantom, up to depths well beyond the Bragg peak. Energy depositions due to ionisation losses of heavy charged particles, like primary protons and ions, nuclear fragments, recoil nuclei and charged secondary particles from neutron interactions are considered; the production and transport of electrons (delta-rays) is disregarded. The production of secondary particles of different LET and their fluences differential in energy have been taken into account. This is important for an accurate evaluation of biologically equivalent doses delivered to patients undergoing radiation therapy with light ions and is well analysed by SHIELD-HIT.

The consistency of the SHIELD-HIT computations with experimental data and other well documented Monte Carlo codes for proton transport like PTRAN and PETRA has been verified by comparing depth-energy deposition profiles of protons and ^{12}C impinging on water.

Developments of the SHIELD-HIT code for ion transport in tissue-like media

The most essential improvement of the SHIELD-HIT code is the inclusion of the fluctuations of ionisation energy losses (straggling) and the multiple Coulomb scattering of heavy charged particles. These processes play a very important role when an accurate patient treatment plan is prepared for hadron therapy of tumours.

The sampling of the range of a projectile or of a secondary nuclear fragment, its energy, direction of motion at the end of the range, as well as the co-ordinates of the endpoint of the range are computed taking into account the mentioned effects. The range of a particle is divided into separate steps, such that the average energy loss at each step is comparatively small. Then for each step the endpoint energy, direction of motion and the transversal displacement are sampled. As a result, the endpoint of the range can be related to an energy and to a geometric zone of the target different from a calculation

without straggling. To study more carefully the influence of different effects on the general features of ion transport, SHIELD-HIT allows switching off the effects of straggling, multiple scattering and/or nucleus reactions in any desired combination.

The physical models of straggling and multiple scattering used in the SHIELD-HIT code are those from the Review of Particle Properties. Fluctuations of particle energy can be sampled according to either Vavilov [5] or Gaussian [6,7] distributions. In the former case, the subroutine VAVRAN and the accompanying routines from the CERN library are used in their original forms. Multiple Coulomb scattering effects are simulated on the basis of the known two-dimension Gaussian model [6,7] (the Fermi distribution) which gives the correlated values of the angular deviation and the transversal displacement of a particle.

An accurate track length algorithm for the evaluation of the fluence differential in energy of the primary ions and their secondaries as well as higher-order generations of all particles has been implemented. The default particle-number-counter fluence estimator has been kept for comparison.

In addition, a few “purely technical” modifications have been implemented in SHIELD-HIT for a more accurate computation of the range-energy and optical depth-energy dependency of charged particles. As incident energies in hadron therapy are below 1 GeV/u, the energy grid for the mentioned dependencies has been narrowed down from 1 TeV/u to 1.25 GeV/u while maintaining the same dimensions. Furthermore, the linear interpolation in the tables has been changed to quadratic interpolation. This enables obtaining higher accuracy in computations of ranges and energies according to the requirements of medical physics.

Applications and results

We shall now present several illustrative results of the performed simulations. Figure 1 shows the profiles of the energy deposition as a function of the depth in a water target for beams of the ions $^1\text{H}^{+1}$, $^2\text{He}^{+2}$, $^7\text{Li}^{+3}$, $^{11}\text{B}^{+5}$ and $^{12}\text{C}^{+6}$. These distributions reproduce the well-known Bragg curves for heavy charged particles stopped in the medium. The projectile energy was chosen to provide the same average range before stopping for each type of ionic projectile: $R_{\text{stop}} = 26.2$ cm. In this analysis a pencil beam impinges on a cylindrical water phantom target ($R = 10$ cm, $L = 30$ cm) along the axis of the cylinder. The target was subdivided into 300 layers of 1 mm in depth along the z-axis. The total energy deposited in each layer due to ionisation losses of all charged particles and nuclear fragments including recoil nuclei has been scored in the simulation. The results presented in Figure 1 correspond to the case of a broad beam irradiation.

As seen from Figure 1, considerable energy deposition is observed at depths $z > R_{\text{stop}}$ in the target for all the ionic projectiles heavier than protons. This is explained by the contribution from the secondary particles and nuclear fragments. The influence of fluctuations of ionisation losses is manifested in a smoothed shape of the Bragg peak for light projectiles such as protons and alpha particles. The influence on the Bragg peak shape is insignificant for heavier projectiles.

The depth-energy deposition curves for protons with energy 200 MeV transported through water are depicted in Figure 2 for simulations using three different Monte Carlo codes – SHIELD-HIT, PTRAN [8] and PETRA [9]; the last two codes have been thoroughly tested in the context of proton radiotherapy. The PTRAN code does not take into account nuclear reactions. However, in the PETRA code the energy losses due to inelastic nuclear interactions, that may generate up to three secondary protons, are included. The shapes of the computed distributions are similar for these three curves and the difference in the integrals under the curves is less than 1%; the lack of nuclear interactions in

Figure 1. Distribution of energy deposition (MeV/cm) as a function of depth along the axis of a cylindrical water target (R = 10 cm, L = 30 cm) irradiated with different ion-projectiles

The incident energy (MeV/u) for each type of ion beam is shown in the plot, chosen to yield a range of 26.2 cm. SHIELD-HIT Monte Carlo calculations.

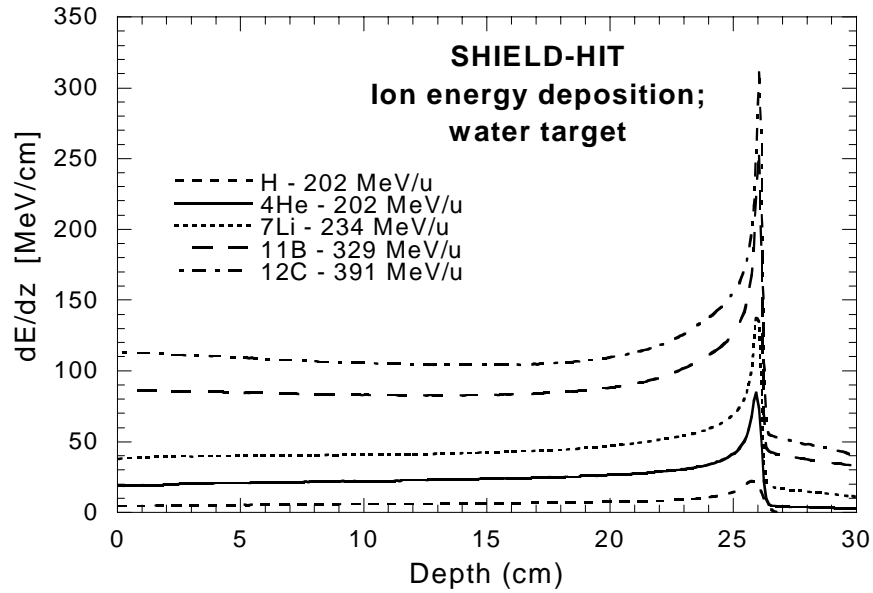
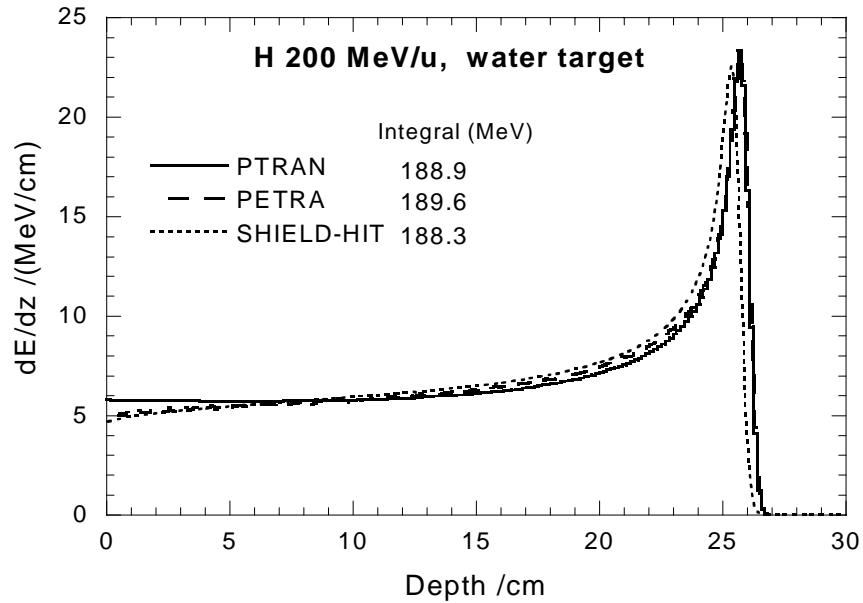


Figure 2. Distribution of energy deposition (MeV/cm) as a function of depth along the axis of a cylindrical water target (R = 10 cm, L = 30 cm) irradiated with 200 MeV proton beams

Comparison of calculations with the Monte Carlo codes PTRAN (excludes nuclear interactions), PETRA (includes nuclear interactions) and SHIELD-HIT

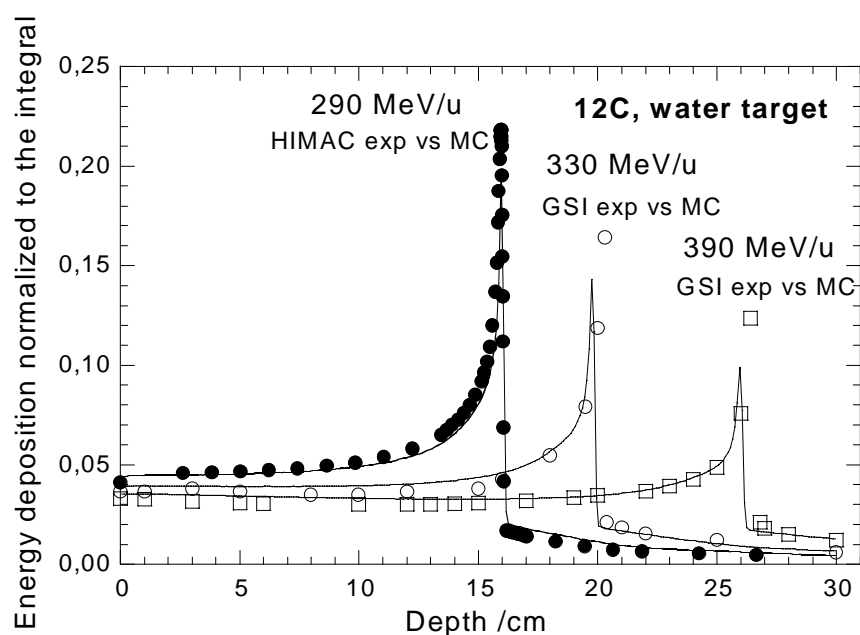


PTRAN can be seen clearly at shallow depths. However, the position of the Bragg peak obtained with the SHIELD-HIT code is shifted by 4-5 mm towards smaller depths relative to the results from the PETRA and PTRAN. A careful study and revision of the stopping power data used in the SHIELD-HIT calculations will be performed in the future.

Figure 3 shows a comparison of the Monte Carlo computed Bragg curves for $^{12}\text{C}^{+6}$ ions at three energies (290, 330 and 390 MeV/u) with experimental data from HIMAC [10] and GSI [11]. It can be seen that the agreement between the results from SHIELD-HIT and the HIMAC measurements for the total energy deposition (normalised to the integral) is quite good. Moreover, the shape of these experimental data is reproduced in a satisfactory manner over the whole depth range. However, the comparison with the GSI measurements shows differences in the projectile maximum range and the height of the Bragg peak. On the other hand, the data from SHIELD-HIT reproduce well the contribution to the energy deposition due to the secondary fragments at depths beyond the Bragg peak for all three experimental cases. A more detailed discussion about the experimental set-up for the GSI and the HIMAC measurements and a revision of the stopping power data used for carbon transport computations are required to explain the differences in the position of the Bragg peak.

Figure 3. Distribution of energy deposition (normalised to integral) as a function of depth along the axis of a cylindrical water target (R = 10 cm, L = 30 cm) irradiated with ^{12}C ion beams of 290, 330 and 390 MeV/u

Comparison of SHIELD-HIT Monte Carlo calculations with measurements at HIMAC and GSI [10,11]



Bragg curves for $^{12}\text{C}^{+6}$ ions with energy 391 MeV/u incident on water and soft tissue computed with the SHIELD-HIT code are presented in Figure 4. The difference in the total energy deposition in these two media does not exceed 0.5%. The small difference in density between the two media produces a slight shift in the position of the Bragg peak.

It is important to consider the contribution to the Bragg curve from the different generations of the hadron cascade. Figure 5 shows the Monte Carlo computed Bragg curve for $^{12}\text{C}^{+6}$ ions with energy 270 MeV/u incident on water. Results are normalised to the entrance energy deposition. The contributions from the primary ^{12}C -beam and from the secondaries of the first generation are presented separately.

Figure 4. Distribution of energy deposition (MeV/cm) as a function of depth along the axis of a cylindrical water target (R = 10 cm, L = 30 cm) irradiated with a 391 MeV/u ^{12}C ion beam

Comparison of SHIELD-HIT Monte Carlo calculations for water and soft tissue targets

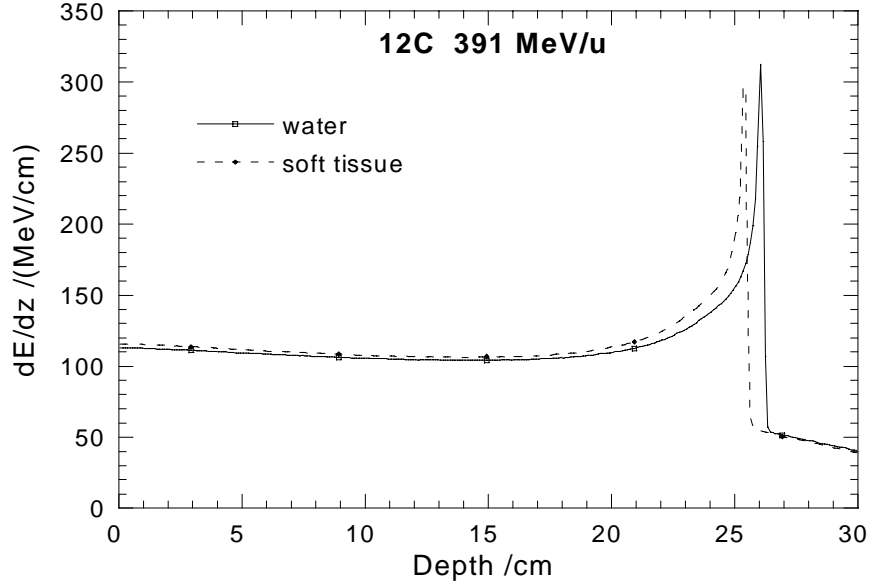
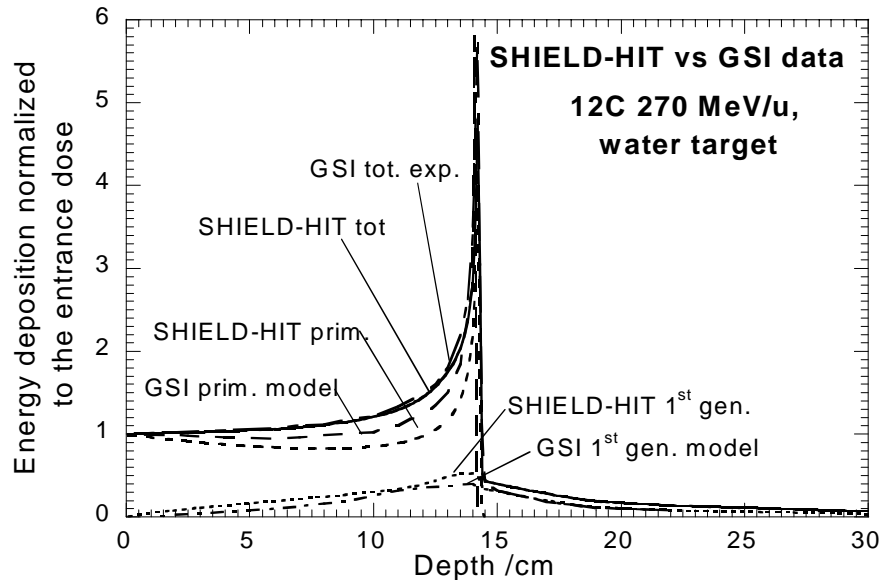


Figure 5. Distribution of energy deposition as a function of depth along the axis of a cylindrical water target (R = 10 cm, L = 30 cm) irradiated with a 270 MeV/u ^{12}C ion beam

Results are normalised to the entrance energy deposition. The total energy deposition, the contributions from primary ^{12}C beam and from secondaries of the first generation are presented separately. Comparison of SHIELD-HIT and GSI [11] data.

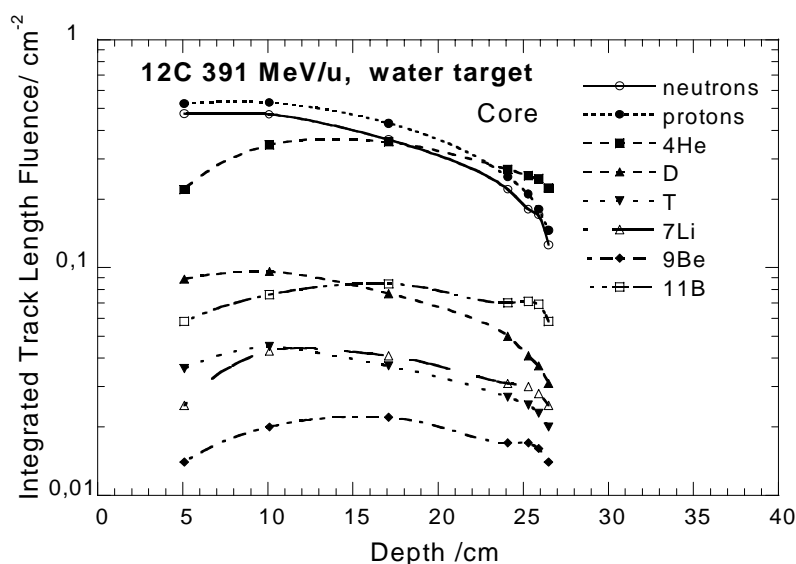


The contributions from secondaries of the second and higher generations are negligible in these studies. Experimental data from GSI [11] on the relative contribution of the total energy deposition, also included in Figure 5, agree very well with the simulated distribution using the SHIELD-HIT code. In this case the position of the Bragg peak is exactly the same for the Monte Carlo and GSI distributions, in contrary to the comparison between Monte Carlo and GSI experimental data presented in Figure 3.

This indicates that the geometry and the projectile energy used in the simulations should exactly match the experimental set-up. The comparison of the calculated relative energy deposition due to the primary beam to the data obtained from the GSI model shows significant discrepancies. However, the same model data for the secondary nuclear fragments of the first generation, also presented in Figure 5, agree satisfactorily with the SHIELD-HIT calculations.

Figure 6 shows the integrated track-length fluence of different secondary particles (neutrons, protons, $^2\text{H}^{+1}$, $^3\text{H}^{+1}$, $^4\text{He}^{+2}$, $^7\text{Li}^{+3}$, $^9\text{Be}^{+4}$ and $^{11}\text{B}^{+5}$ ions) as a function of depth in the core region of a water cylinder irradiated with $^{12}\text{C}^{+6}$ ions of energy 391 MeV/u. The cylindrical water phantom of dimensions $R = 10$ cm, $L = 30$ cm has a core cylindrical region with radius $r = 0.4$ cm which was used to score the track length fluences of the primary ions and their secondaries along the beam axis. The smooth curves are drawn between the symbols by eye.

Figure 6. Integral fluence ($1/\text{cm}^2/\text{projectile}$) of various secondary fragments inside the core region ($r = 0.4$ cm) of a water cylindrical target irradiated with a 391 MeV/u ^{12}C ion beam



In the experiment from Ref. [12] the number of secondary fragments with a given charge Z was measured as a function of depth in a water target. A target of the same dimensions as above was irradiated by ion beams in the energy range between 200 and 670 MeV/u. Several projectiles from ^{10}B to ^{20}Ne were used. Figure 7 displays the number of fragments with $Z = 5$ per ^{12}C projectile with energy 670 MeV/u as a function of the depth z . As can be seen, the agreement between the results of the computations and the experiment is quite satisfactory with a discrepancy which does not exceed 10%.

Figure 8 presents the SHIELD-HIT Monte Carlo calculated depth distributions of the production of radioactive isotopes that are of interest for positron emission tomography (PET), aimed at visualising the energy deposited in a patient treatment. The water target was irradiated by a ^{12}C ion beam with energy 270 MeV/u. It is seen that the shape of the distributions depends on the possible channels for the production of a given isotope. For example, the isotope ^{15}O can be produced only removing one neutron from the oxygen nucleus present in the water molecule. Therefore, production of the isotope ^{15}O weakly depends on the depth in the water absorber. On the contrary, the isotope ^{11}C can be formed both in reactions of spallation of oxygen and via capture of one neutron from the ion projectile ^{12}C . This leads to a sharp maximum in the distribution, corresponding to the area of stopping of the projectile-like fragment ^{11}C .

Figure 7. Number of fragments with $Z = 5$ per incident ^{12}C projectile with energy 670 MeV/u as a function of depth in a cylindrical water target ($R = 10$ cm, $L = 30$ cm)

Comparison of SHIELD-HIT Monte Carlo calculations with experimental data from GSI [12]

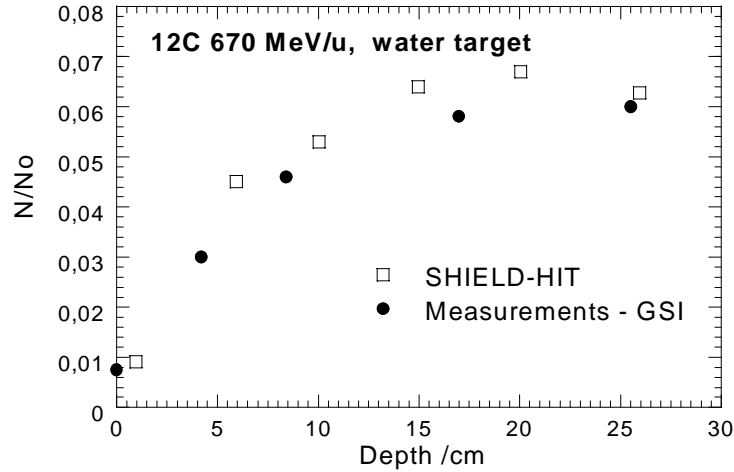
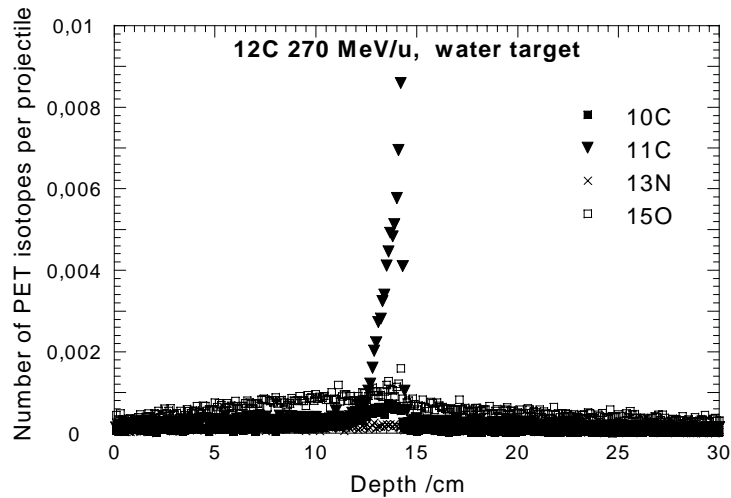


Figure 8. Depth distribution of the production rate (per incident projectile) of some isotopes of interest for PET imaging in a cylindrical water target ($R = 10$ cm, $L = 30$ cm) irradiated with a 270 MeV/u ^{12}C ion beam



Conclusions

The consistency of Monte Carlo calculations performed with the SHIELD-HIT code has been verified comparing with available experimental data and other well-tested Monte Carlo codes for ion transport, including protons. With regard to depth-energy deposition profiles of protons and ^{12}C impinging on water, SHIELD-HIT yields profiles consistent with a proper treatment of nuclear inelastic collisions. Moreover, the energy deposition beyond the Bragg peak due to nuclear fragmentation is also well predicted. Good agreement is also found with experimental determinations of the number of fragments as a function of depth in water produced with ^{12}C ions of 670 MeV/u. These results indicate that the SHIELD-HIT Monte Carlo code can be used with confidence for simulations in the field of ion beam therapy in oncology.

REFERENCES

- [1] Dementyev, A.V., N.M. Sobolevsky, "SHIELD – Universal Monte Carlo Hadron Transport Code: Scope and Applications", *Proc. of 3rd Workshop on Simulating Accelerator Radiation Environments (SARE-3)*, KEK, Tsukuba, Japan, 7-9 May 1997, KEK Proceedings 97-5, H. Hirayama, ed., H/R/D, p. 21, June 1997.
- [2] Sobolevsky, N.M., A.P. Zhukov, "Some Non-typical Tasks of Hadron Transport with the SHIELD Transport Code", *Proc. of 4th Workshop on Simulating Accelerator Radiation Environments (SARE-4)*, Knoxville (TN), USA, 14-16 September 1998, T.A. Gabriel, ed., ORNL, p. 283 (1999).
- [3] Dementyev, A.V., N.M. Sobolevsky, "SHIELD – Universal Monte Carlo Hadron Transport Code: Scope and Applications", *Radiation Measurements*, 30, 553 (1999).
- [4] Sobolevsky, N.M., "The SHIELD Transport Code: A Tool for Computer Study of Interaction of Particles and Nuclei with Complex Media", *Proceedings of the 3rd Yugoslav Nuclear Society International Conference (YUNSC 2000)*, Belgrade, 2-5 October 2000, The VINCA Institute, Belgrade, p. 539 (2001).
- [5] Vavilov, P.V., *ZhETP*, 32, 920 (1957) (in Russian).
- [6] Rossi, R., *High-energy Particles*, New York (1952).
- [7] Remizovich, V.S., D.B. Rogozkin, M.I. Ryazanov, "Fluctuations of Ranges of Charged Particles", Moscow, *Energoatomizdat*, 1988 (in Russian).
- [8] Carlsson, A.K., P. Andreo, A. Brahme, "Monte Carlo and Analytical Calculation of Proton Pencil Beams for Computerized Treatment Plan Optimization", *Phys. Med. Biol.*, 42, 1033 (1997).
- [9] Medin, J., P. Andreo, *PETRA, A Monte Carlo Code for the Simulation of Proton and Electron Transport in Water*, internal report MSF 1997-1, Dept. of Medical Radiation Physics of Karolinska Institutet and Stockholm University, Stockholm (1997).
- [10] Kanai, T., private communication (2000).
- [11] Sihver, L., D. Schardt, T. Kanai, "Depth-dose Distributions of High-energy Carbon, Oxygen and Neon Beams in Water", *Jpn. J. Med. Phys.*, Vol. 18, No. 1, p. 1 (1998).
- [12] Schall, I., D. Schardt, H. Geissel, *et al.*, "Charge-changing Nuclear Reactions of Relativistic Light-ion Beams ($5 \leq Z \leq 10$) Passing Through Thick Absorbers", *Nucl. Instr. Meth.*, B117, 221 (1996).

**ANALYTICAL METHOD FOR MULTI-SCATTERED
NEUTRONS IN CAVITY USED IN THE DUCT-III CODE**

Katsumi Hayashi, Ryuichi Tayama, Hiroyuki Handa

Hitachi Engineering Co., Ltd.
Saiwai-cho, 3-2-1, Hitachi, Ibaraki 317-0073 Japan
E-mail: k_hayashi@psg.hitachi-hec.co.jp

Kazuo Shin

Kyoto University
Sakyo-ku, Kyoto, 606-8317 Japan

Hideo Hirayama

High Energy Accelerator Research Organisation
Oho, Tsukuba, Ibaraki 305-0801 Japan

Hirdeo Nakano, Fumihiro Masukawa, Hiroshi Nakashima, Nobuo Sasamoto

Japan Atomic Energy Research Institute
Tokai-mura, Ibaraki 319-1195 Japan

Abstract

A formula for multi-scattered radiation flux in a spherical cavity based on the albedo analytical method developed by Shin, *et al.* is employed in the DUCT-III code to estimate wall-scattered radiations. The albedo data used in this formula is a neutron albedo library originally stored in the DUCT-III code, the energy of which is thermal to 3 GeV for concrete and iron.

A comparison of calculated cavity-streaming results by DUCT-III and MCNP4B (or MCNPX) was made to validate DUCT-III as a design code. The calculated dose rate by DUCT-III in the duct was 1.1-1.4 times higher than that calculated by MCNP4B (or MCNPX). Although we obtained slightly conservative results, it can be concluded that DUCT-III is suitable for use in cavity-streaming design.

Introduction

Ducts are generally positioned far away from radiation sources in order to decrease leakage (streaming) radiation through them. Because the radiation source is ordinarily surrounded by room walls, the wall-scattered radiation is not negligible compared to radiation which directly reaches the duct entrance in a normal situation. For this reason, some type of method should be used to estimate wall-scattered radiation as a source of duct-streaming radiation at the duct entrance.

Many simple formulae to estimate wall-scattered radiation have been proposed. Nakamura and Uwamino [1,2] proposed a simple dose distribution formula in a cavity using a calculated result determined by the DOT3.5 [3] code. This formula is useful for estimating dose, but does not provide energy spectrum information. Shin, *et al.* [4] proposed a more analytical formula to estimate the multi-scattered radiation flux using albedo data. This formula is useful because it provides energy spectrum information incident to the cavity surface. We thus integrated this formula into the DUCT-III [5-10] code to perform a cavity-streaming calculation.

Formula for wall-scattered radiation current in cavity

A formula for multi-scattered radiation flux in a spherical cavity based on an albedo analytical method developed by Shin, *et al.* [4] is employed to calculate the wall-scattered radiations. The radiation current incident to the duct is given by:

$$S = \frac{J}{2\pi} \quad (1)$$

$$J = \frac{A}{(I - A)} \frac{S_0}{S_a} \quad (2)$$

where S is the isotropic radiation current in $\text{cm}^2\text{sr}^{-1}\text{s}^{-1}$, J is the accumulated radiation current in cm^2s^{-1} , A is the albedo matrix, I is the unit matrix, S_0 is the isotropic radiation source intensity in s^{-1} , and S_a is the inner surface area of the cavity wall in cm^2 . Eq. (2) was corrected from the original equation, $J = I/(I - A) S_0/S_a$ in which the radiation current directly incident to the duct was included. The radiation current S is expressed in DUCT-III as a function of the incident angle. Eq. (1) is rewritten by:

$$S_j = \left(\cos(\theta_j) - \cos(\theta_{j+1}) \right) \frac{A}{(I - A)} \frac{S_0}{S_a} \quad (3)$$

where S_j is the incident current in the j -th angular bin at duct inlet (cm^2s^{-1}), and θ_j is the angular mesh boundary of radiation incident into the duct in degrees. For high-energy neutrons, $A/(I - A)$ in Eq. (3) is changed to the following:

$$\frac{A}{(I - A)} \cong A^1 + A^2 + \dots + A^M \quad (4)$$

where $M = 20$ is used.

The albedo matrix library used is the same library in the DUCT-III code originally prepared to calculate the duct streaming flux. This albedo was calculated from thermal to 3 GeV using the NMTC/JAERI and MCNP4A codes [11,12].

Validation of DUCT-III code using cavity-streaming problem

A comparison of the calculated cavity-streaming results by DUCT-III and MCNP4B [12] (or MCNPX [13]) was made to validate DUCT-III as a design code.

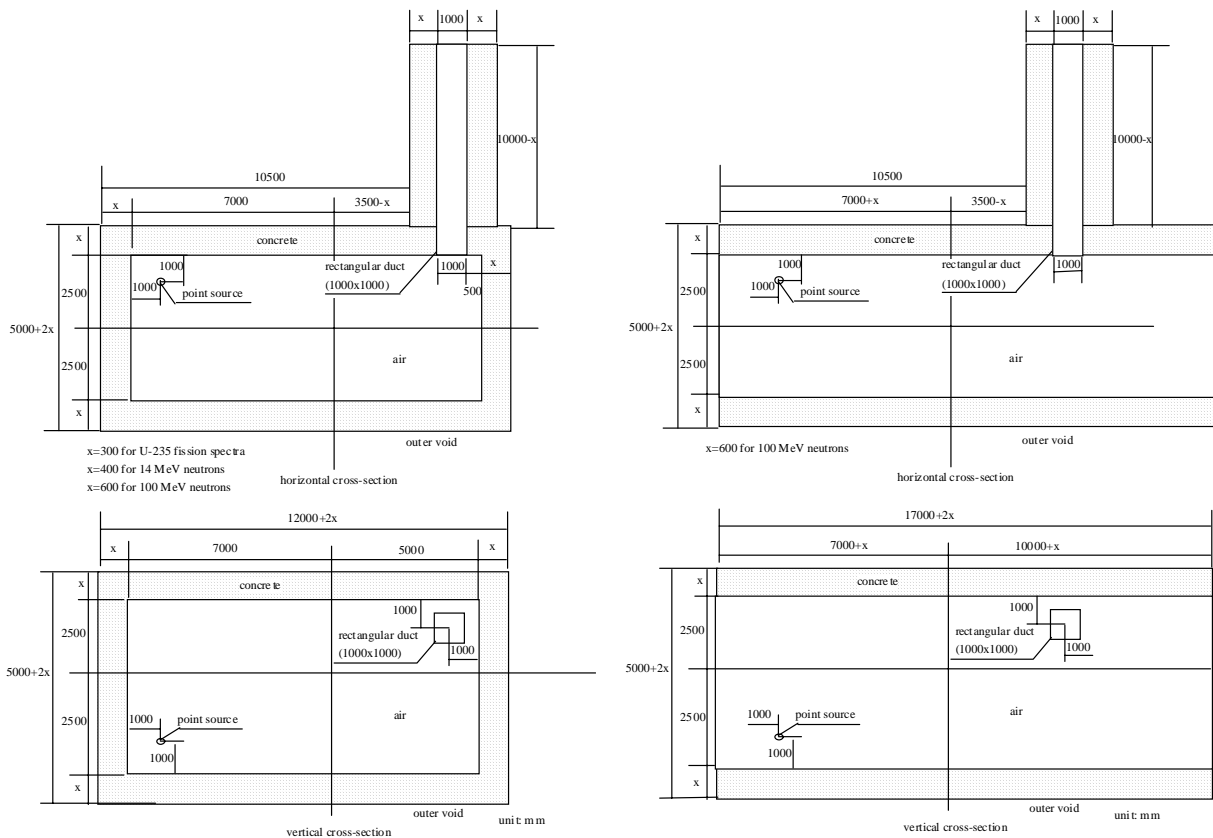
Figure 1(a) shows the geometry used. The neutron source is located near the lower-left-rear corner of a room 12 m wide, 5 m deep and 5 m high. Near the upper-right-rear corner is located a rectangular duct 10 m long, the cross-section of which is 1 m \times 1 m. The distance from the source to the duct entrance is 10.5 m and the incident angle to the duct entrance is 86°. Three kinds of point isotropic neutron source, the energy spectrum of which are ^{235}U fission spectrum (to represent reactor), 14 MeV (fusion facility) and 100 MeV (accelerator), are used for comparison.

Figure 1(b) shows the accelerator tunnel geometry. This geometry is prepared to validate the applicability of the cavity model in DUCT-III for tunnel geometry. A 100 MeV point isotropic source is used for comparison.

Figure 1

(a) MCNP/MCNPX model of duct streaming calculations

(b) MCNPX model of duct streaming calculations (accelerator tunnel)



Monte Carlo calculation

In the Monte Carlo calculation, the thickness of the wall, x , is determined to be the concrete thickness that decreases the dose rate to about 1/4.

MCNP4B [12] and the JENDL-3.2 [14] library were used for fission and the 14 MeV source. MCNPX2.1.5 [13] and the LA150 [15] library were used for the 100 MeV source. Table 1 shows the material composition used in the calculation. Concrete density and composition are the same as those used in the albedo calculation.

Table 1. Atomic number densities of concrete and air

Material	Concrete*		Air	
Density	2.15		1.239E-03	
Element	Fraction (w/o)	Number density ($\times 10^{24} \text{ cm}^{-3}$)	Fraction (w/o)	Number density ($\times 10^{24} \text{ cm}^{-3}$)
H	1.02	1.31E-02		
C	1.00	1.09E-04		
N			76.5	4.25E-05
O	53.85	4.35E-02	23.5	1.14E-05
Mg	0.22	1.17E-04		
Al	3.44	1.65E-03		
Si	34.21	1.57E-02		
K	1.32	4.38E-04		
Ca	4.41	1.42E-03		
Fe	1.41	3.27E-04		

* ANL-5800 [17] type02-a concrete.

Table 2 shows the flux to effective dose conversion factor derived from AP geometry in ICRP Publication 74 [16].

DUCT-III calculation

In the DUCT-III calculation, the room is modelled as a sphere with a 10.5 m radius that is the distance from source to the centre of the duct entrance. Therefore the inner surface area of the room is calculated to be $1.38 \times 10^7 \text{ cm}^2$. The duct was modelled as a 1 m \times 1 m rectangular duct as shown in Figure 1.

In the DUCT-III code, two types of energy group structure are prepared. One is from thermal to 15 MeV and the other is thermal to 3 GeV. The former group structure is used for fission and 14 MeV calculations. The latter group structure is used for 100 MeV calculations.

Table 3 shows the flux to effective dose conversion factor for each group structure derived from AP geometry in ICRP Publication 74 [16]. Energy group collapsing was done by using the neutron spectrum at the duct entrance calculated by MCNP or MCNPX.

Result and discussion

²³⁵U fission spectrum

Figure 2 shows the effective dose distribution in the duct. Figure 3 shows the energy spectra at 2 m and 7.5 m from the duct entrance. The maximum statistical error (1σ) of the effective dose was 1.7%. Statistical errors (1σ) are also shown for the energy spectra (error bar).

Table 2. Flux to effective dose conversion factors for neutrons with HILO energy structure

Energy group	Upper energy (MeV)	Flux to effective dose conversion factors ((Sv·h ⁻¹)/(cm ⁻² ·s ⁻¹))	Energy group	Upper energy (MeV)	Flux to effective dose conversion factors ((Sv·h ⁻¹)/(cm ⁻² ·s ⁻¹))
15	1.00E+02	1.71E-06	41	3.01E+00	1.51E-06
16	9.00E+01	1.68E-06	42	2.46E+00	1.42E-06
17	8.00E+01	1.65E-06	43	2.02E+00	1.33E-06
18	7.00E+01	1.64E-06	44	1.65E+00	1.22E-06
19	6.50E+01	1.63E-06	45	1.35E+00	1.13E-06
20	6.00E+01	1.62E-06	46	1.11E+00	1.02E-06
21	5.50E+01	1.60E-06	47	9.07E-01	9.12E-07
22	5.00E+01	1.60E-06	48	7.43E-01	7.63E-07
23	4.50E+01	1.61E-06	49	4.98E-01	5.90E-07
24	4.00E+01	1.63E-06	50	3.34E-01	4.48E-07
25	3.50E+01	1.64E-06	51	2.24E-01	3.34E-07
26	3.00E+01	1.66E-06	52	1.50E-01	2.37E-07
27	2.75E+01	1.67E-06	53	8.65E-02	1.43E-07
28	2.50E+01	1.69E-06	54	3.18E-02	8.94E-08
29	2.25E+01	1.72E-06	55	1.50E-02	6.67E-08
30	2.00E+01	1.74E-06	56	7.10E-03	5.64E-08
31	1.75E+01	1.77E-06	57	3.35E-03	5.25E-08
32	1.49E+01	1.78E-06	58	1.58E-03	5.11E-08
33	1.35E+01	1.79E-06	59	4.54E-04	5.18E-08
34	1.22E+01	1.80E-06	60	1.01E-04	5.33E-08
35	1.00E+01	1.79E-06	61	2.26E-05	5.44E-08
36	8.19E+00	1.77E-06	62	1.07E-05	5.44E-08
37	6.70E+00	1.74E-06	63	5.04E-06	5.33E-08
38	5.49E+00	1.70E-06	64	2.38E-06	5.14E-08
39	4.49E+00	1.65E-06	65	1.12E-06	4.77E-08
40	3.68E+00	1.47E-06	66	4.14E-07	2.26E-08

Table 3. Collapsed flux to effective dose conversion factors for neutrons with DUCT-III energy structures

Upper energy (MeV)	Collapsed response* ((Sv·h ⁻¹)/(cm ⁻² ·s ⁻¹))		Upper energy (MeV)	Collapsed response* ((Sv·h ⁻¹)/(cm ⁻² ·s ⁻¹))
	²³⁵ U fission spectrum	14 MeV neutrons		100 MeV neutrons
1.50E+01	0.00E+00	1.78E-06	3.00E+03	0.00E+00
1.30E+01	1.76E-06	1.78E-06	1.50E+03	0.00E+00
5.49E+00	1.54E-06	1.57E-06	8.00E+02	0.00E+00
2.47E+00	1.23E-06	1.24E-06	4.00E+02	0.00E+00
9.07E-01	7.64E-07	7.55E-07	1.00E+02	1.70E-06
3.34E-01	3.98E-07	3.91E-07	1.96E+01	1.54E-06
1.11E-01	1.38E-07	1.37E-07	1.35E+00	6.46E-07
9.12E-03	5.30E-08	5.30E-08	8.65E-02	9.65E-08
7.49E-04	5.26E-08	5.26E-08	3.35E-03	5.18E-08
6.14E-05	5.44E-08	5.44E-08	1.01E-04	5.38E-08
5.04E-06	5.05E-08	5.04E-08	5.04E-06	5.05E-08
4.14E-07	2.26E-08	2.26E-08	4.14E-07	2.26E-08

Figure 2. Dose distribution in duct by ^{235}U fission source

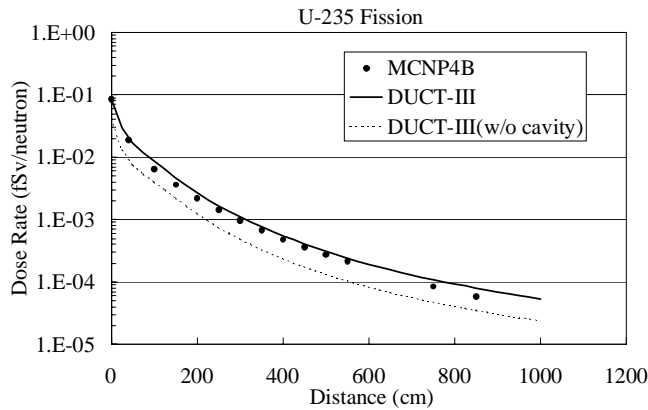
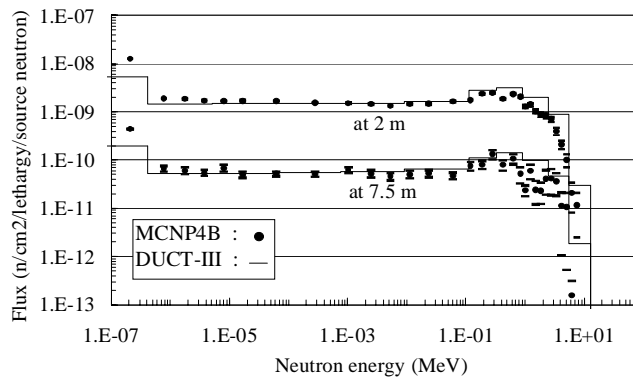


Figure 3. Calculated neutron spectrum for ^{235}U fission neutron source



The dotted line in Figure 2 shows an example calculation using DUCT-III without the cavity model. This calculation was made using three steps. First, neutron flux at the duct entrance $\Phi(E)$ was obtained using $\Phi(E) = S(E)/4\pi r^2$, where $S(E)$ is the source neutron spectrum and r is the distance from the source to the duct entrance. Second, the pseudo point isotropic source at the duct entrance $Sp(E)$ must be calculated using $Sp(E) = \Phi(E)D$, where D is the duct entrance area. Third, duct streaming should be calculated using this source by DUCT-III. This method underestimates by a factor of two or more because the room-scattered neutrons were ignored.

The calculated effective dose at the duct entrance obtained by DUCT-III using a cavity model is shown with a solid line in Figure 2. The result is in good agreement with MCNP4B; it is about 1.3 times higher just after the duct entrance than that of MCNP4B. This discrepancy tends to be smaller with a shorter distance from the entrance. From about 2.5 m from the entrance to the duct exit, the discrepancy is only about 1.1. This results from the difference of angular distribution of the source neutron at the duct entrance. In DUCT-III, axis symmetry angular distribution was assumed but the in MCNP code, realistic angular distribution was used. Figure 3 demonstrates that the energy spectrum in the duct is also well reproduced by DUCT-III.

From the above comparison, it can be concluded that the DUCT-III code is suitable to be used for cavity-streaming geometry for fission reactors.

14 MeV neutron

Figure 4 shows the effective dose distribution in the duct. Figure 5 shows the energy spectra at 2 m and 7.5 m from the duct entrance. The maximum statistical error (1σ) of the effective dose was 1.7%. Statistical errors (1σ) are also shown for the energy spectra (error bar).

Figure 4. Dose distribution in duct by 14 MeV source

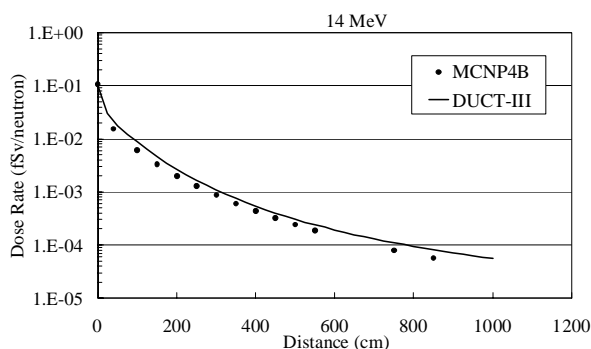
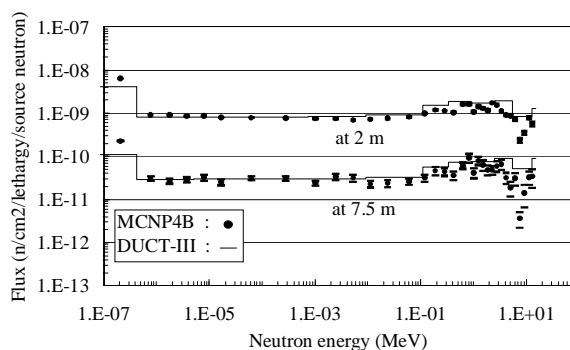


Figure 5. Calculated neutron spectrum for 14 MeV neutron source



The effective dose calculated by DUCT-III at the duct entrance is in good agreement with that obtained by MCNP4B, but is about 1.4 times higher just after the duct entrance than that of MCNP4B. This discrepancy tends to be smaller the shorter the distance from the entrance. From about 2.5 m from the entrance to the duct exit, the discrepancy is only about 1.2. This results from the difference of angular distribution of the source neutron at the duct entrance. In DUCT-III, axis symmetry angular distribution was assumed but the in MCNP, realistic angular distribution was used. Figure 5 shows that the energy spectra in the duct are also well reproduced by DUCT-III.

From the above comparison, it can be concluded that the DUCT-III code is suitable to be used for cavity-streaming geometry for fusion facilities.

100 MeV neutron

Figure 6 shows the effective dose distribution in the duct. Figure 7 shows the energy spectra at 2 m and 7.5 m from the duct entrance. The maximum statistical error (1σ) of the effective dose was 2.7%. Statistical errors (1σ) are also shown for the energy spectra (error bar).

Figure 6. Dose distribution in duct by 100 MeV source

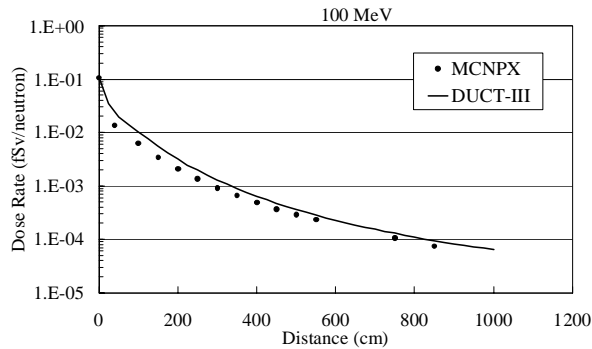
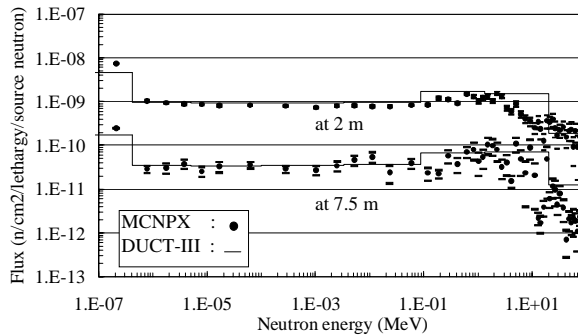


Fig. 6 Dose distribution in duct by 100 MeV source

Figure 7. Calculated neutron spectrum for 100 MeV neutron source



The effective dose calculated by DUCT-III at the duct entrance is in good agreement with MCNPX, but is about 1.6 times higher just after the duct entrance than that obtained by MCNPX. This discrepancy tends to be smaller the shorter the distance from the entrance. From about 2.5 m from the entrance to the duct exit, the discrepancy is only about 1.4. This results from the difference of angular distribution of the source neutron at the duct entrance. In DUCT-III, axis symmetry angular distribution was assumed, but the in MCNP code realistic angular distribution was used. Figure 7 shows that the energy spectrum in the duct is also well reproduced by DUCT-III.

From the above comparison, it can be concluded that the DUCT-III code is suitable to be used for cavity-streaming geometry for accelerators.

100 MeV neutron in accelerator tunnel

Another comparison was made to determine the applicability of the cavity model used in the DUCT-III code to accelerator tunnel geometry. Another MCNPX calculation was performed using the geometry shown in Figure 1(b). This geometry represents an accelerator tunnel with duct streaming problem.

Figure 8 shows the effective dose distribution in the duct. Figure 9 shows the energy spectra at 2 m and 7.5 m from the duct entrance. The maximum statistical error (1σ) of the effective dose was 4.4%. Statistical errors (1σ) are also shown for the energy spectra (error bar). Because DUCT-III has only a cavity model, the result used is the same as that for Figures 6 and 7.

Figure 8. Dose distribution in duct by 100 MeV source in tunnel

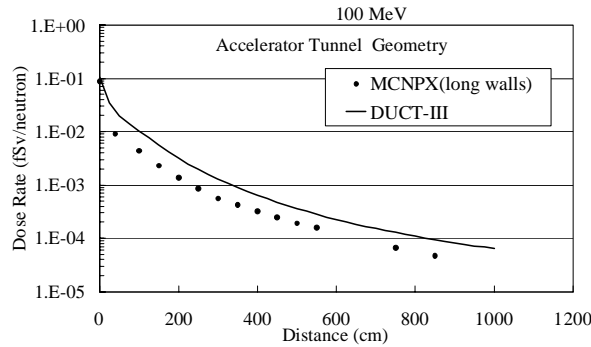
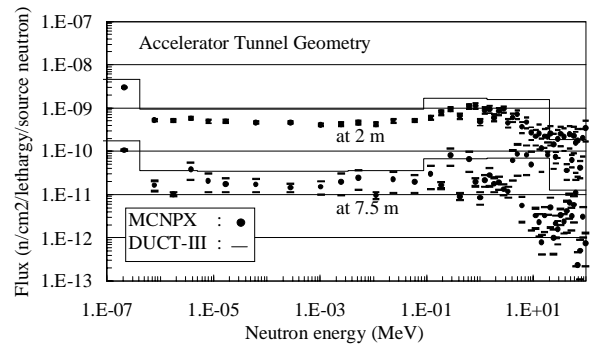


Figure 9. Calculated neutron spectrum for 100 MeV neutron source in tunnel



From the comparison of the two MCNPX result (Figure 6 and Figure 8), it was found that effective dose decreases to about 60% when side walls are removed. Because DUCT-III uses a spherical cavity, it overestimates in tunnel-streaming geometry. Although the discrepancy is larger than that for cavity-streaming geometry, it is only about 2-2.3 times higher than the Monte Carlo result. It can therefore be concluded that the DUCT-III code is suitable to be used in tunnel-streaming geometry for accelerators, taking the overestimation into consideration.

Conclusion

The cavity model developed by Shin was introduced into the DUCT-III code. We used DUCT-III for cavity-streaming geometry. It was found from the comparison to Monte Carlo codes that the dose distribution shape in the duct is well reproduced by DUCT-III. The dose rate calculated by DUCT-III in the duct was 1.1-1.4 times higher than that calculated by MCNP4C (or MCNPX). This overestimation results from the angler distribution of the scattered neutrons at the duct entrance, which was created by the assumption of a spherical cavity. Although we obtain slightly conservative results, it can be concluded that DUCT-III is suitable to be used for cavity-streaming and accelerator tunnel-streaming design.

REFERENCES

- [1] Uwamino, Y., T. Nakamura and T. Ohkubo, *Med. Phys.*, 13, 374 (1986).
- [2] Nakamura, T. and Y. Uwamino, *Radioisotopes*, 35(2), 51 (1986).
- [3] Rhoades, W.A. and F.R. Mynatt, *The DOT-III Two-dimensional Discrete Ordinates Transport Code*, ORNL/TM-4280 (1973).
- [4] Shin, K., *et al.*, “Albedo Analytical Method for Multi-scattered Neutron Flux Calculation in Cavity”, *J. Nucl. Sci. Technol.*, 23, 949 (1986).
- [5] Shin, K., “Semiempirical Formula for Energy-space Distributions of Streamed Neutrons and Gamma-rays in Cylindrical Duct”, *J. Nucl. Sci. Technol.*, 25 [1], 8-18 (1988).
- [6] Shin, K., “An Approximate Formula for Neutron and Gamma-ray Streaming through Ducts and Slits”, *7th Int. Conference on Radiation Shielding*, Bournemouth, UK, 12-16 Sept. (1988).
- [7] Shin, K. and A. Itoh, “A Simple Calculation Method for 14 MeV Gap Streaming”, *International Symposium on Fusion Nuclear Technology*, Tokyo, 11-14 April (1988).
- [8] Hayashi, K., *et al.*, *DUCT-II and SHINE-II: Simple Design Code for Duct-streaming and Skyshine*, JAERI-M 91-013 (1991).
- [9] Tayama, R., *et al.*, *DUCT-III: Simple Design Code for Duct-streaming Radiations*, KEK-Internal 2001-8 (2001)
- [10] Masukawa, F., *et al.*, *Verification of the DUCT-III for Calculation of High-energy Neutron Streaming*, JAERI-Report (to be published).
- [11] Takada, H., *et al.*, *An Upgraded Version of the Nucleon Meson Transport Code: NMTC/JAERI97*, JAERI-Data/Code 98-005 (1998).
- [12] RSICC Computer Code Collection, *MCNP-4B: Monte Carlo N-particle Transport Code System*, CCC-660, Oak Ridge National Laboratory (1997).
- [13] RSICC Computer Code Collection, *MCNPX version 2.1.5*, CCC-705, Oak Ridge National Laboratory (1999).
- [14] Nakagawa, T., *et al.*, “Japanese Evaluated Nuclear Data Library Version 3 Revision 2: JENDL-3.2”, *J. Nucl. Sci. Technol.*, 32, 1259-1271 (1995).
- [15] Chadwick, M.B., *et al.*, “Cross-section Evaluation to 150 MeV for Accelerator-driven Systems and Implementation in MCNPX”, *Nucl. Sci. Eng.*, 131, 293 (1999).

- [16] *Conversion Coefficients for Use in Radiological Protection Against External Radiation*, ICRP Publication 74, The International Commission on Radiological Protection (1996).
- [17] *Reactor Physics Constants*, ANL-5800, Argonne National Laboratory, 660 (1963).
- [18] Alsmiller, Jr., R.G., *et al.*, *Neutron-photon Multi-group Cross-sections for Neutron Energies < 400 MeV*, ORNL/TM-7818 (1981).

DEVELOPMENT OF A GENERAL-PURPOSE HEAVY-ION TRANSPORT CODE

Hiroshi Iwase¹, Koji Niita² and Takashi Nakamura¹

¹Tohoku University, Department of Quantum Science and Energy Engineering

²Advanced Science Research Centre, JAERI

Abstract

The high-energy particle transport code NMTC/JAM [1], which has been developed at JAERI, was improved for the calculation of high-energy heavy-ion transport through the incorporation of the SPAR [2] code and Shen's formula [3]. The new NMTC/JAM is the first general-purpose heavy-ion transport Monte Carlo code.

In this code heavy-ion transport is calculated using the Shen's formula and the SPAR code. The heavy-ion nuclear reaction is calculated with the JQMD [4] code, which is widely used for hadron and heavy-ion reactions based on the quantum molecular dynamics model.

In order to investigate the accuracy of the new NMTC/JAM for heavy-ion transport calculations, systematic calculations were performed to obtain neutron production yields from thick targets so as to compare the measured data. The results of the new NMTC/JAM calculations agree very well with the experimental data.

Background

Recently, high-energy heavy ions have been used in various fields of nuclear physics, material physics and for medical applications, especially cancer therapy, and several heavy-ion accelerator facilities are now operating or planned for construction. High-energy heavy ions are also important constituents of cosmic radiation for space utilisation, such as the international space station project including the Japanese Experiment Module (JEM).

The three-dimensional Monte Carlo code HETC-CYRIC [5] was developed for heavy-ion transport calculation. The HETC-CYRIC code uses the HIC [6] code for the heavy-ion nuclear reaction and also uses Shen's formula and the SPAR code for the heavy-ion transport calculation. The HETC-CYRIC code gives good agreement with the experimental data for the neutron production yield from thick targets. However the HETC-CYRIC code is limited in its output of various calculated results for general use, and the HIC code for heavy-ion nuclear reaction is rather old-fashioned, being based on the intranuclear cascade evaporation model.

We thus developed a new heavy-ion transport code for general-purpose calculation, NMTC/JAM, by upgrading the original NMTC/JAM.

Original NMTC/JAM

The high-energy particle transport code NMTC/JAM is an upgraded version of NMTC/JAERI97 [7]. The applicable energy range of NMTC/JAM is extended in principle up to 200 GeV for nucleons and mesons by introducing the high-energy nuclear reaction code JAM [8] for the intranuclear cascade. For the evaporation and fission processes, NMTC/JAM includes a new code, GEM [9]. The Generalised Evaporation Model (GEM) code can treat the light nucleus production from the excited residual nucleus with good accuracy. According to the extension of the applicable energy, the nucleon-nucleus non-elastic, elastic and differential elastic cross-section data are upgraded by employing new systematics. In addition, particle transport in a magnetic field has been implemented for the beam transport calculations.

The NMTC/JAM code has many tally functions and the format of input and output data has been greatly improved so as to be more user-friendly.

Heavy-ion transport calculation

For heavy-ion transport calculations, Shen's formula and the SPAR code, which have been used in the HETC-CYRIC and JQMD codes (as described later) are included in the NMTC/JAM code.

Shen's formula

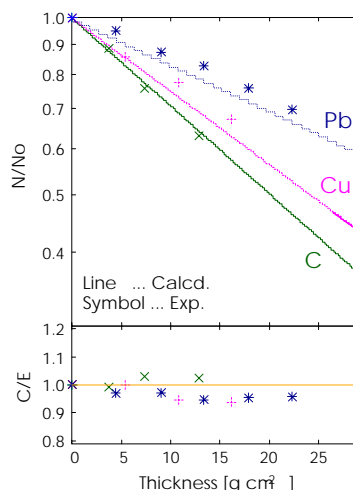
Shen's formula is used to calculate the heavy-ion total reaction cross-sections. In order to check the accuracy of this formula, we calculated the attenuation of incident heavy-ion numbers using the formula of total reaction cross-section σ_t as follows:

$$\frac{N}{N_0} = \exp\left(-\frac{x}{N \cdot \sigma_t}\right) \quad (1)$$

where x is a thickness of a target and N is a number of atoms of a target per unit volume. Figure 1 shows the calculated results of heavy-ion projectile attenuation N/N_0 compared with the measured data by Fukumura, *et al.* [10] for the 290 MeV/nucleon C beam on the C, Cu and Pb targets.

Shen's formula shows good agreement with the experimental data in Figure 1, and the average values of Calculation/Experiment (C/E) are within 5% for these three targets.

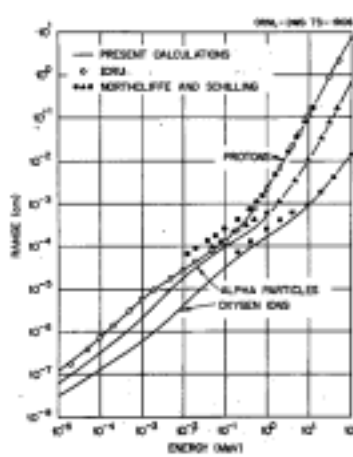
Figure 1. Attenuation of 290 MeV/nucleon C ion with the target thickness. The results calculated by Shen's formula are compared with the measured data. The C/E values are also shown below.



SPAR

The SPAR code is widely used to calculate the stopping powers and ranges for muons, pions, protons and heavy ions in energies from zero to several hundred GeV. Figure 2 shows the calculated ranges of proton, helium and oxygen ions in water [2]. Some differences are found in low energies for helium and oxygen between the calculation and the experiment, but above 10 MeV both data agree well for all projectiles.

Figure 2. Calculated ranges of proton, helium and oxygen in water compared with the ICRU and measured data [14]



JQMD

The JAERI Quantum Molecular Dynamics (JQMD) code, which was developed by Niita, *et al.* [4] based on the QMD model, has been widely used to analyse various aspects of heavy-ion reactions. The JQMD code was included in the original NMTC/JAM code for nucleon-nucleus reaction and the JQMD routine was revised here so as to be able to treat the nucleus-nucleus reaction in the new NMTC/JAM code.

Heavy-ion transport calculation

A distance D at which a heavy-ion projectile travels before colliding with a target nucleus in a medium is determined as follows:

$$D = -\frac{\ln(r)}{\Sigma_t} \quad (2)$$

where Σ_t is the total cross-section of a projectile in a medium and r is a uniform random number.

A range R of a projectile in a medium can be calculated by the SPAR code. It is then decided whether a projectile collides or stops from the comparison of D and R . If $D < R$, a projectile collides with a target nucleus after flying to a distance of D while continuously losing its energy. This energy loss can be calculated by the SPAR code. If $D > R$, a projectile loses its energy completely without collision in a medium, and the transport of this projectile is not traced any further.

After the transport calculation the heavy-ion reaction calculations are treated by the JQMD code. The GEM code developed by Furihata [9] can be used to calculate the evaporation from the excited nucleus after the JQMD calculation.

Comparison of the NMTC/JAM code with measured data

To check the accuracy of the new NMTC/JAM code for heavy-ion transport calculation, we compared the results of this code with the data measured by Kurosawa, *et al.* [11].

Kurosawa, *et al.* measured secondary neutrons produced from thick (stopping length) targets of C, Al, Cu, and Pb by bombarding various heavy ions from He to Xe with energies from 100 MeV/nucleon to 800 MeV/nucleon at the Heavy-ion Medical Accelerator in Chiba (HIMAC) of the National Institute of Radiological Sciences (NIRS), Japan. Table 1 shows the projectile types, its energies and the target thicknesses in their experiment.

We calculated the produced neutron energy spectra for all cases in Table 1. In every case, the calculated results agree well with the measured data within a factor of 3. Figure 3 shows an example of the comparison of the calculated results with the new NMTC/JAM code to the measured neutron spectra for 400 MeV/nucleon iron ion on the lead target.

The NMTC/JAM calculation agrees quite well with the experimental data at all angles from several MeV to several hundreds MeV.

Table 1. Projectile type with its incident energy per nucleon and target thickness used in the experiment by Kurosawa, *et al.* [11]

Projectile and its energy (MeV/u)	Target thickness (cm)			
	C	Al	Cu	Pb
He (100)	C (5.0)	Al (4.0)	Cu (1.5)	Pb (1.5)
He (180)	C (16.0)	Al (12.0)	Cu (4.5)	Pb (5.0)
C (100)	C (2.0)	Al (2.0)	Cu (0.5)	Pb (0.5)
C (180)	C (6.0)	Al (4.0)	Cu (1.5)	Pb (1.5)
C (400)	C (20.0)	Al (15.0)	Cu (5.0)	Pb (5.0)
Ne (100)	C (1.0)	Al (1.0)	Cu (0.5)	Pb (0.5)
Ne (180)	C (4.0)	Al (3.0)	Cu (1.0)	Pb (1.0)
Ne (400)	C (11.0)	Al (8.0)	Cu (3.0)	Pb (3.0)
Ar (400)	C (7.0)	Al (5.5)	Cu (2.0)	Pb (2.0)
Fe (400)	C (4.0)	Al (3.0)	Cu (1.5)	Pb (1.5)
Xe (400)	C (3.0)	Al (2.0)	Cu(1.0)	Pb(1.0)
Si (800)	C (23.0)		Cu(6.5)	

Figure 3. Comparison of the neutron spectra calculated with the NMTC/JAM code and the measured data for 400 MeV/nucleon Fe ion on Pb target

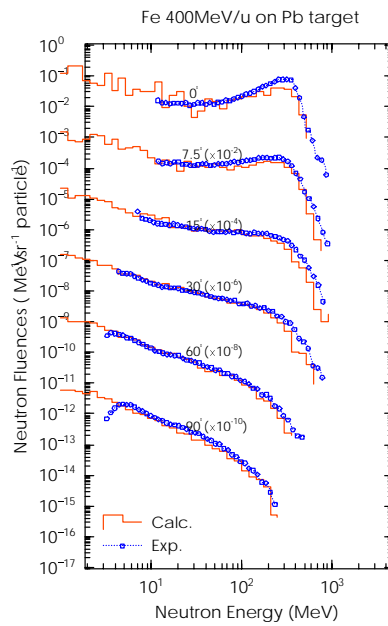
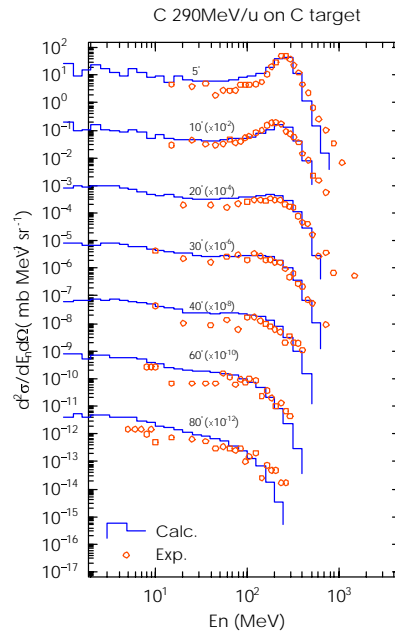


Figure 4 shows the neutron double-differential cross-section (DDX) calculation on a thin C target bombarded by 400 MeV/nucleon C ion compared with the experimental results of Iwata, *et al.* [12]. In this calculation the actual target thickness (1.80 g/cm^2) used in the experiment is considered to obtain the neutron DDX spectrum. In this way we can consider the effect of the energy loss and attenuation of the incident C beams in the target. The NMTC/JAM results agree well with the experimental data.

Figure 4. Comparison of the neutron double-differential cross-section calculated with the NMTC/JAM code and the measured data for 290 MeV/nucleon C ion on C target

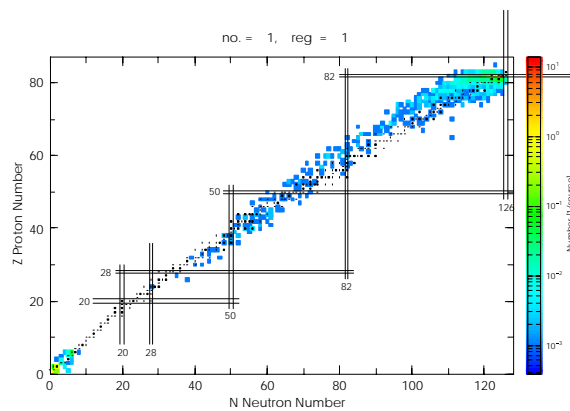


Application to other experiments

The NMTC/JAM code can be applied to various fields, nuclear physics, material physics, shielding design, medical application, space science and so on.

We are currently starting to evaluate nucleus production in the materials induced by high-energy heavy-ion irradiation. Figure 4 shows the output results of the NMTC/JAM code for the nucleus (spallation products) in the Cu target produced by 400 MeV/nucleon C ion. The results will be compared with the measured data of Yashima, *et al.* [13].

Figure 5. Mass yield distribution in the Cu target bombarded by 400 MeV/nucleon C ion calculated by NMTC/JAM



Conclusion

The new NMTC/JAM provides very good results on the angular distributions of the secondary neutron energy spectra produced from thick Pb target bombarded by 400 MeV/nucleon Fe ions.

Further investigations have begun to verify the accuracy of the heavy-ion transport calculations of the NMTC/JAM code and this code can be applied for various heavy-ion studies.

Acknowledgements

We wish to express our gratitude to Dr. Y. Yamaguchi and Dr. Y. Ikeda for helping our stay at JAERI. We also would like to thank Dr. E. Kim, Dr. M. Harada and Dr. S. Meigo for their kind assistance.

REFERENCES

- [1] Niita, K., S. Meigo, H. Takada, Y. Ikeda, JAERI-Data/Code 2001-007 (2001).
- [2] Armstrong, T.W. and K.C. Chandler, ORNL-4869, Oak Ridge National Laboratory (1973).
- [3] Shen, W-Q., B. Wang, J. Feng, W-L. Zhan, Y-T. Zhu, E-P. Feng, *Nucl. Phys.*, A491, 130 (1989).
- [4] Niita, K., S. Chiba, T. Maruyama, H. Takada, T. Fukahori, Y. Nakahara, A. Iwamoto, *Phys. Rev.*, C 52, 2620 (1995).
- [5] Iwase, H., T. Kurosawa, T. Nakamura, N. Yoshizawa and J. Funabiki, *Nucl. Instr. and Meth.* B183, 384 (2001).
- [6] Bertini, H.W., T.A. Gabriel, R.T. Santoro, *et al.*, ORNL-TM-4134, Oak Ridge National Laboratory (1974).
- [7] Takada, H., N. Yoshizawa, K. Kosaka, K. Ishibashi, JAERI-Data/Code 98-005, Japan Atomic Energy Research Institute (1998).
- [8] Nara, Y., N. Otuka, A. Ohnishi, K. Niita and S. Chiba, *Phys. Rev.*, C61, 024901 (1999).
- [9] Furihata, S., *Nucl. Instr. and Meth.*, B171, 251 (2000).
- [10] Fukumura, A., T. Hiraoka, T. Tomitani, *et al.*, *Advances in Hadrontherapy*, 325, Amsterdam (1997).
- [11] Kurosawa, T., N. Nakao, T. Nakamura, *et al.*, *Phys. Rev.*, C 62, 044615 (2000).

- [12] Iwata, Y., L. Heilbronn, H. Sato, *et al.*, *Phys. Rev.*, C 64, 054609 (2001).
- [13] Yashima, H., *et al.*, submitted to *Phys. Rev. C*.
- [14] Northcliffe, L.C. and R.F. Schilling, *Nucl. Data*, A8, 233-463 (1970).

IMPLEMENTATION OF XENON CAPTURE GAMMAS IN FLUKA FOR TRD BACKGROUND CALCULATIONS

A. Fassò¹, A. Ferrari², P.R. Sala², G. Tsileidakis¹

¹GSI and CERN

²INFN and CERN

Abstract

The energy and intensity of gammas produced by thermal neutron capture in xenon must be known in order to simulate the background in the ALICE TRD detector. Because such information is missing from the available evaluated nuclear data files, it has been necessary to reconstruct it by comparing the few existing experimental data with a NNDC database of adopted energy levels. An algorithm based on the resulting data has been implemented in the FLUKA code to simulate the full gamma cascade in all stable xenon isotopes.

Introduction

The ALICE Transition Radiation Detector (TRD) [1] will be a six-layer barrel detector surrounding the interaction point at radial distances from 2.9 to 3.7 meters. Each layer will include a foil stack (radiator) and a wire chamber (Time Expansion Chamber, TEC) filled with a gas mixture containing at least 90% xenon.

The TRD has been designed to provide a separation of pions and electrons with momenta larger than 0.5 GeV/c, based on transition radiation (TR) photons which are produced by electrons when traversing the radiator. Such photons, with typical energies between 4 and 30 keV, have a mean free path of the order of 1 cm in xenon at STP.

Nominal rejection factors for pions can be calculated in principle [2] and have also been measured experimentally with radioactive sources and with test beams for a prototype of the ALICE TRD [3], but the actual separation power will depend in a complex way on the intensity, composition and time structure of the radiation background which will be present in the real LHC environment.

To predict the characteristics of such a background, accurate Monte Carlo simulations are needed, taking into account the particles issued from the initial collision as well as their secondaries, and the interaction of the latter not only with the different parts of the experiment but also with the accelerator structure and with the concrete walls of the tunnel.

Some of the secondaries are neutrons which become thermalised by repeated scattering in the surrounding structures and after a relatively long time (typically several milliseconds) are eventually captured by a nucleus. The resulting nucleus is left in an excited state, generally about 7 or 8 MeV above the ground level, and de-excites by releasing its excitation energy as a cascade of gamma rays. These interact in turn by releasing electrons and producing a signal uncorrelated with the initial particles. Such noise, which tends to hide the signal of the particles issued directly from the collision, should be evaluated by detailed Monte Carlo calculations.

Neutron transport and (n,γ) reactions in FLUKA

In the FLUKA Monte Carlo program [4], the transport of neutrons with energies lower than 20 MeV is performed by a multi-group algorithm. In the standard FLUKA cross-section library [5], the energy range up to 20 MeV is divided into 72 energy groups of approximately equal logarithmic width, one of which is thermal. The angular probabilities for inelastic scattering are obtained by a discretisation of a P5 Legendre polynomial expansion of the actual scattering distribution which preserves its first six moments.

In general, gamma generation (but not transport) is also treated in the frame of a multi-group scheme. A so-called “downscattering matrix” provides the probability for a neutron in a given energy group, to generate a photon in each of 22 gamma energy groups, covering the range 10 keV to 20 MeV. With the exception of a few important gamma lines, such as the 2.2 MeV transition of deuterium, the actual energy of the generated photon is sampled randomly in the energy interval corresponding to its gamma group. Note that the gamma generation matrix includes not only capture gammas, but also gammas produced in other inelastic reactions such as (n,n') .

The gamma generation probabilities, as well as the neutron total and differential cross-sections, kerma factors and information on production of residual nuclei, are derived from Evaluated Nuclear Data Files, distributed by specialised centres such as the NEA Data Bank [6], RSICC [7] and the

IAEA [8], by processing them with an appropriate code [9]. Since several evaluated cross-section sets are available, with variable degrees of completeness and reliability, an effort is constantly being made to include in the FLUKA library the best data available at a particular time. Presently, the library includes about 120 different materials (elements or isotopes, in some cases with the possible choice of different molecular bindings, temperatures or degrees of self-shielding). However, while transport cross-sections are available for all materials of the library, for a few of them it has not yet been possible to find evaluated data concerning some of the complementary information (gamma production, kerma factors or residual nuclei).

As stressed above, a proper simulation of capture gammas in xenon is an essential ingredient of any background prediction for the ALICE TRD, but unfortunately gamma generation information is missing in the xenon entry of the FLUKA neutron cross-section library, since no corresponding evaluated data have been found. However, much of the basic information is available in the form of recommended level energies, published regularly in the journal *Nuclear Data Sheets* and also available on-line [10]. These recommended levels have not necessarily been identified only in (n, γ) reactions, but have also been derived from experiments on beta decay, heavy ion reactions, etc. And indeed, many of them do not play any role in neutron capture because of quantum selection rules, but in most cases it is possible to select the relevant ones by a cross check with xenon capture gamma energies reported by experimental papers and by following all the possible paths of the gamma cascade from the capture level (easily calculated by an energy-mass balance) down to the ground state. Combining all this material together, and making some reasonable physical assumption about the information which is still missing, it has been possible to write a FLUKA subroutine providing an acceptable description of Xe(n, γ) reactions.

A similar work was done some time ago to implement in FLUKA capture gammas from another important nuclide for which evaluated data were missing, ^{113}Cd . However, the approach has not been identical in the two cases. First, in the case of cadmium only the most important isotope was considered, while in the case of xenon all nine stable isotopes have been taken into account. In addition, the type of available experimental data was different for the two elements: for cadmium, in addition to level energies and relative intensities, gamma energies and absolute gamma-ray intensities (probabilities per neutron capture) were available. However, since the existence of unobserved transitions was evident from the intensity balance, a simple de-excitation model has been applied to complete the decay scheme.

Basic nuclear data for xenon

Element xenon (atomic number 54) has nine stable isotopes, with mass number 124, 126, 128, 129, 130, 131, 132, 134, 136 (^{124}Xe and ^{136}Xe are actually unstable, but with an extremely long half-life). Their abundances [11] and their nuclear masses [12] are reported in Table 1. In the same table are also reported the atomic masses* of the nuclei formed by neutron capture in those nuclei, and the respective Q-values for (n, γ) reaction, as given by the formula:

$$Q = u \left({}_{54}^A M + M_n - {}_{54}^{A+1} M \right)$$

where u is the atomic mass unit (931.494013 MeV), and M_n is the neutron mass (939.56533 MeV).

* The evaluated nuclear data refer to *atomic* masses, but internally FLUKA uses *nuclear* masses obtained by the latter by subtracting the electron masses and adding the electron binding energies.

Table 1. Masses and abundances of naturally occurring xenon isotopes, and masses of the nuclei formed by neutron capture

Xenon isotope	${}_{54}^A M$ (amu)	${}_{54}^{A+1} M$ (amu)	Abundance %
${}^{124}\text{Xe}$	123.9058958	124.9063982	0.09
${}^{126}\text{Xe}$	125.9042689	126.9051796	0.09
${}^{128}\text{Xe}$	127.9035304	128.9047795	1.92
${}^{129}\text{Xe}$	128.9047795	129.9035079	26.44
${}^{130}\text{Xe}$	129.9035079	130.9050819	4.08
${}^{131}\text{Xe}$	130.9050819	131.9041545	21.18
${}^{132}\text{Xe}$	131.9041545	132.9059057	26.89
${}^{134}\text{Xe}$	133.9053945	134.907207	10.44
${}^{136}\text{Xe}$	135.907220	136.911563	8.87

Available information on energy levels

Measured and recommended values for the energy levels of all known nuclides are reported monthly in the journal *Nuclear Data Sheets* [14]. The same data and decay schemes can be retrieved on-line from the Evaluated Nuclear Structure Data File (ENSDF) [15]. The NuDat program [10] provided by the National Nuclear Data Center (NNDC) at the Brookhaven National Laboratory allows to extract the recommended values in the form of tables which can be easily read and processed by a user program. For each level, recommended gamma energies, intensities and multiplicities are listed, as well as the level half-life and the spin and parity, when known.

These recommended levels and gamma transitions, which have been derived from a variety of nuclear reaction and decay experiments, do not include virtual excitation levels populated by neutron capture. The energy of latter is easily calculated anyway by adding the Q-value (see Table 1) and the kinetic energy of the captured neutron, but the energies and intensities of gammas emitted from the virtual levels can be obtained only from published experiments on neutron capture (all rather old in the case of xenon). Such data are reported in *Nuclear Data Sheets*, but exactly as they were published, without any evaluation of the gamma energies to make them consistent with the adopted energies of all other levels. Also, only measurements made on single isotopes are considered. Such experimental data are available for ${}^{130}\text{Xe}$ [16,17], ${}^{132}\text{Xe}$ [16,18] and ${}^{137}\text{Xe}$ [19,20] but not for the other six xenon isotopes.

With some difficulty, additional information can also be extracted from experimental data obtained with xenon of natural isotopic composition. The popular ‘‘Lone-Catalog’’ [21] is a compilation of energies and relative intensities of capture gamma rays for all elements up to $Z = 83$. For xenon, 161 gamma lines are reported. However, a comparison with presently recommended values and with the available single-isotope data mentioned above shows that the compilation cannot be considered as very reliable, despite the fact that it is still proposed as a reference by NNDC [22] (for a discussion of the quality of these data see [23]).

A much better source for xenon capture gammas is a paper by Hamada, *et al.* [24], in which 273 gamma lines are reported. The authors have assigned some of these lines to ${}^{130}\text{Xe}$ and ${}^{132}\text{Xe}$, but a systematic comparison with differences between adopted levels has allowed to assign practically each gamma line to one of the stable isotopes of xenon. Several of the gamma energies reported in [24] have also been found to correspond, within small uncertainties, to transitions from the virtual level of one of the xenon isotopes to one of the corresponding adopted levels.

Implementation in FLUKA

As can be understood from the previous survey of available data, it is impossible at the present time to establish a complete database of capture gamma lines for xenon. However, a large number of gamma lines (820) have been identified, corresponding to transitions between 335 levels. More details are given in Table 2. The implementation in FLUKA has been based on the relative branching ratios within each level, which are well established, rather than on the poorly known absolute intensities (number of gammas per capture) or even than on relative intensities over all levels. Gamma lines from a given level for which no relative intensity was reported were assumed to be equally distributed among the known branchings; when the intensity was expressed for instance as “< 80”, half of that value was assumed. In a few cases, when different transitions from the same virtual level were reported by two sources, the values were merged after a re-normalisation of intensities based on all those lines which were common to both.

Table 2. Number of xenon energy levels and gammas adopted in NuDat and implemented in FLUKA

Xenon isotope	Number of levels		Number of gammas			
	adopted in NuDat	used in FLUKA	adopted in NuDat	used in FLUKA, from:	total	
				lower levels	virtual level	
¹²⁴ Xe	234	80	633	175	24	199
¹²⁶ Xe	108	46	233	81	12	93
¹²⁸ Xe	58	28	109	45	9	54
¹²⁹ Xe	103	72	207	144	45	189
¹³⁰ Xe	43	19	66	24	6	30
¹³¹ Xe	75	30	200	87	18	105
¹³² Xe	29	13	56	24	4	28
¹³⁴ Xe	29	15	86	38	3	41
¹³⁶ Xe	164	32	213	53	28	81

The resulting database does not explicitly include gamma energies, but only level energies and, for each level, the possible transitions to lower levels with the respective cumulative probabilities. In this way, each gamma energy is obtained by the difference between its starting and ending level, and exactly the same total gamma energy is emitted for any possible path of the gamma cascade from the virtual to the ground level. Energy conservation on a more global level is ensured by calculating the recoil of the nucleus in the laboratory frame, based on an accurate balance of all masses concerned. The photon emission is assumed to be isotropic.

Of course, several approximations have been necessary. While the energy of the virtual level is calculated correctly taking into account the kinetic energy of the captured neutron, it has been assumed that the possible transitions and their relative intensities do not depend on the neutron energy. This assumption is unlikely to be valid for energies at which the reaction proceeds predominantly through p-wave capture, but a rigorous analysis to identify these energies has not been made. First of all, there is no sufficient experimental or theoretical information which would allow to establish different transitions and intensities. On the contrary, some of the published gamma transitions we have used were not obtained at thermal energies but at some resonance energy [17,18], because this is the simplest way to study transitions in an individual isotope. But even if such information did exist, its implementation in FLUKA should take into account a different situation for each of the nine xenon isotopes, making the database and the dedicated routine exceedingly complex. Also, it could be possible to avoid the problem by implementing gamma production only for thermal neutrons and epithermals

with energies lower than any resonance, but it has been judged better to produce some gammas with the wrong energy or probability rather than producing none at all: at least, the total excitation energy will be correctly accounted for as gamma radiation and the overall energetic balance will be satisfied.

On the other hand, the implementation would be too grossly incorrect – or too complicated to do correctly – if it also extended above the threshold for inelastic neutron scattering. Therefore, an upper limit of 39 keV (isotope-independent for the sake of simplicity) has been set for the energy of any neutron which can be captured in with gamma emission in xenon. Table 3 shows the different thresholds for (n,n') reaction in xenon isotopes, obtained from the ENDF/B-VI evaluated file [13].

Table 3. Q-values for neutron inelastic scattering in the natural xenon isotopes

Xenon isotope	Q (MeV)	Nuclide ${}_{54}^A\text{Xe}$	Q (MeV)	Nuclide ${}_{54}^A\text{Xe}$	Q (MeV)
${}^{124}\text{Xe}$	-0.357	${}^{129}\text{Xe}$	-0.040	${}^{132}\text{Xe}$	-0.668
${}^{126}\text{Xe}$	-0.389	${}^{130}\text{Xe}$	-0.536	${}^{134}\text{Xe}$	-0.847
${}^{128}\text{Xe}$	-0.443	${}^{131}\text{Xe}$	-0.080	${}^{136}\text{Xe}$	-1.313

It is also possible, as was found in the case of cadmium, that not all transitions from the virtual level have been identified. However, too little information is available for xenon concerning absolute gamma emission probabilities. Therefore, no attempt has been made at filling gaps of unknown size.

Discussion

Despite the approximations which have been described above, the new FLUKA description of capture gammas from neutron capture in xenon should provide better results than the default multi-group description used for most FLUKA materials. The energy of each photon is determined as the exact difference between two energy levels, instead of being sampled randomly in a certain energy interval; but – even more important – the correlations between photons emitted by the same excited nucleus will be correctly reproduced in most cases. This should be of particular interest for the simulation of the high-energy physics detector which has triggered this work.

Extensions of the present approach to other nuclides are possible, provided that good data on the transitions from the virtual levels be available. Otherwise, it will be necessary to derive them from a physical model, similar to what has been done for ${}^{113}\text{Cd}$. However, if the number of nuclides considered should increase beyond a certain limit, it could be preferable in the future to read the level data from an external data file, rather than having them hard-wired in a routine specific for each element.

By following each possible sequence of level transitions and compounding the product of their respective probabilities with the abundance and with the relative capture cross-section of the isotope concerned, it is possible to calculate an absolute intensity for each gamma produced. The 689 gamma energies having an intensity larger than 10^{-3} per 100 neutron captures are reported in an ALICE Internal Note [25]. Here the 28 most intense ones are shown in Table 4.

Figure 2 shows a gamma line spectrum obtained in a stand-alone test of the new FLUKA routine which generates capture gammas in xenon. The input neutron energies were randomly sampled from a Maxwellian distribution in the energy range 10^{-5} to 0.4 eV, corresponding to the thermal neutron group of FLUKA, and the target nucleus was sampled according both to its abundance and to its thermal neutron capture cross-section. As it can be expected from Table 4, the most frequent lines belong to ${}^{132}\text{Xe}$ (667.72, 772.60, 1317.93 and 6466.07 keV, the latter corresponding to a transition from the capture level). The 536.09 keV line is from ${}^{130}\text{Xe}$.

Table 4. Number of gammas per 100 thermal neutron captures in nat Xe

Xenon isotope	Gamma energy (keV)	From level (keV)	To level (keV)	I_γ per 100 captures
^{132}Xe	667.72	667.72	0.0	64.73
^{132}Xe	6 466.1	8 935.2	2 469.1	24.07
^{132}Xe	772.61	1 440.3	667.72	22.55
^{130}Xe	536.09	536.09	0.0	16.60
^{132}Xe	1 317.9	1 985.7	667.72	15.88
^{132}Xe	6 379.8	8 935.2	2 555.4	10.66
^{130}Xe	668.52	1 204.6	536.09	10.25
^{132}Xe	483.46	2 469.1	1 985.7	9.824
^{132}Xe	600.03	2 040.4	1 440.3	8.355
^{132}Xe	5 754.4	8 935.2	3 180.8	7.847
^{132}Xe	569.75	2 555.4	1 985.7	7.196
^{132}Xe	1 028.8	2 469.1	1 440.3	6.778
^{132}Xe	1 887.7	2 555.4	667.72	6.404
^{125}Xe	111.78	111.78	0.0	6.344
^{132}Xe	1 140.4	3 180.8	2 040.4	6.278
^{130}Xe	739.48	1 944.1	1 204.6	5.859
^{132}Xe	5 142.9	8 935.2	3 792.3	5.783
^{132}Xe	1 801.4	2 469.1	667.72	5.501
^{130}Xe	752.79	2 696.9	1 944.1	5.344
^{130}Xe	275.45	2 972.3	2 696.9	5.225
^{130}Xe	720.84	3 693.2	2 972.3	4.921
^{125}Xe	140.82	252.60	111.78	4.608
^{132}Xe	630.20	1 297.9	667.72	4.384
^{132}Xe	8 267.5	8 935.2	667.72	4.323
^{132}Xe	5 235.7	8 935.2	3 699.5	4.186
^{130}Xe	854.99	2 059.6	1 204.6	3.992
^{125}Xe	57.940	310.54	252.60	3.917
^{130}Xe	315.60	2 375.2	2 059.6	3.666

A test of the new routine has been done also with a FLUKA run in an idealised geometry: an isotropic 0.025 eV neutron point source in the middle of an “infinite” cube of xenon. Figure 2 shows the calculated track length of photons as a function of photon energy. Comparing this spectrum with that of Figure 1, the following differences can be noticed:

- The presence of a high 511 keV peak, due to positron annihilation.
- A progressive decrease of the gamma line intensity with decreasing energy, due to increasing absorption by photoelectric effect.
- A broad Compton background, hiding most of the lower energy lines.

Real situations should be more complex, of course, since neutron capture in surrounding structural materials would provide additional gammas of different energies and would probably even be dominant. But, due to the high energy of most capture gammas and to their ability to create electron pairs, the largest contribution can still be expected to be that of the annihilation peak.

Figure 1. Gamma lines generated in 10^7 neutron captures in xenon

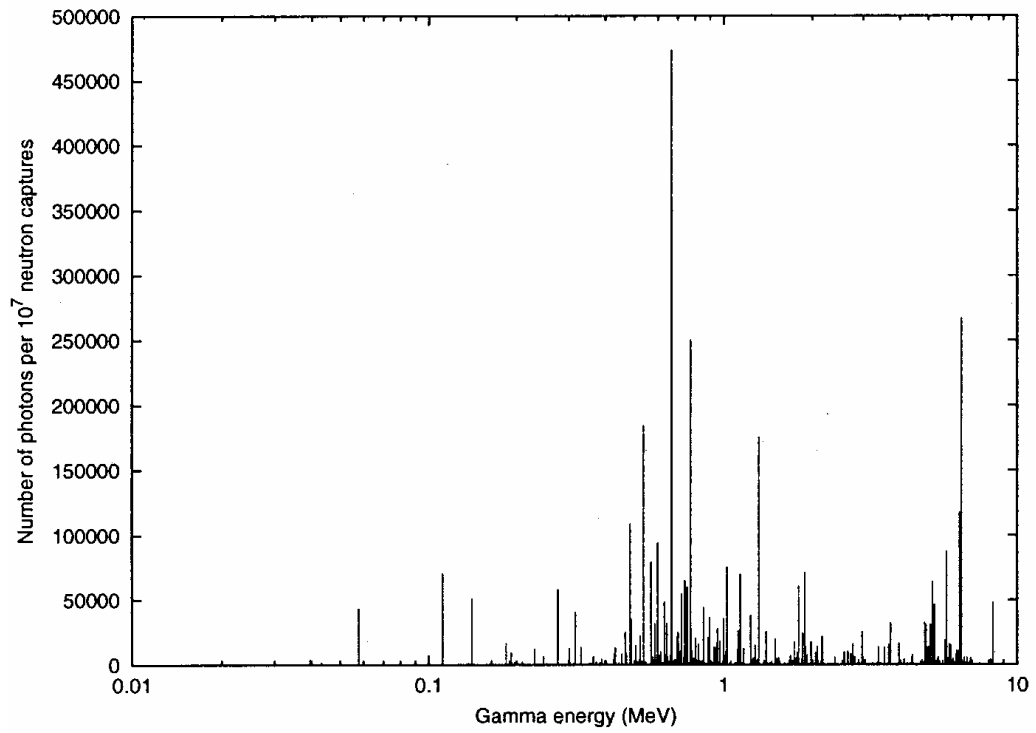
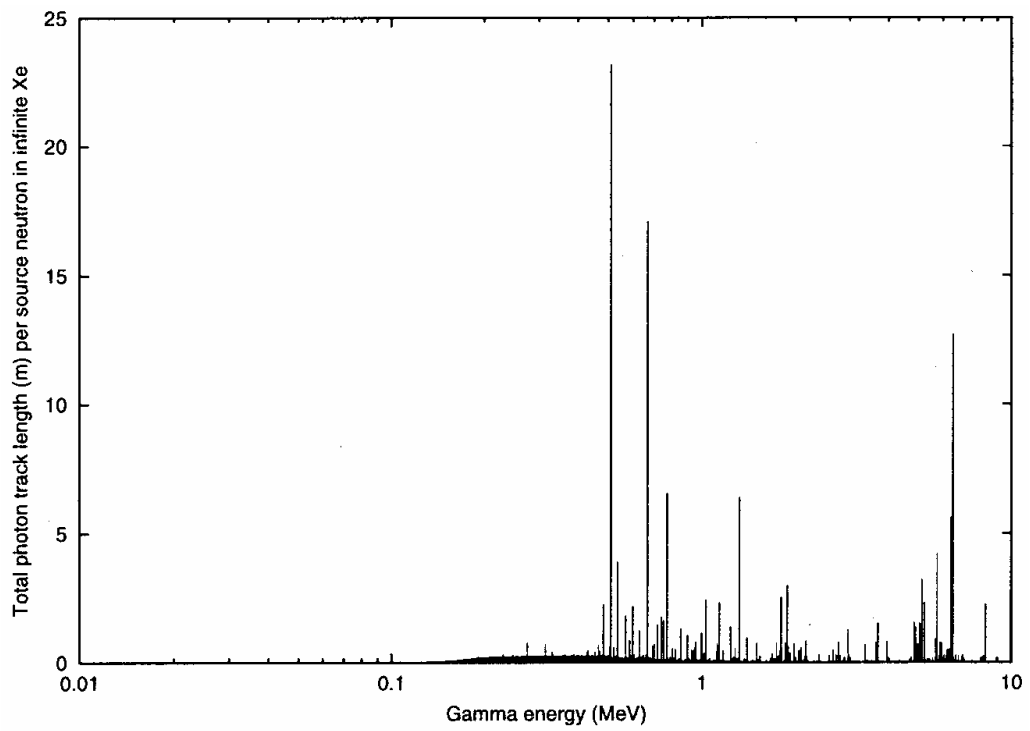


Figure 2. Photon track length spectrum calculated by FLUKA for a thermal neutron source in an infinite xenon volume



REFERENCES

- [1] *A Transition Radiation Detector for Electron Identification with the ALICE Central Detector*, Addendum to ALICE Proposal, CERN/LHCC 99-13, LHCC/P3-Addendum 2, 7 May 1999.
- [2] Mazziotta, M.N., “A Monte Carlo Code for Full Simulation of a Transition Radiation Detector”, *Comp. Phys. Comm.*, 132, 110 (2000).
- [3] Andronic, A., *et al.*, “Prototype Tests for the ALICE TRD”, *IEEE Nuclear Science Symposium and Medical Imaging Conference*, Lyon, France, 15-20 Oct. 2000, ALICE-PUB-2000-034 (2001).
- [4] Ferrari, A., J. Ranft and P.R. Sala, “The FLUKA Radiation Transport Code and its Use for Space Problems”, *Physica Medica*, XVII, Suppl. 1, 72-80 (2001).

Fassò, A., A. Ferrari, J. Ranft and P.R. Sala, “FLUKA: Status and Prospective for Hadronic Applications”, *Monte Carlo 2000 Conference*, Lisbon, 23-26 Oct. 2000, proceedings in press.

Fassò, A., A. Ferrari, P.R. Sala, “Electron-photon Transport in FLUKA: Status”, *Monte Carlo 2000 Conference*, Lisbon, 23-26 Oct. 2000, proceedings in press
- [5] Cuccoli, E., A. Ferrari and G.C. Panini, *A Group Library from JEF-1.1 for Flux Calculations in the LHC Machine Detectors*, JEF-DOC-340 (91) (1991).
- [6] <http://www.nea.fr/html/databank/>.
- [7] <http://www-rsicc.ornl.gov/rsic.html>.
- [8] <http://www-nds.iaea.or.at/>.
- [9] <http://t2.lanl.gov/codes/>.
- [10] <http://www.nndc.bnl.gov/nndc/nudat/>.
- [11] Rosman, K.J.R. and P.D.P. Taylor, “Isotopic Composition of the Elements 1997”, *J. Phys. Chem. Ref. Data*, 27, 1275 (1998).
- [12] Audi, G. and A.H. Wapstra, “The 1995 Update to the Atomic Mass Evaluation”, *Nucl. Phys. A*595, 409 (1995), <http://wwwndc.tokai.jaeri.go.jp/NuC/index.html>.
- [13] <http://t2.lanl.gov/cgi-bin/nuclides/endind>.
- [14] Academic Press, New York.
- [15] <http://www.nndc.bnl.gov/nndc/ensdf/ensdfindex.html>.

- [16] Groshev, L.V., L.I. Govor, A.M. Demidov and A.S. Rakhimov, “Spectra of γ Rays and Level Schemes of ^{130}Xe and ^{132}Xe from the reaction (n,γ) ”, *Yad. Fiz.*, 13, 1129 (1971), also *Sov. J. Nucl. Phys.*, 13, 647 (1971).
- [17] Gelletly, W., W.R. Kane and D.R. MacKenzie, “Neutron-capture Gamma Rays from the 9.47-eV Resonance in $^{129}\text{Xe}(n,\gamma)^{130}\text{Xe}$ ”, *Phys. Rev.*, C9, 2363 (1974).
- [18] Gelletly, W., W.R. Kane and D.R. MacKenzie, “Neutron-capture Gamma Rays from the 14.1-eV Resonance in $^{131}\text{Xe}(n,\gamma)^{132}\text{Xe}$ ”, *Phys. Rev.*, C3, 1678 (1971).
- [19] Fogelberg, B. and W. Mampe, “Determination of the Neutron Binding Energy of the Delayed Neutron Emitter ^{137}Xe ”, *Z. Phys.*, A281, 89 (1977).
- [20] Prussin, S.G., R.G. Lanier, G.L. Struble, L.G. Mann and S.M. Schoenung, “Gamma Rays from Thermal Neutron Capture in ^{136}Xe ”, *Phys. Rev.*, C3, 1001 (1977).
- [21] Lone, M.A., R.A. Leavitt and D.A. Harrison, “Prompt Gamma Rays from Thermal-neutron Capture”, *Atomic Data and Nuclear Data Tables*, 26, 511 (1981).
- [22] Tuli, J.K., *Thermal Neutron Capture Gamma Rays*, can be found at the following address: <http://www-nds.iaea.or.at/wallet/tnc/capgam.shtml>.
- [23] Molnár, G.L., Zs. Révay, T. Belgya and R.B. Firestone, “The New Prompt Gamma-ray Catalogue for PGAA”, *Appl. Rad. Isot.*, 53, 527 (2000).
- [24] Hamada, S.A., W.D. Hamilton and B. Moer, “Gamma-gamma Directional Correlation Measurements in $^{130,132}\text{Xe}$ Following Neutron Capture by Natural Xenon”, *J. Phys.*, G14, 1237 (1988).
- [25] Fassò, A., A. Ferrari, P.R. Sala and G. Tsileidakis, CERN ALICE-INT-2001-28 (2001).

STATUS OF MARS CODE

Nikolai V. Mokhov

Fermi National Accelerator Laboratory
P.O. Box 500, Batavia, Illinois 60510, USA

Abstract

Status and recent developments of the MARS14 Monte Carlo code system for simulation of hadronic and electromagnetic cascades in shielding, accelerator and detector components in the energy range from a fraction of an electronvolt up to 100 TeV are described. These include physics models both in strong and electromagnetic interaction sectors, variance reduction techniques, residual dose, geometry, tracking, histogramming, MAD-MARS Beam Line Builder and Graphical-User Interface. The code is supported world-wide; for more information consult <http://www-ap.fnal.gov/MARS/> and MARS discussion list *mars-forum@fnal.gov*.

Introduction

The MARS code system is a set of Monte Carlo programs for detailed simulation of hadronic and electromagnetic cascades in an arbitrary 3-D geometry of shielding, accelerator and detector components with energy ranging from a fraction of an electronvolt up to 100 TeV. The current MARS14 version [1] combines the well established theoretical models for strong, weak and electromagnetic interactions of hadrons and leptons with a system which can contain up to 105 objects, ranging in dimensions from microns to hundreds of kilometres, made of up to 100 composite materials, with arbitrary 3-D magnetic and electric fields, and a powerful user-friendly graphical-user interface for visualisation of the geometry, materials, fields, particle trajectories and results of calculations. The code has been under development since 1974 at IHEP, SSCL and Fermilab.

In an inclusive mode, the code is capable of fast cascade simulations even at very high energies. MARS tabulates the particles which pass through various portions of the geometry (which can be very simple to very complex), and produces results on particle fluxes, spectra, energy deposition, material activation and many other quantities. The results are presented in tables, histograms and other specialised formats. The system also includes physics of the MCNP code for low-energy neutron transport, and interfaces to ANSYS for thermal and stress analyses, MAD for accelerator and beam-line lattice description and STRUCT for multi-turn particle tracking in accelerators. Various biasing and other variance reduction techniques are implemented in the code. MARS14 allows the user extensive control over the simulation's physics processes, tabulation criteria and runtime optimisations via a wide variety of options and switches implemented from an input file, and via the provided customisable user subroutines.

The code is used in numerous applications world-wide (US, Japan, Europe, Russia) at existing accelerator facilities, in planned experiments and accelerator projects (pp , e^+e^- and $\mu^+\mu^-$ colliders and detectors, kaon and neutrino fixed target experiments, neutrino factories, spallation neutron sources, etc.) and in cosmic ray physics. Its reliability has been demonstrated in many benchmark studies. Physics models, geometry, tracking algorithms, graphical-user interface (GUI) and other details of the MARS14 code are described in Ref. [1]. Here we highlight the most recent developments to the current version which further increase the code reliability, applicability and user friendliness.

Physics model

Event generator

Hadron and photonuclear interactions at $1 \text{ MeV} < E_0 < 2 \text{ GeV}$ are done via full exclusive simulation with the latest version of the Cascade-exciton Model CEM [2]. Inclusive particle production via a set of improved phenomenological models is used as a default for hA and γA interactions at $5 \text{ GeV} < E_0 < 100 \text{ TeV}$, dA at $20 \text{ MeV} < E_0 < 50 \text{ GeV}$ and νA at $0.1 \text{ GeV} < E_0 < 100 \text{ TeV}$. A model which combines both of the above approaches is used at $2 \text{ GeV} < E_0 < 5 \text{ GeV}$ for a smooth transition between high and low energy regions. Figure 1 shows the calculated pion spectra in comparison with recent BNL data. In exclusive mode, the latest version DPMJET-III of the Dual Parton Model [3] can be used for full event generation of a first nuclear collision hA , AA , γA and νA at $E_0 > 5 \text{ GeV}$. In the same manner, the LAQGSM code based on the Quark-gluon String Model [4] has recently been implemented into MARS at $E_0 < 100 \text{ GeV}$ and successfully used for the first time as described in Ref. [5]. Nuclide production simulation has been added to the code. Antiproton annihilation algorithms have been substantially improved in MARS14.

Figure 1. π^- in pBe at 12.3 GeV/c (left) and in pAu at 17.5 GeV/c (right) as calculated with MARS14 (histogram) and measured in the BNL E-910 (symbols)

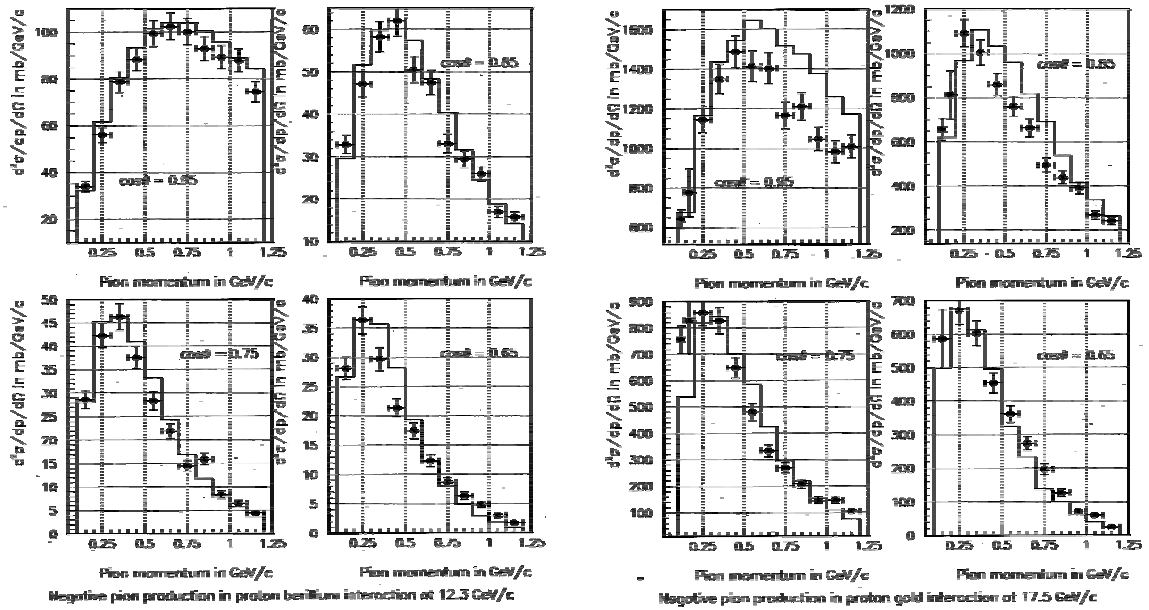


Figure 2. Calculated and measured neutron elastic scattering distributions on carbon (left) and copper (right) nuclei

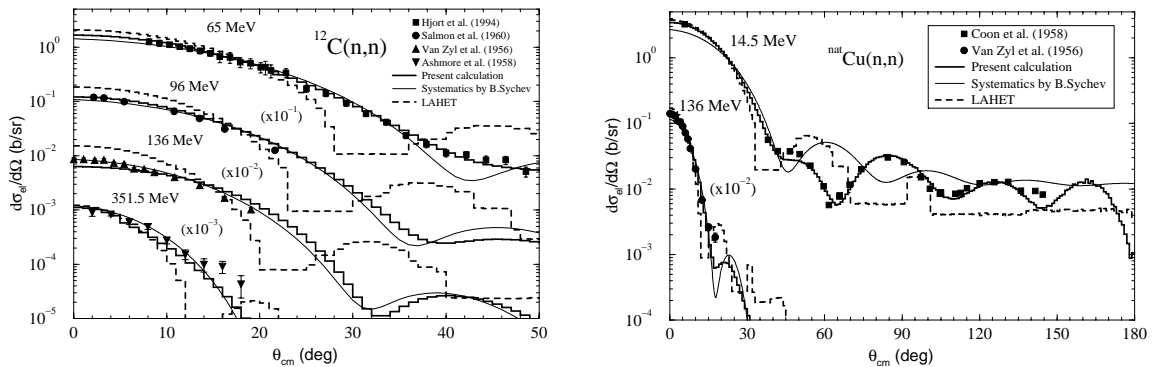
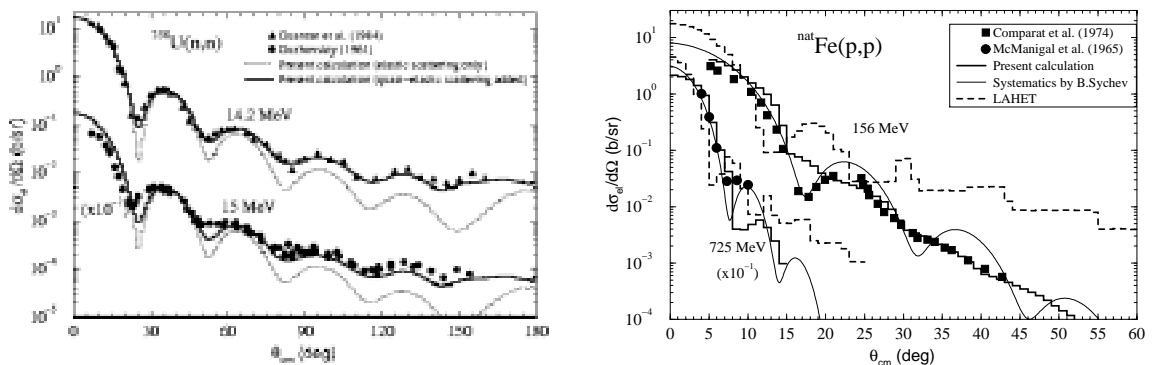


Figure 3. Calculated and measured elastic scattering distributions for neutrons on uranium (left) and protons on iron (right)



Elastic scattering

The MARS14 elastic model at $E < 5$ GeV is based on evaluator nuclear data from the LA-150 and ENDF/HE-VI libraries [6] and Ref. [7,8], supplied with phenomenology where needed [9]. For protons, nuclear and Coulomb elastic scattering as well as their interference are taken into account. At $E < 5$ GeV, a simple analytical description used in the code for both coherent and incoherent components of $d\sigma/dt$ is quite consistent with experiment.

Interface to MCNP

Once the energy of neutrons falls below 14 MeV, all subsequent neutron interactions are described using the appropriate MCNP4C2 [10] subroutine modules. Secondaries generated at this stage by neutrons – protons, photons and deuterons – are directed back to the MARS modules for a corresponding treatment. This implementation, along with algorithms developed for heavier recoils and photons from the thermal neutron capture on ${}^6\text{Li}$ and ${}^{10}\text{B}$, allows the detailed description of corresponding effects in hydrogenous, borated and lithium-loaded materials. The interface includes several other modifications to the dynamically allocated storage, material handling, optional writing of low-energy neutrons and other particles to a file for further treatment by a stand-alone MCNP code and MCNP geometry description (see below).

Coulomb scattering

Since 1985 multiple Coulomb scattering was modelled in MARS from the Moliere distribution with the Gaussian nuclear form-factor included. Just recently, a new algorithm was developed and implemented into MARS14. It provides about a per cent accuracy for step sizes ranging from a few collisions to thousands of radiation lengths in arbitrary mixtures, taking into account nuclear screening with an arbitrary form-factor. The algorithm is based on splitting scattering into “soft” and “hard” parts with a cut-off angle θ_{max} calculated automatically depending on the step size and other input parameters. A “soft” small-angle distribution is sampled from a near-Gaussian asymptotic, while “hard” discrete collisions ($0 \leq N_{disc} \leq 20$, $\langle N_{disc} \rangle \sim 1$) are sampled from a single scattering differential cross-section.

Variance reduction

Many processes in MARS14, such as electromagnetic showers, most of the hadron-nucleus interactions, decays of unstable particles, emission of synchrotron photons, photohadron production and muon pair production, can be treated either analogously or inclusively with corresponding statistical weights. The choice of method is left for the user to decide, via the input settings. Other variance reduction techniques are used in the code: weight-window, splitting and Russian roulette, exponential transformation, probability scoring, step/energy cut-offs. Depending on a problem, these techniques are thoroughly utilised in the code to maximise computing efficiency, which is proportional to t_0/t . Here t is CPU time needed to get a RMS error σ equal to the one the reference method with CPU time t_0 , provided $\sigma \leq 20\text{-}30\%$. An example of one history for a 1-GeV positron on a 2-cm tungsten target calculated in MARS14 in exclusive and leading particle biasing modes is given in Figure 4. It was found empirically that the biasing scheme for hA vertex shown in Figure 5 and used in the code for years, provides the highest efficiency ε detector, accelerator and shielding applications. Here a fixed number and types of secondaries are generated with the appropriate statistical weights.

Figure 4. 1-GeV positron on 2-cm tungsten target: one history simulated in exclusive mode (left) and leading particle biasing mode (right)

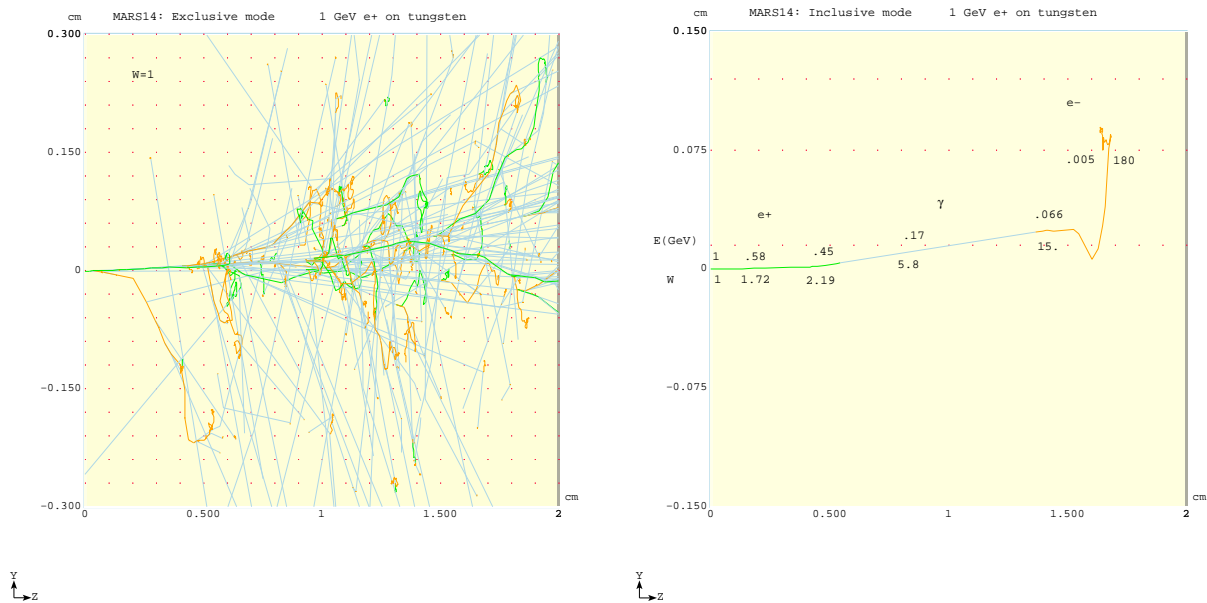
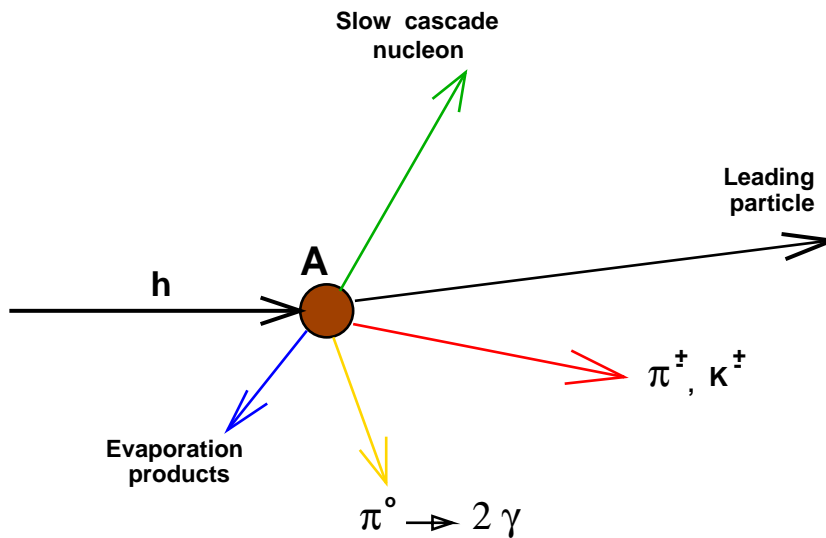


Figure 5. MARS inclusive nuclear interaction vertex

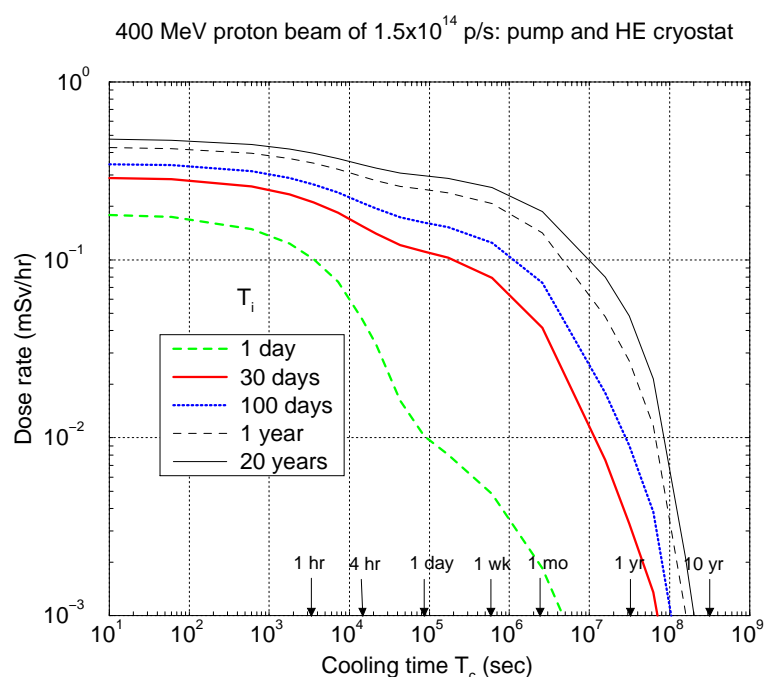


Residual dose

A substantially improved ω -factor based algorithm [11] to calculate residual dose rates in arbitrary composite materials for arbitrary irradiation and cooling times was developed and implemented into the code. The algorithm distinguishes three major energy groups responsible for radionuclide production: (1) above 20 MeV, (2) 1 to 20 MeV and (3) below 0.5 eV. The energy groups are chosen to consider separately the most important nuclear reactions responsible for induced radioactivation in the regions: high-energy inelastic interactions (mostly spallation reactions), threshold reactions ($n,2n$), (n,p), etc., and (n,γ) reactions, respectively. Neutrons in the energy region from 0.5 eV to 1 MeV do

not produce a significant number of radionuclides. Creation of the residual nuclides was pre-calculated with a version [12] of the FLUKA code for cascades induced by energetic hadrons in cylindrical samples of 17 elements: C, O, Na, Mg, Al, Si, K, Ca, Cr, Fe, Ni, Cu, Nb, Ag, Ba, W, Pb. The decay chains of the created radionuclides were followed with the DETRA code in order to determine the emission rates of de-excitation photons for irradiation time $12 \text{ hours} < T_i < 20 \text{ years}$ and cooling time $1 \text{ sec} < T_c < 20 \text{ years}$. Corresponding dose rates on the outer surfaces were calculated from photon fluxes and related to the star density above 20 MeV (first group), and neutron fluxes in two other group). Results were collected in a database, that – along with a sophisticated interpolation algorithm linked to this database – was implemented into MARS14. An example of residual dose calculation for a pump and cryostat of the Fermilab MUCOOL experiment for a 400-MeV proton beam at $1.5 \times 10^{14} \text{ p/s}$ is shown in Figure 6.

Figure 6. Example of MARS14 residual dose calculation in the Fermilab MUCOOL experiment

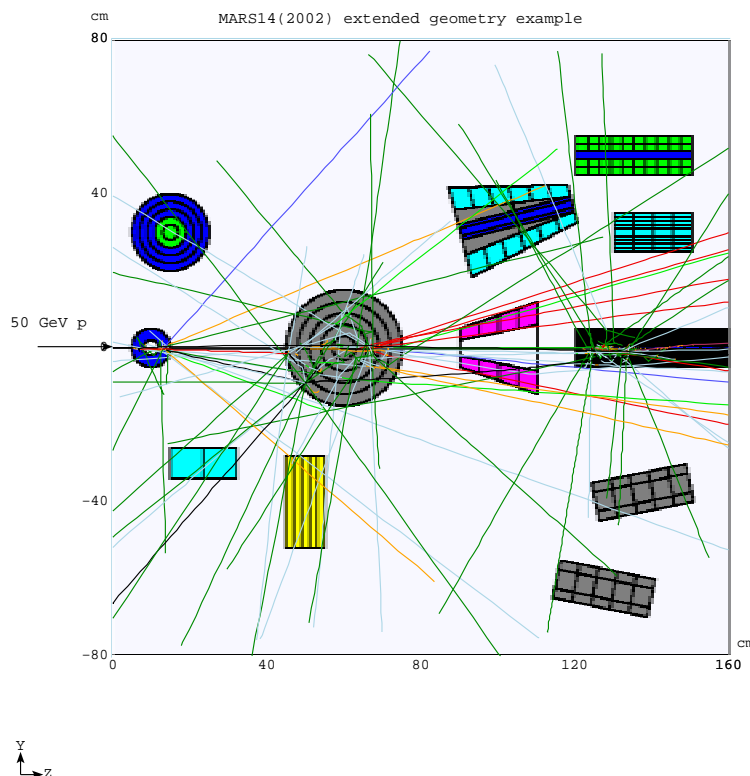


Geometry

Volumes of *non-standard* regions in MARS14 can now be calculated in a short Monte Carlo session. A corresponding output file provides calculated volumes with statistical errors, global and non-standard region numbers, and is directly linked to the main code.

In addition to widely used *Standard* and *Non-standard* geometries in MARS14, a drastically improved *Extended Geometry* option is now available in the code. *Extended* zones are constructed from a set of contiguous or overlapping geometrical shapes, currently, boxes, spheres, cylinders, and truncated cones and tetrahedrons. A variety of new features, such as up to 100 000 extended volumes, subdivision of volumes into subregions, up to 500 arbitrary transformation matrices, etc., are there. There is no worry now about missing a small object in a large mother volume. Figure 7 shows an example of an extended geometry set-up with particle tracks induced by a 50-GeV proton.

Figure 7. An example of MARS14 extended geometry with particle tracks



A new fourth geometry option is now available in MARS14, *MCNP*. A MCNP geometry description can now be put in the MCNP section of the MARS.INP input file and used directly by the MARS14 code. The MCNP community interested in high-energy applications can now use MARS14 with their MCNP geometry packages.

Materials, tracking and histograming

There are 135 built-in materials in MARS14 plus arbitrary user-defined compounds. A maximum of 100 materials can be used within any simulation. A material can be declared multiple times in the input file, so that different step-size or energy thresholds can be applied to the same material. This feature allows noticeable improvement of both a CPU performance and physics description accuracy in the regions of interest. The precise treatment of individual elements in mixtures and compounds defined through the weight or atomic fractions is done for all the electromagnetic and nuclear elastic and inelastic processes. The appropriate parameters for particle transport in arbitrary magnetic fields are chosen automatically, providing extremely high accuracy of tracking. The phase-space/geometry tagging module was further improved. A *Global Shielding* parameter set was added to the code allowing substantial CPU time savings for a “deep penetration” problem and other cases with thick extended shieldings. A variety of built-in and user-defined histograming was further extended. Recently, a possibility for histograming with a histogram origin that follows the curvature of beam lines and accelerator arcs (see next section) was added to MARS14.

MAD-MARS beam line builder

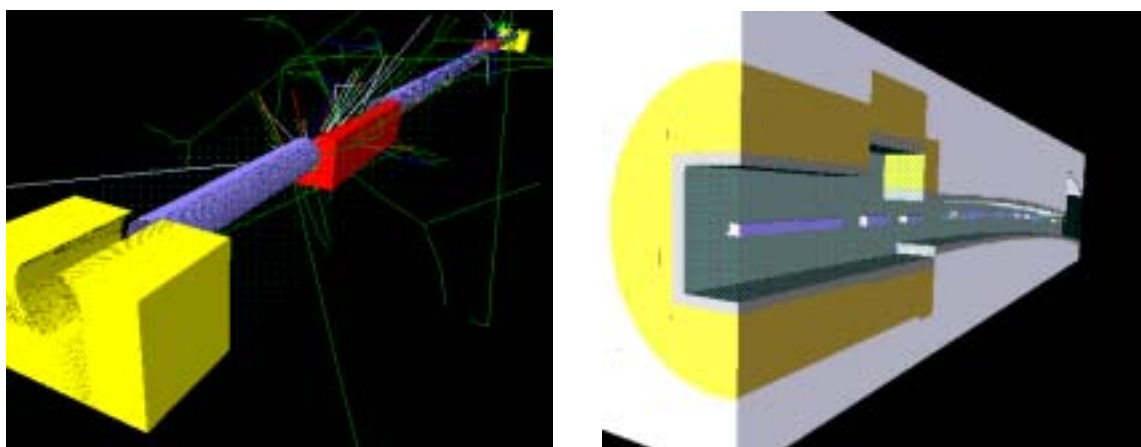
A further developed interface system – MAD-MARS Beam Line Builder (MMBLB) – reads a MAD lattice file and puts the elements in the same order into MARS geometry. Each element is assigned six functions which provide information about the element type/name, geometry, materials, field, volume and initialisation. The user specifies the element type and an optional element name. A building algorithm first tries to match the type/name pair and then substitutes a generic element if needed. Once an element is described, it is registered with the system and its name is bound with the respective geometry, materials, volume and field descriptions. For each region search during tracking, MMBLB finds the corresponding type/name pair and calls its appropriate functions. MMBLB calculates a local rotation matrix R_i and a local translation vector L_i . Then a global rotation matrix M_i and a position P_i are calculated and stored for each element.

Graphical-user interface

The graphical-user interface, MARS-GUI-SLICE was further developed. It is based on *Tcl/Tk* and is linked in to the user's executable. The interface displays all the details of the encoded geometry, showing the encoded zone numbers, materials and magnetic fields; it is a valuable tool for checking complex geometries before executing event generation. Arbitrary 3-D rotation of a slice is possible. During event generation runs, the user can specify output files holding histograms and particle tracks; these output files can be opened by the GUI interface, post-run and projected onto the visual display of the geometry.

A new three-dimensional visualisation engine has recently been developed [13] for the MARS14 code. It further extends the power of visualisation adding a crucial (in many instances) three-dimensional view of the system studied. It is based on the OPENINVENTOR graphics library, integrated with MARS-GUI-SLICE and uses a sophisticated optimisation algorithm developed for arbitrary *non-standard* geometry in MARS. Figure 8 presents two recent examples at Fermilab Booster and NuMI created with this new powerful tool.

Figure 8. Details of the Fermilab Booster collimation section with “L” shaped collimators and particle tracks (left) and a fragment of the NuMI beam line and tunnel (right)



Acknowledgements

Thanks to K. Gudima, M. Huhtinen, C. James, M. Kostin, O. Krivosheev, S. Mashnik, I. Rakhno, J. Ranft, S. Roesler, J. Rzepecki, S. Striganov, I. Tropin, A. Wehmann for collaboration and useful discussions.

REFERENCES

- [1] Mokhov, N.V., *The MARS Code System User's Guide*, Fermilab-FN-628 (1995); Mokhov, N.V., O.E. Krivosheev, "MARS Code Status", *Proc. Monte Carlo 2000 Conf.*, p. 943, Lisbon, 23-26 October 2000; Fermilab-Conf-00/181 (2000); <http://www-ap.fnal.gov/MARS/>.
- [2] Mashnik, S.G., A.J. Sierk, "CEM2k – Recent Developments in CEM", *Proc. AccApp00*, Washington DC, USA, pp. 328–341, La Grange Park, IL, USA, 2001 (nucl-th/00116); Mashnik, S.G., A.J. Sierk, "Recent Developments of the Cascade-exciton Model of Nuclear Reactions", *Proc. ND2001*, Tsukuba, Japan, *J. Nucl. Sci. Techn.*, Supplement 2, 720-725, 2002; Eprint: *nucl-th/0208074*.
- [3] Ranft, J., "Dual Parton Model at Cosmic Ray Energies", *Phys. Rev.*, D51, 64-85 (1995); Gran Sasso Report INFN/AE-97/45 (1997); Roesler, S., R. Engel, J. Ranft, "The Monte Carlo Event Generator DPMJET-III", *Proc. Monte Carlo 2000 Conf.*, p. 1033, Lisbon, 23-26 Oct. 2000; Roesler, S., R. Engel, J. Ranft, "The Event Generator DPMJET-III at Cosmic Ray Energies", *Proc. ICRC-2011 Conference*, 439, Copernicus Gesellschaft (2001).
- [4] Gudima, K.K., S.G. Mashnik, A.J. Sierk, *User Manual for the Code LAQGSM*, Los Alamos National Report LA-UR-01-6804 (2001).
- [5] Cossairt, J.D., N.V. Mokhov, *Assessment of the Prompt Radiation Hazards of Trapped Antiprotons*, Fermilab-Pub-02/043-E-REV (2002).
- [6] Chadwick, M.B., P.G. Young, S. Chiba, *et al.*, "Cross-section Evaluations to 150 MeV for Accelerator-driven Systems and Implementation in MCNPX", *Nucl. Sci. Eng.*, 131, 293 (1999).
- [7] Chiba, S., O. Iwamoto, E.Sh. Sukhovitski, *et al.*, "Coupled-channels Optical Potential for Interaction of Nucleons with ^{12}C up to 150 MeV in Soft-rotator Model", *J. of Nuclear Science and Technology*, 37, 498 (2000).
- [8] Sukhovitski, E.Sh., Y-O. Lee, J. Chang, *et al.*, "Nucleon Interaction with ^{58}Ni up to 150 MeV Studied in the Coupled-channels Approach Based on the Soft-rotator Nuclear Structure Model", *Phys. Rev. C*, 62, 044605-1 (2000).

- [9] Rakhno, I.L., N.V. Mokhov, E. Sukhovitski, S. Chiba, “Simulation of Nucleon Elastic Scattering in the MARS14 Code System”, *Proc. of the ANS Topical Meeting on Accelerator Applications/ Accelerator-driven Transmutation Technology Applications, AccApp/ADTTA’01*, Reno, Nevada, 11-15 Nov. 2001, Ominpress CD ROM (2002), ISBN: 0-89448-666-7; Fermilab-Conf-01/343-T (2001).
- [10] *MCNP – A General Monte Carlo N-particle Transport Code*, Version 4A, J.F. Briesmeister, ed., pub. LA-12625-M, LANL (1993).
- [11] Rakhno, I.L., N.V. Mokhov, A. Elwyn, N. Grossman, M. Huhtinen, L. Nicolas, “Benchmarking Residual Dose Rates in a NuMI-like Environment”, in Ref. [9]; Fermilab-Conf-01/304-E (2001).
- [12] Aarnio, P., *et al.*, CERN/TIS-RP/93-10; Fassò, A., *et al.*, *Proc. IV Int. Conf. on Calorimetry in High Energy Physics*, La Biodola, 20-25 Sept 1993, A. Menzione and A. Scribano, eds., World Scientific, p. 493 (1993); Fassò, A., *et al.*, *Proc. Specialists Meeting on Shielding Aspects of Accelerators, Targets and Irradiation Facilities (SATIF)*, Arlington, Texas, 28-29 April 1994, NEA/OECD doc., p. 287 (1995).
- [13] Rzepecki, J.P., M.A. Kostin, N.V. Mokhov, *3-D Visualization for the MARS14 Code*, Fermilab-TM-2197 (2003).

SESSION VI

**Shielding in Medical
Accelerator Applications**

Chairs: J.C. Liu, P. Vaz

PRINCIPLE OF RADIOLOGICAL SHIELDING OF MEDICAL CYCLOTRONS

Bhaskar Mukherjee

Safety Division, Australian Nuclear Science and Technology Organisation (ANSTO)

PMB 1, Menai, NSW 2234, Australia

E-mail: mukherjee@ieee.org

Abstract

Medical cyclotrons are primarily used to produce high yields of short half-life, neutron deficient radioisotopes for diagnostic nuclear medicine. Modern medical cyclotrons are predominantly installed in urban hospitals or specialist clinics, and usually accelerate low energy H^- (10-17 MeV) and d^- (3-8 MeV) ions to a high beam current level ($\sim 100 \mu A$). During routine operation of such cyclotrons, intense parasitic neutron and gamma radiation fields are generated and thereby increase the risk of radiological hazards to patients and members of the public. This report reviews the principle of shielding calculation methods for medical cyclotrons. The practical aspects of optimised shielding thickness calculations of the cyclotron containment and properties of some common shielding materials are also presented.

Introduction

Efficient radiation shielding is vitally important for safe operation of modern hospital-based medical cyclotrons producing large activities of short-lived radioisotopes [1]. These radioisotopes are generally used as the main ingredients to manufacture dedicated radiopharmaceuticals for positron emission tomography (PET) scanning. The list of common PET radiopharmaceuticals produced by a medical cyclotron is presented in Table 1. During routine operation of a medical cyclotron, selected target materials encapsulated in small chambers are bombarded with an intense beam (up to 100 μ A) of 10-17 MeV protons or 3-8 MeV deuterons. Strong fields of prompt fast neutrons and gamma rays are produced as a result of the nuclear reactions, which take place when the projectile (proton or deuterons) beam hits the target materials and the irradiation chamber wall [2]. Unlike large nuclear research establishments, PET (nuclear medicine) clinics sometimes lack large radiation-shielded and secured areas for the work involved with high radiation levels, and are often visited by members of the public with little radiation protection awareness. Hence, an adequate radiological shielding of the cyclotron and a well-planned building design are of paramount importance for a safe and economical operation of the medical cyclotron facility.

Table 1. Important physical data of some common PET radiopharmaceuticals manufactured by modern medical cyclotrons

Radiopharmaceutical	Half-life	Target	Phase	Nuclear reaction
^{18}F , $^{18}\text{FDG}^{(1)}$	109 min	$\text{H}_2\text{}^{18}\text{O}$	Liquid ⁽²⁾	$^{18}\text{O}(\text{p},\text{n})^{18}\text{F}$
$^{13}\text{N}_2$, $^{13}\text{NH}_3$	10 min	$\text{H}_2\text{}^{16}\text{O}$	Liquid ⁽³⁾	$^{16}\text{O}(\text{p},\alpha)^{13}\text{N}$
^{11}CO , $^{11}\text{CO}_2$	20 min	$^{14}\text{N}_2$	Gas ⁽³⁾	$^{14}\text{N}(\text{p},\alpha)^{11}\text{C}$
$^{15}\text{O}_2$, $\text{H}_2\text{}^{15}\text{O}$	2 min	$^{14}\text{N}_2$	Gas ⁽³⁾	$^{14}\text{N}(\text{d},\text{n})^{15}\text{O}$

⁽¹⁾ Fluoro-deoxyglucose, ⁽²⁾ Enriched target, ⁽³⁾ Natural target

The main purpose of the radiological shielding of the medical cyclotron is to provide an adequate personnel and environmental dose reduction with a minimal capital and maintenance expenditure. In addition to the radiological shielding of the cyclotron itself, the overall layout plan of the PET facility considering the organisational aspects of the associated laboratories, patient handling operations and radiological safety procedures for the staff, visitors (i.e. members of the public) and the environment must be taken into account. This paper highlights the major aspects of the radiological shielding design of hospital-based medical cyclotrons.

Types of PET medical cyclotron

Modern medical cyclotrons accelerate high-intensity negatively charged particles. In a medical cyclotron almost 100% of the accelerated negative (H^- or d^-) ions are extracted out of the acceleration chamber using a thin carbon stripper foil and guided to the target (T), hence, the risk of radio-activation of the major cyclotron components [3], particularly the “Dees”, which are made of thick copper plates and magnet poles, made of iron alloy, is completely eliminated. Medical cyclotrons can either be housed within a self-contained compact shielding (self-shielded) or supplied without a shielding for later installation in a shielded vault (externally shielded). Evidently, these differences have no influence on the shielding calculation method. Table 2 displays the number and shielding type of medical cyclotrons presently in operation [4]. From the standpoint of user-friendliness and lower capital and operation costs the self-shielded negative ion medical cyclotrons (145 units are in operation) are more popular than other cyclotron types (83 units are in operation).

Table 2. Present status of different types of medical cyclotrons operating world-wide

Medical cyclotron type	Shielding type		Total number of cyclotrons
	Self-shielded	Externally shielded	
Negative ion	145	28	228
Positive ion*	12	36	
Superconducting	–	7	

* Earlier models of medical cyclotron.

From the perspective of material properties, the medical cyclotron shielding could be divided into three major categories:

- 1) Annular tank filled with aqueous solution of a suitable boron compound [5].
- 2) Vertical tank filled with a composite material consisting of iron shots and high-density hydrocarbon fluid [6].
- 3) Walls made of standard high-density concrete with a high water content [7].

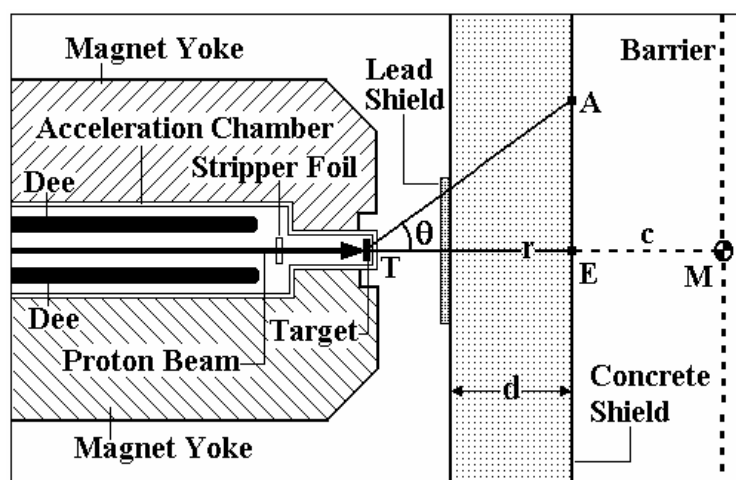
Due to lower material cost and easier handling and fabrication processes, high-density concrete is found to be the most popular shielding material for medical cyclotrons.

Shielding calculation

Method

The principle of medical cyclotron shielding is displayed in Figure 1. Unlike conventional high-energy research cyclotrons, the radiological shielding of a “self-shielded” medical cyclotron is placed close to the targets that produce intense fields of prompt neutron and gamma radiation fields. The targets are usually situated at the periphery of the acceleration chamber. Furthermore, this unique configuration also provides an additional shielding contributed by the solid iron yoke of the cyclotron electromagnet surrounding the target.

Figure 1. Schematic diagram of the principle of medical cyclotron shielding



The phenomenological neutron attenuation model with a point kernel source has been used for shielding thickness calculations [8]. Neutrons and gamma rays are produced during the interaction of low-energy (10-17 MeV) protons with the cyclotron target predominantly via the nuclear “evaporation process”. The by-product neutrons are emitted in a spatially isotropic manner and with a Maxwellian energy distribution [9]. The neutron dose equivalent rate at point “A” at contact with the external surface of a sufficiently thick concrete shield is given by [8,10]:

$$H_A [\text{Svh}^{-1}] = 2.25 \times 10^{16} I H_0 (r/\cos\theta)^{-2} \exp(-d \cos\theta \rho/\lambda) \quad (1)$$

where H_0 ($\text{Svh}^{-1}\text{m}^2/\text{proton}$) is the neutron source term, i.e. neutron dose equivalent rate per impinging proton at 1 m from the cyclotron target, λ ($\text{kg}\cdot\text{m}^{-2}$) is the neutron attenuation length of the shielding concrete, ρ ($\text{kg}\cdot\text{m}^{-3}$) is the density of the shielding concrete, d (m) is the concrete shield thickness, r (m) is the distance between the cyclotron target (T) and reference point (E) external to the shield and I (μA) is the proton beam current ($1 \mu\text{A} = 6.25 \times 10^{12}$ protons per second).

The neutron dose equivalent rate for the most conservative case (H_E), i.e. at 0° with the cyclotron target can be derived from Eq. (1):

$$H_E [\text{Svh}^{-1}] = 2.25 \times 10^{16} I H_0 r^{-2} \exp(-d \rho/\lambda) \quad (2)$$

In some cases the relevant regulatory authority imposes an additional mandatory dose reduction, compared to radiation workers, for the members of the public. This could be conveniently achieved by placing a barrier or fence at the location of interest (M) near the cyclotron shielding (Figure 1). The neutron dose equivalent rate (H_M) at the barrier placed at a distance c from the shielding wall and corresponding the dose reduction factor (f) are calculated as:

$$H_M [\text{Svh}^{-1}] = 2.25 \times 10^{16} I H_0 (r + c)^{-2} \exp(-d \rho/\lambda) \quad (3)$$

$$f = r^2 (r + c)^{-2} \quad (4)$$

Neutron source term

The neutron source term (H_0) is the most important parameter required for the shielding thickness calculation. The energy distribution of neutron fluence, generated during various proton-induced (p,n) reactions relevant to PET radioisotope production with medical cyclotrons was adopted from Ref. [2] and graphically presented in Figure 2. The neutrons produced by the $^{13}\text{C}(p,n)^{13}\text{N}$ reaction were found to possess the highest energy, ~10 MeV (hardest) and the most intense neutron fluence was found to be generated during the $^{18}\text{O}(p,n)^{18}\text{F}$ reaction. It was also established that the neutron yield from proton (~10.4 MeV) bombardment of a “thick” H_2^{18}O target (used for the production of the most common PET product ^{18}F FDG) was 1.82 times higher than the neutron yield from a proton-induced nuclear reaction with a thick copper target [2]. The above information was utilised to assess the neutron source term for shielding calculations from the data related to proton bombardment of a copper target [11]. In Figure 3 the neutron source term ($^{\text{Cu}}H_0$) for a thick copper target bombarded with energetic protons is shown as a function of proton energy.

Figure 2. The relative neutron fluence produced during important (p,n) reactions relevant to PET isotope production with a medical cyclotron

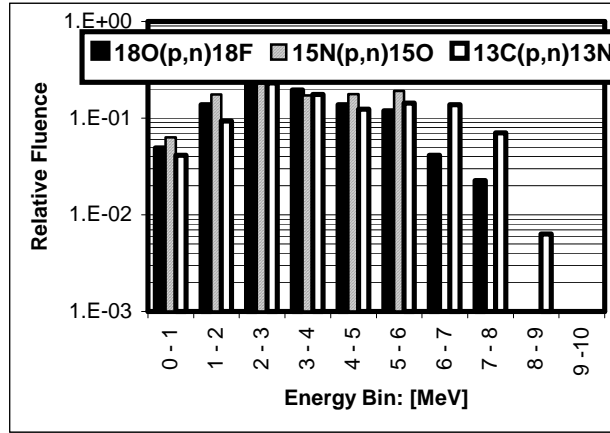
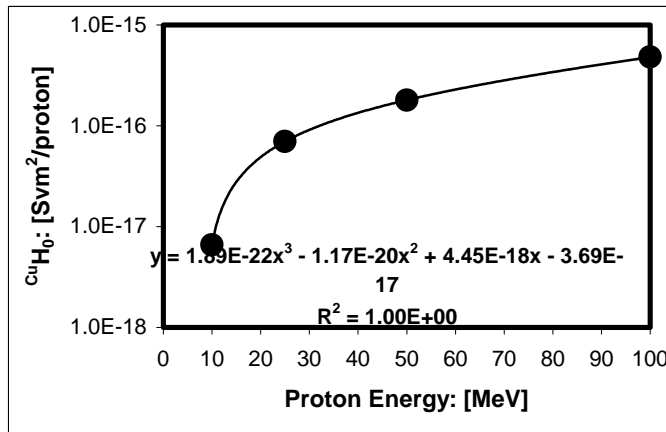


Figure 3. Neutron source term for copper ^{64}Cu is shown as a function of proton energy. The function was fitted with a 3rd order polynomial shown inset.



Assuming the most conservative case, the neutron yield during the production of ^{18}F via the $^{18}\text{O}(p,n)^{18}\text{F}$ reaction was used as the source term of the shielding calculation. The source term for a thick H_2^{18}O target ($^{0-18}\text{H}_0$) bombarded with monoenergetic protons from a medical cyclotron is given as:

$$^{0-18}\text{H}_0 = 1.82 I_{\text{Cu}} H_0 \quad (5)$$

By transforming the source term for $^{18}\text{O}(p,n)^{18}\text{F}$ reaction given in Eqs. (2) and (3) as a function of the copper target source term using Eq. (5) one obtains:

$$H_E [\text{Svh}^{-1}] = 4.1 \times 10^{16} I_{\text{Cu}} H_0 r^{-2} \exp(-d\rho/\lambda) \quad (6)$$

$$H_M [\text{Svh}^{-1}] = 4.1 \times 10^{16} I_{\text{Cu}} H_0 (r+c)^{-2} \exp(-d\rho/\lambda) \quad (7)$$

The source term $^{0-18}\text{H}_0$ at any given proton energy could be calculated by substituting the source term for copper ($I_{\text{Cu}} H_0$) in Eq. (4). The value of $I_{\text{Cu}} H_0$ could be interpolated from Figure 3 using the 3rd order fitting polynomial.

Neutron attenuation length

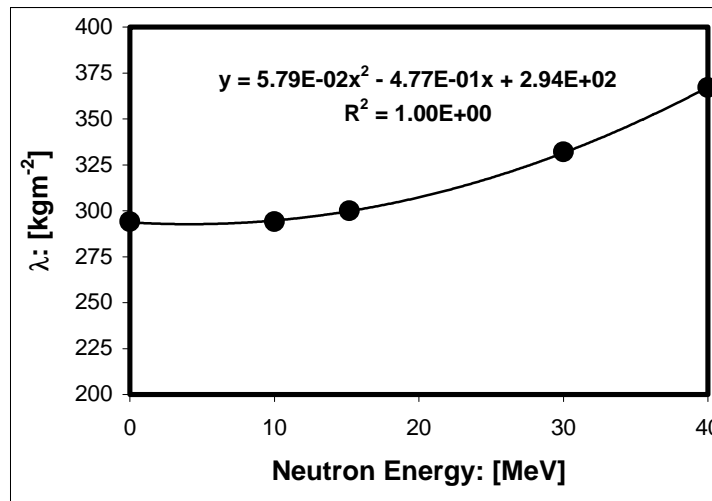
The neutron attenuation length is defined as the thickness of the shielding material required to attenuate the impinging radiation field by a factor of e^{-1} (3.68×10^{-1}). In the medical cyclotron environment the neutrons are the major source of radiation exposure (dose equivalent) external to a sufficiently thick shielding. An ideal neutron shielding material must attenuate neutrons of a wide energy range and thereby needs to satisfy two important criteria:

- 1) It shall contain high Z (high-density) material to slow down (thermalise) the high-energy neutrons by inelastic scattering.
- 2) It shall incorporate sufficient hydrogenous (low-density) material to remove the thermalised neutrons by neutron capture (n, γ) reaction.

Due to its lower cost, non-toxicity and a simple handling and manufacturing capability the standard high-density concrete ($\rho = 2\,400 \text{ kg}\cdot\text{m}^{-3}$) with at least 5% w/w water content [7] was found to be most suitable for medical cyclotron shielding purposes.

The attenuation length of broad beam monoenergetic neutrons of a wide energy range in shielding concrete ($\rho = 2\,400 \text{ kg}\cdot\text{m}^{-3}$) has been reported elsewhere [11]. Within the neutron energy band of 0-20 MeV, i.e. relevant to the present work, the attenuation length was found to be nearly energy independent. However, for the purpose of an accurate shielding evaluation the neutron attenuation lengths were plotted as a function of neutron energy and fitted with a 2nd order polynomial and shown in Figure 4.

Figure 4. The attenuation length of shielding concrete ($\rho = 2\,400 \text{ kg}\cdot\text{m}^{-3}$) is shown as a function of neutron energy. The function was fitted with a 2nd order polynomial shown inset.



Shielding of gamma rays

During routine PET isotope production operations of medical cyclotrons intense fields of high energy prompt gamma rays ($\sim 8 \text{ MeV}$) are produced via the inelastic proton scattering (p,p') reaction in the cyclotron target. Evidently, the thick concrete shielding originally designed for neutrons will be

sufficient to effectively attenuate those gamma rays. However, an adequately thick lead shield placed between the cyclotron target and concrete shielding (Figure 1) could further reduce this high-energy gamma radiation field. The major source of gamma radiation field outside the shielding is primarily caused by the neutron capture photons (2.2 MeV) mostly produced in the outer layer of the concrete shielding [9]. A ~1% w/w inclusion of commercial grade boron carbide (B_4C) with the shielding concrete will significantly reduce the radiation exposure [12].

Example of shielding calculation

The shielding thickness for a generic self-shielded medical cyclotron was calculated using Eq. (6). The starting parameters at various cyclotron operational conditions used in this calculation are given below. The results are summarised in Table 3.

- Proton energy (E_p): 11, 13, 15 and 17 MeV.
- Proton beam current (I): 10, 20, 30, 40, 50, 75 and 100 μA .
- Maximum allowable neutron dose equivalent rate at contact with the external surface of the concrete shielding (H_E): 20 $\mu Sv h^{-1}$.
- Distance between the cyclotron target and external shielding surface (r): 2.7 m.

Table 3. The results of shielding thickness calculation for self-shielded medical cyclotron

The concrete shielding thickness (d) is presented as a function of proton energy (E_p) and beam current (I). The neutron dose equivalent rate (H_E) at contact (E) with the external shielding wall (Figure 1) was set at 20 $\mu Sv h^{-1}$.

I [μA]	Shielding thickness: d [m]			
	$E_p = 11$ MeV	$E_p = 13$ MeV	$E_p = 15$ MeV	$E_p = 17$ MeV
10	1.27	1.34	1.39	1.45
20	1.36	1.43	1.47	1.54
30	1.41	1.48	1.52	1.59
40	1.44	1.51	1.56	1.63
50	1.47	1.54	1.59	1.66
75	1.52	1.59	1.64	1.71
100	1.55	1.63	1.67	1.75

The tenth value layer (TVL)

In many cases it becomes necessary to implement additional shielding to achieve a further dose (radiation exposure) reduction at certain critical locations (i.e. ducts, voids, penetration) of the medical cyclotron shielding. In such circumstances the minor shielding thickness could be calculated using the concept of tenth value layer (TVL) thickness. The TVL (i.e. the thickness of the shielding material required for an $1/10^{\text{th}}$ dose reduction) thickness for gamma rays in concrete, iron and lead [13] and for neutrons in concrete, polyethylene and water [14] were evaluated using the reference data and presented as multi-order polynomials in Tables 4(a) and 4(b) respectively. The radiological shielding engineers could readily use these polynomials.

Table 4(a). The TVL thickness of gamma rays (y) within the energy band 0.5-10 MeV in lead, iron and concrete is shown as function of photon energy, f(x)

Material	Tenth value layer (TVL) thickness
Concrete	$y = 15.944x^{0.453}, R^2 = 0.995$
Iron	$y = -0.002x^4 + 0.054x^3 - 0.641x^2 + 3.557x + 1.931, R^2 = 1.000$
Lead	$y = -0.005x^4 + 0.121x^3 - 1.095x^2 + 4.041x - 0.236, R^2 = 0.992$

Table 4(b). The TVL thickness of neutrons at 0° incidence (y) within the energy band 0.5-10 MeV in concrete, polyethylene and water is shown as function of neutron energy, f(x)

Material	Tenth value layer (TVL) thickness
Concrete	$y = 18.366x^{0.46}, R^2 = 0.966$
Polyethylene	$y = -0.2311x^2 + 4.4735x + 4.9923, R^2 = 0.995$
Water	$y = -0.0064x^3 - 0.2808x^2 + 5.9052x + 4.5912, R^2 = 0.991$

Shielding optimisation and ALARA

The cost of radiological shielding constitutes a major part of the total capital investment of a medical cyclotron facility producing various PET radioisotopes on a commercial basis. The ultimate success of the well-designed radiological shielding of a medical cyclotron depends on a careful choice of radiological safety, financial expenditure for construction and running cost facility and often the socio-political factors, including the recent public awareness on potential radiation hazards. The mathematical methods for the optimisation of radiological shielding of particle accelerators under the auspices of ALARA (as low as reasonably achievable) have been reported elsewhere [15,16].

The total monetary value of a commercial medical cyclotron facility is comprised of two major factors:

- 1) Cost for the shielding construction, $X(i,k)$.
- 2) Cost of the radiological health detriment and cyclotron operation, $Y(j,k)$.

$$X(i,k) = f(a, b, h, s, x, I, W, p) \quad (8)$$

$$Y(j,k) = f(\alpha, \lambda, \rho, \eta, N, T, I, l, a, x) \quad (9)$$

In Table 5 the list of variables belonging to the above functions $X(i,k)$ and $Y(j,k)$ are explicitly shown. The main “goal” of the optimisation process is to achieve the “maximum” radiological safety at “minimum” material (shielding) and operational cost and is expressed as follows:

$$X(i,k) + Y(j,k) \Rightarrow \text{Minimum} \quad (10)$$

The optimisation of the above multi-variable objective function using analytical methods is a difficult task. A genetic algorithm (evolutionary computing) based optimisation technique has been developed to optimise the radiological shielding of medical cyclotrons [12].

Table 5. Showing the variable list of the functions used for optimisation calculation of the radiological shielding of a medical cyclotron using a genetic algorithm

Item	Description [Unit]	Remarks
α	Cost of radiation protection [\$/person.Sv]	Monetary values (Index: k)
s	Cost of shielding concrete [$\$/\text{m}^3$]	
l	Cost of real estate (surface area) [$\$/\text{m}^2$]	
p	Cost of waste disposal [$\$/\text{GBq}^{-1}$]	
a	Length of the shielding [m]	Engineering design parameters (Index: i)
b	Breadth of the shielding [m]	
h	Height of the shielding [m]	
λ	Neutron attenuation length of concrete [m]	
T	Expected life of the shielding [y]	
W	Total weight of iron (activation) [kg]	
N	Number of exposed persons	Radiological and cyclotron operational parameters (Index: j)
η	Occupancy factor	
I	Proton beam current [μA]	
H_L	Allowable dose equivalent [mSv]	
H_X	Maximum dose equivalent [mSv]	
ρ	H_L/H_X	
X(i,k)	Total optimised cost of the shielding [\\$]	Optimisation goals (genetic algorithm)
H_{XR}	Dose equivalent rate at external reference point [μSvh^{-1}]	
x	Concrete shield thickness [m]	

Summary and conclusion

The shielding calculation method for medical cyclotrons using the “deterministic” neutron attenuation model has been highlighted. The proton-induced $^{18}\text{O}(p,n)^{18}\text{F}$ reaction produces the most copious neutrons with the hardest (~ 9 MeV) average energy compared to other PET radioisotope production pathways, including the deuteron-induced $X(d,n)Y$ reactions. Hence, the $^{18}\text{O}(p,n)^{18}\text{F}$ reaction (most conservative case) was chosen as the source term for the shielding calculation procedure for all common PET radioisotope-producing medical cyclotrons. The thickness of concrete ($\rho = 2400 \text{ kg}\cdot\text{m}^{-3}$) shielding for the proton energy of 11, 13, 15 and 17 MeV and proton beam currents of 10, 20, 30, 50, 75 and 100 μA was evaluated for the reference dose equivalent rate of $20 \mu\text{Svh}^{-1}$ (at contact with the external surface of the concrete shield). A “cost effective” method for further dose reduction at the location of the members of the public by installing a barrier (fence) near the cyclotron shield has been suggested.

At proton energies higher than 17 MeV the concrete shield thickness becomes prohibitively high and it inhibits the trouble-free movement of the heavy shielding mass while accessing the cyclotron target and acceleration chamber during maintenance work. In such case the installation of the medical cyclotron in a shielded vault [8] becomes inevitable. The shielding thickness calculation method for cyclotron vault (external shielding) has also been indicated. The tenth value thickness (TVL) for gamma rays and fast neutrons in various important shielding materials are presented in form of multi-order polynomials for practical applications.

Although an intense field of prompt high-energy (~ 8 MeV) gamma rays are produced in the vicinity of the cyclotron target, this radiation is completely stopped in the thick concrete shielding originally intended to attenuate the neutrons. The gamma ray dose is primarily contributed by the 2.2 MeV neutron capture gamma rays produced in the outer layer of the concrete shield. In order to reduce the intensity of this gamma radiation field the inclusion of an additional $\sim 1\%$ w/w of boron carbide (B_4C) in the concrete shield has been suggested.

The important aspects of the optimisation of the radiological shielding of medical cyclotrons in light of the ALARA principle have been discussed. The “global optimisation” of the function of multiple variables, such as the “best” shield thickness using an “evolutionary computing technique” (genetic algorithm) has been highlighted.

The shielding calculation method presented in this paper could be useful for the following purposes:

- Assessment and quality control (QC) of the self-shielded medical cyclotrons supplied by the commercial cyclotron manufacturers.
- Calculation of the thickness of additional (corrective) shielding required by the new operating condition of the cyclotron facility, i.e. the upgrade of the targets, introduction of new isotope production schedule.
- Design of the radiological shielding of a new medical cyclotron.

Recommendations

The important cyclotron shielding design parameters such as the neutron source terms (^{64}Cu and ^{18}O) and attenuation length (λ) used in this work have been adopted from the reference work carried out in 1980s, i.e. the early days of medical cyclotron technology. With a view to coping with the rapidly advancing accelerator (cyclotron) technology, greater radiological safety awareness of society and new requirements of the nuclear medicine fraternities the following actions have been suggested:

- Renewed experimental and theoretical investigations for the accurate and reliable assessment of neutron and gamma source terms for all relevant PET radioisotope production reactions (targets).
- Renewed experimental evaluation and Monte Carlo simulation of the relaxation length of monoenergetic neutrons (1-20 MeV) in various shielding materials.
- Establishment of a suitable benchmark for the radiological shielding of medical cyclotrons under the auspices of the ALARA principle.

REFERENCES

- [1] Kearfott, K.J., J.E. Carey, M.N. Clemenshaw and D.B. Faulkner, “Radiation Protection Design for a Clinical Positron Emission Tomography Imaging Suite”, *Health Phys.*, 63, 581-589 (1992).
- [2] Votaw, J.A. and R.J. Nickles, “Radionuclide Production for Positron Emission Tomography: Choosing an Appropriate Accelerator”, *Nucl. Inst. Meth.*, B40/41, 1093-1099 (1989).
- [3] Bol, J.L., *et al.*, “High Intensity H^- Cyclotron for Radioisotope Production”, Proc. of the Cyclotrons and Their Applications-89, 8-12 May 1989, Berlin, Germany, pp. 149-151.

- [4] *Directory of Cyclotrons Used for Radionuclide Production in Member States*, IAEA-TECHDOC-1007 (1998).
- [5] Tochon-Danguy, H., *et al.*, “Occupational Radiation Exposure at the Self-shielded IBA CYCLONE 10/5 Cyclotron of the A&RMC, Melbourne, Australia”, *Proc. of the Cyclotrons and Their Applications-98*, 14-19 June 1998, Caen, France, pp. 105-107.
- [6] Mukherjee, B. and T.J. Ruth, “Radiation Shielding Aspects of Compact Medical Cyclotrons”, *European Jour. Nucl. Med.*, 21(Supplement), 218-218 (1994).
- [7] *Radiation Protection Design Guidelines for 0.1-100 MeV Particle Accelerator Facilities*, NCRP Report No.51 (1977).
- [8] Mukherjee, B., “A Cook-book-method of Shielding Design for Compact Medical Cyclotrons”, *Proc. of the Cyclotrons and Their Applications-95*, 8-13 October 1995, Cape Town, South Africa, pp. 330-333.
- [9] Moritz, L.E., “Radiation Protection at Low Energy Proton Accelerators”, *Radiation Prot. Dosim.*, 96(4), 297-309 (2001).
- [10] Tesch, K., “A Simple Estimation of the Lateral Shielding for Proton Accelerators in the Energy Range 50 to 1 000 MeV”, *Radiation Prot. Dosim.*, 11(4), 165-172 (1985).
- [11] *Radiological Safety Aspects of the Operation of Proton Accelerators*, IAEA Technical Reports Series No. 283 (1988).
- [12] Mukherjee, B., “Optimisation of the Radiation Shielding of Medical Cyclotrons Using a Genetic Algorithm”, *Proc. of the 10th International Congress of the International Radiation Protection Association (IRPA)*, 14-19 May 2000, Hiroshima, Japan, pp. 9/111-121.
- [13] Nachtigall, D., “Physikalische Grundlagen für Dosimetrie und Strahlenschutz”, *Verlag Karl Thieme KG, München* (1970).
- [14] *Protection Against Neutron Radiation*, NCRP Report No.38 (1971).
- [15] Auxier, J.A. and H.W. Dickson, “Concern over Recent Use of the ALARA Philosophy”, *Health Phys.*, 44(6), 595-600 (1983).
- [16] Sarkar, P.K., “Optimization of Radiation Protection in Accelerators: Decision Making Under Uncertainty and Risk”, *Indian Jour. Phys.*, 65A(8), 451-454 (1991).

AN OVERVIEW OF SHIELDING CONSIDERATIONS IN CONSTRUCTING A PROTON-RADIATION CANCER-THERAPY FACILITY

Wayne D. Newhauser^{1,2} and Uwe Titt^{2,1}

¹M.D. Anderson Cancer Center, Houston, TX, USA

²Massachusetts General Hospital, Boston, MA, USA

Abstract

Radiation protection considerations strongly influence the layout and cost of a proton-radiation cancer-therapy facility. Standard radiation shielding designs do not exist for proton therapy facilities, due to the relatively small number of such centres in existence world-wide. Therapy equipment, clinical workloads and local radiation-control regulations typically have varied substantially from one facility to the next. Consequently, the shielding design will likely comprise a significant engineering effort that involves health physicists, medical physicists, physicians, architects and civil engineers. This report provides an overview of the major tasks in the shielding design process including caseload estimations, shielding attenuation calculations, administrative controls, construction issues, acceptance testing of the shielding, trends in shielding design methods, complicating factors and costs.

Introduction

Radiation therapy with high-energy proton beams has emerged as the treatment of choice for several types of cancer patients. The principal advantage of proton beams over, for example, photon beams, is their ability to cover the tumour with a high and uniform radiation dosage while simultaneously sparing the surrounding normal tissue [1]. Most of the major medical aspects of proton therapy are now sufficiently well understood so to allow the treatment of diverse types of cancers at various anatomical sites [2]. As proton therapy emerges from a long research phase and enters into the mainstream of radiation oncology, an increasing level of effort will be required in order to design proton facilities that can treat large numbers of patients efficiently and economically.

Economic considerations present special challenges for building designers. Specifically, high-energy protons can generate fields of unwanted stray radiation, with neutrons predominating the hazard to humans. To maintain a safe working environment, two basic techniques are applied to mitigate radiation hazards: strict *administrative controls* limit the production of radiation and prevent personnel from occupying radiation areas, and physical *shielding* enclosures attenuate stray radiation to safe levels. The shielding thickness required to attenuate high-energy neutron beams is quite large. A 250-MeV proton beam generates neutrons with energies up to about the same energy and one meter of ordinary concrete will attenuate the associated dose equivalent to approximately 14% of the unshielded value. (The dose equivalent attenuation length, λ , in ordinary concrete is approximately 50 cm.) Typical shielding barriers are 1 to 3 m thick. With proton gantries in excess of 13 m diameter, the size of the shielded rooms are large. Consequently, an enormous amount of shielding material is required and it comprises a significant fraction of the total facility cost.

Over the last few years, we have provided technical guidance on shielding issues related to building a proton therapy centre [3]. This work aims to familiarise the reader with the overall scope of work in designing the shielding for new proton therapy facilities including, design methods, safety margins and economic considerations.

Overview of work associated with neutron shielding

We begin by clarifying the scope of work associated with neutron shielding of a proton therapy centre. It is significantly more time consuming and expensive than is the case for typical electron linear accelerator-based radiation therapy installations. In some cases, this fact has become apparent late in the facility's conceptual design process, resulting in a drastic underestimation in the associated design time, effort and cost. In sequential order, the major tasks include estimating the facility proton usage rates, neutron source strengths, a review of all applicable state and federal regulations, the shielding attenuation predictions, construction of the shields, verification measurements of the shielding performance under a variety of operating conditions, and periodic reviews to ensure that the shielding is adequate as the facility usage changes over time. In the remainder of this section, we explore each of these tasks in turn.

Proton usage rates at the patient location

Perhaps most importantly, the shielding design must carefully take into account the long-term clinical goals of the facility. Specifically, the design must provide adequate protection given projected patient treatment rates. The projections must specify the total proton beam fluence rates required as functions of beam orientation (e.g. for facilities equipped with rotating gantries), energy, range modulation width, field size, etc. Average rates are estimated for periods of a year, a week and an

hour. For the one-hour interval, the peak rate is also needed. Typically, the rates vary from one facility to another due to differences in the hospitals' and medical staffs' specialities. Hence, input from the medical staff is recommended. As the medical practice of proton therapy is evolving rapidly, accurate predictions are difficult to make. At the present time, we recommend that a best estimate of the total proton usage rate should be inflated by a safety factor of at least 1.5 for shielding design purposes.

Shielding design

For proton therapy facilities, the physics and engineering techniques for performing the neutron production and shielding attenuation are mature and reasonably well understood. Recently, the analytical techniques were verified with measurements in an operational proton therapy facility and with Monte Carlo simulations of that same facility [4,5]. These studies, conducted at the Northeast Proton Therapy Center (NPTC) in Boston, suggest that the analytical and Monte Carlo methods, when applied with care and attention to detail, may be employed with confidence. In most situations, analytical models provide predictions of adequate accuracy for preliminary and/or final design calculations. However, when applied to complex geometry situations and at high angles of obliquity to the primary proton beam, the accuracy can be poor. We shall briefly review how the analytical techniques were applied to NPTC design. That facility contains a 235-MeV cyclotron, two rotational gantries and two fixed horizontal beam rooms [5].

The concrete shields were designed with Moyer's analytical model [6,7] that predicts the neutron dose equivalent behind a simple concrete slab. The model's two basic assumptions are that the high-energy neutrons determine the neutron dose equivalent rates behind thick shields and that the low-energy neutrons are in radiation equilibrium with high-energy neutrons at locations deep in the shield. Attenuation in the mazes was modelled with multiple exponential terms for each leg of the maze based on the technique from Tesch [8].

Nine neutron sources were modelled along the beam line, the strength of which were specified in neutron dose equivalent per incident proton per solid angle of the emitted neutrons. Separate terms were given for neutrons produced by intranuclear cascades and by evaporation from compound nuclei. Source strengths for (isotropic) evaporation neutrons are from Awschalom [9]. The forward-peaked cascade sources were estimated over the 30° to 120° interval with a power-law relation to proton energy based on the methods from Tesch [7]. At angles larger than 120°, a conservative approach was made, using the 120° values. At 0°, a value of 20 times the 90° value was used. Additional simplifications and conservative approximations were made, which included the neglecting of self-shielding for all sources except for the cyclotron. In addition, at locations where the angle of obliquity exceeded 45°, the attenuation was approximated by the value at 45°.

A comparison with survey measurements at the NPTC revealed that the analytical models over-predicted the dose equivalent rates in virtually all cases examined [5] by factors ranging from 11 to 124. Those studies revealed that detailed Monte Carlo simulations with MCNPX [10] overestimate the dose equivalent rates in most cases, with the ratio of simulated to predicted values ranging from 0.7 to 7 [4]. Hence, the Monte Carlo results are in substantially better agreement with the measurements than are the analytical calculations. This is attributable to the better suitability of the Monte Carlo method to complex geometries and the fact that, in the simulations, the sources and shield barriers were modelled in much richer detail. An implicit finding of these studies is that in order to obtain accurate results, great detail is required in the Monte Carlo representation of the neutron sources and shields. In fact, the NPTC study included more than 500 proton sources, distributed throughout a detailed model of the facility, taking four different energies, as well as eight treatment angles of each of the two gantries into account. Virtual receptors provided the resulting neutron dose equivalent per

incident proton at more than 200 locations in and around the facility. These results were weighted with the transmission efficiency of the beam producing and transportation system, and finally summed using a predicted facility usage pattern.

A second important finding from the NPTC studies is that the required computational resources are relatively modest. For example, the NPTC studies relied on a cluster of 20 LINUX/INTEL (200 MHz Pentium II) computers. The complete set of simulations required 18 months on this cluster. Today with 20 2-GHz PCs, this work could be completed in less than two months. However, quick calculations may be needed several times per day, particularly during the initial phase of the design process. Hence, it will probably take a few years before Monte Carlo calculations will overtake analytical methods as the most-frequently used design tool.

Administrative controls

The physical shielding barriers do not alone provide adequate protection from potential radiation hazards. Administrative controls further preserve the safe working environment by ensuring that the facility is not operated beyond the designed capacity and that humans are not present in areas of intense radiation fields (excepting the patients receiving treatment). These administrative controls comprise a variety of manual procedures and automated safety systems, of which we describe a few aspects of each type here.

In the United States, all radiation therapy facilities must have an extensive radiation safety programme. It must provide radiation safety training for personnel, as well as a significant amount of written documentation that may be needed in order to maintain or demonstrate a safe working environment. This typically includes a shielding design document, standard operating procedures, emergency operation procedures, etc. The local regulatory authority may require that some or all of these be submitted for approval prior to the facility construction or start-up. The entire radiation protection programme must be reviewed and updated at periodic intervals.

Proton beam monitoring systems and area monitoring systems for secondary radiation (mainly neutrons) are also needed. Proton beam currents should be logged and compared at periodic intervals to the shielding design limits. Hardware limits on the injected proton beam current are needed in cases where the accelerator is capable of greatly exceeding the shielding design limits. Passive integrating dosimeters can provide an independent check of ambient dose levels, which is particularly useful for outdoor locations. However, of all these systems, perhaps the most important is the active neutron area monitoring system. It provides acoustic and visual alarms in case the secondary radiation approaches the regulatory limits [11] and, at the NPTC, it has provided a valuable tool to verify that the long-term neutron exposures to personnel are below the regulatory limits.

Construction issues

During the facility construction, it is necessary to supervise the fabrication of the shielding barriers in order to ensure that they are built according to the shielding design. Specifically, the barrier dimensions should be verified, concrete samples should be analysed for mass density and composition (hydrogen content is particularly important), concrete should be poured in a manner that ensures it is free of voids and conduits or ducts in the shield barriers must be verified to be consistent with the shielding design. The proton transmission efficiency of the beam production and transport systems should be verified for consistency with those values used in the shielding design calculations.

Acceptance testing of the facility shielding

To demonstrate the adequacy of the shielding, and as a part of the radiation protection programme, a radiation survey must be conducted and an area monitoring system must be provided in order to ensure that the dose limits to workers, patients and visitors are not exceeded at any time. The area monitoring system alerts individuals to the potential or actual change in the safe working environment and provides a record of the measured neutron dose equivalent rates. A survey includes fully shielded areas (occupied by facility staff and members of the general public) and partially shielded areas (e.g. patients and staff inside the treatment rooms). It is convenient to report the survey results in terms of dose equivalent per proton delivered to isocentre (roughly the patient's position during treatment), which facilitates comparisons to predictions that are also so normalised. Additional discussions on neutron survey measurement methods and instrumentation are given elsewhere ([5] and references therein).

Traditionally, predictions of the neutron exposure to patients while receiving proton beam therapy is not included in the facility (building) shielding design. In the future, these calculations will probably be done by the hospital or by the therapy equipment manufacturer. It is difficult to predict since it strongly depends on the hardware set-up and the treatment conditions. Several studies have been made that investigate the neutron dose to patients at different facilities [12-15]. These studies report disparate results that were obtained at different facilities, each with distinct and different beam delivery and shaping equipment. A consensus has not yet been achieved on this topic. Additional discussion is given elsewhere [3].

Future evolution in design methods

Proton usage rates introduce the predominant component in the total uncertainty in the shielding design. The designer may increase the best estimate of the true usage rates by some safety factor, e.g. 1.5 or more, in order to minimise the possibility of constructing an under-shielded facility. We are working on this problem by developing simple semi-empirical methods for estimating proton usage rates for several treatment sites (e.g. for prostate, lung and intra-cranial treatments). The methods are based on clinical data from the Boston project and may be published in late 2003. Regarding the radiation transport models, Monte Carlo simulations will eventually become the principal design tool, although simulation times and ease-of-use must still be improved. Benchmark calculations and measurements will be increasingly important, particularly measurements that correlate the facility usage patterns and ambient neutron dose equivalent rates (i.e. from active area monitors). This should result in increased feedback in design process, e.g. the acceptance test measurements from one facility will provide benchmark data for the models used to design subsequent facilities.

A number of new design tools will emerge, such as a facility simulator that will allow the designer to explore the ramifications of various facility usage scenarios (e.g. for treatments of different energies, modulation widths and gantry positions), providing a database of neutron dose equivalent rates for each kind of treatment. When combined with treatment load data from existing facilities and/or projections, one will then be able to quickly assess the adequacy of a given design. When combined with analytical shielding models, this technique will be extended to automatically design a unique shielding configuration for each facility usage scenario. These results will be used to refine new shielding designs or, in operational facilities, to restructure or balance some patient treatments in order to avoid excessive radiation exposure, e.g. as might otherwise result from higher-than-anticipated caseload.

Finally, we expect that the continued commercial growth in the proton therapy market will bring increased economic pressure to minimise the total shielding and radiation protection costs. This will be achieved with better shielding design tools which, with their greater accuracy and lower uncertainties, will allow the shielding designer to eliminate much of the large and non-uniform over-shielding that exists in contemporary facilities. The design tools will also significantly reduce the need for comprehensive, extensive neutron surveys during the facility pre-clinical phase. These tools will also make possible the design of smarter shields, e.g. small local shields on a beam line that allow the exterior room walls to be much thinner, but that must be easily removable for servicing the beam line.

Complicating factors

Methods for calculating the neutron shielding at proton therapy facilities have advanced dramatically in recent years [5]. However, they remain more cumbersome than analogous methods for standard applications, e.g. for the shielding of an electron linear accelerator used in conventional radiation therapy. In addition, each facility will have a combination of features that strongly influence the shielding requirements including the clinical workload, the selection of a cyclotron or synchrotron accelerator and the efficiency of beam delivery hardware. Compounding a difficult situation, the uncertainties in such shielding predictions are large and difficult to estimate. This necessitates very conservative design margins and safety factors. In turn, this results in shield barriers that are thicker, more expensive and more obtrusive in the facility layout. The latter problem inflates costs and is particularly acute for facilities located in major metropolitan centres, where land and construction costs are high and the immediately adjacent areas are subsequently inhabited.

Financial aspects

Cost estimates of the radiation shielding design and construction are not available in the literature. In many cases, the total cost is split between the several autonomous groups, e.g. the shielding designers, the architects, the building engineers, the beam equipment manufacturer, the building construction firm and the hospital's radiation oncology and safety departments. Based on our experience with the construction of the NPTC and the M.D. Anderson Cancer Center Proton Therapy Center (PTC-H) in Houston, we crudely estimate that the costs of the shielding design, radiation protection instrumentation and radiation protection activities (during the pre-clinical phase) at approximately 2% of the overall facility cost. (This estimate does not include the shielding materials, their installation, nor the cost of the massive load-bearing foundation required to carry this weight.) From an economic standpoint, it is crucial to avoid shielding-related problems that could cause delays in the facility start-up or in reduced clinical usage compared with the design parameters. A delay of one day in the pre-clinical phase can cost approximately \$30 000 (US) in capital costs alone.

Above all, under-shielding is to be avoided, as it will lead to the installation of expensive remedial shielding, a delay in the facility start-up, or a restriction on the clinical workload. Hence, it is imperative to over-shield the facility somewhat. It is also important to prepare for the radiation surveys in order that they begin on schedule and are completed quickly. In addition, it is prudent to have available benchmarked shielding design tools that allow the facility operator to substitute some of the measurements with less-expensive calculations.

Conclusions

The shielding design process for a contemporary proton therapy centre is not an exact science: educated guesses are necessary and numerous choices must be made on the basis of subjective

assessments. Recently there has been much progress on improving shielding design methods and we expect this trend to continue. Simultaneously, there is an increased economic incentive to further refine future shielding designs to minimise wasted costs associated with today's degree of over-shielding. This paper presents an overview of several major aspects of the shielding design, construction and verification processes.

Acknowledgements

This work was supported in part by a grant from the Bechtel Infrastructure Corporation (WN, UT) and by a subcontract of that grant (WN).

REFERENCES

- [1] Wilson R.R., "Radiological Use of Fast Protons", *Radiol.*, 47, 487-491 (1946).
- [2] Miller D.W., "A Review of Proton Beam Radiation Therapy", *Med. Phys.*, 22, 1943-1954 (1995).
- [3] Newhauser, W.D., D.T. Dexheimer and U. Titt, "Shielding of Proton Therapy Facilities – A Review of Recent Advances", *Proc. Am. Nucl. Soc. Radiat. Prot. Shielding Division Conf.*, Santa Fe, NM, 14-17 April 2002, pp. 168-178, J. Briesmeister and R.C. Little (eds.), American Nuclear Society, Chicago, IL (2002).
- [4] Titt, U., W.D. Newhauser, X. Yan and D.T. Dexheimer, "Neutron Shielding Calculations for a 230-MeV Proton Therapy Facility", *Adv. Monte Carlo for Radiat. Phys., Part. Transp. Simul. Appl. Proc. Monte Carlo 2000 Conf.*, Lisbon, Portugal, 23-26 October 2000, pp. 1075-1080, A. Kling, M. Nakagawa, L. Tavora and P. Vaz (eds.), Springer Verlag, Heidelberg, Germany (2001).
- [5] Newhauser, W.D., U. Titt, D.T. Dexheimer, X. Yan and S. Nill, "Neutron Shielding Verification Measurements and Simulations for a 235-MeV Proton Therapy Center", *Nucl. Instr. Meth.*, A 476, 80-84 (2002).
- [6] Moyer, B.J., "Method of Calculation of the Shielding Enclosure for the Berkeley Bevatron", *Proc. First Int. Conference on Shielding Around High-energy Accelerators*, Saclay, France, 18-20 January 1962, pp. 65-70, Press Universitaires de France, Paris (1962).
- [7] Tesch, K., "A Simple Estimation of the Lateral Shielding for Proton Accelerators in the Energy Range 50 to 1 000 MeV", *Radiat. Prot. Dosim.*, 11, 165-172 (1985).
- [8] Tesch, K., "The Attenuation of the Neutron Dose Equivalent in a Labyrinth Through an Accelerator Shield", *Particle Accel.*, 12, 169- (1982).

- [9] Awschalom, M., *Radiation Shielding for 250 MeV Protons*, Fermilab report TM-1354 1100.050, Rev. 4/1/87.
- [10] Hughes, H.G., H.W. Egdorf, F. Gallmeier, R.C. Little, R.E. Prael, E. Snow, L.S. Waters, M. White, *MCNPX User's Manual*, TPO-E83-G-UG-X-0001, Revision 0 (1999).
- [11] Nill, S. and W.D. Newhauser, *Users Manual for TNRS: A Tool for Neutron Radiation Surveillance*, Northeast Proton Therapy Center Report NPTC-HD-103, August 2000.
- [12] Binns, P.J. and J.H. Hough, "Secondary Dose Exposures during 200 MeV Proton Therapy", *Rad. Prot. Dosim.*, 70, 441-444 (1997).
- [13] Agosteo, S., C. Birattari, M. Caravaggio, M. Silari and G. Tosi, "Secondary Neutron and Photon Dose in Proton Therapy", *Radiother. Oncol.*, 48, 293-305 (1998).
- [14] Yan, X., W.D. Newhauser, U. Titt and A.M. Koehler, "Measurement of Neutron Dose Equivalent to Proton Therapy Patients Outside of the Proton Radiation Field", *Nucl. Instr. Meth.*, A 476, 429-434 (2002).
- [15] Schneider U., S. Agosteo, E. Pedroni, J. Besserer, "Secondary Neutron Dose during Proton Therapy using Spot Scanning", *Int. J. Radiat. Oncol. Biol. Phys.*, 53, 244-251 (2002).

Additional references

Coutrakon G.B., "Proton Synchrotrons for Cancer Therapy", *Proc. 16th Int. Conf. App. Accel. in Res. and Industry*, Denton, TX, 1-5 November, 2000, pp. 861-864, J.L. Duggan and I.L. Morgan (eds.), American Association of Physics, Melville, New York (2001).

Yongen Y., "The Proton Therapy System for MGH's NPTC: Equipment Description and Progress Report", *Proc. NIRS Int. Sem. Appl. Heavy Ion Accel. Radiat. Ther. Cancer in Connection with XXI PTCOG Meeting*, Chiba-shi, Japan, 14-16 November 1994, pp. 59-71, T. Kanai and E. Takada (eds.), National Institute of Radiological Sciences, Chiba-shi, Japan, 1995.

LIST OF PARTICIPANTS

AUSTRALIA

MUKHERJEE, Bhaskar
ANSTO – Safety Division
Building 55
PMB-1
New Illawara Road
Menai, NSW 2234

Tel: +61 2 9717 3404
Fax: +61 2 9389 8444
Eml: mukherjee@ieee.org

AUSTRIA

KOPRIVNIKAR, Igor
TU-Graz
Institute for Theoretical Physics
Dept. Strahlenphysik
Steyrergasse 17
8010 Graz

Tel: +43 316 8738697
Fax: +43 316 8738699
Eml: koprivnikar@itp.tu-graz.ac.at

FRANCE

RIDIKAS, Danas
CEA Saclay
DSM/DAPNIA/SPhN
F-91191 Gif-sur-Yvette Cedex

Tel: +33 1 69087847
Fax: +33 1 69087584
Eml: ridikas@cea.fr

GERMANY

KUENKEL, Renate
GSI Darmstadt
Planckstr. 1
D-64291 Darmstadt

Tel: +49 6159 71 2414
Fax: +49 6159 71 2109
Eml: R.Kuenkel@gsi.de

LEUSCHNER, Albrecht
Deutsches Elektronen-Synchrotron (DESY)
Notkestrasse 85
D-22607 Hamburg

Tel: +49 (0) 40 8998 2043
Fax: +49 (0) 40 8998 3282
Eml: Albrecht.Leuschner@desy.de

MARES, Vladimir
GSF
Institute of Radiation Protection
Ingolstaedter Landstr. 1
D-85764 Neuherberg

Tel: +49 (89) 3187 2652
Fax: +49 (89) 3187 3323
Eml: mares@gsf.de

ITALY

MENAPACE, Enzo
ENEA CR E Clementel
Applied Physics Division
Via Don G. Fiammelli 2
I-40128 Bologna

Tel: +39 051 60 98 239
Fax: +39 051 60 98 359
Eml: menapace@bologna.enea.it

PELLICIONI, Maurizio
Laboratori Nazionali di Frascati (INFN)
Casella Postale 56
I-00044 Frascati

Tel: +39 (06) 940 32246
Fax: +39 (06) 940 32364
Eml: maurizio.pellicioni@lnf.infn.it

JAPAN

HAYASHI, Katsumi
Hitachi Engineering Company, Ltd.
Saiwai-cho, 3-2-1
Hitachi
Ibaraki 317-0073

Tel: +81 (294) 55 4501
Fax: +81 (294) 55 9900
Eml: k_hayashi@psg.hitachi-hec.co.jp

HIRAYAMA, Hideo
Radiation Science Center
High Energy Accelerator Res. Org. KEK
1-1 Oho
Tsukuba-shi
Ibaraki-ken 305-0801

Tel: +81 (298) 64 5489
Fax: +81 (298) 64 1993
Eml: hideo.hirayama@kek.jp

IWASE, Hiroshi
Tohoku University
Dept. of Quantum Science & Energy Eng.
Aoba, Aramaki, Aoba-ku
Sendai 980-8579

Tel: +81 22 217 7910
Fax: +81 22 217 7910
Eml: gan@cyric.tohoku.ac.jp

NAKAMURA, Takashi
Dept. of Quantum Science and Energy Eng.
Tohoku University
Aramaki, Aoba-ku, Sendai-shi
Miyagi-ken 980-8579

Tel: +81 (22) 217 7805
Fax: +81 (22) 217 7808/7809
Eml: nakamura@cyric.tohoku.ac.jp

* NAKASHIMA, Hiroshi
Japan Atomic Energy Research Institute
Center for Neutron Science
Shirakata-Shirane 2-4
Tokai
Ibaraki 319-1195

Tel: +81 29 282 6144
Fax: +81 29 282 5996
Eml: nakasima@shield4.tokai.jaeri.go.jp

* *Regrets not having been able to attend.*

- * NAKAO, Noriaki
KEK, High Energy Accelerator
Research Organisation
1-1 Oho
Tsukuba-shi, Ibaraki-ken 305-0801
Tel: +81 (298) 79 6004
Fax: +81 (298) 64 4051
Eml: noriaki.nakao@kek.jp
- NUNOMIYA, Tomoya
Cyclotron and Radioisotope Center
Dept. of Quantum Science & Energy Eng.
Tohoku University
Aramaki, Aoba, Aoba-ku
Sendai 980-8579
Tel: +81 (22) 217 7910
Fax: +81 (22) 217 7910
Eml: nunomiya@cyric.tohoku.ac.jp
- SAKAMOTO, Yukio
External Dosimetry Laboratory
Department of Health Physics
JAERI
Tokai-mura, Naka-gun
Ibaraki-ken 319-1195
Tel: +81 (29) 282 5803
Fax: +81 (29) 282 6063
Eml: sakamoto@frs.tokai.jaeri.go.jp
- TANIGUCHI, Shingo
Japan Synchrotron Radiation Research Inst.
Koto 1-1-1, Mihazuki-cho
Sayou-gun
Hyogo 679-5198
Tel: +81 791 58 2723
Fax: +81 791 58 0830
Eml: shingo@spring8.or.jp
- YASHIMA, Hiroshi
Tohoku University
Dept. of Quantum Science & Energy Eng.
Cyclotron and Radioisotope Center
Aoba, Aramaki, Aoba-ku
Sendai 980-8579
Tel: +81 22 217 7806
Fax: +81-22-217-7809
Eml: yashima@cyric.tohoku.ac.jp
- YONAI, Sunsuke
Tohoku University
Dept. of Quantum Science & Energy Eng.
Cyclotron and Radioisotope Center
Aoba, Aramaki, Aoba-ku
Sendai 980-8579
Tel: +81 22 217 7806
Fax: +81 22 217 7809
Eml: yonai@cyric.tohoku.ac.jp

PORTUGAL

- VAZ, Pedro
Instituto Tecnológico e Nuclear
Estrada Nacional 10
P-2686-953 Sacavém
Tel: +351 21 994 62 30
Fax: +351 21 994 10 39
Eml: pedrovaz@itn.mces.pt

* *Regrets not having been able to attend.*

SWEDEN

GUDOWSKA, Irena
Dept. of Medical Radiation Physics
Karolinska Institute
P.O. Box 260
S-171 76 Stockholm

Tel: +46 (8) 517 75447
Fax: +46 (8) 34 35 25
Eml: irena@radfys.ks.se

SWITZERLAND

TEICHMANN, Sabine
Paul Scherrer Institut
AEA Division WMHA/C44
CH-5232 Villigen PSI

Tel: +41 (0) 56 310 4375
Fax: +41 (0) 56 310 3717
Eml: sabine.teichmann@psi.ch

UNITED STATES OF AMERICA

ASAI, Makoto
SLAC
2575 Sand Hill Road, MS97
Menlo Park, CA 94025

Tel: +1 650-926-3772
Fax: +1 650-926-3329
Eml: asai@slac.stanford.edu

ALDERMAN, Julie M.
Argonne National Laboratory
Advanced Photon Source
9700 S. Cass Avenue
Building 431Z-010
Argonne, IL 60439

Tel: +1 630-252-1183
Fax: +1 630-252-1664
Eml: alderman@aps.anl.gov

BAIRD, Ken
Stanford Linear Accelerator Center
MS 20
2575 Sand Hill Road
Menlo Park, CA 94025

Tel: +1 650 926 2728
Fax: +1 650 926 2521
Eml: baird@slac.stanford.edu

CASEY, Robert
Brookhaven National Laboratory
NSLS
Bld. 725c
Upton, NY 11786

Tel: +1 631-344-4654
Fax: +1 631-344-5842
Eml: casey1@bnl.gov

* COKINOS, Dimitrios
Brookhaven National Laboratory
Building 197C
P.O. Box 5000
Upton, NY 11973-5000

Tel: +1 (516) 344 2146
Fax: +1 (516) 344 3374
Eml: cokinos@bnl.gov

* *Regrets not having been able to attend.*

DEGTIARENKO, Pavel V.
Radiation Control Group
Jefferson Laboratory MS3A
12000 Jefferson Avenue
Newport News, VA 23606

Tel: +1 (757) 269 6274
Fax: +1 (757) 269 7352
Eml: pavel@jlab.org

* DONAHUE, Richard J.
Lawrence Berkeley Laboratory
1 Cyclotron Road, MS 2-400
Berkeley, CA 94720

Tel: +1 (510) 486 5597
Fax: +1 (510) 486 7304
Eml: rjdonahue@lbl.gov

GALLMEIER, Franz X.
Oak Ridge National Laboratory
Building 6011, MS 6474
P.O. Box 2008
Oak Ridge, TN 37830

Tel: +1 865 5749675
Fax: +1 865 5746080
Eml: gallmeierfz@ornl.gov

HEILBRONN, Lawrence H.
Lawrence Berkeley National Laboratory
MS 74-197
Berkeley, CA 94720

Tel: +1 510 486 4002
Fax: +1 510 486 6949
Eml: lhheilbronn@lbl.gov

HUNTER, Hamilton T.
Director, RSICC
Oak Ridge National Laboratory
P.O. Box 2008
Oak Ridge, TN 37831-6362

Tel: +1 (865) 574 6297
Fax: +1 (865) 574 6182
Eml: h3o@ornl.gov

JOB, Pankakkal K.
Advanced Photon Source
Argonne National Laboratory
9700 South Cass Avenue
Argonne, IL 60439-4803

Tel: +1 (630) 252 6573
Fax: +1 (630) 252 1664
Eml: pkj@aps.anl.gov

KHATER, Hesham Y.
Stanford Linear Accelerator Center
2575 Sand Hill Road, MS 48
Menlo Park, CA 94070

Tel: +1 650 926 2048
Fax: +1 650 926 3569
Eml: khater@slac.stanford.edu

* KIRK, Bernadette L.
Radiation Information Analysis Section
Oak Ridge National Laboratory
P.O. Box 2008
Oak Ridge, TN 37831-6362

Tel: +1 (865) 574 6176
Fax: +1 (865) 574 6182
Eml: kirkbl@ornl.gov

LIU, James C.
Radiation Physics Department
Bin 48 – SLAC
P.O. Box 4349
Stanford, CA 94309

Tel: +1 650 926 4728
Fax: +1 650 926 3569
Eml: james@slac.stanford.edu

* *Regrets not having been able to attend.*

MAO, Xiaotian Stan
Stanford Linear Accelerator Center
P.O. Box 4349
MS 48
Stanford, CA 94309

Tel: +1 650 926 4317
Fax: +1 650 926 3569
Eml: mao@slac.stanford.edu

MASHNIK, Stepan G.
Nuclear Physics Group, T-16
Los Alamos National Laboratory
MS B283
Los Alamos, NM 87545

Tel: +1 (505) 667 9946
Fax: +1 (505) 667 1931
Eml: mashnik@lanl.gov

MOKHOV, Nikolai V.
FERMILAB
MS 220
P.O. Box 500
Batavia, IL 60510-500

Tel: +1 (630) 840 4409
Fax: +1 (630) 840 6039
Eml: mokhov@fnal.gov

NELSON, W. Ralph
Radiation Physics Department
Stanford Linear Accelerator Center
MS 48 – SLAC
2575 Sand Hill Road
Menlo Park, CA 94025

Tel: +1 (650) 926 2047
Fax: +1 (650) 926 3569
Eml: wrnrp@slac.stanford.edu

NEUHAUSER, Wayne D.
M.D. Anderson Cancer Center
Department of Radiation Physics
Proton Therapy Group, Box 94
1515 Holcombe Blvd
Houston, TX 77030

Tel: +1 (713) 745 0048
Fax:
Eml: wnewhaus@mail.mdanderson.org

PRAEL, Richard E.
Los Alamos National Laboratory
Group X-5
MS F663
P.O. Box 1663
Los Alamos, NM 87545

Tel: +1 (505) 667 7283
Fax: +1 (505) 665 3046
Eml: rep@lanl.gov

PRINZ, Alyssa
SLAC
MS 48
2575 Sand Hill Road
Menlo Park, CA 94025

Tel: +1 (650) 926 4062
Fax: +1 (650) 926 3569
Eml: aaprinz@slac.stanford.edu

RAKHNO, Igor
Fermi National Accelerator Laboratory
MS 220, P.O.Box 500
Batavia, IL 60510-0500

Tel: +1 (630) 840 6763
Fax: +1 (630) 840 6039
Eml: rakhno@fnal.gov

ROKNI, Sayed H.
Stanford Linear Accelerator Center
MS 48
2575 Sand Hill Road
Menlo Park, CA 94025

Tel: +1 (650) 926 3544
Fax: +1 (650) 926 3569
Eml: rokni@slac.stanford.edu

* WATERS, Laurie S.
Los Alamos National Laboratory
MS H816
Los Alamos, NM 87544

Tel: +1 (505) 665 4127
Fax: +1 (505) 667 7443
Eml: lsw@lanl.gov

WRIGHT, Dennis H.
SLAC
2575 Sand Hill Road, MS 41
Menlo Park, CA 94025

Tel: +1 (650) 926-4743
Fax: +1 (650) 926-3767
Eml: dwright@slac.stanford.edu

INTERNATIONAL ORGANISATIONS

BRUGGER, Markus
CERN TIS-RP
865-RC-0009
CH-1211 Genève 23

Tel: +41 22 767 6556
Fax: +41 22 767 5700
Eml: Markus.Brugger@cern.ch

FASSÒ, Alberto
CERN/GSI
EP/AIP
CH-1211 Genève 23

Tel: +41 22 767 2398
Fax: +41 22 767 9480
Eml: Alberto.Fasso@cern.ch

ROESLER, Stefan
CERN
TIS-RP
CH-1211 Genève 23

Tel: +41 22 7679891
Fax: +41 22 7675700
Eml: Stefan.Roesler@cern.ch

SARTORI, Enrico
OECD/NEA Data Bank
Le Seine-Saint Germain
12, boulevard des Iles
F-92130 Issy-les-Moulineaux

Tel: +33 1 45 24 10 72 / 78
Fax: +33 1 45 24 11 10 / 28
Eml: sartori@nea.fr

SILARI, Marco
CERN
TIS-RP
CH-1211 Genève 23

Tel: +41 (22) 767 3937
Fax: +41 (22) 767 9360
Eml: marco.silari@cern.ch

* STEVENSON, Graham Roger
CERN
CH-1211 Genève 23

Tel: +41 (22) 767 4623
Fax: +41 (22) 767 9800
Eml: Graham.Stevenson@cern.ch

* *Regrets not having been able to attend.*

VINCKE, Heinz
CERN
CH-1211 Genève 23

Tel: +41 22 767 8864
Fax: +41 22 767 9080
Eml: Heinz.Vincke@cern.ch

VLACHOUDIS, Vasilis
CERN
Div. SL
CH-1211 Genève 23

Tel: +41 22 76 79 851
Fax: +41 22 76 75 555
Eml: Vasilis.Vlachoudis@cern.ch

Questionnaire on the quality of OECD publications

We would like to ensure that our publications meet your requirements in terms of presentation and editorial content. We would welcome your feedback and any comments you may have for improvement. Please take a few minutes to complete the following questionnaire. Answers should be given on a scale of 1 to 5 (1 = poor, 5 = excellent).

Fax or post your answer before 31 December 2004, and you will automatically be entered into the prize draw to win a year's subscription to *OECD's Observer magazine*.*

A. Presentation and layout

1. What do you think about the presentation and layout in terms of the following:

	Poor	Adequate		Excellent	
Readability (font, typeface)	1	2	3	4	5
Organisation of the book	1	2	3	4	5
Statistical tables	1	2	3	4	5
Graphs	1	2	3	4	5

B. Printing and binding

2. What do you think about the quality of the printed edition in terms of the following:

Quality of the printing	1	2	3	4	5
Quality of the paper	1	2	3	4	5
Type of binding	1	2	3	4	5
Not relevant, I am using the e-book	<input type="checkbox"/>				

3. Which delivery format do you prefer for publications in general?

Print CD E-book (PDF) via Internet Combination of formats

C. Content

4. How accurate and up to date do you consider the content of this publication to be?

1 2 3 4 5

5. Are the chapter titles, headings and subheadings...

Clear Yes No
Meaningful Yes No

6. How do you rate the written style of the publication (e.g. language, syntax, grammar)?

1 2 3 4 5

D. General

7. Do you have any additional comments you would like to add about the publication?

.....
.....
.....

Tell us who you are:

Name: E-mail:

Fax:

Which of the following describes you?

IGO NGO Self-employed Student
Academic Government official Politician Private sector

Thank you for completing the questionnaire. Please fax your answers to:

(33-1) 49 10 42 81 or mail it to the following address:

Questionnaire qualité PAC/PROD, Division des publications de l'OCDE
23, rue du Dôme – 92100 Boulogne Billancourt – France.

Title: Shielding Aspects of Accelerators, Targets and Irradiation Facilities

OECD Code (printed version): 66 2004 10 1 p

* Please note: This offer is not open to OECD staff.

OECD PUBLICATIONS, 2, rue André-Pascal, 75775 PARIS CEDEX 16

PRINTED IN FRANCE

(66 2004 10 1 P) No. 53631 2004